ISRAEL ION CHANNEL AND TRANSPORTERS MEETING 2019

EDITED BY: Moran Rubinstein, Rami Yaka and Avi Priel
PUBLISHED IN: Frontiers in Pharmacology

frontiers Research Topics

ISSN 1664-8714
ISBN 978-2-88971-055-3
DOI 10.3389/978-2-88971-055-3

About Frontiers

Frontiers is more than just an open-access publisher of scholarly articles: it is a pioneering approach to the world of academia, radically improving the way scholarly research is managed. The grand vision of Frontiers is a world where all people have an equal opportunity to seek, share and generate knowledge. Frontiers provides immediate and permanent online open access to all its publications, but this alone is not enough to realize our grand goals.

Frontiers Journal Series

The Frontiers Journal Series is a multi-tier and interdisciplinary set of open-access, online journals, promising a paradigm shift from the current review, selection and dissemination processes in academic publishing. All Frontiers journals are driven by researchers for researchers; therefore, they constitute a service to the scholarly community. At the same time, the Frontiers Journal Series operates on a revolutionary invention, the tiered publishing system, initially addressing specific communities of scholars, and gradually climbing up to broader public understanding, thus serving the interests of the lay society, too.

Dedication to Quality

Each Frontiers article is a landmark of the highest quality, thanks to genuinely collaborative interactions between authors and review editors, who include some of the world's best academicians. Research must be certified by peers before entering a stream of knowledge that may eventually reach the public - and shape society; therefore, Frontiers only applies the most rigorous and unbiased reviews.
Frontiers revolutionizes research publishing by freely delivering the most outstanding research, evaluated with no bias from both the academic and social point of view. By applying the most advanced information technologies, Frontiers is catapulting scholarly publishing into a new generation.

What are Frontiers Research Topics?

Frontiers Research Topics are very popular trademarks of the Frontiers Journals Series: they are collections of at least ten articles, all centered on a particular subject. With their unique mix of varied contributions from Original Research to Review Articles, Frontiers Research Topics unify the most influential researchers, the latest key findings and historical advances in a hot research area! Find out more on how to host your own Frontiers Research Topic or contribute to one as an author by contacting the Frontiers Editorial Office: frontiersin.org/about/contact

ISRAEL ION CHANNEL AND TRANSPORTERS MEETING 2019

Topic Editors:
Moran Rubinstein, Tel Aviv University, Israel
Rami Yaka, Hebrew University of Jerusalem, Israel
Avi Priel, Hebrew University of Jerusalem, Israel

Citation: Rubinstein, M., Yaka, R., Priel, A., eds. (2021). Israel Ion Channel and Transporters Meeting 2019. Lausanne: Frontiers Media SA. doi: 10.3389/978-2-88971-055-3

Table of Contents

frontiers in Pharmacology

ORIGINAL RESEARCH
published: 15 October 2019
doi: 10.3389/fphar.2019.01198

2-APB and CBD-Mediated Targeting of Charged Cytotoxic Compounds Into Tumor Cells Suggests the Involvement of TRPV2 Channels

*Hagit Neumann-Raizel[1,2], Asaf Shilo[3], Shaya Lev[1,2], Maxim Mogilevsky[3], Ben Katz[1,2], David Shneor[3], Yoav D. Shaul[3], Andreas Leffler[4], Alberto Gabizon[5], Rotem Karni[3], Alik Honigman[3] and Alexander M. Binshtok[1,2]**

[1] Department of Medical Neurobiology, Institute for Medical Research Israel-Canada, Faculty of Medicine, The Hebrew University of Jerusalem, Jerusalem, Israel, [2] The Edmond and Lily Safra Center for Brain Sciences, The Hebrew University, Jerusalem, Israel, [3] Department of Biochemistry and Molecular Biology, Institute for Medical Research Israel-Canada, Faculty of Medicine, The Hebrew University of Jerusalem, Jerusalem, Israel, [4] Department of Anesthesiology and Intensive Care Medicine, Hannover Medical School, Hannover, Germany, [5] Shaare Zedek Medical Center and Faculty of Medicine, The Hebrew University of Jerusalem, Jerusalem, Israel

OPEN ACCESS

Edited by:
Moran Rubinstein,
Tel Aviv University, Israel

Reviewed by:
Michael Christian Puljung,
University of Oxford,
United Kingdom
Irene Frischauf,
Johannes Kepler
University of Linz, Austria

***Correspondence:**
Alexander M. Binshtok
alexander.binshtok@ekmd.huji.ac.il

Specialty section:
This article was submitted to Pharmacology of Ion Channels and Channelopathies, a section of the journal Frontiers in Pharmacology

Received: *26 July 2019*
Accepted: *17 September 2019*
Published: *15 October 2019*

Citation:
Neumann-Raizel H, Shilo A, Lev S, Mogilevsky M, Katz B, Shneor D, Shaul YD, Leffler A, Gabizon A, Karni R, Honigman A and Binshtok AM (2019) 2-APB and CBD-Mediated Targeting of Charged Cytotoxic Compounds Into Tumor Cells Suggests the Involvement of TRPV2 Channels. Front. Pharmacol. 10:1198. doi: 10.3389/fphar.2019.01198

Targeted delivery of therapeutic compounds to particular cell types such that they only affect the target cells is of great clinical importance since it can minimize undesired side effects. For example, typical chemotherapeutic treatments used in the treatment of neoplastic disorders are cytotoxic not only to cancer cells but also to most normal cells when exposed to a critical concentration of the compound. As such, many chemotherapeutics exhibit severe side effects, often prohibiting their effective use in the treatment of cancer. Here, we describe a new means for facilitated delivery of a clinically used chemotherapy compound' doxorubicin, into hepatocellular carcinoma cell line (BNL1 ME). We demonstrate that these cells express a large pore, cation non-selective transient receptor potential (TRP) channel V2. We utilized this channel to shuttle doxorubicin into BNL1 ME cells. We show that co-application of either cannabidiol (CBD) or 2-APB, the activators of TRPV2 channels, together with doxorubicin leads to significantly higher accumulation of doxorubicin in BNL1 ME cells than in BNL1 ME cells that were exposed to doxorubicin alone. Moreover, we demonstrate that sub-effective doses of doxorubicin when co-applied with either 2-APB or CBD lead to a significant decrease in the number of living BNL1 ME cell and BNL1 ME cell colonies in comparison to application of doxorubicin alone. Finally, we demonstrate that the doxorubicin-mediated cell death is significantly more potent, requiring an order of magnitude lower dose, when co-applied with CBD than with 2-APB. We suggest that CBD may have a dual effect in promoting doxorubicin-mediated cell death by facilitating the entry of doxorubicin *via* TRPV2 channels and preventing its clearance from the cells by inhibiting P-glycoprotein ATPase transporter. Collectively, these results provide a foundation for the use of large pore cation-non selective channels as "natural" drug delivery systems for targeting specific cell types.

Keywords: TRPV2 channels, targeted delivery, hepatocellular carcinoma, BNL1 ME cells, membrane permeation, doxorubicin, cannabidiol, 2-APB

INTRODUCTION

Inhibition of specific enzymes, formation of protein complexes, or modification of transcription factors' activity affects either cell state, such as excitability or activity, or even cell fate, by modulating survival, growth, division, etc. Therefore, it can be useful to alter the function of cells in diverse ways for the treatment of many different disease states. Some of the anticancer chemotherapeutics—for example, affect tumor cells by acting on enzymes that are involved in replication or uncoiling of DNA together with activation of various complex molecular signals, which ultimately induces apoptosis (Tacar et al., 2013; Dobbelstein and Moll, 2014). A limitation of this approach is that it is not cell-type-specific, resulting in damage to healthy tissue. The effect on DNA or the enzymes, or their isoforms, which are widely expressed in many cell types implies that chemotherapy also produces undesired effects. Hence, the relative effectiveness of chemotherapeutics should always be considered together with the underlying chemotherapeutic-mediated toxicity. This toxicity may affect both rapidly dividing and postmitotic non-cancer cells, thus leading to substantial side effects (Bagnyukova et al., 2010). The ultimate goal in anticancer drug development is to target only cancer cells, sparing normal cells. Several approaches are currently being used to enhance the effect of anticancer drugs on tumor cells. Some of these strategies are tuned to target cancer-specific cellular machinery. Others, by using polymeric drug carriers, liposomes, and other nanoparticles, enhance the delivery of non-specific chemotherapeutics to the tumor cells by modifying the drug tissue biodistribution (Gabizon et al., 2014). Here, we unveil a different method for the selective targeting of tumor cells. We target otherwise membrane-impermeable hydrophilic chemotherapy agents into cancer cells *via* the pore of cation non-selective transient receptor potential (TRP) channels, expressed in a differential manner by many types of tumor cells. These channels such as TRPV1, TRPV2, as well as other numerous members of TRP channel family play a critical role in tumorigenesis, tumor vascularization, and the ability of tumor cells to proliferate and migrate (Prevarskaya et al., 2007; Santoni and Farfariello, 2011; Fiorio Pla and Gkika, 2013; Chen et al., 2014). Here, we hypothesized that TRP channels could be utilized as cell-specific "natural" drug delivery system for targeting charged molecules that are cytotoxic or anti-proliferative when inside the cells, but relatively innocuous outside, specifically into cancer cells. Recently, we showed that the pore of the TRPV1 and TRPA1 channels, members of TRP channel family, which are expressed by pain- and itch-related neurons but not by other peripheral neurons, is large enough to allow passage of a charged derivative of lidocaine, QX-314. QX-314 was shown to be ineffective when applied extracellularly but blocks sodium channels and consequently neuronal excitability when it gains access to the inside of cells (Binshtok et al., 2007; Roberson et al., 2011). We have shown that activation of TRPV1 and TRPA1 channels provides a pathway for selective entry of QX-314 into pain-related (nociceptive) neurons and therefore inhibition of pain signals without effecting non-nociceptive sensory and motor neurons (Binshtok et al., 2007; Binshtok et al., 2009b; Binshtok et al., 2009a). We also have demonstrated that this approach is not limited to nociceptive neurons and could be used to selectively block other types of cells that express TRP channels (Roberson et al., 2013). We and others have suggested that this method could also be used for targeted delivery of charged cytotoxic compounds into tumor cells that express large cationic channels (Bean et al., 2007; Santoni and Farfariello, 2011; Nabissi et al., 2013). Here, we tested this hypothesis by targeting mouse hepatocellular carcinoma BNL1 ME cells with a clinically used chemotherapy drug, doxorubicin. Doxorubicin is one of the most commonly used chemotherapeutic drugs for the treatment of hepatocellular carcinoma (HCC (Bruix and Sherman, 2011) and other cancers such as lymphomas, leukemia, breast, lung, ovarian, gastric and thyroid malignancies (Lal et al., 2010). However, due to its relatively high dissociation constant (pKa), doxorubicin resides in part in its protonated, membrane impermeant form even in physiological pH (Webb et al., 2011). Considering that the tumor cell environment is of a lower than normal physiological extracellular pH (Gallagher et al., 2008; Webb et al., 2011), the protonated fraction of doxorubicin in the vicinity of tumor cells is even higher. Hence, its relative membrane impermeability is lower. Therefore, in order to increase the probability of drug permeation into tumor cells, the application of high doses is required when applying the standard therapeutic strategy. The usage of high doses, however, promotes drug off-target side effects.

Here, we show that, differently from non-cancerous liver and heart cells, mouse hepatocellular carcinoma BNL1 ME cells express a large-pore cationic channel receptor, TRPV2. Application of compounds that activates and opens TRPV2 channels facilitates the entry of doxorubicin into BNL1 ME cells, leading to its substantial accumulation within BNL1 ME cells. Moreover, we show that low sub-effective doses of doxorubicin, which do not lead to cell death, become effective and sufficient to cease proliferation and induce cell death of BNL1 ME cells when doxorubicin is co-applied with TRPV2 activators. Such CBD- or 2-APB-mediated facilitated entry will minimize the off-target effect of doxorubicin and therefore will substantially reduce adverse side effects.

MATERIALS AND METHODS

Cell Culture

Murine BNL1 ME A.7R.1 cells (American Type Culture Collection, Manassas, VA) were plated on γ-irradiated mouse embryonic fibroblasts or 0.1% gelatin-coated six-well plates and maintained in DMEM (high glucose, Invitrogen) with 10% FBS, 2mM L-glutamine, 100 U/ml penicillin, and 100 U/ml streptomycin. Medium was changed every other day.

HEK293T cells were grown at 37°C with 5% CO_2 in DMEM with 10% FCS and 1% penicillin-streptomycin (Biological Industries). HEK293T cells were transfected using TRPV2 cDNA and DsRed cDNA (Clontech). Transfections were performed with the TransIt (Mirus) Transfection Reagent, with equal amounts of cDNA, according to the manufacturer's instructions and protocol.

qPCR

Total RNA was extracted with TRI Reagent (Sigma), and 2 μg of total RNA was reverse transcribed using the M-MLV reverse transcriptase (Promega). Quantitative PCR was performed on the cDNA using SYBR Green (Roche) and the CFX96 (Bio-Rad) real-time PCR machine. TRPV2 mRNA levels were examined from mouse liver, heart tissues, and mouse HCC BNL1 ME. Samples were compared to a standard curve, which was established by serial dilutions of a known concentration of cDNA. GAPDH was used from normalization. Primers: TRPV2: 5'-TAC GGT CCT GCT CGA GTG TC-3' and 5'-TGG CTC TAA AAC CAC CAT GC-3.' GAPDH: 5'-CCC AGC ACA ATG AAG ATC AA-3' and 5'-TAG AAG CAT TTG CGG TGG AC-3.'

Immunoblotting

Cells were lysed in Laemmli buffer and analyzed for total protein concentration as described (Karni et al., 2007). Fifty micrograms of total protein from each cell lysate was separated by SDS-PAGE and transferred onto a nitrocellulose membrane. The membranes were blocked with 5% milk and probed with specific antibodies. Bands were visualized using enhanced chemiluminescence detection. Primary antibodies were as follows: RL-1 antibody (1:1,000, Santa Cruz) human origin (Caprodossi et al., 2008; Nabissi et al., 2010) and β-tubulin (1:2,000, Sigma). Secondary antibodies used were as follows: HRP-conjugated goat anti-mouse, goat anti-rabbit, and donkey anti-goat IgG (1:10,000 Jackson Laboratories).

Ratiometric Calcium Imaging

Cultured BNL1 ME cells were loaded for 45 min with 1 μM FURA-2 AM dye (stock in DMSO) in a standard external solution (SES) composed of (in mM) 5 KCl, 145 NaCl, 2 CsCl, 1 MgCl, 10 HEPES, and 10 glucose and then rinsed for 45 min for de-esterification of intracellular acetoxymethyl esters. Cells were perfused continuously at a rate of ~1 ml per min with SES and examined with an inverted microscope equipped with Epi-Fl attachment, perfect focus system (Nikon) and EXi Aqua monochromator (Q-imaging) and X40 lens. Intracellular Ca^{2+} concentrations were measured fluorometrically as the absorbance ratio at 340 and 380 nm ($\Delta F340/380$, 510 nm for emission, Lambda DG4, Sutter Instruments). Images were taken every 1 s, monitored online, and analyzed offline using Nikon Elements AR Software (Nikon). 2-Aminoethoxydiphenyl borate (2-APB, 200 μM) or cannabidiol (CBD, 10 μM) were briefly bath applied (as indicated in the figures) using a fast-step valve control perfusion system. In some experiments, CBD was applied after cells were pre-treated with 1 μM doxorubicin. For a positive control of imaging, an ionophore, ionomycin (1 μM, Sigma), was briefly bath applied, at the end of the experiment. In some experiments, cells were treated with 1 μM thapsigargin for 5–15 min, in order to deplete endoplasmic reticulum Ca^{2+} stores (Thastrup et al., 1990). We considered the cells as responsive only if the changes in ratio (ΔF) following application of 2-APB (200 μM) or CBD (10 μM) were larger than $0.1\Delta F$, and were easily distinguishable from optic noise which was about 0.02 ΔF.

Doxorubicin Imaging

Cultured BNL1 ME cells were perfused continuously at 2 ml per min with DMEM and examined with an inverted microscope equipped with Epi-Fl attachment, perfect focus system (Nikon) and EXi Aqua monochromator (QImaging). Doxorubicin fluorescence was measured as absorbance at 480 nm (580 nm for emission, Lambda DG4, Sutter Instruments). Images were taken every 10 min, monitored online, and analyzed offline using Nikon Elements AR Software (Nikon). 2-APB (200 μM) or CBD (10 μM) and doxorubicin (1 and 5 μM) were bath applied using a fast-step valve control perfusion system, at a rate of ~1 ml per min.

In Vitro Cell Growth Assay

This assay was carried out as previously described (Shneor et al., 2017). Briefly, BNL1 ME cells were plated in 96-well plates for 24 h. Then, each one of the treatment groups was added. Dose responses of doxorubicin and each one of the activators were used to find the optimal doses for the drugs. Cells were then incubated with DMEM with one of the drugs for 24, 48, and 72 h. Then, cells were incubated for 30 min with substrate of CellTiter-Fluor Cell Viability Assay (Promega; excitation: 380–400 nm; emission 505 nm). Live cells took up the substrate, and constitutive protease activity cleaved it to the fluorescent form, which generated a fluorescent signal proportional to the number of live cells. The fluorescent signal was detected in a flow cytometer.

Clonogenic Cell Survival Method

BNL1 ME cell populations were prepared by trypsinization. Cells were counted using a hemocytometer, and appropriate cell numbers were seeded in six-well plates and treated for 24 h with doxorubicin alone or together with TRPV2 activators. Colonies were fixed and stained with methylene blue (Karni et al., 1999; Karni et al., 2007); for quantification, the number of colonies in each well was calculated using a stereomicroscope. Digital images of the colonies were obtained using a CCD camera (Nikon, Japan). Colonies were counted using ImageJ analysis software (Fiji version 1.44a). Due to the high confluence of the colonies after the treatment with DMSO or CBD alone, the examined parameters of the number of colonies, the size of the individual colony, and the inner density of each colony were undetectable. Treatment with 2 μM doxorubicin alone completely prevented colony formation. Therefore, only colonies following treatment with doxorubicin and colonies treated with both CBD and doxorubicin were analyzed and compared.

Doxorubicin Uptake Assay

Intracellular doxorubicin concentrations were measured with or without TRPV2 activators. BNL1 ME cells were plated on six-well plates at concentrations of 2×10^5 cells/well and treated with DMEM for 24 h, after incubation at 37°C for 1 h. With each one of the treatments, each culture medium was removed, and cells were washed three times with PBS. The cells were lysed in 1 ml HCL-acidified isopropanol for 24 h (centrifuged at 2,000 rpm for 10 min). For fluorometric analysis, total cellular doxorubicin

in BNL1 ME cells was determined by measuring the fluorescent emission of the solution (λ_{ex} = 480 nm, λ_{em} = 590 nm) in the cell lysate with a fluorometer, as described elsewhere (Patil et al., 2018). The drug concentration was calculated with the standard curve of doxorubicin.

Calcein Accumulation Assay

BNL1 ME cells were seeded at 20 × 104 cells/well in 24-well plates. Experiments were performed 2 days after achieving confluent monolayers. Before the experiment, cells were incubated for 1 h with 1 ml DMEM, supplemented with 5 mM HEPES, pH 7.3, in the presence or the absence of a P-gp inhibitor, verapamil (200 μM). In the accumulation phase, cells were co-incubated with 0.25 μM calcein-AM in the presence or absence of the inhibitor. Control cells were incubated with equal volumes of solvents of all substances (DMSO). After 1 h, the cells were washed three times with ice-cold PBS. Intracellular fluorescence of calcein-AM was measured within 1 h with λ_{ex} = 485 nm and λ_{em} = 528 nm using a plate reader (Synergy HT, BioTek, Winooski, VT, USA).

Chemicals

Doxorubicin and 2-APB were purchased from Sigma. CBD was kindly provided by the lab of Prof. Raphael Mechoulam, School of Pharmacy, Hebrew University of Jerusalem, Hadassah Ein Kerem. Calcein was kindly provided by the lab of Dr. Sara Eyal, School of Pharmacy, Hebrew University of Jerusalem, Hadassah Ein Kerem.

Experimental Design and Statistical Analysis

Data are shown as mean ± S.E.M. Differences between groups were analyzed using a two-tailed Student's *t*-test or one-way ANOVA analysis of variance followed by Bonferroni *post hoc* tests, when appropriate. The criterion for statistical significance was $p < 0.05$.

Sample size calculation: we did not carry out a power analysis because we were studying the effect of a new drug combination and had no way to estimate the effect size.

The number of replicates (n for cells and n for the number of plates/repetitions) for each experiment is given either in the Figure legends or in the *Results*. For each treatment group, we calculated the average value for the repetitions and ran the statistical comparisons between the treatments. If a representative example is shown, we explain how representative it is, i.e., how many cells/plates showed a similar effect. When relevant, the inclusion criteria for the experiments are described in the *Materials and Methods* section above.

RESULTS

Mouse Hepatocellular Carcinoma BNL1 ME Cells Express Functional TRPV2 Channels

Amongst the large pore-cation non-selective ion channels, the TRP vanilloid subtype 2 channel (TRPV2), a member of the TRP superfamily, is highly expressed by a variety of tumor cells (Santoni and Farfariello, 2011; Liberati et al., 2014). It has been shown that urothelial carcinoma cells (Caprodossi et al., 2008; Mizuno et al., 2014), human leukemic cells (Pottosin et al., 2015), prostate cancer cells (Monet et al., 2010), esophagus squamous cell carcinoma cells (Zhou et al., 2014), and hepatocellular carcinoma cells (Liu et al., 2010) overexpress TRPV2 channels. Here, we sought to examine whether a pore of TRPV2 channels expressed by a murine model of hepatocellular carcinoma cells [BNL1 ME (Kuriyama et al., 1999; Tatsumi et al., 1999; Ogunwobi and Liu, 2011)] could be used to shuttle doxorubicin into these cells selectively. First, we examined whether BNL1 ME cells overexpress TRPV2 similarly to previous reports of hepatocellular carcinoma cells (Liu et al., 2010). We compared the expression levels of TRPV2 in BNL1 ME cells to a mouse embryonic fibroblast cell line (MEF), which served as a negative control, and to normal mouse liver cells from a direct, first passage culture. We used RT-qPCR and showed that BNL1 ME cells possess significantly higher levels of TRPV2 mRNA than MEF and normal liver cells (**Figure 1A**). We next compared the protein level of TRPV2 channel in BNL1 ME, dissociated mouse liver cells, and pheochromocytoma 12 cell line (PC12) transfected with TRPV2 as a positive control (**Figure 1B**). We demonstrated that, while the levels of the TRPV2 protein are undetectable in liver cells, BNL1 ME cells express substantial levels of TRPV2.

Considering that cardiotoxicity is one of the significant side effects of doxorubicin (Singal and Iliskovic, 1998; Chatterjee et al., 2010) and that expression of TRPV2 was previously shown in a variety of heart cells e.g., cardiomyocytes, fibroblasts, endothelial cells, and vascular smooth muscle cells (Watanabe et al., 2009), we also compared the levels of TRPV2 mRNA and TRPV2 channel protein in short-term cultured heart cells from mouse heart to BNL1 ME cells. Indeed, we confirmed that heart cells express TRPV2 mRNA (**Figure 1A**); however, these cells did not show expression of the TRPV2 protein (**Figure 1B**). This inconsistency implies posttranslational modulation, which is a common mechanism to strictly regulate protein levels (Maier et al., 2009; Vandewauw et al., 2013). This posttranslational regulation is also true for TRPV2 regulation (Uhlen et al., 2015). These data indicate that mouse BNL1 ME cells express TRPV2 channel protein, unlike liver or heart cells.

To assess whether TRPV2 channels expressed by BNL1 ME cells are functional, we examined changes in intracellular Ca^{2+} [$(Ca^{2+})_i$] in BNL1 ME cells loaded with the Ca^{2+} indicator FURA-2AM, following bath application of the TRPV2 channel activator, 2-aminoethoxydiphenyl borate [2-APB (Hu et al., 2004; Juvin et al., 2007)]. We first perfused the cells with a bath solution containing nominally free Ca^{2+} (Ca^{2+}—free bath solution) in order to examine possible 2-ABP-mediated release of Ca^{2+} from internal stores, as previously shown (Maruyama et al., 1997). In these conditions, bath application of 2-APB produced a small increase in $[Ca^{2+}]_i$ (**Figure 1C**). Reperfusion of cells with bath solution containing 2 mM Ca^{2+} (SES) led to a slow, gradual increase in $[Ca^{2+}]_i$ reaching a plateau after about 4 min, as expected. The second application of 2-APB in these conditions led to a substantial increase in $[Ca^{2+}]_i$ in all monitored cells (**Figure 1C**). These data suggest that 2-APB produces a large

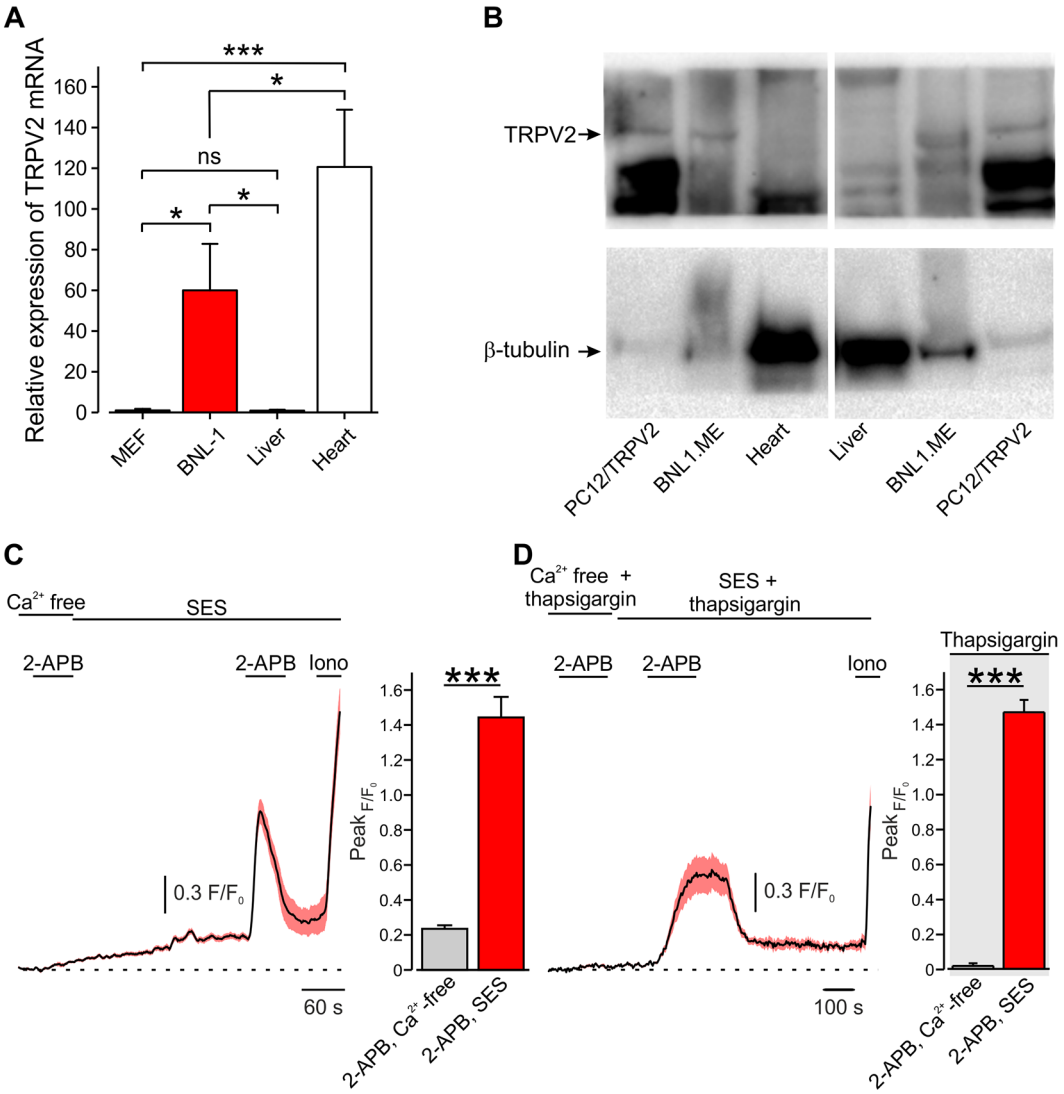

FIGURE 1 | Mouse hepatocellular carcinoma BNL1 ME cells, but not liver or heart cells express functional TRPV2 channels. **(A)** Bar graph depicting relative expression levels, assessed by RT-PCR, of TRPV2 mRNA in BNL1 ME cells compared to MEF, non-cancerous mice liver, and mice heart cells (GAPDH was used for normalization; *see Methods*). *—$p < 0.05$; ***—$p < 0.001$, one-way ANOVA with *post hoc* Bonferroni, n = 3 replications. **(B)** Western blot analysis of TRPV2 protein levels in BNL1 ME cells compared to pheochromocytoma 12 cell line (PC12) constitutively expressing TRPV2 (PC12/TRPV2), non-cancerous mice liver cells, and mice heart cells. β-Tubulin served as a control (for a blot containing all the lanes; see **Supplementary Figure 1**). The size of the proteins (95 kD for TRPV2 and 51 kD for β-tubulin) was determined relative to pre-stained size markers. Representative of five experiments. **(C)** *Left,* Mean ± SEM of changes in cytosolic $[Ca^{2+}]_i$ following bath application of 200 μM 2-APB. Note that application of 2-APB leads to a small increase in intracellular Ca^{2+} when external solution contains nominal Ca^{2+} concentration (Ca^{2+} free) but produces a substantial and significant (***—$p < 0.001$, one-way ANOVA) increase in intracellular Ca^{2+} when calcium is present in the bath solution (standard external solution, SES), n = 26 cells. For a positive control of imaging, 1 μM ionomycin (Iono) was added to the bath solution at the end of each experiment. *Right,* bar graph comparing peak changes in cytosolic $[Ca^{2+}]_i$ following application of 2-APB in Ca^{2+} free-solution with changes in cytosolic $[Ca^{2+}]_i$ following application of 2-APB in 2 mM Ca^{2+} containing SES; ***—$p < 0.001$, paired Student *t*-test, n = 43 cells, from three plates. **(D)** Same as in *C*, but with SES containing thapsigargin. Note that, under these conditions, the increase in intracellular Ca^{2+} occurs only when calcium is present in the external solution (SES) n = 28 cells. *Right,* ***—$p < 0.001$, paired Student *t*-test, n = 34 cells, from three plates. ns, not significant.

transmembrane Ca^{2+} influx into BNL1 ME cells, in addition to a small 2-APB-mediated increase, possibly *via* 2-ABP-mediated activation of IP_3 receptors (Maruyama et al., 1997). To examine the latter possibility, we treated BNL1 ME cells for 5–15 min with 1 μM thapsigargin to deplete endoplasmic reticulum Ca^{2+} stores (Thastrup et al., 1990). 2-APB applied on thapsigargin-treated cells, perfused with Ca^{2+}—free bath solution did not produce any change in $[Ca^{2+}]_i$. Changing the bath to a solution containing 2 mM Ca^{2+} did not result in the rise of intracellular Ca^{2+}. However, the second application of 2-APB in cells treated with bath solution containing 2 mM Ca^{2+} led to a substantial increase in $[Ca^{2+}]_i$ (**Figure 1D**), suggesting that the 2-APB-induced $[Ca^{2+}]_i$ rise is due to TRPV2 and not store-operated channels. Collectively, these data suggest that 2-APB induces a

transmembrane Ca^{2+} influx, indicating that BNL1 ME express functional TRPV2 channels on their plasma membrane.

To further study the functionality of TRPV2 channels, we measured changes in $[Ca^{2+}]_i$ in BNL1 ME cells following bath application of another well-established TRPV2 activator, cannabidiol (CBD, (Qin et al., 2008). It was previously demonstrated that CBD leads to $[Ca^{2+}]_i$ increase, mainly due to TRPV2-mediated Ca^{2+} influx, since CBD-mediated Ca^{2+} transients *via* TRPV2 were abolished when extracellular Ca^{2+} was removed from the external solution (Eubler et al., 2018). First, we showed that 10 μM CBD applied onto HEK293T cells, transfected with human TRPV2 (hTRPV2) led to an increase in $[Ca^{2+}]_i$ only in the TRPV2 transfected HEK cells, which were labeled with DsRed-expressing fluorescent protein (**Supplementary Figure 2**). Application of CBD on HEK293T cells, which were not labeled with DsRed, and therefore do not express hTRPV2, did not produce a change in $[Ca^{2+}]_i$ (n = 19 cells, *data not shown*). Bath applications of 10 μM CBD onto BNL1 ME cells, similarly to the effect of 2-APB, led to a robust increase in $[Ca^{2+}]_i$ (**Supplementary Figure 3**), further supporting the functional expression of TRPV2 on the plasma membrane of BNL1 ME cells.

2-APB- or CBD-Mediated Activation of TRPV2 Channels Is Sufficient to Produce Entry and Accumulation of Doxorubicin Into BNL1 ME Cells

In developing our platform for facilitated entry of charged compounds into cancer cells, through TRP channels, we used the relatively small (543 Da) chemotherapeutic drug, doxorubicin, which in physiological pH resides mostly in the charged form (Webb et al., 2011). We first examined whether activation of TRPV2 channels is sufficient to allow the entry of doxorubicin into BNL1 ME cells. To that end, we exploited the endogenous fluorescence property of doxorubicin (Scalori et al., 1988) and measured the intensity of its intracellular fluorescence, that reflects doxorubicin "trapped" in the cytoplasm. To ensure that the fluorescence originates from doxorubicin which is "trapped" inside the cell and does not originate from doxorubicin in the extracellular solution, we performed the measurements of doxorubicin-induced intracellular fluorescence after 1 h of doxorubicin washout. This time frame is sufficient to allow an exchange of all extracellular solution about 50 times, suggesting that all extracellular doxorubicin is washed out. In these conditions, bath application (*see Methods*) of either 1 μM doxorubicin alone (**Figures 2A**, *left*, **B**) or 200 μM 2-APB alone (**Figure 2B**) did not cause any changes in the fluorescent levels, beyond basal control levels (**Figure 2B**). However, the co-application of doxorubicin, together with 2-APB, led to a significant increase in intracellular fluorescence (**Figures 2A**, *right*, **B**), implying that doxorubicin enters the cells only in conjunction with the activation of TRPV2.

Next, we examined whether CBD-mediated activation of TRPV2 is also sufficient to shuttle doxorubicin into BNL1 ME cells. The previously described method of measuring doxorubicin fluorescence following treatment with CBD could be inappropriate, due to CBD-mediated inhibition of the P-glycoprotein ATPase transporter (Zhu et al., 2006). This transporter has been shown to participate in the removal of doxorubicin from the cells (Giavazzi et al., 1984; Ferry, 1998) and appears to be present in BNL1 ME cells (*see below and* **Supplementary Figure 6**). Thus, increased fluorescence following the application of doxorubicin and CBD could result not only because of facilitated entry of doxorubicin but also due to its accumulation following the inhibition of the transporter. We, therefore, examined the CBD-mediated doxorubicin entry

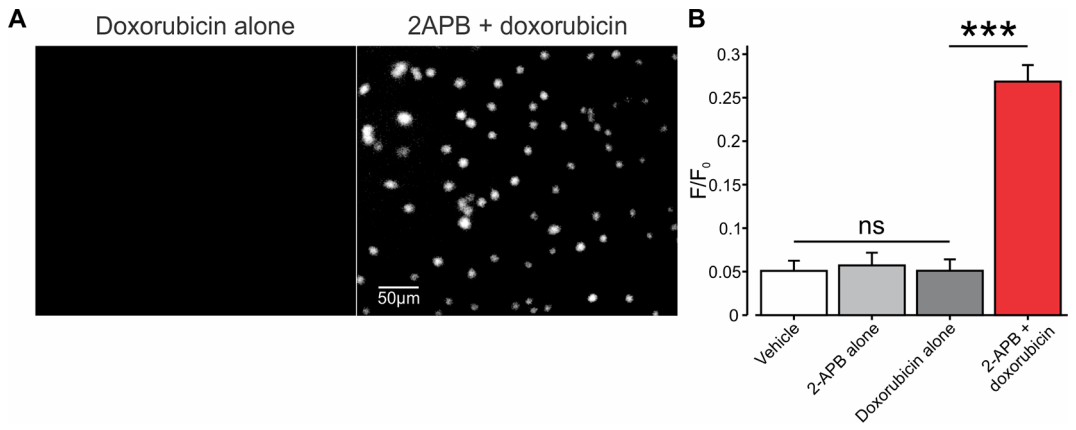

FIGURE 2 | Co-application of 2-APB with doxorubicin leads to facilitated entry of doxorubicin into mouse BNL1 ME cells. **(A)** Representative epifluorescent images of cultured BNL1 ME cells, 5 min after application 1 μM doxorubicin alone (*left*) and co-application of 200 μM 2-APB with 1 μM doxorubicin (*right*). Note that doxorubicin-based fluorescence (*see Methods*) was detected only when co-applied with 2-APB. **(B)** Bar graph depicting means ± SEM of changes in intensity of intracellular fluorescence following application of vehicle, 2-APB alone, doxorubicin alone, or doxorubicin together with 2-APB at the indicated concentrations. The values for vehicle and 2-APB alone were measured 30 min after application. 2-APB was then washed out for 30 min, and the values for doxorubicin alone or doxorubicin together with 2-APB were measured after 60 min each. Note that doxorubicin-based intracellular fluorescence was above the noise levels (0.05 F/F_0) only after the co-application of doxorubicin with 2-APB. ***$p < 0.001$, compared to doxorubicin alone, paired *t*-test, ns, not significant, n = 60 cells, three repetitions.

into BNL1 ME cells by measuring changes in the Ca^{2+} fluxes following the application of doxorubicin together with CBD. We hypothesized that, if doxorubicin permeates through the pore of TRPV2 channels, it would impair the penetration of Ca^{2+} and therefore would lead to a decrease in the FURA2-induced fluorescence, similarly to other charged molecules such as QX-314 (Puopolo et al., 2013). Accordingly, we loaded BNL1 ME cells with FURA-2AM and compared CBD-induced increase in $[Ca^{2+}]_i$ in cells treated with standard bath solution (SES; *see Methods*) with cells treated with bath solution containing doxorubicin. When cells were perfused with SES, the application of 10 μM CBD produced a substantial increase in $[Ca^{2+}]_i$ in all cells (**Figure 3**; see also **Supplementary Figure 3**). Application of CBD onto cells treated with SES containing 1 μM doxorubicin led to significantly smaller increase in $[Ca^{2+}]_i$ ($p < 0.001$, n = 30 cells; **Figure 3**). When the doxorubicin-containing bath solution was washed out, CBD-mediated increase in $[Ca^{2+}]_i$ partially recovered (**Figure 3**). It is noteworthy that, when cells were perfused with SES, consecutive applications of CBD produced a similar increase in $[Ca^{2+}]_i$ ($p > 0.05$, n = 36 cells; **Supplementary Figure 3**).

Because CBD has been shown to activate other Ca^{2+} permeable ion channels (Bisogno et al., 2001), we examined whether TRPV2 channels specifically provide a pathway for the doxorubicin to enter the cells following CBD-mediated activation. To that end, we measured how doxorubicin, when added to SES, changes CBD-mediated Ca^{2+} influx into HEK293T cells, transfected with human TRPV2 (hTRPV2). Similar to our results from BNL1 ME cells, the addition of doxorubicin to the SES leads to a significant decrease in CBD-mediated Ca^{2+} influx (**Supplementary Figure 4A**). When doxorubicin was not added to the SES, subsequent applications of CBD produced similar increases in $[Ca^{2+}]_i$ (**Supplementary Figure 4B**). These results from the minimally reconstituted system of TRPV2-expressing HEK cells indicate that CBD-activated TRPV2 channels is sufficient to shuttle doxorubicin into the cells.

Collectively, these data imply that doxorubicin enters BNL1 ME cells *via* active TRPV2 channels. Importantly, these data also suggest that doxorubicin enters BNL1 ME cells *via* the pore of TRPV2 channels.

Finally, to examine directly whether activation of TRPV2 channels would lead to increased accumulation of doxorubicin in BNL1 ME cells, we measured the intracellular concentration of doxorubicin. We used an *in vitro* uptake method in which intracellular doxorubicin concentrations were measured in BNL1 ME cells by fluorometric analysis. We assessed the intracellular concentration of doxorubicin at different time points after treating BNL1 ME cells with 1 μM doxorubicin alone or together with activation of the TRPV2 channels. To prevent the possible effect of enhanced doxorubicin accumulation caused by CBD-mediated inhibition of P-glycoprotein ATPase transporter on doxorubicin concentrations, we activated TRPV2 channels using 200 μM 2-APB. We found that at all measured time points, the total cellular concentration of doxorubicin in BNL1 ME cells, was significantly higher when doxorubicin was co-applied with 2-APB than when doxorubicin was applied alone (**Figure 4**). These data suggest that activation of TRPV2 channels enhances the accumulation of doxorubicin in BNL1 ME cells.

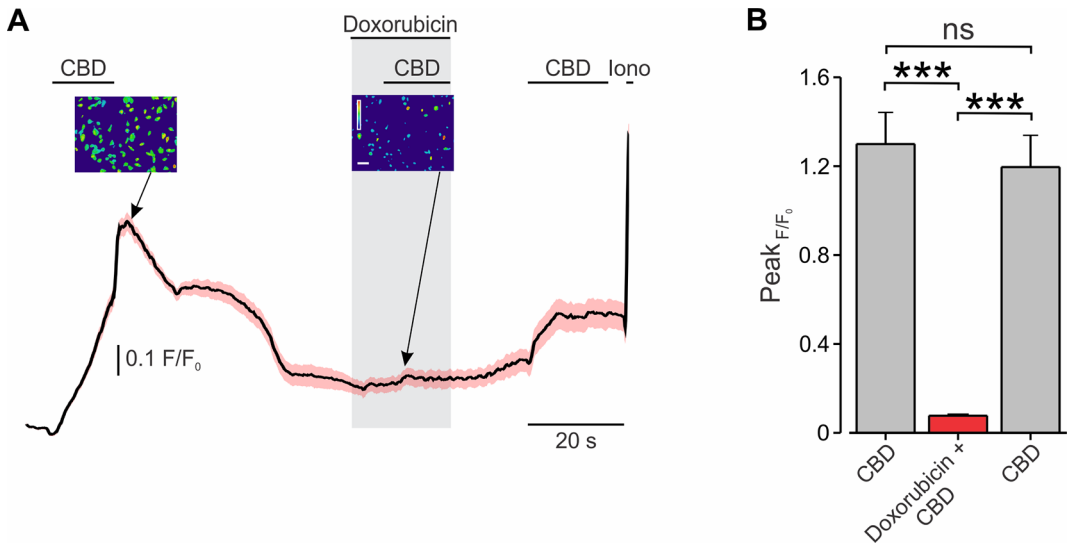

FIGURE 3 | Co-application of CBD with doxorubicin attenuates TRPV2-mediated Ca^{2+} entry into BNL1 ME cells. **(A)** Mean ± SEM of changes in cytosolic $[Ca^{2+}]_i$ following bath application of 10 μM CBD in SES, 10 μM CBD in SES containing 1 μM doxorubicin, and 10 μM CBD in after washout of doxorubicin, n = 36 cells. *Insets*, photomicrographs of blue-green-red pseudocolor radiometry images (taken at the time points indicated by arrows) demonstrated a decrease of F/F_0 after treatment of doxorubicin. Bar, 50 μm. The pseudocolor scale depicts changes in F/F_0 between 0 (*blue*) to 1.5 (*red*). For a positive control of imaging, 1 μM ionomycin (Iono) was added to the bath solution at the end of each experiment. **(B)** Bar graph depicting mean ± SEM of changes in peak FURA-2AM fluorescence following bath application of 10 μM CBD in SES, 10 μM CBD in SES containing 1 μM doxorubicin, and 10 μM CBD in after washout of doxorubicin. Note a significant decrease in response to CBD when doxorubicin is present in the extracellular solution. Note also that the response to CBD is partially rescued after doxorubicin is washed out. ***—$p < 0.001$, ns, not significant; RM one-way ANOVA with *post hoc* Bonferroni, n = 54 cells, from three plates.

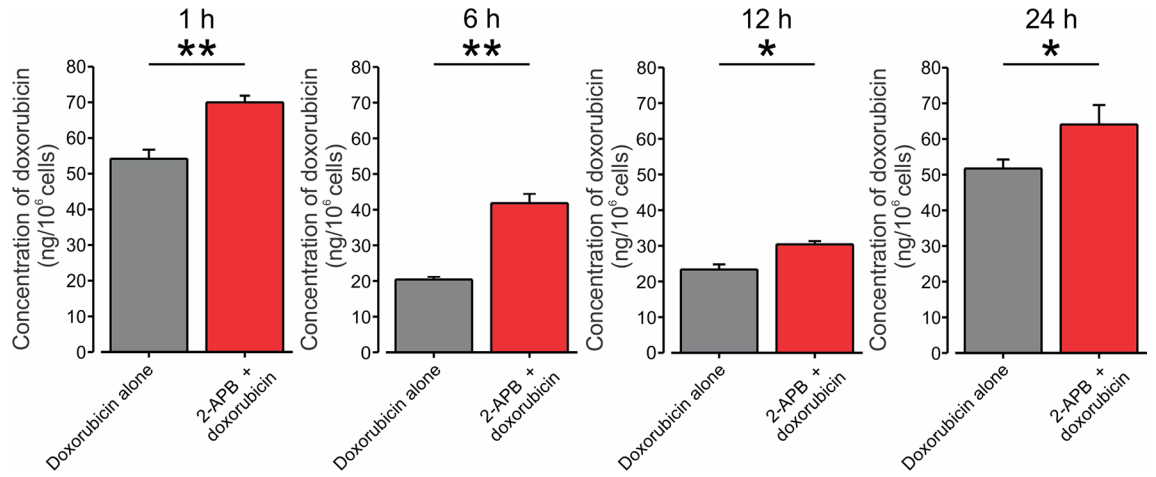

FIGURE 4 | Co-application of doxorubicin with 2-APB leads to an increased amount of intracellular doxorubicin in BNL1 ME cells. Bar graphs depicting the amount of doxorubicin in BNL1 ME cells (in ng/10^6 cells) measured using fluorometric analysis, 1, 6, 12, and 24 h following treatment with 1 μM doxorubicin alone (*gray*) or with 1 μM doxorubicin co-applied with 200 μM 2-APB (*red*). Note that the amount of intracellular doxorubicin was significantly increased when doxorubicin was co-applied together with 2-APB, *—$p < 0.05$, **—$p < 0.01$, Student's *t*-test, n = 3 repetitions for 1-, 6-, and 12-h time points, n = 2 repetitions for 24-h time point, n = 3 repetitions, for each treatment group.

Activation of TRPV2 by 2-APB Leads to Facilitated Entry of Doxorubicin Into BNL1 ME Cells

We hypothesized that activation of TRPV2 by virtue of opening aqueous pores, which are permeable for the protonated fraction of doxorubicin, will facilitate the permeation of doxorubicin and therefore augment its cytotoxic effect on TRPV2-expressing cancer cells, while sparing other cell types and therefore minimizing off-target side effects, as the effective concentration of doxorubicin can be lowered. To examine this hypothesis, we used a cell survival assay that measures cell viability expressed by the level of fluorescence (*see Methods*). We first determined a concentration range at which the application of doxorubicin alone does not affect the viability of BNL1 ME cells. We show here that 24-h treatment of BNL1 ME cells at concentrations of up to 2 μM doxorubicin do not lead to significant cell death (**Figure 5A**). Treatment with higher than 2 μM doxorubicin led to a significant decrease in the number of live cells (**Figure 5A**). We then chose the maximal sub-effective concentration of doxorubicin (2 μM) and co-applied it with 2-APB, which by itself did not affect cell viability in a concentration range of 25 to 200 μM, when treated for 24 h (**Figure 5B**). Co-application of 2 μM doxorubicin with 200 μM 2-APB led to a significant decrease in cell viability after 24 h (**Figures 5C, D**). The observed effect of co-application of doxorubicin and 2-APB showed a ~70% decrease after 24 h. This decrease was higher than the additive effect of the two treatments (~ 40% after 24 h, **Figure 5D**). These results suggest that activation of the TRPV2 channels leads to facilitated entry of doxorubicin into BNL1 ME cells such that previously sub-effective doses of doxorubicin alone when co-applied with the activator of the TRPV2 channels are sufficient to significantly affect cell viability. At these concentrations, at the later time points of 48 and 72 h, both doxorubicin and 2-APB applied alone had a substantial effect on the number of living cells such that there was no facilitated effect of co-application of 2-APB and doxorubicin (**Supplementary Figures 5A, B**). These data show that the optimal effect of 200 μM 2-APB-mediated facilitated entry of 2 μM doxorubicin on cell vitality is achieved 24 h after initiation of treatment.

CBD Facilitates Both the Entry and Accumulation of Doxorubicin in BNL1 ME Cells

CBD has been shown to inhibit the P-glycoprotein ATPase transporter (Zhu et al., 2006), which participates in the removal of doxorubicin from the cells (Giavazzi et al., 1984; Ferry, 1998). We therefore hypothesize that CBD may amplify the efficacy of the doxorubicin-mediated effect specifically in cancer cells by (1) providing selective entry of doxorubicin into cancer cells *via* TRPV2 activation (see **Figure 3**) and by (2) enhancing doxorubicin accumulation by P-gp ATPase inhibition. To examine the latter notion, we examined whether BNL1 ME cells express functional P-gp ATPase by measuring the accumulation of the P-gp ATPase substrate, calcein, (Hollo et al., 1994) in BNL1 ME cells following application of the well-established P-gp antagonist, verapamil (Cornwell et al., 1987). We show that the application of verapamil significantly increases the intracellular concentration of calcein (**Supplementary Figure 6**), suggesting that BNL1 ME cells express functional P-gp ATPase. Accordingly, the co-application of verapamil and doxorubicin significantly increases intracellular doxorubicin concentrations, compared with doxorubicin alone (**Figure 6A**). Notably, doxorubicin accumulation following co-application with CBD was significantly higher than the accumulation following co-application of verapamil with doxorubicin (**Figure 6A**), implying that, in addition to a possible

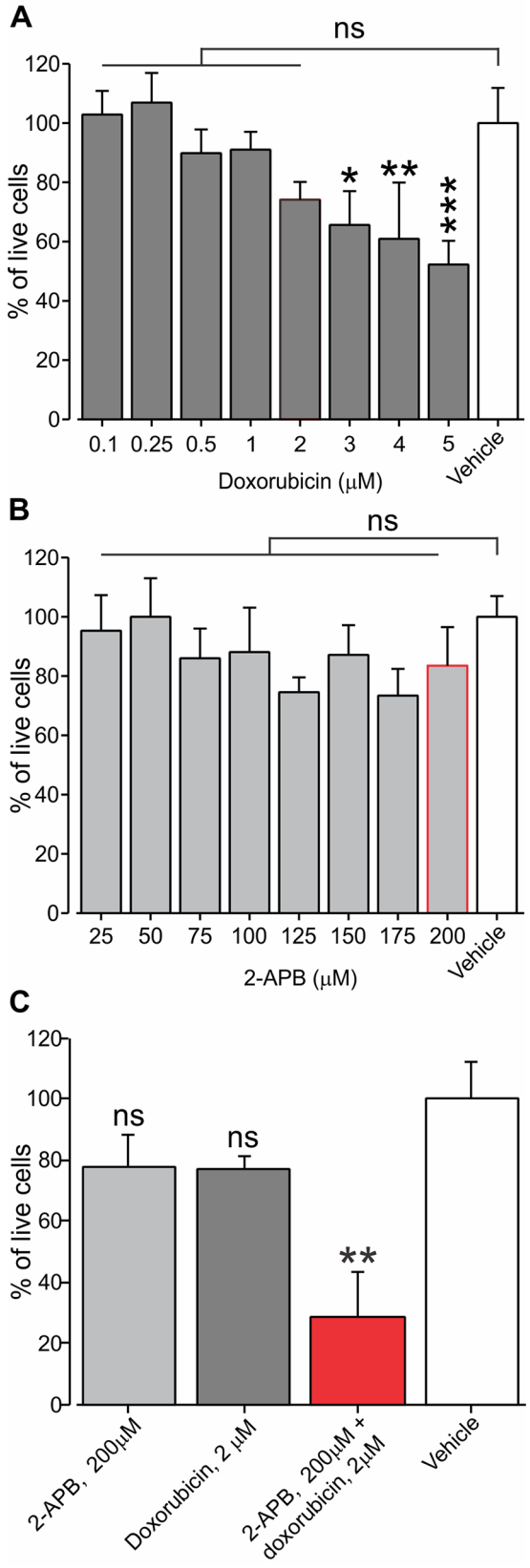

FIGURE 5 | Continued

FIGURE 5 | Application of sub-effective dose of doxorubicin together with 2-APB leads to a decrease in living BNL1 ME cells. **(A)** Live-cell fluorescence measurements from cultured BNL1 ME cells 24 h after treatment with doxorubicin alone at the indicated doses. Note that only treatment with doses higher than 2 μM leads to a significant reduction in the number of live cells (measured as a relative level of fluorescence; *see Methods*). **(B)** Same as in *A* but cells were treated for 24 h with 2-APB at the indicated dosed. Note that 2-APB does not affect cell viability at all examined doses. **(C)** Live-cell fluorescence measurements from cultured BNL1 ME cells show 24-h treatment with previously ineffective 2 μM doxorubicin applied together with 200 μM 2-APB leads to a significant decrease tumor cells viability, *$p < 0.05$, **$p < 0.01$, ***$p < 0.001$, ns, not significant; one-way ANOVA, comparison between the vehicles to all other groups, n = 6 wells for each group, three repetitions.

effect of CBD on P-gp ATPase, CBD facilitates doxorubicin accumulation by other mechanisms, possibly, as our data suggest, by promoting its entry *via* TRPV2 channels. These results also suggest that CBD co-applied with doxorubicin may be beneficial, compared to 2-APB, in causing cell death. Indeed, we were able to achieve about 40% facilitative effect (40% ΔSyn) using 10 μM CBD (**Supplementary Figure 7A**), which by itself did not affect cell viability (**Supplementary Figure 7B**), when co-applied with 0.1 μM doxorubicin (**Figure 6B**). A similar facilitative effect was achieved with 2-APB when co-applied with 2 μM doxorubicin (see **Figure 5**). Interestingly, higher concentrations of doxorubicin together with 10 μM CBD did not significantly change this facilitative effect (**Supplementary Figure 7A**).

Co-Application of Doxorubicin With CBD Inhibits the Formation of BNL1 ME Cell Colonies

A decrease in the number of viable cells measured using cell survival assay may be attributed to a decrease in cell proliferation, an increase in cell death, or both. We therefore examined if facilitated entry of doxorubicin affects cell proliferation, using the clonogenic cell survival method (*see Methods*). We analyzed the colony formation of BNL1 ME cells treated with DMSO, 0.1 μM 2-APB alone, 10 μM CBD alone, and doxorubicin alone, at two different sub-effective doses (0.1 and 2 μM), which were used in the cell viability experiments in combination with either CBD or 2-APB, respectively. The number of colonies that developed 10–15 days post-treatment was quantified. The size of the individual colonies and inner density of each colony were analyzed as well. Treatment with DMSO (*data not shown*) as well as CBD led to similar high confluences of the colonies such that it was impossible to determine specific parameters describing the properties of the single colony (**Figure 7A**, *left*). Treatment with 2 μM doxorubicin alone, which we previously used together with 2-APB in the cell viability assay, completely prevented colony formation (*data not shown*). Therefore, we did not examine the effect of 2 μM doxorubicin co-applied with 2-APB and analyzed only the colonies treated with doxorubicin and those treated with a combination of CBD and doxorubicin. Treatment with 0.1 μM doxorubicin alone substantially reduced the number of colonies, the average size of the colonies, and the inner density of the colonies (**Figures 7A**, *middle*, and **B–D**). The co-application

of 0.1 μM doxorubicin and 10 μM CBD, which by itself did not affect colony formation (**Figure 7A**, *left*), enhanced the effect of doxorubicin, reducing by about 20-fold the number of colonies and significantly decreasing the size and the inner density of the colonies (**Figures 7A**, *right*, **B–D**). These results suggest that, following co-application of doxorubicin and CBD, fewer cells propagate from a single surviving cell in a given time, implying that this approach reduces cell proliferation, possibly affecting also doxorubicin-resistant cell population.

Collectively, our results show that activation of TRPV2 channels provides a pathway for facilitated entry of doxorubicin into BNL1 ME cells. Our data suggest that doxorubicin, in doses that do not affect cell viability, when co-applied with TRPV2 activators, significantly reduces viability and proliferation of cancer cells.

DISCUSSION

The ultimate goal of developing an anticancer drug is to target cancer cells in a selective and specific manner while sparing healthy cells. To achieve this goal, some strategies are tuned to develop new drugs targeting cancer cell-specific molecular machinery. Other strategies aim at achieving specificity by using nanomedicines polymeric drug carriers such as liposomes and nanoparticles, restricting the delivery of non-specific chemotherapeutics primarily to the tumor tissues (Gabizon et al., 2014). In this study, we introduced a method of targeted delivery of cytotoxic compounds into cells harboring large-pore cation non-selective channels such as the TRPV2 channel. TRPV2 is a member of the TRP channel family. TRP channels were shown to be overexpressed by many tumor cells, playing critical roles in tumorigenesis, tumor vascularization, and the ability of the tumor cell to proliferate and migrate (Prevarskaya et al., 2007; Santoni and Farfariello, 2011; Fiorio Pla and Gkika, 2013; Chen et al., 2014). Here, we exploited these channels as cell-specific "natural" drug delivery systems for targeted application of charged molecules which are cytotoxic or antiproliferative, when inside the cells, but relatively non-toxic when outside the cells, to cancer cells, minimizing unwanted effects on other, non-TRP expressing cells.

Doxorubicin and other anthracyclines are widely used in chemotherapy, due to their efficacy in treating a broad spectrum of cancer types, such as sarcomas, carcinomas, and hematological cancers. However, their use is limited, particularly by their cardiac toxicity (Swain et al., 2003). Doxorubicin causes cumulative and mostly irreversible damage to the cardiac muscle (Ewer et al., 2004), restricting the repeated use of this drug. In addition, doxorubicin is also a prominent myelosuppressive agent. Therefore, the concentration of doxorubicin used must be strictly limited to avoid those and other doxorubicin' side effects.

However, the weak base chemical properties of doxorubicin will reduce the rate of drug uptake, particularly in the acidic environment of cancer cells, in which doxorubicin will persist mostly in the charged form. This property of doxorubicin substantially impedes doxorubicin permeation across the membrane, such that its concentration may be around three-fold higher outside of the cell than on the inside, as suggested by some studies (Webb et al., 2011). Here, we utilized the usually ineffective charged fraction of doxorubicin and shuttled it into cancer cells *via* cation permeable TRPV2 channels, allowing us to achieve the desired effect using substantially lower doses of doxorubicin.

We and others have previously demonstrated that the pore of TRPV1 and TRPA1 channels, which are predominantly expressed by pain- and itch-related peripheral neurons, are large enough to allow passage of QX-314, a charged derivative of lidocaine that is ineffective when applied extracellularly but blocks sodium channels and consequently neuronal excitability when inside of cells (Binshtok et al., 2007; Puopolo et al., 2013; Roberson et al., 2013). By showing QX-314-mediated decrease of TRPV1-induced inward current, it was previously suggested that that activation of TRPV1 channels provided a pathway for entry of QX-314 into pain-related neurons, with QX-314 acting as a permeant blocker (Puopolo et al., 2013). Co-application of TRPV1 or TRPA1 activators enabled specific inhibition of pain and itch transmission without affecting other sensory and motor neurons (Binshtok et al., 2007; Binshtok et al., 2009b; Binshtok et al., 2009a; Roberson et al., 2013). Here, we demonstrated that the application of doxorubicin inhibited TRPV2-induced Ca^{2+} influx, which implies that doxorubicin permeates into BNL1 ME cells *via* the pore of the TRPV2 channels.

TRPV2 is overexpressed by a variety of cancer cells and plays a functional role in hepatocellular carcinoma, prostate cancer, bladder cancer, and glioblastoma development (Liu et al., 2010; Monet et al., 2010; Nabissi et al., 2013). It also is one of the factors of dystrophic cardiomyopathy (Iwata et al., 2003; Lorin et al., 2015). The latter implies that, if heart cells express functional TRPV2 channels on their membrane, the activation of TRPV2 may lead to entry of doxorubicin into heart cells and thus enhance doxorubicin-based cardiotoxicity. We, however, demonstrated that, although heart cells express a high level of TRPV2 mRNA, the expression of the TRPV2 protein in heart cells was barely detectable. Importantly, we also did not detect the expression of TRPV2 protein in liver cells.

Several explanations can be provided for the difference in expression of TRPV2 at the mRNA and protein levels. Accumulating evidence shows a weak correlation between mRNA and protein levels. Different post-transcriptional regulatory mechanisms involving cis-acting and trans-acting mechanisms generate different systems that enhance or repress the synthesis of proteins from a certain copy number of mRNA molecules (Maier et al., 2009). Moreover, mRNA levels do not always correlate with the relative expression of TRP channels at the protein level or in their functional state (Vandewauw et al., 2013). Therefore, while mRNA expression values are used in the diagnosis and classification of cancers, the abundance of proteins and their interactions are far more critical in determining cellular functionality (Greenbaum et al., 2003). However, it is noteworthy that, in order to retain normalization of the liver and heart cells, we used here normal liver and heart tissue and compared the TRPV2 expression between cell line (hepatocellular carcinoma) and these tissues. Such a comparison between cell lines and cultures tissues can by itself cause discrepancies.

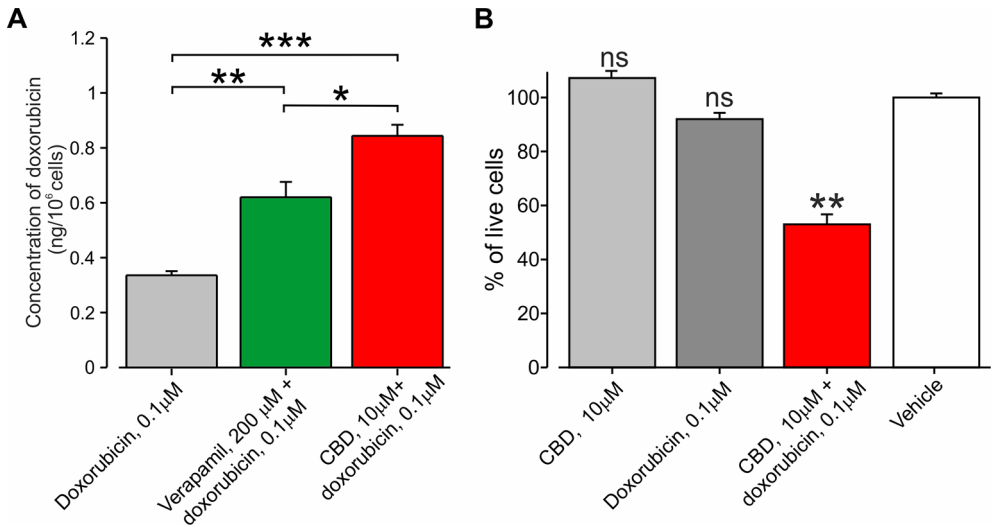

FIGURE 6 | Co-application of doxorubicin with CBD led to an increased amount of intracellular doxorubicin and increased cell death. **(A)** The concentration of doxorubicin in BNL1 ME cells (in ng/10^6 cells; *see Methods*) following a 24-h treatment with 0.1 μM doxorubicin alone, 0.1 μM doxorubicin together with 200 μM verapamil, or 0.1 μM doxorubicin together with 10 μM CBD, measured using fluorometric analysis; n = 3 repetitions for each time point for each treatment group. **(B)** Live-cell fluorescence measurements from cultured BNL1 ME cells treated for 24 h with 10 μM CBD alone, 0.1 μM doxorubicin alone or co-application of 10 μM. CBD, and 0.1 μM doxorubicin. Note that only the co-application of CBD with doxorubicin produced a significant decrease in the number of living cells. *$p < 0.05$, **$p < 0.01$, ***$p < 0.001$, ns, not significant; one-way ANOVA, comparison between the vehicle to all other groups, n = 6 wells for each group, three repetitions.

To activate TRPV2 channels, we used the well-known activators of TRPV2-2-APB (Hu et al., 2004; Juvin et al., 2007) and CBD (Qin et al., 2008). We showed that the application of 2-APB onto BNL1 ME cells leads to Ca^{2+} influx in the presence of thapsigargin only when Ca^{2+} is present in the external solution. This rules out the possibility that 2-APB leads to an increase of intracellular Ca^{2+} *via* intracellular mechanisms. Notably, 2-APB activates mouse and rat TRPV2 channels with different potencies, while the human TRPV2 channel is insensitive to 2-APB when expressed in HEK293 (Neeper et al., 2007). To emphasize on the translational aspect of our findings, we have also examined other activators of TRPV2 and demonstrated that CBD-mediated activation of TRPV2 allows facilitated entry of doxorubicin into BNL1 ME cells. However, neither 2-APB nor CBD are selective TRPV2 agonists, activating other large pore channels (Bisogno et al., 2001; Hu et al., 2004; DeHaven et al., 2008). The similar effects shown here by two separate TRPV2 agonists suggest TRPV2 involvement in facilitated entry of doxorubicin into BNL1 ME cells. At this stage, we cannot exclude other possible mechanisms for doxorubicin penetration.

We show that the effect of 24-h co-treatment of doxorubicin and 2-APB on cell viability led to a decrease of about 70% in the number of living cells, while application of each of the drugs separately did not produce any significant cell death, suggesting a facilitative effect of 2-APB (see **Figure 5D**). However, considering that prolonged treatment with 2-APB or doxorubicin did produce a toxic effect (as shown in **Supplementary Figure 5**), an alternative explanation could be that the 24-h application of 2-APB and/or doxorubicin did not kill the cells but stressed them in a way which was not detected by the live essay. In this case, the cumulative effect of co-application might have led to cell death. Our data showing that the substantial facilitative effect, which was achieved using a relatively less toxic activator, CBD, suggests that the latter explanation is less likely and implies that co-application of TRPV2 activators with doxorubicin leads to facilitative entry of doxorubicin and thus increased BNL1 ME cell death.

The effect of 2-APB and doxorubicin, applied alone, on the cell viability after 48 and 72 h, suggests that that the optimal effect of 2-APB-mediated facilitated entry of doxorubicin on cell vitality is achieved at 24 h after initiation of treatment. Systemic application of doxorubicin reaches maximal concentrations within 30 to 60 min and is cleared very quickly from the organism (Gabizon et al., 2003). Thus, the 24-h facilitative window could be achieved by either prolonged infusion of doxorubicin together with the channel activators or by using slow-released pegylated liposomal doxorubicin (Tahover et al., 2015), paired with prolonged infusion of the channel agonist.

Importantly, according to the human protein atlas database (Uhlen et al., 2015), TRPV2 is highly expressed in many organs, such as endocrine tissues, kidneys, and skin, but not in the liver cells. These data imply that, in translation from our proof-of-concept results to the clinic, local liver application of the treatment would assure a specific effect on hepatocellular carcinoma cells but not an off-target effect of normal liver cells (as they do not express TRPV2 protein), and no other tissues, by virtue of its local application.

Our data from transfected HEK293T cells expressing TRPV2 demonstrate that CBD-mediated activation of TRPV2 channels leads to doxorubicin entry into TRPV2 expressing HEK293T cells *via* the pore of TRPV2 channels, emphasizing that TRPV2 could be utilized as natural drug delivery system. Importantly,

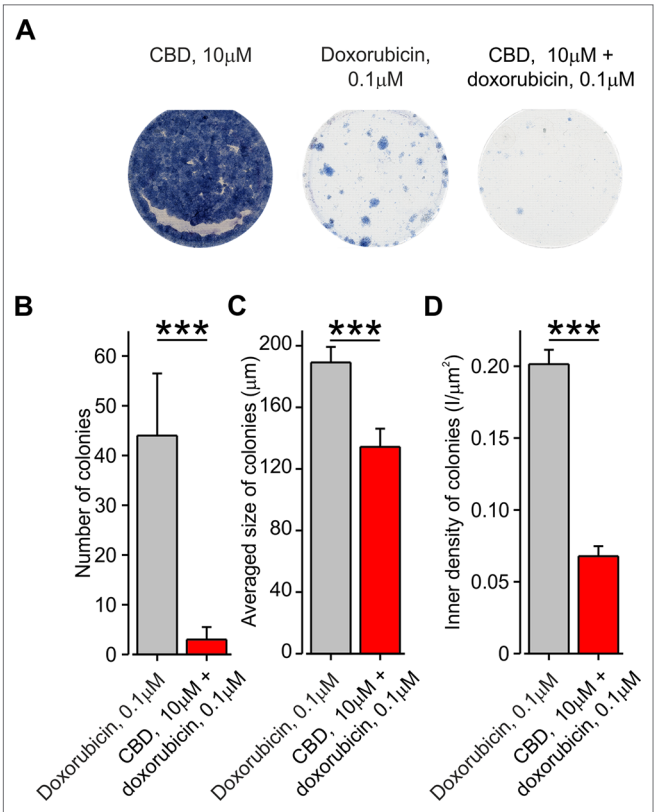

FIGURE 7 | Co-application of doxorubicin with CBD, but not alone, inhibits the formation of BNL1 ME cell colonies. **(A)** A collage image of BNL1 ME cell colonies 24 h after treatment with 10 μM CBD alone (*left*), 0.1 μM doxorubicin (*middle*), and 10 μM CBD with 0.1 μM doxorubicin (*right*). **(B–D)** Bar graphs plotting the number of colonies **(B)**, averaged size of colonies **(C)**, and inner density of colonies **(D)** treated with either 0.1 μM doxorubicin (*gray*) or 10 μM CBD with 0.1 μM doxorubicin (*red*). ***—$p < 0.001$, Student's *t-test*, n = 6 colonies for each treatment.

since CBD is widely used in the clinic (Kogan and Mechoulam, 2007), our results showing CBD-mediated facilitated entry of doxorubicin opens up the possibility of clinical utilization of the platform we describe here.

The observed effect of CBD together with doxorubicin on BNL1 ME cell viability was significantly stronger than the effect of 2-APB together with doxorubicin. We, therefore, assumed that CBD might have an additional facilitative effect on tumor cell death. We ruled out an effect of CBD alone on cell viability. Our next assumption was that, in addition to the facilitation of doxorubicin entry, CBD might also affect doxorubicin removal from cells. Indeed, CBD was demonstrated to inhibit the P-gp ATPase, which affects the removal of doxorubicin from the cells (Zhu et al., 2006). Using the well-described P-gp ATPase antagonist verapamil (Cornwell et al., 1987), we show that (1) BNL1 ME cells, similarly to many tumor cells (Kartner et al., 1983), express functional P-gp ATPase, and (2) blockade of P-gp ATPase by verapamil leads to increase in doxorubicin concentration. These results render P-gp ATPase as a possible target for CBD inhibition, thus underlying the substantial effects of previously ineffective 0.1 μM doxorubicin on cell viability. Moreover, our data showing that the application of CBD together with doxorubicin leads to an increase in doxorubicin concentration which was significantly higher than when doxorubicin was co-applied with verapamil emphasizes the importance of CBD-induced, TRPV2-mediated facilitated entry of doxorubicin into BNL1 ME cells.

The effect of TRPV2-mediated entry of doxorubicin on colony survival, in addition to its effects on cell viability, may also be significant in terms of drug resistance to doxorubicin (Broxterman et al., 2009). It is possible that the colonies which survived the application of doxorubicin alone were generated from cells with resistance to doxorubicin. Importantly, these colonies were annulled when doxorubicin was co-applied with CBD, implying that this combined platform could potentially be beneficial against doxorubicin drug resistance. Since P-gp transporter expression was correlated with drug resistance in cancer cells (Kartner et al., 1983), CBD-mediated inhibition of P-gp ATPase could underlie this effect of CBD and doxorubicin on inhibition of cell colonies in addition to TRPV2-mediated entry of doxorubicin.

In summary, we have demonstrated here a platform for facilitated entry of doxorubicin into cancer cells. Such facilitated entry may allow the use of lower doses of the cytotoxic agent minimizing the off-target toxic effects and therefore may allow an improved therapeutic index. The methodology proposed here is based on the biological properties of specific cells harboring large cationic channels. These large-pore cationic channels are expressed at high levels by cancer cells provide a "natural" drug delivery system. This drug delivery system, when activated, could be used to introduce cytotoxic drugs selectively into cancer cells. Thus, our approach suggests a novel method for the delivery of a variety of drugs that are (1) selective to the target cells and (2) will not require complex manipulations of cells or drugs. Another important aspect of the strategy is that it promises to open up a large new chemical space of potential anti-cancer agents (cytotoxic, antiproliferative, as well as anticancer peptides and nucleic acid medicines), i.e., cationic molecules that are poorly cell-permeant, to be effectively introduced by permeation through large cationic channels. The results of our work may provide a basis for the development of novel tools to modulate intracellular signal transduction and metabolic pathways and thereby to treat cancer with significantly fewer side effects and higher efficacy. The data we show, in conjunction with the differential expression profile of large pore cation non-selective channels, as seen in the human protein atlas database (Uhlen et al., 2015), and data related to differential expression of these channels in cancer cells (*de novo*, expression, upregulation, or downregulation; *see for example* Shapovalov et al., 2016), would suggest that the translation of our platform is not trivial. It implies the need for careful profiling when considering this strategy for different cancers.

DATA AVAILABILITY STATEMENT

The raw data supporting the conclusions of this manuscript will be made available by the authors, without undue reservation, to any qualified researcher.

AUTHOR CONTRIBUTIONS

Conceptualization, AB; Methodology, AL, YS, RK, AG, AH, and AB; Investigation, HN-R, AS, SL, MM, BK, DS; Writing - Original Draft, HN-R, AL, YS, RK, AG, AH, and AB; Funding Acquisition, AB; Supervision, AB.

FUNDING

Support is gratefully acknowledged from the Deutsch-Israelische Projectkooperation program of the Deutsche Forschungsgemeinschaft (DIP) grant agreement BI 1665/1-1ZI1172/12-1 (HN-R, BK, SL, and AB); the Israeli Science Foundation - grant agreement 1470/17 (HN-R, BK, SL and AB); Rosetrees Foundation A1777 and M139 (AB) and the Marie Curie International Reintegration Grant and Rosetrees Trust (AB).

ACKNOWLEDGMENTS

We want to acknowledge Dr. Sara Eyal for fruitful discussions and help in designing the verapamil experiments.

SUPPLEMENTARY MATERIAL

The Supplementary Material for this article can be found online at: https://www.frontiersin.org/articles/10.3389/fphar.2019.01198/full#supplementary-material

REFERENCES

Bagnyukova, T. V., Serebriiskii, I. G., Zhou, Y., Hopper-Borge, E. A., Golemis, E. A., and Astsaturov, I. (2010). Chemotherapy and signaling: how can targeted therapies supercharge cytotoxic agents? *Cancer Biol. Ther.* 10, 839–853. doi: 10.4161/cbt.10.9.13738

Bean, B. P., Binshtok, A. M., and Woolf, C. J. (2007). Harvard Office of Technology Development: targeting anti-cancer drugs intracellularly *via* TRP channels. http://www.techtransfer.harvard.edu/technologies/tech.php?case=3059.

Binshtok, A. M., Bean, B. P., and Woolf, C. J. (2007). Inhibition of nociceptors by TRPV1-mediated entry of impermeant sodium channel blockers. *Nature* 449, 607–610. doi: 10.1038/nature06191

Binshtok, A. M., Roberson, D. P., Bean, B. P., and Woolf, C. J. (2009a). *Activation of TRPA1 as well as TRPV1 channels by lidocaine allows entry of QX-314 into nociceptors to produce a pain selective sodium channel block*. Chicago, IL: Society for Neuroscience Meeting.

Binshtok, A. M., Gerner, P., Oh, S. B., Puopolo, M., Suzuki, S., Roberson, D. P., et al. (2009b). Coapplication of lidocaine and the permanently charged sodium channel blocker QX-314 produces a long-lasting nociceptive blockade in rodents. *Anesthesiology* 111, 127–137. doi: 10.1097/ALN.0b013e3181a915e7

Bisogno, T., Hanus, L., De Petrocellis, L., Tchilibon, S., Ponde, D. E., Brandi, I., et al. (2001). Molecular targets for cannabidiol and its synthetic analogues: effect on vanilloid VR1 receptors and on the cellular uptake and enzymatic hydrolysis of anandamide. *Br. J. Pharmacol.* 134, 845–852. doi: 10.1038/sj.bjp.0704327

Broxterman, H. J., Gotink, K. J., and Verheul, H. M. (2009). Understanding the causes of multidrug resistance in cancer: a comparison of doxorubicin and sunitinib. *Drug Resist Update* 12, 114–126. doi: 10.1016/j.drup.2009.07.001

Bruix, J., and Sherman, M. (2011). Management of hepatocellular carcinoma: an update. *Hepatology* 53, 1020–1022. doi: 10.1002/hep.24199

Caprodossi, S., Lucciarini, R., Amantini, C., Nabissi, M., Canesin, G., Ballarini, P., et al. (2008). Transient receptor potential vanilloid type 2 (TRPV2) expression in normal urothelium and in urothelial carcinoma of human bladder: correlation with the pathologic stage. *Eur. Urol.* 54, 612–620. doi: 10.1016/j.eururo.2007.10.016

Chatterjee, K., Zhang, J., Honbo, N., and Karliner, J. S. (2010). Doxorubicin cardiomyopathy. *Cardiology* 115 (2), 155–162. doi: 10.1159/000265166

Chen, J., Luan, Y., Yu, R., Zhang, Z., Zhang, J., and Wang, W. (2014). Transient receptor potential (TRP) channels, promising potential diagnostic and therapeutic tools for cancer. *Biosci. Trends* 8, 1–10. doi: 10.5582/bst.8.1

Cornwell, M. M., Pastan, I., and Gottesman, M. M. (1987). Certain calcium channel blockers bind specifically to multidrug-resistant human KB carcinoma membrane vesicles and inhibit drug binding to P-glycoprotein. *J. Biol. Chem.* 262, 2166–2170.

DeHaven, W. I., Smyth, J. T., Boyles, R. R., Bird, G. S., and Putney, J. W., Jr. (2008). Complex actions of 2-aminoethyldiphenyl borate on store-operated calcium entry. *J. Biol. Chem.* 283, 19265–19273. doi: 10.1074/jbc.M801535200

Dobbelstein, M., and Moll, U. (2014). Targeting tumour-supportive cellular machineries in anticancer drug development. *Nat. Rev. Drug Discov.* 13, 179–196. doi: 10.1038/nrd4201

Eubler, K., Herrmann, C., Tiefenbacher, A., Kohn, F. M., Schwarzer, J. U., Kunz, L., et al. (2018). Ca(2+) Signaling and IL-8 secretion in human testicular peritubular cells involve the cation channel TRPV2. *Int. J. Mol. Sci.* 19 (9), 2829. doi: 10.3390/ijms19092829

Ewer, M. S., Martin, F. J., Henderson, C., Shapiro, C. L., Benjamin, R. S., and Gabizon, A. A. (2004). Cardiac safety of liposomal anthracyclines. *Semin. Oncol.* 31, 161–181. doi: 10.1053/j.seminoncol.2004.08.006

Ferry, D. R. (1998). Testing the role of P-glycoprotein expression in clinical trials: applying pharmacological principles and best methods for detection together with good clinical trials methodology. *Int. J. Clin. Pharmacol. Ther.* 36, 29–40.

Fiorio Pla, A., and Gkika, D. (2013). Emerging role of TRP channels in cell migration: from tumor vascularization to metastasis. *Front. Physiol.* 4, 311. doi: 10.3389/fphys.2013.00311

Gabizon, A., Shmeeda, H., and Barenholz, Y. (2003). Pharmacokinetics of pegylated liposomal doxorubicin: review of animal and human studies. *Clin. Pharmacokinet.* 42, 419–436. doi: 10.2165/00003088-200342050-00002

Gabizon, A., Bradbury, M., Prabhakar, U., Zamboni, W., Libutti, S., and Grodzinski, P. (2014). Cancer nanomedicines: closing the translational gap. *Lancet* 384, 2175–2176. doi: 10.1016/S0140-6736(14)61457-4

Gallagher, F. A., Kettunen, M. I., Day, S. E., Hu, D. E., Ardenkjaer-Larsen, J. H., Zandt, R., et al. (2008). Magnetic resonance imaging of pH *in vivo* using hyperpolarized 13C-labelled bicarbonate. *Nature* 453, 940–943. doi: 10.1038/nature07017

Giavazzi, R., Kartner, N., and Hart, I. R. (1984). Expression of cell surface P-glycoprotein by an adriamycin-resistant murine fibrosarcoma. *Cancer Chemother. Pharmacol.* 13, 145–147. doi: 10.1007/BF00257134

Greenbaum, D., Colangelo, C., Williams, K., and Gerstein, M. (2003). Comparing protein abundance and mRNA expression levels on a genomic scale. *Genome Biol.* 4, 117. doi: 10.1186/gb-2003-4-9-117

Hollo, Z., Homolya, L., Davis, C. W., and Sarkadi, B. (1994). Calcein accumulation as a fluorometric functional assay of the multidrug transporter. *Biochim. Biophys. Acta* 1191, 384–388. doi: 10.1016/0005-2736(94)90190-2

Hu, H. Z., Gu, Q., Wang, C., Colton, C. K., Tang, J., Kinoshita-Kawada, M., et al. (2004). 2-aminoethoxydiphenyl borate is a common activator of TRPV1, TRPV2, and TRPV3. *J. Biol. Chem.* 279, 35741–35748. doi: 10.1074/jbc.M404164200

Iwata, Y., Katanosaka, Y., Arai, Y., Komamura, K., Miyatake, K., and Shigekawa, M. (2003). A novel mechanism of myocyte degeneration involving the Ca2+-permeable growth factor-regulated channel. *J. Cell Biol.* 161, 957–967. doi: 10.1083/jcb.200301101

Juvin, V., Penna, A., Chemin, J., Lin, Y. L., and Rassendren, F. A. (2007). Pharmacological characterization and molecular determinants of the activation of transient receptor potential V2 channel orthologs by 2-aminoethoxydiphenyl borate. *Mol. Pharmacol.* 72, 1258–1268. doi: 10.1124/mol.107.037044

Karni, R., Jove, R., and Levitzki, A. (1999). Inhibition of pp60c-Src reduces Bcl-XL expression and reverses the transformed phenotype of cells overexpressing EGF and HER-2 receptors. *Oncogene* 18, 4654–4662. doi: 10.1038/sj.onc.1202835

Karni, R., de Stanchina, E., Lowe, S. W., Sinha, R., Mu, D., and Krainer, A. R. (2007). The gene encoding the splicing factor SF2/ASF is a proto-oncogene. *Nat. Struct. Mol. Biol.* 14, 185–193. doi: 10.1038/nsmb1209

Kartner, N., Riordan, J. R., and Ling, V. (1983). Cell surface P-glycoprotein associated with multidrug resistance in mammalian cell lines. *Science* 221, 1285–1288. doi: 10.1126/science.6137059

Kogan, N. M., and Mechoulam, R. (2007). Cannabinoids in health and disease. *Dialogues Clin. Neurosci.* 9, 413–430.

Kuriyama, S., Masui, K., Kikukawa, M., Sakamoto, T., Nakatani, T., Nagao, S., et al. (1999). Complete cure of established murine hepatocellular carcinoma is achievable by repeated injections of retroviruses carrying the herpes simplex virus thymidine kinase gene. *Gene Ther.* 6, 525–533. doi: 10.1038/sj.gt.3300869

Lal, S., Mahajan, A., Chen, W. N., and Chowbay, B. (2010). Pharmacogenetics of target genes across doxorubicin disposition pathway: a review. *Curr. Drug Metab.* 11, 115–128. doi: 10.2174/138920010791110890

Liberati, S., Morelli, M. B., Amantini, C., Santoni, M., Nabissi, M., Cardinali, C., et al. (2014). Advances in transient receptor potential vanilloid-2 channel expression and function in tumor growth and progression. *Curr. Protein Pept. Sci.* 15, 732–737. doi: 10.2174/1389203715666140704115913

Liu, G., Xie, C., Sun, F., Xu, X., Yang, Y., Zhang, T., et al. (2010). Clinical significance of transient receptor potential vanilloid 2 expression in human hepatocellular carcinoma. *Cancer Gene. Cytogenet.* 197, 54–59. doi: 10.1016/j.cancergencyto.2009.08.007

Lorin, C., Vogeli, I., and Niggli, E. (2015). Dystrophic cardiomyopathy: role of TRPV2 channels in stretch-induced cell damage. *Cardiovasc Res.* 106, 153–162. doi: 10.1093/cvr/cvv021

Maier, T., Guell, M., and Serrano, L. (2009). Correlation of mRNA and protein in complex biological samples. *FEBS Lett.* 583, 3966–3973. doi: 10.1016/j.febslet.2009.10.036

Maruyama, T., Kanaji, T., Nakade, S., Kanno, T., and Mikoshiba, K. (1997). 2APB, 2-aminoethoxydiphenyl borate, a membrane-penetrable modulator of Ins(1,4,5)P3-induced Ca2+ release. *J. Biochem.* 122, 498–505. doi: 10.1093/oxfordjournals.jbchem.a021780

Mizuno, H., Suzuki, Y., Watanabe, M., Sokabe, T., Yamamoto, T., Hattori, R., et al. (2014). Potential role of transient receptor potential (TRP) channels in bladder cancer cells. *J. Physiol. Sci.* 64, 305–314. doi: 10.1007/s12576-014-0319-6

Monet, M., Lehen'kyi, V., Gackiere, F., Firlej, V., Vandenberghe, M., Roudbaraki, M., et al. (2010). Role of cationic channel TRPV2 in promoting prostate cancer migration and progression to androgen resistance. *Cancer Res.* 70, 1225–1235. doi: 10.1158/0008-5472.CAN-09-2205

Nabissi, M., Morelli, M. B., Santoni, M., and Santoni, G. (2013). Triggering of the TRPV2 channel by cannabidiol sensitizes glioblastoma cells to cytotoxic chemotherapeutic agents. *Carcinogenesis* 34, 48–57. doi: 10.1093/carcin/bgs328

Nabissi, M., Morelli, M. B., Amantini, C., Farfariello, V., Ricci-Vitiani, L., Caprodossi, S., et al. (2010). TRPV2 channel negatively controls glioma cell proliferation and resistance to Fas-induced apoptosis in ERK-dependent manner. *Carcinogenesis* 31, 794–803. doi: 10.1093/carcin/bgq019

Neeper, M. P., Liu, Y., Hutchinson, T. L., Wang, Y., Flores, C. M., and Qin, N. (2007). Activation properties of heterologously expressed mammalian TRPV2: evidence for species dependence. *J. Biol. Chem.* 282, 15894–15902. doi: 10.1074/jbc.M608287200

Ogunwobi, O. O., and Liu, C. (2011). Hepatocyte growth factor upregulation promotes carcinogenesis and epithelial-mesenchymal transition in hepatocellular carcinoma *via* Akt and COX-2 pathways. *Clin. Exp Metastasis* 28, 721–731. doi: 10.1007/s10585-011-9404-x

Patil, Y., Shmeeda, H., Amitay, Y., Ohana, P., Kumar, S., and Gabizon, A. (2018). Targeting of folate-conjugated liposomes with co-entrapped drugs to prostate cancer cells *via* prostate-specific membrane antigen (PSMA). *Nanomedicine* 14, 1407–1416. doi: 10.1016/j.nano.2018.04.011

Pottosin, I., Delgado-Enciso, I., Bonales-Alatorre, E., Nieto-Pescador, M. G., Moreno-Galindo, E. G., and Dobrovinskaya, O. (2015). Mechanosensitive Ca(2)(+)-permeable channels in human leukemic cells: pharmacological and molecular evidence for TRPV2. *Biochim. Biophys. Acta* 1848, 51–59. doi: 10.1016/j.bbamem.2014.09.008

Prevarskaya, N., Zhang, L., and Barritt, G. (2007). TRP channels in cancer. *Biochim. Biophys. Acta* 1772, 937–946. doi: 10.1016/j.bbadis.2007.05.006

Puopolo, M., Binshtok, A. M., Yao, G. L., Oh, S. B., Woolf, C. J., and Bean, B. P. (2013). Permeation and block of TRPV1 channels by the cationic lidocaine derivative QX-314. *J. Neurophysiol.* 109, 1704–1712. doi: 10.1152/jn.00012.2013

Qin, N., Neeper, M. P., Liu, Y., Hutchinson, T. L., Lubin, M. L., and Flores, C. M. (2008). TRPV2 is activated by cannabidiol and mediates CGRP release in cultured rat dorsal root ganglion neurons. *J. Neurosci.* 28, 6231–6238. doi: 10.1523/JNEUROSCI.0504-08.2008

Roberson, D. P., Binshtok, A. M., Blasl, F., Bean, B. P., and Woolf, C. J. (2011). Targeting of sodium channel blockers into nociceptors to produce long-duration analgesia: a systematic study and review. *Br. J. Pharmacol.* 164, 48–58. doi: 10.1111/j.1476-5381.2011.01391.x

Roberson, D. P., Gudes, S., Sprague, J. M., Patoski, H. A., Robson, V. K., Blasl, F., et al. (2013). Activity-dependent silencing reveals functionally distinct itch-generating sensory neurons. *Nat. Neurosci.* 16, 910–918. doi: 10.1038/nn.3404

Santoni, G., and Farfariello, V. (2011). TRP channels and cancer: new targets for diagnosis and chemotherapy. *Endocr. Metab. Immune Disord. Drug Targets* 11, 54–67. doi: 10.2174/187153011794982068

Scalori, V., Alessandri, M. G., Giovannini, L., Bertelli, A. A., and Mian, M. (1988). Adriamycin, aclacinomycin and thepirubicin intracardiac distribution examined by fluorescence microscopy. *Chemioterapia* 7, 179–183.

Shapovalov, G., Ritaine, A., Skryma, R., and Prevarskaya, N. (2016). Role of TRP ion channels in cancer and tumorigenesis. *Semin. Immunopathol.* 38, 357–369. doi: 10.1007/s00281-015-0525-1

Shneor, D., Folberg, R., Pe'er, J., Honigman, A., and Frenkel, S. (2017). Stable knockdown of CREB, HIF-1 and HIF-2 by replication-competent retroviruses abrogates the responses to hypoxia in hepatocellular carcinoma. *Cancer Gene Ther.* 24, 64–74. doi: 10.1038/cgt.2016.68

Singal, P. K., and Iliskovic, N. (1998). Doxorubicin-induced cardiomyopathy. *N. Engl. J. Med.* 339, 900–905. doi: 10.1056/NEJM199809243391307

Swain, S. M., Whaley, F. S., and Ewer, M. S. (2003). Congestive heart failure in patients treated with doxorubicin: a retrospective analysis of three trials. *Cancer* 97, 2869–2879. doi: 10.1002/cncr.11407

Tacar, O., Sriamornsak, P., and Dass, C. R. (2013). Doxorubicin: an update on anticancer molecular action, toxicity and novel drug delivery systems. *J. Pharm. Pharmacol.* 65, 157–170. doi: 10.1111/j.2042-7158.2012.01567.x

Tahover, E., Patil, Y. P., and Gabizon, A. A. (2015). Emerging delivery systems to reduce doxorubicin cardiotoxicity and improve therapeutic index: focus on liposomes. *Anticancer Drugs* 26, 241–258. doi: 10.1097/CAD.0000000000000182

Tatsumi, T., Takehara, T., Kanto, T., Kuzushita, N., Ito, A., Kasahara, A., et al. (1999). B7-1 (CD80)-gene transfer combined with interleukin-12 administration elicits protective and therapeutic immunity against mouse hepatocellular carcinoma. *Hepatology* 30, 422–429. doi: 10.1002/hep.510300219

Thastrup, O., Cullen, P. J., Drobak, B. K., Hanley, M. R., and Dawson, A. P. (1990). Thapsigargin, a tumor promoter, discharges intracellular Ca2+ stores by specific inhibition of the endoplasmic reticulum Ca2(+)-ATPase. *Proc. Natl. Acad. Sci. U. S. A.* 87, 2466–2470. doi: 10.1073/pnas.87.7.2466

Uhlén M., Fagerberg L., Hallström B.M., Lindskog C., Oksvold P., Mardinoglu A. (2015). Proteomics. Tissue-based map of the human proteome. *Science* 347, 1260419. doi: 10.1126/science.1260419

Vandewauw, I., Owsianik, G., and Voets, T. (2013). Systematic and quantitative mRNA expression analysis of TRP channel genes at the single trigeminal and dorsal root ganglion level in mouse. *BMC Neurosci.* 14, 21. doi: 10.1186/1471-2202-14-21

Watanabe, H., Murakami, M., Ohba, T., Ono, K., and Ito, H. (2009). The pathological role of transient receptor potential channels in heart disease. *Circ J.* 73, 419–427. doi: 10.1253/circj.CJ-08-1153

Webb, B. A., Chimenti, M., Jacobson, M. P., and Barber, D. L. (2011). Dysregulated pH: a perfect storm for cancer progression. *Nat. Rev. Cancer.* 11 (9), 671–677. doi: 10.1038/nrc3110

Zhou, K., Zhang, S. S., Yan, Y., and Zhao, S. (2014). Overexpression of transient receptor potential vanilloid 2 is associated with poor prognosis in patients with esophageal squamous cell carcinoma. *Med. Oncol.* 31, 17. doi: 10.1007/s12032-014-0017-5

Zhu, H. J., Wang, J, S., Markowitz, J. S., Donovan, J, L., Gibson, B. B, Gefroh, H. A, Devane, C. L. (2006). Characterization of P-glycoprotein inhibition by major cannabinoids from marijuana. *J. Pharmacol. Exp. Ther*. 317, 850–857.

Conflict of Interest: The authors declare that the research was conducted in the absence of any commercial or financial relationships that could be construed as a potential conflict of interest.

frontiers in Pharmacology

MINI REVIEW
published: 13 December 2019
doi: 10.3389/fphar.2019.01487

Modulation of Transient Receptor Potential C Channel Activity by Cholesterol

*Rita Gutorov[1], Maximilian Peters[1], Ben Katz[1], Tal Brandwine[1], Nicolas A. Barbera[2], Irena Levitan[2] and Baruch Minke[1]**

[1] *Institute for Medical Research Israel-Canada (IMRIC), Edmond and Lily Safra Center for Brain Sciences (ELSC), Faculty of Medicine, The Hebrew University, Jerusalem, Israel,* [2] *Division of Pulmonary, Critical Care, Sleep and Allergy, Department of Medicine, University of Illinois at Chicago, Chicago, IL, United States*

Changes of cholesterol level in the plasma membrane of cells have been shown to modulate ion channel function. The proposed mechanisms underlying these modulations include association of cholesterol to a single binding site at a single channel conformation, association to a highly flexible cholesterol binding site adopting multiple poses, and perturbation of lipid rafts. These perturbations have been shown to induce reversible targeting of mammalian transient receptor potential C (TRPC) channels to the cholesterol-rich membrane environment of lipid rafts. Thus, the observed inhibition of TRPC channels by methyl-β-cyclodextrin (MβCD), which induces cholesterol efflux from the plasma membrane, may result from disruption of lipid rafts. This perturbation was also shown to disrupt multimolecular signaling complexes containing TRPC channels. The *Drosophila* TRP and TRP-like (TRPL) channels belong to the TRPC channel subfamily. When the *Drosophila* TRPL channel was expressed in S2 or HEK293 cells and perfused with MβCD, the TRPL current was abolished in less than 100 s, fitting well the fast kinetic phase of cholesterol sequestration experiments in cells. It was thus suggested that the fast kinetics of TRPL channel suppression by MβCD arise from disruption of lipid rafts. Accordingly, lipid raft perturbation by cholesterol sequestration could give clues to the function of lipid environment in TRPC channel activity and its mechanism.

Keywords: TRP-like (TRPL) channel, lipid rafts, methyl-β-cyclodextrin, cholesterol recognition amino acid consensus sequence (CRAC), caveolae

OPEN ACCESS

Edited by:
Moran Rubinstein, Tel Aviv University, Israel

Reviewed by:
Bernard Attali, Tel Aviv University, Israel
Ehud Ohana, Ben-Gurion University of the Negev, Israel

****Correspondence:***
Baruch Minke
baruchm@ekmd.huji.ac.il

Specialty section:
This article was submitted to Pharmacology of Ion Channels and Channelopathies, a section of the journal Frontiers in Pharmacology

Received: *28 August 2019*
Accepted: *15 November 2019*
Published: *13 December 2019*

Citation:
Gutorov R, Peters M, Katz B, Brandwine T, Barbera NA, Levitan I and Minke B (2019) Modulation of Transient Receptor Potential C Channel Activity by Cholesterol. Front. Pharmacol. 10:1487. doi: 10.3389/fphar.2019.01487

INTRODUCTION

Cholesterol molecules are intercalated among the phospholipids of cell membrane forming an integral part of the plasma membrane, which is essential for the proper function of ion channels. Plasma membrane cholesterol includes domains known as lipid rafts (Pike, 2006). However, cholesterol is located in both rafts and non-raft fractions.

An efficient method to modulate the content of plasma membrane cholesterol is by methyl-β-cyclodextrin (MβCD), which is a cyclic oligosaccharide (Ohtani et al., 1989; Davis and Brewster, 2004). The β-cyclodextrins (seven glucose units) have high affinity for encapsulating cholesterol (Ohtani et al., 1989). MβCD is quite specific for cholesterol, allowing enrichment or a relatively rapid sequestration of cholesterol from living cells. Cholesterol-saturated MβCD is efficient as cholesterol donor. The degree of cholesterol enrichment is between ~30% to ~threefold, according to the type

of cell (Christian et al., 1997; Levitan et al., 2000). When cells are incubated with high concentration of "empty" MβCD (5–10 mM) for hours (> 2 h), 80–90% of total cellular cholesterol can be sequestered (Kilsdonk et al., 1995; Levitan et al., 2000). The amount of cholesterol sequestration from different cell types is a highly variable parameter (Matthews et al., 1985; Kilsdonk et al., 1995; Christian et al., 1997; Niu et al., 2002). Cholesterol sequestration leads to dis-association of proteins from lipid rafts (Scheiffele et al., 1997; Kabouridis et al., 2000; Predescu et al., 2005) and to decrease in clustering of raft-associated molecules (Harder et al., 1998). Cholesterol depletion also disrupts caveolae structure; it does not result in the disappearance of caveolin but leads to a shift of caveolin from raft to non-raft fractions (Hissa et al., 2017) and to ruffling (Grimmer et al., 2002). It was shown that βCDs sequestered cholesterol from both cholesterol-rich and cholesterol-poor membrane domains (Ottico et al., 2003; Gaus et al., 2005; Rouquette-Jazdanian et al., 2006; Tikku et al., 2007).

In this mini-review, we discuss physiological effects of modulating plasma membrane cholesterol. We focus on modulations of transient receptor potential C (TRPC) channels activity following application MβCD, with emphasis on fast modulations (in less than 100 s).

THE KINETICS OF CHOLESTEROL REMOVAL BY MβCD

Cholesterol sequestration by βCD from several cell types revealed bi-exponential kinetics, when monitored with radiolabeled [H^3] cholesterol: a fast (τ 1/2 of 19–23 s) and a slow (τ 1/2 of 15–30 min) kinetics, suggesting the existence of two separate pools of cholesterol (Yancey et al., 1996). It was further suggested that the "fast" pool of cholesterol corresponds to the outer leaflet of the plasma membrane, while the identity of the slow pool was unclear (Yancey et al., 1996). Recently, imaging studies showed that cholesterol level in the inner leaflet of the plasma membrane was ~12-fold smaller than cholesterol concentration in the outer leaflet (Liu et al., 2017). Interestingly, two pools of MβCD extracts were observed, with half-lives similar to those reported previously (Yancey et al., 1996; Haynes et al., 2000). However, it was also found that the slower cholesterol efflux (from the "slow" pool) was absent from energy-depleted cells (Hao et al., 2002).

The existence of a fast-modulated pool of cholesterol is important for the interpretation of studies showing fast responses of ion channels to modulations of cholesterol (see below). Unfortunately, most studies used prolonged incubations of cells and tissues with cyclodextrins, thus precluding the ability to observe fast kinetics of cholesterol modulations.

MODULATION OF MAMMALIAN TRPC CHANNEL ACTIVITY BY CHOLESTEROL

Cholesterol-ion channels interactions have been studied both computationally and experimentally. Earlier studies identified two types of cholesterol binding motifs: the cholesterol consensus motif (CCM) and the cholesterol recognition amino acid consensus sequence (CRAC), as well as the so-called CARC motif, in which the amino acid sequence appears in reverse. These motifs have been found in many ion channels, such as nicotinic acetylcholine receptor (nAChR), BK, P2X7, Kv1.3, as well as TRPV1 channels (Picazo-Juárez et al., 2011; Singh et al., 2012; Balajthy et al., 2017; Murrell-Lagnado, 2017). However, a recent analysis of the solved crystal structures of 24 cholesterol–protein complexes with 38 distinct cholesterol binding sites showed that fewer than 40% of these sites contained a CRAC or CARC motif, indicating that these motifs at best form only a subset of potential cholesterol binding sites (Rosenhouse-Dantsker, 2017). Furthermore, the relatively loose definition of the motif, (L/V)-X_{1-5}-(Y)-X_{1-5}-(K/R), where X can be one to five residues of any kind, has raised concerns about the predictive nature of the motif and the risk of identifying false positives (Epand, 2006; Jaipuria et al., 2018). Notably, while for many channels, there is little or no experimental confirmation for cholesterol interacting with these motifs, it was shown that a CRAC motif has a significant effect on cholesterol modulation of TRPV1 channel activity (Picazo-Juárez et al., 2011).

Because the above cholesterol binding motifs represent only a subset of potential cholesterol binding sites, there is a risk in using this approach. Consequently, more recent strategies for identifying binding sites have utilized computational approaches such as docking analyses and molecular dynamics simulations to identify potential sites in an unbiased manner. In particular, cholesterol binding sites were identified on nAChR, as well as on inwardly rectifying potassium (Kir) channels, voltage-dependent anion channel (VDAC), and $GABA_A$ receptors (Brannigan et al., 2008; Rosenhouse-Dantsker et al., 2013; Hénin et al., 2014; Weiser et al., 2014). In these studies, docking analyses were first used to predict a set of candidate binding sites, which were then refined through short atomistic simulations and tested experimentally. Importantly, these binding sites did not contain the previously described cholesterol binding motifs. A limitation of this approach, however, is that atomistic simulations usually are not long enough to observe the dynamic behavior of the cholesterol molecule moving from the bilayer to the binding site. This limitation is addressed most recently, with the development of coarse-grained force fields such as the Martini force field, long (μs) time-scale simulations of membrane proteins allowing for the dynamic binding and unbinding of cholesterol to target proteins, providing deeper insight into the mechanisms of cholesterol regulation (Cang et al., 2013; Genheden et al., 2017; Rouviere et al., 2017; Barbera et al., 2018). Using these approaches, most recent studies discovered that in contrast to most other ligands, cholesterol binding is highly flexible and cholesterol dynamically explores its binding site, adopting multiple poses in a "cloud," rather than occupying a single conformation (Gimpl, 2016; Genheden et al., 2017; Rouviere et al., 2017; Barbera et al., 2018). Recently electron cryo-microscopy structure of zebra fish TRPC4 ($TRPC4_{DR}$) channel in its unliganded closed state, at an overall resolution of 3.6 Å was published (Vinayagam et al., 2018). The transmembrane S1–S6 helices structure revealed that in the pre-S1 elbow domain inside the membrane, a cavity is formed with helices S1 and S4, in which a density corresponding to a sterol is formed (**Figure 1**). Since the authors added cholesteryl hemisuccinate (CHS) during the purification of $TRPC4_{DR}$, they

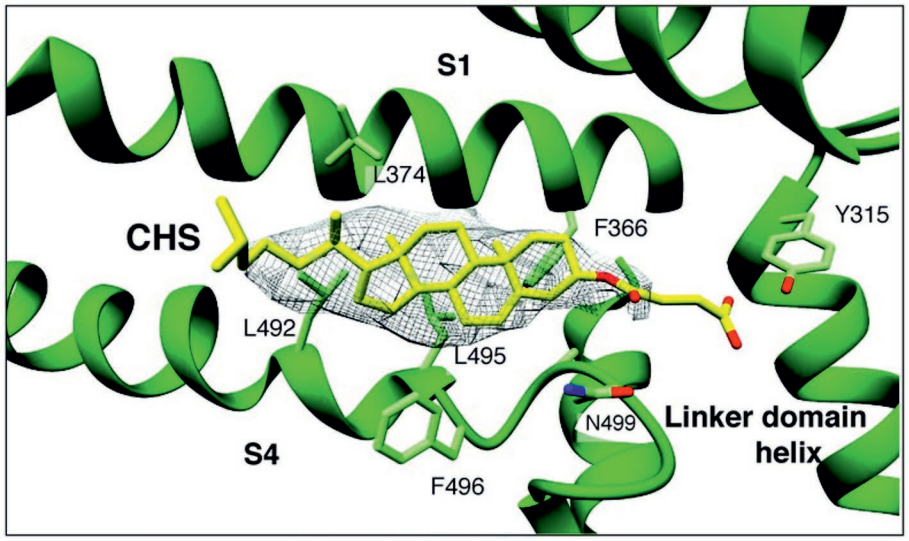

FIGURE 1 | A sterol binding pocket in the $TRPC4_{DR}$ structure. Electron cryo-microscopy structure of zebra fish TRPC4 ($TRPC4_{DR}$) channel in its unliganded closed state, at an overall resolution of 3.6 Å. The transmembrane S1–S6 helices structure revealed that in the pre-S1 elbow domain inside the membrane, a cavity is formed with helices S1 and S4, in which a density corresponding to a sterol is formed. (Reproduced from Vinayagam et al. (2018) with permission from eLife.)

fitted this molecule into the density. This density in the S1–S4 cavity is consistent with the above notion that sterol binding to channel proteins is flexible.

Cholesterol changes in the plasma membrane of cells have been shown to modulate ion channels function, and these modulations include perturbation of specific lipid environments. Experimental observations have suggested reversible targeting of mammalian TRPC channels to cholesterol-rich membrane environment of lipid rafts. This led to the suggestion that the observed inhibition of mammalian TRPC channels by MβCD-inducing cholesterol efflux may result in part from disruption of lipid rafts, including disruption of multimolecular signaling complexes (Svobodova and Groschner, 2016). Below we give examples for the role of lipid rafts in several types of TRPC channels.

TRPC1

The mammalian TRPC1 was shown to interact with caveolin-1 (Cav-1), which is a scaffolding protein that binds cholesterol (Lockwich et al., 2000). This interaction is mediated *via* both N-terminal Cav-1 binding motif and C-terminal Cav-scaffolding consensus. The important role of caveolae in TRPC1 activation was supported by the finding that TRPC1 activity was dependent on Cav-1 (Murata et al., 2007), while TRPC1 was found mainly in caveolae (Lockwich et al., 2000). The experiments indicated that TRPC1 mainly resides in lipid rafts and exposed to the cholesterol-rich membrane of caveolae (Lockwich et al., 2000). Inhibition of TRPC1 currents by MβCD-induced cholesterol sequestration may result from both disruption of lipid raft architecture, including impaired local assembly of signaling molecules, and inhibition of a gating mechanism. The above two effects of cholesterol on TRPC1 function (i.e. disruption of lipid raft architecture and inhibition of a gating mechanism) was demonstrated for several cell types (Bergdahl et al., 2003; Brownlow and Sage, 2005; Kannan et al., 2007).

TRPC3

Cholesterol sensitivity of the TRPC3 channel was demonstrated by using acute administration of cholesterol-saturated MβCD to modify membrane cholesterol content. Cholesterol application elevated conductance in TRPC3-expressing HEK293 cell culture. The membrane conductance derived from I–V curves was typical for phospholipase C (PLC)–mediated TRPC3 currents, showing fast rise time of several seconds. Thus, increased cholesterol concentrations induced a relatively fast TRPC3-mediated current in HEK293 cells (Graziani et al., 2006). Surface biotinylation experiments revealed a significant increase of TRPC3 level at the plasma membrane caused by cholesterol addition. This result suggests that TRPC3-mediated current and the ensuing Ca^{2+} influx that were induced by cholesterol elevation may resulted from a cholesterol-induced expression of TRPC3 in the surface membrane (Graziani et al., 2006).

Like TRPC1, the TRPC3 channels reside in caveolae. The significance of caveolae in mediating inositol 1,4,5 trisphosphate (IP_3)–induced non-selective cation current (I_{Cat}) activation and arterial smooth muscle constriction was studied in smooth muscles of cerebral arteries (Adebiyi et al., 2011). Immunoprecipitation and immunoFRET experiments revealed that Cav-1, TRPC3, and IP_3 receptor1 (IP_3R1-1) formed a multimolecular signaling complex *via* Cav-1 scaffolding domain that was reversibly disrupted by MβCD and by a peptide with Cav-1 scaffolding domain. These experiments revealed close association of the signaling proteins in smooth muscles of cerebral arteries. In other experiments, caveolae disassembly was obtained by: (1) MβCD, (2) Cav-1 knockdown using RNAi, or (3)

application of Cav-1 scaffolding domain. Caveolae disassembly inhibited the I_{Cat} currents and vasoconstriction. The data thus indicated that the multimolecular signaling complex *via* Cav-1 scaffolding domain allowed signal-induced vasoconstriction (Adebiyi et al., 2011).

TRPC6

Podocytes are multipolar cells that cover the external surface of glomerular capillaries and form an essential component of the kidney ultrafiltration apparatus (Pavenstädt et al., 2003). Importantly, in order for podocytes to respond to distending forces, their Ca^{2+}-dependent contractile elements must be coupled to a Ca^{2+} signaling pathway. The major source of regulated Ca^{2+} influx into podocytes is Ca^{2+}-permeable TRPC6 channel, which like other mammalian TRPC channels are activated *via* PLC-mediated signaling cascade (Dryer and Reiser, 2010; Katz et al., 2017). Several mutations in the TRPC6 channel result in autosomal-dominant nephrotic syndromes (Reiser et al., 2005; Winn et al., 2005; Heeringa et al., 2009). Podocin is a cholesterol binding protein, which interacts, in a still unclear manner, with the TRPC6 channel (Reiser et al., 2005; Huber et al., 2006). The ability of podocin, which resides in lipid raft domains (Lei et al., 2014), to bind cholesterol may be central to TRPC6 gating (Huber et al., 2006). Inhibition of TRPC6 channels by application of MβCD or by expression of dominant-negative Cav-1 isoform indicated that TRPC6 activation requires lipid rafts regions at the surface membrane (Lei et al., 2014), suggesting that podocin coordinates TRPC6 channel activity (Anderson et al., 2013).

FAST INHIBITION OF THE *DROSOPHILA* TRP-LIKE CHANNEL ACTIVITY BY MβCD

The *Drosophila* light-sensitive TRP and TRP-like (TRPL) channels are the first members of the TRPC subfamily that were discovered (review Katz et al., 2017). It is well established that the TRP/TRPL channels are the target of the rhodopsin-activated-phosphoinositide cascade, which leads to production of lipids that may function as second messenger in a variety of cells and tissues. Cyclodextrins, both α-cyclodextrin and MβCD, are known to sequester phospholipids (Ohtani et al., 1989) that are involved directly or indirectly in gating of TRPC channels.

Light activation of PLC in *Drosophila* photoreceptors leads to the formation of diacylglycerol (DAG) and IP_3, which are then recycled back to form *phosphatidylinositol 4,5-bisphosphate* [PtdIns(4,5)P_2, designated the phosphoinositide (PI) cycle, **Figure 2A**). The mechanism by which the PI cycle activates the TRP/TRPL channels is not entirely clear (e.g. see Hardie, 2003). Nevertheless, the involvement of lipids in TRP/TRPL channel activation may account for the effects of MβCD on the TRPL channel (see below).

To characterize the *Drosophila* light-sensitive channels, TRPL channels were expressed in tissue-cultured S2 (Hardie et al., 1997; Chyb et al., 1999; Parnas et al., 2009; Lev et al., 2012b; Peters et al., 2017) and HEK293 cells (Hambrecht et al., 2000; Lev et al., 2012b; Peters et al., 2017). TRPL channels expressed in the *Drosophila* S2 cells showed basal activity that could be amplified by polyunsaturated fatty acid [PUFA, e.g. linoleic acid (LA), Lev and Minke, 2010; Lev et al., 2012a; Lev et al., 2012b]. The pronounced basal TRPL current obtained at positive voltage was virtually abolished by MβCD, in less than 100 s (**Figures 2B–D**). This quick effect of cholesterol sequestration is in marked contrast to the previously shown slow effect (of many minutes) of cholesterol sequestration (Singh et al., 2011). Inhibition of the TRPL current persisted long after removal of MβCD, excluding direct inhibition of TRPL by MβCD (**Figure 2C**). In further experiments, cholesterol was first depleted by means of MβCD in S2 cells expressing TRPL; then the excess of MβCD was washed out, and the cells were perfused with the TRPL channel activator LA. This protocol initially resulted, as expected, in reduction of TRPL currents (see **Figure 2**), but surprisingly, LA could activate the TRPL channels independent of MβCD. These results suggest that in S2 cells, MβCD does not affects the TRPL channels directly but affected G-protein coupled related signaling proteins upstream of TRPL in the cascade. Also, it is possible that cholesterol and LA share common mechanism of action, or that LA activation does not require cholesterol for its action.

To further examine at what stage of the transduction cascade MβCD operates, we expressed the Pleckstrin Homology domain of PLC-δ attached to the green fluorescent protein (GFP) in tissue culture cells. The Pleckstrin Homology domain, which binds specifically PtdIns(4,5)P_2 (and IP_3), marks plasma membrane PtdIns(4,5)P_2 in living cells (Balla and Varnai, 2002; Suh et al., 2006; Lev et al., 2012b). Since it is technically difficult to perform these experiments in S2 cells, HEK293 cells were used. In HEK293 cells expressing TRPL, no basal (constitutive) TRPL current was observed [(**Figure 3A**), unlike the situation in S2 cells (**Figures 2B, C**, Lev et al., 2012a)]. Under control conditions, the Pleckstrin Homology domain–GFP was associated with PtdIns(4,5)P_2 of the surface membrane (**Figures 3C–H**). However, when PtdIns(4,5)P_2 concentrations were reduced [e.g. by PLC-dependent hydrolysis of PtdIns(4,5)P_2], the GFP-associated peptide diffused to the cell body (**Figures 3C–H**). PLC was activated by the expressed muscarinic receptor (hM1, which was activated by carbachol, CCH, **Figures 3C, D**), before (**Figure 3C**) and after application of MβCD (**Figure 3D**). These experiments showed that MβCD had no effect on PtdIns(4,5)P_2 hydrolysis by PLC, thus indicating that inhibition of TRPL-dependent current by cholesterol sequestration takes place after activation of PLC in the transduction cascade in HEK293 cells. Strikingly, application of LA, which is a highly potent activator of the TRPL channels, acting directly on the channels (Parnas et al., 2009) had virtually no effect (**Figure 3B**). Thus, in HEK293 cells, LA applied after response suppression by MβCD had virtually no effect on TRPL channel activity, suggesting that in HEK293 cells unlike S2 cells, cholesterol depletion suppress directly TRPL channel activation.

CONCLUSION

Cholesterol molecules are essential for the proper function of ion channels, including TRPC channels. Sequestration of cholesterol by MβCD from the plasma membrane of cells expressing TRPC

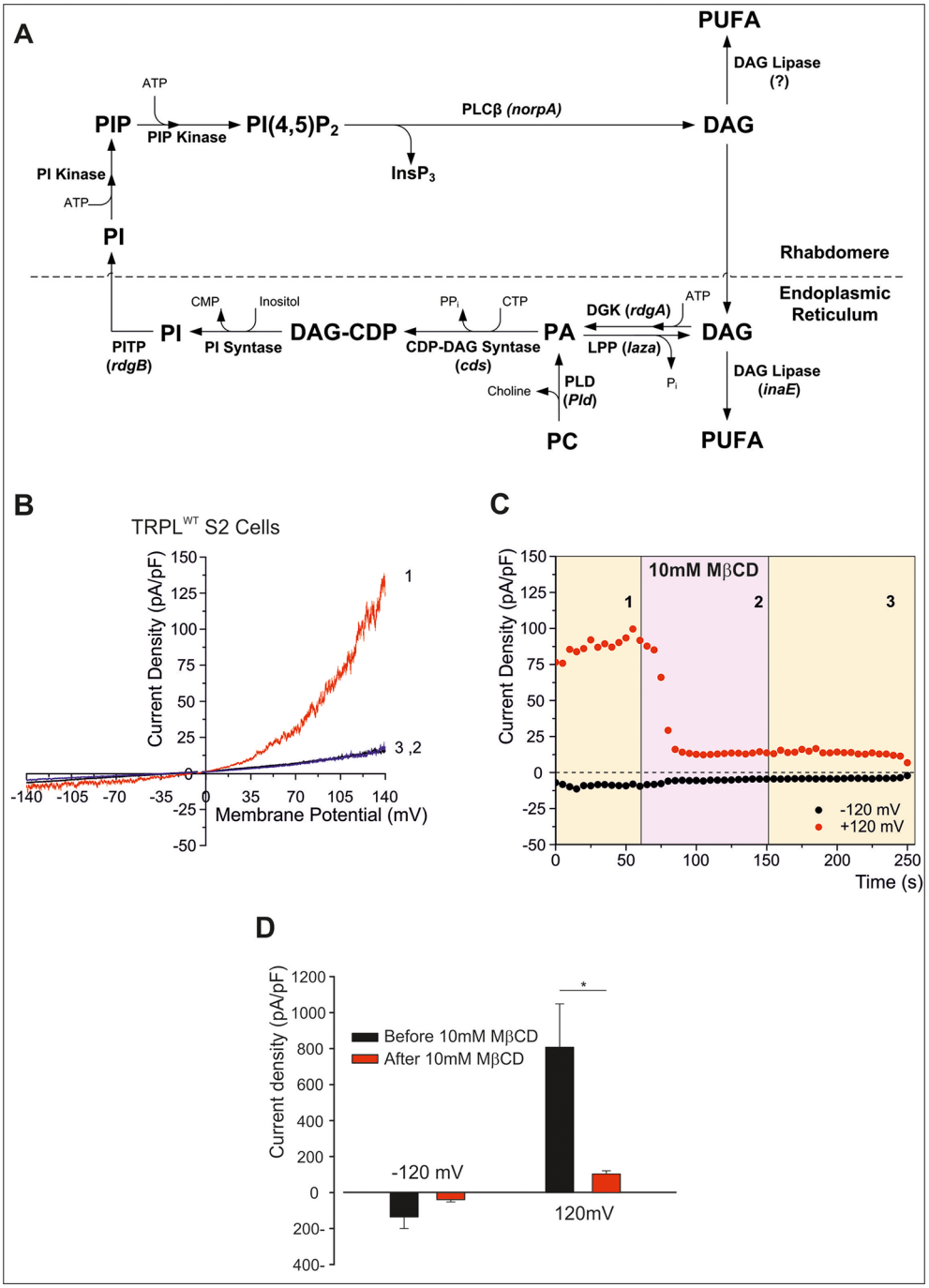

FIGURE 2 | (A) *The phosphoinosite (PI) cycle*. In the phototransduction cascade, light triggers the activation of phospholipase Cβ (PLCβ, encoded by *norpA*). This catalyzes hydrolysis of the membrane phospholipid $PI(4,5)P_2$ (PIP_2) into IP_3 and diacylglycerol (DAG). DAG is transported by endocytosis to the endoplasmic reticulum and inactivated by phosphorylation converting it into phosphatidic acid (PA) *via* DAG kinase (DGK, encoded by *rdgA*) and to CDP-DAG *via* CDP-DAG synthase. Subsequently, CDP-DAG is converted into phosphatidyl inositol (PI), which is transferred back to the microvillar membrane, by the PI transfer protein (encoded by *rdgB*). PIP and PIP_2 are produced at the microvillar membrane by PI kinase and PIP kinase, respectively. PA can also be converted back to DAG by lipid phosphate phosphohydrolase (Lpp, encoded by laza). PA is also produced from phosphatidyl choline (PC) by phospholipase D (PLD). DAG is also converted in two enzymatic stages, one of them is by DAG lipase (encoded by *inaE*), into polyunsaturated fatty acids (PUFAs). **(B–D)** *MβCD blocks constitutive TRPL channels activity*. **(B)** Current–voltage relationships (I–V curves) measuring TRPL-dependent currents. I–V curves obtained in response to voltage ramp (of 1 s duration) from S2 cells expressing TRPL and showing basal channel activity with strong outward rectification, typical for TRPL-dependent current (1). The TRPL channel activity was highly reduced after perfusion with 10 mM methyl-β-cyclodextrin (MβCD) (2) and the effect was irreversible, even after washout of MβCD (3) (n > 10). **(C)** Time course of the MβCD effects on TRPL currents in S2 cells. Current densities are shown as a function of time. Series of I–V curves were derived from repeatedly applied voltage ramps every 5 s, and currents were measured at ±120 mV holding potentials as a function of time under the various experimental conditions as indicated. The numbers correspond to the numbers on the I–V curves in **(B)**. **(D)** Statistics of the cholesterol depletion experiments in S2 cells. **(A)** Cholesterol depletion by MβCD had a significant effect on the positive TRPL currents at 120 mV (n = 5, values are average ± SEM, paired Student t-test, $*p \leq 0.05$). Reproduced from Katz and Minke, 2009 with permission from Frontiers. **(B–D)** Reproduced from Peters et al., 2017 with permission from Elsevier, license number 4676401165468.)

channels suppressed channel activity. It is still not entirely clear what is the mechanism underlying suppression of TRPC channels activity by MβCD. Possible mechanisms include association of cholesterol to a highly flexible cholesterol binding site or perturbation of specific lipid environments. Mammalian TRPC1 and TRPC6 channels require for their activity binding to scaffold proteins located in cholesterol-rich lipid rafts. For these channels, inhibition resulting from cholesterol sequestration by MβCD possibly resulted from disruption of lipid rafts at the plasma membrane, rather than direct inhibition of a gating mechanism. Nevertheless, channel–cholesterol interactions similar to those reported for Kir channels cannot be excluded. Future availability of atomic structure of TRPC channel subfamilies nanodisks can be very useful to determine the possibility that in contrast

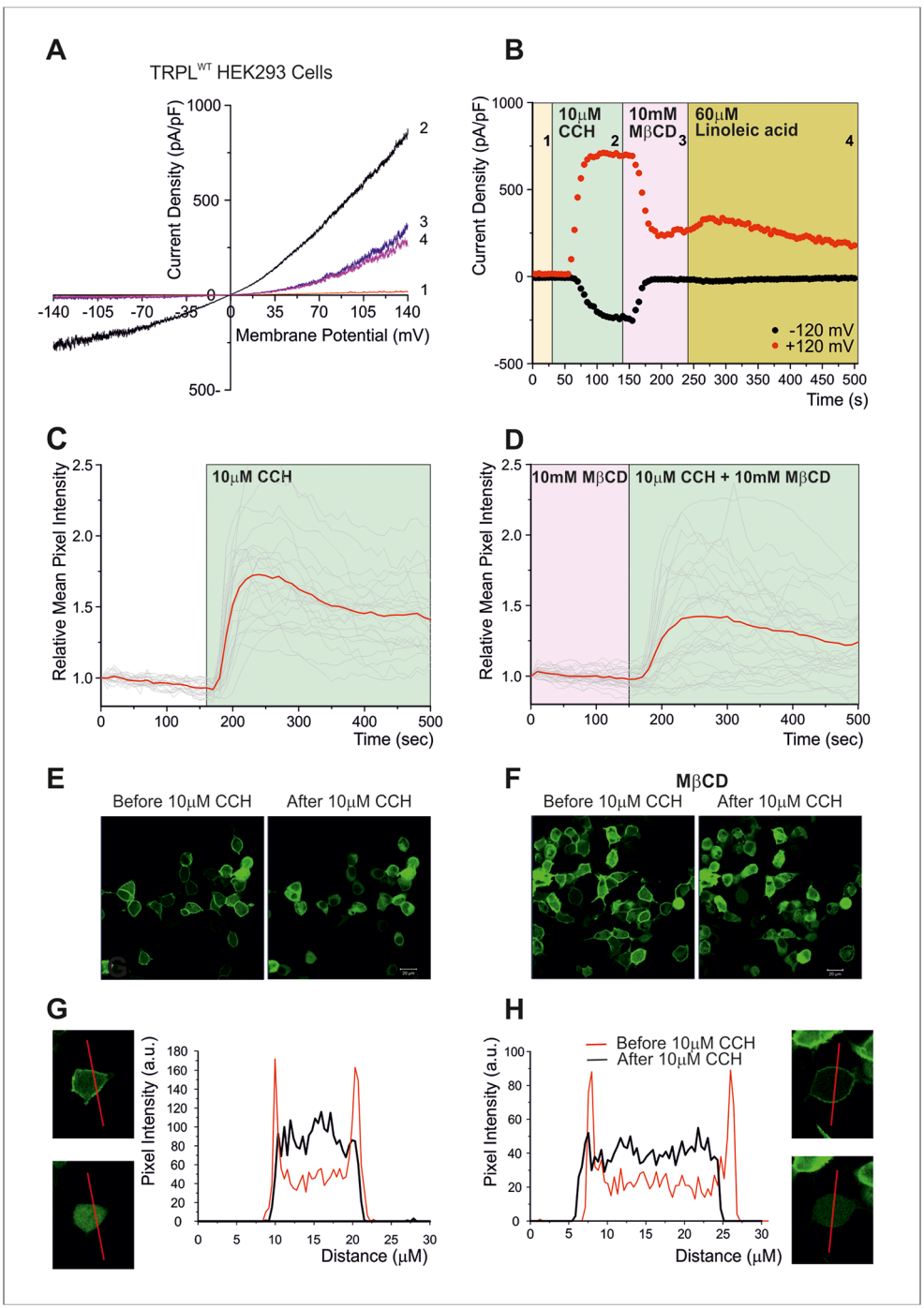

FIGURE 3 | Continued

FIGURE 3 | (A–B) *Cholesterol depletion suppressed receptor-activated TRPL-dependent current.* **(A)** TRP-like–green fluorescent protein (TRPL–GFP) did not show any spontaneous activity in HEK293 cells, but it could be readily activated *via* PLC and blocked by MβCD: current–voltage relationships measured from HEK293 cells expressing TRPL–GFP, showing no basal channel activity (1). However, coexpression of the hM1 muscarinic receptor and application of carbachol (CCH) activated the expressed TRPL–GFP channels *via* endogenous PLC-mediated cascade (2) and the TRPL-dependent current in the presence of CCH was suppressed by application of MβCD (3), while subsequent application of LA, a strong activator of TRPL channels, did not activate the channels after the application of MβCD (4). **(B)** Time course of the receptor-activated TRPL-dependent current and the effect of cholesterol depletion on the receptor-activated TRPL currents in HEK293 cells. Current densities are shown as a function of time. Series of i–V curves were derived from repeatedly applied voltage ramps every 5 s, and currents were measured at ±120 mV holding potentials as a function of time under the various experimental conditions as indicated **(C–H)** *Cholesterol depletion did not affect receptor-induced PLC activity*. No effects of cholesterol depletion on PLC activity as monitored by translocation of the PIP_2 sensor PH–GFP: representative series of multiphoton images of HEK293 cells coexpressing eGFP-tagged PH domain and hM1 receptor. Application of CCH to the bathing solution, in a concentration that activated the TRPL channels (10 μM CCH), induced similar translocation of the eGFP-tagged PH domain to the cell body, with and without MβCD, indicating the PLC-mediated hydrolysis of PIP_2 is not affected by MβCD. **(C)** The time course of fluorescence changes measured in the cytosol before application of MβCD: graph plotting the relative mean pixels' intensity (red curve) as a function of time measured from multiphoton images of HEK293 cells expressing PH–GFP and hM1 receptors. Before PLC stimulation by CCH application (white background), the GFP–PH is associated with the plasma membrane where most PIP_2 is located and the cell body fluorescence is low (for quantification, see **G**, **H**). Once PLC is activated and PIP_2 is hydrolyzed (green background), the PH–GFP translocates to the cytosol and there is a marked increase in fluorescence intensity at the cytosol. The individual single-cell measurements are shown by noisy dim gray traces. **(D)** The time course of fluorescence changes measured in the cytosol after application of MβCD: similar graph as in **(C)**, but measured following application of MβCD. **(E)** Multiphoton images of HEK293 cells expressing PH–GFP and hM1 receptor without application of MβCD: Left: GFP fluorescence of cells before application of CCH, little PH–GFP translocation was observed. Right: GFP fluorescence of cells after perfusion with the M1 agonist CCH. Translocation of PH–GFP is observed. MβCD was not applied (n > 50). **(F)** Multiphoton images of HEK293 cells expressing PH–GFP and hM1 receptor after application of MβCD: Similar images of HEK293 cells expressing TRPL PH–GFP and hM1 receptor before (left) and after application of CCH (right). MβCD was applied, but it did not affect PH–GFP translocation (n > 50). **(G**, **H)** Graphs plotting the PH–GFP fluorescence intensity as a function of cell position: fluorescence intensity of images showing cross sections of two representative cells along the red line, before application of CCH (red curve), and after application of CCH (black curve) in the absence of MβCD **(G)** and after application of MβCD **(H)**. (Reproduced from Peters et al., 2017 with permission from Elsevier, license number 4676401165468.)

to most other ligands, cholesterol binding to TRPC channels is highly flexible and cholesterol dynamically explores its binding site, adopting multiple poses in a "cloud," rather than occupying a single conformation and in this way affects channel gating. For the *Drosophila* TRPL channel, where the gating mechanism of the channel is still unknown, elucidating the mechanism of cholesterol action may help solve the long-standing enigma of channel gating.

AUTHOR CONTRIBUTIONS

RG presented the lecture in the Israel Ion Channel and Transporters Meeting 2019, conducted a wide literature search, drafted the manuscript, and participated in the writing. MP performed the experimental part of the review and conducted part of the literature search. TB conducted part of the literature search. BK participated in the writing and drafting of the manuscript. NB wrote the section on the Computational Approach and inserted the relevant literature. IL covered the Computational Approach, searched for the relevant literature, and participated in the writing. BM initiated the review, drafted the manuscript, and wrote the paper.

ACKNOWLEDGMENTS

This study was supported by the United States–Israel Binational Science Foundation grant no. 2015014 (BM and IL).

REFERENCES

Adebiyi, A., Narayanan, D., and Jaggar, J. H. (2011). Caveolin-1 assembles type 1 inositol 1,4,5-trisphosphate receptors and canonical transient receptor potential 3 channels into a functional signaling complex in arterial smooth muscle cells. *J. Biol. Chem.* 286, 4341–4348. doi: 10.1074/jbc.M110.179747

Anderson, M., Kim, E. Y., Hagmann, H., Benzing, T., and Dryer, S. E. (2013). Opposing effects of podocin on the gating of podocyte TRPC6 channels evoked by membrane stretch or diacylglycerol. *Am. J. Physiol. Cell Physiol.* 305, C276–C289. doi: 10.1152/ajpcell.000952013

Balajthy, A., Hajdu, P., Panyi, G., and Varga, Z. (2017). Sterol Regulation of Voltage-Gated K. *Curr. Top. Membr* 80, 255–292. doi: 10.1016/bs.ctm.2017.05.006

Balla, T., and Varnai, P. (2002). Visualizing cellular phosphoinositide pools with GFP-fused protein-modules. *SciSTKE* L3. 1–17. doi: 10.1126/scisignal.1252002pl3

Barbera, N., Ayee, M. A. A., Akpa, B. S., and Levitan, I. (2018). Molecular dynamics simulations of kir2.2 interactions with an ensemble of cholesterol molecules. *Biophys. J.* 115, 1264–1280. doi: 10.1016/j.bpj.2018.07.041

Bergdahl, A., Gomez, M. F., Dreja, K., Xu, S. Z., Adner, M., Beech, D. J., et al. (2003). Cholesterol depletion impairs vascular reactivity to endothelin-1 by reducing store-operated Ca2+ entry dependent on TRPC1. *Circ. Res.* 93, 839–847. doi: 10.1161/01.RES.0000100367.45446.A3

Brannigan, G., Hénin, J., Law, R., Eckenhoff, R., and Klein, M. L. (2008). Embedded cholesterol in the nicotinic acetylcholine receptor. *Proc. Natl. Acad. Sci. U.S.A.* 105, 14418–14423. doi: 10.1073/pnas.0803029105

Brownlow, S. L., and Sage, S. O. (2005). Transient receptor potential protein subunit assembly and membrane distribution in human platelets. *Thromb. Haemost.* 94, 839–845. doi: 10.1160/TH05-06-0391

Cang, X., Du, Y., Mao, Y., Wang, Y., Yang, H., and Jiang, H. (2013). Mapping the functional binding sites of cholesterol in β2-adrenergic receptor by long-time molecular dynamics simulations. *J. Phys. Chem. B* 117, 1085–1094. doi: 10.1021/jp3118192

Christian, A. E., Haynes, M. P., Phillips, M. C., and Rothblat, G. H. (1997). Use of cyclodextrins for manipulating cellular cholesterol content. *J. Lipid Res.* 38, 2264–2272.

Chyb, S., Raghu, P., and Hardie, R. C. (1999). Polyunsaturated fatty acids activate the Drosophila light-sensitive channels TRP and TRPL. *Nature* 397, 255–259. doi: 10.1038/16703

Davis, M. E., and Brewster, M. E. (2004). Cyclodextrin-based pharmaceutics: past, present and future. *Nat. Rev. Drug Discovery* 3, 1023–1035. doi: 10.1038/nrd1576

Dryer, S. E., and Reiser, J. (2010). TRPC6 channels and their binding partners in podocytes: role in glomerular filtration and pathophysiology. *Am. J. Physiol. Renal Physiol.* 299, F689–F701. doi: 10.1152/ajprenal.002982010

Epand, R. M. (2006). Cholesterol and the interaction of proteins with membrane domains. *Prog. Lipid Res.* 45, 279–294. doi: 10.1016/j.plipres.2006.02.001

Gaus, K., Rodriguez, M., Ruberu, K. R., Gelissen, I., Sloane, T. M., Kritharides, L., et al. (2005). Domain-specific lipid distribution in macrophage plasma membranes. *J. Lipid Res.* 46, 1526–1538. doi: 10.1194/jlr.M500103-JLR200

Genheden, S., Essex, J. W., and Lee, A. G. (2017). G protein coupled receptor interactions with cholesterol deep in the membrane. *Biochim. Biophys. Acta Biomembr.* 1859, 268–281. doi: 10.1016/j.bbamem.2016.12.001

Gimpl, G. (2016). Interaction of G protein coupled receptors and cholesterol. *Chem. Phys. Lipids* 199, 61–73. doi: 10.1016/j.chemphyslip.2016.04.006

Graziani, A., Rosker, C., Kohlwein, S. D., Zhu, M. X., Romanin, C., Sattler, W., et al. (2006). Cellular cholesterol controls TRPC3 function: evidence from a novel dominant-negative knockdown strategy. *Biochem. J.* 396, 147–155. doi: 10.1042/BJ20051246

Grimmer, S., van Deurs, B., and Sandvig, K. (2002). Membrane ruffling and macropinocytosis in A431 cells require cholesterol. *J. Cell Sci.* 115, 2953–2962.

Hénin, J., Salari, R., Murlidaran, S., and Brannigan, G. (2014). A predicted binding site for cholesterol on the GABAA receptor. *Biophys. J.* 106, 1938–1949. doi: 10.1016/j.bpj.2014.03.024

Hambrecht, J., Zimmer, S., Flockerzi, V., and Cavalie, A. (2000). Single-channel currents through transient-receptor-potential-like (TRPL) channels. *Pflugers Arch.* 440, 418–426. doi: 10.1007/s004240000301

Hao, M., Lin, S. X., Karylowski, O. J., Wüstner, D., McGraw, T. E., and Maxfield, F. R. (2002). Vesicular and non-vesicular sterol transport in living cells. The endocytic recycling compartment is a major sterol storage organelle. *J. Biol. Chem.* 277, 609–617. doi: 10.1074/jbc.M108861200

Harder, T., Scheiffele, P., Verkade, P., and Simons, K. (1998). Lipid domain structure of the plasma membrane revealed by patching of membrane components. *J. Cell Biol.* 141, 929–942. doi: 10.1083/jcb.141.4.929

Hardie, R. C., Reuss, H., Lansdell, S. J., and Millar, N. S. (1997). Functional equivalence of native light-sensitive channels in the Drosophila trp 301 mutant and TRPL cation channels expressed in a stably transfected Drosophila cell line. *Cell Calcium* 21, 431–440. doi: 10.1016/S0143-4160(97)90054-3

Hardie, R. C. (2003). Regulation of trp channels via lipid second messengers. *AnnuRevPhysiol* 65, 735–759. doi: 10.1146/annurev.physiol.65.092101.142505

Haynes, M. P., Phillips, M. C., and Rothblat, G. H. (2000). Efflux of cholesterol from different cellular pools. *Biochemistry* 39, 4508–4517. doi: 10.1021/bi992125q

Heeringa, S. F., Möller, C. C., Du, J., Yue, L., Hinkes, B., Chernin, G., et al. (2009). A novel TRPC6 mutation that causes childhood FSGS. *PloS One* 4, e7771. doi: 10.1371/journal.pone.0007771

Hissa, B., Oakes, P. W., Pontes, B., Ramírez-San Juan, G., and Gardel, M. L. (2017). Cholesterol depletion impairs contractile machinery in neonatal rat cardiomyocytes. *Sci. Rep.* 7, 43764. doi: 10.1038/srep43764

Huber, T. B., Schermer, B., Müller, R. U., Höhne, M., Bartram, M., Calixto, A., et al. (2006). Podocin and MEC-2 bind cholesterol to regulate the activity of associated ion channels. *Proc. Natl. Acad. Sci. U.S.A.* 103, 17079–17086. doi: 10.1073/pnas.0607465103

Jaipuria, G., Giller, K., Leonov, A., Becker, S., and Zweckstetter, M. (2018). Insights into Cholesterol/Membrane Protein Interactions Using Paramagnetic Solid-State NMR. *Chemistry* 24, 17606–17611. doi: 10.1002/chem.201804550

Kabouridis, P. S., Janzen, J., Magee, A. L., and Ley, S. C. (2000). Cholesterol depletion disrupts lipid rafts and modulates the activity of multiple signaling pathways in T lymphocytes. *Eur. J. Immunol.* 30, 954–963. doi: 10.1002/1521-4141(200003)30:3<954::AID-IMMU954>3.0.CO;2-Y

Kannan, K. B., Barlos, D., and Hauser, C. J. (2007). Free cholesterol alters lipid raft structure and function regulating neutrophil Ca2+ entry and respiratory burst: correlations with calcium channel raft trafficking. *J. Immunol.* 178, 5253–5261. doi: 10.4049/jimmunol.178.85253

Katz, B., and Minke, B. (2009). Drosophila photoreceptors and signaling mechanisms. (FL: Boca Raton) *Front. Cell Neurosci.* 3, 2. doi: 10.3389/neuro.03.0022009

Katz, B., Payne, R., and Minke, B. (2017). *TRP Channels in Vision* (Boca Raton (FL): CRC Press, Taylor & Francis Group). doi: 10.4324/9781315152837-3

Kilsdonk, E. P., Yancey, P. G., Stoudt, G. W., Bangerter, F. W., Johnson, W. J., Phillips, M. C., et al. (1995). Cellular cholesterol efflux mediated by cyclodextrins. *J. Biol. Chem.* 270, 17250–17256. doi: 10.1074/jbc.270.29.17250

Lei, L., Lu, S., Wang, Y., Kim, T., and Mehta, D. (2014). The role of mechanical tension on lipid raft dependent PDGF-induced TRPC6 activation. *Biomaterials* 35, 2868–2877. doi: 10.1016/j.biomaterials.2013.12.030

Lev, S., and Minke, B. (2010). Constitutive activity of TRP channels methods for measuring the activity and its outcome. *Methods Enzymol.* 484, 591–612. doi: 10.1016/B978-0-12-381298-8.00029-0

Lev, S., Katz, B., and Minke, B. (2012a). The activity of the TRP-like channel depends on its expression system. *Channels (Austin)* 6, 86–93. doi: 10.4161/chan.19946

Lev, S., Katz, B., Tzarfaty, V., and Minke, B. (2012b). Signal-dependent hydrolysis of phosphatidylinositol 4,5-bisphosphate without activation of phospholipase C: implications on gating of Drosophila TRPL (transient receptor potential-like) channel. *J. Biol. Chem.* 287, 1436–1447. doi: 10.1074/jbc.M111.266585

Levitan, I., Christian, A. E., Tulenko, T. N., and Rothblat, G. H. (2000). Membrane cholesterol content modulates activation of volume-regulated anion current in bovine endothelial cells. *J. Gen. Physiol.* 115, 405–416. doi: 10.1085/jgp.115.4.405

Liu, S. L., Sheng, R., Jung, J. H., Wang, L., Stec, E., O'Connor, M. J., et al. (2017). Orthogonal lipid sensors identify transbilayer asymmetry of plasma membrane cholesterol. *Nat. Chem. Biol.* 13, 268–274. doi: 10.1038/nchembio2268

Lockwich, T. P., Liu, X., Singh, B. B., Jadlowiec, J., Weiland, S., and Ambudkar, I. S. (2000). Assembly of Trp1 in a signaling complex associated with caveolin-scaffolding lipid raft domains. *J. Biol. Chem.* 275, 11934–11942. doi: 10.1074/jbc.275.16.11934

Matthews, D. A., Bolin, J. T., Burridge, J. M., Filman, D. J., Volz, K. W., Kaufman, B. T., et al. (1985). Refined crystal structures of Escherichia coli and chicken liver dihydrofolate reductase containing bound trimethoprim. *J. Biol. Chem.* 260, 381–391.

Murata, T., Lin, M. I., Stan, R. V., Bauer, P. M., Yu, J., and Sessa, W. C. (2007). Genetic evidence supporting caveolae microdomain regulation of calcium entry in endothelial cells. *J. Biol. Chem.* 282, 16631–16643. doi: 10.1074/jbc.M607948200

Murrell-Lagnado, R. D. (2017). Regulation of P2X purinergic receptor signaling by cholesterol. *Curr. Top. Membr.* 80, 211–232. doi: 10.1016/bs.ctm.2017.05.004

Niu, S. L., Mitchell, D. C., and Litman, B. J. (2002). Manipulation of cholesterol levels in rod disk membranes by methyl-beta-cyclodextrin: effects on receptor activation. *J. Biol. Chem.* 277, 20139–20145. doi: 10.1074/jbc.M200594200

Ohtani, Y., Irie, T., Uekama, K., Fukunaga, K., and Pitha, J. (1989). Differential effects of alpha-, beta- and gamma-cyclodextrins on human erythrocytes. *Eur. J. Biochem.* 186, 17–22. doi: 10.1111/j.1432-1033.1989.tb15171.x

Ottico, E., Prinetti, A., Prioni, S., Giannotta, C., Basso, L., Chigorno, V., et al. (2003). Dynamics of membrane lipid domains in neuronal cells differentiated in culture. *J. Lipid Res.* 44, 2142–2151. doi: 10.1194/jlr.M300247-JLR200

Parnas, M., Peters, M., and Minke, B. (2009). Linoleic acid inhibits TRP channels with intrinsic voltage sensitivity: implications on the mechanism of linoleic acid action. *Channels (Austin)* 3, 164–166. doi: 10.4161/chan.3.38873

Pavenstädt, H., Kriz, W., and Kretzler, M. (2003). Cell biology of the glomerular podocyte. *Physiol. Rev.* 83, 253–307. doi: 10.1152/physrev.000202002

Peters, M., Katz, B., Lev, S., Zaguri, R., Gutorov, R., and Minke, B. (2017). Depletion of Membrane Cholesterol Suppresses Drosophila Transient Receptor Potential-Like (TRPL) Channel Activity. *Curr. Top. Membr* 80, 233–254. doi: 10.1016/bs.ctm.2017.05.005

Picazo-Juárez, G., Romero-Suárez, S., Nieto-Posadas, A., Llorente, I., Jara-Oseguera, A., Briggs, M., et al. (2011). Identification of a binding motif in the S5 helix that confers cholesterol sensitivity to the TRPV1 ion channel. *J. Biol. Chem.* 286, 24966–24976. doi: 10.1074/jbc.M111.237537

Pike, L. J. (2006). Rafts defined: a report on the Keystone Symposium on Lipid Rafts and Cell Function. *J. Lipid Res.* 47, 1597–1598. doi: 10.1194/jlr.E600002-JLR200

Predescu, S. A., Predescu, D. N., Shimizu, K., Klein, I. K., and Malik, A. B. (2005). Cholesterol-dependent syntaxin-4 and SNAP-23 clustering regulates caveolar fusion with the endothelial plasma membrane. *J. Biol. Chem.* 280, 37130–37138. doi: 10.1074/jbc.M505659200

Reiser, J., Polu, K. R., Möller, C. C., Kenlan, P., Altintas, M. M., Wei, C., et al. (2005). TRPC6 is a glomerular slit diaphragm-associated channel required for normal renal function. *Nat. Genet.* 37, 739–744. doi: 10.1038/ng1592

Rosenhouse-Dantsker, A., Noskov, S., Durdagi, S., Logothetis, D. E., and Levitan, I. (2013). Identification of novel cholesterol-binding regions in Kir2 channels. *J. Biol. Chem.* 288, 31154–31164. doi: 10.1074/jbc.M113.496117

Rosenhouse-Dantsker, A. (2017). Insights into the molecular requirements for cholesterol binding to ion channels. *Curr. Top. Membr* 80, 187–208. doi: 10.1016/bs.ctm.2017.05.003

Rouquette-Jazdanian, A. K., Pelassy, C., Breittmayer, J. P., and Aussel, C. (2006). Revaluation of the role of cholesterol in stabilizing rafts implicated in T cell receptor signaling. *Cell Signal* 18, 105–122. doi: 10.1016/j.cellsig.2005.03.024

Rouviere, E., Arnarez, C., Yang, L., and Lyman, E. (2017). Identification of two new cholesterol interaction sites on the A. *Biophys. J.* 113, 2415–2424. doi: 10.1016/j.bpj.2017.09.027

Scheiffele, P., Roth, M. G., and Simons, K. (1997). Interaction of influenza virus haemagglutinin with sphingolipid-cholesterol membrane domains via its transmembrane domain. *EMBO J.* 16, 5501–5508. doi: 10.1093/emboj/16.185501

Singh, D. K., Shentu, T. P., Enkvetchakul, D., and Levitan, I. (2011). Cholesterol regulates prokaryotic Kir channel by direct binding to channel protein. *Biochim. Biophys. Acta* 1808, 2527–2533. doi: 10.1016/j.bbamem.2011.07.006

Singh, A. K., McMillan, J., Bukiya, A. N., Burton, B., Parrill, A. L., and Dopico, A. M. (2012). Multiple cholesterol recognition/interaction amino acid consensus (CRAC) motifs in cytosolic C tail of Slo1 subunit determine cholesterol sensitivity of Ca2+- and voltage-gated K+ (BK) channels. *J. Biol. Chem.* 287, 20509–20521. doi: 10.1074/jbc.M112.356261

Suh, B. C., Inoue, T., Meyer, T., and Hille, B. (2006). Rapid chemically induced changes of PtdIns(4,5)P2 gate KCNQ ion channels. *Science* 314, 1454–1457. doi: 10.1126/science.1131163

Svobodova, B., and Groschner, K. (2016). Reprint of "Mechanisms of lipid regulation and lipid gating in TRPC channels". *Cell Calcium* 60, 133–141. doi: 10.1016/j.ceca.2016.06.010

Tikku, S., Epshtein, Y., Collins, H., Travis, A. J., Rothblat, G. H., and Levitan, I. (2007). Relationship between Kir2.1/Kir2.3 activity and their distributions between cholesterol-rich and cholesterol-poor membrane domains. *Am. J. Physiol. Cell Physiol.* 293, C440–C450. doi: 10.1152/ajpcell.004922006

Vinayagam, D., Mager, T., Apelbaum, A., Bothe, A., Merino, F., Hofnagel, O., et al. (2018). Electron cryo-microscopy structure of the canonical TRPC4 ion channel. *Elife* 7, 1–23. doi: 10.7554/eLife.36615

Weiser, B. P., Salari, R., Eckenhoff, R. G., and Brannigan, G. (2014). Computational investigation of cholesterol binding sites on mitochondrial VDAC. *J. Phys. Chem. B* 118, 9852–9860. doi: 10.1021/jp504516a

Winn, M. P., Conlon, P. J., Lynn, K. L., Farrington, M. K., Creazzo, T., Hawkins, A. F., et al. (2005). A mutation in the TRPC6 cation channel causes familial focal segmental glomerulosclerosis. *Science* 308, 1801–1804. doi: 10.1126/science.1106215

Yancey, P. G., Rodrigueza, W. V., Kilsdonk, E. P., Stoudt, G. W., Johnson, W. J., Phillips, M. C., et al. (1996). Cellular cholesterol efflux mediated by cyclodextrins. Demonstration Of kinetic pools and mechanism of efflux. *J. Biol. Chem.* 271, 16026–16034. doi: 10.1074/jbc.271.27.16026

Conflict of Interest: The authors declare that the research was conducted in the absence of any commercial or financial relationships that could be construed as a potential conflict of interest.

frontiers in Pharmacology

ORIGINAL RESEARCH
published: 14 January 2020
doi: 10.3389/fphar.2019.01532

Thrombin as Key Mediator of Seizure Development Following Traumatic Brain Injury

Marina Ben Shimon[1†], *Efrat Shavit-Stein*[1,2†], *Keren Altman*[1], *Chaim G. Pick*[3] *and Nicola Maggio*[1,2,4*]

[1] Department of Neurology, The Chaim Sheba Medical Center, Ramat Gan, Israel, [2] Department of Neurology and Neurosurgery, Sackler Faculty of Medicine and Sagol School of Neuroscience, Tel Aviv University, Tel Aviv, Israel, [3] Department of Anatomy and Anthropology, Sackler Faculty of Medicine and Sagol School of Neuroscience, Tel Aviv University, Tel Aviv, Israel, [4] Talpiot Medical Leadership Program, The Chaim Sheba Medical Center, Ramat Gan, Israel

OPEN ACCESS

Edited by:
Moran Rubinstein,
Tel Aviv University, Israel

Reviewed by:
Livio Luongo,
Second University of Naples, Italy
Heike Wulff,
University of California,
Davis, United States

***Correspondence:**
Nicola Maggio
Nicola.maggio@sheba.health.gov.il

[†]These authors have contributed equally to this work

Specialty section:
This article was submitted to Pharmacology of Ion Channels and Channelopathies, a section of the journal Frontiers in Pharmacology

Received: 10 October 2019
Accepted: 27 November 2019
Published: 14 January 2020

Citation:
Ben Shimon M, Shavit-Stein E, Altman K, Pick CG and Maggio N (2020) Thrombin as Key Mediator of Seizure Development Following Traumatic Brain Injury. Front. Pharmacol. 10:1532. doi: 10.3389/fphar.2019.01532

Traumatic brain injury (TBI) commonly leads to development of seizures, accounting for approximately 20% of newly diagnosed epilepsy. Despite the high clinical significance, the mechanisms underlying the development of posttraumatic seizures (PTS) remain unclear, compromising appropriate management of these patients. Accumulating evidence suggest that thrombin, the main serine protease of the coagulation cascade, is involved in PTS genesis by mediating inflammation and hyperexcitability following blood brain barrier breakdown. In order to further understand the role of thrombin in PTS, we generated a combined mild TBI (mTBI) and status epilepticus mice model, by injecting pilocarpine to mice previously submitted to head injury. Interestingly, mTBI was able to reduce seizure onset in the pilocarpine animal model as well as increase the death rate in the treated animals. In turn, pilocarpine worsened spatial orientation of mTBI treated mice. Finally, thrombin activity as well as the expression of IL1-β and TNF-α was significantly increased in the mTBI-pilocarpine treated animals. In conclusion, these observations indicate a synergism between thrombin and mTBI in lowering seizure in the pilocarpine model and possibly aggravating inflammation. We believe that these results will improve the understanding of PTS pathophysiology and contribute to the development of more targeted therapies in the future.

Keywords: mild traumatic brain injury, epilepsy, thrombin, Protease Activated Receptor 1 (PAR1), N-Methyl-D-Aspartate (NMDA)

INTRODUCTION

Traumatic brain injury (TBI) significantly increases the risk of seizures and is a major cause of intractable epilepsy (Hunt et al., 2013), accounting for nearly 20% of acquired epilepsy in the general population (Garga and Lowenstein, 2006). Posttraumatic seizures (PTS) may occur with a long delay of up to 20 years after the traumatic event (Piccenna et al., 2017) and involve a significant heterogeneity of seizures (Piccenna et al., 2017). The variety of PTS events includes focal seizures with or without generalization, a coexistence of both, or non-convulsive seizures (Agrawal et al., 2006). In addition to the miscellany of seizures, up to 8% of patients with PTS develop Status

Epilepticus (SE) (Peets et al., 2005), a neurological emergency and significant cause of morbidity and mortality (Betjemann and Lowenstein, 2015).

Alarmingly, PTS pathophysiology is yet to be fully understood, thus management of patients and outcomes are compromised. To better understand the underlying mechanism of PTS, prior studies first tried to identify a number of risk factors involved. A major one is TBI severity (Annegers et al., 1998), especially penetrating injuries, with a significant 50% risk of epilepsy (Agrawal et al., 2006). Additional risk factors include subdural hematoma (Verellen and Cavazos, 2010) and alcohol abuse (Xu et al., 2017). However, none of them is categorical about the impact of mild TBI (mTBI) to the pathophysiology of seizures and epilepsy. As mTBI accounts for nearly 80% of the hospitalized head injury cases in the United States (Kushner, 1998), and is also related to seizure development (Webb et al., 2015), it is critical to identify the role of mTBI in the onset and progression of PTS.

To study epileptogenesis following mTBI, animal models were generated to replicate the complex implications of human mTBI and PTS. A commonly used model is the closed weight free drop mTBI rodent (Kalish and Whalen, 2016), which permits the evaluation of a great spectrum of the biological changes involved in PTS (Itsekson-Hayosh et al., 2016). Among those, blood brain barrier (BBB) breakdown (Korn et al., 2005), blood vessel disruption and vascular permeability changes (Gaetz, 2004) are crucial for PTS development. As a consequence of this circumstances, glutamate is released leading to calcium influx and therefore to development of a hyperexcitable state (Xiong et al., 2013), facilitating seizures. Additionally, intense inflammatory response, diffuse axonal injury and cell death play a central role in late structural modification and adaptive neuroplasticity occurs following TBI (Povlishock and Christman, 1995; Ziebell and Morganti-Kossmann, 2010).

The hyperexcitable state found in PTS points toward possible involvement of blood components, especially thrombin, as they were recently found to be central mediators of seizures related to BBB breakdown (Heinemann et al., 2012). Thrombin, a serine protease participating in the coagulation cascade, is originated from prothrombin cleavage by activated factor X (Krishnaswamy, 2013). After binding to its protease activated receptor (PAR1), Thrombin-PAR1 activation leads to NMDA receptors potentiation and massive calcium influx, followed by a glutamate mediated hyperexcitable state, and a lowered threshold for seizure development (Gingrich et al., 2000; Maggio et al., 2008) Critically, thrombin-PAR1 complex also participates in mTBI mechanism, causing *in vivo* synaptic disfunction and amnesia, effects that were reversed after the administration of thrombin inhibitors (Itzekson et al., 2014).

As the participation of thrombin in epileptogenesis and in BBB breakdown conditions is well known, here we chose to focus on the possibility of a synergistic effect between thrombin and mTBI in seizure development. Using a combined mice model of mTBI (free weight drop) and temporal lobe epilepsy (pilocarpine injection), we found that seizures intensity and death rate during SE were increased in the animals exposed to both treatments compared to those that experience a single one. In addition, the expression of both thrombin as well as inflammatory markers was higher in the former group than in the latter. We therefore conclude that our findings highlight the importance of thrombin in PTS pathophysiology, suggesting new directions in the management and treatment of these patients.

MATERIALS AND METHODS

Experimental Setting

The experiments were approved by the Institutional Animal Care and Use Committee of the Sheba Medical Center which obeys to national and NIH approved rules (ANIM 1089-17). The minimal number of animals was used and all efforts were made to minimize suffering. The study was carried out in 8 weeks old male C57BL/6J mice and mTBI was induced using a free weight drop concussive device as previously described (Itzekson et al., 2014). Briefly, the device consisted of an 80-cm high metal tube (13 mm in diameter) placed vertically over the head of the mouse. Minutes prior to the injury, the animals were slightly anesthetized by isoflurane (gaseous), as previously described (Edut et al., 2014). Trauma was induced by a 50-gr metal weight dropped down the metal tube on the right anterolateral side of the head (just anterior to the right ear). The mouse was placed on a sponge immobilization board which allowed head rotation following the impact thus mimicking the natural condition of head rotation in a whiplash injury. Control mice underwent a similar procedure, however, were un-injured. Twenty-four hours after the trauma, SE was induced by a single intraperitoneal (i.p.) injection of pilocarpine hydrochloride. The trauma effect on SE development was tested in experimental settings of 250 mg/kg (low dose pilocarpine) and 350 mg/kg (high dose pilocarpine). In order to avoid side effects induced by peripheral cholinergic activation, mice were treated with atropine sulphate monohydrate (1 mg/kg, i.p.) 30 min before pilocarpine injection. Seizures were monitored and scored every 10 min using a modified Racine's scale (0—no response, 1—freezing, 2—head nodding, 3—orofacial seizure, 4—clonic seizure, and 5—tonic seizure) (Racine, 1972), during 90 min following pilocarpine administration. After 90 min mice received diazepam (3 mg/kg; i.p.) to halt convulsions, or before in case of tonic seizure. All experimental groups received both atropine and diazepam similarly to pilocarpine treated mice.

Open Field

Open field was performed to evaluate cognitive function and anxiety in mice upon 24 h from low pilocarpine administration. This task takes advantage of rodents aversions to large, brightly lit, open, and unknown environment. Mice were placed in the middle of the open field apparatus consisted of square box (47 cm × 47 cm × 29 cm) and given 5 min to explore. Time in the center and crossing center frequencies were recorded and analyzed using EthoVision software (Noldus information technology). The mobility index was defined as: Total duration in the center/Crossing center frequency.

Thrombin Activity

Mice were anesthetized with pentobarbital (0.8 mg/kg) and rapidly decapitated for hippocampi dissections. Right hippocampus was dissected, and dorsal hippocampus used for thrombin activity. Thrombin enzymatic activity was measured using a fluorometric assay based on the cleavage rate of the synthetic substrate Boc-Asp (OBzl)-ProArg-AMC (I-1560; Bachem, Bubendorf, Switzerland) and defined by the linear slope of the fluorescence intensity versus time, as previously described (Bushi et al., 2013). The hippocampal tissue placed into 96-well black microplate (Nunc, Roskilde, Denmark) containing the substrate buffer. Measurements were carried out using a microplate reader (Tecan; Infinite 200; Switzerland) with excitation and emission filters of 360 nm ± 35 nm and 460 nm ± 35 nm, respectively. Reported values are normalized to protein concentration of each sample and normalized to control group values (±SEM).

Gene Expression

Right hemisphere hippocampi were dissected and prepared as described before (Maggio and Segal, 2007). The RNA tissue was extracted using the TRIzol (Thermo Fisher 15596026) solubilization method followed by phase separation with chloroform. Samples were placed in 1 ml TRIzol and homogenized with bullet blender homogenizer (Next Advance) at a maximum speed for 1 min. RNA phase cleaning was performed using Bio-Rad Aurum Kit (Bio-Rad Laboratories 732-6820, Hercules, CA, USA). Total RNA (2 μg) was used for reverse transcription using high-capacity cDNA reverse transcription kit (Applied Biosystems). Quantitative real-time polymerase chain reaction was performed on the StepOne™ Real-Time PCR System (Applied Biosystems, Rhenium, Israel) using Fast SYBR Green Master (ROX) (Applied Biosystems). Hypoxanthine guanine phosphoribosyltransferase (HPRT) served as a reference gene (primers list). A standard amplification program was used (1 cycle of 95°C for 20 s and 40 cycles of 95°C for 3 s and 60°C for 30 s). The primers used in this analysis are listed in Table 1. The results were normalized to reference gene expression within the same cDNA sample and calculated using the ΔCt method with results reported as fold changes relative to control brains of sham animals and reported as mean ± SEM **Table 1**.

RESULTS

mTBI Lowers Threshold for Seizures in a Pilocarpine Animal Model of SE

Administration of pilocarpine in rodents is commonly used to model SE induction and subsequent mechanisms leading to epileptogenesis (Scorza et al., 2009; Vezzani, 2009). Similarly, the weight drop model in rodents is an established mTBI model, since it mimics important characteristics of human mTBI, including PTS (Glushakov et al., 2016). In our study, we chose to combine those well-known models in order to examine the possibility that mTBI may lower seizure under epileptic prone conditions. To better examine the effect of the combined model, we used both a high dose (350 mg/kg) and a low dose (250 mg/kg) of pilocarpine.

Primarily, we focused on the effect of both pilocarpine doses, and the consequent death that might result from those treatments. The experimental timeline included 50-gr weight drop followed by pilocarpine administration and seizure analysis (**Figure 1A**). As expected, the Racine score, used to evaluate seizure severity, was found to be worse in the high dose pilocarpine group compared to the low dose group (3.8 ± 0.45 vs. 1.9 ± 0.09, respectively, $p < 0.005$, at 70 min post injection, **Figures 1B, C**). Next, we chose to repeat our assessment with the mTBI and pilocarpine combined group. Interestingly, the combination of high dose pilocarpine group with mTBI did not result in a higher Racine score (**Figure 1C**). However, on the other hand, a significant difference was found when the low dose pilocarpine group was combined with mTBI (**Figure 1B**). Indeed, a low dose pilocarpine group only showed a mild seizure severity (as seen in Racine score). In contrast, the combination of low dose pilocarpine group with mTBI resulted in a higher seizure score at the onset with the highest seizures severity score achieved upon 20 min post injection (2.8 ± 0.24 vs. 1.6 ± 0.18, respectively, $p < 0.004$, **Figure 1B**). Strikingly, in this animal group, seizures severity dropped significantly toward the end of the experimental time window (70 min: 1.4 ± 0.22 vs. 1.9 ± 0.09 $p < 0.03$; 80 min: 1.2 ± 0.17 vs. 1.9 ± 0.12 $p < 0.03$; 90 min: 1.2 ± 0.17 vs. 1.8 ± 0.11, $p < 0.05$, respectively). While the groups treated with low dose pilocarpine both with and without the combination of mTBI survived the procedure (**Figure 1D**), the high dose pilocarpine combined mTBI group experienced a higher mortality rate when compared to the correspective high dose pilocarpine group (31% vs. 8.6%, **Figure 1E**). Altogether, these data show that mTBI may facilitate seizures and severity as well as worsen the epilepsy related mortality in SE.

mTBI Worsen Cognitive Abilities in Pilocarpine Treated Animals

Pilocarpine treatment as well as exposure to mTBI are both known to affect cognitive functions, i.e., spatial orientation both in humans (de Freitas Cardoso et al., 2019) and in animal models (Chauvière et al., 2009). In a previous study, the cognitive effects of an mTBI only protocol were thoroughly characterized, and

TABLE 1 | Set of primers used for real-time PCR analysis.

Gene	Forward	Reverse
HPRT	GATTAGCGATGATGAACCAGGTT	**CCTCCCATCTCCTTCATGA CA**
Fx (factor X)	GTGGCCGGGAATGCAA	**AACCCTTCATTGTCTTCGTTAATGA**
TNFα	GACCCTCACACTCAGATCATCTTCT	**CCTCCACTTGGTGGTTTGCT**
IL1β	CTGGTGTGTGACGTTCCCATTA	**CCGACAGCACGAGGCTTT**

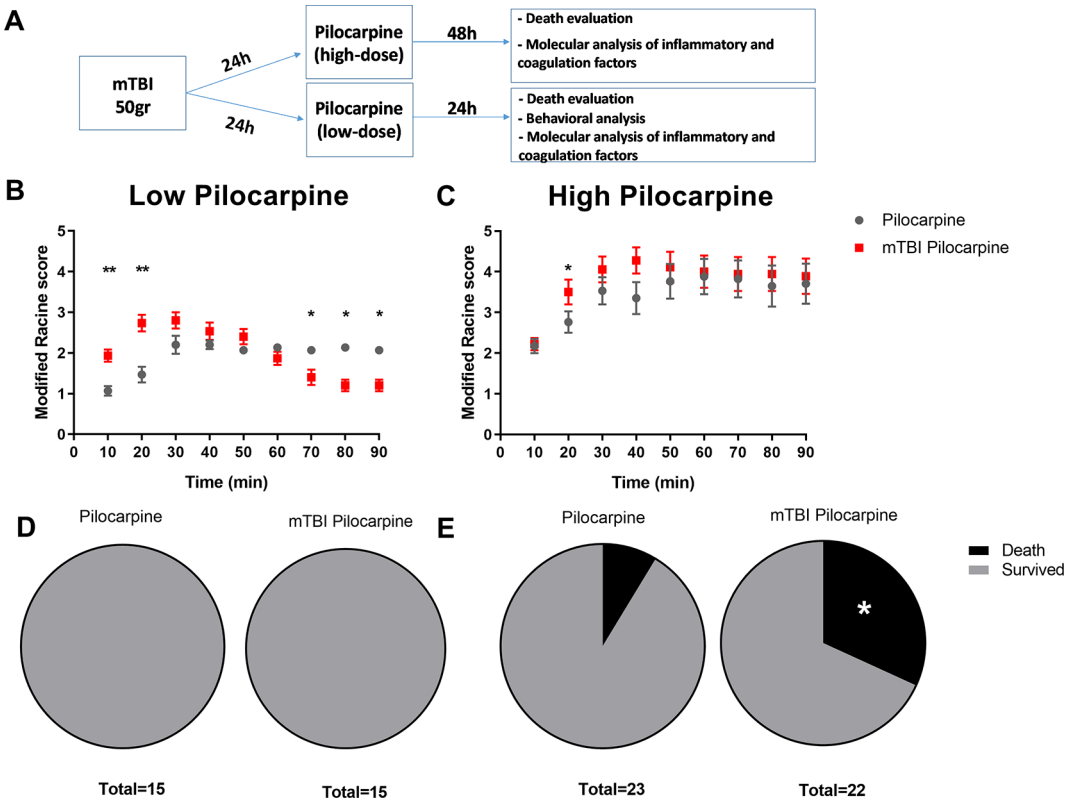

FIGURE 1 | Minimal traumatic brain injury (mTBI) lowers the threshold of seizure in the pilocarpine mouse model of status epilepticus. **(A)** Timeline of the experimental procedure. **(B)** mTBI increased seizure severity upon treatment with a subthreshold low dose concentration of pilocarpine (n = 15 mice/group) while **(C)** no effect was detected when mTBI and high dose of pilocarpine were combined (n = 22-23 mice/group). While mTBI did not affect mortality in a setting of subthreshold low dose concentration of pilocarpine **(D)**, a higher mortality rate **(E)** was detected when mTBI was combined with a high dose concentration. Data is presented as mean ± SEM, ∗ $p \leq 0.05$, ∗∗ $p \leq 0.01$.

showed deficits in spatial orientation (Heim et al., 2017). In this study, we studied whether a synergistic effect of both pilocarpine and mTBI might occur in worsening spatial coordination. We decided to test our hypothesis by evaluating exploratory behavior in an open field setting. Here, mTBI animals exhibited a higher exploratory behavior resulting in both a higher time spent at the center of the arena (7.2 ± 1.46 vs. 5.0 s ±0.89 s, p = 0.1, respectively, **Figure 2A**) as well as in an increased frequency of entries in this compartment (6.1 ± 1.22 vs. 4.2 ± 1.01, p = 0.15, respectively, **Figure 2B**). In parallel, treatment with pilocarpine resulted in a lower exploratory behavior compared to untreated controls. Interestingly, a combined pilocarpine and mTBI

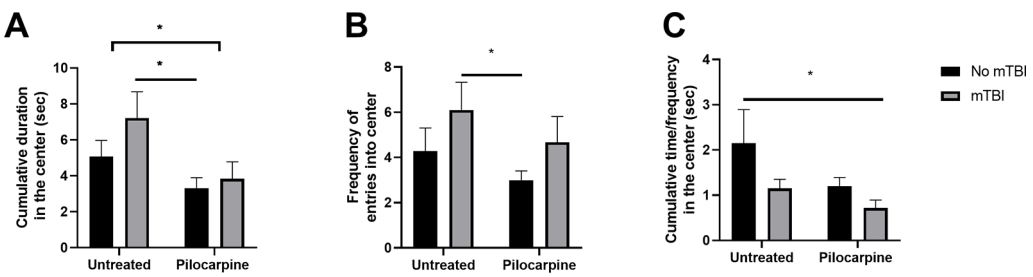

FIGURE 2 | Minimal traumatic brain injury (mTBI) worsens cognitive abilities in pilocarpine treated animals. mTBI animals (n = 7–10 mice/group) exhibited a higher exploratory behavior resulting in both a higher time spent at the center of the arena **(A)** as well as in increased frequency of entries in the compartments **(B)**. In parallel, a pilocarpine treatment (n = 11 mice) resulted in a lower exploratory behavior. **(C)** A combined mTBI pilocarpine treatment (n = 6 mice) dramatically reduced the mobility index of the animals. Data is presented as mean ± SEM ∗ $p \leq 0.05$.

treatment resulted in a worsening of spatial orientation for mTBI treated animals (3.8 ± 0.94 vs. 7.2 s ± 1.46 s, p = 0.06; 4.6 ± 1.14 vs. 3.0 ± 0.40, p = 0.05, **Figures 2A, B**) with a dramatic reduction in their mobility index (0.7 ± 0.17 vs. 2.1 ± 0.73, respectively, p = 0.05, **Figure 2C**). These results indicate that a combined mTBI pilocarpine treatment worsens spatial orientation.

PTS Occurrence Is Related to Thrombin Activity

To investigate the possible mechanisms involved in PTS using our mice model, we focused on thrombin which is known to play a key role both in epilepsy (Maggio et al., 2013b) and in mTBI (Xi et al., 2002). In order to investigate whether thrombin might be related to the effects of mTBI on seizures severity, thrombin activity was measured in the hippocampi of mice treated either with pilocarpine or mTBI alone, or in a combination of both. Thrombin was upregulated in all the experimental groups (**Figure 3A**) with the highest activity found in the combined groups compared to the others, (3.0 ± 0.40 and 2.0 ± 0.25 fold increase in the mTBI combined with high pilocarpine and low pilocarpine groups respectively, compared to 2.0 ± 0.27 and 1.3 ± 0.15 in the non-mTBI corresponding groups, $p < 0.05$) either mTBI or pilocarpine alone. Interestingly, the expression of Factor X, an enzyme responsible for the rate limiting reaction for thrombin activity, was significantly enhanced the combined group (11.98 ± 6.66 p = 0.03, **Figure 3B**). These data, might suggest a synergistic effect of mTBI and epileptic activity in upregulating thrombin levels.

Seizures Severity Correlates With the Expression of Inflammatory Markers

Thrombin upregulation in the combined group can lead to harmful downstream effect, as thrombin has been pointed out as an important mediator of neuroinflammation and vascular disruption (Popović et al., 2012). To examine the possible effects of the thrombin upregulation, we measured the levels of proinflammatory mediators, TNF- alpha and IL1- beta that were shown to enhance brain tissue damage following trauma (Xiong et al., 2018). Interestingly, high dose of pilocarpine either alone or combined with mTBI resulted in an increased expression of both TNF-alpha (70.9 ± 27.49 and 125.1 ± 24.60 fold increase, respectively, $p < 0.005$) as well as IL1-beta (7.9 ± 2.80 and 9.4 ± 3.32 fold increase, respectively, $p < 0.007$, **Figures 3C, D**), suggesting an intense inflammatory response occurring in this setting. Contrarily, the exposure to a lower dose of pilocarpine resulted in a higher expression of inflammatory markers only in combination with mTBI (TNF-alpha: 2.8 ± 1.87 and 10.7 ± 6.50, p = 0.9, and p = 0.7, respectively; IL1-beta: 1.1 ± 0.10 and 2.2 ± 1.07, p = 0.9, and p = 0.7, respectively, **Figures 3C, D**). Altogether, these findings might highlight the possibility that seizures severity correlates with a higher expression of inflammatory markers in the brain.

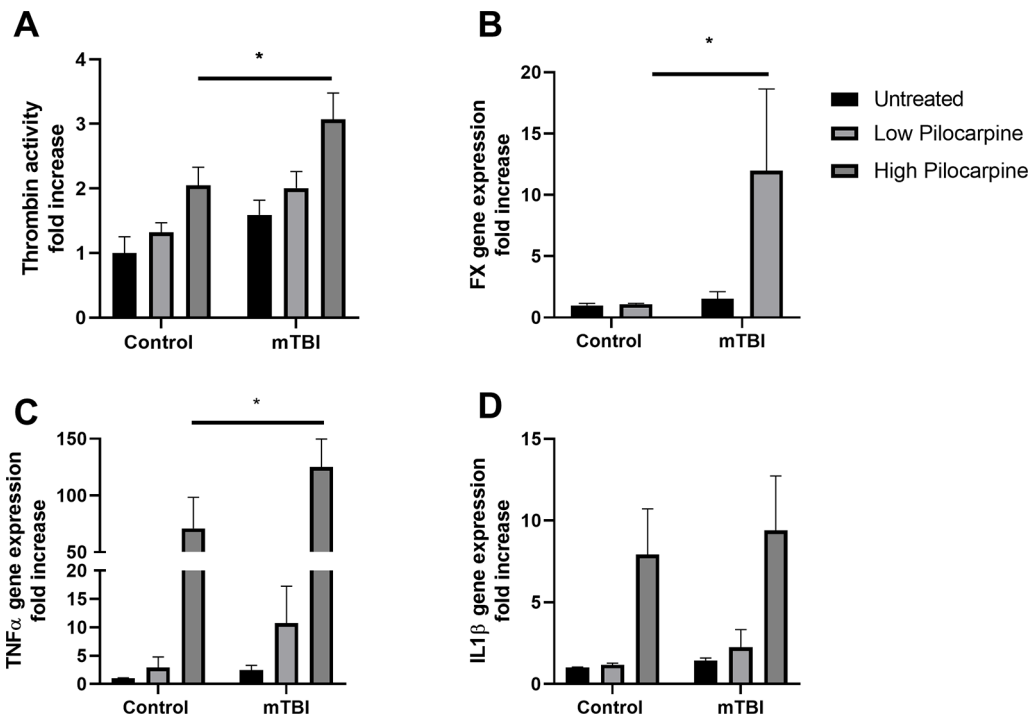

FIGURE 3 | Thrombin and proinflammatory markers expression correlate with seizure severity. Thrombin activity **(A)** as well as Factor X mRNA expression **(B)** were increased in animals that underwent a combined treatment with minimal traumatic brain injury (mTBI) and pilocarpine. The mRNA expression of proinflammatory markers such as TNFa **(C)** and IL1b **(D)** were also enhanced in the same group (n = 5-19 mice/group). Data is presented as mean ± SEM, ∗ $p \leq 0.05$.

DISCUSSION

In this study, we evaluated the impact of mTBI on seizure outcomes in an animal model of seizures and epilepsy. While it is known that TBI significantly increases the risk of seizures and is a major cause of intractable epilepsy (Hunt et al., 2013), no information is currently available concerning the impact of mTBI on seizures and epilepsy. By combining two animal models, the pilocarpine model with the drop weight model of mTBI, we found that mTBI worsens seizures severity and increases epilepsy related death upon induction of SE. In addition, animals that underwent a combined treatment exhibited an impaired spatial orientation. Finally, the proteases thrombin and Factor X as well as additional inflammatory markers were upregulated in the hippocampi of the mice that underwent a combined treatment compared to the respective controls (as summarized in **Figure 4**).

Interestingly, our data show that mTBI was able to affect the seizure onset in the pilocarpine animal model of SE. While a low dose of pilocarpine is usually associated to a lower seizure's severity score, the combination of this treatment with mTBI resulted in a faster onset, higher severity of seizures compared to controls. This finding supports the possibility that mTBI could predispose the brain such that an additional low threshold stimulus, i.e., a low dose of pilocarpine, might result in a bigger effect than if the same stimulus would have been delivered alone. In other words, mTBI could act as a "conditioning stimulus" (Statler et al., 2008; Pitkänen and Immonen, 2014) and thus affect seizures in our setting. However, if preexposure to mTBI may result in a faster seizure onset in animals treated with a low dose of pilocarpine, in the same group of animals the decay of seizure severity seems quicker. While this result may seem puzzling, a possible explanation for this phenomenon might be linked to a higher inhibitory tone in this group of animals. Indeed, as a response to the faster onset of seizures, inhibitory networks may be quickly recruited in order to shunt the over-excitatory response. Alternatively, a lower seizure onset in the low dose pilocarpine treated group might be less efficient in recruiting inhibitory networks and thus an asymptote response could arise. Additional experiments are needed to be performed in order to address this intriguing hypothesis.

Mortality due to seizures is also affected by a previous exposure to mTBI. This is an interesting observation which guarantees further exploration due to its potential clinical impact: could patients that have been exposed to mTBI and then developed epilepsy be more prone to SUDEP?

The combination of both mTBI and seizures seems to affect spatial orientation as well. Indeed, while in mTBI, spatial orientation seems to be preserved, the advent of seizures worsens it. A possible explanation of this observation may lie in the hyperexcitable state of the hippocampal network following pilocarpine treatment. As the hippocampus is the major brain area involved in spatial orientation (Burgess et al., 2002), upon seizures, the hyperexcitability of the hippocampal network might saturate the molecular and cellular mechanisms responsible for spatial orientation and memory functions (Ben Shimon et al., 2015; Maggio et al., 2017; Maggio et al., 2018) In this respect, it could be interesting to speculate about the longer time scale of this phenomenon. Our behavioral experiments were carried a day after the exposure to pilocarpine and two days after mTBI induction. Previous reports indicated that mTBI mice develop long term neuropsychiatric condition of increased anxiety and later depression (Guida et al., 2017; Belardo et al., 2019). In this sense, could a bigger time lag from the seizures restore the hippocampal abilities of the mTBI treated animals? Would the impairment in spatial orientation observed in mTBI animals upon seizure be reversible? Would a

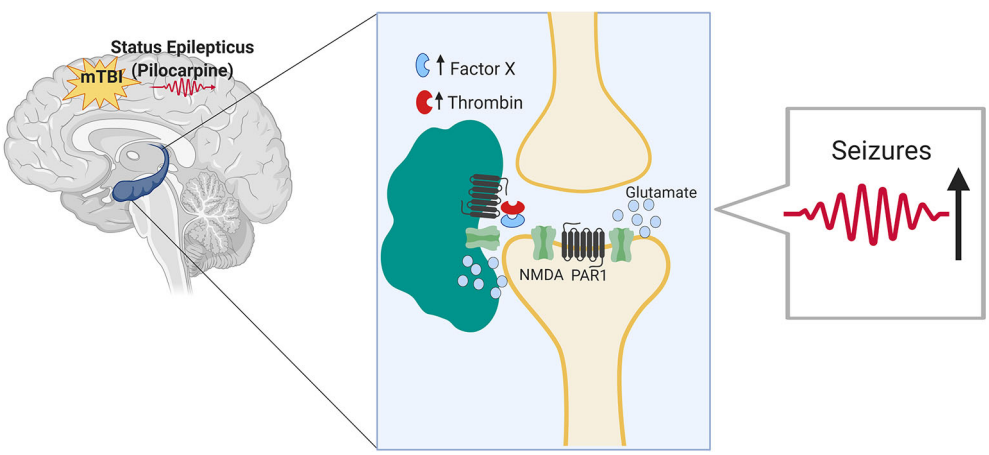

FIGURE 4 | Minimal traumatic brain injury (mTBI) lowers the threshold of seizures in the pilocarpine mouse model of status epilepticus through Thrombin-PAR1 mediated excitatory pathway. Thrombin is known to rise in the brain both in hyperexcitable state as well as upon BBB breakdown following mTBI. Thrombin at high concentrations leads to the activation of NMDA receptor through a pathway mediated by PAR1. NMDA receptor activation and the subsequent massive influx of calcium lead to hyperexcitability and lower threshold for seizures to occur.

long term follow up of the impacted animals show a different behavioral phenotype, which was not observed in an mTBI only model? Future experiments are required in order to assess these hypotheses.

In several, previous contributions, we have highlighted the role of thrombin, a serine protease, in the pathogenesis of epilepsy and mTBI (Itsekson-Hayosh et al., 2016). Therefore, in this study, we aimed at assessing both thrombin activity and the expression of inflammatory markers in the mTBI-pilocarpine setting. The rationale of our assumption was that thrombin is known to rise in the brain both in hyperexcitable state as well as upon BBB breakdown following mTBI (Ben Shimon et al., 2017; De Luca et al., 2017). In the present study, thrombin was upregulated in all the experimental groups with the highest activity found in the combined mTBI-pilocarpine groups compared to the respective others. This observation was followed by the increased expression of inflammatory markers such as TNF-alpha and IL1-beta in the same group of animals, thus suggesting that this setting may cause an intense inflammatory response. Therefore, it is interesting to speculate about the possible mechanism that may link thrombin with the "conditioning" effect of mTBI on seizures. Following BBB breakdown, thrombin enters into the brain and binds to its protease activated receptor (PAR1) (Maggio et al., 2013a). Thrombin-PAR1 activation leads to NMDA receptors potentiation and massive calcium influx, followed by a glutamate mediated hyperexcitable state, and a lowered threshold for seizure development (Gingrich et al., 2000; Maggio et al., 2008). Activation of the inflammatory response may reverberate the BBB breakdown (Chodobski et al., 2011; Krenzlin et al., 2016) causing more thrombin efflux into the brain. Critically, the thrombin-PAR1 complex could also cause the impairment of spatial orientation in the treated mice due to occurrence of synaptic dysfunction and amnesia (Itzekson et al., 2014).

While additional experiments need to be performed, our observations point to an important link between mTBI and seizures. More studies are therefore needed in order to further evaluate this link for developing better therapeutical strategies for patients.

DATA AVAILABILITY STATEMENT

The datasets generated for this study are available on request to the corresponding author.

ETHICS STATEMENT

The animal study was reviewed and approved by the Institutional Animal Care and Use Committee of the Sheba Medical Center.

AUTHOR CONTRIBUTIONS

ES-S supervised the project, conceived and planned the experiments, contributed to the analysis and interpretation of the results, and wrote the manuscript. MS conducted the experiments and data analysis and contributed to the writing of the manuscript. NM supervised the project, conceived and planned the experiments, gave a detailed interpretation of the results, and wrote the manuscript. KA wrote the manuscript. CP consulted regarding the project setting and results interpretation and reviewed the manuscript.

REFERENCES

Agrawal, A., Timothy, J., Pandit, L., and Manju, M. (2006). Post-traumatic epilepsy: an overview. *Clin. Neurol. Neurosurg.* 108 (5), 433–439. doi: 10.1016/j.clineuro.2005.09.001

Annegers, J. F., Hauser, W. A., Coan, S. P., and Rocca, W. A. (1998). A population-based study of seizures after traumatic brain injuries. *New Engl. J. Med.* 338 (1), 20–24. doi: 10.1056/NEJM199801013380104

Belardo, C., Iannotta, M., Boccella, S., Rubino, R. C., Ricciardi, F., Infantino, R., et al. (2019). Oral cannabidiol prevents allodynia and neurological dysfunctions in a mouse model of mild traumatic brain injury. *Front. In Pharmacol.* 10. doi: 10.3389/fphar.2019.00352

Ben Shimon, M., Lenz, M., Ikenberg, B., Becker, D., Shavit Stein, E., Chapman, J., et al. (2015). Thrombin regulation of synaptic transmission and plasticity: implications for health and disease. *Front. In Cell. Neurosci.* 9, 151. doi: 10.3389/fncel.2015.00151

Ben Shimon, M., Zeimer, T., Shavit Stein, E., Artan-Furman, A., Harnof, S., Chapman, J., Maggio, N., et al. (2017). Recovery from trauma induced amnesia correlates with normalization of thrombin activity in the mouse hippocampus. *PloS One* 12 (11), e0188524. doi: 10.1371/journal.pone.0188524

Betjemann, J. P., and Lowenstein, D. H. (2015). Status epilepticus in adults. *Lancet Neurol.* 14 (6), 615–624. doi: 10.1016/S1474-4422(15)00042-3

Burgess, N., Maguire, E. A., and O'Keefe, J. (2002). The human hippocampus and spatial and episodic memory. *Neuron* 35 (4), 625–641. doi: 10.1016/s0896-6273(02)00830-9

Bushi, D., Chapman, J., Katzav, A., Shavit-Stein, E., Molshatzki, N., Maggio, N., et al. (2013). Quantitative detection of thrombin activity in an ischemic stroke model. *J. Mol. Neurosci.* 51 (3), 844–850. doi: 10.1007/s12031-013-0072-y

Chauvière, L., Rafrafi, N., Thinus-Blanc, C., Bartolomei, F., Esclapez, M., and Bernard, C. (2009). Early deficits in spatial memory and theta rhythm in experimental temporal lobe epilepsy. *J. Neurosci. Off. J. Soc. Neurosci. Soc. Neurosci.* 29 (17), 5402–5410. doi: 10.1523/JNEUROSCI.4699-082009

Chodobski, A., Zink, B. J., and Szmydynger-Chodobska, J. (2011). Blood-brain barrier pathophysiology in traumatic brain injury. *Trans. stroke Res.* 2 (4), 492–516. doi: 10.1007/s12975-011-0125-x

de Freitas Cardoso, M. G., Faleiro, R. M., de Paula, J. J., Kummer, A., Caramelli, P., Teixeira, A. L., et al. (2019). Cognitive impairment following acute mild traumatic brain injury. *Front. In Neurol.* 10, 198. doi: 10.3389/fneur.2019.00198

De Luca, C., Virtuoso, A., Maggio, N., and Papa, M. (2017). Neuro-Coagulopathy: blood coagulation factors in central nervous system diseases. *Int. J. Mol. Sci.* 18 (10), 2128. doi: 10.3390/ijms18102128

Edut, S., Rubovitch, V., Rehavi, M., Schreiber, S., and Pick, C. G. (2014). A study on the mechanism by which mdma protects against dopaminergic dysfunction after minimal traumatic brain injury (mTBI) in Mice. *J. Mol. Neurosci.* 54 (4), 684–697. doi: 10.1007/s12031-014-0399-z

Gaetz, M. (2004). The neurophysiology of brain injury. *Clin. Neurophysiol.* 115 (1), 4–18. doi: 10.1016/S1388-2457(03)00258-X

Garga, N., and Lowenstein, D. H. (2006). Posttraumatic epilepsy: a major problem in desperate need of major advances. *Epilepsy Curr.* 6 (1), 1. doi: 10.1111/J.1535-7511.2005.00083.X

Gingrich, M. B., Junge, C. E., Lyuboslavsky, P., and Traynelis, S. F. (2000). Potentiation of NMDA receptor function by the serine protease thrombin. *J. Neurosci. Off. J. Soc. Neurosci. Soc. Neurosci.* 20 (12), 4582–4595. doi: 10.1523/JNEUROSCI.20-12-04582.2000

Glushakov, A. V., Glushakov, O. Y., Doré, S., Carney, P. R., and Hayes, R. L. (2016). Animal Models of Posttraumatic Seizures and Epilepsy. *Methods In Mol. Biol.* 1462pp, 481–519. doi: 10.1007/978-1-4939-3816-2_27

Guida, F., Boccella, S., Iannotta, M., De Gregorio, D., Giordano, C., Belardo, C., et al. (2017). Palmitoylethanolamide reduces neuropsychiatric behaviors by restoring cortical electrophysiological activity in a mouse model of mild traumatic brain injury. *Front. In Pharmacol. Front. Res. Found.* 8. doi: 10.3389/fphar.2017.00095

Heim, L. R., Bader, M., Edut, S., Rachmany, L., Baratz-Goldstein, R., Lin, R., et al. (2017). The invisibility of mild traumatic brain injury: impaired cognitive performance as a silent symptom. *J. Neurotrauma* 34 (17), 2518–2528. doi: 10.1089/neu.2016.4909

Heinemann, U., Kaufer, D., and Friedman, A. (2012). Blood-brain barrier dysfunction, TGFβ signaling, and astrocyte dysfunction in epilepsy. *Glia. NIH Public Access* 60 (8), 1251–1257. doi: 10.1002/glia.22311

Hunt, R. F., Boychuk, J. A., and Smith, B. N. (2013). Neural circuit mechanisms of post–traumatic epilepsy. *Front. In Cell. Neurosci.* 7, 89. doi: 10.3389/fncel.2013.00089

Itsekson-Hayosh, Z., Shavit-Stein, E., Katzav, A., Rubovitch, V., Maggio, N., Chapman, J., et al. (2016). Minimal traumatic brain injury in mice: protease-activated receptor 1 and thrombin-related changes. *J. Neurotrauma* 33 (20), 1848–1854. doi: 10.1089/neu.2015.4146

Itzekson, Z., Maggio, N., Milman, A., Shavit, E., Pick, C. G., and Chapman, J. (2014). Reversal of trauma-induced amnesia in mice by a thrombin receptor antagonis. *J. Mol. Neurosci.* 53 (1), 87–95. doi: 10.1007/s12031-013-0200-8

Kalish, B. T., and Whalen, M. J. (2016). Weight drop models in traumatic brain injury, in *Meth. Mol. Biol.* 1462, 193–209. doi: 10.1007/978-1-4939-3816-2_12

Korn, A., Golan, H., Melamed, I., Pascual-Marqui, R., and Friedman, A. (2005). Focal cortical dysfunction and blood-brain barrier disruption in patients with Postconcussion syndrome. *J. Clin. Neurophysiol. Off. Publ. Am. Electroencephalographic Soc.* 22 (1), 1–9. doi: 10.1097/01.wnp.0000150973.24324.a7

Krenzlin, H., Lorenz, V., Danckwardt, S., Kempski, O., and Alessandri, B. (2016). The Importance of Thrombin in Cerebral Injury and Disease. *Int. J. Mol. Sci.* 17 (1), 84. doi: 10.3390/ijms17010084

Krishnaswamy, S. (2013). The Transition of Prothrombin to Thrombin. *J. Thromb. Haemostasis JTH* 11 Suppl 1 (0 1), 265–276. doi: 10.1111/Jth.12217

Kushner, D. (1998). Mild traumatic brain injury. *Arch. Internal Med.* 158 (15), 1617. doi: 10.1001/archinte.158.15.1617

Maggio, N., Blatt, I., Vlachos, A., Tanne, D., Chapman, J., and Segal, M. (2013a). Treating seizures and epilepsy with anticoagulants? *Front. In Cell. Neurosci.* 7, 19. doi: 10.3389/fncel.2013.00019

Maggio, N., Cavaliere, C., Papa, M., Blatt, I., Chapman, J., and Segal, M. (2013b). Thrombin regulation of synaptic transmission: Implications for seizure onset. *Neurobiol. Dis.* 50, 171–178. doi: 10.1016/j.nbd.2012.10.017

Maggio, N., and Segal, M. (2007). Striking variations in corticosteroid modulation of long-term potentiation along the septotemporal axis of the hippocampus. *J. Neurosci. Off. J. Soc. Neurosci. Soc. Neurosci.* 27 (21), 5757–5765. doi: 10.1523/JNEUROSCI.0155-07.2007

Maggio, N., Shavit Stein, E., and Segal, M. (2017). Complex modulation by stress of the effect of seizures on long term potentiation in mouse hippocampal slices. *Hippocampus* 27pp (8), 860–870. doi: 10.1002/hipo.22736

Maggio, N., Shavit Stein, E., Segal, M., and Frontiers Media, S. A. (2018). Cannabidiol regulates long term potentiation following status epilepticus: mediation by calcium stores and serotonin. *Front. In Mol. Neurosci.* 11, 32. doi: 10.3389/fnmol.2018.00032

Maggio, N., Shavit, E., Chapman, J., and Segal, M. (2008). Thrombin induces long-term potentiation of reactivity to afferent stimulation and facilitates epileptic seizures in rat hippocampal slices: toward understanding the functional consequences of cerebrovascular insults. *J. Neurosci.* 28 (3), 732–736. doi: 10.1523/JNEUROSCI.3665-07.2008

Peets, A. D., Berthiaume, L. R., Bagshaw, S. M., Federico, P., Doig, C. J., and Zygun, D. A. (2005). Prolonged refractory status epilepticus following acute traumatic brain injury: a case report of excellent neurological recovery. *Crit. Care BioMed. Cent.* 9 (6), R725. doi: 10.1186/cc3884

Piccenna, L., Shears, G., and OBrien, T. J. (2017). Management of post-traumatic epilepsy: an evidence review over the last 5 years and future directions. *Epilepsia Open* 2 (2), 123–144. doi: 10.1002/epi4.12049

Pitkänen, A., and Immonen, R. (2014). Epilepsy related to traumatic brain injury. *Neurotherapeutics* 11 (2), 286–296. doi: 10.1007/s13311-014-0260-7

Popović, M., Smiljanić, K., Dobutović, B., Syrovets, T., Simmet, T., and Isenović, E. R. (2012). Thrombin and vascular inflammation. *Mol. Cell. Biochem.* 359 (1–2), 301–313. doi: 10.1007/s11010-011-1024-x

Povlishock, J. T., and Christman, C. W. (1995). The pathobiology of Traumatically induced axonal injury in animals and humans: a review of current thoughts. *J. Neurotrauma* 12 (4), 555–564. doi: 10.1089/neu.1995.12.555

Racine, R. J. (1972). Modification of seizure activity by electrical stimulation: II. Motor seizure. *Electroencephalography Clin. Neurophysiol.* 32 (3), 281–294. doi: 10.1016/0013-4694(72)90177-0

Scorza, F. A., Arida, R. M., Naffah-Mazzacoratti, M., da, G., Scerni, D. A., Calderazzo, L., and Cavalheiro, E. A. (2009). The pilocarpine model of epilepsy: what have we learned? *Anais da Academia Brasileira de Ciencias*, 81(3), 345–65.

Statler, K. D., Swank, S., Abildskov, T., Bigler, E. D., and White, H. S. (2008). Traumatic brain injury during development reduces minimal clonic seizure thresholds at maturity. *Epilepsy Res.* 80 (2–3), 163–170. doi: 10.1016/j.eplepsyres.2008.04.001

Verellen, R. M., and Cavazos, J. E. (2010). *Post-traumatic epilepsy: an overview. Therapy* Vol. 7 (London, England : 2004: NIH Public Access), 527–531. doi: 10.2217/THY.10.57

Vezzani, A. (2009). Pilocarpine-induced seizures revisited: what does the model mimic? *Epilepsy Curr.* 9 (5), 146–148. doi: 10.1111/j.1535-7511.2009.01323.x

Webb, T. S., Whitehead, C. R., Wells, T. S., Gore, R. K., and Otte, C. N. (2015). Neurologically-related sequelae associated with mild traumatic brain injury. *Brain Inj.* 29 (4), 430–437. doi: 10.3109/02699052.2014.989904

Xi, G., Reiser, G., and Keep, R. F. (2002). The role of thrombin and thrombin receptors in ischemic, hemorrhagic and traumatic brain injury: deleterious or protective? *J. Neurochem.* 84 (1), 3–9. doi: 10.1046/j.1471-4159.2003.01268.x

Xiong, Y., Mahmood, A., and Chopp, M. (2013). Animal models of traumatic brain injury. *Nat. Rev. Neurosci.* 14 (2), 128. doi: 10.1038/NRN3407

Xiong, Y., Mahmood, A., and Chopp, M. (2018). Current understanding of neuroinflammation after traumatic brain injury and cell-based therapeutic opportunities. *Chin. J. traumatology Zhonghua chuang shang za zhi* 21 (3), 137–151. doi: 10.1016/j.cjtee.2018.02.003

Xu, T., Yu, X., Ou, S., Liu, X., Yuan, J., Huang, H., et al. (2017). Risk factors for posttraumatic epilepsy: a systematic review and meta-analysis. *Epilepsy Behav.* 67, 1–6. doi: 10.1016/j.yebeh.2016.10.026

Ziebell, J. M., and Morganti-Kossmann, M. C. (2010). Involvement of proinflammatory and antiinflammatory cytokines and chemokines in the pathophysiology of traumatic brain injury. *Neurotherapeutics* 7 (1), 22–30. doi: 10.1016/j.nurt.2009.10.016

Conflict of Interest: The authors declare that the research was conducted in the absence of any commercial or financial relationships that could be construed as a potential conflict of interest.

The handling editor declared a shared affiliation, though no other collaboration, with one of the authors, CP, at time of review.

frontiers in Pharmacology

ORIGINAL RESEARCH
published: 17 January 2020
doi: 10.3389/fphar.2019.01567

GTL-1, a Calcium Activated TRPM Channel, Enhances Nociception

Emiliano Cohen[1], *Rakesh Kumar*[2], *Tal Zinger*[1], *Avi Priel*[2] *and Millet Treinin*[1]*

[1] Department of Medical Neurobiology, Hadassah-Medical School, Jerusalem, Israel, [2] Faculty of Medicine, School of Pharmacy, The Institute for Drug Research, Hebrew University, Jerusalem, Israel

C. elegans PVD neurons are conserved for morphology, function and molecular determinants with mammalian polymodal nociceptors. Functions of polymodal nociceptors require activities of multiple ion channels and receptors including members of the TRP family. GTL-1, a member of the TRPM subclass of TRP channels, was previously shown to amplify PVD-mediated responses to optogenetic stimuli. Here we characterize effects of GTL-1 on PVD-mediated behavioral responses to noxious stimuli. We show that GTL-1 is required within PVD for the immediate and enduring response to thermal (cold) stimuli. But, find no significant reduction in percent animals responding to single or to repeated noxious mechanical stimuli. Nevertheless, PVD specific knockdown of *gtl-1* expression reduces the magnitude of responses to noxious mechanical stimuli. To understand GTL-1's mechanism of action we expressed it in HEK293 cells. Our results show GTL-1-dependent currents induced by activation of a Gαq-coupled Designer Receptor Exclusively Activated by Designer Drugs (DREADD). In addition, using excised patches we show that GTL-1 can be activated by internal calcium. Our results are consistent with indirect, calcium dependent, activation of GTL-1 by noxious stimuli. This mechanism explains the GTL-1-dependent amplification of responses to multiple stimuli optogenetic and sensory in PVD.

Keywords: TRPM, *C. elegans*, nociceptors, calcium, behavior

OPEN ACCESS

Edited by:
Domenico Tricarico, University of Bari Aldo Moro, Italy

Reviewed by:
Lishuang Cao, Vertex Pharmaceuticals (United Kingdom), United Kingdom
Isaac Jardin, University of Extremadura, Spain

***Correspondence:**
Millet Treinin
millet.treinin@mail.huji.ac.il

Specialty section:
This article was submitted to Pharmacology of Ion Channels and Channelopathies, a section of the journal Frontiers in Pharmacology

Received: *19 August 2019*
Accepted: *03 December 2019*
Published: *17 January 2020*

Citation:
Cohen E, Kumar R, Zinger T, Priel A and Treinin M (2020) GTL-1, a Calcium Activated TRPM Channel, Enhances Nociception. Front. Pharmacol. 10:1567. doi: 10.3389/fphar.2019.01567

INTRODUCTION

Responding appropriately to noxious, potentially injurious or injurious signals is essential for survival. This response requires polymodal nociceptors, multi dendritic sensory neurons innervating the skin or internal organs and responding to high threshold thermal and mechanical stimuli and to noxious chemicals (Woolf and Ma, 2007; Smith and Lewin, 2009). *C. elegans* PVD neurons are multi dendritic neurons, conserved for structure, function, and molecular determinants with mammalian polymodal nociceptors (Chatzigeorgiou et al., 2010; Albeg et al., 2011). These neurons respond to high threshold mechanical stimuli and to cold temperatures, responses mediated, respectively, by the DEG/ENaC channel subunits, MEC-10 and DEGT-1, and the TRPA channel, TRPA-1 (Chatzigeorgiou et al., 2010).

Transcriptomic analysis of PVD neurons identified multiple ion channel subunits likely to express in these neurons (Smith et al., 2010). Several of these channel subunits were examined for their effects on the behavioral response to optogenetic activation of PVD (Husson et al., 2012); this study identified GTL-1 as an ion channel needed within PVD for amplification of the behavioral

response to optogenetic stimuli. GTL-1, Gon-Two Like protein, belonging to the TRPM subfamily of the TRP superfamily was previously shown to function together with GON-2 in maintaining Mg^{2+} homeostasis in the *C. elegans* intestine, as well as in controlling IP_3-dependent Ca^{2+} oscillations to control defecation (Teramoto et al., 2005; Kwan et al., 2008; Xing et al., 2008; Xing and Strange, 2010). However, roles of GTL-1 in responses to PVD-mediated, physiological, noxious stimuli have not been studied.

Members of the TRP superfamily play key roles in nociception (Clapham, 2003; Dhaka et al., 2006; Julius, 2013). TRP proteins form nonspecific cation channels shown to respond to noxious heat, noxious cold, pH, and mechanical stimuli. For example, TRPV1, also known as the capsaicin receptor, is expressed in mammalian nociceptors and is important for mediating responses to heat, acid and vanilloid toxins (Caterina and Julius, 1999; Caterina et al., 2000); TRPM3 functions as a noxious heat sensor (Vriens et al., 2011); and TRPM8 functions as a cold sensor (Dhaka et al., 2007). Functions of TRPs in polymodal nociceptors are not limited to nociception as they were also shown to modulate nociceptor activity. For example, in the *Drosophila* DA-IV polymodal nociceptors, TRP channels functioning downstream to hedgehog signaling sensitize responses to noxious stimuli (Babcock et al., 2009). Indeed, several TRPs, including TRPM channels, were shown to be activated by intracellular Ca^{2+}, suggesting that in certain cases they function downstream to Gαq-coupled GPCRs, other TRP channels, or voltage activated calcium channels (Launay et al., 2002; Zurborg et al., 2007).

Here, we examine whether, GTL-1-dependent amplification of optogenetic stimuli (Husson et al., 2012) represents a physiological role for this channel in enhancing responses to noxious stimuli. For this, we examined effects of loss-of-function mutation or PVD-specific knockdown of this gene on PVD-dependent responses to thermal and mechanical stimuli. Results of this analysis show defects in these responses, supporting a role for GTL-1 in PVD-mediated responses. In addition, we expressed GTL-1 in HEK293 cells to show that, like other TRPM channels, it is activated by internal calcium and can function downstream to Gαq-coupled GPCRs.

MATERIALS AND METHODS

Strains

The wild type is N2. The *gtl-1(ok375)* mutation is a loss-of-function mutation due to a deletion of 2.7Kb encoding for all the transmembrane domains of GTL-1, the strain carrying this mutation is referred to as *gtl-1(lf)*. The *trpa-1(ok999)* mutation encodes a loss-of-function mutation of *trpa-1* due to a deletion of 1.3Kb, encoding for most of the intracellular N-terminal domain. The *mec-4(1611)* mutation is a gain-of-function mutation leading to degeneration of the six touch receptor neurons (AVM, ALM, PVM, PLM). This strain was crossed with the *gtl-1(lf)* strain for the high threshold mechanical stimulation assay, and also served as a control in that assay. The integrated *ser-2prom3::deg-3(N293I)* transgene which eliminates PVDs via degeneration (-P animals), was previously described in (Albeg et al., 2011).

Plasmids

To knockdown expression of *gtl-1* in PVD we used the method developed in (Esposito et al., 2007) for expressing double stranded RNA of genes of interest in specific cells. Specifically, coding inserts of *gtl-1* were amplified from the *C. elegans* RNAi library (Source BioScience, clone IV-6A13,(Kamath et al., 2003)) using primers L4440F (5' CGACGGTATCGATAAGCTTGAT-'3) and L4440R ('5- CGACGGTATCGATAAGCTTGAT-'3) each containing a HindIII site. The resulting 1.1 Kb fragment was cloned in both orientations downstream to a 1.7 Kb *ser-2prom3* promoter (expressing in PVD and OLL (Tsalik et al., 2003)) in the pBluescript SKII(−) HindIII site. The plasmids expressing both orientations were injected at 50 ng/µl each with a *ser-2prom3*::GFP plasmid as a marker into wild-type N2 animals.

A full length cDNA of *gtl*-1 cloned into pGEM-T was a kind gift from Howard Baylis (University of Cambridge). For expression of GTL-1 in HEK293 cells, a 5kb KpnI-BamH1 cDNA fragment containing *gtl-1* was cloned into pCDNA4/TO.

Behavioral Analysis

Response to Cold Temperature Following Prolonged Exposure

The assay was performed as previously described (Albeg et al., 2011; Cohen et al., 2014). In brief, for movement analysis animals were transferred as L4 larvae to fresh plates and grown overnight to adulthood at 20°C. Prior to locomotion analysis single adults were transferred to a fresh NGM plate pre-equilibrated at 20°C or 15°C and having a thin layer of OP50 bacteria as food (overnight growth) and allowed to acclimate for 10 min at 20°C or 15°C. Movement of each animal was then recorded at a 25× magnification and at a rate of 10 frames per second. Animals were recorded for 60 sec or until they moved out of the frame. These movies were analyzed using software developed for this purpose [(Albeg et al., 2011), detailed description of this software is provided in http://www.cs.huji.ac.il/~feit/worms/user-manual.pdf] .

Immediate Response to Cold

For rapid and precise temperature control of a thin agar surface on which the animal's movement is recorded we developed the following experimental setup: one animal was transferred to a small piece of NGM agar. To keep the animal within the imaging field it was placed on a dot (approximately 2mm in diameter) of bacteria. The agar was placed on a cover slip and put on top of a thermoelectric plate (peltier, European Thermodynamics ET-127-20-25) and a thermocouple unit (National Instruments TC01) was inserted in the agar. The peltier unit was connected to a programmable power supply unit (Thurlby Thandar Instruments PL-155-P) and a digital microscope (DinoLite Pro AM413T). The power supply unit, the thermocouple unit and the microscope were connected to a PC running a Matlab program that can record the movement of the worm, receive the information from the thermocouple and adjust the voltage of

the power supply, thus, maintaining or changing the incubation temperature.

The automated protocol to test the effects of cooling on animal behavior was as follows. First the temperature of the agar was equilibrated to 20°C. 10 min after this temperature was achieved and stabilized, the temperature was dropped to 15°C or maintained at 20°C for control purposes. The animal remained at this temperature for 10 min, followed by a return of the temperature to 20°C. Recording and analysis of control and temperature drop experiments were randomized and blind to the animal's genotype. Using this imaging setup we were only able to examine reversal frequency (direction changes from forward to backward movement) and this analysis was done manually. Reversals were counted for a period of 30 sec just before the temperature drop, immediately after the temperature reached 15° C, after 10 min at 15°C, immediately after the temperature returned to 20°C, or at the same time frames for control animals maintained at 20°C,.

Mechanical Stimuli

For response to high threshold mechanical stimulus young adult (picked as L4 to fresh plates, 10 animals per plate, and grown at 20°C overnight) *mec-4(e1611)* and *mec-4(e1611); gtl-1(ok375)* animals were examined for their response to prodding with a platinum wire pick. Animals reversing or increasing their forward speed were considered as having responded (Way and Chalfie, 1989). To test adaptation to high threshold mechanical stimulus, young adults (picked as L4 to fresh plates and grown at 20°C overnight) N2, *gtl-1(ok375)*, and -PVD animals were examined for their response to prodding with a platinum wire pick every 10 sec (Husson et al., 2012).

Prolonged response to noxious mechanical stimulus (transfer with a wire pick) was examined as described in (Cohen et al., 2012). Briefly, animals were grown at 20°C on standard nematode growth media (NGM) plates seeded with the *E. coli* strain OP50. For each assay, L4 animals were transferred for overnight growth to fresh NGM plates and examined as young adults. At the start of each experiment a single animal was transferred with a platinum wire pick to a fresh newly seeded NGM plate and worm tracking was initiated at the moment that the animal's image was captured, up to half a minute following transfer. All movies track the animals for 20 min.

Cell Culture (HEK293T) and Transfection

Cell culture and transfection were performed as described (Geron et al., 2018). Briefly, human embryonic kidney 293T (HEK293T) cells were transfected with a total of 1 µg of DNA (GTL-1 pCNA4/TO alone or GTL-1 pCNA4/TO + hM3D(Gq) (a gift from Bryan Roth (Addgene plasmid # 45547; Gq/Dreadd)) and with pCDNA3.1(+) using Mirus LT1 transfection reagent (Mirus Bio, Madison, WI) according to manufacturer's protocol. Co-transfection with EGFP in the pCDNA3.1(+) vector was carried for quick identification of successful transfection. Transfections were performed in 12-well plates containing $3x10^5$ cells 48h before analysis. Cells were plated on 0.05 mg/ml PDL-coated glass coverslips (12 mm) and incubated at 37°C (5% CO2) for at least 16h before electrophysiological analysis.

Patch Clamp Recordings

Voltage-clamp recordings from transfected HEK293T cell were carried out as previously described (Kumar et al., 2017; Geron et al., 2018). Briefly, membrane currents were recorded under the voltage-clamp using an Axopatch 200B patch-clamp amplifier (Molecular Devices, Sunnyvale, CA, USA). Membrane currents were digitized using a Digidata 1440A interface board and pCLAMP 10.6 software (Molecular Devices, Sunnyvale, CA, USA) with sampling frequency set to 5 kHz and were low-pass filtered at 2 kHz. Holding voltage was −40 mV for transfected HEK293T. Patch electrodes were fabricated from borosilicate glass using the P1000 Micropipette Puller (Sutter Instrument) and fire-polished using the Microforge MF-900 (Narishige, Japan) to a resistance of 2–4 MΩ for both the inside-out and perforated patch recordings.

The inside-out configuration was performed as previously described (Kumar et al., 2017). Briefly, both the pipette solution and intracellular solutions constituted (mM): 150 NaCl, 2.8 KCl, 2 $CaCl_2$, and 10 HEPES, adjusted to pH 7.4 with NaOH. Following the establishment of the excised inside-out multichannel patch, patches were continuously superfused with extracellular solutions with or without calcium *via* the ValveBank perfusion system (AutoMate Scientific, Berkeley, CA, USA).

The perforated-patch configuration was carried out as previously described (Priel and Silberberg, 2004; Kumar et al., 2017). Briefly, the pipette solution constituted (mM): 75 K_2SO_4, 55 KCl, 5 $MgSO_4$, 10 HEPES, adjusted to pH 7.2 with KOH. Nystatin (Sigma, St. Louis, MO, USA) was used for patch perforation at a working concentration of 200 µM. To this end, it was dissolved in Dimethyl Sulfoxide (DMSO; Sigma, St. Louis, MO, USA) to obtain a 55 mM stock solution, which following 1 min ultra-sonication was diluted in pipette solution to obtain working solution. Nystatin solutions were freshly prepared in the dark every 2 h. Only cells with series resistance of ≤15 MΩ were used for analysis. The extracellular solution contained (mM): 140 NaCl, 2.8 KCl, 2 $MgSO_4$, 1.8 $CaCl_2$, 10 HEPES, 10 D-glucose, adjusted to pH 7.4 with NaOH (Ringer solution). Once the perforated-patch or the standard whole cell configuration was established, cells were continuously superfused with extracellular solutions. To avoid effects from pre-exposure of the recorded cells to the applied agonist, cells were exposed to them once, allowing the recording of a single cell from each coverslip.

Statistical Analysis

Statistical analyses were performed using the Matlab statistical analysis toolbox and Prism 7 (GraphPad Software, La Jolla, CA, USA). Student's t-test and ANOVA were used to determine statistical significance. Electrophysiological analysis was performed by using pClamp 10.6 software.

RESULTS

GTL-1 Participates in the Response to Cold Temperatures

Previous analysis showed that PVD neurons respond to temperature downshift *via* the TRP channel, TRPA-1, as

demonstrated by findings showing that *trpa-1(lf)* animals have an impaired response to rapid cooling. Specifically, in response to cooling *trpa-1(lf)* animals show no calcium transients within PVD and no increase in omega turns when examined in a liquid drop (Chatzigeorgiou et al., 2010). We have previously shown that TRPA-1 is required for the altered locomotion of animals at cold (15°C) relative to warm (20°C) temperatures (Cohen et al., 2014). To examine the role of GTL-1 in this behavioral response we used the same locomotion assay (Cohen et al., 2014). At 20°C, wild-type (N2) animals moved at an average speed of 0.225mm/sec and had a low rate of pauses and direction reversals (**Figure 1**). After 10 min at 15°C wild-type (N2) animals' speed was significantly reduced and the rate of pauses was significantly increased relative to 20°C (**Figures 1A, B**, black bars vs. grey bars). In *gtl-1* mutants effects of temperature on speed were smaller, although significant; no significant effect of temperature on speed was detected in *trpa-1* mutants; and, no significant effect of temperature on the rate of pauses was seen in *gtl-1* and *trpa-1* loss of function mutants (**Figures 1A, B**). Temperature affected the rate of reversals similarly to its effect on the rate of pauses, but, in none of the strains was this effect significant (**Figure 1C**). The similar effects of GTL-1 and TRPA-1 in reducing the response to cold temperature relative to the response of wild-type animals are consistent with GTL-1, like TRPA-1, being required for this response (**Figures 1A, B**). We note that *gtl-1(lf)* also affects locomotion at 20°C; having significantly reduced speed and increased rate of pauses relative to wild-type (N2) animals ($p < 0.0001$ two-way ANOVA). However, contribution of genotype to the variance in locomotion is only significant when examining the rate of pauses (two-way ANOVA, $p < 0.0001$).

Effects of GTL-1 on the Response to Cold Temperature Require Its Expression in PVD

Results in **Figures 1A–C** show altered locomotion of *gtl-1(lf)* animals at normal growth temperature (20°C). Such differences may mask the effect of temperature reduction on locomotion. Moreover, *gtl-1* is widely expressed and some of its effects may not depend on PVD expression. To examine whether the reduced response to cold temperatures depends on function of GTL-1 in PVD cells, we specifically knocked down its expression in PVD neurons using cell specific dsRNA-mediated knockdown (Esposito et al., 2007). Indeed, results in **Figures 1D, E** show that effects of GTL-1 on locomotion at 20°C do not depend on its

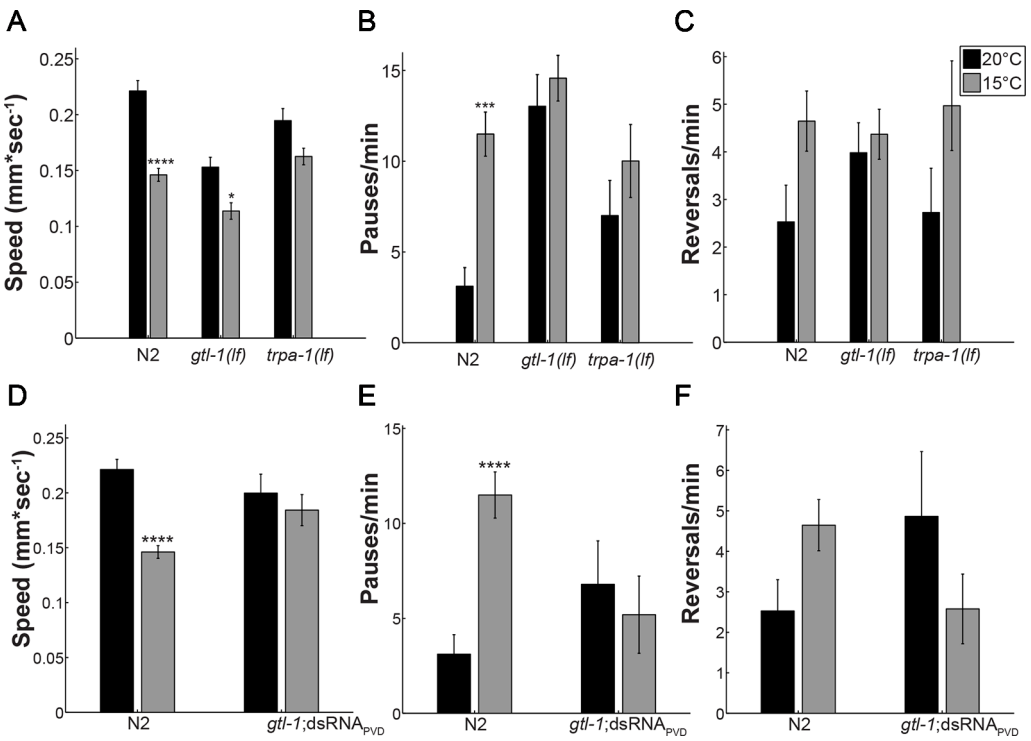

FIGURE 1 | GTL-1 is required within PVD for the effects of temperature on locomotion. Effects of temperature on locomotion were compared between wild type (N2), *gtl-1(lf)*, and *trpa-1(lf)* animals **(A–C)** and between wild-type (N2) animals and animals expressing *gtl-1*dsRNA specifically in PVD (*gtl-1;*dsRNA$_{PVD}$) **(D–F)**, at 20° C (black bars) or 15°C (grey bars). Number of animals, 24, 36, 29, 22, 18, and 15 **(A–C)** and 24, 36, 13, and 12 **(D–F)** in order of appearance. Significant differences for the same strain at 15°C relative to 20°C were examined using two-way ANOVA with bonferroni's multiple comparisons correction (*-$p < 0.05$, ***-$p < 0.01$, ****-$p < 0.0001$). Temperature contributes significantly to the variance in A ($p < 0.0001$), B ($p = 0.0018$), C ($p = 0.0112$), D ($p < 0.0001$) and E ($p = 0.042$); genotype contributes significantly to the variance only in B ($p < 0.0001$); and effects of the interaction are significant in A ($p = 0.0069$), B ($p = 0.0476$), D ($p = 0.0069$), E ($p = 0.0032$), and F (0.026).

expression in PVD. Moreover, genotype does not significantly contribute to the variance in locomotion when comparing wild-type animals to animals in which *gtl-1* was specifically silenced in PVD (two-way ANOVA). Importantly, effects of cold temperature on locomotion are eliminated in the transgenic animals in which *gtl-1* was specifically knocked-down in PVD. In addition, the residual effects of temperature on locomotion speed seen in *gtl-1(lf)* animals are not seen when *gtl-1* is specifically silenced in PVDs (compare **Figures 1A–D**). Thus, GTL-1's function in PVD is required for the behavioral response of *C.elegans* to cold temperatures while effects of GTL-1 on locomotion under normal growth temperature are independent of PVD expression.

Effects of GTL-1 on the Immediate Response to Cold

Results described above (**Figure 1**) show locomotion following adaptation to cold temperatures (10 min after transfer to 15°C) and may also include an enduring response to transfer, a strong mechanical stimulus (Cohen et al., 2012). To examine whether *gtl-1* participates in the immediate response to temperature downshift we used a setup that allows us to rapidly cool the agar surface on which the animals is placed while recording the animal's locomotion (see Methods). Due to poor image quality in this setup movies were manually analyzed. Therefore, only one parameter was tested, the number of reversals. Reversals were counted during a 30 sec interval immediately before temperature downshift and immediately after temperature downshift and compared to the number of reversals in animals that were continuously maintained at 20°C. To reduce effects of transfer to the test surface on locomotion, animals were allowed to recover from the noxious mechanical stress (transfer with a wire pick) for 10 min before being examined.

After 10 min at 20°C, wild-type (N2) animals had a reversal rate of 4.25 ± 0.73 reversals/minute, when maintained at 20°C for another 10 min this rate slightly increased (5.25 ± 0.69 reversals/minute (**Figures 2A, B**, black bars)). Immediately after the temperature drop to 15°C wild-type animals reduced their rate of reversals (a 3.4-fold reduction to 1.25 ± 0.4 reversals/minute; **Figure 2A**), a reduction likely to represent an escape response i.e., increased forward speed, reduced pauses and reduced reversals (Cohen et al., 2012). This reduction is maintained for 10 min at the noxious temperature of 15°C (**Figure 2B**). Since, the response observed using this assay differs from the response to lower temperature seen in the previous assay [**Figure 1** and (Cohen et al., 2014)] we examined whether it represents a PVD-mediated response to temperature downshift. For this, we examined animals lacking PVD neurons [-PVD animals (Albeg et al., 2011)]. Indeed, -PVD animals exhibit a weaker, statistically insignificant reduction in reversals immediately after the temperature downshift (**Figure 2A**) and no reduction in the rate of reversals following 10 min at 15°C (**Figure 2B**). Thus, reduced rate of reversals following temperature downshift requires PVD neurons allowing us to use this assay to examine the role of GTL-1 in the immediate response to thermal stimuli. Indeed, this assay demonstrates the similarity between *gtl-1(lf)* and -PVD animals in their immediate and enduring responses to temperature downshift (**Figures 2A, B**). Together, our results (**Figures 1** and **2**) demonstrate an important role for GTL-1 in the response to cold temperatures.

GTL-1 and the Response to Mechanical Stimuli

GTL-1 was shown to amplify optogenetic stimuli to PVD, a result suggesting that it functions downstream to nocisensors (Husson et al., 2012). Thus, GTL-1 is unlikely to function

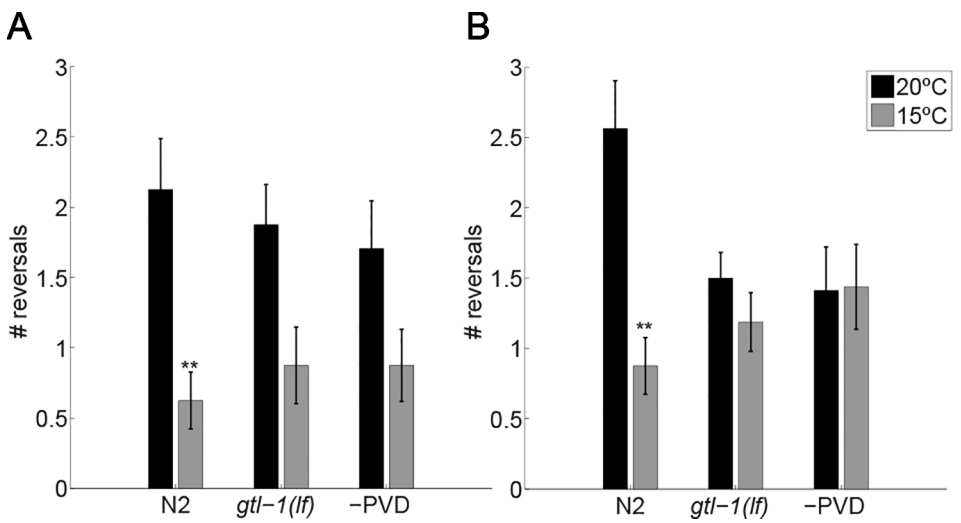

FIGURE 2 | GTL-1 is required for the immediate and enduring response to cold temperatures. Number of reversals was counted over 30 sec immediately after the temperature drop **(A)** and 10 min later **(B)**. n = 16 each. Significant differences relative to controls, maintained at 20°C (black bars) throughout the experiments, were examined using two-way ANOVA **-p< 0.01).

specifically in the response to thermal stimuli and is likely to also affect the response to noxious mechanical stimuli. To examine the role of GTL-1 in the response to mechanical stimuli we first examined its effects on percent animals responding to single noxious mechanical stimulus (prodding with a platinum wire pick). Since this response depends on both PVD and touch receptor neurons (Way and Chalfie, 1989) we compared responses of *mec-4(e1611)* animals, in which touch receptor neurons degenerate (Driscoll and Chalfie, 1991), to responses of *gtl-1(lf);mec-4(e1611)* lacking GTL-1 and touch receptor neurons. Using this assay we found a small but insignificant effect of GTL-1 on percent animals responding to noxious mechanical stimuli (**Figure 3A**). Thus *gtl-1* is not essential for a reliable response to a single high-threshold mechanical stimulus.

Responses to noxious stimuli habituate to a lower extent relative to responses to similar non noxious stimuli; as shown when comparing responses to repeated optogenetic activation of PVD neurons relative to responses to repeated optogenetic activation of the low threshold touch receptor neurons (Husson et al., 2012). To examine whether GTL-1 is required for maintaining the response to repeated mechanical stimuli we compared decay in percent animals responding to repeated noxious mechanical stimuli between wild-type, *gtl-1(lf)* and –PVD animals. Results of this analysis are consistent with PVD neurons being needed for maintaining the response to repeated mechanical stimuli as, animals lacking PVD neurons show a stronger decay in the response to repeated prodding with a platinum wire pick relative to wild type animals (**Figure 3B**). Our results, however, show that GTL-1 is not required for maintaining the response to repeated noxious mechanical stimuli as its responses to repeated prodding are indistinguishable from these of wild-type animals (**Figure 3B**).

Results in **Figure 3** show that GTL-1 is not required for producing a reliable behavioral response to high threshold mechanical stimuli or for maintaining a reliable response to repeated high threshold mechanical stimuli. However, these assays did not examine magnitude of the response to such stimuli. To examine whether GTL-1 affects response magnitude to mechanical stimuli, we imaged locomotion of animals for 20 min following transfer of the animal to a new plate with a platinum wire pick; this assay provides a sensitive and quantitative measure for roles of genes and neurons in the response to mechanical stimuli (Cohen et al., 2012). Results of this analysis show that both N2 and gtl-1(lf) animals show similar reduction of forward speed over time and a similar ratio between speed at the start point and the end point (1.59 and 1.68, respectively). However, the starting speed of gtl-1(lf) is lower then that of wild-type animals (**Figure 4A**). Analysis of two other locomotion parameters, percent time moving forward and percent time pausing (**Figures 4B, C**) show a similar starting point but larger changes over time relative to wild-type. To better understand the role of PVD expressed GTL-1 in locomotion following noxious mechanical stimuli we examined animals following PVD-specific knockdown of gtl-1 expression, as described above (**Figures 1D–F**). Results of this analysis show reduced initial speed following transfer of the animal with a platinum wire pick, a difference that is maintained 3 to 4 min following transfer (**Figure 4D**). Other parameters examined show no difference between wild-type animals and transgenic animals (**Figures 4E, F**). These results demonstrate a role for PVD-expressed GTL-1 in determining the magnitude of the escape response (enhanced forward speed) following a noxious mechanical stimulus. Other effects of GTL-1 on locomotion in this assay are likely to depend on its expression in yet unidentified cells. Previously published results show that

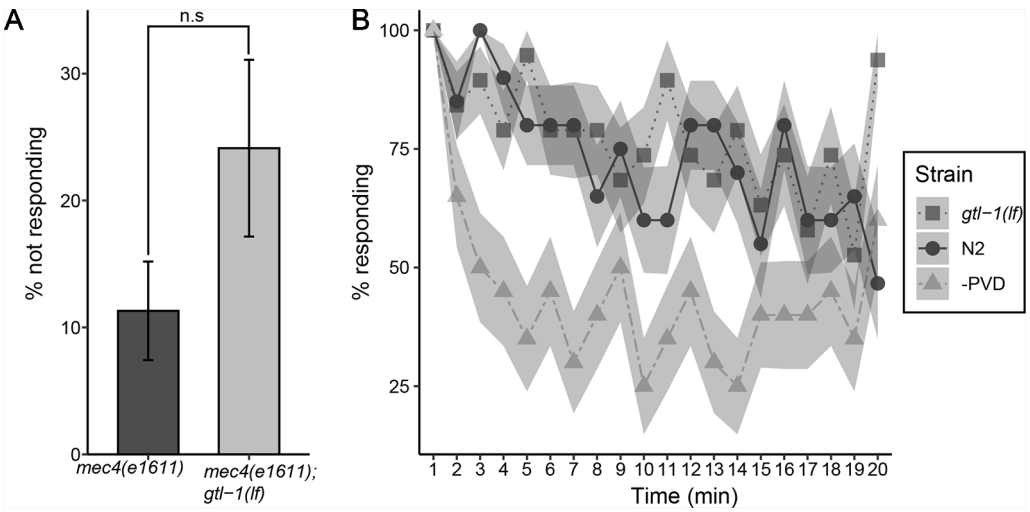

FIGURE 3 | GTL-1 is not essential for the response to single or repeated mechanical stimuli. **(A)** Percent animals not responding to a single high threshold mechanical stimuli in *mec-4(e1611);*gtl-1(lf) and in *mec-4(1611)* animals (20 and 11 plates, respectively, 10 animals each plate). Statistical analysis was performed using n.s, p = 0.086. **(B)** Responses to repeated high threshold mechanical stimuli in *gtl-1(lf)* animals (n = 20), wild-type (N2, n = 20), and -PVD (n = 20) animals.

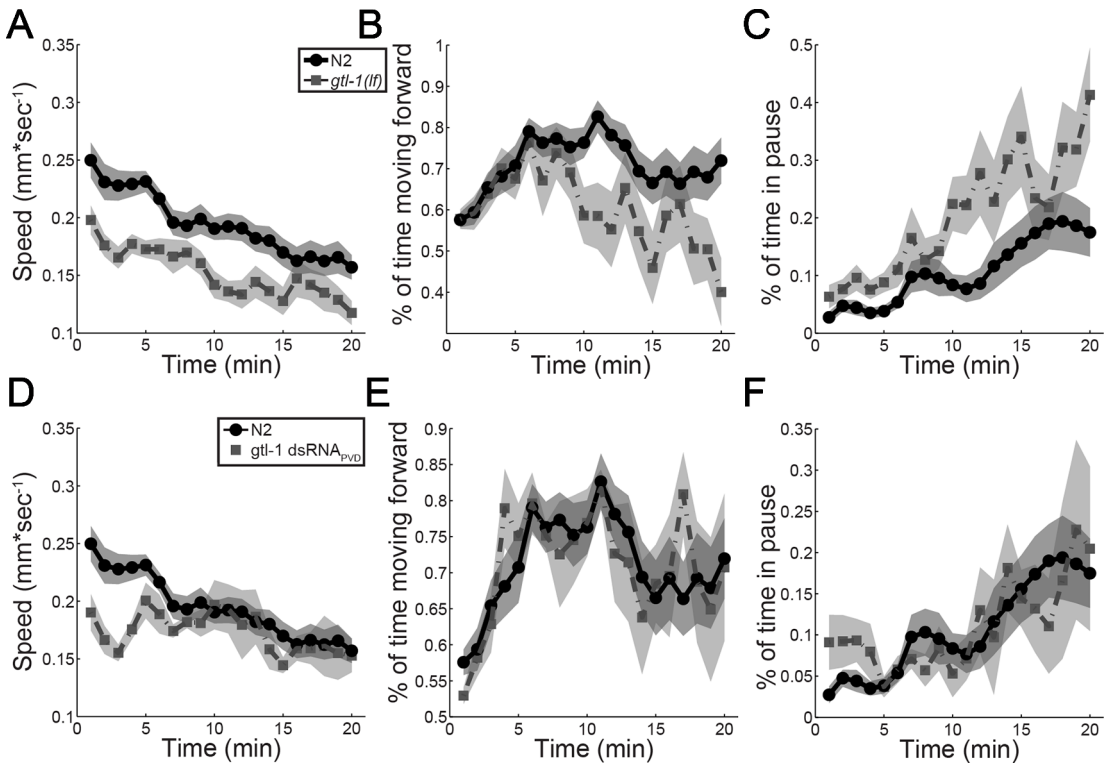

FIGURE 4 | GTL-1 affects the magnitude of the response to noxious mechanical stimuli. Immediate and enduring responses to a noxious mechanical stimulus of wild-type (N2, N = 19, circles) compared to *gtl-1(lf)* (n = 13, squares) **(A–C)** and wild-type (N2, n = 19, circles) compared to *gtl-1* dsRNA$_{PVD}$ (n = 5, squares) **(D–F)**.

animals lacking PVD show a similar reduction in the escape response, relative to wild-type animals, i.e. reduced speed immediately following transfer with a wire pick, a reduction that lasts for a few min (Cohen et al., 2012). Thus, GTL-1 is likely to be an important determinant of this PVD-mediated escape response to noxious mechanical stimuli.

Heterologous Expression of GTL-1

Behavioral analysis (above) together with the previously published optogenetic analysis (Husson et al., 2012) show that GTL-1 functions in PVDs to enhance responses to multiple modalities. Previous studies suggest that GTL-1 might be a calcium-activated non-selective cation channel (CAN) (Xing et al., 2008; Xing and Strange, 2010), a mode of gating similar to that of TRPM4 and TRPM5 (Launay et al., 2002; Hofmann et al., 2003). Activation by cytosolic calcium may explain the role of GTL-1 in amplifying responses to multiple distinct stimuli activating PVDs.

To examine whether internal calcium activates GTL-1-dependent currents we used the multi-channel inside-out configuration of the patch clamp technique in HEK293 cells; excised patches were exposed to Ca^{2+} at different membrane voltages; this analysis showed voltage and internal calcium dependent gating of GTL-1 (**Figures 5A, B**). Specifically, in cells expressing GTL-1 and in the presence of internal calcium we observed outwardly rectifying currents (**Figure 5A**). Although, these currents were small they were significantly larger then currents seen in the absence of calcium (**Figure 5B**). No difference was observed between effects of 0.1 mM and 1 mM calcium on current amplitudes (**Figure 5B**); a result consistent with results obtained in the *C. elegans* intestine where GTL-1 and GON-2 function together to produce calcium oscillations and the defecation rhythm; these calcium oscillation were attributed to calcium having two opposing effects on these channels; activation at low concentrations and inhibition at higher concentrations (Estevez and Strange, 2005). Importantly, activation of GTL-1 by internal calcium enables its activation by receptors and channels affecting cytosolic calcium levels, directly or indirectly (**Figure 6**).

In the intestine GTL-1 was suggested to function downstream to PLC and IP_3, known to function as part of signaling pathways leading to calcium release from internal stores (Xing and Strange, 2010). To examine whether $G_{\alpha}q$-dependent signaling, leading to PLC activation and IP_3 signaling, activates GTL-1 we used a Designer Receptor Exclusively Activated by Designer Drugs (DREADD) developed for expression in HEK293 cells (Lee et al., 2014; Roth, 2016). Previously published results show that in HEK293 cells CNO-dependent currents are only detected when this DREADD receptor is co-expressed with a TRP channel and are abolished in the presence of a PLC inhibitor

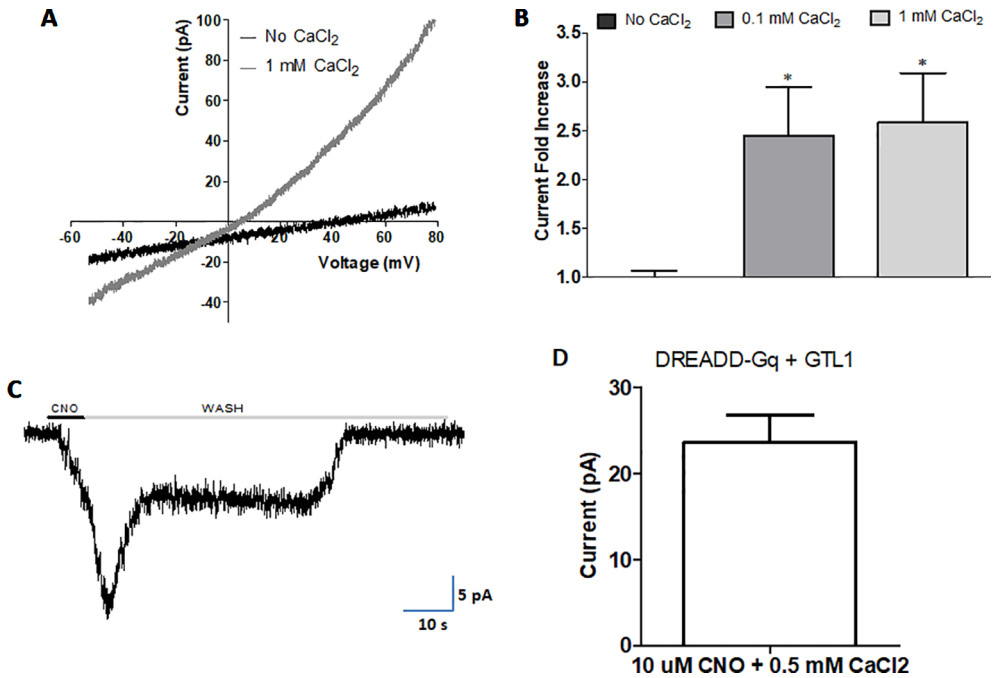

FIGURE 5 | Internal calcium and Gαq activity gate GTL-1. GTL-1 was expressed in HEK293 cells. **(A and B)** Calcium enhances GTL-1 dependent currents. **(A)** Representative IV recording with and without calcium applied to the inner side of the excised inside-out patch. **(B)** Fold effect on current amplitudes of Calcium applied to the excised inside-out patch at +80mV. Effects of calcium are significant, $p < 0.05$, ($n = 8$), one-way ANOVA with correction for multiple variables **(C** and **D)** GTL-1 is activated by DREADD-Gαq. **(C)** Representative response. **(D)** Average response, $n = 5$. Of note, no currents are detected in the absence of CNO or in cells not expressing GTL-1.

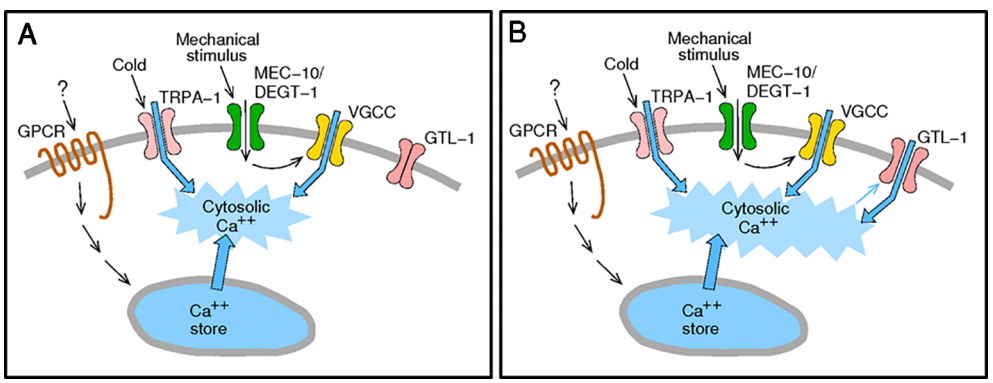

FIGURE 6 | Activation of GTL-1 by internal calcium enables amplification of sensory stimuli. **(A)** Sensory stimuli *via* nocisensor activation directly (TRPA-1) or indirectly (GPCRs and MEC-10/DEGT-1) elevate cytosolic calcium. **(B)** Elevated cytosolic calcium activates GTL-1 channels to amplify the calcium signal.

(Kumar et al., 2017). Thus, results (**Figures 5C, D**) showing reproducible CNO-activated currents when co-expressing GTL-1 with this DREADD receptor are a clear indication for GTL-1 being activated downstream to $G_{\alpha}q$-dependent signaling and are consistent with results obtained in the *C. elegans* intestine (Xing and Strange, 2010).

DISCUSSION

GTL-1, a member of the TRPM family of ion channels, was previously shown to amplify behavioral responses to optogenetic activation of PVD (Husson et al., 2012). Here, we set out to characterize the role of GTL-1in PVD-mediated responses to

noxious, physiological, stimuli. PVD cells mediate the response to temperature downshift, a response requiring PVD expression of TRPA-1 (Chatzigeorgiou et al., 2010). Our results demonstrate similar defects in the behavioral responses to cold temperatures in *gtl-1(lf)* animals, *trpa-1(lf)* animals, and animals lacking PVD. Analysis of the PVD mediated response to mechanical stimuli, however, shows milder GTL-1-dependent behavioral effects. Specifically our results show reduced response magnitude to a noxious mechanical stimulus. But, no significant reduction in the reliability of the response (percent animal responding) to a single or to repeated mechanical stimuli. To understand the mechanism enabling effects of GTL-1 on responses to thermal, mechanical, and optogenetic stimuli, we examined its gating using electrophysiology in HEK293 cells. Results of this analysis show that internal calcium and Gαq-signaling gate this channel. Thus, GTL-1 like other TRPM channels, and as described in **Figure 6**, enables amplification of responses to receptors and channels that, directly or indirectly, enhance internal calcium levels (Launay et al., 2002; Zurborg et al., 2007).

Our results suggest that GTL-1 is mainly required for responses to immediate and enduring cold temperatures while having a relatively minor role in the response to high threshold mechanical stimuli. Non-sensor channels that are required for a specific modality within a polymodal nociceptor have previously been reported. For example, inhibition of the voltage-gated potassium channel, $k_v1.1$, leads to severe mechanical allodynia (i.e., lowers the threshold and causes non-painful stimuli to be sensed as painful) without affecting the threshold for noxious heat (Hao et al., 2013); the voltage-gated sodium channel, $Na_v1.8$, on the other hand, has been shown to specifically affect transmission of cold sensation, by being the only voltage-gated sodium channel active at low temperatures (Matthews et al., 2006; Zimmermann et al., 2007). Additional analysis of GTL-1 channel's properties is needed to better understand its modality specific effects.

In mammals, the TRPM family consists of 8 different channels TRPM1-8. Members of this family are implicated in various biological processes, e.g., regulation of Ca^{2+} oscillations following T-lymphocyte activation (TRPM4) (Launay et al., 2004), regulation of magnesium absorption in kidneys and the intestine (TRPM6) (Voets et al., 2004; Vriens et al., 2011), gustatory transduction (TRPM5) and innocuous and noxious thermal sensing (TRPM3 and 8)(Zhang et al., 2003; Bautista et al., 2007; Dhaka et al., 2007; Vriens et al., 2011). *C. elegans* expresses three TRPM channels, *gon-2, gtl-1*, and *gtl-2.* These channels express widely including the intestine, the gonad, excretory cells, and the nervous system. Functions of these channels include, maintaining Ca^{2+} and Mg^{2+} homeostasis in the intestines and in extracellular fluids (Teramoto et al., 2005; Stawicki et al., 2011), controlling defecation rhythm (Kwan et al., 2008; Xing et al., 2008), and regulating the onset and continuation of post-embryonic mitotic cell divisions in the somatic gonad (Sun and Lambie, 1997; West et al., 2001). Our results combined with the results in (Husson et al., 2012) show for the first time a neuronal function for GTL-1; enhancing responses to noxious stimuli.

Previous work showed that in the *C. elegans* intestine GTL-1 functions together with GON-2 to produce a strong inwardly rectifying current, I_{ORCa}. The role of GTL-1 in this current was deduced from comparing currents in *gtl-1, gon-2*, or *gon-2;gtl-1* loss of function animals to wild-type animals. These studies suggested that GTL-1 has a minor role in I_{ORCa} and that it is likely to be activated by cytosolic Ca^{2+} and to function downstream of PLC signaling (Teramoto et al., 2005; Xing et al., 2008; Xing and Strange, 2010). This study, for the first time, characterizes properties of the GTL-1 channel in a heterologous expression system. Results of this analysis are consistent with the *in-vivo* results, showing mild outward rectification of the GTL-1 dependent currents, activation by internal calcium and by Gαq signaling. Importantly, our findings suggest a mechanism, summarized in **Figure 6**, whereby GTL-1 is activated downstream of channels, receptors and signaling pathways whose activation directly or indirectly increases cytosolic calcium; thus enabling GTL-1 dependent enhancement of multiple and distinct sensory modalities as demonstrated by its effects on behavioral responses to thermal and mechanical stimuli.

DATA AVAILABILITY STATEMENT

The datasets generated for this study are available on request to the corresponding author.

AUTHOR CONTRIBUTIONS

EC performed behavioural analysis, cloned *gtl-1* cDNA into mammalian cell expression vector, organized results for article, and participated in writing the article. RK performed and analyzed heterologous expression studies. TZ set up the system enabling imaging and analysis of the response to rapid temperature downshift, performed the experiments, and analyzed them. AP supervised the heterologous expression studies and participated in writing the article. MT supervised behavioral analysis and wrote the article.

FUNDING

This work was supported by the Prusiner-Abramsky research award to MT, the Israel Science Foundation (Grants 1444/16 to AP), the Brettler Center and David R. Bloom Center, School of Pharmacy (The Hebrew University of Jerusalem; to AP), a Jerusalem Brain Committee Postdoctoral Fellowship (to RK).

ACKNOWLEDGMENTS

We thank the *C. elegans* Genetics Stock Center for strains, Howard Baylis for the *gtl-1* cDNA, and Anatoly Shapochnikov for assistance with setting up the immediate cooling device.

REFERENCES

Albeg, A., Smith, C. J., Chatzigeorgiou, M., Feitelson, D. G., Hall, D. H., Schafer, W. R., et al. (2011). C. elegans multi-dendritic sensory neurons: morphology and function. *Mol. Cel Neurosci.* 46, 308–317. doi: 10.1016/j.mcn.2010.10.001

Babcock, D. T., Landry, C., and Galko, M. J. (2009). Cytokine signaling mediates UV-induced nociceptive sensitization in Drosophila larvae. *Curr. Biol.* 19, 799–806. doi: 10.1016/j.cub.2009.03.062

Bautista, D. M., Siemens, J., Glazer, J. M., Tsuruda, P. R., Basbaum, A. I., Stucky, C. L., et al. (2007). The menthol receptor TRPM8 is the principal detector of environmental cold. *Nature* 448, 204–208. doi: 10.1038/nature05910

Caterina, M. J., and Julius, D. (1999). Sense and specificity: a molecular identity for nociceptors. *Curr. Opin. In Neurobiol.* 9, 525–530. doi: 10.1016/S0959-4388(99)00009-4

Caterina, M. J., Leffler, A., Malmberg, A. B., Martin, W. J., Trafton, J., Petersen-Zeitz, K. R., et al. (2000). Impaired nociceptrion and pain sensation in mice lacking the capsaicin receptor. *Science* 288, 306–313. doi: 10.1126/science.288.5464.306

Chatzigeorgiou, M., Yoo, S., Watson, J. D., Lee, W. H., Spencer, W. C., Kindt, K. S., et al. (2010). Specific roles for DEG/ENaC and TRP channels in touch and thermosensation in C. elegans nociceptors. *Nat. Neurosci.* 13, 861–868. doi: 10.1038/nn.2581

Clapham, D. (2003). TRP channels as cellular sensors. *Nature* 426, 519–524. doi: 10.1038/nature02196

Cohen, E., Yemini, E., Feitelson, D. G., Schaffer, W. R., and Treinin, M. (2012). Locomotion analysis identifies roles of mechanosensory neurons in governing locomotion dynamics of *C. elegans*. *J. Exp. Biol.* 215, 3639–3648. doi: 10.1242/jeb.075416

Cohen, E., Chatzigeorgiou, M., Husson, S. J., Steuer-Costa, W., Gottschalk, A., Schafer, W. R., et al. (2014). C. elegans nicotinic acetylcholine receptors are required for nociception. *Mol. Cell Neurosci.* 59, 85–96. doi: 10.1016/j.mcn.2014.02.001

Dhaka, A., Viswanath, V., and Patapoutian, A. (2006). Trp ion channels and temperature sensation. *Annu. Rev. Neurosci.* 29, 135–161. doi: 10.1146/annurev.neuro.29.051605.112958

Dhaka, A., Murray, A. N., Mathur, J., Earley, T. J., Petrus, M. J., and Patapoutian, A. (2007). TRPM8 is required for cold sensation in mice. *Neuron* 54, 371–378. doi: 10.1016/j.neuron.2007.02.024

Driscoll, M., and Chalfie, M. (1991). The mec-4 gene is a member of a family of Caenorhabditis elegans genes that can mutate to induce neuronal degeneration. *Nature* 349, 588–593. doi: 10.1038/349588a0

Esposito, G., Schiavi, E. D., Bergamasco, C., and Bazzicalupo, P. (2007). Efficient and cell specific knock-down of gene function in targeted C. elegans neurons. *Gene* 395, 170–176. doi: 10.1016/j.gene.2007.03.002

Estevez, A. Y., and Strange, K. (2005). Calcium feedback mechanisms regulate oscillatory activity of a TRP-like Ca2+ conductance in C. elegans intestinal cells. *J. Physiol.* 567, 239–251. doi: 10.1113/jphysiol.2005.091900

Geron, M., Kumar, R., Zhou, W., Faraldo-Gómez, J. D., Vásquez, V., and Priel, A. (2018). TRPV1 pore turret dictates distinct DkTx and capsaicin gating. *Proc. Natl. Acad. Sci. U.S.A.* 115, E11837–E11846. doi: 10.1073/pnas.1809662115

Hao, J., Padilla, F., Dandonneau, M., Lavebratt, C., Lesage, F., Noël, J., et al. (2013). Kv1.1 channels act as mechanical brake in the senses of touch and pain. *Neuron* 77, 899–914. doi: 10.1016/j.neuron.2012.12.035

Hofmann, T., Chubanov, V., Gudermann, T., and Montell, C. (2003). TRPM5 is a voltage-modulated and Ca(2+)-activated monovalent selective cation channel. *Curr. Biol.* 13, 1153–1158. doi: 10.1016/s0960-9822(03)00431-7

Husson, S. J., Steuer Costa, W., Wabnig, S., Stirman, J. N., Watson, J. D., Spencer, W. C., et al. (2012). Optogenetic analysis of a nociceptor neuron and network reveals modulatory ion channels acting downstream of nociceptive sensors. *Curr. Biol.* 22, 743–752. doi: 10.1016/j.cub.2012.02.066

Julius, D. (2013). TRP channels and pain. *Annu. Rev. Cell Dev. Biol.* 29, 355–384. doi: 10.1146/annurev-cellbio-101011-155833

Kamath, R. S., Fraser, A. G., Dong, Y., Poulin, G., Durbin, R., Gotta, M., et al. (2003). Systematic functional analysis of the Caenorhabditis elegans genome using RNAi. *Nature* 421, 231–237. doi: 10.1038/nature01278

Kumar, R., Hazan, A., Geron, M., Steinberg, R., Livni, L., Matzner, H., et al. (2017). Activation of transient receptor potential vanilloid 1 by lipoxygenase metabolites depends on PKC phosphorylation. *FASEB J.* 31, 1238–1247. doi: 10.1096/fj.201601132R

Kwan, C. S., Vázquez-Manrique, R. P., Ly, S., Goyal, K., and Baylis, H. A. (2008). TRPM channels are required for rhythmicity in the ultradian defecation rhythm of C. elegans. *BMC Physiol.* 8, 11. doi: 10.1186/1472-6793-8-11

Launay, P., Fleig, A., Perraud, A. L., Scharenberg, A. M., Penner, R., and Kinet, J. P. (2002). TRPM4 is a Ca2+-activated nonselective cation channel mediating cell membrane depolarization. *Cell* 109, 397–407. doi: 10.1016/s0092-8674(02)00719-5

Launay, P., Cheng, H., Srivatsan, S., Penner, R., Fleig, A., and Kinet, J. P. (2004). TRPM4 regulates calcium oscillations after T cell activation. *Science* 306, 1374–1377. doi: 10.1126/science.1098845

Lee, H. M., Giguere, P. M., and Roth, B. L. (2014). DREADDs: novel tools for drug discovery and development. *Drug Discovery Today* 19, 469–473. doi: 10.1016/j.drudis.2013.10.018

Matthews, E. A., Wood, J. N., and Dickenson, A. H. (2006). Na(v) 1.8-null mice show stimulus-dependent deficits in spinal neuronal activity. *Mol. Pain* 2, 5. doi: 10.1186/1744-8069-2-5

Priel, A., and Silberberg, S. D. (2004). Mechanism of ivermectin facilitation of human P2X4 receptor channels. *J. Gen. Physiol.* 123, 281–293. doi: 10.1085/jgp.200308986

Roth, B. L. (2016). DREADDs for Neuroscientists. *Neuron* 89, 683–694. doi: 10.1016/j.neuron.2016.01.040

Smith, E. S., and Lewin, G. R. (2009). Nociceptors: a phylogenetic view. *J. Comp. Physiol. A* 195, 1089–1106. doi: 10.1007/s00359-009-0482-z

Smith, C. J., Watson, J. D., Spencer, W. C., OÕBrien, T., Cha, B., Albeg, A., et al. (2010). Time-lapse imaging and cell-specific expression profiling reveal dynamic branching and molecular determinants of a multi-dendritic nociceptor in C. elegans. *Dev. Biol.* 345, 18–33. doi: 10.1016/j.ydbio.2010.05.502

Stawicki, T. M., Zhou, K., Yochem, J., Chen, L., and Jin, Y. (2011). TRPM channels modulate epileptic-like convulsions *via* systemic ion homeostasis. *Curr. Biol.* 21, 883–888. doi: 10.1016/j.cub.2011.03.070

Sun, A. Y., and Lambie, E. J. (1997). gon-2, a gene required for gonadogenesis in Caenorhabditis elegans. *Genetics* 147, 1077–1089.

Teramoto, T., Lambie, E. J., and Iwasaki, K. (2005). Differential regulation of TRPM channels governs electrolyte homeostasis in the C. elegans intestine. *Cell Metab.* 1, 343–354. doi: 10.1016/j.cmet.2005.04.007

Tsalik, E. L., Niacaris, T., Wenick, A. S., Pau, K., Avery, L., and Hobert, O. (2003). LIM homeobox gene-dependent expression of biogenic amine receptors in restricted regions of the C. elegans nervous system. *Dev. Biol.* 263, 81–102. doi: 10.1016/s0012-1606(03)00447-0

Voets, T., Nilius, B., Hoefs, S., van der Kemp, A. W., Droogmans, G., Bindels, R. J., et al. (2004). TRPM6 forms the Mg2+ influx channel involved in intestinal and renal Mg2+ absorption. *J. Biol. Chem.* 279, 19–25. doi: 10.1074/jbc.M311201200

Vriens, J., Owsianik, G., Hofmann, T., Philipp, S. E., Stab, J., Chen, X., et al. (2011). TRPM3 is a nociceptor channel involved in the detection of noxious heat. *Neuron* 70, 482–494. doi: 10.1016/j.neuron.2011.02.051

Way, J. C., and Chalfie, M. (1989). The mec-3 gene of Caenorhabditis elegans requires its own product for maintained expression and is expressed in three neuronal cell types. *Genes Dev.* 3, 1823–1833. doi: 10.1101/gad.3.12a.1823

West, R. J., Sun, A. Y., Church, D. L., and Lambie, E. J. (2001). The C. elegans gon-2 gene encodes a putative TRP cation channel protein required for mitotic cell cycle progression. *Gene* 266, 103–110. doi: 10.1016/s0378-1119(01)00373-0

Woolf, C. J., and Ma, Q. (2007). Nociceptors–noxious stimulus detectors. *Neuron* 55, 353–364. doi: 10.1016/j.neuron.2007.07.016

Xing, J., and Strange, K. (2010). Phosphatidylinositol 4,5-bisphosphate and loss of PLCgamma activity inhibit TRPM channels required for oscillatory Ca2+ signaling. *Am. J. Physiol. Cell Physiol.* 298, C274–C282. doi: 10.1152/ajpcell.00394.2009

Xing, J., Yan, X., Estevez, A., and Strange, K. (2008). Highly Ca2+-selective TRPM channels regulate IP3-dependent oscillatory Ca2+ signaling in the C. elegans intestine. *J. Gen. Physiol.* 131, 245–255. doi: 10.1085/jgp.200709914

Zhang, Y., Hoon, M. A., Chandrashekar, J., Mueller, K. L., Cook, B., Wu, D., et al. (2003). Coding of sweet, bitter, and umami tastes: different receptor cells sharing similar signaling pathways. *Cell* 112, 293–301. doi: 10.1016/s0092-8674(03)00071-0

Zimmermann, K., Leffler, A., Babes, A., Cendan, C. M., Carr, R. W., Kobayashi, J., et al. (2007). Sensory neuron sodium channel Nav1.8 is essential for pain at low temperatures. *Nature* 447, 855–858. doi: 10.1038/nature05880

Zurborg, S., Yurgionas, B., Jira, J. A., Caspani, O., and Heppenstall, P. A. (2007). Direct activation of the ion channel TRPA1 by Ca2+. *Nat. Neurosci.* 10, 277–279. doi: 10.1038/nn1843

Conflict of Interest: The authors declare that the research was conducted in the absence of any commercial or financial relationships that could be construed as a potential conflict of interest.

frontiers in Pharmacology

ORIGINAL RESEARCH
published: 17 January 2020
doi: 10.3389/fphar.2019.01566

The Hyperpolarization-Activated Cyclic-Nucleotide-Gated Channel Blocker Ivabradine Does Not Prevent Arrhythmias in Catecholaminergic Polymorphic Ventricular Tachycardia

Hanna Bueno-Levy[1†], David Weisbrod[1†], Dor Yadin[2†], Shiraz Haron-Khun[1,2], Asher Peretz[1], Edith Hochhauser[3], Michael Arad[2] and Bernard Attali[1*]*

[1] Department of Physiology and Pharmacology, The Sackler Faculty of Medicine, Tel Aviv University, Tel Aviv, Israel, [2] Leviev Heart Center, Sheba Medical Center, Tel Aviv, Israel, [3] The Cardiac Research Laboratory, Felsenstein Medical Research Center, Rabin Medical Center, Tel Aviv University, Petah Tikva, Israel

OPEN ACCESS

Edited by:
Avi Priel,
Hebrew University of Jerusalem, Israel

Reviewed by:
Alexander Binshtok,
Hebrew University of Jerusalem, Israel
Noam Zilberberg,
Ben-Gurion University of the Negev, Israel

***Correspondence:**
Michael Arad
michael.arad@sheba.health.gov.il
Bernard Attali
battali@tauex.tau.ac.il

[†]These authors have contributed equally to this work

Specialty section:
This article was submitted to Pharmacology of Ion Channels and Channelopathies, a section of the journal Frontiers in Pharmacology

Received: *17 September 2019*
Accepted: *03 December 2019*
Published: *17 January 2020*

Citation:
Bueno-Levy H, Weisbrod D, Yadin D, Haron-Khun S, Peretz A, Hochhauser E, Arad M and Attali B (2020) The Hyperpolarization-Activated Cyclic-Nucleotide-Gated Channel Blocker Ivabradine Does Not Prevent Arrhythmias in Catecholaminergic Polymorphic Ventricular Tachycardia. Front. Pharmacol. 10:1566. doi: 10.3389/fphar.2019.01566

Catecholaminergic polymorphic ventricular tachycardia (CPVT) is an inherited, stressed-provoked ventricular arrhythmia. CPVT is treated by β-adrenergic receptor blockers, Na^+ channel inhibitors, sympathetic denervation, or by implanting a defibrillator. We showed recently that blockers of SK4 Ca^{2+}-activated K^+ channels depolarize the maximal diastolic potential, reduce the heart rate, and attenuate ventricular arrhythmias in CPVT. The aim of the present study was to examine whether the pacemaker channel inhibitor, ivabradine could demonstrate anti-arrhythmic properties in CPVT like other bradycardic agents used in this disease and to compare them with those of the SK4 channel blocker, TRAM-34. The effects of ivabradine were examined on the arrhythmic beating of human induced pluripotent stem cells derived cardiomyocytes (hiPSC-CMs) from CPVT patients, on sinoatrial node (SAN) calcium transients, and on ECG measurements obtained from transgenic mice model of CPVT. Ivabradine did neither prevent the arrhythmic pacing of hiPSC-CMs derived from CPVT patients, nor preclude the aberrant SAN calcium transients. In contrast to TRAM-34, ivabradine was unable to reduce *in vivo* the ventricular premature complexes and ventricular tachyarrhythmias in transgenic CPVT mice. In conclusion, ivabradine does not exhibit anti-arrhythmic properties in CPVT, which indicates that this blocker cannot be used as a plausible treatment for CPVT ventricular arrhythmias.

Keywords: ivabradine, SK4, potassium channel, catecholaminergic polymorphic ventricular tachycardia, cardiac arrhythmia, ventricular arrhythmias, pacemaker

INTRODUCTION

Catecholaminergic polymorphic ventricular tachycardia (CPVT) is a rare, potentially fatal, inherited arrhythmia disease. It is often triggered by stress leading to polymorphic ventricular tachycardia in otherwise structurally normal hearts (Priori and Chen, 2011; Lieve et al., 2016). The pathophysiological mechanism of this disorder is suggested to involve diastolic Ca^{2+} leakage from

the sarcoplasmic reticulum (SR), thereby producing local increase in cytosolic Ca^{2+} that is extruded by the Na^{+}–Ca^{2+} exchanger NCX1. The increased NCX1 depolarizing activity generates early- or delayed-afterdepolarizations (EADs or DADs) that trigger premature beats and fatal polymorphic ventricular tachycardia (Priori and Chen, 2011). CPVT is a heterogeneous genetic disease, including autosomal dominant mutations in ryanodine receptor type 2 (RyR2, CPVT1), autosomal recessive mutations in calsequestrin 2 (CASQ2, CPVT2), and more rarely mutations in triadin or calmodulin. While CASQ2 mutants are "loss of function" mutations, the RyR2 mutations are "gain of function" mutations, both of which lead to diastolic Ca^{2+} leakage (Priori et al., 2002; Chopra and Knollmann, 2011; Priori and Chen, 2011; Arad et al., 2012; Lieve et al., 2016; Roston et al., 2017).

In addition to β-adrenergic receptor blockers, CPVT treatment includes inhibitors of Na^{+} channels such as flecainide, implantable defibrillator, and sympathetic denervation (Priori et al., 2002; Hayashi et al., 2009; Lieve et al., 2016; Roston et al., 2017). We have recently showed that SK4 K^{+} channels could be an additional therapeutic target for ventricular arrhythmias in CPVT (Haron-Khun et al., 2017). Recently, we found that TRAM-34, a selective blocker of SK4 K^{+} channels, decreased the β-adrenergic-triggered DADs and arrhythmic Ca^{2+} transients in human induced pluripotent stem cells derived cardiomyocytes (hiPSC-CMs) of CPVT2 patients bearing a mutation in calsequestrin 2 (CASQ2-D307H) and in sinoatrial node (SAN) from CASQ2-D307H knock-in (CASQ2 KI) mice (Haron-Khun et al., 2017). *In vivo* telemetric electrocardiograms (ECG) measurements showed that treatment with the SK4 channel blockers, TRAM-34 and clotrimazole, triggered sinus bradycardia and greatly reduced the ventricular arrhythmias of CASQ2-D307H KI and CASQ2 knockout mice at rest and following exercise (Haron-Khun et al., 2017).

Recently, the pacemaker channel inhibitor ivabradine was found to decrease digitalis-induced ventricular arrhythmias and short QT-induced arrhythmic features in Langendorff-perfused rabbit heart preparations (Frommeyer et al., 2017a; Frommeyer et al., 2017b). Ivabradine is usually prescribed to treat stable angina pectoris and in association with β-blockers to cure heart failure with left ventricular systolic dysfunction (Koruth et al., 2017). Ivabradine inhibits the pacemaker or funny current (If) in the SAN tissue, which is conveyed by hyperpolarization-activated, cyclic nucleotide-gated cation 4 (HCN4) channels and results in a decrease in the rate of diastolic depolarization and, consequently, the heart rate. Ivabradine also inhibits the human cardiac human ether-à-go-go related gene (hERG) K^{+} channel (IKr current), in a use-dependent manner, thereby prolonging the ventricular repolarization (Melgari et al., 2015). Overall, this causes an increase in the effective refractory period and in the post repolarization refractoriness, thus preventing premature excitations, which are usually a prelude of ventricular tachycardia.

The aim of the present work was to examine whether ivabradine could decrease the occurrence of arrhythmias found in cellular and animal model of CPVT. Results indicate that ivabradine was unsuccessful in reducing the occurrence of DADs in hiPSC-CMs derived from a CPVT2 patient. Similarly, ivabradine was unable to prevent the aberrant Ca^{2+} transients found in SAN and to reduce the ventricular arrhythmias observed in the ECG from CASQ2-D307H KI mice.

METHODS

Drugs

Isoproterenol, clotrimazole, and ivabradine hydrochloride were purchased from Sigma, while TRAM-34 from Tocris. For *in-vivo* telemetric recordings, ivabradine-HCl was dissolved in saline while TRAM-34 was solubilized into peanut oil.

Animals

SvEv mice (3–6 months old) homozygous for the CASQ2 D307H mutation (CASQ2 D307H KI) and matched wild-type (WT) mice were used in this study (Song et al., 2007). Mice were maintained and bred in a pathogen-free facility on regular rodent chow with free access to water and 12-h light and dark cycles. The procedures followed for experimentation and maintenance of the animals were approved by the Animal Research Ethics Committee of Tel Aviv University (M-14-063) in accordance with Israeli law and in accordance with the Guide for the Care and Use of Laboratory Animals (1996, National Academy of Sciences, Washington, DC).

Human Induced-Pluripotent Stem Cell Culture and Cardiac Differentiation

Human induced pluripotent stem cells (hiPSC) derived from normal healthy individuals and from patients bearing the CASQ2 D307H mutation (CPVT2) were grown on mitomycin C-inactivated mouse embryonic fibroblasts (MEF), in order to maintain them in an undifferentiated state. Cells were maintained pluripotent in a culture medium containing 80% Dulbecco's modified Eagle medium (DMEM) F-12 (Biological Industries), 20% Knock Out SR (Invitrogen), 2 mM L-glutamine, 0.1 mM β-mercaptoethanol (Gibco), and 1% nonessential amino acids (NEA) (Gibco), supplemented with 4 ng/ml basic fibroblast growth factor (bFGF) (Invitrogen). The medium was replaced daily until the colonies were ready to passage (every 4–5 days). For embryoid bodies (EBs) induction (d0), hiPSC colonies were removed from their MEF feeder by collagenase IV treatment and collected. After centrifugation, the cells were resuspended in EBs medium containing 80% DMEM (Gibco), 20% fetal bovine serum (FBS) (Biological Industries), 1% NEA, and 1 mM L-glutamine and plated on 58-mm Petri dishes. After 7 days of culture in suspension, EBs were plated on 0.1% gelatin-coated plates and checked daily until a spontaneous beating activity was visible. Because CASQ2 is lately expressed in hiPSC-CMs, 25 days-old EBs were used. The beating clusters were mechanically dissected from EBs, following a three-step dissociation protocol (Weisbrod et al., 2013). The hiPSC-CMs were isolated and plated on Matrigel-coated glass coverslips (13 mm diameter) in 24-well plates. The coverslips were then incubated at 37°C, and a recovery period of 2 days was given before any electrophysiological experiment was performed.

Mouse Sinoatrial Node Dissection and Calcium Transient Measurements

WT and CASQ2 D307H KI mice were anesthetized with isoflurane and sacrificed by cervical dislocation. The heart was rapidly removed and transferred into Tyrode solution containing heparin. After the atria were pinned and the superior and inferior vena cava localized, the ventricles were removed. The SAN was anatomically identified between the superior and inferior vena cava, the crista terminalis, and the interatrial septum. SAN tissue preparations were dissected *ex vivo* from WT and CASQ2-D307H KI mice as previously described (Torrente et al., 2015). The dissected whole SAN tissue was pinned on a hand-made chamber and was incubated in a Tyrode solution containing 10 μM Fluo-4 AM (Thermo Fisher Scientific) and pluronic acid for 1 h at 37°C in the dark. The SAN tissue was washed in Tyrode at 37°C in the dark for 10 min before experiments. Fluorescence of calcium transients was recorded using a photomultiplier (PTi D-104) at 35°C and the analog signals were digitized using Digidata 1440 (Molecular Devices) and analyzed with pCLAMP 10.5 software.

Electrophysiology

In all experiments, the coverslips were perfused at 33°C with an external solution containing (in mM): 140 NaCl, 4 KCl, 11 glucose, 1.2 MgCl2, 1.8 CaCl2, 5.5 4-(2-hydroxyethyl)-1-piperazineethanesulfonic acid (HEPES) titrated to pH 7.4 with NaOH and adjusted at 320 mOsm with sucrose. Whole-cell patch-clamp recordings were performed with an Axopatch 700B amplifier (Molecular Devices) and pCLAMP 10.5 software (Molecular Devices). Signals were digitized at 5 kHz and filtered at 2 kHz using microelectrodes with resistances of 4–7 MΩ were pulled from borosilicate glass capillaries (Harvard Apparatus) and filled with an intracellular solution containing (in mM): 130 KCl, 5 MgATP, 5 ethylene glycol-bis(β-aminoethyl ether)-*N*,*N*,*N*′,*N*′-tetraacetic acid (EGTA), 10 HEPES titrated to pH 7.3 with KOH and adjusted at 290 mOsm with sucrose. Unless otherwise stated, internal free calcium concentrations were 100 nM for current-clamp experiments and were titrated with EGTA and CaCl2 using the MaxChelator software (www.stanford.edu/~cpatton/maxc.html).

In Vivo Telemetric Recordings

Telemetric ambulatory long-term ECG recordings, analogous to Holter monitoring in humans, were obtained with implantable transmitters. The investigator was blinded for the mice genotypes. WT, CASQ2-D307H KI SvEv mice were anesthetized with ketamine (75–90 mg/kg) and xylazine (5–8 mg/kg) intraperitoneally (IP) (Kepro, Holland), and a midline incision was made along the spine. An implantable 3.5 g wireless radiofrequency transmitter (DSI MM USA, device weight 3.8 g) was aseptically inserted into a subcutaneous tissue pocket in the back as previously described (Katz et al., 2010). Animals were allowed to recover after surgery at least 6 days before any experiments. Baseline ECG were obtained 15 min after IP injection of the appropriate vehicle (saline for ivabradine or peanut oil for TRAM-34). For pharmacological experiments, the same mouse was used a few hours after baseline ECG recordings (vehicle injection) and for subsequent ECG recordings upon IP injection of 6 mg/kg ivabradine or 20 mg/kg TRAM-34. Telemetered ECG tracings were obtained in conscious mice at rest for 1 min and during peak exercise (i.e. the first minute of recovery). In the treadmill exercise, mice were forced to exercise on a rodent treadmill; gradually increasing the speed up to a maximum of 15 m/min. Ventricular tachycardia (VT) was defined as four or more consecutive ventricular beats. If this phenotype was consecutively observed for more than 15 s, it was defined as "sustained" ventricular tachycardia (SVT). Shorter VTs were characterized as "non-sustained" (NSVT). All other ventricular arrhythmias, such as premature beats, ventricular bigeminy, couplets, and triplets were all defined as ventricular premature contractions (VPCs) (Katz et al., 2010).

Data Analysis

Rate, DADs, and calcium transients were analyzed with the Clampfit program (pCLAMP 10.5; Molecular Devices). Sinus rhythm, PR interval, and ECG arrhythmic features were analyzed with the LabChart 8 Reader (ADInstruments). Data were analyzed with Excel (Microsoft) and Prism 5.0 (GraphPad Software) and are expressed as mean ± SEM. Statistical analysis was performed using the two-tailed paired Student t test and the linear regression for correlation or by one way ANOVA followed by Tukey's or Bonferroni's multiple comparison test. P values of less than 0.05 were assumed significant.

RESULTS

Ivabradine Does Neither Affect the Firing Rate nor Prevent the Occurrence of Delayed-Afterdepolarizations in Human Induced Pluripotent Stem Cells Derived Cardiomyocytes Derived From CPVT2 (CASQ2-D307H) Patients

Isolated spontaneously beating hiPSC-CMs (25 days-old EBs) derived from normal (healthy) and CPVT2 patients carrying the CASQ2 D307H mutation (Novak et al., 2012) were used and their spontaneous firing properties were examined as previously shown (Haron-Khun et al., 2017). We recorded spontaneous action potentials fired from single hiPSC-CM cells in the current-clamp mode of the patch-clamp technique. Shown are representative traces of a spontaneously beating CPVT2-derived hiPSC-CM cell, which indicates that the application of 3 μM of ivabradine alone did not affect the beating rate (**Figures 1A, C**). In line with our previous findings (Haron-Khun et al., 2017), 100 nM isoproterenol did not increase the beating rate of CPVT2 hiPSC-CMs, in contrast to that of control healthy patients, but instead triggered DADs (**Figures 1A–C**). The number of DADs for each treatment was normalized to that obtained in the same cell before the addition of any drug. The records revealed a significant increase in the normalized number of DADs in the presence of 100 nM isoproterenol *versus* control

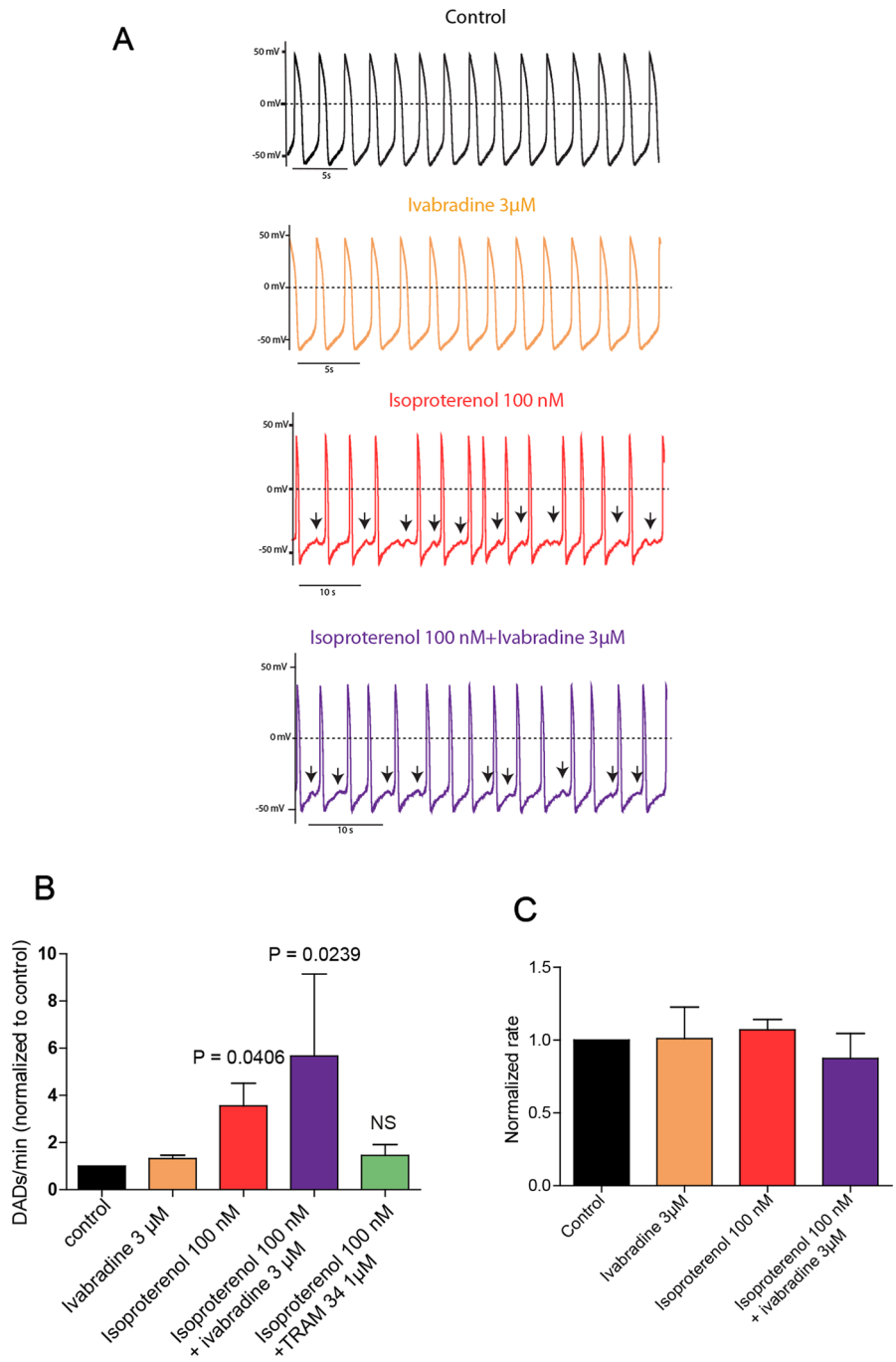

FIGURE 1 | Ivabradine does not prevent the occurrence of delayed-afterdepolarizations (DADs) in human induced pluripotent stem cells derived cardiomyocytes (hiPSC-CMs) derived from CPVT2 (CASQ2-D307H) patients. **(A)** Representative traces of spontaneous action potential (AP) recorded in CASQ2 D307H hiPSC-CMs are shown from the same cell in the absence of any drug (black trace, control), then in the presence of 3 µM ivabradine (orange trace), 100 nM of isoproterenol (red trace), and both isoproterenol + ivabradine (purple trace). **(B)** Data summary for each treatment of the numbers of DADs, which were normalized to those obtained in the same cell before the addition of any drug. Isoproterenol (100 nM) increased DADs by 3.56 ± 0.96-fold [n = 19, P = 0.0147, one-way ANOVA (F = 3.402; P = 0.0147); Dunnett's multiple comparisons test, P = 0.0406]; ivabradine (3 µM) + isoproterenol (100 nM) increased DADs by 5.67 ± 3.47-fold, n = 4, one-way ANOVA (F = 3.402; P = 0.0147); Dunnett's multiple comparisons test, P = 0.0239; TRAM-34 (1 µM) + isoproterenol (100 nM) increased DADs by only 1.45 ± 0.41–fold, which is not significant (NS) compared to control; n = 15, one-way ANOVA (F = 3.402; P = 0.0147); Dunnett's multiple comparisons test, P = 0.983. **(C)** Data summary of the normalized beating rates for each treatment. Beating rates were normalized those obtained in the same cell before the addition of any drug (control).The ANOVA test found no significant differences.

[3.56 ± 0.96-fold, n = 19, one-way ANOVA (F = 3.402; P = 0.0147); Dunnett's multiple comparisons test, P = 0.0406]. When 3 μM ivabradine was added together with isoproterenol, no bradycardic effect was seen and yet a significant increase in the normalized number of DADs was observed when compared to control [5.67 ± 3.47-fold, n = 4, one-way ANOVA (F = 3.402; P = 0.0147); Dunnett's multiple comparisons test, P = 0.0239] (**Figures 1A–C**). Very similar results were obtained with a rather selective blocker of the If current, ZD7288 (25 μM), which in the presence of isoproterenol, was unable to prevent the occurrence of DADs compared to control [3.58 ± 0.8-fold, n = 5, one way ANOVA (F = 7.14; P = 0.0029), Dunnett's multiple comparison test, P = 0.0224]. In agreement with our previous data (Haron-Khun et al., 2017), when the SK4 K^+ channel blocker TRAM-34 (1 μM) was added to isoproterenol, no significant increase in the normalized number of DADs was revealed when compared to control [1.45 ± 0.46–fold, n = 15, one-way ANOVA (F = 3.402; P = 0.0147); Dunnett's multiple comparisons test, P = 0.983] (**Figure 1B**). Taken together, our data show that in contrast to SK4 channel blockade, ivabradine, which inhibits I_f and hERG currents does not prevent the occurrence of arrhythmic features like DADs that accompany the spontaneous beating of CASQ2-D307H hiPSC-CMs in the presence of isoproterenol.

Ivabradine Does Not Reduce the Arrhythmic Phenotype of Calcium Transients in Sinoatrial Node From CASQ2-D307H KI Mice

The spontaneous calcium transients of the SAN were investigated by exposing intact SAN tissue preparations dissected *ex vivo* from WT and CASQ2-D307H KI mice to Fluo-4 AM, as previously described (Torrente et al., 2015; Haron-Khun et al., 2017). We formerly showed that in SAN from WT mice, the rate of calcium transients was significantly larger in presence of 100 nM isoproterenol (Haron-Khun et al., 2017). Here, the exposure of WT SAN to 100 nM isoproterenol increased the rate of Ca^{2+} transients (from 2.9 ± 0.4 to 4.5 ± 0.3 Hz, n = 5, P = 0.015, one-way ANOVA and Tukey's multiple comparison test). In contrast, the calcium transient rate of SANs from CASQ2-D307H KI mice was not significantly affected by the exposure to isoproterenol and/or ivabradine (**Figure 2A**). Importantly, the pattern of the calcium transients of SANs from CASQ2-D307H KI mice showed different

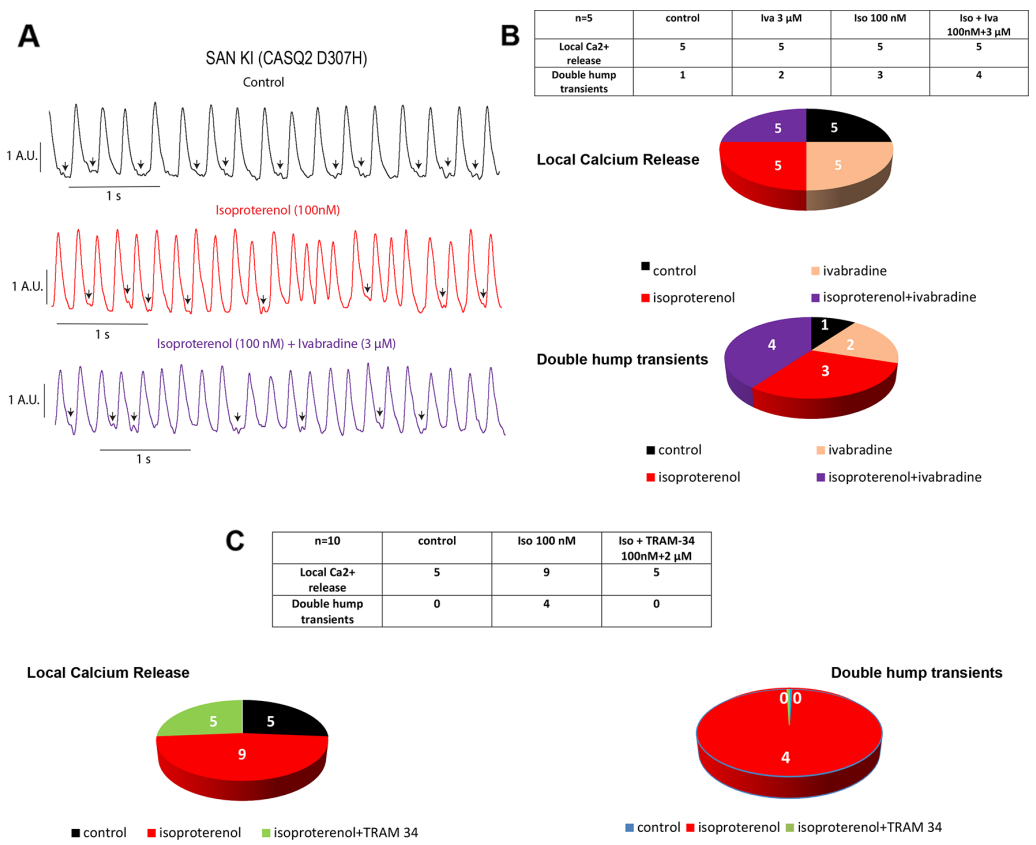

FIGURE 2 | Ivabradine does not reduce the arrhythmic phenotype of calcium transients in sinoatrial node (SAN) from CASQ2-D307H KI mice. **(A)** Representative traces of calcium transients obtained from the same SAN of knock-in (KI) CASQ2 D307H mice under control (black trace), 100 nM isoproterenol (red trace), and isoproterenol + ivabradine (purple trace). **(B)** Data summary of the aberrant calcium transients observed in SAN from KI CASQ2 D307H mice under the described conditions (n = 5). **(C)** Data summary of the aberrant calcium transients observed in SAN from KI CASQ2 D307H mice under the described conditions (n = 10).

abnormal features such as "local calcium release" (**Figure 2A**, arrows) and "double humps transients" both in control and isoproterenol conditions (**Figures 2A, B**). However, application of 3 μM ivabradine either alone or in the presence of 100 nM isoproterenol did not prevent the occurrence of "local calcium release" and "double humps transients" (**Figures 2A, B**). In line with our previous data (Haron-Khun et al., 2017), the SK4 channel blocker TRAM-34 (2 μM) behaved differently by decreasing the arrhythmic Ca^{2+} transient features events in the presence of isoproterenol (**Figure 2C**).

Ivabradine Does Not Decrease *In Vivo* the Ventricular Arrhythmias Recorded in Electrocardiogram From CASQ2-D307H KI Mice

To record continuously ECGs at rest and during treadmill exercise, a heart telemetry device was implanted in WT and CASQ2-D307H KI mice. For each session, continuous ECG recording was performed with the same animals receiving first IP injection of vehicle (saline or peanut oil) and then the blocker. In WT mice, ivabradine (6 mg/kg) exhibited, as expected, a bradycardic effect at rest, thereby decreasing the heart rhythm (from 771 ± 19 to 503 ± 26 beats/min for saline and ivabradine injection, respectively; n = 4, paired t-test P = 0.0003) and increasing the PR interval (from 29 ± 1 to 32 ± 1 ms, for saline and ivabradine injection, respectively; n = 4, paired t-test P = 0.0045) (**Figures 3A, B**, see arrows). Ivabradine produced similar bradycardic effects on WT mice during treadmill exercise (heart rate of 747 ± 35 and 518 ± 28 beats/min, for saline and ivabradine injection, respectively; n = 4, paired t-test P = 0.0068 and PR interval of 29 ± 2 *versus* 31 ± 1 ms for saline and ivabradine injection, respectively, n = 4, paired t-test P = 0.0217) (**Figures 4A, B**). In CASQ2-D307H KI mice, ivabradine (6 mg/kg) still produced bradycardic effect at rest (from 652 ± 18 to 444 ± 68 beats per min, for saline and ivabradine injection, respectively n = 4, paired t-test P = 0.0192), but not following treadmill exercise. Ivabradine poorly prevented the ECG arrhythmic features of CASQ2-D307H KI mice, where at rest three out of six mice still exhibited ventricular tachycardia or premature ventricular complexes (**Figures 3C, D**, **Table 1**). During treadmill exercise, ivabradine was completely ineffective since all six ivabradine-treated CASQ2-D307H KI mice showed ventricular tachycardia (**Figures 4C, D**, **Table 1**). In contrast, 9 out of 12 TRAM-34-treated (20 mg/kg) CASQ2-D307H KI mice exhibited normal sinus rhythm at rest, while following treadmill exercise, 4 out of 12 animals remained with normal sinus rhythm without significant ventricular arrhythmia (**Figures 3E, F** and **Figures 4E, F** and **Table 1**). These results show that ivabradine is unable to decrease the ventricular arrhythmias observed in ECG of CASQ2-D307H KI mice, as opposed to TRAM-34, which greatly reduces them (Haron-Khun et al., 2017).

DISCUSSION

In a recent study, we showed that SK4 channel blockers decrease the heart rate, depolarize the maximal diastolic potential (MDP), and attenuate ventricular arrhythmias in transgenic CPVT mice. In this work, we examined both *in vitro* and *in vivo* whether ivabradine could exhibit anti-arrhythmic properties in CPVT as other bradycardic agents such as β-adrenergic receptor blockers or SK4 channel inhibitors. Ivabradine is a blocker of the hyperpolarization-activated cyclic-nucleotide gated-channel, which mediates the cation non-selective "funny" current If, and is mainly encoded by the HCN4 protein in the sinoatrial node (Bucchi et al., 2013). In the SAN tissue, the If current is responsible for the cardiac pacemaker activity by generating the diastolic depolarization. Ivabradine blocks the HCN4 inner pore leading to a reduction in the slope of the diastolic depolarization, thereby slowing the heart rate (Bucchi et al., 2013). Ivabradine blocks the HCN channel in its open state and exhibits a use-dependence effect, becoming more potent at faster heart rates. As a bradycardic agent, ivabradine has been evaluated and is currently used in selected patients with systolic heart failure and stable angina (Koruth et al., 2017). Indeed, various experimental and epidemiological studies have found that atherosclerosis, heart failure, coronary artery disease, stroke, and arrhythmias are linked to elevated heart rate (Koruth et al., 2017). In addition to blocking HCN channels, studies showed that ivabradine prolonged ventricular action potentials by blocking the IKr current (hERG) in ventricular myocytes (Melgari et al., 2015). Moreover, it was shown that ivabradine blocks the recombinant hERG current over a range of concentrations overlapping with those required to block HCN4 (Melgari et al., 2015). Because of its concurrent inhibitory action on If and IKr currents, ivabradine was suggested to be a potential antiarrhythmic drug thanks to an increase in both the effective refractory period and the post-repolarization refractoriness (Frommeyer et al., 2017a; Frommeyer et al., 2017b). The bradycardic features of ivabradine raise the question of whether it could be effective in ventricular arrhythmias. Recently, ivabradine was found to decrease digitalis-induced ventricular arrhythmias and short QT-induced arrhythmic features in Langendorff-perfused rabbit heart preparations (Frommeyer et al., 2017a; Frommeyer et al., 2017b). Along with this rationale, we asked in the present work whether ivabradine could prevent the ventricular arrhythmias found in cellular and animal models of CPVT2. We found that ivabradine did not prevent the occurrence of DADs in the presence of isoproterenol in hiPSC-CMs of CPVT2 patients (**Figure 1**). In contrast, the SK4 channel blocker TRAM-34, significantly reduced the number of DADs, in line with our recent data (Haron-Khun et al., 2017) (**Figure 1**). Similarly, we showed that ivabradine was ineffective in preventing the arrhythmic calcium transients recorded in the presence of isoproterenol in SAN intact tissue from CASQ2 KI mice (**Figure 2**). However, TRAM-34 significantly decreased the occurrence of local Ca^{2+} release and double hump transient events in agreement with our previous results (Haron-Khun et al., 2017). Along the same line, ivabradine did not prevent the ventricular arrhythmias revealed by telemetry in CASQ2-D307H KI mice at rest and was totally ineffective during treadmill exercise (**Figures 3** and **4**, **Table 1**). A contrasting picture was obtained with TRAM-34,

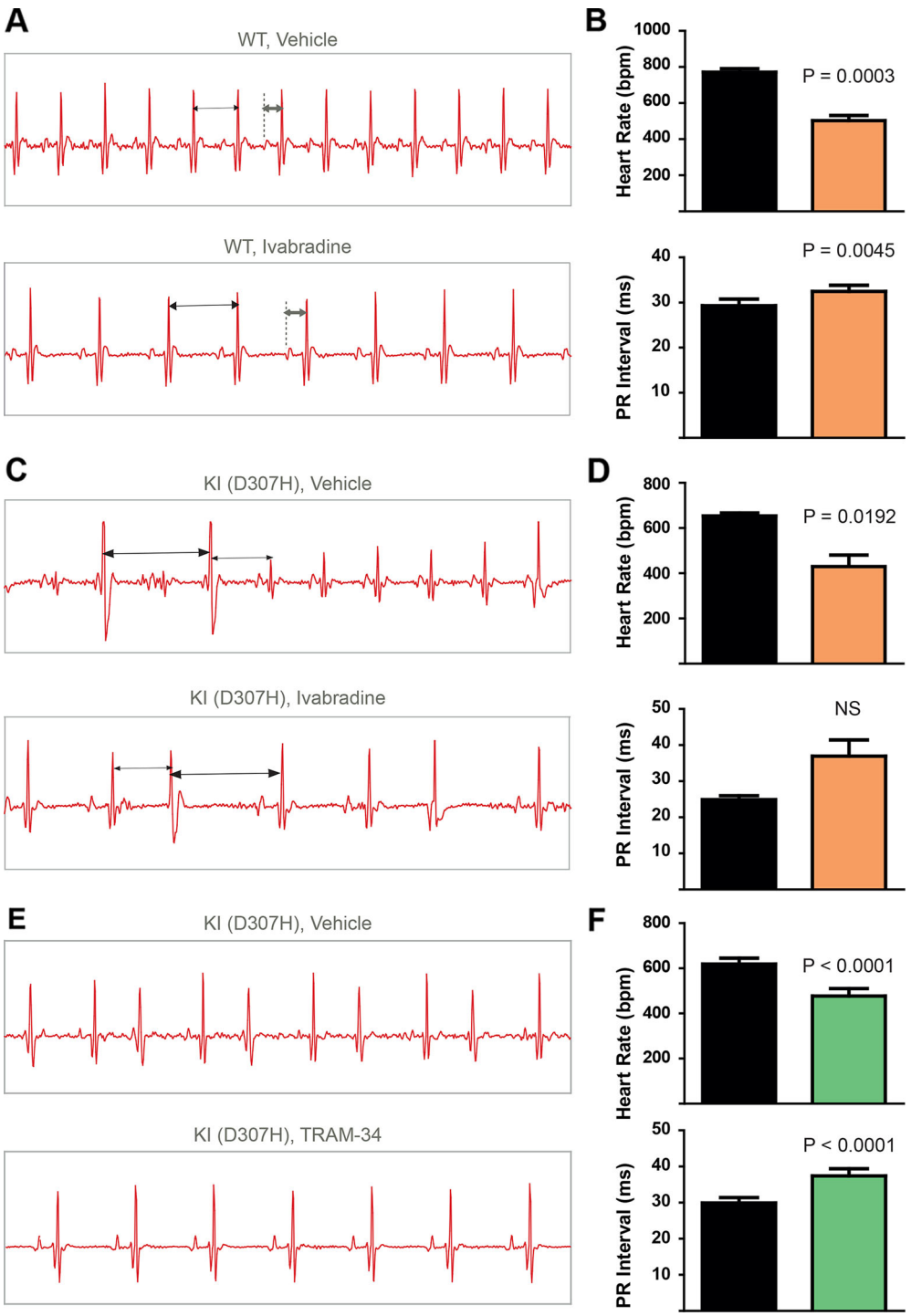

FIGURE 3 | In contrast to TRAM-34, ivabradine does not prevent the ventricular arrhythmias recorded in ECG from CASQ2-D307H KI mice at rest. **(A)** Representative ECG recording following intraperitoneal (IP) injection of vehicle (saline, upper) and 6 mg/kg ivabradine (lower), in WT mice at rest. Sequential vehicle and ivabradine injections were performed on the same animal. **(B)** Data summary of heart rate (paired t test, P = 0.0003, n = 4) and PR interval (paired t test, P = 0.0045, n = 4) after IP injection of ivabradine. **(C)** Representative ECG recordings following IP injection of vehicle (saline, upper) and 6 mg/kg ivabradine (lower) in CASQ2 D307H knock-in (KI) mice at rest. **(D)** Data summary of the heart rate (paired t test, P = 0.0192, n = 4) and PR interval [not significant (NS), n = 4] after IP injection of ivabradine. **(E)** Representative ECG recording following IP injection of vehicle (peanut oil, upper) and 20 mg/kg TRAM-34 (lower) in CASQ2 D307H KI mice at rest. **(F)** Data summary of heart rate (paired t-test; P < 0.0001, n = 12) and PR interval (paired t-test; P < 0.0001, n = 12) in CASQ2 D307H KI mice at rest.

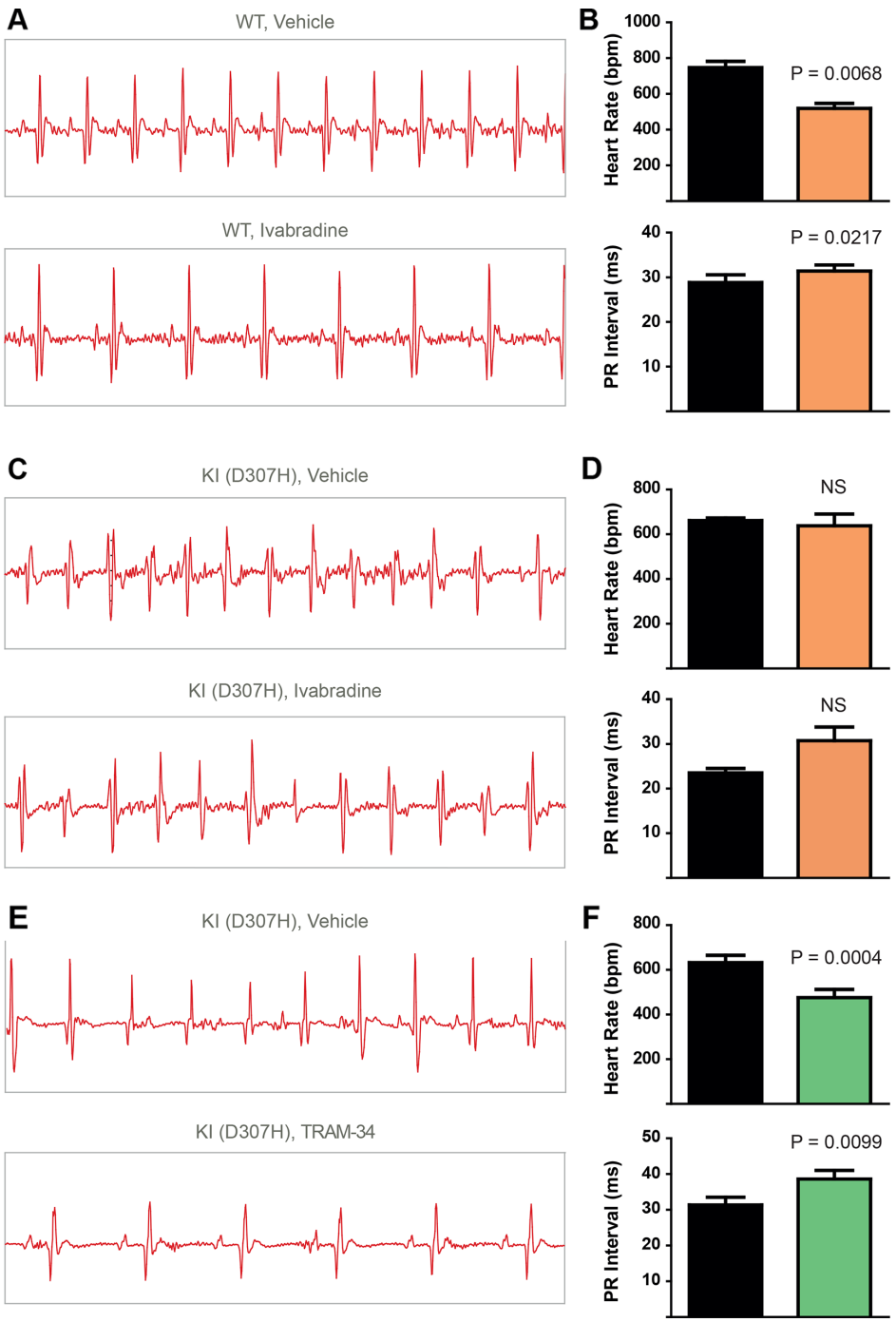

FIGURE 4 | In contrast to TRAM-34, ivabradine does not prevent the ventricular arrhythmias recorded in ECG from CASQ2 D307H KI mice following treadmill exercise. **(A)** Representative ECG recording following intraperitoneal (IP) injection of vehicle (saline, upper) and 6 mg/kg ivabradine (lower), in WT mice following treadmill exercise. **(B)** Data summary of heart rate (paired t test, n = 4, P = 0.0068) and PR interval (paired t test, n = 4, P = 0.0217) in WT mice after treadmill exercise and IP injection of ivabradine. **(C)** Representative ECG recording following IP injection of vehicle (saline, upper) and 6 mg/kg ivabradine (lower) in CASQ2 D307H knock-in (KI) mice following treadmill exercise. **(D)** Data summary of heart rate [not significant (NS), n = 4] and PR interval [not significant (NS), n = 4] after IP injection of ivabradine. **(E)** Representative ECG recording following IP injection of vehicle (peanut oil, upper) and 20 mg/kg TRAM-34 (lower) in CASQ2 D307H KI mice following treadmill exercise. **(F)** Data summary of heart rate (paired t-test; P = 0.0004, n = 11) and PR interval (paired t-test; P = 0.0099, n = 11) in CASQ2 D307H KI mice following treadmill exercise.

TABLE 1 | Comparative effects of ivabradine and TRAM-34 on the arrhythmogenic features of CPVT2 CASQ2-D307H knock-in (KI) mice at rest or during treadmill exercise.

Number of mice (n)	Vehicle 6	Ivabradine (6 mg/kg) 6	Vehicle 12	TRAM-34 (20 mg/kg) 12
KI at rest				
Normal sinus rhythm	0	3	3	9
VPC	2	1	6	3
NSVT	0	0	3	0
SVT	4	2	0	0
KI treadmill exercise				
Normal sinus rhythm	0	0	1	4
VPC	1	0	2	4
NSVT	0	0	9	4
SVT	5	6	0	0

The data show the comparative effects of ivabradine and TRAM-34 on the arrhythmogenic features of CPVT2 CASQ2-D307H KI mice at rest or during treadmill exercise. Ivabradine (6 mg/kg) was dissolved in saline, while TRAM-34 (20 mg/kg) was prepared in peanut oil and were injected intraperitoneally into 100 µl vehicle. VPC, ventricular premature complexes; NSVT, non-sustained ventricular tachycardia; SVT, sustained ventricular tachycardia. The types of arrhythmic features were classified following their severity: sinusal rhythm (normal), ventricular premature contractions (VPC), NSVT, and SVT.

which significantly reduced the occurrence of ventricular arrhythmias at rest and to lesser extent upon treadmill exercise (**Figures 3** and **4**, **Table 1**).

We and others previously showed that CASQ2 knockout (CASQ2 KO) and CASQ2-D307H KI mice are significantly bradycardic (Glukhov et al., 2015; Haron-Khun et al., 2017). It is interesting to note that isoproterenol did increase neither the beating rate of hiPSC-CMs derived from CPVT2 patients nor the rate of Ca^{2+} transients of SAN taken from CASQ2 KI mice upon isoproterenol application. Similarly, in the ECG recording from CASQ2-D307H KI mice, the heart rate at rest was not increased following treadmill exercise (652 ± 18 and 658 ± 15 beats/min, respectively). A recent work (Ho et al., 2018) found that sympathetic stimulation failed to accelerate heart rate in exercised CASQ2 KO mice, suggesting a sympathetic-parasympathetic imbalance in CASQ2 KO and CASQ2-D307H KI mice, possibly due to autonomic adaptation.

Therapies for CPVT include exercise restriction, β-blockers, additional drugs, primarily flecainide, implantable cardioverter defibrillators (ICD) in high-risk patients to prevent sudden death, and sympathetic denervation (Priori et al., 2002; Hayashi et al., 2009; Lieve et al., 2016; Roston et al., 2017). Administration of β-blockers remains the longstanding cornerstone of treatment. However, the response to β-blockers is partial and often decreases with time because of an escape phenomenon (Priori et al., 2002; Hayashi et al., 2009). In addition, β-blockers exhibit undesirable side effects, including psychological depression, bronchospasm, peripheral vasoconstriction, hypotension, leg tiredness, and erectile dysfunction. Flecainide was recently shown to possess antiarrhythmic properties in CPVT through either a stabilizing effect on RyR2 by decreasing its opening probability or by increasing the threshold for triggered activity through its Na^+ channel blocking activity (Lieve et al., 2016; Roston et al., 2017). However, routine use of flecainide monotherapy is not recommended yet because of lack of large retrospective studies. ICD implantation in young and active patients necessitates routine device replacement and is associated with device malfunction, including inappropriate shocks, infection, and psychological problems. The major clinical indications for left cardiac sympathetic denervation (LCSD) are ß-blocker intolerance or refractoriness, high risk of sudden death with ß-blocker treatment, or frequent ICD shocks (Lieve et al., 2016; Roston et al., 2017). However, LCSD is still rarely used as a supplementary therapy to ß-blocker administration and ICD implantation. Although tremendous progress has been made in the recent years in the treatment of CPVT, there is still a great need to develop additional or alternative new therapies. The gene therapy is of great potential in this context but is not yet ready for clinical use (Kurtzwald-Josefson et al., 2017).

A common feature of most pharmacological agents in use is their negative chronotropic effect. In this context, ivabradine treatment was a legitimate candidate drug to be tested in cellular and animal models of CPVT. Despite its bradycardic action, ivabradine was unable to prevent *in vitro* the occurrence of DADs and abnormal Ca^{2+} transients in the presence of isoproterenol as well as *in vivo* the ventricular arrhythmias in CASQ2-D307H KI mice. In contrast, we previously showed the SK4 channel blockers TRAM-34 and clotrimazole, though similarly reducing the heart rate and increasing the PR interval, could successfully reduce the occurrence of ventricular arrhythmias (Haron-Khun et al., 2017). This raises the question of why ivabradine and the SK4 channel blockers (TRAM-34 and clotrimazole) do not exert the same beneficial effect in CPVT ventricular arrhythmias, although both are bradycardic agents. First, it suggests that bradycardia and increase in the effective refractory period and in the post repolarization refractoriness are not sufficient to prevent ventricular arrhythmias in CPVT. Second, although the precise mechanism of action of SK4 K^+ channels in the cardiac SAN cycle remains to be determined, normal SAN automaticity is regulated by coupling between an "M clock," the ensemble of surface membrane ion channels, and a "Ca^{2+} clock," the SR (Lakatta and DiFrancesco, 2009). According to the coupled-clock hypothesis, the M and Ca^{2+} clocks should crosstalk. Ca^{2+}-calmodulin-activated adenylyl cyclase in pacemaker cells generates high cyclic AMP (cAMP)

activity that activates the If channel by positively shifting the If channel activation. In addition, cAMP production controls protein kinase A (PKA)-dependent phosphorylation activity. PKA, together with Ca^{2+}-activated calmodulin-dependent kinase II, phosphorylates various membrane clock channels (e.g., L-type Ca^{2+} channels and K^+ channels), as well as Ca^{2+} clock proteins (Behar and Yaniv, 2016). Because of this coupling mechanism, it is possible that treatment with ivabradine alone is not sufficient to prevent ventricular arrhythmias in CPVT. Nevertheless, it was previously shown that the bradycardic effect of ivabradine was accompanied by reduced SR Ca^{2+} load, slowed intracellular Ca^{2+} cycling kinetics, and prolongation of the period of spontaneous local Ca^{2+} releases occurring during diastolic depolarization (Yaniv et al., 2013). It is possible that reduction in adenylate cyclase-cAMP/PKA activity (e.g., by β-blockers) in parallel to treatment with ivabradine could provide a more effective anti-arrhythmic therapy in CPVT. In line with this idea, a recent case report showed that ivabradine in combination with the β-blocker nadolol, successfully suppressed non-sustained polymorphic ventricular tachycardia in two patients heterozygous for RyR2 mutation (CPVT1) (Vaksmann and Klug, 2018). We recently suggested by a numerical model that SK4 channel contribution becomes significant only at the late repolarization, a crucial period for the Ca^{2+} clock and for the coupling to the voltage clock, thereby contributing to the MDP hyperpolarization, facilitating activation of If and recovery from inactivation of voltage-gated Ca^{2+} channels (Haron-Khun et al., 2017). Thus, inhibitors of SK4 Ca^{2+}-activated K^+ channels are ideally suited to suppress the coupling between the two clocks and their subsequent blockade may favorably act to prevent premature excitations, which are a prelude of ventricular arrhythmias.

In all, in contrast to SK4 channel blockers ivabradine does not exhibit anti-arrhythmic properties in CPVT and this drug alone cannot be used to treat CPVT ventricular arrhythmias.

DATA AVAILABILITY STATEMENT

All datasets generated for this study are included in the article.

ETHICS STATEMENT

The animal study was reviewed and approved by the Animal Research Ethics Committee of Tel Aviv University (M-14-063) in accordance with Israeli law and in accordance with the Guide for the Care and Use of Laboratory Animals (1996, National Academy of Sciences, Washington, DC).

AUTHOR CONTRIBUTIONS

HB-L, DW, DY, SH-K, and AP performed the experiments and analyses. EH provided experimental tools. MA and BA conceived the project, planned the experiments, and wrote the manuscript.

ACKNOWLEDGMENTS

BA holds the Andy Libach Professorial Chair in clinical pharmacology and toxicology. We thank Prof. Dario DiFrancesco, Dr. Andrea Barbuti, and Manuel Paina (The Pacelab, Milano) and Dr. Pietro Mesirca (IGF-CNRS, Montpellier) for their kind training and advices in isolating the mouse sinoatrial node preparation. We are grateful to Profs. Jonathan G. Seidman and Christine E. Seidman for initially providing us with the SvEv mice. This work was supported by a grant from the Israel Science Foundation (763/10) to MA and (ISF 1215/13 and 2092/14) and the Fields Fund for Cardiovascular Research to BA.

REFERENCES

Arad, M., Glikson, M., El-Ani, D., and Monserrat-Inglesias, L. (2012). A family with recurrent sudden death and no clinical clue. *Ann. Noninvasive Electrocardiol.* 17 (4), 387–393. doi: 10.1111/anec.12024

Behar, J., and Yaniv, Y. (2016). Dynamics of PKA phosphorylation and gain of function in cardiac pacemaker cells: a computational model analysis. *Am. J. Physiol. Heart Circ. Physiol.* 310 (9), H1259–H1266. doi: 10.1152/ajpheart.00076.2016

Bucchi, A., Baruscotti, M., Nardini, M., Barbuti, A., Micheloni, S., Bolognesi, M., et al. (2013). Identification of the molecular site of ivabradine binding to HCN4 channels. *PloS One* 8 (1), e53132. doi: 10.1371/journal.pone.0053132

Chopra, N., and Knollmann, B. C. (2011). Genetics of sudden cardiac death syndromes. *Curr. Opin. Cardiol.* 26 (3), 196–203. doi: 10.1097/HCO.0b013e3283459893

Frommeyer, G., Weller, J., Ellermann, C., Bogeholz, N., Leitz, P., Dechering, D. G., et al. (2017a). Ivabradine Reduces Digitalis-induced Ventricular Arrhythmias. *Basic Clin. Pharmacol. Toxicol.* 121 (6), 526–530. doi: 10.1111/bcpt.12829

Frommeyer, G., Weller, J., Ellermann, C., Kaese, S., Kochhauser, S., Lange, P. S., et al. (2017b). Antiarrhythmic properties of ivabradine in an experimental model of Short-QT- Syndrome. *Clin. Exp. Pharmacol. Physiol.* 44 (9), 941–945. doi: 10.1111/1440-1681.12790

Glukhov, A. V., Kalyanasundaram, A., Lou, Q., Hage, L. T., Hansen, B. J., Belevych, A. E., et al. (2015). Calsequestrin 2 deletion causes sinoatrial node dysfunction and atrial arrhythmias associated with altered sarcoplasmic reticulum calcium cycling and degenerative fibrosis within the mouse atrial pacemaker complex1. *Eur. Heart J.* 36 (11), 686–697. doi: 10.1093/eurheartj/eht452

Haron-Khun, S., Weisbrod, D., Bueno, H., Yadin, D., Behar, J., Peretz, A., et al. (2017). SK4 K+ channels are therapeutic targets for the treatment of cardiac arrhythmias. *EMBO Mol. Med.* 9 (4), 415–429. doi: 10.15252/emmm.201606937

Hayashi, M., Denjoy, I., Extramiana, F., Maltret, A., Buisson, N. R., Lupoglazoff, J. M., et al. (2009). Incidence and risk factors of arrhythmic events in catecholaminergic polymorphic ventricular tachycardia. *Circulation* 119 (18), 2426–2434. doi: 10.1161/CIRCULATIONAHA.108.829267

Ho, H. T., Thambidorai, S., Knollmann, B. C., Billman, G. E., Gyorke, S., and Kalyanasundaram, A. (2018). Accentuated vagal antagonism paradoxically increases ryanodine receptor calcium leak in long-term exercised Calsequestrin2 knockout mice. *Heart Rhythm.* 15 (3), 430–441. doi: 10.1016/j.hrthm.2017.10.008

Katz, G., Khoury, A., Kurtzwald, E., Hochhauser, E., Porat, E., Shainberg, A., et al. (2010). Optimizing catecholaminergic polymorphic ventricular tachycardia therapy in calsequestrin-mutant mice. *Heart Rhythm.* 7 (11), 1676–1682.doi: 10.1016/j.hrthm.2010.07.004

Koruth, J. S., Lala, A., Pinney, S., Reddy, V. Y., and Dukkipati, S. R. (2017). The Clinical Use of Ivabradine. *J. Am. Coll. Cardiol.* 70 (14), 1777–1784. doi: 10.1016/j.jacc.2017.08.038

Kurtzwald-Josefson, E., Yadin, D., Harun-Khun, S., Waldman, M., Aravot, D., Shainberg, A., et al. (2017). Viral delivered gene therapy to treat catecholaminergic polymorphic ventricular tachycardia (CPVT2) in mouse models. *Heart Rhythm.* 14 (7), 1053–1060. doi: 10.1016/j.hrthm.2017.03.025

Lakatta, E. G., and DiFrancesco, D. (2009). What keeps us ticking: a funny current, a calcium clock, or both? *J. Mol. Cell Cardiol.* 47 (2), 157–170. doi: 10.1016/j.yjmcc.2009.03.022

Lieve, K. V., van der Werf, C., and Wilde, A. A. (2016). Catecholaminergic polymorphic ventricular tachycardia. *Circ. J.* 80 (6), 1285–1291. doi: 10.1253/circj.CJ-16-0326

Melgari, D., Brack, K. E., Zhang, C., Zhang, Y., El Harchi, A., Mitcheson, J. S., et al. (2015). hERG potassium channel blockade by the HCN channel inhibitor bradycardic agent ivabradine. *J. Am. Heart Assoc.* 4 (4). doi: 10.1161/JAHA.115.001813

Novak, A., Barad, L., Zeevi-Levin, N., Shick, R., Shtrichman, R., Lorber, A., et al. (2012). Cardiomyocytes generated from CPVTD307H patients are arrhythmogenic in response to beta-adrenergic stimulation. *J. Cell Mol. Med.* 16 (3), 468–482. doi: 10.1111/j.1582-4934.2011.01476.x

Priori, S. G., and Chen, S. R. W. (2011). Inherited Dysfunction of Sarcoplasmic Reticulum Ca2+ Handling and Arrhythmogenesis. *Circ. Res.* 108 (7), 871–883. doi: 10.1161/CIRCRESAHA.110.226845

Priori, S. G., Napolitano, C., Memmi, M., Colombi, B., Drago, F., Gasparini, M., et al. (2002). Clinical and molecular characterization of patients with catecholaminergic polymorphic ventricular tachycardia. *Circulation* 106 (1), 69–74. doi: 10.1161/01.CIR.0000020013.73106.D8

Roston, T. M., Van Petegem, F., and Sanatani, S. (2017). Catecholaminergic polymorphic ventricular tachycardia: a model for genotype-specific therapy. *Curr. Opin. Cardiol.* 32 (1), 78–85.doi: 10.1097/HCO.0000000000000360

Song, L., Alcalai, R., Arad, M., Wolf, C. M., Toka, O., Conner, D. A., et al. (2007). Calsequestrin 2 (CASQ2) mutations increase expression of calreticulin and ryanodine receptors, causing catecholaminergic polymorphic ventricular tachycardia. *J. Clin. Invest.* 117 (7), 1814–1823. doi: 10.1172/JCI31080

Torrente, A. G., Zhang, R., Zaini, A., Giani, J. F., Kang, J., Lamp, S. T., et al. (2015). Burst pacemaker activity of the sinoatrial node in sodium-calcium exchanger knockout mice. *Proc. Natl. Acad. Sci. U.S.A.* 112 (31), 9769–9774. doi: 10.1073/pnas.1505670112

Vaksmann, G., and Klug, D. (2018). Efficacy of ivabradine to control ventricular arrhythmias in catecholaminergic polymorphic ventricular tachycardia. *Pacing Clin. Electrophysiol.* 41, 1378–1380. doi: 10.1111/pace.13446

Weisbrod, D., Peretz, A., Ziskind, A., Menaker, N., Oz, S., Barad, L., et al. (2013). SK4 Ca2+ activated K+ channel is a critical player in cardiac pacemaker derived from human embryonic stem cells. *Proc. Natl. Acad. Sci. U.S.A.* 110 (18), E1685–E1694. doi: 10.1073/pnas.1221022110

Yaniv, Y., Sirenko, S., Ziman, B. D., Spurgeon, H. A., Maltsev, V. A., and Lakatta, E. G. (2013). New evidence for coupled clock regulation of the normal automaticity of sinoatrial nodal pacemaker cells: bradycardic effects of ivabradine are linked to suppression of intracellular Ca(2)(+) cycling. *J. Mol. Cell Cardiol.* 62, 80–89. doi: 10.1016/j.yjmcc.2013.04.026

Conflict of Interest: The authors declare that the research was conducted in the absence of any commercial or financial relationships that could be construed as a potential conflict of interest.

frontiers in Pharmacology

MINI REVIEW
published: 29 January 2020
doi: 10.3389/fphar.2019.01644

Bridging the Molecular-Cellular Gap in Understanding Ion Channel Clustering

Valerie Abigail Nirenberg and Ofer Yifrach *

Department of Life Sciences and the Zlotowski Center for Neurosciences, Ben-Gurion University of the Negev, Be'er Sheva, Israel

The clustering of many voltage-dependent ion channel molecules at unique neuronal membrane sites such as axon initial segments, nodes of Ranvier, or the post-synaptic density, is an active process mediated by the interaction of ion channels with scaffold proteins and is of immense importance for electrical signaling. Growing evidence indicates that the density of ion channels at such membrane sites may affect action potential conduction properties and synaptic transmission. However, despite the emerging importance of ion channel density for electrical signaling, how ion channel-scaffold protein molecular interactions lead to cellular ion channel clustering, and how this process is regulated are largely unknown. In this review, we emphasize that voltage-dependent ion channel density at native clustering sites not only affects the density of ionic current fluxes but may also affect the conduction properties of the channel and/or the physical properties of the membrane at such locations, all changes that are expected to affect action potential conduction properties. Using the concrete example of the prototypical *Shaker* voltage-activated potassium channel (Kv) protein, we demonstrate how insight into the regulation of cellular ion channel clustering can be obtained when the molecular mechanism of ion channel-scaffold protein interaction is known. Our review emphasizes that such mechanistic knowledge is essential, and when combined with super-resolution imaging microscopy, can serve to bridge the molecular-cellular gap in understanding the regulation of ion channel clustering. Pressing questions, challenges and future directions in addressing ion channel clustering and its regulation are discussed.

Keywords: action potential, clustering, coupling, ion channel density, potassium channels, sodium channels post-synaptic density–95, scaffold proteins

OPEN ACCESS

Edited by:
Moran Rubinstein,
Tel Aviv University, Israel

Reviewed by:
Daniel Yakubovich,
Tel Aviv University, Israel
Carlos Alberto Villalba-Galea,
University of the Pacific, United States

***Correspondence:**
Ofer Yifrach
ofery@bgu.ac.il

Specialty section:
This article was submitted to Pharmacology of Ion Channels and Channelopathies, a section of the journal Frontiers in Pharmacology

Received: *24 September 2019*
Accepted: *16 December 2019*
Published: *29 January 2020*

Citation:
Nirenberg VA and Yifrach O (2020) Bridging the Molecular-Cellular Gap in Understanding Ion Channel Clustering. Front. Pharmacol. 10:1644. doi: 10.3389/fphar.2019.01644

INTRODUCTION

The precise localization, distribution, and density of voltage-activated ion channels at specific neuronal membrane sites are essential for action potential (AP) generation and propagation and for synaptic transmission (Hille, 1992). Ion channels are not randomly distributed in the membrane, as would be assumed by the Singer-Nicolson fluid mosaic membrane model (Singer and Nicolson, 1972), but instead are targeted to specific sites, such as axon initial segments (AIS), nodes of Ranvier (NR) or the post-synaptic density (PSD), where they are usually part of highly regulated multi-protein macromolecular complexes (Lai and Jan, 2006). Transcriptional activators and suppressors,

cytoskeletal proteins, cell adhesion molecules, post-translational signaling molecules, ion channel auxiliary subunits, and scaffold proteins are co-targeted with ion channels to such sites. The final endpoint in assembling such complexes is not only the proximity of the ion channel and its auxiliary subunits and/or modulatory proteins but also the clustering of many ion channel molecules together, potentially, within interaction distances (Engelman, 2005; Han and Kim, 2008; Freeman et al., 2016; Capera et al., 2019). The density of ion channel molecules at these sites, i.e., the number of molecules per membrane area, is thus an important parameter, and the question then arises what are the potential functional consequences of having many neighboring ion channel molecules aggregated together in one site with respect to electrical signaling? Furthermore, how the density of ion channel proteins at their specific membrane targeting sites are spatially and temporally regulated, to affect AP conduction properties, is largely unknown.

In the current review, we highlight the importance of ion channel clustering and its regulation for electrical signaling. We begin by concisely surveying where and how different voltage-activated ion channels are targeted to primary sites along the polarized neuron in the direction of AP propagation. We then present cases where ion channel density was shown to affect not only the density of ionic current fluxes at their site of expression but also the gating properties of ion channels, relative to their function in an isolated context, and the physical properties of the membrane. We discuss the functional consequences of such changes on AP conduction properties and further emphasize the important role played by scaffold proteins in mediating voltage-dependent ion channel clustering. Finally, by using the concrete example of the voltage-activated potassium channel protein, we highlight that when the molecular mechanism underlying the ion channel-scaffold protein interaction is known, cellular understanding regarding the regulation of ion channel density can be obtained. This example demonstrates the strength of adopting a mechanistic view in bridging the molecular-cellular gap in the understanding of ion channel clustering. We end with a summary of current challenges and consider future directions that can be taken for better understanding ion channel clustering.

SITE-SPECIFIC CLUSTERING OF ION CHANNELS AFFECTS SIGNAL GENERATION, PROPAGATION, AND TRANSMISSION

Action potentials are transient changes in membrane polarization that spread in space and time along neurons or muscle cells, for example. Such perturbations result from choreographed changes in membrane conductance, primarily by Na^+ and K^+ ions, brought about by opening, closing, and inactivation gating transitions of voltage-activated sodium (NaV) and potassium (Kv) ion channels, respectively. One can encounter clusters of the various voltage-dependent ion channels starting at the neuronal soma, continuing along the axon and across the synapse (**Figure 1**). AP generation relies on proper enrichment of Na^+ and K^+ voltage-gated ion channels to the AIS, where the axon begins to extend from the soma

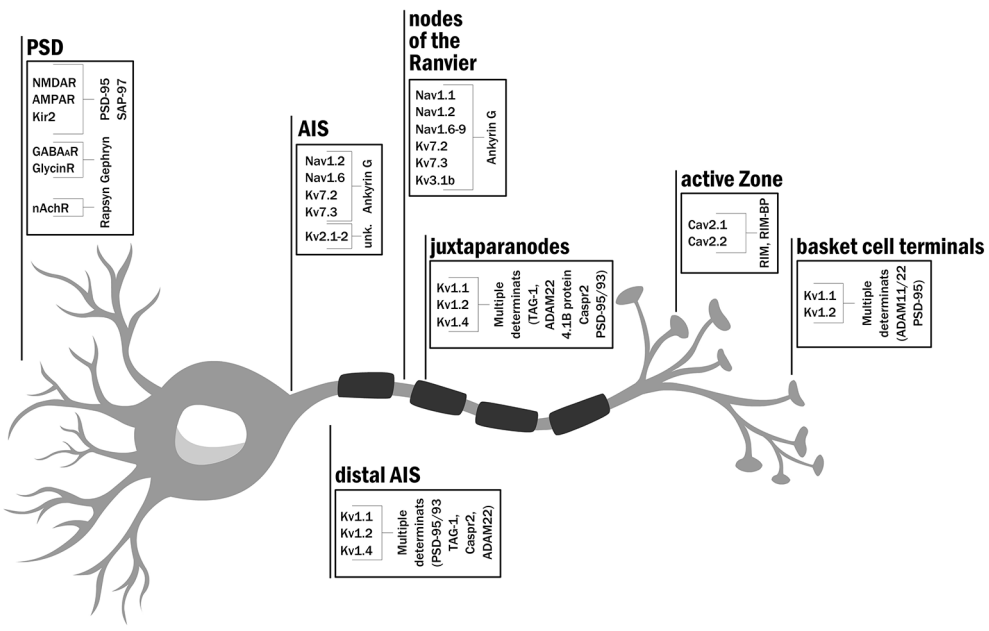

FIGURE 1 | Clustering geography: the distribution of ion channels and scaffold proteins along the neuron. Schematic representation of a typical neuron specifying the type of ion channel and scaffold proteins targeted and clustered to the axon initial segment, node of Ranvier, active zone and at the postsynaptic densities (in dendrites). A full reference list supporting the indicated location for each channel subtype is given in **SI Text 1**.

(Hille, 1992; Kole et al., 2007; Kole et al., 2008; Jensen et al., 2017). Membrane depolarization occurs with high efficiency at the AIS, with voltage-activated sodium channel subtypes 1.2 and 1.6 (NaV1.2 and NaV1.6) corresponding to the dominant ion channel types clustered at this region (Tian et al., 2014) (**Figure 1**). Disruption of NaV channel cluster formation at the AIS in mouse cerebellum Purkinje cells led to delayed AP initiation and a reduced maximal firing rate (Zhou et al., 1998). These effects emphasize the importance of NaV channel clusters at the AIS for normal electrical signaling. Kv channels were also shown to be part of the high-density channel repertoire at the AIS (**Figure 1**). While Kv2.1 channel clusters are seen at specific subdomain patches of the AIS (Trimmer, 1991; Scannevin et al., 1996; Sarmiere et al., 2008), Kv7, and Kv1 channel subtypes (KCNQ and *Shaker*-type channels), respectively, reside at the proximal (Klinger et al., 2011) and distal regions of the AIS (Kole et al., 2007), adjusting the threshold, inter-spike interval, and firing frequency characteristics of the action potential.

As the AP propagates down the myelinated axon, high densities of NaV and Kv channels are encountered at nodes of the Ranvier (**Figure 1**). Here, targeting and clustering of these channels are essential for AP saltatory conduction along the axon (Rasband and Trimmer, 2001). The nodal membrane was reported to express clusters of multiple NaV channel subtypes, including NaV1.1, NaV1.2, NaV1.6, NaV1.7, Nav1.8, and NaV1.9 channels (Chang and Rasband, 2013). Kv channel subtypes 1, 3, and 7 were also reported to reside and cluster at nodal sites. Whereas Kv7.2, Kv7.3, and Kv3.1 channels were shown to be responsible for the repolarization of the axonodal membrane (Devaux et al., 2003; Devaux et al., 2004; Klinger et al., 2011; Trimmer, 2015), the Kv1 channel subfamily (Kv1.1, Kv1.2, and Kv1.4) is clustered at juxtaparanodal regions (Poliak et al., 2003; Rasband, 2004) and serves to adjust AP propagation along the myelinated axon. Pharmacologically blocking these channels resulted in prolonged action potentials (Devaux et al., 2002).

Progressing along the axon towards its terminal, one reaches the active zone (AZ), the next site where ion channels are clustered (**Figure 1**). In this region, proteins of the vesicle release machinery involved in synaptic transmission are tightly docked (Südhof, 2012). In particular, voltage-activated Ca^{2+} channels (N and P/Q types, specifically CaV2.1 and 2.2, respectively) are clustered at this site to ensure the economic and directed release of neurotransmitters into the synaptic cleft (Kaeser et al., 2011; Gundelfinger and Fejtova, 2012). Following the release, neurotransmitters diffuse across the synaptic cleft and bind to excitatory or inhibitory ligand-gated ionotropic receptors that are aggregated at the post-synaptic density membrane (PSD). The PSD has mostly been studied in glutamatergic neurons, where AMPA and NMDA ionotropic receptors are clustered, proximal to the pre-synaptic AZ sites (Boeckers, 2006; Chen et al., 2015; Tang et al., 2016; Scheefhals and MacGillavry, 2018). Ionotropic glycine receptor clustering was also reported in the membrane of the postsynaptic cell (Patrizio et al., 2017; Schaefer et al., 2018). Such clusters are found in motor neuronal membranes of the adult spinal cord, brain stem, and retina, and were shown to be essential for proper neuron hyperpolarization. Impaired clustering of glycine receptors is associated with startle disease in mice (Patrizio et al., 2017; Schaefer et al., 2018). The clustering of different ion channels and receptors in proximity to other intracellular signaling and cytoskeletal structural proteins at the PSD is also essential for ensuring a robust response to neurotransmitter binding and for modulating the evoked synaptic potential, whether inhibitory or excitatory, of the post-synaptic cell membrane (Boeckers, 2006). A robust response to neurotransmitter release also occurs at the neuromuscular junction (NMJ) where it is essential for muscle contraction. Thousands of copies of nicotinic acetylcholine receptors (nAchRs) are clustered at the post-synaptic muscle cell (Peng and Poo, 1986; Bruneau et al., 2008). The opening of these non-selective ligand-gated cation channels in response to acetylcholine release allows the diffusion of primarily Na^+ ions across the muscle cell membrane to achieve efficient muscle cell membrane depolarization and subsequently contraction (Bruneau et al., 2008; Slater, 2017; Burden et al., 2018). A detailed reference list summarizing available information attesting to the targeting of a specific ion channel subtype to the indicated neuronal membrane sites is given in **SI Text 1**.

THE HIDDEN DIMENSION OF ION CHANNEL CLUSTERING: THE DIFFERENT MODES BY WHICH ION CHANNEL DENSITY MAY AFFECT AP CONDUCTION PROPERTIES

The density of aggregated voltage-dependent ion channel molecules at their unique sites of targeting may affect AP conduction properties *via* three distinct, non-mutually-exclusive modes. First and straightforward, voltage-dependent ion channel density at the sites of channel expression directly dictates the density of inward or outward Na^+ or K^+ ionic currents, upon changes in membrane polarization. Second, ion channel density by itself may affect activation and/or inactivation gating transitions of the channel, as compared to the isolated channel scenario. Last, the accumulation of densely-packed voltage-activated ion channel molecules, with their multiple positively charged voltage-sensing domains, might affect the capacitance property of the membrane at such sites, potentially affecting the cable properties of the axon. As we concisely summarize below, all three functional consequences of changes in ion channel density are expected to affect AP conduction properties.

Several years before the seminal papers of Hodgkin and Huxley, describing the theory behind action potential generation (Hodgkin and Huxley, 1952; Huxley, 1964), Hodgkin described a set of experiments on *Carcinus maenas* crab axons demonstrating two, low- and high-frequency, repetitive firing modes (Hodgkin, 1948). These experiments provided a solid base for the current understanding of AP firing modes exhibited by pyramidal neurons (Tateno and Robinson, 2006) and interneurons (Tateno and

Robinson, 2007). The two neuronal excitability modes were used to rationalize coding properties of neurons (Rinzel and Ermentrout, 1998; St-Hilaire and Longtin, 2004; Tateno et al., 2004; Tateno and Robinson, 2006; Tateno and Robinson, 2007). It has long been thought that different combinations of ion channel types may explain the observed differences in firing patterns (Prescott et al., 2008). In recent years, however, theoretical and experimental evidence has been accumulated to show that changes in the densities of voltage-gated Na^+ and K^+ channels alone can explain the dynamic switch of a neuron between the low and high-frequency firing modes (Århem et al., 2006; Århem and Blomberg, 2007; Zeberg et al., 2010; Zeberg et al., 2015). Such changes in ionic current densities are reflected by changes in the membrane permeability to Na^+ and K^+ ions when all channels are open. In the native channel context, such modulation of ion channel densities may be brought about by specific channel blockers that serve to reduce the nominal number of active channels per site (Zeberg et al., 2010). These later studies directly demonstrate how changes in ionic current densities may affect AP conduction properties and information coding.

Changes in ion channel densities at their native clustering sites may further affect the gating properties of the ion channel. Ion channel gating is often studied in an isolated channel context, with the ion channel being expressed in the membrane of a heterologous expression system (Furutani and Kurachi, 2012). Activation and slow or fast channel inactivation of voltage-dependent channels are then studied using electrophysiological recording techniques, with the single-channel recording being one of the most direct and thorough methods for studying ion channel gating and regulation (Sakmann and Neher, 1984). Clearly, the targeting of ion channels to native sites along with their adjacent modulatory subunits and regulatory proteins affects the gating properties of the channels (O'Connell et al., 2010; Zhang et al., 2016; Vivas et al., 2017). What we wish to emphasize here is that the density of ion channels at native clustering sites by itself may affect the channel activation and inactivation gating properties, thus affecting AP conduction properties. This dimension is frequently overlooked when addressing channel clustering. Several examples of such density-mediated modulation of channel gating have been reported. First, the density of the prototypical bacterial KcsA K^+ channel expressed in liposomes was shown to affect the open probability of the channel (Molina et al., 2006; Sumino et al., 2014). The mechanism underlying such effects on channel activation gating is, however, not yet clear. Another example is the L-type CaV1.2 channel expressed in native cardio-myocyte cells. CaV1.2 channels were shown reside within small clusters (5–10 molecules) and appear to open synchronously in response to membrane depolarization (Dixon et al., 2015). Furthermore, prolonged open channel duration was observed for the clustered channels, as compared to the isolated channel case, suggesting that activation gating is affected (Dixon et al., 2015; Folci et al., 2018). The functional coupling between multiple ion channels can also be inhibitory. For instance, Kv2.1 channels were reported to exhibit a non-conductive phenotype when clustered at high densities (Scannevin et al., 1996; O'Connell et al., 2010; Fox et al., 2013; Liu et al., 2016). Clearly, in all these examples, although no mechanisms were suggested, it is reasonable to assume that short-range inter-molecular allosteric interactions are responsible for the observed coupling effects. Such changes in ion channel gating properties due to changes in channel density would affect the kinetics of ionic current development with time (i.e. the rate constants for activation and inactivation channel processes) and are expected to affect AP shape and conduction properties (Debanne et al., 1997; Giese et al., 1998; Johnston et al., 1999).

Another dimension of voltage-dependent ion channel density concerns their potential effect(s) on the physical properties of the membrane at the clustering site. Such effects may be brought about by the proximity of many charged voltage sensor domains resulting in changes in membrane thickness and/or its effective dielectric constant, both properties that affect membrane capacitance. The first report concerning potential effects of channel overexpression on membrane properties concerned the channelrhodopsin-2 light-gated ion channel (Zimmermann et al., 2008). Overexpression of the protein in HEK293 cells resulted in changes in the morphology of the cell mabrane reflected in an increase in membrane capacitance. This effect was not observed upon physiological expression levels of the channel (Zimmermann et al., 2008). Furthermore, recordings from tsA201 and PC12 cells overexpressing *the Ciona intestinalis* voltage-sensing phosphatase protein (Ci-VSP) revealed an increase of the local membrane capacitance upon voltage activation of the protein (Hossain et al., 2008; Lundby et al., 2008). The additional capacitance component termed "sensing capacitance" was further investigated by computational simulations of neuronal model cells expressing the voltage-sensing fluorescent proteins VSFP2.3 and VSFP3.1 (Akemann et al., 2009). The results revealed that changes in expression levels of these proteins resulted in changes in membrane capacitance due to changes membrane topology and/or mobility of channel gating, leading to changes in the effective diaelectric constant of the membrane. The simulations revealed that such changes lead to an increase of the threshold for AP spike initiation (Akemann et al., 2009). Although these studies relate to changes in the expression levels of these voltage-sensing domain-containing proteins as causing changes in membrane capacitance, such changes, are of course, related to changes in the density of these proteins per membrane area. The end result is that for voltage-sensor containing proteins, regulation of protein clustering affects membrane capacitance properties and hence, cable properties of the axon. It remains to be shown whether such "sensing capacitance" effects are also observed for native voltage-dependent sodium and potassium ion channel proteins.

Taken together, the results summarized here emphasize that understanding of how ion channel density within clustering sites is regulated is of paramount importance in considering electrical signaling, with changes in ion channel density exerted through changes in membrane ionic current densities, in channel gating properties and/or membrane capacitance, dramatically affecting AP shape, frequency and information coding in neurons.

MOLECULAR AND CELLULAR GAPS IN UNDERSTANDING ION CHANNEL CLUSTERING

The family of scaffold proteins is central for targeting and clustering of ion channels at native membrane sites (Good et al., 2011). Such clustering can be revealed by confocal light microscopy imaging of heterologous cells transfected to express both the ion channel and scaffold proteins and is manifested as a speckled co-localization pattern of fluorescently-tagged versions of both proteins in the cell membrane (Tejedor et al., 1997). Scaffold proteins correspond to many different and structurally unrelated protein subfamilies that seem to share similar functional roles. They are multi-domain proteins that interact with ion channels and membrane receptors (as well as with other membrane-embedded proteins) on the one hand, and with other intracellular signaling and skeletal proteins on the other. Scaffold proteins thus link membrane-associated events with downstream signaling pathways (Good et al., 2011; Zheng et al., 2011; Lee et al., 2014).

Here, we consider several examples of scaffold proteins encountered along the length of the neuron (**Figure 1**). Ankyrin G scaffold proteins interact with NaV channel isoforms at nodal and AIS sites and further bind to the intracellular βIV-spectrin protein (Zhou et al., 1998; Komada and Soriano, 2002). This latter protein further interacts with actin, a major component of the cytoskeletal network. The interaction between ankyrin G and NaV channels in the rat is mediated by a nine amino acid motif within the second intracellular loop of the NaV1.2 channel and leads to NaV channel clustering (Lemaillet et al., 2003). How ankyrin G serves to dock and cluster NaV channel molecules is not yet known. The clustering of calcium channels at the pre-synaptic AZ offers another example. Here, the scaffold protein of focus is the RIM (Rab3-interacting molecule) protein (Südhof, 2012). RIM proteins were proposed to interact *via* their PDZ protein-protein interaction modules with a cytoplasmic C-terminal PDZ-binding motif presented by N and P/Q type voltage-activated Ca^{2+} channels (Kaeser et al., 2011). Such interaction allows for tethering these channels at the AZ in high copy numbers. For example, around 100 CaV1.3 and ~10 CaV2.1 channel molecules reside in AZ clusters of hippocampal Purkinje neurons, with several such clusters being noted per AZ (Miki et al., 2017). RIM proteins also interact with several other vesicle-release proteins in the AZ complex (Krinner et al., 2017). The RIM scaffold protein thus mediates coupling between the CaV channel and vesicle docking machinery proteins and is essential for synchronous neurotransmitter release at the AZ. Still, it remains to be determined whether or not CaV channel-RIM protein-protein interactions affect Cav gating. The last example concerns the scaffold protein-mediated clustering of different ion channels and receptors at the PSD (Gomperts, 1996). Here, the dominating scaffold protein family is the membrane-associated guanylate kinase (MAGUK) family, the most intensively studied of all scaffold proteins. Relying on their multiple domains, MAGUKs serve as linker proteins that couple membrane events with downstream intracellular signaling (Zheng et al., 2011; Chen et al., 2015). Similar to RIMs, MAGUK proteins also carry PDZ domains capable of binding the C-terminal motifs of several membrane-embedded ion channels, receptors, and cell adhesion proteins (Li et al., 2000; Lee and Zheng, 2010). Other modular domains of MAGUKs, such as its SH3 and guanylate kinase-like domains, serve as hubs for signaling control and interact with other PSD components, such as the adhesion protein ADAM22, A-kinase anchor proteins (AKAPs), actin dynamic modulators (such as SPIN90/WISH) (Lee et al., 2006; Han and Kim, 2008; Verpelli et al., 2012; Frank and Grant, 2017) and other scaffolding proteins [such as *guanylate kinase-associated protein* (GKAP) family members]. PSD-95 and SAP-97, two members of the MAGUK family of scaffold proteins, were shown to be responsible for AMPAR, NMDAR and Kir2 channel clustering at the PSD site of glutamatergic synapses (Cohen et al., 1996; Gomperts, 1996; Chen et al., 2015; Hoffmann et al., 2015). PSD-95 and SAP-97 were also shown to interact with members of the Kv1 (*Shaker*-type) subfamily (Gomperts, 1996; Tiffany et al., 2000). PSD-95 and PSD-93 were also reported to be essential for the proper clustering of *Shaker* channels at the AIS (Ogawa et al., 2008), at membranes of basket cell terminals (Rasband, 2010) and in smooth muscle cells (Joseph et al., 2011) but not in the juxtaparanodes (Rasband et al., 2002). Although Kv1 channels and PSD-95 co-localize at the juxtaparanode (Rasband, 2004; Arancibia-Carcamo and Attwell, 2014), clustering does not seem to depend on PSD-95 and as such, its role in the juxtaparanodal scaffold is still questioned. A detailed reference list supporting the findings indicated above is provided in **SI Text 1**.

The examples above, and others not addressed here demonstrate that ion channel clustering at distinct neuronal membrane sites primarily involves the direct binding of the channel to its cognate scaffold protein partner. In some cases, the ion channel and the scaffold protein binding partners are known. However, how this molecular binding event leads to cellular ion channel clustering involving many molecules is utterly unknown for almost all ion channel proteins. Furthermore, we generally do not know if and how ion channel membrane density is regulated in the spatial and/or temporal dimensions. These questions reflect what we refer to as a molecular-cellular gap that hampers our understanding of ion channel clustering. Indeed, many questions concerning the scaffold protein–ion channel interacting pair have yet to be answered. What is the stoichiometry of the interaction? How is ion channel density regulated in both the spatial and temporal dimensions? How is cluster area size determined? How do other proteins serve to regulate the clustering process? How many ion channel molecules usually reside in such clusters? Are there direct inter-molecular channel–channel interactions within clusters? To begin answering these questions, insight into the molecular mechanism underlying the binding of a channel to its cognate scaffold protein must be obtained. As will be demonstrated in the following section using the concrete example of the *Shaker* Kv channel-PSD-95 interaction, where such mechanistic knowledge is available, valuable insight into the mechanism of ion channel clustering is at hand.

BRIDGING THE MOLECULAR-CELLULAR GAP IN UNDERSTANDING KV CHANNEL CLUSTERING

Members of the *Shaker* Kv channel family were previously discovered to cluster upon channel interaction with the PSD-95 scaffold protein (Kim et al., 1995; Tejedor et al., 1997). This interaction is mediated by PDZ-binding motifs located at the extended C-terminal region of the channel that binds to the PSD-95 PDZ domains. Mutations in the PDZ-binding motif of the prototypical *Drosophila melanogaster Shaker* Kv channel were found to impair both PSD-95 association and clustering. Eliminating this motif resulted in a diffusive channel expression pattern in the membrane of heterologous cells transfected to express the mutant channel and PSD-95 (Kim et al., 1995; Tejedor et al., 1997; Tiffany et al., 2000). In recent years, our lab has revealed the molecular mechanism underlying the *Shaker* Kv channel-PSD-95 interaction (Magidovich et al., 2007; Zandany et al., 2015a). This mechanism is referred to as a 'ball and chain' binding mechanism and is depicted in **Figure 2** (upper panel). According to this mechanism, and in analogy to the fast inactivation gating of NaV and Kv channels (Armstrong and Bezanilla, 1977; Armstrong, 1981; Hoshi et al., 1990), the channel's cytoplasmic C-terminal tail contains an extended intrinsically disordered amino acid "chain" (Magidovich et al., 2007), bearing a conserved PDZ-binding motif (the "ball") at its tip (Magidovich et al., 2007; Zandany et al., 2015a). The random walk motion of the "chain" serves to search and recruit the PSD-95 scaffold protein partner (**Figure 2** upper panel), in a manner analogous to the role of the extended N-terminal Kv channel tail in regulating fast channel inactivation (Hoshi et al., 1990). In this inactivation process, the stretch comprising the terminal 20 amino acids of the channel, corresponding to the inactivation "ball", is guided by a random walk search of the attached "chain" for its receptor site in the inner cavity of the open ion conduction pore domain, thus blocking the flow of K^+ current through the channel. In both "ball and chain" mechanisms, either the N- or C-terminal "chains" belong to the class of entropic chains of intrinsically-disordered proteins (Dunker et al., 2001; Dunker et al., 2002; Uversky and Dunker, 2010) and function as entropic clocks (Dunker et al., 2001) to time channel entry into inactivation or PSD-95 binding, respectively (Hoshi et al., 1990; Zandany et al., 2015a; Zandany et al., 2015b).

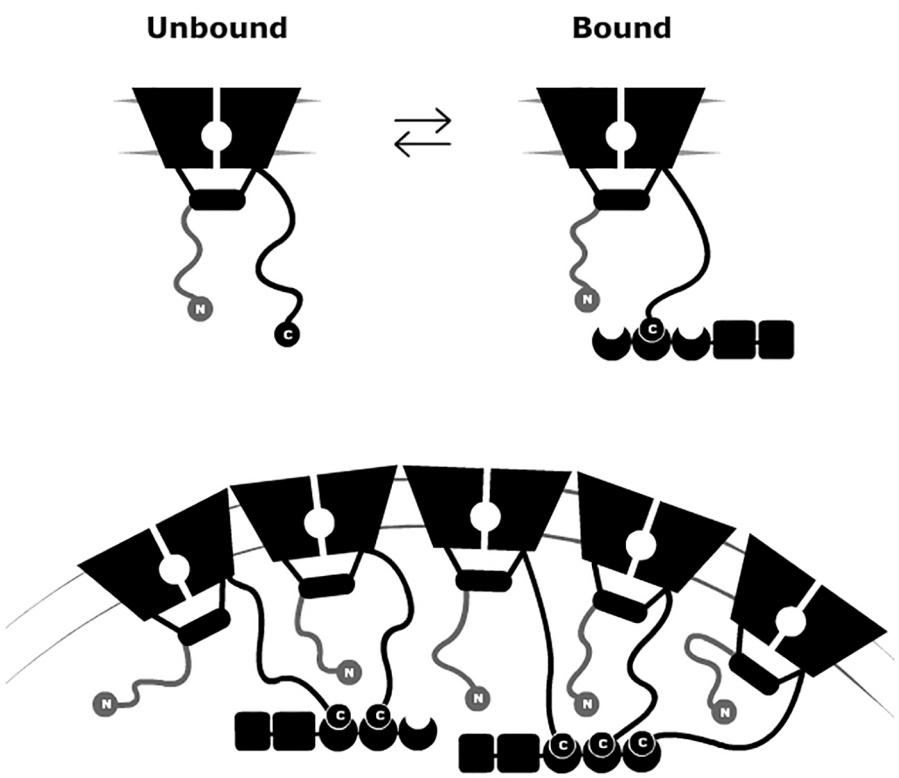

FIGURE 2 | A "ball and chain" mechanism for Kv channel clustering. Schematic representation of the "ball and chain" mechanism for channel binding to PSD-95 (upper panel). In the inter-molecular 'ball and chain' binding mechanism, the interaction of the Kv channel with the membrane-associated PSD-95 scaffold protein is precisely timed, as determined by C-terminal chain length, upon binding of the "chain"-tethered peptide "ball" to the PSD-95 PDZ domain(s). Given the stoichiometry of the interaction and the ability of PSD-95 to aggregate, channel clustering results (lower panel). The membrane-embedded portion corresponds to the channel voltage-sensor and pore domains, while the rectangular shape corresponds to the T1 assembly domain. The crescent, box, and rectangular shapes represent the PDZ, SH3, and guanylate kinase-like domains of the PSD-95 protein, respectively. PSD, post-synaptic density.

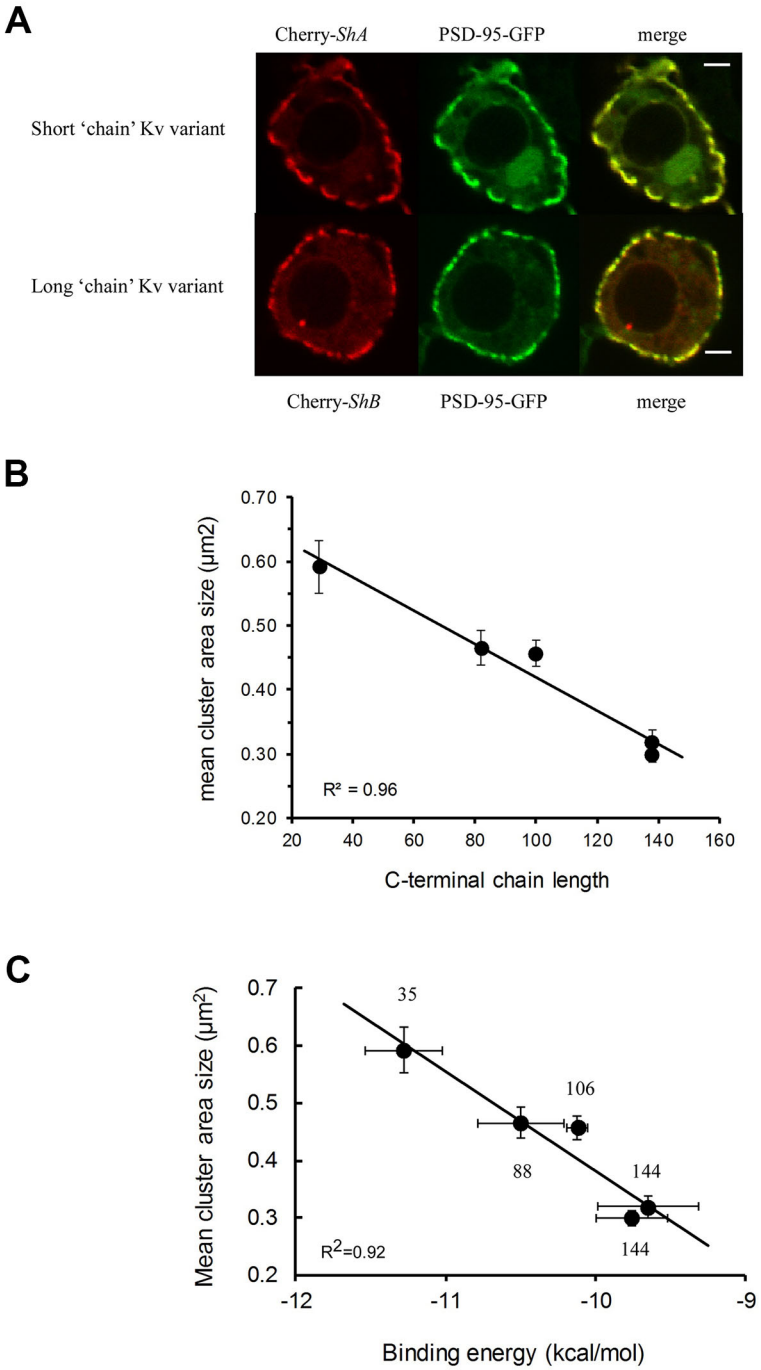

FIGURE 3 | Molecular and cellular correlates in PSD-95–mediated Kv channel clustering. **(A)** Typical confocal microscopy analysis of *Drosophila* Schneider S2 cells co-expressing PSD-95–GFP and either the short or long native (alternatively-spliced) Kv channel "chain" length variants. For each cell, three images are shown, with the red channel-associated and green PSD-95-associated fluorescence signals presented in the left and middle columns, respectively. The merged image is shown in the right column. Scale bars correspond to 2 µ;m. Numbers next to each channel notation indicate C-terminal amino acid "chain" length (adopted with permission from Zandany et al., 2015a). **(B)** Dependence of the mean mega-cluster area size of different Kv channel "chain" length variants on the C-terminal "chain" length. The solid curve corresponds to linear regression with an R^2 value of 0.96. **(C)** Correlation plot relating the mean cluster area size of the different Kv channel "chain" length variants, as supported by PSD-95, and the binding affinity of the different variants to PSD-95. The solid curve represents linear regression between the compared quantities (R^2 = 0.92). It is possible that such a linear correlation breaks down for too short "chains" due to steric considerations stemming from the inability of multiple Kv channel molecules to bind PSD-95 when the "chain" is too short. Numbers next to each channel notation indicate C-terminal "chain" length in terms of amino acid numbers. PSD, post-synaptic density.

Two major criteria support the proposed "ball and chain" mechanism for channel binding to PSD-95 (Zandany et al., 2015a; Zandany et al., 2015b). First, thermodynamic binding analyses showed that the association of the Kv channel C-terminal "chain" peptide with PSD-95 is entropy -controlled in a manner dictated by "chain" length. Second, the association rate constant of the two proteins depends on "chain" length according to a power-law relation, as predicted by polymer chain theory (Zandany et al., 2015a). Direct support for the analogy between the fast inactivation and channel binding to PSD-95 "ball and chain mechanisms" was recently obtained using a "chain"-level chimeric channel approach, where it was shown that different alternatively spliced and intrinsically-disordered N- and C-terminal "chain" variants were able to replace one another in the corresponding fast inactivation or PSD-95 binding processes (Lewin et al., 2019). Furthermore, the swapped "chains" affected the relevant fast inactivation or PSD-95 binding processes in a length-dependent manner, as predicted by the random flight "chain" theory underlying the "ball and chain" mechanism (Lewin et al., 2019).

What is the relevance of the molecular "ball and chain" mechanism to cellular *Shaker* channel clustering (**Figure 2**, lower panel)? Clearly, one important aspect is the stoichiometry of the interaction involving the three PDZ domains of PSD-95 and the four "chains" of the tetrameric Kv channel (Gomperts, 1996). Furthermore, the ability of PSD-95 protein to self-aggregate may also help rationalize how multiple ion channels and/or PSD-95 molecules realize close proximity (Hsueh et al., 1997; Ghosh et al., 2018). Given the "chain"-length dependence of the Kv channel-PSD-95 interaction, combined with stoichiometry considerations, one can ask whether Kv channel "chain" length affects attributes of channel clustering, such as cell surface expression, cluster area size or density. These questions are particularly interesting given that alternative splicing of the Kv channel gene produces Kv channel variants exhibiting distinct "chain" lengths yet which present identical terminal "ball" motifs (Kamb et al., 1988; Schwarz et al., 1988). It has been shown that the level of PSD-95-mediated channel membrane surface expression is dependent on "chain" length, with the shorter "chain" length native *Shaker* channel splice variant exhibiting higher affinity to PSD-95 and higher levels of expression, as compared to the longer, lower affinity native channel variant (Zandany et al., 2015a). The same variants further exhibited differences in cluster area size, with the short "chain" variant presenting clusters covering larger areas (**Figure 3A**) (Zandany et al., 2015a). Moreover, confocal imaging analyses of embryonic *Drosophila* Schneider cells transfected to express PSD-95, together with a series of Kv channel native and artificial "chain"-length variants, revealed "chain length"-dependence of Kv channel cluster area size (Lewin et al., 2019). Specifically, the shorter the Kv channel C-terminal "chain", the larger was the cluster area size observed (**Figure 3B**) (Lewin et al., 2019). Furthermore, the cluster area size of any Kv channel-PSD-95 protein pair was found to linearly correlate with the observed affinity between the two proteins (**Figure 3C**). These results carry important consequences for understanding the regulation of Kv channel clustering. Fine-tuning of channel clustering may not only be achieved by differences in spatial-temporal expression of the PSD-95-related affinity variants (Mottes and Iverson, 1995; Ingleby et al., 2009) but also can result from heterologous subunit assembly (Isacoff et al., 1990; McCormack et al., 1990). Different combinations of long and short C-terminal "chain" variants may thus lead to the appearance of channels with a repertoire of affinities towards PSD-95 and hence, possibly to distinct channel cluster area sizes and densities. Such regulation is expected to have a profound implication on electrical signaling. Taken together, the results summarized in **Figure 3** reveal the cellular correlates of the molecular "ball and chain" mechanism concerning channel clustering. Kv channel "chain" length not only affects affinity to the PSD-95 scaffold protein but further determines Kv channel surface expression and cluster area size. Given the extended intrinsically-disordered nature of this random "chain", this emphasizes the entropy-based regulation mode of Kv channel clustering, which mirrors the thermodynamic entropy signature of the preceding Kv channel-PSD-95 molecular binding step (Zandany et al., 2015b).

Nevertheless, several questions related to the regulation of *Shaker* Kv channel clustering await answers. What regulation strategies are employed at the "chain" and "ball" levels to control channel binding to PSD-95, and as such, Kv channel clustering? Does Kv channel "chain" length affect ion channel density? Does the C-terminal "chain" play an active or a passive role in channel clustering? Does crosstalk exist between the inactivation and clustering "ball and chain" mechanisms? Is "chain" length a primary factor that determines the binding specificity of PSD-95 towards its multiple membrane protein partners, or post-translational modifications are also involved? While these questions remain to be answered, the "ball and chain" description of Kv channel binding to scaffold proteins provides a simple mechanistic framework for studying Kv channel clustering. It offers a reference framework to analyze, compare, and interpret data and allows for rationalizing different regulation strategies for channel clustering.

FUTURE CHALLENGES AND DIRECTIONS

While a known mechanism for the ion channel-scaffold protein interaction is definitely valuable for answering the questions posed above, it is not enough. We still need a reliable quantitative approach to ion channel clustering that can presently only be achieved *via* high-resolution imaging of channel clustering. In the past, ion channel clustering was usually studied using conventional confocal imaging light microscopy that allows for resolutions up to 250 nm in the lateral direction. At such low resolution, quantitative assessment of channel clustering yields only limited basic information on surface expression and mega-cluster area size (Zandany et al, 2015a; Lewin et al., 2019). Recent advances in imaging techniques, in particular, in super-resolution imaging methodologies, offer improved spatial resolution reaching 30 nm, a value that may enable the further studying of clustering at the single-molecule level (Sieben et al., 2018; Schermelleh et al., 2019). Such methodologies, particularly single-molecule localization methods (SML), will further enable evaluating important quantitative attributes of channel clustering,

such as ion channel densities within cluster sites, number of clusters per membrane area and average number of molecules in a cluster, to mention only a few. It may further enable understanding the various regulation strategies that may affect ion channel density. The premise of such an approach was elegantly demonstrated in a recent paper by Shapiro and colleagues studying ion channel clustering using stochastic optical reconstruction SML microscopy (STORM) (Zhang et al., 2016). In this study, the authors demonstrated scaffold protein (the AKAP protein)-mediated cluster formation involving direct association of different ion channel types. The analysis reported the distribution of clusters according to area size and the relative proximity of the clusters. Their results provided unexpected and novel insight into the role of coupling among different channel types for electrical signaling. As in all reported cases of ion channel coupling due to channel clustering, the channel determinants responsible for such potentially inter-molecular allosteric coupling remain to be identified (Zhang et al., 2016).

Additional important insight into ion channel clustering can be obtained by employing crystallographic and X-ray scattering analyses. Relying on these methods, combined with thermodynamic analyses, Rodzli and colleagues recently showed that the isolated C-terminal peptide of the Kir 2.1 channel, when fused to the first two PDZ domains of PSD-95, forms a cubic-packed, highly organized oligomeric scaffold (Rodzli et al., 2019). These data suggest that 'chain' binding to PSD-95 provides a switch with which to initiate channel clustering, probably *via* self-assembly of repeating scaffold units. It would be interesting to examine how changes in length and composition of the peptide "chain" would impact the properties of this compound scaffold.

CONCLUDING REMARKS

In the current review, using the concrete example of PSD-95-mediated *Shaker* Kv channel clustering, we emphasized that insight into cellular ion channel clustering can be obtained when the molecular mechanism controlling ion channel-scaffold protein interaction is known. Identifying the interacting scaffold protein partners responsible for active ion channel clustering is only the first step towards understanding the clustering process. Knowing the molecular mechanism underlying this interaction, combined with super-resolution confocal microscopy, in particular, single-molecule localization microscopy that allows direct observation of channel clustering at the molecular level, may serve to bridge the molecular and cellular gap in understanding channel clustering. This strategy may further provide a framework to analyze pressing questions regarding the specific clustering of the ion channel under study, in particular, those related to the manner(s) by which the ion channel clustering process is regulated to affect ion channel density. Given the seminal importance of ion channel density in affecting action potential conduction properties, brought about by changes in ionic current densities, ion channel gating properties and/or membrane capacitance, efforts to reveal such mechanisms are paramount and are expected to shed more light on the hidden dimension of ion channel density regulation.

AUTHOR CONTRIBUTIONS

VN and OY wrote the manuscript.

ACKNOWLEDGMENTS

This research was supported by the Israel Science Foundation (grant 294/16 to OY).

SUPPLEMENTARY MATERIAL

The Supplementary Material for this article can be found online at: https://www.frontiersin.org/articles/10.3389/fphar.2019.01644/full#supplementary-material

REFERENCES

Arancibia-Carcamo, I. L., and Attwell, D. (2014). The node of Ranvier in CNS pathology. *Acta Neuropathol.* 128, 161–175. doi: 10.1007/s00401-014-1305-z

Århem, P., and Blomberg, C. (2007). Ion channel density and threshold dynamics of repetitive firing in a cortical neuron model. *BioSystems* 89, 117–125. doi: 10.1016/j.biosystems.2006.03.015

Århem, P., Klement, G., and Blomberg, C. (2006). Channel density regulation of firing patterns in a cortical neuron model. *Biophys. J.* 90, 4392–4404. doi: 10.1529/biophysj.105.077032

Akemann, W., Lundby, A., Mutoh, H., and Knöpfel, T. (2009). Effect of voltage sensitive fluorescent proteins on neuronal excitability. *Biophys. J.* 96, 3959–3976. doi: 10.1016/j.bpj.2009.02.046

Armstrong, C. M., and Bezanilla, F. (1977). Inactivation of the sodium channel. II. Gating current experiments. *J. Gen. Physiol.* 70, 567–590. doi: 10.1085/jgp.70.5.567

Armstrong, C. M. (1981). Sodium channels and gating currents. *Physiol. Rev.* 61, 644–683. doi: 10.1152/physrev.1981.61.3.644

Boeckers, T. M. (2006). The postsynaptic density. *Cell Tiss. Res.* 326, 409–422. doi: 10.1007/s00441-006-0274-5

Bruneau, E. G., Brenner, D. S., Kuwada, J. Y., and Akaaboune, M. (2008). Acetylcholine receptor clustering is required for the accumulation and maintenance of scaffolding proteins. *Curr. Biol.* 18, 109–115. doi: 10.1016/j.cub.2007.12.029

Burden, S. J., Huijbers, M. G., and Remedio, L. (2018). Fundamental molecules and mechanisms for forming and maintaining neuromuscular synapses. *Int. J. Mol. Sci.* 19, 490. doi: 10.3390/ijms19020490

Capera, J., Serrano-Novillo, C., Navarro-Pérez, M., Cassinelli, S., and Felipe, A. (2019). The potassium channel odyssey: mechanisms of traffic and membrane arrangement. *Int. J. Mol. Sci.* 20, 734. doi: 10.3390/ijms20030734

Chang, K.-J., and Rasband, M. N. (2013). Excitable domains of myelinated nerves: axon initial segments and nodes of Ranvier. *Curr. Top. Membr.* 5, 159–192. doi: 10.1016/B978-0-12-417027-8.00005-2

Chen, X., Levy, J. M., Hou, A., Winters, C., Azzam, R., Sousa, A. A., et al. (2015). PSD-95 family MAGUKs are essential for anchoring AMPA and NMDA receptor complexes at the postsynaptic density. *Proc. Natl. Acad. Sci. U. S. A.* 112, 6983–6992. doi: 10.1073/pnas.1517045112

Cohen, N. A., Brenman, J. E., Snyder, S. H., and Bredt, D. S. (1996). Binding of the inward rectifier K+ channel Kir 2.3 to PSD-95 is regulated by protein kinase A phosphorylation. *Neuron* 17, 759–767. doi: 10.1016/S0896-6273(00)80207-X

Debanne, D., Guérineau, N. C., Gähwiler, B. H., and Thompson, S. M. (1997). Action-potential propagation gated by an axonal I(A)-like K+ conductance in hippocampus. *Nature* 389, 286–289. doi: 10.1038/38502

Devaux, J., Gola, M., Jacquet, G., and Crest, M. (2002). Effects of K^+ channel blockers on developing rat myelinated CNS axons: identification of four types of K^+ channels. *J. Neurophysiol.* 87, 1376–1385. doi: 10.1152/jn.00646.2001

Devaux, J., Alcaraz, G., Grinspan, J., Bennett, V., Joho, R., Crest, M., et al. (2003). Kv3.1b is a novel component of CNS nodes. *J. Neurosci.* 23, 4509–4518. doi: 10.1523/JNEUROSCI.23-11-04509.2003

Devaux, J. J., Kleopa, K. A., Cooper, E. C., and Scherer, S. S. (2004). KCNQ2 is a nodal K^+ channel. *J. Neurosci.* 24, 1236–1244. doi: 10.1523/JNEUROSCI.4512-03.2004

Dixon, R. E., Moreno, C. M., Yuan, C., Opitz-Araya, X., Binder, M. D., Navedo, M. F., et al. (2015). Graded Ca2+/calmodulin-dependent coupling of voltage-gated CaV1.2 channels. *eLife* 4, e05608. doi: 10.7554/eLife.05608

Dunker, A. K., Lawson, J. D., Brown, C. J., Williams, R. M., Romero, P., Oh, J. S., et al. (2001). Intrinsically disordered protein. *J. Mol. Graph. Model.* 19, 26–59. doi: 10.1016/S1093-3263(00)00138-8

Dunker, A. K., Brown, C. J., Lawson, J. D., Iakoucheva, L. M., and Obradović, Z. (2002). Intrinsic disorder and protein function. *Biochemistry* 41, 6573–6582. doi: 10.1021/bi012159+

Engelman, D. M. (2005). Membranes are more mosaic than fluid. *Nature* 438, 578–580. doi: 10.1038/nature04394

Folci, A., Steinberger, A., Lee, B., Stanika, R., Scheruebel, S., Campiglio, M., et al. (2018). Molecular mimicking of C-terminal phosphorylation tunes the surface dynamics of CaV1.2 calcium channels in hippocampal neurons. *J. Biol. Chem.* 293, 1040–1053. doi: 10.1074/jbc.M117.799585

Fox, P. D., Loftus, R. J., and Tamkun, M. M. (2013). Regulation of Kv2.1 K^+ conductance by cell surface channel density. *J. Neurosci.* 33, 1259–1270. doi: 10.1523/JNEUROSCI.3008-12.2013

Frank, R. A., and Grant, S. G. (2017). Supramolecular organization of NMDA receptors and the postsynaptic density. *Curr. Opin. Neurobiol.* 45, 139–147. doi: 10.1016/j.conb.2017.05.019

Freeman, S. A., Desmazières, A., Fricker, D., Lubetzki, C., and Sol-Foulon, N. (2016). Mechanisms of sodium channel clustering and its influence on axonal impulse conduction. *Cell. Mol. Life Sci.* 73, 723–735. doi: 10.1007/s00018-015-2081-1

Furutani, K., and Kurachi, Y. (2012). "Heterologous expression systems and analyses of ion channels," in *Patch Clamp Techniques* (Tokyo): Springer Protocols Handbooks (Springer), 353–370. doi: 10.1007/978-4-431-53993-3_23

Ghosh, A., Ramagopal, U. A., Bonanno, J. B., Brenowitz, M., and Almo, S. C. (2018). Structures of the L27 domain of Disc large homologue 1 protein illustrate a self-assembly module. *Biochemistry* 57, 1293–1305. doi: 10.1021/acs.biochem.7b01074

Giese, K. P., Storm, J. F., Reuter, D., Fedorov, N. B., Shao, L. R., Leicher, T., et al. (1998). Reduced K^+ channel inactivation, spike broadening, and after hyperpolarization in Kvbeta1.1-deficient mice with impaired learning. *Learn. Mem.* 5, 257–273. doi: 10.1101/lm.5.4.257

Gomperts, S. N. (1996). Clustering membrane proteins: it's all coming together with the PSD-95/SAP90 protein family. *Cell* 84, 659–662. doi: 10.1016/S0092-8674(00)81043-0

Good, M. C., Zalatan, J. G., and Lim, W. A. (2011). Scaffold Proteins: Hubs for controlling the flow of cellular information. *Science* 332, 680–686. doi: 10.1126/science.1198701

Gundelfinger, E. D., and Fejtova, A. (2012). Molecular organization and plasticity of the cytomatrix at the active zone. *Curr. Opin. Neurobiol.* 22, 423–430. doi: 10.1016/j.conb.2011.10.005

Han, K., and Kim, E. (2008). Synaptic adhesion molecules and PSD-95. *Prog. Neurobiol.* 84, 263–283. doi: 10.1016/j.pneurobio.2007.10.011

Hille, B. (1992). Ionic channels of excitable membranes (second edition). *FEBS Lett.* 306, 277–278. doi: 10.1016/0014-5793(92)81020-M

Hodgkin, A. L., and Huxley, A. F. (1952). A quantitative description of membrane current and its application to conduction and excitation in nerve. *J. Physiol. (Lond.)* 117, 500–544. doi: 10.1113/jphysiol.1952.sp004764

Hodgkin, A. L. (1948). The local electric changes associated with repetitive action in a non-medullated axon. *J. Physiol.* 107, 165–181. doi: 10.1113/jphysiol.1948.sp004260

Hoffmann, B., Klöcker, N., Benndorf, K., and Biskup, C. (2015). Visualization of the dynamics of PSD-95 and Kir2.1 interaction by fluorescence lifetime-based resonance energy transfer imaging. *Medical Photonics* 27, 70–82. doi: 10.1016/j.medpho.2014.11.001

Hoshi, T., Zagotta, W. N., and Aldrich, R. W. (1990). Biophysical and molecular mechanisms of Shaker potassium channel inactivation. *Science* 250, 533–538. doi: 10.1126/science.2122519

Hossain, M. I., Iwasaki, H., Okochi, Y., Chahine, M., Higashijima, S., Nagayama, K., et al. (2008). Enzyme domain affects the movement of the voltage sensor in ascidian and zebrafish voltage-sensing phosphatases. *J. Biol. Chem.* 283, 18248–18259. doi: 10.1074/jbc.M706184200

Hsueh, Y. P., Kim, E., and Sheng, M. (1997). Disulfide-linked head-to-head multimerization in the mechanism of ion channel clustering by PSD-95. *Neuron* 18, 803–814. doi: 10.1016/S0896-6273(00)80319-0

Huxley, A. F. (1964). Excitation and conduction in nerve: quantitative analysis. *Science* 145, 1154–1159. doi: 10.1126/science.145.3637.1154

Ingleby, L., Maloney, R., Jepson, J., Horn, R., and Reenan, R. (2009). Regulated RNA editing and functional epistasis in Shaker potassium channels. *J. Gen. Physiol.* 133, 17–27. doi: 10.1085/jgp.200810133

Isacoff, E. Y., Jan, Y. N., and Jan, L. Y. (1990). Evidence for the formation of heteromultimeric potassium channels in Xenopus oocytes. *Nature* 345, 530–534. doi: 10.1038/345530a0

Jensen, C. S., Watanabe, S., Stas, J. I., Klaphaak, J., Yamane, A., Schmitt, N., et al. (2017). Trafficking of Kv2.1 channels to the axon initial segment by a novel nonconventional secretory pathway. *J. Neurosci.* 37, 11523–11536. doi: 10.1523/JNEUROSCI.3510-16.2017

Johnston, D., Hoffman, D. A., Colbert, C. M., and Magee, J. C. (1999). Regulation of back-propagating action potentials in hippocampal neurons. *Curr. Opin. Neurobiol.* 9, 288–292. doi: 10.1016/s0959-4388(99)80042-7

Joseph, B. K., Thakali, K. M., Pathan, A. R., Kang, E., Rusch, N. J., and Rhee, S. W. (2011). Postsynaptic density-95 scaffolding of Shaker-type K^+ channels in smooth muscle cells regulates the diameter of cerebral arteries. *J. Physiol. (Lond.)* 589, 5143–5152. doi: 10.1113/jphysiol.2011.213843

Kaeser, P. S., Deng, L., Wang, Y., Dulubova, I., Liu, X., Rizo, J., et al. (2011). RIM proteins tether Ca^{2+}-channels to presynaptic active zones *via a* direct PDZ-domain interaction. *Cell* 144, 282–295. doi: 10.1016/j.cell.2010.12.029

Kamb, A., Tseng-Crank, J., and Tanouye, M. A. (1988). Multiple products of the Drosophila Shaker gene may contribute to potassium channel diversity. *Neuron* 1, 421–430. doi: 10.1016/0896-6273(88)90192-4

Kim, E., Niethammer, M., Rothschild, A., Jan, Y. N., and Sheng, M. (1995). Clustering of Shaker-type K^+ channels by interaction with a family of membrane-associated guanylate kinases. *Nature* 378, 85–88. doi: 10.1038/378085a0

Klinger, F., Gould, G., Boehm, S., and Shapiro, M. S. (2011). Distribution of M-channel subunits KCNQ2 and KCNQ3 in rat hippocampus. *Neuroimage.* 58, 761–769. doi: 10.1016/j.neuroimage.2011.07.003

Kole, M. H. P., Letzkus, J. J., and Stuart, G. J. (2007). Axon initial segment Kv1 channels control axonal action potential waveform and synaptic efficacy. *Neuron* 55, 633–647. doi: 10.1016/j.neuron.2007.07.031

Kole, M. H. P., Ilschner, S. U., Kampa, B. M., Williams, S. R., Ruben, P. C., and Stuart, G. J. (2008). Action potential generation requires a high sodium channel density in the axon initial segment. *Nat. Neurosci.* 11, 178–186. doi: 10.1038/nn2040

Komada, M., and Soriano, P. (2002). βIV-spectrin regulates sodium channel clustering through ankyrin-G at axon initial segments and nodes of Ranvier. *J. Cell Biol.* 156, 337–348. doi: 10.1083/jcb.200110003

Krinner, S., Butola, T., Jung, S., Wichmann, C., and Moser, T. (2017). RIM-binding protein 2 promotes a large number of CaV1.3 Ca^{2+}-channels and contributes to fast synaptic vesicle replenishment at hair cell active zones. *Front. Cell Neurosci.* 11, 334. doi: 10.3389/fncel.2017.00334

Lai, H. C., and Jan, L. Y. (2006). The distribution and targeting of neuronal voltage-gated ion channels. *Nat. Rev. Neurosci.* 7, 548–562. doi: 10.1038/nrn1938

Lee, H.-J., and Zheng, J. J. (2010). PDZ domains and their binding partners: structure, specificity, and modification. *CCS*, 8, 8. doi: 10.1186/1478-811X-8-8

Lee, S., Lee, K., Hwang, S., Kim, S. H., Song, W. K., Park, Z. Y., et al. (2006). SPIN90/WISH interacts with PSD-95 and regulates dendritic spinogenesis *via*

an N-WASP-independent mechanism. *EMBO J.* 25, 4983–4995. doi: 10.1038/sj.emboj.7601349

Lee, A., Fakler, B., Kaczmarek, L. K., and Isom, L. L. (2014). More than a pore: ion channel signaling complexes. *J. Neurosci.* 34, 15159–15169. doi: 10.1523/JNEUROSCI.3275-14.2014

Lemaillet, G., Walker, B., and Lambert, S. (2003). Identification of a conserved Ankyrin-binding motif in the family of sodium channel α subunits. *J. Biol. Chem.* 278, 27333–27339. doi: 10.1074/jbc.M303327200

Lewin, L., Nirenberg, V., Yehezkel, R., Naim, S., Abdu, U., Orr, I., et al. (2019). Direct evidence for a similar molecular mechanism underlying Kv channel fast inactivation and clustering. *J. Mol. Biol.* 431, 542–556. doi: 10.1016/j.jmb.2018.12.002

Li, D., Takimoto, K., and Levitan, E. S. (2000). Surface expression of Kv1 channels is governed by a C-terminal motif. *J. Biol. Chem.* 275, 11597–11602. doi: 10.1074/jbc.275.16.11597

Liu, R., Yang, G., Zhou, M.-H., He, Y., Mei, Y.-A., and Ding, Y. (2016). Flotillin-1 downregulates K^+ current by directly coupling with Kv2.1 subunit. *Protein Cell* 7, 455–460. doi: 10.1007/s13238-016-0276-3

Lundby, A., Mutoh, H., Dimitrov, D., Akemann, W., and Knöpfel, T. (2008). Engineering of a genetically encodable fluorescent voltage sensor exploiting fast Ci-VSP voltage-sensing movements. *PloS One* 3, e2514. doi: 10.1371/journal.pone.0002514

Magidovich, E., Orr, I., Fass, D., Abdu, U., and Yifrach, O. (2007). Intrinsic disorder in the C-terminal domain of the Shaker voltage-activated K+ channel modulates its interaction with scaffold proteins. *Proc. Natl. Acad. Sci. U. S. A.* 104, 13022–13027. doi: 10.1073/pnas.0704059104

McCormack, K., Lin, J. W., Iverson, L. E., and Rudy, B. (1990). Shaker K^+ channel subunits from heteromultimeric channels with novel functional properties. *Biochem. Biophys. Res. Commun.* 171, 1361–1371. doi: 10.1016/0006-291x(90)90836-c

Miki, T., Kaufmann, W. A., Malagon, G., Gomez, L., Tabuchi, K., Watanabe, M., et al. (2017). Numbers of presynaptic Ca^{2+} channel clusters match those of functionally defined vesicular docking sites in single central synapses. *Proc. Natl. Acad. Sci. U. S. A.* 114, 5246–5255. doi: 10.1073/pnas.1704470114

Molina, M. L., Barrera, F. N., Fernández, A. M., Poveda, J. A., Renart, M. L., Encinar, J. A., et al. (2006). Clustering and coupled gating modulate the activity in KcsA, a potassium channel model. *J. Biol. Chem.* 281, 18837–18848. doi: 10.1074/jbc.M600342200

Mottes, J. R., and Iverson, L. E. (1995). Tissue-specific alternative splicing of hybrid Shaker/lacZ genes correlates with kinetic differences in Shaker K+ currents *in vivo*. *Neuron* 14, 613–623. doi: 10.1016/0896-6273(95)90318-6

O'Connell, K. M. S., Loftus, R., and Tamkun, M. M. (2010). Localization-dependent activity of the Kv2.1 delayed-rectifier K^+ channel. *Proc. Natl. Acad. Sci. U. S. A.* 107, 12351–12356. doi: 10.1073/pnas.1003028107

Ogawa, Y., Horresh, I., Trimmer, J. S., Bredt, D. S., Peles, E., and Rasband, M. N. (2008). Postsynaptic density-93 clusters Kv1 channels at axon initial segments independently of Caspr2. *J. Neurosci.* 28, 5731–5739. doi: 10.1523/JNEUROSCI.4431-07.2008

Patrizio, A., Renner, M., Pizzarelli, R., Triller, A., and Specht, C. G. (2017). Alpha subunit-dependent glycine receptor clustering and regulation of synaptic receptor numbers. *Sci. Rep.* 7, 1–11. doi: 10.1038/s41598-017-11264-3

Peng, H. B., and Poo, M. (1986). Formation and dispersal of acetylcholine receptor clusters in muscle cells. *Trends Neurosci.* 9, 125–129. doi: 10.1016/0166-2236(86)90041-X

Poliak, S., Salomon, D., Elhanany, H., Sabanay, H., Kiernan, B., Pevny, L., et al. (2003). Juxtaparanodal clustering of *Shaker*-like K^+ channels in myelinated axons depends on Caspr2 and TAG-1. *J. Cell Biol.* 162, 1149–1160. doi: 10.1083/jcb.200305018

Prescott, S. A., De Koninck, Y., and Sejnowski, T. J. (2008). Biophysical basis for three distinct dynamical mechanisms of action potential initiation. *PloS Comput. Biol.* 4, e1000198. doi: 10.1371/journal.pcbi.1000198

Rasband, M. N., and Trimmer, J. S. (2001). Developmental clustering of ion channels at and near the node of ranvier. *Dev. Biol.* 236, 5–16. doi: 10.1006/dbio.2001.0326

Rasband, M. N., Park, E. W., Zhen, D., Arbuckle, M. I., Poliak, S., Peles, E., et al (2002). Clustering of neuronal potassium channels is independent of their interaction with PSD-95. *J. Cell Biol.* 159, 663–672. doi: 10.1083/jcb.200206024

Rasband, M. N. (2004). It's "juxta" potassium channel! *J. Neurosci. Res.* 76, 749–757. doi: 10.1002/jnr.20073

Rasband, M. N. (2010). Clustered K+ channel complexes in axons. *Neurosci. Lett.* 486, 101–106. doi: 10.1016/j.neulet.2010.08.081

Rinzel, J., and Ermentrout, B. (1998). "Analysis of neural excitability and oscillations," in *Methods in Neuronal Modeling: From Ions to Networks*. Eds. C. Koch and I. Segev (Cambridge MA: The MIT Press), 251–291.

Rodzli, N., Lockhart-Cairns, M., Levy, C., Chipperfield, J., Bird, L., Baldock, C., et al. (2019). How the dual PDZ domain from Postsynaptic density protein 95 clusters ion channels and receptors. *bioRxiv*, 775726. doi: 10.1101/775726

Südhof, T. C. (2012). The presynaptic active zone. *Neuron* 75, 11–25. doi: 10.1016/j.neuron.2012.06.012

Sakmann, B., and Neher, E. (1984). Patch clamp techniques for studying ionic channels in excitable membranes. *Annu. Rev. Physiol.* 46, 455–472. doi: 10.1146/annurev.ph.46.030184.002323

Sarmiere, P. D., Weigle, C. M., and Tamkun, M. M. (2008). The Kv2.1 K+ channel targets to the axon initial segment of hippocampal and cortical neurons in culture and in situ. *BMC Neurosci.* 9, 112. doi: 10.1186/1471-2202-9-112

Scannevin, R. H., Murakoshi, H., Rhodes, K. J., and Trimmer, J. S. (1996). Identification of a cytoplasmic domain important in the polarized expression and clustering of the Kv2.1 K^+ channel. *J. Cell Biol.* 135, 1619–1632. doi: 10.1083/jcb.135.6.1619

Schaefer, N., Roemer, V., Janzen, D., and Villmann, C. (2018). Impaired glycine receptor trafficking in neurological diseases. *Front. Mol. Neurosci.* 11, 291. doi: 10.3389/fnmol.2018.00291

Scheefhals, N., and MacGillavry, H. D. (2018). Functional organization of postsynaptic glutamate receptors. *Mol. Cell. Neurosci.* 91, 82–94. doi: 10.1016/j.mcn.2018.05.002

Schermelleh, L., Ferrand, A., Huser, T., Eggeling, C., Sauer, M., Biehlmaier, O., et al. (2019). Super-resolution microscopy demystified. *Nat. Cell Biol.* 21, 72–84. doi: 10.1038/s41556-018-0251-8

Schwarz, T. L., Tempel, B. L., Papazian, D. M., Jan, Y. N., and Jan, L. Y. (1988). Multiple potassium-channel components are produced by alternative splicing at the Shaker locus in Drosophila. *Nature* 331, 137–142. doi: 10.1038/331137a0

Sieben, C., Douglass, K. M., Guichard, P., and Manley, S. (2018). Super-resolution microscopy to decipher multi-molecular assemblies. *Curr. Opin. Struct. Biol.* 49, 169–176. doi: 10.1016/j.sbi.2018.03.017

Singer, S. J., and Nicolson, G. L. (1972). The fluid mosaic model of the structure of cell membranes. *Science* 175, 720–731. doi: 10.1126/science.175.4023.720

Slater, C. R. (2017). The structure of human neuromuscular junctions: some unanswered molecular questions. *Int. J. Mol. Sci.* 18, 2183. doi: 10.3390/ijms18102183

St-Hilaire, M., and Longtin, A. (2004). Comparison of coding capabilities of Type I and Type II neurons. J. *Comput. Neurosci.* 16, 299–313. doi: 10.1023/B:JCNS.0000025690.02886.93

Sumino, A., Yamamoto, D., Iwamoto, M., Dewa, T., and Oiki, S. (2014). Gating-associated clustering–dispersion dynamics of the KcsA potassium channel in a lipid membrane. *J. Phys. Chem. Lett.* 5, 578–584. doi: 10.1021/jz402491t

Tang, A.-H., Chen, H., Li, T. P., Metzbower, S. R., MacGillavry, H. D., and Blanpied, T. A. (2016). A trans-synaptic nanocolumn aligns neurotransmitter release to receptors. *Nature* 536, 210–214. doi: 10.1038/nature19058

Tateno, T., and Robinson, H. P. C. (2006). Rate coding and spike-time variability in cortical neurons with two types of threshold dynamics. *J. Neurophysiol.* 95, 2650–2663. doi: 10.1152/jn.00683.2005

Tateno, T., and Robinson, H. P. C. (2007). Phase resetting curves and oscillatory stability in interneurons of rat somatosensory cortex. *Biophys. J.* 92, 683–695. doi: 10.1529/biophysj.106.088021

Tateno, T., Harsch, A., and Robinson, H. P. C. (2004). Threshold firing frequency-current relationships of neurons in rat somatosensory cortex: type 1 and type 2 dynamics. *J. Neurophysiol.* 92, 2283–2294. doi: 10.1152/jn.00109.2004

Tejedor, F. J., Bokhari, A., Rogero, O., Gorczyca, M., Zhang, J., Kim, E., et al. (1997). Essential role for dlg in synaptic clustering of Shaker K^+ channels *in vivo*. *J. Neurosci.* 17, 152–159. doi: 10.1523/JNEUROSCI.17-01-00152.1997

Tian, C., Wang, K., Ke, W., Guo, H., and Shu, Y. (2014). Molecular identity of axonal sodium channels in human cortical pyramidal cells. *Front. Cell Neurosci.* 8, 297. doi: 10.3389/fncel.2014.00297

Tiffany, A. M., Manganas, L. N., Kim, E., Hsueh, Y. P., Sheng, M., and Trimmer, J. S. (2000). PSD-95 and SAP97 exhibit distinct mechanisms for regulating K^+ channel

surface expression and clustering. *J. Cell Biol.* 148, 147–157. doi: 10.1083/jcb.148.1.147

Trimmer, J. S. (1991). Immunological identification and characterization of a delayed rectifier K^+ channel polypeptide in rat brain. *Proc. Natl. Acad. Sci. U. S. A.* 88, 10764–10768. doi: 10.1073/pnas.88.23.10764

Trimmer, J. S. (2015). Subcellular localization of K^+ channels in mammalian brain neurons: remarkable precision in the midst of extraordinary complexity. *Neuron* 85, 238–256. doi: 10.1016/j.neuron.2014.12.042

Uversky, V. N., and Dunker, A. K. (2010). Understanding protein non-folding. *Biochim. Biophys. Acta* 1804, 1231–1264. doi: 10.1016/j.bbapap.2010.01.017

Verpelli, C., Schmeisser, M. J., Sala, C., and Boeckers, T. M. (2012). Scaffold proteins at the postsynaptic density. *Adv. Exp. Med. Biol.* 970, 29–61. doi: 10.1007/978-3-7091-0932-8_2

Vivas, O., Moreno, C. M., Santana, L. F., and Hille, B. (2017). Proximal clustering between BK and CaV1.3 channels promotes functional coupling and BK channel activation at low voltage. *Elife* 6. doi: 10.7554/eLife.28029

Zandany, N., Lewin, L., Nirenberg, V., Orr, I., and Yifrach, O. (2015a). Entropic clocks in the service of electrical signaling: "Ball and chain"mechanisms for ion channel inactivation and clustering. *FEBS Lett.* 589, 2441–2447. doi: 10.1016/j.febslet.2015.06.010

Zandany, N., Marciano, S., Magidovich, E., Frimerman, T., Yehezkel, R., Shem-Ad, T., et al. (2015b). Alternative splicing modulates Kv channel clustering through a molecular ball and chain mechanism. *Nat. Commun.* 6, 6488. doi: 10.1038/ncomms7488

Zeberg, H., Blomberg, C., and Arhem, P. (2010). Ion channel density regulates switches between regular and fast spiking in soma but not in axons. *PloS Comput. Biol.* 6, e1000753. doi: 10.1371/journal.pcbi.1000753

Zeberg, H., Robinson, H. P. C., and Århem, P. (2015). Density of voltage-gated potassium channels is a bifurcation parameter in pyramidal neurons. *J. Neurophysiol.* 113, 537–549. doi: 10.1152/jn.00907.2013

Zhang, J., Carver, C. M., Choveau, F. S., and Shapiro, M. S. (2016). Clustering and functional coupling of diverse ion channels and signaling poteins revealed by super-resolution STORM microscopy in neurons. *Neuron* 92, 461–478. doi: 10.1016/j.neuron.2016.09.014

Zheng, C.-Y., Seabold, G. K., Horak, M., and Petralia, R. S. (2011). MAGUKs, Synaptic development, and synaptic plasticity. *Neuroscientist* 17, 493–512. doi: 10.1177/1073858410386384

Zhou, D., Lambert, S., Malen, P. L., Carpenter, S., Boland, L. M., and Bennett, V. (1998). AnkyrinG is required for clustering of voltage-gated Na channels at axon initial segments and for normal action potential firing. *J. Cell Biol.* 143, 1295–1304. doi: 10.1083/jcb.143.5.1295

Zimmermann, D., Zhou, A., Kiesel, M., Feldbauer, K., Terpitz, U., Haase, W., et al. (2008). Effects on capacitance by overexpression of membrane proteins. *Biochem. Bioph. Res. Commun.* 369, 1022–1026. doi: 10.1016/j.bbrc.2008.02.153

Conflict of Interest: The authors declare that the research was conducted in the absence of any commercial or financial relationships that could be construed as a potential conflict of interest.

frontiers in Pharmacology

MINI REVIEW
published: 19 February 2020
doi: 10.3389/fphar.2020.00070

Hydrogen-Deuterium Exchange Mass-Spectrometry of Secondary Active Transporters: From Structural Dynamics to Molecular Mechanisms

Moshe Giladi[1,2]* *and Daniel Khananshvili*[1]*

[1] Department of Physiology and Pharmacology, Sackler Faculty of Medicine, Tel Aviv University, Tel Aviv, Israel, [2] Tel Aviv Sourasky Medical Center, Tel Aviv University, Tel Aviv, Israel

OPEN ACCESS

Edited by:
Avi Priel,
Hebrew University of Jerusalem, Israel

Reviewed by:
Baruch Kanner,
Hebrew University of Jerusalem, Israel
Israel Sekler,
Ben-Gurion University of the Negev, Israel

***Correspondence:**
Moshe Giladi
moshegil@post.tau.ac.il
Daniel Khananshvili
dhanan@tauex.tau.ac.il

Specialty section:
This article was submitted to Pharmacology of Ion Channels and Channelopathies, a section of the journal Frontiers in Pharmacology

Received: 03 October 2019
Accepted: 24 January 2020
Published: 19 February 2020

Citation:
Giladi M and Khananshvili D (2020) Hydrogen-Deuterium Exchange Mass-Spectrometry of Secondary Active Transporters: From Structural Dynamics to Molecular Mechanisms. Front. Pharmacol. 11:70. doi: 10.3389/fphar.2020.00070

Membrane transporters allow the selective transport of otherwise poorly permeable solutes across the cell membrane and thus, play a key role in maintaining cellular homeostasis in all kingdoms of life. Importantly, these proteins also serve as important drug targets. Over the last decades, major progress in structural biology methods has elucidated important structure-function relationships in membrane transporters. However, structures obtained using methods such as X-ray crystallography and high-resolution cryogenic electron microscopy merely provide static snapshots of an intrinsically dynamic, multi-step transport process. Therefore, there is a growing need for developing new experimental approaches capable of exploiting the data obtained from the high-resolution snapshots in order to investigate the dynamic features of membrane proteins. Here, we present the basic principles of hydrogen-deuterium exchange mass-spectrometry (HDX-MS) and recent advancements in its use to study membrane transporters. In HDX-MS experiments, minute amounts of a protein sample can be used to investigate its structural dynamics under native conditions, without the need for chemical labelling and with practically no limit on the protein size. Thus, HDX-MS is instrumental for resolving the structure-dynamic landscapes of membrane proteins in their apo (ligand-free) and ligand-bound forms, shedding light on the molecular mechanism underlying the transport process and drug binding.

Keywords: mass spectrometry, hydrogen-deuterium exchanger, secondary transport, membrane proteins, structural dynamics

INTRODUCTION

Membrane proteins participate in fundamental physiological events in every biological system from bacteria to humans. >50% of marketed drugs target membrane proteins, whereas the pharmacological targeting of many other membrane proteins is considered potentially beneficial in numerous biomedical applications (Overington et al., 2006; Yıldırım et al., 2007; Arinaminpathy et al., 2009). However, the molecular mechanisms underlying their function and regulation remain largely unknown due to the lack of structural information. Indeed, while membrane proteins

account for ~26% of the human proteome, their structures represent only ~2% of the structures in the Protein Data Bank (Fagerberg et al., 2010; Pandey et al., 2016). Several obstacles hamper the structural investigation of membrane proteins, requiring the development of state-of-the-art technologies for elucidating their molecular architectures (Pandey et al., 2016; Masson et al., 2017; Hagn et al., 2018; Ravula and Ramamoorthy, 2019; Redhair et al., 2019). The major obstacles are that their overexpression and purification and structural studies by most techniques (e.g., X-ray crystallography) remain limited in many cases. These obstacle consequently hamper the rational development of drug candidates targeting disease-related membrane proteins (Vinothkumar and Henderson, 2010; Lounnas et al., 2013; Marciano et al., 2014).

Secondary transporters are membrane-bound proteins that selectively catalyze the movement of poorly permeable solutes (e.g., ions, neurotransmitters, drugs) across the cell membrane, supporting diverse cellular functions in health and disease. Secondary transporters comply with the alternating access paradigm, according to which the protein ligand-binding pocket becomes alternatively accessible at opposite sides of the membrane by adopting the inward-facing (IF) and outward-facing (OF) states in succession (Jardetzky, 1966; Forrest et al., 2011). Recent breakthroughs in the structural biology of membrane proteins provided a wealth of structures of membrane-bound transporters in different conformational states (Drew and Boudker, 2016; Bai et al., 2017), providing insights into their transport and solute recognition mechanisms. However, they provide static snapshots of an inherently multi-step process (Seeger, 2018). Thus, there is a growing need for developing new approaches to investigate membrane proteins dynamics (Konermann et al., 2011; Smith et al., 2012; Sim et al., 2017; Mandala et al., 2018; Burke, 2019). These include a combination of molecular dynamics (MD) simulations (Roux et al., 2011; Zdravkovic et al., 2012; Zhekova et al., 2016; Zhekova et al., 2017; Harpole and Delemotte, 2018) with advanced experimental techniques, including spectroscopic techniques and single-particle cryogenic electron microscopy (Smith et al., 2012; Pandey et al., 2016; Castell et al., 2018; Hagn et al., 2018; Ravula and Ramamoorthy, 2019; Sun and Gennis, 2019).

Hydrogen-deuterium exchange mass-spectrometry (HDX-MS) gained attention in recent years for studying membrane proteins dynamics, even though it has been used for decades to characterize soluble proteins (Konermann et al., 2011; Vadas et al., 2017). HDX-MS monitors time-dependent exchange of solvent D_2O with proteins backbone amide hydrogens under native conditions. The deuterium exchange rate depends on the solvent accessibility, secondary structure, and structural rigidity (Konermann et al., 2011). Coupled with proteolytic digestion and peptide separation, HDX-MS allows the quantification of exchange rates in short protein segments, up to single-residue resolution. Two major advantages of HDX-MS are that small protein amounts (< 0.1 mg) are required for analysis and that chemical protein labeling is not required, avoiding unwanted structural perturbations. Here, we summarize recent advancements and applications in the use of HDX-MS for studying the structural dynamics of transporters.

HYDROGEN-DEUTERIUM EXCHANGE MASS-SPECTROMETRY PRINCIPLES

HDX-MS principles are briefly and qualitatively described below, to allow a discussion of its applications for studying transporters. For in-depth explanations, several excellent review articles are available (Konermann et al., 2011; Rand et al., 2014; Engen and Wales, 2015; Masson et al., 2017; Oganesyan et al., 2018; Masson et al., 2019; Redhair et al., 2019).

In HDX experiments, deuterium exchanges with labile protein hydrogens in a time-dependent manner following protein dilution in a D_2O buffer (Masson et al., 2017) (**Figure 1**). HDX-MS monitors mainly the exchange of backbone amide hydrogens since *i*) at neutral pH they are exchanged in rates that can be detected using HDX-MS (seconds to days) and *ii*) their exchange can be effectively quenched (Marcsisin and Engen, 2010; Gallagher and Hudgens,

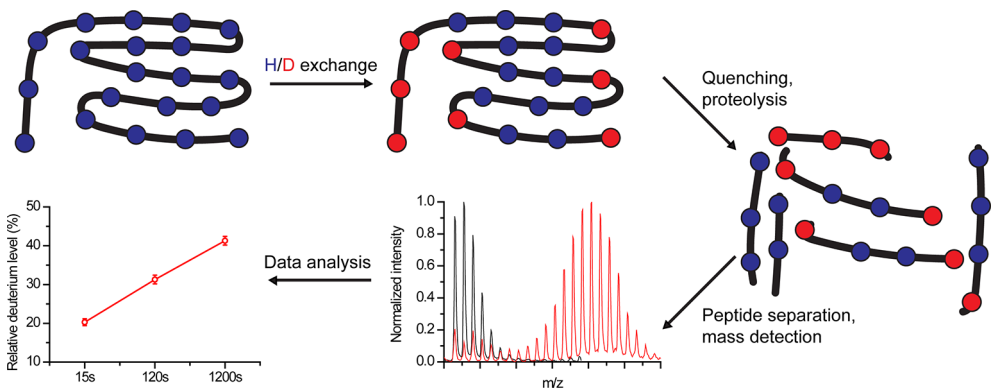

FIGURE 1 | Schematic overview of hydrogen-deuterium exchange mass-spectrometry (HDX-MS) workflow. Proteins are labeled in D_2O buffer for a predefined time, followed by exchange quenching and proteolysis. The peptides are separated, and their mass is detected using MS. Finally, the amount of incorporated deuterium within each peptide is calculated for each time point.

2016). The HDX rate depends on several parameters. Amide hydrogens can exhibit a "closed state," stemming from participation in stable hydrogen bonds in secondary structures or from solvent inaccessibility, which does not allow their exchange with solvent deuterium, or an "open state" where proton abstraction, the rate-limiting step of HDX, can occur (Oganesyan et al., 2018). In addition, the reaction has an intrinsic chemical rate constant, which depends on the pH, temperature, and the residue environment (Oganesyan et al., 2018).

The transition between the closed and open states occurs by local unfolding events. Under native conditions, in which proteins are well folded, the HDX rate mainly depends on the rate of transition back to the closed state (Weis et al., 2006). If the unfolded protein region returns to the closed state at a rate much slower than the chemical exchange rate, EX1 kinetics are observed, resulting in correlated deuterium uptake in neighboring residues. This results in two populations: one with low *m/z* and one with a high *m/z*, reflecting peptides from protein molecules that have not and that have undergone exchange, respectively. With time, the high *m/z* population becomes more prominent at the expense of the low *m/z* population. EX1 kinetics are considered rare in folded proteins under native conditions, but can be induced, for example, by the addition of denaturants (Weis et al., 2006; Oganesyan et al., 2018). If the protein returns to the closed state at a rate much faster than the chemical exchange rate, EX2 kinetics are observed. Here, the exchange depends on the transition of individual residues between the open and closed state, occurring in an uncorrelated fashion. Thus, with time, a single population with gradually increasing *m/z* values is observed (Weis et al., 2006).

Following deuteration, the reaction is quenched at pre-defined time points by changing the pH from neutral (7) to pH_{min} (2.5–3), resulting in ~10,000-fold reduction in HDX (Konermann et al., 2011; Masson et al., 2017; Oganesyan et al., 2018); and by reducing the temperature from 25 to 0°C, leading to ~14-fold decrease in HDX (Englander, 2006; Oganesyan et al., 2018). Next, the protein is digested using a protease and the peptides are separated using analytic reverse-phase chromatography. Currently, the major technical bottleneck of HDX-MS experiments lies in obtaining a high sequence coverage, which is limited by the resistance to digestive enzymes and by proteolytic conditions. Finally, eluted peptides are identified using MS and the degree of HDX is calculated based on the obtained *m/z* values. The experimental details and pitfalls of protein digestion, peptide separation, and MS identification are beyond the scope of this review (Konermann et al., 2011; Masson et al., 2017; Masson et al., 2019).

HYDROGEN-DEUTERIUM EXCHANGE MASS-SPECTROMETRY STUDIES OF MEMBRANE PROTEINS

Despite sharing the alternating access paradigm, ligand-induced conformational changes differ among transporters due to differences in ligand-protein interactions. For example, symporters (co-transporting two or more ligands) can transition between the IF and OF states without bound ligands, whereas ligand binding is obligatory for swapping between the IF and OF states in antiporters (exchanging ligands at opposite sides of the membrane) (Forrest et al., 2011; Drew and Boudker, 2016; Bai et al., 2017).

In general, detecting local ligand-induced dynamic changes in proteins is difficult. For example, the crystal structures of membrane proteins in both the ligand-free and ligand-bound forms are frequently unavailable, precluding the detection of ligand-induced conformational changes even for proteins with known structures. Moreover, high-resolution structural snapshots of the apo and ligand-bound states may not resolve significant conformational differences. However, small ligand-induced conformational changes can be detected using HDX-MS at specific protein subdomains under native conditions by measuring the differential deuterium uptake (ΔHDX) in the presence and absence of ligands. This ability of HDX-MS provides unique opportunities for addressing the most challenging issues in elucidating the mechanisms of ligand-protein and protein-protein interactions (Rand et al., 2014; Masson et al., 2019; Redhair et al., 2019), as reviewed here for a number of recently studied transporter proteins.

Conformational Transitions Underlying Alternating Access: The Na^+/H^+ Antiporter

Nha proteins regulate cellular pH, $[Na^+]$, and volume throughout the kingdoms of life (Padan and Landau, 2016). The main structural model used to study Nha orthologs is *Escherichia coli* NhaA, for which a crystallographic structure of the inactive state at acidic pH is available (Hunte et al., 2005). To study the structural dynamics of NhaA under physiological pH, HDX-MS was recently used (Eisinger et al., 2017). Crucial to the insights obtained in this study, HDX-MS provides global dynamic data, in contrast to methods based on site-specific labeling, which only detect movements of pre-defined protein regions.

In this study, an exceptionally high sequence coverage of 88.5% was obtained for NhaA in detergent, providing insights into the mechanism underlying alternating access upon ligand binding. By comparing the HDX patterns between apo- and substrate-bound Nha, a recurring pattern of HDX change was observed in several helices, where increased deuterium uptake in one terminus was accompanied by decreased deuterium uptake at the other terminus. The uptake at the middle of the helices was largely unchanged.

Based on the observed pattern of HDX change, although not directly providing spatial information, it was suggested that translation of the transmembrane helices relative to the membrane occurs, as reflected in the reciprocal HDX changes observed for the two termini within specific transmembrane helices. This model is consistent with the "elevator-like" mechanism of alternating access, implying a vertical translation of transmembrane helices during the transport cycle (Ryan and Vandenberg, 2016). In summary, HDX-MS provided novel insights into the structural transitions involved in alternating access, unattainable by the previously resolved structures of the inactive NhaA.

Effect of Protein-Lipid Interactions on Transporters' Conformation Landscapes

Most secondary transporters belong to the major facilitator superfamily (MFS), sharing a conserved architecture despite their diverse functions (Radestock and Forrest, 2011). Although the crystal structures of MFS members are available, they provided little information on protein-lipid interactions and their effect on the equilibrium between the OF and IF states. Thus, Martens et al. combined MD simulations with HDX-MS to study the effects of the lipid environment on three well-characterized transporters: lactose permease, xylose transporter, and glycerol-3-phosphate antiporter (Martens et al., 2018).

First, a mutation known to shift the equilibrium toward the OF-state was introduced at the extracellular vestibule of all transporters (Kumar et al., 2014). Comparing the WT and mutated transporters using HDX-MS revealed that the method detects the conformational change, with regions on the extracellular vestibule taking up more deuterium in the mutants *vs.* the WT, whereas the opposite occurs for residues at the intracellular vestibule. Next, the transporters were reconstituted into nanodisks composed of phosphatidylglycerol, tetraoleyl cardiolipin, and either phosphatidylcholine or phosphatidylethanolamine. Interestingly, the presence of phosphatidylethanolamine shifted the equilibrium toward the IF state. Subsequently, MD simulations of the transporters in lipid bilayers identical to the nanodisks' composition predicted direct interactions between the charged phosphatidylethanolamine headgroup and a conserved cytoplasmic network of charged residues, stabilizing the OF state (Doki et al., 2013). Mutating the charged residues abolished the effect of phosphatidylethanolamine, strongly suggesting that specific phosphatidylethanolamine-protein interactions control the intrinsic equilibrium of the transporters. This study is a stark example of combining experimental and computational methods in order to identify subtle but functionally significant protein-lipid interactions.

Helix Unwinding During Transport: Studies of LeuT

LeuT is a prokaryotic homolog of the neurotransmitter/Na^+ symporters (NSS) family, which includes important drug targets such as the serotonin, dopamine, and norepinephrine transporters (Kristensen et al., 2011). LeuT was extensively studied, and its crystallographic structures along the transport cycle are available (Focke et al., 2013). These structures suggested that large-scale structural rearrangements are required during alternating access (Krishnamurthy and Gouaux, 2012). However, the conformational landscape allowing the transition between the IF and OF states remains elusive and controversial.

To study the transition between different states, detergent-solubilized LeuT was investigated under conditions that favor the IF or OF states (Merkle et al., 2018). Surprisingly, many peptides, mainly at the intracellular side of the transporter, exhibited EX1 kinetics. This is rather unusual in folded proteins under native conditions and considered to reflect a long-lived unfolding of secondary structure elements. Based on the spatial distribution of peptides exhibiting EX1 kinetics, along with the available crystallographic structures, it was proposed that specific helices undergo partial unwinding during alternating access and that these conformational changes also contribute to substrate release. This study highlights the functional importance of slow (seconds time scale) conformational changes that can be well resolved using HDX-MS, in contrast to other experimental or computational (e.g., MD) methods.

Hydrogen-Deuterium Exchange Mass-Spectrometry of Membrane Proteins in Lipid Nanodisks

The interactions of membrane proteins with surrounding lipids can dramatically modulate their function (Vadas et al., 2017). Indeed, the activity of eukaryotic NSS members significantly depends on specific lipid-protein interactions that modulate the protein dynamics and consequently, substrate interactions (Divito and Amara, 2009). Therefore, Adhikary et al. studied LeuT reconstituted into phospholipid bilayer nanodisks (Adhikary et al., 2017). Using this approach, LeuT was investigated under conditions that favor the IF and OF conformations. Comparison of the HDX patterns between these states revealed specific alterations in regions previously implicated in the transport cycle, reflecting functionally significant structural changes. Interestingly, the HDX-MS data, consistent with previous biophysical and computational studies, supported a smaller tilt angle for the first transmembrane helix in the IF conformation compared to that observed in the crystal structures. This difference was attributed to the lipid environment, since the crystal structure was obtained in detergent with minute amount of lipid. To summarize, HDX-MS provides a flexible platform to study membrane proteins in different hydrophobic environments and under conditions that favor specific conformational states, without the need for site-specific labeling.

Ion Interactions With Multiple Sites: The Na^+/Ca^{2+} Exchanger

NCX participates in cellular Ca^{2+} homeostasis by extruding Ca^{2+} from the cells against its electrochemical gradient (Blaustein and Lederer, 1999). NCX exchanges $3Na^+$:$1Ca^{2+}$, where Na^+ and Ca^{2+} are transported in separate steps (Khananshvili, 1990). Surprisingly, the crystal structure of NCX from *Methanocaldococcus jannaschii* (NCX_Mj) revealed four ion binding sites, simultaneously occupied by three Na^+ ions at sites termed S_{int}, S_{mid}, S_{ext}, and one Ca^{2+} ion at a site termed S_{Ca} (Liao et al., 2012). Since this binding mode was inconsistent with previous studies, MD simulations and ion flux analyses of mutants were performed, suggesting that Na^+ ions occupy S_{int}, S_{Ca}, and S_{ext}, whereas Ca^{2+} occupies S_{Ca} (Marinelli et al., 2014; Giladi et al., 2016b; Giladi et al., 2017; van Dijk et al., 2018). Thus, the Na^+ and Ca^{2+} ions are bound in a mutually exclusive manner along the transport cycle.

To experimentally establish the assignment of ion binding sites, we compared the apo-state with the ion-bound states of NCX_Mj using HDX-MS (Giladi et al., 2016a; Giladi et al., 2017). Despite low sequence coverage, our analysis included 10 out of 12 ion-coordinating residues. We detected a Na^+-dependent

decrease in deuterium uptake at S_{int}, S_{Ca}, and S_{ext}, but not S_{mid}, whereas in the presence of Ca^{2+} the decrease in deuterium uptake was mainly observed at S_{Ca}. This is consistent with the predictions made by the MD simulations and mutational analyses foreseeing the occupation of S_{mid} by a water molecule but not by Na^+ or Ca^{2+} in the ground state (Marinelli et al., 2014; Giladi et al., 2016a; Giladi et al., 2017; van Dijk et al., 2018). Notably, subsequent crystallographic studies have validated our binding sites' assignment (Liao et al., 2016). Thus, HDX-MS corroborated the ion binding mode suggested by the computational and functional studies.

Ion Selectivity of a Li^+-Transporting NCX Mutant

The mitochondrial Na^+/Ca^{2+} exchanger (NCLX) exhibits exceptional ion selectivity, exchanging Ca^{2+} with either Na^+ or Li^+, whereas NCXs do not transport Li^+ (Palty et al., 2010). Although the physiological relevance of this ion selectivity remains puzzling, it is notable that 9 (out of 12) ion-coordinating residues in NCLX differ from those in NCXs and other members of the Ca^{2+}/cation antiporter superfamily. To understand how these differences affect the ion binding recognition and transport, we performed structure-based replacement of ion-coordinating residues in NCX_Mj to imitate the NCLX binding sites (Refaeli et al., 2016). Strikingly, the newly designed construct (termed NCLX_Mj) mediates Na^+/Ca^{2+} and Li^+/Ca^{2+} with comparable K_m values (Refaeli et al., 2016).

Next, we sought to determine whether the ion binding sites in NCLX_Mj are reminiscent of those of NCX_Mj (Giladi et al., 2019). HDX-MS analyses of ion-induced conformational changes revealed that S_{Ca} binds Na^+, Li^+, or Ca^{2+}, whereas one or more additional Na^+/Li^+ sites of NCLX_Mj are incompatible with the original Na^+ sites (S_{ext} and S_{int}) assigned to NCX_Mj. These results suggested that NCLX_Mj may transport ions with an electroneutral stoichiometry of $2Na^+:1Ca^{2+}$ or $2Li^+:1Ca^{2+}$. Consistent with the HDX-MS data, voltage clamping accelerates the Na^+/Ca^{2+} exchange rates in NCX_Mj-reconstituted proteoliposomes (due to a stoichiometry of $3Na^+:1Ca^{2+}$), whereas it has no appreciable effect on the Na^+/Ca^{2+} or Li^+/Ca^{2+} exchange rates in NCLX_Mj (Giladi et al., 2019).

Our studies have demonstrated the utility of HDX-MS in identifying and validating binding sites in ion transporters, where relatively small differences in the ion-induced ΔHDX signals provide important information on ion selectivity and conformational changes occurring upon ion binding at distinct sites. Thus, combined with MD simulations and X-ray crystallography, HDX-MS is especially appealing for elucidating the structural determinants of ion selectivity and ion-induced conformational changes in ion transport systems comprising multiple ion binding sites.

CONCLUSIONS

Over the past decades, structural biology has enormously contributed to our understanding of membrane protein function, mainly by providing static snapshots of discrete states in high resolution. To fully decipher the structure-function relationships underlying the complex process of solute transport, a growing number of experimental and computational methods have been developed to bridge the gap between these static snapshots and determine the underlying conformational landscapes. HDX-MS is increasingly used to study intact membrane proteins under various near-native conditions, providing novel opportunities to study membrane-protein interactions, substrate recognition, and transport-related conformational transitions. Future developments in instrumentation and data analysis automation may allow the use of HDX-MS in high-throughput, fully exploiting its potential use in basic research and biomedical applications such as drug design.

AUTHOR CONTRIBUTIONS

MG and DK reviewed the literature and wrote the manuscript.

FUNDING

This work was supported by the Israel Science Foundation (Grant #1351/18) (D.K) and by the Israel Cancer Research Foundation (Grant #19202) (MG). Financial support from the Shmuel Shalit award to DK is gratefully acknowledged.

REFERENCES

Adhikary, S., Deredge, D. J., Nagarajan, A., Forrest, L. R., Wintrode, P. L., and Singh, S. K. (2017). Conformational dynamics of a neurotransmitter: Sodium symporter in a lipid bilayer. *Proc. Natl. Acad. Sci. U. S. A.* 114, E1786–E1795. doi: 10.1073/pnas.1613293114

Arinaminpathy, Y., Khurana, E., Engelman, D. M., and Gerstein, M. B. (2009). Computational analysis of membrane proteins: the largest class of drug targets. *Drug Discovery Today* 14, 1130–1135. doi: 10.1016/j.drudis.2009.08.006

Bai, X., Moraes, T. F., and Reithmeier, R. A. F. (2017). Structural biology of solute carrier (SLC) membrane transport proteins. *Mol. Membr. Biol.* 34, 1–32. doi: 10.1080/09687688.2018.1448123

Blaustein, M. P., and Lederer, W. J. (1999). Sodium/calcium exchange: its physiological implications. *Physiol. Rev.* 79, 763–854. doi: 10.1152/physrev.1999.79.3.763

Burke, J. E. (2019). Dynamic structural biology at the protein membrane interface. *J. Biol. Chem.* 294, 3872–3880. doi: 10.1074/jbc.AW118.003236

Castell, O. K., Dijkman, P. M., Wiseman, D. N., and Goddard, A. D. (2018). Single molecule fluorescence for membrane proteins. *Methods* 147, 221–228. doi: 10.1016/j.ymeth.2018.05.024

Divito, C. B., and Amara, S. G. (2009). Close encounters of the oily kind: regulation of transporters by lipids. *Mol. Interv.* 9, 252–262. doi: 10.1124/mi.9.5.8

Doki, S., Kato, H. E., Solcan, N., Iwaki, M., Koyama, M., Hattori, M., et al. (2013). Structural basis for dynamic mechanism of proton-coupled symport by the

peptide transporter POT. *Proc. Natl. Acad. Sci. U. S. A.* 110, 11343–11348. doi: 10.1073/pnas.1301079110

Drew, D., and Boudker, O. (2016). Shared molecular mechanisms of membrane transporters. *Annu. Rev. Biochem.* 85, 543–572. doi: 10.1146/annurev-biochem-060815-014520

Eisinger, M. L., Dörrbaum, A. R., Michel, H., Padan, E., and Langer, J. D. (2017). Ligand-induced conformational dynamics of the Escherichia coli Na+/H+ antiporter NhaA revealed by hydrogen/deuterium exchange mass spectrometry. *Proc. Natl. Acad. Sci. U. S. A.* 114, 11691–11696. doi: 10.1073/pnas.1703422114

Engen, J. R., and Wales, T. E. (2015). Analytical aspects of hydrogen exchange mass spectrometry. *Annu. Rev. Anal. Chem.* 8, 127–148. doi: 10.1146/annurev-anchem-062011-143113

Englander, S. W. (2006). Hydrogen exchange and mass spectrometry: a historical perspective. *J. Am. Soc Mass Spectrom.* 17, 1481–1489. doi: 10.1016/j.jasms.2006.06.006

Fagerberg, L., Jonasson, K., Von Heijne, G., Uhlén, M., and Berglund, L. (2010). Prediction of the human membrane proteome. *Proteomics* 10, 1141–1149. doi: 10.1002/pmic.200900258

Focke, P. J., Wang, X., and Larsson, H. P. (2013). Neurotransmitter transporters: structure meets function. *Structure* 21, 694–705. doi: 10.1016/j.str.2013.03.002

Forrest, L. R., Krämer, R., and Ziegler, C. (2011). The structural basis of secondary active transport mechanisms. *Biochim. Biophys. Acta - Bioenerg.* 1807, 167–188. doi: 10.1016/j.bbabio.2010.10.014

Gallagher, E. S., and Hudgens, J. W. (2016). "Mapping Protein-Ligand Interactions with Proteolytic Fragmentation, Hydrogen/Deuterium Exchange-Mass Spectrometry," in *Methods in Enzymology* (Netherlands: Elsevier), 357–404. doi: 10.1016/bs.mie.2015.08.010

Giladi, M., Almagor, L., Van Dijk, L., Hiller, R., Man, P., Forest, E., et al. (2016a). Asymmetric preorganization of inverted pair residues in the sodium-calcium exchanger. *Sci. Rep.* 6, 20753. doi: 10.1038/srep20753

Giladi, M., Shor, R., Lisnyansky, M., and Khananshvili, D. (2016b). Structure-functional basis of ion transport in sodium–calcium exchanger (NCX) proteins. *Int. J. Mol. Sci.* 17, 1949. doi: 10.3390/ijms17111949

Giladi, M., Van Dijk, L., Refaeli, B., Almagor, L., Hiller, R., Man, P., et al. (2017). Dynamic distinctions in the Na^+/Ca^{2+}exchanger adopting the inward- and outward-facing conformational states. *J. Biol. Chem.* 292, 12311–12323. doi: 10.1074/jbc.M117.787168

Giladi, M., Lee, S. Y., Refaeli, B., Hiller, R., Chung, K. Y., and Khananshvili, D. (2019). Structure-dynamic and functional relationships in a Li+-transporting sodium–calcium exchanger mutant. *Biochim. Biophys. Acta - Bioenerg.* 1860, 189–200. doi: 10.1016/j.bbabio.2018.11.015

Hagn, F., Nasr, M. L., and Wagner, G. (2018). Assembly of phospholipid nanodiscs of controlled size for structural studies of membrane proteins by NMR. *Nat. Protoc.* 13, 79–98. doi: 10.1038/nprot.2017.094

Harpole, T. J., and Delemotte, L. (2018). Conformational landscapes of membrane proteins delineated by enhanced sampling molecular dynamics simulations. *Biochim. Biophys. Acta - Biomembr.* 1860, 909–926. doi: 10.1016/j.bbamem.2017.10.033

Hunte, C., Screpanti, E., Venturi, M., Rimon, A., Padan, E., and Michel, H. (2005). Structure of a Na+/H+ antiporter and insights into mechanism of action and regulation by pH. *Nature* 435, 1197–1202. doi: 10.1038/nature03692

Jardetzky, O. (1966). Simple allosteric model for membrane pumps [27]. *Nature* 211, 969–970. doi: 10.1038/211969a0

Khananshvili, D. (1990). Distinction between the two basic mechanisms of cation transport in the cardiac Na+-Ca2+ exchange system. *Biochemistry* 29, 2437–2442. doi: 10.1021/bi00462a001

Konermann, L., Pan, J., and Liu, Y. H. (2011). Hydrogen exchange mass spectrometry for studying protein structure and dynamics. *Chem. Soc Rev.* 40, 1224–1234. doi: 10.1039/c0cs00113a

Krishnamurthy, H., and Gouaux, E. (2012). X-ray structures of LeuT in substrate-free outward-open and apo inward-open states. *Nature* 481, 469–474. doi: 10.1038/nature10737

Kristensen, A. S., Andersen, J., Jorgensen, T. N., Sorensen, L., Eriksen, J., Loland, C. J., et al. (2011). SLC6 neurotransmitter transporters: Structure, function, and regulation. *Pharmacol. Rev.* 63, 585–640. doi: 10.1124/pr.108.000869

Kumar, H., Kasho, V., Smirnova, I., Finer-Moore, J. S., Kaback, H. R., and Stroud, R. M. (2014). Structure of sugar-bound LacY. *Proc. Natl. Acad. Sci. U. S. A.* 111, 1784–1788. doi: 10.1073/pnas.1324141111

Liao, J., Li, H., Zeng, W., Sauer, D. B., Belmares, R., and Jiang, Y. (2012). Structural insight into the ion-exchange mechanism of the sodium/calcium exchanger. *Sci. (80-.)* 335, 686–690. doi: 10.1126/science.1215759

Liao, J., Marinelli, F., Lee, C., Huang, Y., Faraldo-Gómez, J. D., and Jiang, Y. (2016). Mechanism of extracellular ion exchange and binding-site occlusion in a sodium/calcium exchanger. *Nat. Struct. Mol. Biol.* 23, 590–599. doi: 10.1038/nsmb.3230

Lounnas, V., Ritschel, T., Kelder, J., McGuire, R., Bywater, R. P., and Foloppe, N. (2013). Current progress in structure-based rational drug design marks a new mindset in drug discovery. *Comput. Struct. Biotechnol. J.* 5, e201302011. doi: 10.5936/csbj.201302011

Mandala, V. S., Williams, J. K., and Hong, M. (2018). Structure and dynamics of membrane proteins from solid-state NMR. *Annu. Rev. Biophys.* 47, 201–222. doi: 10.1146/annurev-biophys-070816-033712

Marciano, D. P., Dharmarajan, V., and Griffin, P. R. (2014). HDX-MS guided drug discovery: Small molecules and biopharmaceuticals. *Curr. Opin. Struct. Biol.* 28, 105–111. doi: 10.1016/j.sbi.2014.08.007

Marcsisin, S. R., and Engen, J. R. (2010). Hydrogen exchange mass spectrometry: what is it and what can it tell us? *Anal. Bioanal. Chem.* 397, 967–972. doi: 10.1007/s00216-010-3556-4

Marinelli, F., Almagor, L., Hiller, R., Giladi, M., Khananshvili, D., and Faraldo-Gómez, J. D. (2014). Sodium recognition by the Na^+/Ca^{2+} exchanger in the outward-facing conformation. *Proc. Natl. Acad. Sci.* 111, E5354–E5362. doi: 10.1073/pnas.1415751111

Martens, C., Shekhar, M., Borysik, A. J., Lau, A. M., Reading, E., Tajkhorshid, E., et al. (2018). Direct protein-lipid interactions shape the conformational landscape of secondary transporters. *Nat. Commun.* 9, 4151. doi: 10.1038/s41467-018-06704-1

Masson, G. R., Jenkins, M. L., and Burke, J. E. (2017). An overview of hydrogen deuterium exchange mass spectrometry (HDX-MS) in drug discovery. *Expert Opin. Drug Discovery* 12, 981–994. doi: 10.1080/17460441.2017.1363734

Masson, G. R., Burke, J. E., Ahn, N. G., Anand, G. S., Borchers, C., Brier, S., et al. (2019). Recommendations for performing, interpreting and reporting hydrogen deuterium exchange mass spectrometry (HDX-MS) experiments. *Nat. Methods* 16, 595–602. doi: 10.1038/s41592-019-0459-y

Merkle, P. S., Gotfryd, K., Cuendet, M. A., Leth-Espensen, K. Z., Gether, U., Loland, C. J., et al. (2018). Substrate-modulated unwinding of transmembrane helices in the NSS transporter LeuT. *Sci. Adv.* 4, eaar6179. doi: 10.1126/sciadv.aar6179

Oganesyan, I., Lento, C., and Wilson, D. J. (2018). Contemporary hydrogen deuterium exchange mass spectrometry. *Methods* 144, 27–42. doi: 10.1016/j.ymeth.2018.04.023

Overington, J. P., Al-Lazikani, B., and Hopkins, A. L. (2006). How many drug targets are there? *Nat. Rev. Drug Discovery* 5, 993–996. doi: 10.1038/nrd2199

Padan, E., and Landau, M. (2016). "Sodium-Proton (Na+/H+) Antiporters: Properties and Roles in Health and Disease," in *Metal Ions in Life Sciences* (Germany: Springer), 391–458. doi: 10.1007/978-3-319-21756-7-12

Palty, R., Silverman, W. F., Hershfinkel, M., Caporale, T., Sensi, S. L., Parnis, J., et al. (2010). NCLX is an essential component of mitochondrial Na+/Ca 2+ exchange. *Proc. Natl. Acad. Sci. U. S. A.* 107, 436–441. doi: 10.1073/pnas.0908099107

Pandey, A., Shin, K., Patterson, R. E., Liu, X. Q., and Rainey, J. K. (2016). Current strategies for protein production and purification enabling membrane protein structural biology1. *Biochem. Cell Biol.* 94, 507–527. doi: 10.1139/bcb-2015-0143

Radestock, S., and Forrest, L. R. (2011). The alternating-access mechanism of MFS transporters arises from inverted-topology repeats. *J. Mol. Biol.* 407, 698–715. doi: 10.1016/j.jmb.2011.02.008

Rand, K. D., Zehl, M., and Jørgensen, T. J. D. (2014). Measuring the hydrogen/deuterium exchange of proteins at high spatial resolution by mass spectrometry: overcoming gas-phase hydrogen/deuterium scrambling. *Acc. Chem. Res.* 47, 3018–3027. doi: 10.1021/ar500194w

Ravula, T., and Ramamoorthy, A. (2019). Magnetic-alignment of polymer macro-nanodiscs enables residual dipolar couplings based high-resolution structural

studies by NMR. *Angew. Chemie Int. Ed.* 58, 14925–14928. doi: 10.1002/anie.201907655

Redhair, M., Clouser, A. F., and Atkins, W. M. (2019). Hydrogen-deuterium exchange mass spectrometry of membrane proteins in lipid nanodiscs. *Chem. Phys. Lipids* 220, 14–22. doi: 10.1016/j.chemphyslip.2019.02.007

Refaeli, B., Giladi, M., Hiller, R., and Khananshvili, D. (2016). Structure-based engineering of lithium-transport capacity in an archaeal sodium-calcium exchanger. *Biochemistry* 55, 1673–1676. doi: 10.1021/acs.biochem.6b00119

Roux, B., Bernèche, S., Egwolf, B., Lev, B., Noskov, S. Y., Rowley, C. N., et al. (2011). Ion selectivity in channels and transporters. *J. Gen. Physiol.* 137, 415–426. doi: 10.1085/jgp.201010577

Ryan, R. M., and Vandenberg, R. J. (2016). Elevating the alternating-access model. *Nat. Struct. Mol. Biol.* 23, 187–189. doi: 10.1038/nsmb.3179

Seeger, M. A. (2018). Membrane transporter research in times of countless structures. *Biochim. Biophys. Acta - Biomembr.* 1860, 804–808. doi: 10.1016/j.bbamem.2017.08.009

Sim, D. W., Lu, Z., Won, H. S., Lee, S. N., Seo, M. D., Lee, B. J., et al. (2017). Application of solution NMR to structural studies on α-helical integral membrane proteins. *Molecules* 22, 1347. doi: 10.3390/molecules22081347

Smith, R. D., Engdahl, A. L., Dunbar, J. B., and Carlson, H. A. (2012). Biophysical limits of protein-ligand binding. *J. Chem. Inf. Model.* 52, 2098–2106. doi: 10.1021/ci200612f

Sun, C., and Gennis, R. B. (2019). Single-particle cryo-EM studies of transmembrane proteins in SMA copolymer nanodiscs. *Chem. Phys. Lipids.* 221, 114–119. doi: 10.1016/j.chemphyslip.2019.03.007

Vadas, O., Jenkins, M. L., Dornan, G. L., and Burke, J. E. (2017). "Using Hydrogen–Deuterium Exchange Mass Spectrometry to Examine Protein–Membrane Interactions," in *Methods in Enzymology* (Netherlands: Elsevier), 143–172. doi: 10.1016/bs.mie.2016.09.008

van Dijk, L., Giladi, M., Refaeli, B., Hiller, R., Cheng, M. H., Bahar, I., et al. (2018). Key residues controlling bidirectional ion movements in Na+/Ca2+ exchanger. *Cell Calcium* 76, 10–22. doi: 10.1016/j.ceca.2018.09.004

Vinothkumar, K. R., and Henderson, R. (2010). Structures of membrane proteins. *Q. Rev. Biophys.* 43, 65–158. doi: 10.1017/S0033583510000041

Weis, D. D., Wales, T. E., Engen, J. R., Hotchko, M., and Ten Eyck, L. F. (2006). Identification and characterization of EX1 kinetics in H/D exchange mass spectrometry by peak width analysis. *J. Am. Soc Mass Spectrom.* 17, 1498–1509. doi: 10.1016/j.jasms.2006.05.014

Yıldırım, M. A., Goh, K. I., Cusick, M. E., Barabási, A. L., and Vidal, M. (2007). Drug—target network. *Nat. Biotechnol.* 25, 1119–1126. doi: 10.1038/nbt1338

Zdravkovic, I., Zhao, C., Lev, B., Cuervo, J. E., and Noskov, S. Y. (2012). Atomistic models of ion and solute transport by the sodium-dependent secondary active transporters. *Biochim. Biophys. Acta - Biomembr.* 1818, 337–347. doi: 10.1016/j.bbamem.2011.10.031

Zhekova, H., Zhao, C., Schnetkamp, P. P. M., and Noskov, S. Y. (2016). Characterization of the cation binding sites in the NCKX2 Na +/Ca 2+ -K + exchanger. *Biochemistry* 55, 6445–6455. doi: 10.1021/acs.biochem.6b00591

Zhekova, H. R., Ngo, V., da Silva, M. C., Salahub, D., and Noskov, S. (2017). Selective ion binding and transport by membrane proteins – A computational perspective. *Coord. Chem. Rev.* 345, 108–136. doi: 10.1016/j.ccr.2017.03.019

Conflict of Interest: The authors declare that the research was conducted in the absence of any commercial or financial relationships that could be construed as a potential conflict of interest.

frontiers in Pharmacology

ORIGINAL RESEARCH
published: 07 April 2020
doi: 10.3389/fphar.2020.00405

Novel Human Polymorphisms Define a Key Role for the SLC26A6-STAS Domain in Protection From Ca^{2+}-Oxalate Lithogenesis

Liana Shimshilashvili[1], *Sara Aharon*[1], *Orson W. Moe*[2,3,4] *and Ehud Ohana*[1]*

[1] Department of Clinical Biochemistry and Pharmacology, Faculty of Health Sciences, Ben-Gurion University of the Negev, Beer-Sheva, Israel, [2] Department of Internal Medicine, University of Texas Southwestern Medical Center, Dallas, TX, United States, [3] Charles and Jane Pak Center of Mineral Metabolism and Clinical Research, University of Texas Southwestern Medical Center, Dallas, TX, United States, [4] Department of Physiology, University of Texas Southwestern Medical Center, Dallas, TX, United States

OPEN ACCESS

Edited by:
Avi Priel,
Hebrew University of Jerusalem, Israel

Reviewed by:
Daniel Khananshvili,
Tel Aviv University, Israel
Yoni Haitin,
Tel Aviv University, Israel

***Correspondence:**
Ehud Ohana
ohanaeh@bgu.ac.il

Specialty section:
This article was submitted to Pharmacology of Ion Channels and Channelopathies, a section of the journal Frontiers in Pharmacology

Received: *16 December 2019*
Accepted: *17 March 2020*
Published: *07 April 2020*

Citation:
Shimshilashvili L, Aharon S, Moe OW and Ohana E (2020) Novel Human Polymorphisms Define a Key Role for the SLC26A6-STAS Domain in Protection From Ca^{2+}-Oxalate Lithogenesis. Front. Pharmacol. 11:405. doi: 10.3389/fphar.2020.00405

Impaired homeostasis of the carboxylic acids oxalate and citrate, dramatically increases the risk for the formation of Ca^{2+}-oxalate kidney stones, which is the most common form of kidney stones in humans. Renal homeostasis of oxalate and citrate is controlled by complex mechanisms including epithelial transport proteins such as the oxalate transporter, SLC26A6, and the citrate transporters, the SLC13's. These transporters interact *via* the SLC26A6-STAS domain *in vitro*, however, the role of the Sulfate Transporter and Anti-Sigma factor antagonist (STAS) domain in Ca^{2+}-oxalate stone formation was not investigated in humans. Here, we report two novel human SLC26A6 polymorphisms identified in the STAS domain of SLC26A6 in two heterozygous carriers. Intriguingly, these individuals have low urinary citrate, but different clinical manifestations. Our *in vitro* experiments indicate that the homolog mutations of SLC26A6(D23H/D673N) and SLC26A6(D673N) alone abolished the expression and function of SLC26A6, and impaired the regulation of SLC13-mediated citrate transport by SLC26A6. On the other hand, the SLC26A6(R621G) variant showed reduced SLC26A6 protein expression and membrane trafficking, retained full transport activity, but impaired the regulation of the citrate transporter. Accordingly, the human SLC26A6(D23H/D673N) carrier showed a dramatic reduction in urinary citrate concentrations which resulted in Ca^{2+}-oxalate stones formation, as opposed to the carrier of SLC26A6(R621G). Our findings indicate that the human SLC26A6-STAS domain mutations differentially impair SLC26A6 expression, function, and regulation of citrate transporters. This interferes with citrate and oxalate homeostasis thus potentially predisposes to Ca^{2+}-oxalate kidney stones.

Keywords: SLC26A6, citrate, oxalate, kidney stones, NaDC-1

INTRODUCTION

The majority of kidney stone formers develop Ca^{2+}-oxalate stones, which is a significant health problem that may lead to loss of renal function (Moe, 2006; Evan et al., 2010) and is associated with other morbidities such as hypertension and increased risk of fractures (Borghi et al., 1999; Obligado and Goldfarb, 2008). In fact, more than 85% of kidney stone formers has Ca^{2+}-oxalate as part of the stone composition (Evan et al., 2003; Moe, 2006). Ca^{2+}-oxalate kidney stones are caused by elevated urinary Ca^{2+} and oxalate, termed hypercalciuria and hyperoxaluria, respectively (Moe, 2006). In addition, low urine concentrations of the Ca^{2+}-chelator, citrate, can also contribute to calcium lithogenesis, when coupled to hyperoxaluria, even in the absence of hypercalciuria (Moe, 2006). Sufficient urinary citrate concentrations are crucial to protect against stone formation. We have previously reported that the SLC26A6/NaDC-1 complex of transporters protects against stone formation in a dual fashion (Moe, 2006; Ohana et al., 2013). On one hand, SLC26A6 exclusively mediates oxalate clearance in the intestine and, as a result, *Slc26a6* deletion in mice causes Ca^{2+}-oxalate stone formation driven by hyperoxalemia and increased filtered load (Jiang et al., 2006; Knauf et al., 2011). On the other hand, SLC26A6 interacts with the proximal tubule citrate transporter, SLC13A2 or NaDC-1 (sodium dicarboxylate cotransporter-1), to inhibit citrate uptake from the urine. This mechanism controls citrate re-absorption, thus regulating urinary citrate excretion rate and concentrations (Ohana et al., 2013). More specifically, the intracellular STAS domain of SLC26A6 interacts with a specific structural determinant on NaDC-1, namely, the f domain, which is common to all members of the SLC13 transporter family (Khamaysi et al., 2019). Similarly, the STAS domain is located in the intracellular C-terminal of all members of the SLC26 family of transporters (Sharma et al., 2011). Importantly, mutations in or deletion of the entire STAS segment impair SLC26 proteins trafficking to the plasma membrane and their interaction with partner proteins. This underscores the quintessential role that STAS plays in controlling SLC26 function and expression (Ko et al., 2004; Dorwart et al., 2008; Ohana et al., 2013; Geertsma et al., 2015). Remarkably, numerous human mutations were identified in the STAS domain of different SLC26 transporters causing many diseases including, diastrophic dysplasia (SLC26A2) (Cai et al., 2015), congenital chloride diarrhea (SLC26A3) (Dorwart et al., 2008), Pendred syndrome (SLC26A4) (Everett et al., 1997), and infertility (SLC26A8/A3) (Dirami et al., 2013; Rapp et al., 2017; Wedenoja et al., 2017). Notably, the *Slc26a6*/*Nadc-1* complex was shown to control blood pressure by regulating succinate reabsorption at the proximal tubule, which, in turn, regulates the renin-angiotensin system (Khamaysi et al., 2019). This was suggested as one molecular mechanism that underlies the association between hypertension and kidney stone formation (Borghi et al., 1999; Cappuccio et al., 1999; Obligado and Goldfarb, 2008). Several SLC26A6 polymorphisms were identified in Ca^{2+}-oxalate stone formers, however, the vast majority of the polymorphisms are located in the catalytic transmembrane domain (Corbetta et al., 2009; Lu et al., 2016). For example, the SLC26A6(V206M) polymorphism, which we also found in our cohort, was shown to be associated with kidney stones development and primary hyperparathyroidism patients (Monico et al., 2008; Corbetta et al., 2009). Here, we report two novel polymorphisms in the STAS domain of SLC26A6 found in two individuals. One compound polymorphism (D23H/D673N) was identified in a Ca^{2+}-oxalate stone former. The other polymorphism, R621G, was identified in an individual that did not have clinically detectable stones to date. Identification of the mechanism that leads to these different clinical outcomes will help delineate the role that the regulatory SLC26A6-STAS domain plays in controlling citrate/oxalate homeostasis and modifies Ca^{2+}-oxalate lithogenic propensity. Therefore, we pose the question: What is the mechanism by which SLC26A6-STAS domain polymorphisms impair citrate homeostasis that may lead to Ca^{2+}-oxalate stone formation?

MATERIALS AND METHODS

Clinical Studies

Stone-formers were recruited from the Mineral Metabolism Clinic at the Pak Center of Mineral Metabolism and Clinical Research at the University of Texas Southwestern Medical Center. Healthy non-stone formers were recruited from the staff and students on campus with a protocol approved by the University of Texas Southwestern Institutional Review Board and informed consent was obtained from each of the

TABLE 1 | Demographics of human study subjects. Caucasian stone-formers and healthy non-stone formers were recruited as described in the *Materials and Methods* section. Outpatient 24 h urines were collected on random *ad lib* outpatient diets and urinary stone risk profile was assayed by the Clinical Laboratory Improvement Amendments (CLIA)-certified laboratory and genotyping was performed by the Sequencing Core at the Pak Center of Mineral Metabolism and Clinical Research (Reed et al., 2002).

	Non-stone formers			Stone formers		
	WT	R621G–Het	V206M–Het	WT	D23H–Het D673N–Het	V206M–Het
Ethnicity (NH/H)*	20/1	1/0	2/0	18/0	1/0	8/1
Gender (M/F)	7/14	1/0	1/1	13/5	0/1	7/2
Age, years	45 ± 11	33	50 ± 7	44 ± 14	43	43 ± 14
(Min–max)	(20–57)		(45–55)	(8–61)		(18–61)

**All subjects are Caucasian.*

participating subjects. Subject characteristics are shown in **Table 1**. Calcium stone formers all had stone analysis showing 70–100% calcium oxalate in the stone samples. Outpatient 24 h urines were collected on random *ad lib* outpatient diets and urinary stone risk profile was assayed by the Clinical Laboratory Improvement Amendments (CLIA)-certified laboratory and genotyping was performed by the Sequencing Core at the Pak Center of Mineral Metabolism and Clinical Research (Reed et al., 2002). The clinical chemistry methods are standard, in particular, citrate was measured enzymatically by citrate lyase (Cobas Fara, Roche, NJ), creatinine by picric acid method (Olympus AU400), and oxalate by ion chromatography (Dionex, Sunnyvale, CA).

Plasmid Constructs

The plasmids used were the human SLC26A6 clone (NM_022911) in the pCMV6-AC vector or pCMV6-AC-mkate vector and the human NaDC1 clone (BC096277) in the pCMV6-AC-Myc-His vector. Site-directed mutants were generated with the QuikChange Lightning Mutagenesis Kit (Agilent, Santa Clara, CA) and the appropriate primers. The products were verified by Sanger sequencing (Hylabs).

Intracellular pH Measurements and Fluorescent Images Acquisition

Intracellular pH was measured using a single cell real-time imaging system equipped with anEclipse Ti inverted microscope (Nikon, Japan), PE-4000 LED monochromator (CoolLEd, UK), andHamamatsu Flash 4.0LT camera (Hamamatsu photonics, Japan). This system was also utilized foracquisition of the mKate images in **Figure 4C**. HEK293 cells, transiently expressing either SLC26A6(WT), or SLC26A6 (R621G), SLC26A6(D674N), SLC26A6(D23H/D674N) and an empty vector as a control, were seeded on coverslips (D674 is the homolog of D673 in SLC26A6 isoform No. 1; NCBI accession No. NP_075062.2). Cells were stained on stage using 2 μM BCECF-AM (Biotium Inc, CA) and signal was measured ratiometrically, using excitation wavelength of 490 nm *versus* 435 nm and detected at 530 nm. Cells were incubated with BCECF at room temperature for 5 min and washed with regular solution [prepared with 10 mM 4-(2-hydroxyethyl)-1-piperazineethanesulfonic acid (HEPES), 10 mM glucose, 140 mM NaCl, 5 mM KCl, 1 mM $MgCl_2$, 1 mM $CaCl_2$, and pH was adjusted to 7.4)] for at least 10 min until stabilization of the fluorescent signal. Subsequently, the cells were perfused with regular solution until establishment of a base line. Next, regular solution was replaced with a HCO_3^- buffered solution (regular solution was adjusted to 120 mM NaCl, 25 mM $NaHCO_3^-$, and 2.5 mM HEPES) or, with a Cl^- free solution (HCO_3^- buffered solution was papered with gluconate to replace Cl^-). All HCO_3^- buffered solutions were gassed with 5% CO_2 and 95% O_2.

Immunoblot and Co-Immunoprecipitation

HEK293T cells were transfected with the indicated plasmids and after 2 days, lysates were prepared [lysis buffer contained phosphate-buffered saline (PBS), 10 mM Na^+-pyrophosphate, 50 mM NaF, and pH was adjusted to 7.4. 1 mM Na^+-orthovanadate, 1% Triton X-100, and a cocktail of protease inhibitors (Roche) were freshly added before each use]. The cells were placed on ice and scraped after addition of lysis buffer. Protein extracts were incubated with Protein G Sepharose beads (Sigma-Aldrich, St. Louis, MO) and anti-His antibody (1:100) (Thermo Fisher Scientific, Waltham, MA) overnight at 4°C. The beads-protein complexes were incubated for 4 h at 4°C, centrifuged, and washed with lysis buffer four times. Samples were prepared for running on sodium dodecyl sulfate polyacrylamide gel electrophoresis (SDS-PAGE) by heating (37°C for 30 min) in SDS sample buffer. Subsequently, the samples were transferred to nitrocellulose membranes and incubated overnight at 4°C with anti-SLC26A6 (1:500) (ab 172684, Abcam) and the next day exposed to the appropriate secondary antibody. Signal was developed using enhanced-chemiluminescence (ECL) substrate (CYANAGEN).

Cell Surface Expression

Surface expression was analyzed using biotinylation assay. HEKT cells transfected with the appropriate plasmids were incubated with 0.5 mg/ml EZ-LINK Sulfo-NHS-LC-Biotin (Thermo Fisher Scientific, Waltham, MA) for 30 min on ice. The biotin was quenched using 50 mM glycine and lysates were prepared as previously described. Total protein concentration was assessed by BCA method. The lysates were incubated with Neutravidin agarose resin (Thermo Fisher Scientific, Waltham, MA) for 2 h at 4°C and washed three times using lysis buffer. Protein were isolated by adding 50 μl sample buffer and western blot analysis was performed as previously described. The blots were analyzed after incubation of the membranes overnight either with anti-SLC26A6, anti-tRFP (Evrogen) antibodies, or anti-β-actin (Sigma-Aldrich, St. Louis, MO) antibody for 1 h at room temperature.

Succinate Uptake Measurements

Succinate is an established substrate for transport by NaDC-1 and is an accepted surrogate for citrate. HEK293T cells were transfected with the indicated plasmids and washed with PBS (biological industries). Subsequently, an incubation solution containing 5 mM KCl, 10 mM HEPES, 10 mM glucose, and 140 mM NaCl (pH adjusted to 7.4) was supplemented with 1 mM Na^+ succinate and 1 mCi ^{14}C succinic acid (ViTrax, Inc., Fullerton, CA) per 1.6 mM cold succinate and added to the cells. The cells were then washed twice with incubation solution and 0.5 ml NaOH (1M) was immediately added to lyse the cells. The lysates were then transferred to scintillation vials containing 0.250 ml of HCl (2M). Finally, radioactivity was determined by liquid scintillation counting using a Packard 1900CA TRI-CARB analyzer.

3D Protein Model Prediction

The putative structure of SLC26A6 (NCBI accession No. NP_075062.2) was predicted using HHPred software (Soding et al., 2005) with high homology to the cryo-EM structure of SLC26A9 (PDB_ID: 6RTC) (Walter et al., 2019). Prediction parameters: probability=100, E-value = 2.2e−85, score=774.77, identities=39%, similarity=0.742, SS = 54.8, Cols = 632, length =

643. The final model was generated and visualized using PyMOl software (Schrödinger, Germany) (Pettersen et al., 2004).

RESULTS

Two Human SLC26A6-STAS Domain Polymorphisms Have Different Clinical Manifestations

We genotyped a cohort of 27 Ca^{2+}-oxalate kidney stone formers and 23 healthy non-stone formers, and identified two SLC26A6 polymorphisms located in the region that encodes for the intracellular STAS domain (**Supplementary Figure 1**). Interestingly, one compound polymorphism, SLC26A6(D23H/D673N), was found in a kidney stone former, while the other, SLC26A6(R621G), was found in a non-stone former. We compared the urinary oxalate and citrate concentrations of these individuals to either SLC26A6(WT) or SLC26A6 (V206M) polymorphism carriers, which were either healthy (non-stone formers) or stone-formers, as indicated. Interestingly, stone formers who carry the catalytic transmembrane domain polymorphism, SLC26A6(V206M), showed a trend of higher urinary oxalate levels compared to non-stone formers, which was not statistically significant due to the low number of SLC26A6(V206M) carriers in our cohort (**Figure 1A**). However, the SLC26A6(V206M) carriers citrate concentrations were not different (**Figure 1B**). Moreover, the SLC26A6(V206M) urinary oxalate and citrate values were similar to WT in both healthy and stone forming patients (**Figures 1A, B**). Unexpectedly, the (R621G) carrier did not develop kidney stones to our knowledge, in spite of high urinary oxalate and relatively low citrate compared to both WT and V206M individuals. This subject left our institution soon after the original assessment and it is plausible that kidney stones formed later and did not enter our record. However, the individual with (D23H/D673N) polymorphism had normal urinary oxalate levels, but dramatically low urinary citrate compared to all other groups. Remarkably, only three other stone formers in our cohort reached citrate values as low or lower than the D23H/D673N polymorphism carrier. These findings suggest that, in humans, point mutations and polymorphisms in the SLC26A6-STAS domain can interfere with citrate/oxalate homeostasis, but may be not be sufficient to lead to frank disturbances in urinary chemistry or Ca^{2+}-oxalate stone formation. Nevertheless, the level of urinary citrate concentrations obtained as an outpatient on a random diet is unlikely sufficient for determining the risk of stone formation.

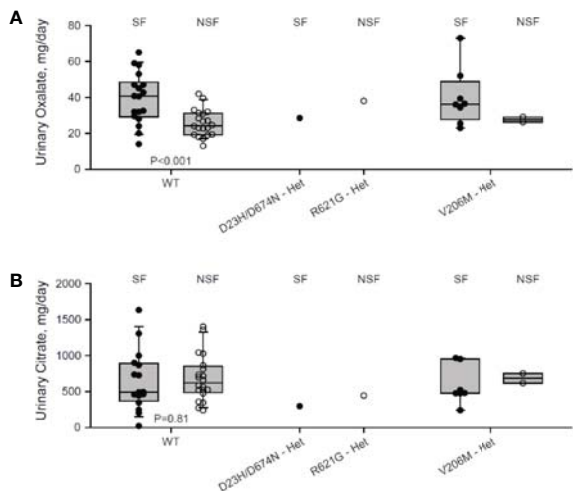

FIGURE 1 | Two individuals carrying heterozygous SLC26A6-STAS domain polymorphisms show hypocitraturia. We monitored urinary oxalate **(A)** and citrate **(B)** concentrations in hyperoxaluric stone formers (SF) and non-stone formers (NSF) that carry the V206M, D23H/D673N, R621G polymorphisms, or WT. P values by ANOVA are indicated. It is noteworthy that both hyperoxaluria and hypocitraturia are risk factors in the general Ca^{2+}-oxalate SF population but cohort who underwent genotyping was biased for hyperoxaluric patient and hence hypocitraturia was "selected out".

The Transport Function of SLC26A6(D673N) Homolog Mutant Is Abolished While the Activity of SLC26A6(R621G) Is Retained

As previously reported, SLC26A6 controls oxalate clearance in the intestine and also regulates citrate reabsorption in the kidney proximal tubule (Jiang et al., 2006; Ohana et al., 2013). Either of these functions or both are crucial to control oxalate/citrate homeostasis and modify stone risk. To test whether the STAS domain polymorphisms SLC26A6(R621G) and SLC26A6 (D23H/D673N) affect the function of SLC26A6, we generated an SLC26A6(R621G) as well as SLC26A6(D23H/D674N) and SLC26A6(D674N) point mutations. Notably, D674 is the homolog of D673 in SLC26A6 isoform No. 1 (NCBI accession No. NP_075062.2). Therefore, the only mutation used for the *in vitro* studies is D674N or the double mutant D23H/D674N, which are equivalent to D673N and D23H/D673 in the isoform we used. Next, we monitored SLC26A6-mediated Cl^-/HCO_3^- exchange activity in HEK293 cells expressing either SLC26A6 (WT) or mutants. As shown in **Figure 2A**, while the transport function of the SLC26A6(D23H/D674N) double mutant (and SLC26A6(D674N)) is completely abolished, the function of SLC26A6(R621G) is fully retained indicating the completely different biologic consequences of these base changes. Notably, these findings suggest that SLC26A6 function is in correlation with the clinical manifestation described in **Figure 1**; showing that the individual with SLC26A6(D23H/D673N) polymorphism forms kidney stones, while the individual with SLC26A6(R621G) does not.

The Sulfate Transporter and Anti-Sigma Factor Antagonist Domain Polymorphisms Hamper SLC26A6 Mediated Inhibition of the Citrate Transporter, NaDC-1

The essential function of the SLC26 transporters STAS domain in the interaction and regulation of partner proteins, including NaDC-1, suggests that mutations in this protein region may affect SLC26A6 interaction with and regulation of NaDC-1. To address this, we monitored NaDC-1 function by measuring

succinate uptake into HEK293 cells expressing NaDC-1 alone or in the presence of either SLC26A6(WT) or mutants. Our results indicate that SLC26A6 significantly inhibits NaDC-1, yet, both STAS mutations dramatically impair the ability of SLC26A6 to inhibit NaDC-1 (**Figure 2B**). This suggests that the SLC26A6-STAS mutations affect either the interaction with NaDC-1, the regulation of NaDC-1 by SLC26A6, or both.

The STAS Domain Polymorphisms Impair SLC26A6 Expression

To explain the different functional effects of the human polymorphisms, we transfected HEK293 cells with either SLC26A6(WT), SLC26A6(D674N), or SLC26A6(R621G) and monitored the expression by immunoblot. As presented in **Figure 3A**, we found that the total cellular expression of SLC26A6(R621G) was higher than SLC26A6(D674N), but both were significantly lower than WT. This indicates that both mutations down-regulate the total expression of SLC26A6 protein. Next, we aimed to test whether the reduced expression also affects the trafficking of the mutants to the plasma membrane. To this end, we monitored the cell surface expression of either WT or mutant SLC26A6 proteins using a surface biotinylation assay after adjusting the input protein levels. We found that the membrane expression of D674N is dramatically low compared to R621G and WT (**Figure 3B**). This explains both the nearly abolished function of this mutant and corresponds to the failure to inhibit NaDC-1 transport by the D674N mutant. Nonetheless, the membrane expression of R621G is also significantly lower than WT (**Figure 3B**), but apparently this level of R621G expression is sufficient to retain full SLC26A6 function.

The Interaction of Both D674N and R621G With NaDC-1 Is Similar to SLC26A6(WT)

As shown in **Figure 1**, the carriers of both mutants exhibit low urinary citrate concentrations. Therefore, we hypothesized that the mutations may interfere with SLC26A6-NaDC-1 interaction, which is mediated by the STAS domain. To this end, we tested the level of interaction between NaDC-1 and SLC26A6 mutants compared to WT utilizing co-immunoprecipitation (Co-IP),

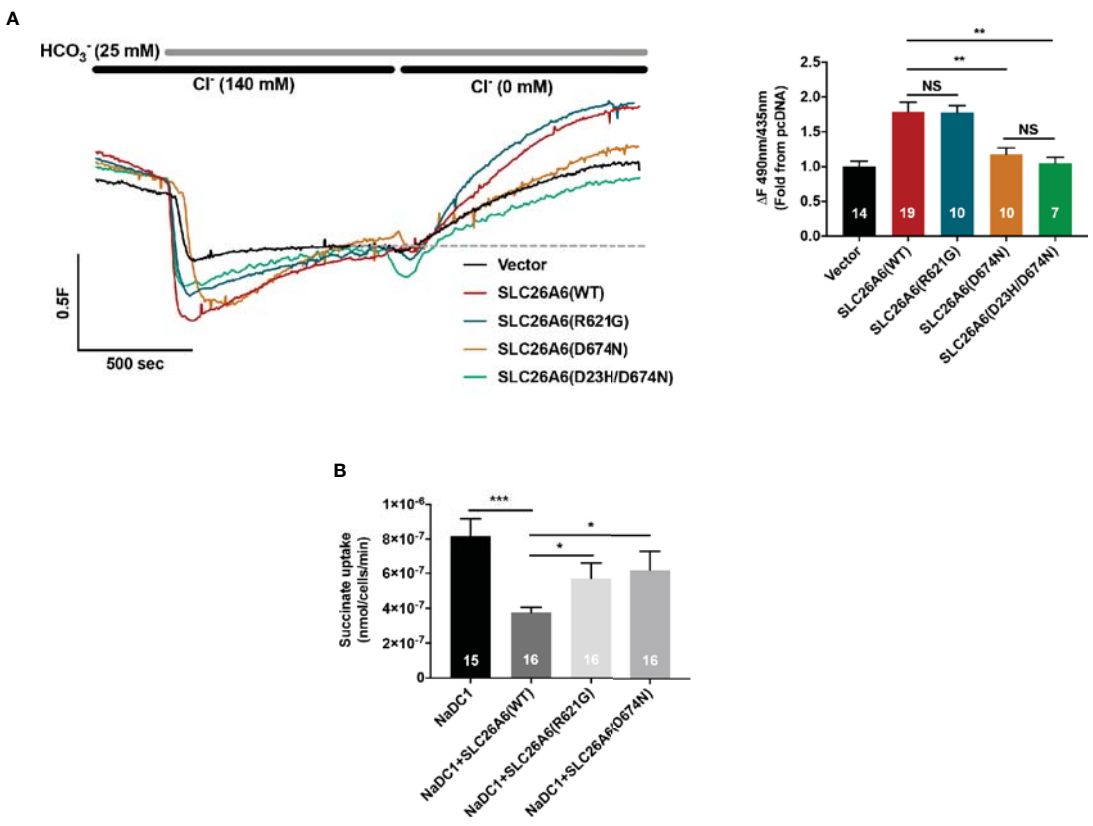

FIGURE 2 | Functional and regulatory properties of SLC26A6 are compromised by the sulfate transporter and anti-sigma factor antagonist (STAS) domain polymorphisms (D23H/D673N) and (R621G). **(A)** Representative traces and summary of the human SLC26A6 Cl^-/HCO_3^- exchange activity monitored in cells transfected with either an empty vector (control), SLC26A6(WT), SLC26A6(D674N), SLC26(D23H/D674N), or SLC26A6 (R621G), as indicated. Transport activity was monitored as the fluorescence change from the new baseline (dashed line) to peak after prefusion with 0 Cl^-. **(B)** NaDC-1-mediated succinate uptake was monitored using a radiolabeled ^{14}C-succinate flux assay in cells expressing NaDC-1 in the presence or absence of WT or mutant SLC26A6, as indicated. The background signal monitored in control cells (transfected with and empty vector) was subtracted. *P < 0.05, **P < 0.01, ***P < 0.001, NS = P > 0.05.

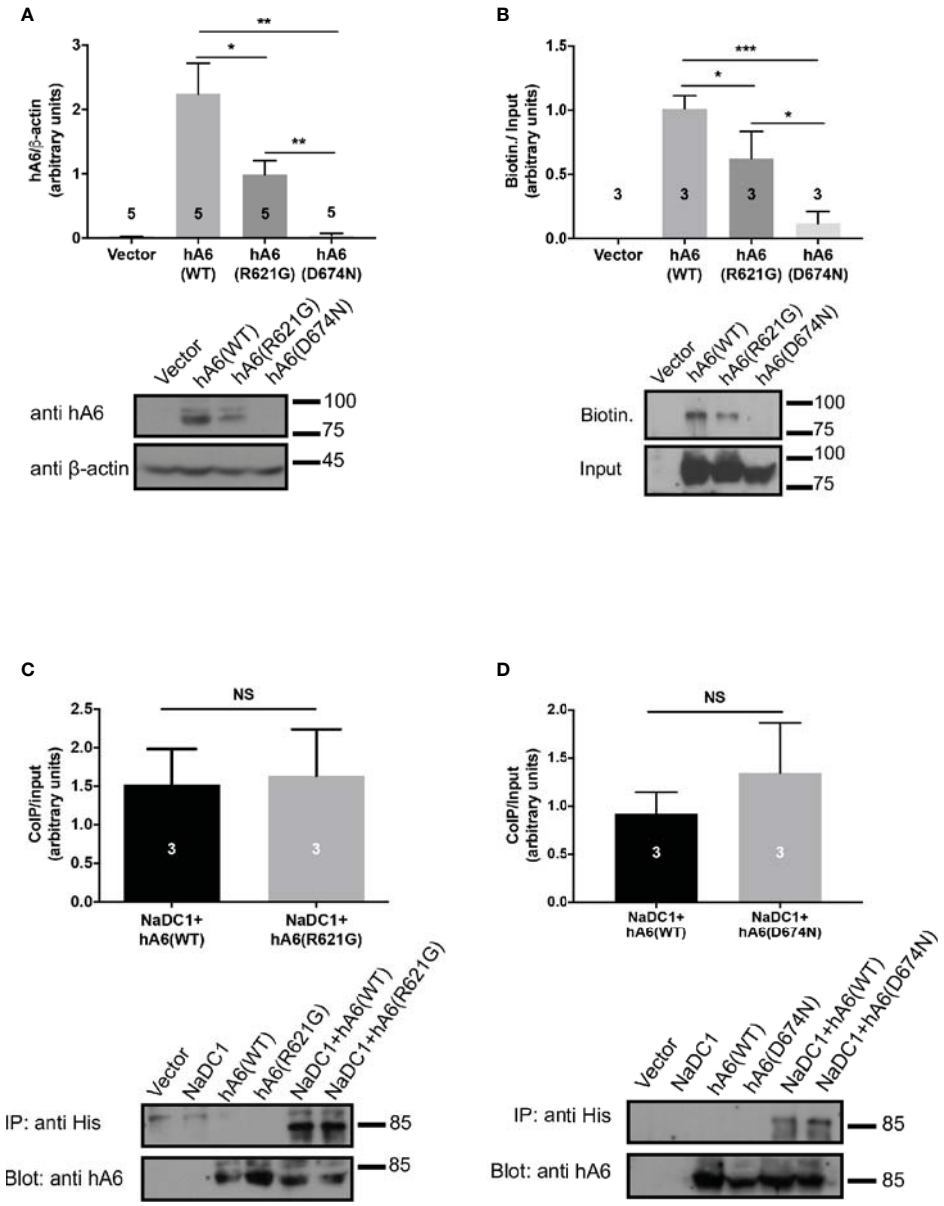

FIGURE 3 | The sulfate transporter and anti-sigma factor antagonist (STAS) domain mutations impair protein expression, trafficking to the plasma membrane but not the interaction with NaDC-1. **(A)** The expression of human SLC26A6 (hA6) monitored in lysates of HEK293T cells transfected with an empty vector SLC26A6 (WT), SLC26A6(D674N), or SLC26A6 (R621G) compared to β-actin expression. **(B)** The membrane expression of the indicated proteins was monitored using a biotinylation assay after adjustment of the total protein levels as shown in the input blot. The interaction between NaDC-1, SLC26A6, and mutants was monitored using a co-immunoprecipitation (Co-IP) assay. The western blot analyses in **(C, D)** indicate that the SLC26A6-STAS domain mutations retain interaction with NaDC-1. *P < 0.05, **P < 0.01, ***P < 0.001, NS = P > 0.05.

following adjustment of SLC26A6 expression levels. As shown in **Figures 3C, D**, the interaction level of both D674N and R621G with NaDC-1 is similar to the interaction between NaDC-1 and SLC26A6(WT). This may suggest that the mutations do not interfere with NaDC-1 interaction, or that the STAS domain region that encompasses R621 and D674 does not mediate SLC26A6-NaDC-1 binding.

Together, our results, thus far, indicate that D674N (which corresponds to the human polymorphism D673N) dramatically impairs the expression of SLC26A6, and abolishes the trafficking of SLC26A6 to the plasma membrane and, consequently, hampers SLC26A6 transport function. On the other hand, the R621G mutant lowers SLC26A6 total expression and trafficking, however, the residual expression is sufficient to retain full

transport activity. Notably, the low surface expression of both mutants relative to WT is insufficient to inhibit NaDC-1, since NaDC-1 inhibition is eliminated by D674N and R621G (**Figure 2B**).

Potential Rescue of SLC26A6(D674N) Membrane Expression

The trafficking of transport proteins to the membrane may be rescued by partner proteins that form complexes in the membrane, as demonstrated for CFTR (Bosch and De Boeck, 2016). Therefore, we monitored the membrane expression of SLC26A6(D674N) in the presence of NaDC-1. The results in **Figure 4A** suggest that the surface expression of the D674N mutant is not improved and even hampered by NaDC-1 expression. However, monitoring the membrane expression of the same mutant with a fluorescent protein tag at the C-terminus increased the protein membrane expression (**Figures 4B, C**). This suggests that adding a soluble peptide to the STAS domain slightly compensates for the trafficking impairment caused by the STAS(D674N) mutant. Therefore, the SLC26A6-STAS domain is a potential therapeutic target for diseases caused by impaired trafficking of SLC26 transporters.

DISCUSSION

Many factors increase the risk for kidney stone formation, including, abnormal urine pH, high urine calcium, high urine oxalate, and low concentrations of the major urine Ca^{2+} buffer, citrate. Elevated urine oxalate coupled with low urinary citrate is a dire combination and imposes a major risk for Ca^{2+}-oxalate kidney stones formation, even in the absence hypercalciuria (Moe, 2006; Moe and Preisig, 2006). Interestingly, the homeostasis of oxalate and citrate is controlled by the SLC26A6/NaDC-1 complex of transport proteins (Ohana et al., 2013). SLC26a6 and NaDC-1 reciprocally regulate their function —SLC26A6 strongly inhibits NaDC-1, while NaDC-1 slightly activates SLC26A6 (Ohana et al., 2013). These are teleogically logical interactions that control the luminal concentrations of citrate (anti-lithogenic) and oxalate (pro-lithogenic). This occurs due to interaction between the SLC26A6-STAS and the NaDC-1-H4c domains (Ohana et al., 2013; Khamaysi et al., 2019). However, the role of the SLC26A6-STAS domain in human Ca^{2+}-oxalate stone formation has not been explored and is poorly understood. In the current study, we report of two novel SLC26A6 polymorphisms found in two different individuals. Intriguingly, one individual that carries the

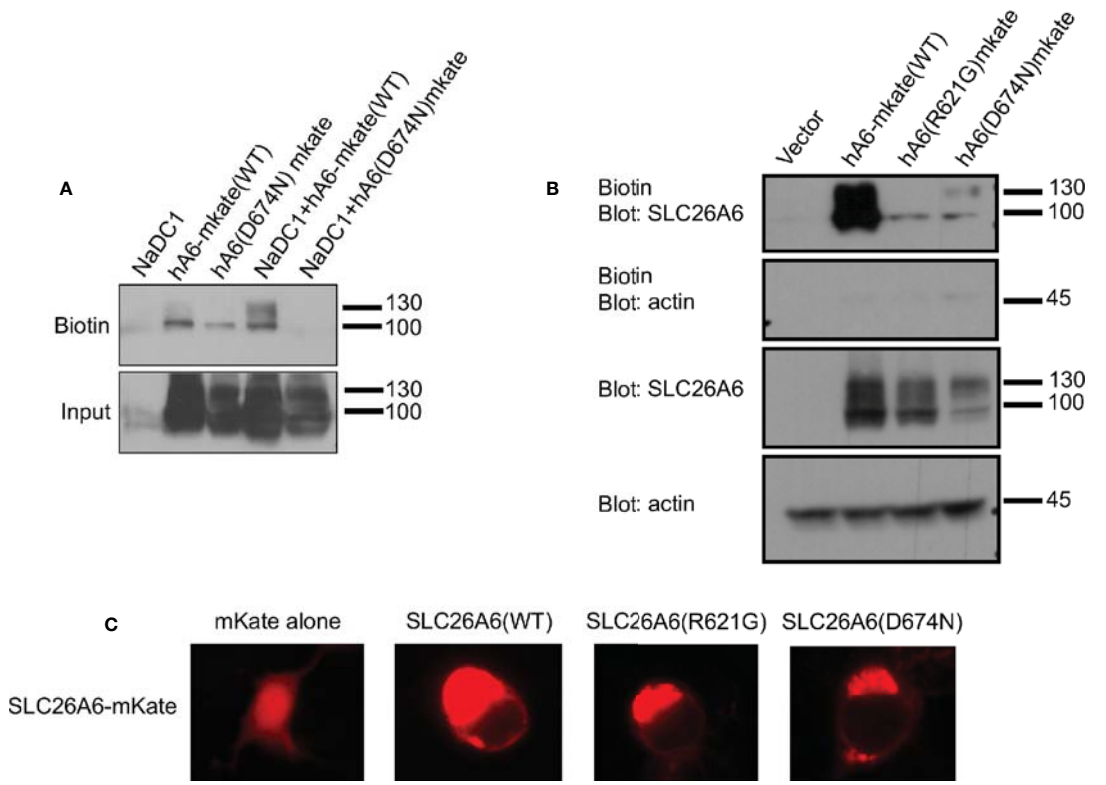

FIGURE 4 | The membrane expression of SLC26A6(D674N) is recovered by the mKate tag, but not by NaDC-1 expression. We monitored human SLC26A6 (hA6) trafficking to the plasma membrane by biotinylation using similar total protein concentrations (no adjustment). As shown in **(A)**, in the presence of NaDC-1, the expression of slc26a6 was even lower than in the absence of NaDC-1. However, the mKate tagged SLC26A6(D674N)mKate protein showed membrane expression similar to that of SLC26A6(R621G)mKate **(B)**. The images in **(C)** describe the cellular distribution of the indicated mKate tagged proteins compared to the cytoplasmic distribution of mKate alone.

heterogeneous single nucleotide polymorphism, R621G, has high urinary oxalate and low urinary citrate, but has not form kidney stones to date. The other individual was diagnosed with Ca^{2+}-oxalate kidney stones showing significant hypocitraturia with normal urinary oxalate concentrations (**Figure 1**). We studied the role of the STAS domain mutations *in vitro*, and found that the D674N mutation (which is homologous to D673N) abolished SLC26A6 expression, trafficking, transport function, and regulation of the citrate transporter, NaDC-1. Although the patient carries a compound D23H/D673N polymorphism, we focused on the STAS domain missense mutation D673N (we tested the homologous mutant D674N), which impaired protein expression even in the absence of D23H (**Figure 3A**). These findings are in agreement with the clinical manifestation of Ca^{2+}-oxalate kidney stone formers, since impaired SLC26A6 function hampers the exclusive intestinal oxalate clearance pathway as well as proximal tubule citrate transport regulation (Aronson, 2010). Indeed, the D23H/D673N carrier had lower citrate concentrations compared to other stone formers (**Figure 1B**). Yet, the normal urinary oxalate concentrations in D23H/D673N carrier are unexpected and require further investigation (**Figure 1A**).

On the other hand, the heterogeneous polymorphism R621G impaired SLC26A6 expression and trafficking, but to a lesser extent compared to D674N (**Figures 3A, B**). Consequently, the SLC26A6 activity was retained, however, the membrane expression was not sufficient to preserve the NaDC-1 inhibition by SLC26A6, which was largely abolished (**Figures 2A, B**). Nonetheless, the R621G carrier showed hyperoxaluria and relatively low urinary citrate, which was less dramatic compared to that of the D673N carrier (**Figures 1A, B**).

We present findings in humans and *in vitro*, that the SLC26A6-STAS domain plays a key role in controlling citrate homeostasis. Based on our previous reports, we suggest that specific STAS domain mutations are expected to cause low urinary citrate due to impaired inhibition of SLC13-mediated citrate transport and subsequent elevated citrate absorption. This would potentially lower urinary citrate as we, indeed, measured in urine samples that were collected from STAS-polymorphism carriers (**Figure 1**). Notably, our results suggest that the extent of urinary citrate reduction may contribute to the clinical outcome. The D23H/D673N polymorphism carriers had a dramatic reduction in urinary citrate compared to other stone formers that likely induced lithogenesis even in the absence of hyperoxaluria. Nevertheless, the citrate concentrations monitored in urine samples of the R621G carrier were 50% higher compared to the D23H/D673N carrier, who also had high urinary oxalate, but did not develop stones (**Figures 1A, B**). This may indicate that a substantial decrease in urinary citrate caused by impaired SLC26A6 regulation of citrate absorption is sufficient to cause stone formation even in the absence of hyperoxaluria. These observations are rather intriguing but the clinical conclusions are limited since we identified only one individual that carries either of the polymorphisms in our cohort. Finally, our previous report indicated that in mice *Slc26a6\Slc13* complex also controls blood pressure by regulating succinate homeostasis (Khamaysi et al., 2019). Hence, the effects of impaired SLC26A6-STAS domain function may extend beyond kidney stone formation and could also lead to hypertension, which is, indeed, strongly associated with kidney stones (Obligado and Goldfarb, 2008).

Numerous studies by others and us have shown that the STAS domain is essential for transporter trafficking and regulation of partner proteins *via* interaction (Sharma et al., 2011). As a result, human mutations within the STAS domain of many SLC26 family members can cause diseases (Rapp et al., 2017). For example, a specific STAS domain mutation in SLC26A3, which is associated with male subfertility, impairs SLC26A3 interaction with CFTR (Wedenoja et al., 2017). Another study showed that a specific SLC26A2-STAS mutation associated with the skeletal disease, diastrophic dysplasia, impairs SLC26A2 trafficking to the plasma membrane (Rapp et al., 2017). Therefore, a potential therapeutic strategy could be rescuing the mutant SLC26A2 surface expression. Remarkably, a similar therapeutic strategy underlies the cystic fibrosis treatment by Lumacaftor® that increases surface expression of mutated CFTR channels (Van Goor et al., 2011). Our results in **Figures 4B, C** suggest that a C-terminal fluorescent tag may improve the membrane trafficking of SLC26A6(D674N), however, further analysis is required to test the effects of the tag on STAS domain structure and function. Our findings indicate that SLC26 transporters trafficking or protein-protein interactions caused by STAS domain mutations may be rescued. In the future, the screening and development of compounds that specifically target different SLC26 STAS domains and regions may increase trafficking or correct regulatory defects to treat SLC26 related diseases including kidney stones and hypertension.

DATA AVAILABILITY STATEMENT

The raw data supporting the conclusions of this article will be made available by the authors, without undue reservation, to any qualified researcher.

ETHICS STATEMENT

The studies involving human participants were reviewed and approved by The University of Texas Southwestern Institutional Review Board. The patients/participants provided their written informed consent to participate in this study.

AUTHOR CONTRIBUTIONS

EO designed the study. LS performed experiments. SA generated clones. EO, LS, and OM were involved in data analysis. Human data acquisition was performed by OM. Funding was acquired by EO and OM. EO, LS, and OM wrote the manuscript. All authors contributed to critical revision of the manuscript and approved the final version.

FUNDING

This work was supported by BSF grant (No. 2015003) to EO and by the Israel Science Foundation grants No. 271/16 and 2164/16 to EO. OM was supported by the National Institutes of Health R01DK081423, R01 DK115703, R01 DK091392, and P30 DK079328) and the Charles Pak Foundation.

ACKNOWLEDGMENTS

The authors thank John Poindexter for his assistance in bioinformatics with the human data.

SUPPLEMENTARY MATERIAL

The Supplementary Material for this article can be found online at: https://www.frontiersin.org/articles/10.3389/fphar.2020.00405/full#supplementary-material

SUPPLEMENTARY FIGURE 1 | A putative 3D model of SLC26A6 and multiple sequence alignment (MSA) of human isoforms. We generated a putative 3D model of the human SLC26A6 based on the cryo-EM model reported for the SLC26A9 transporter. The model was generated as described in the methods section. The model shows the SLC26A6 transmembrane domain (green), the STAS domain (yellow) and the D674 residue location (red). The model lacks the IVS region of STAS (dashed line) which is flanked by the blue residues and harbors R621. The MSA analysis shows R621 (dark grey) and D674 (red) conservation between different human SLC26A6 isoforms. The IVS residues of human SLC26A6 isoform 1, which was used in our study, are highlighted in light grey.

REFERENCES

Aronson, P. S. (2010). Role of SLC26A6-mediated Cl(-)-oxalate exchange in renal physiology and pathophysiology. *J. Nephrol.* 23 Suppl 16, S158–S164.

Borghi, L., Meschi, T., Guerra, A., Briganti, A., Schianchi, T., Allegri, F., et al. (1999). Essential arterial hypertension and stone disease. *Kidney Int.* 55, 2397–2406. doi: 10.1046/j.1523-1755.1999.00483.x

Bosch, B., and De Boeck, K. (2016). Searching for a cure for cystic fibrosis. A 25-year quest in a nutshell. *Eur. J. Pediatr.* 175, 1–8. doi: 10.1007/s00431-015-2664-8

Cai, T., Yang, L., Cai, W., Guo, S., Yu, P., Li, J., et al. (2015). Dysplastic spondylolysis is caused by mutations in the diastrophic dysplasia sulfate transporter gene. *Proc. Natl. Acad. Sci. U. S. A* 112, 8064–8069. doi: 10.1073/pnas.1502454112

Cappuccio, F. P., Siani, A., Barba, G., Mellone, M. C., Russo, L., Farinaro, E., et al. (1999). A prospective study of hypertension and the incidence of kidney stones in men. *J. hypertens.* 17, 1017–1022. doi: 10.1097/00004872-199917070-00019

Corbetta, S., Eller-Vainicher, C., Frigerio, M., Valaperta, R., Costa, E., Vicentini, L., et al. (2009). Analysis of the 206M polymorphic variant of the SLC26A6 gene encoding a Cl- oxalate transporter in patients with primary hyperparathyroidism. *Eur. J. Endocrinol.* 160, 283–288. doi: 10.1530/EJE-08-0623

Dirami, T., Rode, B., Jollivet, M., Da Silva, N., Escalier, D., Gaitch, N., et al. (2013). Missense mutations in SLC26A8, encoding a sperm-specific activator of CFTR, are associated with human asthenozoospermia. *Am. J. Hum. Genet.* 92, 760–766. doi: 10.1016/j.ajhg.2013.03.016

Dorwart, M. R., Shcheynikov, N., Yang, D., and Muallem, S. (2008). The solute carrier 26 family of proteins in epithelial ion transport. *Physiology* 23, 104–114. doi: 10.1152/physiol.00037.2007

Evan, A. P., Lingeman, J. E., Coe, F. L., Parks, J. H., Bledsoe, S. B., Shao, Y., et al. (2003). Randall's plaque of patients with nephrolithiasis begins in basement membranes of thin loops of Henle. *J. Clin. Invest.* 111, 607–616. doi: 10.1172/JCI17038

Evan, A. P., Lingeman, J. E., Worcester, E. M., Bledsoe, S. B., Sommer, A. J., Williams, J. C.Jr., et al. (2010). Renal histopathology and crystal deposits in patients with small bowel resection and calcium oxalate stone disease. *Kidney Int.* 78, 310–317. doi: 10.1038/ki.2010.131

Everett, L. A., Glaser, B., Beck, J. C., Idol, J. R., Buchs, A., Heyman, M., et al. (1997). Pendred syndrome is caused by mutations in a putative sulphate transporter gene (PDS). *Nat. Genet.* 17, 411–422. doi: 10.1038/ng1297-411

Geertsma, E. R., Chang, Y. N., Shaik, F. R., Neldner, Y., Pardon, E., Steyaert, J., et al. (2015). Structure of a prokaryotic fumarate transporter reveals the architecture of the SLC26 family. *Nat. Struct. Mol. Biol.* 22, 803–808. doi: 10.1038/nsmb.3091

Jiang, Z., Asplin, J. R., Evan, A. P., Rajendran, V. M., Velazquez, H., Nottoli, T. P., et al. (2006). Calcium oxalate urolithiasis in mice lacking anion transporter Slc26a6. *Nat. Genet.* 38, 474–478. doi: 10.1038/ng1762

Khamaysi, A., Anbtawee-Jomaa, S., Fremder, M., Eini-Rider, H., Shimshilashvili, L., Aharon, S., et al. (2019). Systemic Succinate Homeostasis and Local Succinate Signaling Affect Blood Pressure and Modify Risks for Calcium Oxalate Lithogenesis. *J. Am. Soc. Nephrol.* 30 (3), 381–392. doi: 10.1681/ASN.2018030277

Knauf, F., Ko, N., Jiang, Z., Robertson, W. G., Van Itallie, C. M., Anderson, J. M., et al. (2011). Net intestinal transport of oxalate reflects passive absorption and SLC26A6-mediated secretion. *J. Am. Soc. Nephrol. : JASN* 22, 2247–2255. doi: 10.1681/ASN.2011040433

Ko, S. B., Zeng, W., Dorwart, M. R., Luo, X., Kim, K. H., Millen, L., et al. (2004). Gating of CFTR by the STAS domain of SLC26 transporters. *Nat. Cell Biol.* 6, 343–350. doi: 10.1038/ncb1115

Lu, X., Sun, D., Xu, B., Pan, J., Wei, Y., Mao, X., et al. (2016). In Silico Screening and Molecular Dynamic Study of Nonsynonymous Single Nucleotide Polymorphisms Associated with Kidney Stones in the SLC26A6 Gene. *J. Urol.* 196, 118–123. doi: 10.1016/j.juro.2016.01.093

Moe, O. W., and Preisig, P. A. (2006). Dual role of citrate in mammalian urine. *Curr. Opin. Nephrol. Hypertens.* 15, 419–424. doi: 10.1097/01.mnh.0000232882.35469.72

Moe, O. W. (2006). Kidney stones: pathophysiology and medical management. *Lancet* 367, 333–344. doi: 10.1016/S0140-6736(06)68071-9

Monico, C. G., Weinstein, A., Jiang, Z., Rohlinger, A. L., Cogal, A. G., Bjornson, B. B., et al. (2008). Phenotypic and functional analysis of human SLC26A6 variants in patients with familial hyperoxaluria and calcium oxalate nephrolithiasis. *Am. J. Kidney Dis.* 52, 1096–1103. doi: 10.1053/j.ajkd.2008.07.041

Obligado, S. H., and Goldfarb, D. S. (2008). The association of nephrolithiasis with hypertension and obesity: a review. *Am. J. hypertens.* 21, 257–264. doi: 10.1038/ajh.2007.62

Ohana, E., Shcheynikov, N., Moe, O. W., and Muallem, S. (2013). SLC26A6 and NaDC-1 transporters interact to regulate oxalate and citrate homeostasis. *J. Am. Soc. Nephrol. : JASN* 24, 1617–1626. doi: 10.1681/ASN.2013010080

Pettersen, E. F., Goddard, T. D., Huang, C. C., Couch, G. S., Greenblatt, D. M., Meng, E. C., et al. (2004). UCSF Chimera–a visualization system for exploratory research and analysis. *J. Comput. Chem.* 25, 1605–1612. doi: 10.1002/jcc.20084

Rapp, C., Bai, X., and Reithmeier, R. A. F. (2017). Molecular analysis of human solute carrier SLC26 anion transporter disease-causing mutations using 3-dimensional homology modeling. *Biochim. Biophys. Acta Biomembr.* 1859, 2420–2434. doi: 10.1016/j.bbamem.2017.09.016

Reed, B. Y., Gitomer, W. L., Heller, H. J., Hsu, M. C., Lemke, M., Padalino, P., et al. (2002). Identification and characterization of a gene with base substitutions associated with the absorptive hypercalciuria phenotype and low spinal bone density. *J. Clin. Endocrinol. Metab.* 87, 1476–1485. doi: 10.1210/jcem.87.4.8300

Sharma, A. K., Rigby, A. C., and Alper, S. L. (2011). STAS domain structure and function. *Cell. Physiol. Biochem.* 28, 407–422. doi: 10.1159/000335104

Soding, J., Biegert, A., and Lupas, A. N. (2005). The HHpred interactive server for protein homology detection and structure prediction. *Nucleic Acids Res.* 330, W244–W248. doi: 10.1093/nar/gki408

Van Goor, F., Hadida, S., Grootenhuis, P. D., Burton, B., Stack, J. H., Straley, K. S., et al. (2011). Correction of the F508del-CFTR protein processing defect in vitro by the investigational drug VX-809. *Proc. Natl. Acad. Sci. U. States America* 108, 18843–18848. doi: 10.1073/pnas.1105787108

Walter, J. D., Sawicka, M., and Dutzler, R. (2019). Cryo-EM structures and functional characterization of murine Slc26a9 reveal mechanism of uncoupled chloride transport. *eLife* 8, e46986. doi: 10.7554/eLife.46986

Wedenoja, S., Khamaysi, A., Shimshilashvili, L., Anbtawe-Jomaa, S., Elomaa, O., Toppari, J., et al. (2017). A missense mutation in SLC26A3 is associated with human male subfertility and impaired activation of CFTR. *Sci. Rep.* 7, 14208. doi: 10.1038/s41598-017-14606-3

Conflict of Interest: The authors declare that the research was conducted in the absence of any commercial or financial relationships that could be construed as a potential conflict of interest.

frontiers in Pharmacology

ORIGINAL RESEARCH
published: 15 May 2020
doi: 10.3389/fphar.2020.00672

Andersen–Tawil Syndrome Is Associated With Impaired PIP_2 Regulation of the Potassium Channel Kir2.1

Reem Handklo-Jamal[1], Eshcar Meisel[1,2], Daniel Yakubovich[1,3], Leonid Vysochek[2], Roy Beinart[1,2], Michael Glikson[1,2†], Julie R. McMullen[4], Nathan Dascal[1], Eyal Nof[1,2] and Shimrit Oz[1,2†]*

[1] Sackler School of Medicine, Tel Aviv University, Tel Aviv, Israel, [2] Heart Center, Sheba Medical Center, Ramat-Gan, Israel, [3] Neonatology Department, Schneider Children's Medical Center, Petah-Tikva, Israel, [4] Baker Heart and Diabetes Institute, Melbourne, VIC, Australia

OPEN ACCESS

Edited by:
Avi Priel,
Hebrew University of Jerusalem, Israel

Reviewed by:
Bernard Attali,
Tel Aviv University, Israel
Yael Stern-Bach,
Hebrew University of Jerusalem, Israel

***Correspondence:**
Shimrit Oz
shimrit.oz.fr@gmail.com

†Present address:
Michael Glikson,
Shaare Zedek Medical Center, Jerusalem, Israel
Shimrit Oz,
Rappaport Faculty of Medicine, Technion, Haifa, Israel

Specialty section:
This article was submitted to Pharmacology of Ion Channels and Channelopathies, a section of the journal Frontiers in Pharmacology

Received: 28 November 2019
Accepted: 23 April 2020
Published: 15 May 2020

Citation:
Handklo-Jamal R, Meisel E, Yakubovich D, Vysochek L, Beinart R, Glikson M, McMullen JR, Dascal N, Nof E and Oz S (2020) Andersen–Tawil Syndrome Is Associated With Impaired PIP_2 Regulation of the Potassium Channel Kir2.1. Front. Pharmacol. 11:672. doi: 10.3389/fphar.2020.00672

Andersen–Tawil syndrome (ATS) type-1 is associated with loss-of-function mutations in *KCNJ2* gene. *KCNJ2* encodes the tetrameric inward-rectifier potassium channel Kir2.1, important to the resting phase of the cardiac action potential. Kir-channels' activity requires interaction with the agonist phosphatidylinositol-4,5-bisphosphate (PIP_2). Two mutations were identified in ATS patients, V77E in the cytosolic N-terminal "slide helix" and M307V in the C-terminal cytoplasmic gate structure "G-loop." Current recordings in Kir2.1-expressing HEK cells showed that each of the two mutations caused Kir2.1 loss-of-function. Biotinylation and immunostaining showed that protein expression and trafficking of Kir2.1 to the plasma membrane were not affected by the mutations. To test the functional effect of the mutants in a heterozygote set, Kir2.1 dimers were prepared. Each dimer was composed of two Kir2.1 subunits joined with a flexible linker (i.e. WT-WT, WT dimer; WT-V77E and WT-M307V, mutant dimer). A tetrameric assembly of Kir2.1 is expected to include two dimers. The protein expression and the current density of WT dimer were equally reduced to ~25% of the WT monomer. Measurements from HEK cells and *Xenopus* oocytes showed that the expression of either WT-V77E or WT-M307V yielded currents of only about 20% compared to the WT dimer, supporting a dominant-negative effect of the mutants. Kir2.1 sensitivity to PIP_2 was examined by activating the PIP_2 specific voltage-sensitive phosphatase (VSP) that induced PIP_2 depletion during current recordings, in HEK cells and *Xenopus* oocytes. PIP_2 depletion induced a stronger and faster decay in Kir2.1 mutant dimers current compared to the WT dimer. BGP-15, a drug that has been demonstrated to have an anti-arrhythmic effect in mice, stabilized the Kir2.1 current amplitude following VSP-induced PIP_2 depletion in cells expressing WT or mutant dimers. This study underlines the implication of mutations in cytoplasmic regions of Kir2.1. A newly developed calibrated VSP activation protocol enabled a quantitative assessment of changes in PIP_2 regulation caused by the mutations. The results suggest an impaired function and a dominant-negative effect of the Kir2.1

variants that involve an impaired regulation by PIP_2. This study also demonstrates that BGP-15 may be beneficial in restoring impaired Kir2.1 function and possibly in treating ATS symptoms.

Keywords: Andersen–Tawil syndrome, cardiac arrhythmia, PIP_2, inward-rectifier potassium channel, slide helix, G-loop, voltage-sensitive phosphatase, BGP-15

INTRODUCTION

Andersen–Tawil syndrome (ATS, also known as long-QT7) is a channelopathy, typically characterized by a triad of symptoms: cardiac arrhythmias, periodic paralysis, and dysmorphic features (Tawil et al., 1994). However, variable symptom severity and incomplete penetrance are associated with the syndrome, in addition to a phenotypic mimicry of catecholaminergic polymorphic ventricular tachycardia (CPVT) characterized by bidirectional ventricular tachycardia (VT) (Barajas-Martinez et al., 2011).

KCNJ2 encodes the inwardly-rectifying potassium channel Kir2.1, a major component of the cardiac action potential repolarization phase. Pathogenic variants of *KCNJ2* gene account for 60-70% of clinical ATS cases, termed type-1 ATS (Plaster et al., 2001). Most of the pathogenic variants cause Kir2.1 loss-of-function and exert a dominant-negative effect, attributed to trafficking or gating defects (Tristani-Firouzi et al., 2002; Hosaka et al., 2003; Ma et al., 2011). Type-2 ATS is caused by mutations in genes other than *KCNJ2* (Kokunai et al., 2014).

Kir channels are homotetramers composed of four identical subunits that form a K^+-selective transmembrane pore. Kir2.1 subunit topology includes two transmembrane domains (TMDs) with the outer and inner helices that form the transmembrane conduction pathway. Regulatory cytoplasmic regions are the N-terminal "slide helix" that lays in parallel to the plasma membrane, and a large cytosolic C-terminal domain (CTD). The assembled CTD structures form a tightening in the cytosolic ion permeation pathway through a gate termed the "G-loop," aligned below the transmembrane ion permeation pathway (**Figure 1C**).

Kir channels are activated by the phosphoinositide $PI(4,5)P_2$ (PIP_2) (Huang et al., 1998). ATS-associated mutations in Kir2.1 were linked to reduced PIP_2 affinity (Lopes et al., 2002). The crystal structure of Kir2.2 showed that PIP_2 interacts with an interface between the inner TMD and the CTD complex,

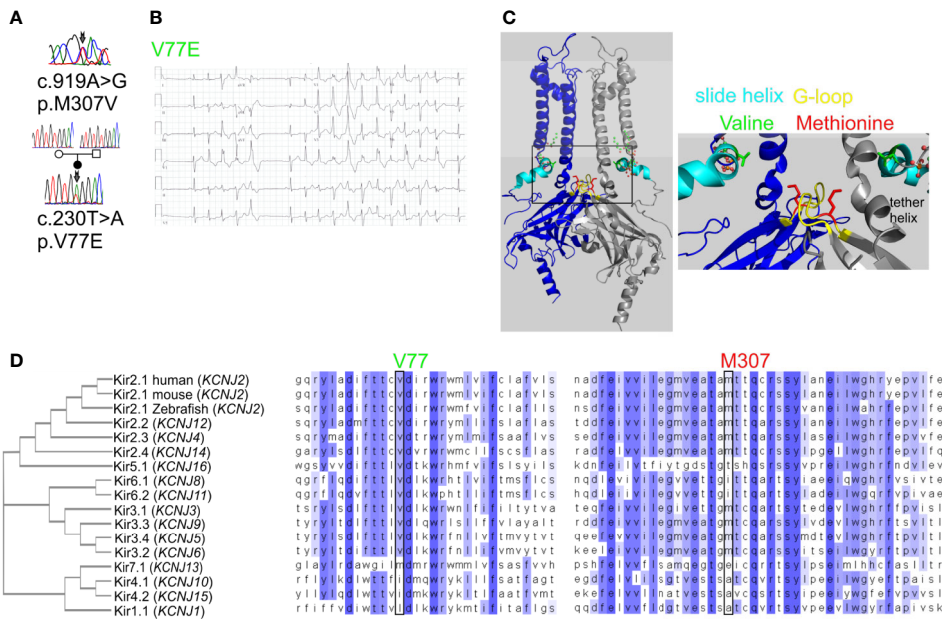

FIGURE 1 | Mutations in Kir2.1 associated with Andersen–Tawil syndrome. **(A)** DNA sequencing of two patients revealed mutations in Kir2.1. **(B)** Representative ECG from the carrier of V77E variant showing bidirectional ventricular tachycardia, prolonged QT interval with ST and T wave abnormalities. **(C)** Left, cartoon presentation of two subunits (blue and gray) out of four, of the inwardly rectifying potassium channel protein (Kir2.2 with PIP_2, PDB ID: 3SPI (Hansen et al., 2011)). PIP_2 is in ball-and-stick (atom code: oxygen, red; carbon, green; phosphorous, orange). The N-terminal slide helix is in cyan and the cytoplasmic gate G-loop is in yellow. Side chains as sticks of V75 and M308 in Kir2.2, homologous to V77 and M307 in Kir2.1, are in green and red, respectively. The plasma membrane is in light gray. Right, zoom on the mutated residues' location. **(D)** Kir channels phylogenetic tree. Amino acid sequence alignments of 15 human Kir proteins, in addition to mouse and Zebrafish Kir2.1.

inducing the formation of a cytoplasmic extension of the TMD: the tether helix. The tether helix is pivotal for both the direct binding of PIP_2 and for the conformational gating transduction (**Figure 1C**) (Hansen et al., 2011; Lacin et al., 2017).

The hydroxylamine derivative BGP-15 is a small molecule that showed beneficial and cytoprotective effects in diabetes, cancer, cardiomyopathy, heart failure, atrial fibrillation (AF), and muscle dysfunction (Gehrig et al., 2012; Literati-Nagy et al., 2014; Sapra et al., 2014; Nascimento et al., 2018). BGP-15 has been well-tolerated in phase I–II human clinical trials as an insulin sensitizer. The putative target pathways include heat-shock proteins induction (Crul et al., 2013), poly ADP-ribose polymerase 1 (PARP-1) inhibition (Racz et al., 2002), and phosphorylation of IGF1R (Sapra et al., 2014). The exact mode of action is not clear, but several reports suggest that BGP-15 modulates plasma membrane composition, dynamics, and fluidity, involving lipid-rafts reorganization (Gombos et al., 2011; Sapra et al., 2014; Balogi et al., 2019).

In the current work, we report two ATS-associated Kir2.1 mutations. Using molecular and electrophysiological methods we show that these mutations are loss-of-function with a dominant-negative effect. We developed a calibrated protocol to asses Kir2.1 functional sensitivity to PIP_2 using voltage-sensitive phosphatase (VSP) and investigated the effect of BGP-15 on Kir2.1 regulation.

MATERIALS AND METHODS

Clinical and Genetic Assessment

The participants in this study provided written informed consent for both the clinical and genetic studies, which were approved by the Institutional Ethics Committee of the Sheba Medical Center, Tel-Hashomer (approval 0379-13-SMC). Genetic findings were obtained by a sequence screening of the following genes: *KCNQ1*, *HERG*, *SCN5A*, *KCNE1*, *KCNE2*, *KCNJ2*, and *RYR2*. Patients were clinically evaluated by 12-lead electrocardiogram (ECG), exercise testing, and 24-h Holter monitoring.

Cellular Expression Models

HEK cells were maintained in Dulbecco's modified Eagle's medium (DMEM) supplemented with 10% fetal bovine serum (FBS), 100 U/ml penicillin, 10 mg/ml streptomycin, and 2 mM L-glutamine (Biological Industries, Kibbutz Beit-Haemek, Israel) at 37°C with 5% CO_2. Transfections for electrophysiological experiments were using Trans-ITx2 (Mirus, Madison, WI, USA) in 35-mm dishes and biotinylation experiments were using the calcium-phosphate method in 10-cm dishes. 90%–100% confluent dishes were split 1:2 on day 1 and transfected on day 2. On day 3, cells were split on coverslips for patch-clamp experiments and recorded on days 4-5. Biotinylation procedures started on day 4.

HL-1 cells were cultured on gelatin/fibronectin pre-coated dishes, in Claycomb media supplemented with 10% FBS, 100 μM norepinephrine (Sigma-Aldrich, St. Louis, Mo, USA), 100 U/ml penicillin, 10 mg/ml streptomycin, and 2 mM L-glutamine (Biological Industries). For imaging, cells were plated on gelatin/fibronectin-coated culture slides (Lab-Tek Nalge Nunc International, IL, USA) and transfected using Lipofectamine 2000 (Thermo Fisher Scientific, Waltham, MA, USA).

Xenopus laevis oocytes experiments were approved by Tel-Aviv University Institutional Animal Care and Use Committee (permits M-08-081 and M-13-002). Maintenance and operation of female frogs were essentially as previously described (Oz et al., 2017). Briefly, frogs were maintained at 20 ± 2°C on a 10-h light/14-h dark cycle. Portions of ovary were removed from anesthetized frogs [0.17% procainemethanesulphonate (MS222)]. Oocytes were defolliculated by collagenase, injected with RNA and incubated for 2–3 days at 22°C in NDE solution (in mM: 96 NaCl, 2 KCl, 1 $MgCl_2$, 1 $CaCl_2$, 5 HEPES, 2.5 pyruvic acid; 50 mg l^{-1} gentamycin).

DNA Constructs

DNA of GFP was C-terminally fused to the human *KCNJ2* coding sequence (accession number NM_000891.2), following the elimination of *KCNJ2* stop codon and cloned into pcDNA3 vector using restriction enzymes (BamHI-*KCNJ2*-EcoRI-GFP-ApaI). This is the Kir2.1-GFP monomer. DNA sequence encoding the HA-tag (a.a. YPYDVPDYA) was inserted after alanine 115 in the extracellular domain, using a Q5 site-directed mutagenesis kit (New England Biolabs, Ipswich, MA, USA). Point mutations were introduced using PCR [KAPA HiFi HotStart (Kapa Biosciences, Wilmington, MA, USA)]. DNA constructs of Kir2.1 concatenated dimers were prepared using the HA-tagged *KCNJ2* constructs. Kir2.1 WT-WT construct is the WT dimer and WT-V77E, WT-M307V, or WT-R67W construct are mutant dimers. The first Kir2.1 subunit was created with BamHI at the 5′ end, then the stop codon was eliminated and four codons for glycine were inserted, followed by the SalI site at the 3′ end. The second Kir2.1 subunit was WT or mutated, with SalI site at the 5′ end that followed by four codons for glycine, ending with EcoRI site at the 3′. Thus, the linker between two Kir2.1 subunits was composed of (a.a.) GGGGVDGGGG. Kir2.1 dimers between SalI and EcoRI sites were cloned into pcDNA3 vector for mammalian cell's expression and pGSB vector [modified pGEMHE (Shistik et al., 1998)] for RNA *in-vitro* synthesis. For HEK cells expression danio rerio voltage-sensing phosphatase (dr-VSP) was in pcDNA vector, and for *Xenopus* oocytes expression dr-VSP was in pGEM vector (Hossain et al., 2008).

RNA was transcribed *in vitro* using a standard procedure, from a template cDNA in oocyte expression vectors containing 5′ and 3′ untranslated sequences of *Xenopus* β-globin (Dascal and Lotan, 1992).

Immunocytochemistry and Imaging

Cells expressing extracellular HA-tag on Kir2.1-GFP were fixed in 1% paraformaldehyde in phosphate buffer saline (PBS) for 10 min to retain GFP fluorescence, without permeabilization, then blocked with CAS blocking agent (Thermo Fisher Scientific) for 30 min at room temperature. Cells were incubated with mouse anti-HA antibody (Millipore, Burlington, MA, USA), washed with PBS, and incubated with Alexa-594 conjugated anti-mouse secondary antibody (ThermoFisher Scientific). Cell nuclei were

counterstained with DAPI. Images were captured with an LSM 700 confocal microscope using Zen software (ZEISS, Oberkochen, Germany). Three channels (blue, green, red) were acquired sequentially.

Biotinylation Assay

Biotinylation of surface proteins was carried out essentially as described (Nof et al., 2019). Briefly, transfected HEK cells were incubated with 0.5 mg/ml EZ-Link Sulfo-NHS-SS-Biotin (Pierce, Rockford, IL, USA) in PBS pH 8, supplemented with 1 mM Ca^{2+} and 0.5 mM Mg^{2+}, for 30 min at 4°C. Incubation in 50 mM glycine for 10 min ended the reaction. Cells were scraped, washed and lysed for 30 min at 4°C in (mM): 20 Tris–HCl pH 8, 150 NaCl, 1 EGTA, and 1% NP40 supplemented with 0.5 phenylmethylsulfonyl fluoride (PMSF), protease inhibitor cocktail (Roche, Basel, Switzerland), 25 β-glycerol phosphate, and 1 sodium orthovanadate (Sigma-Aldrich). Equal amounts of total protein were incubated with streptavidin-agarose beads (Pierce) for 2 h at 4°C in a rotating device. Proteins were eluted in sample buffer for 1 h at room temperature, followed by 5-min incubation at 65°C, then resolved by SDS-PAGE and Western blotted.

Electrophysiology

Whole-cell currents were recorded from HEK cells using the patch-clamp technique, at 23°C. Signals were amplified using an Axopatch 200B patch-clamp amplifier (Molecular Devices, San Jose, CA, USA), sampled at 1 kHz, and filtered with a low-pass Bessel filter at 10 kHz. Data were acquired with DigiData1440A (Molecular Devices). Patch pipettes (Harvard apparatus, Holliston, MA, USA) were pulled with a resistance of 3–5 MΩ. Series resistance was compensated by 80%–90%. The intracellular pipette solution contained (in mM): 130 KCl, 2 $MgCl_2$, 4 MgATP, 10 EGTA, 10 HEPES, adjusted with KOH to pH 7.2 (295 mOsm). The external solution contained (in mM): 135 NaCl, 4 KCl, 10 glucose, 10 HEPES, 1.8 $CaCl_2$, 1 $MgCl_2$, adjusted with NaOH to pH 7.4 (305 mOsm). For Ba^{2+}-sensitive currents (**Figure 2**), cells were additionally perfused with the Ba^{2+}-containing external solution (in mM): 10 $BaCl_2$, 120 NaCl, 4 KCl, 10 glucose, 10 HEPES, 1.8 $CaCl_2$, 1 $MgCl_2$. The net Ba^{2+}-sensitive current was a subtraction of the current evoked in the presence of perfused $BaCl_2$ from the current evoked in the standard external solution without $BaCl_2$, using the same protocol in one cell.

HEK cells were held at −60 mV in the voltage step protocol (**Figure 2**) and at 0 mV in the voltage ramp protocol. Ramps were set from −120 to 0 mV in 1 s. In the double-ramp protocol (example in **Figure 5A**), a 10-s sweep was followed by 80 s at holding potential before the next sweep. Often, the maximal amplitude of the first ramp in sweeps II–IV was smaller than the maximal amplitude of the first ramp in the previous sweep (probably due to a partial replenishment of PIP_2 between the sweeps). Using voltage ramps enabled to distinguish Kir2.1 from leak currents that may have developed due to deterioration of the cell during the protocol. When the ramp waveform did not have a typical Kir2.1 rectification the sweep was excluded. VSP effect was quantified from currents elicited by voltage ramps as the ratio between the maximal amplitude at −120 mV after (I2) and

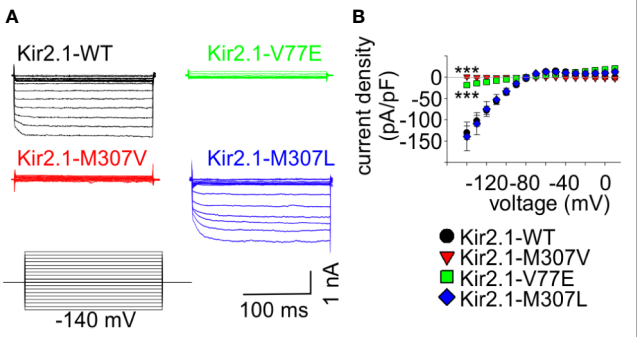

FIGURE 2 | Mutations V77E and M307V induce Kir2.1 loss-of-function. Net Ba^{2+}-sensitive currents recorded from HEK cells expressing Kir2.1-GFP (WT, V77E, M307V, M307L) elicited by a voltage-steps protocol. **(A)** Representative currents. **(B)** Average current density (WT, n = 12; V77E, n = 10; M307V, n = 6; M307L, n = 8). Statistical analysis in the voltage step to −140 mV using one-way ANOVA (Dunnett's test, comparison to WT). M307L, not significant; V77E and M307V, ***$p < 0.001$.

before (I1) the depolarizing step, and as % VSP effect according to ((1 − (I2/I1)) * 100). When the amplitude ratio was 1, the VSP effect was 0%, and if VSP activation abolished the current completely, I2/I1 was 0 and the VSP effect was 100%. Normalized ramp-elicited currents were divided by the maximal inward current at −120 mV and plotted against the voltage. The current density was calculated as the current amplitude divided by the capacitance of each cell. Normalized current density was compared to the mean current density of the control group at −120 mV. Cells transfected on the same day and recorded during a 2-day session were considered as one experiment. 50 μM BGP-15 (Cayman Chemical, Ann Arbor, MI, USA) were incubated overnight in cell culture medium and were added to the bath solution during recording.

Xenopus oocytes were injected with RNAs of Kir2.1 concatenated dimers (0.05, 0.1, or 1 ng of the WT dimer, as indicated, and 1 ng of the mutant dimers) and VSP (10 ng). Currents were recorded using the two-electrode voltage clamp (TEVC) technique. Oocytes were held at −30 mV and current–voltage relationships were produced by voltage ramps from −120 to 30 mV in 2 s. Bath solution contained (in mM): 24 KCl, 72 NaCl, 1 $CaCl_2$, 1 $MgCl_2$, and 5 HEPES, in pH = 7.4. Naïve cells' endogenous, depolarization-induced, inward currents (possibly *via* sodium or stretch-activated ion channels) were partially blocked by 50 μM Gd^{3+} (Baud et al., 1982; Yang and Sachs, 1989). The net Kir2.1 currents were obtained by subtraction of the mean current obtained with the same VSP activation protocol from four naïve oocytes from the same batch of oocytes in the same experiment or in the presence of 50 μM Gd^{3+}. VSP effect was quantified from currents elicited by voltage ramps as the ratio between the maximal amplitude at −80 mV. The reversal potential, V_{rev}, was the potential at which the net current was zero. The rectification index was calculated by the division of the current 50 mV positive to V_{rev} by the current 50 mV negative to V_{rev}.

Software and Data Analysis and Presentation

The structure of Kir2.2-V75E was generated by PyMOL (Molecular Graphics System, Version 2.0 Schrödinger) based on the crystal structure of Kir2.2 channel (PDB ID:3SPI). The rotamer with minimal steric clashes was selected. Subsequently, the energy minimization procedure was conducted by YASARA force field server default values (http://www.yasara.org) (Krieger et al., 2009).

DNA chromatogram was visualized by BioEdit. Multiple DNA sequence alignments were using CLUSTAL Omega 1.2.4. Western blot bands were quantified using ImageJ (NIH, United States). Figures were prepared using CorelDraw 2018 (Corel Corp., Ottawa, Canada). SigmaPlot 13 and 14 (Systat Software, CA, USA) and Prism (GraphPad, San Diego, CA, USA) were used for graph preparation and statistical assays. Currents were analyzed using Clampfit 10.7.

Data were presented as mean ± standard error or box plots indicating 25–75 percentiles (box borders), median (black line), mean (dotted red line), and 5–95 percentiles (whiskers). Statistical tests were performed on raw data. Two-group comparisons were performed using unpaired t-test if the data passed the Shapiro-Wilk normality test, otherwise, Mann–Whitney rank-sum test was used. Multiple group comparisons were done using one-way ANOVA, followed by Dunnet's tests for normally distributed data and Kruskal-Wallis one-way ANOVA on ranks followed by Dunn's test, otherwise. Two-way ANOVA with repeated measures was performed to compare current courses in voltage ramp protocol, between groups. ***, $p < 0.001$; **, $p < 0.01$; *, $p < 0.05$; ns, not significant.

RESULTS

Kir2.1 Variants V77E and M307V Are Associated With ATS

We have previously described a case of familial almost incessant polymorphous and bidirectional VT. Association of the disease with mutations in several calcium-handling related genes was excluded (Nof et al., 2004). Years later, a larger gene screening detected a c.919A > G substitution in the *KCNJ2* gene encoding the inward-rectifier potassium channel Kir2.1. This missense mutation led to a substitution of methionine at position 307 to valine (p.M307V) in the Kir2.1 protein (**Figure 1A**). Shortly after the report, one family member had a syncope while driving, and implantable cardioverter defibrillator (ICD) was implanted. Symptomatic arrhythmia events were not documented since then. Another family member was implanted with an ICD due to her ventricular arrhythmias. A few years later, she had a ventricular fibrillation (VF) storm which the ICD was able to terminate. All other family members described in the previous report (Nof et al., 2004) remained asymptomatic and were not implanted with ICD despite the heavy arrhythmic burden.

In another case, a 35-year-old woman with multiple premature ventricular contractions (PVCs) and non-sustained ventricular tachycardia (NSVT) was genetically and clinically evaluated. She reported a lower limb muscle weakness. A thigh-muscle biopsy, performed at another institute, was normal. ECG recording showed polymorphic and bidirectional VT at rest and exercise. Missense variation c.230T > A in *KCNJ2* was detected, leading to substitution of valine 77 to glutamic acid (p.V77E) in Kir2.1. Both parents did not carry the mutation in *KCNJ2*, and kinship genetic test based on single-nucleotide polymorphism (SNP) confirmed parenthood. Thus, V77E mutation is a *de-novo* mutation in the proband (**Figures 1A, B**). She developed tachycardia-induced cardiomyopathy with 40% left ventricular ejection fraction (LVEF). An ablation attempt was aborted due to the polymorphic nature of her PVCs, and an ICD was implanted. She did not receive any ICD shocks during follow up.

Following the association of the *KCNJ2* mutations with cardiac arrhythmia symptoms, ATS type-1 was diagnosed in the carriers of both mutations. The clinical manifestations included ventricular arrhythmias but without periodic paralysis or facial/skeletal dysmorphic features that have been previously reported, with a variable penetrance, in other ATS cases.

Residue M307 is located at the G-loop in Kir2.1 C-terminus. Residue V77 is located at the regulatory slide helix in Kir2.1 N-terminus (**Figure 1C**). Both residues are conserved among species and different inward-rectifier potassium channels. The hydrophobic valine 77 is highly conserved among 11 out of 15 *KCNJ* genes, and in all 15 *KCNJ* genes this position is occupied by hydrophobic residues. The hydrophobic methionine 307 is conserved in 8 out of 15 *KCNJ* genes (**Figure 1D**).

Both V77E and M307V Cause Kir2.1 Loss-of-Function Without Affecting Cell Surface Expression

In order to study the functional properties of the mutants, Kir2.1-GFP constructs were expressed in HEK cells, and currents were measured using whole-cell patch-clamp technique. During a voltage-step protocol, cells expressing Kir2.1-GFP WT showed large inward voltage-dependent currents at voltages negative to −80 mV that were blocked by 10 mM Ba^{2+}. The net Ba^{2+}-sensitive currents were inwardly rectifying with a reversal potential close to the calculated K^+ equilibrium potential (according to the calculated Nernst potential of −90 mV and liquid junction potential of 3.9 mV, the calculated reversal potential of K^+ is ~−86 mV), and small outward currents were recorded with voltage steps between −80 to −20 mV (**Figure 2**).

Expression of the Kir2.1-GFP V77E and M307V mutants produced almost no Ba^{2+}-sensitive currents, indicating that these are loss-of-function mutations. The substitution of M307 with the hydrophobic residue leucine (M307L) did not affect the current density and rectification that were similar to that of Kir2.1-GFP WT (**Figure 2**).

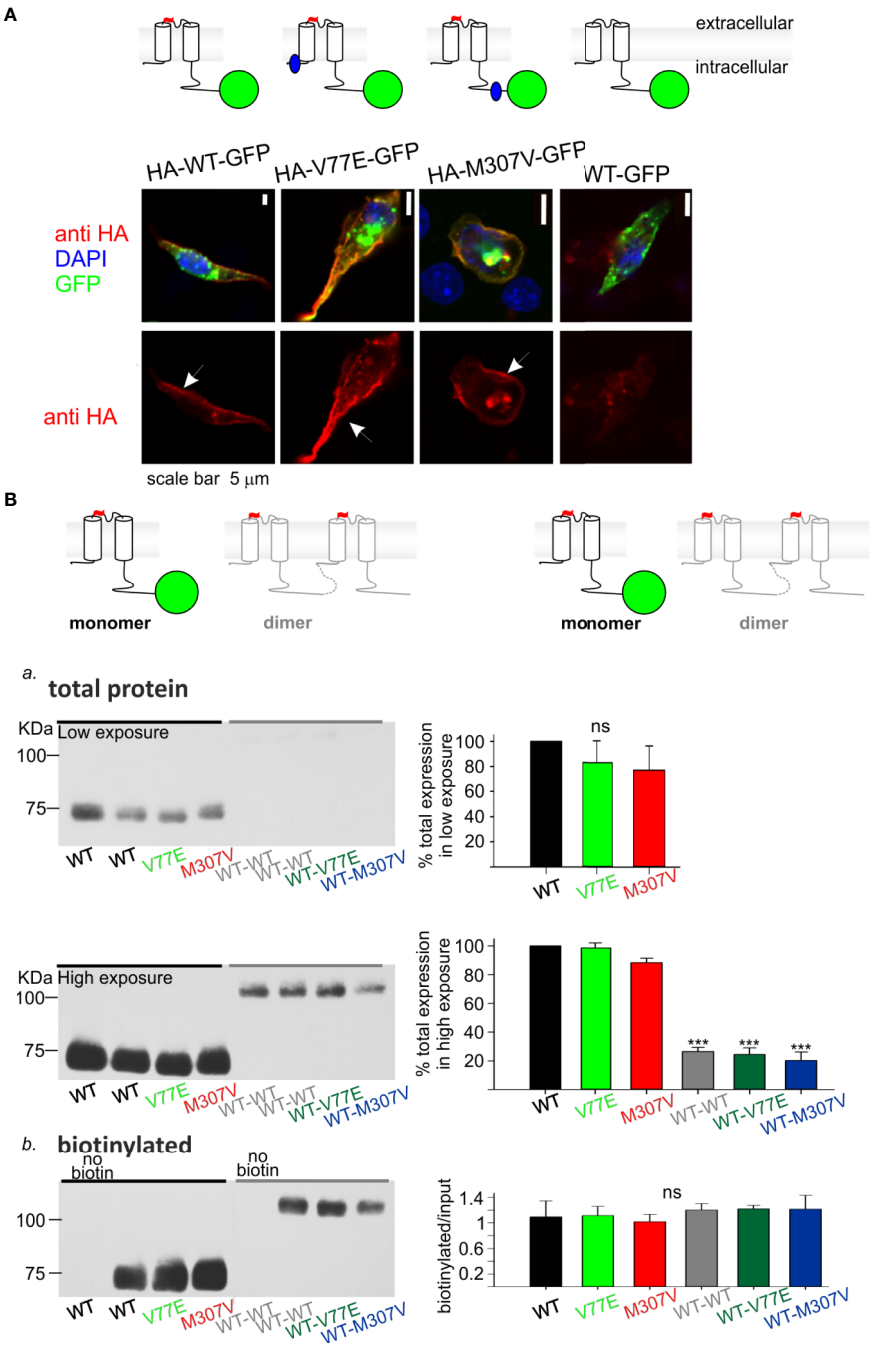

FIGURE 3 | Loss-of-function Kir2.1 mutations express on the cell surface. **(A)** Immunostaining of HL-1 cells transfected with Kir2.1-GFP with and without an extracellular HA-tag. Top, an illustration of the Kir2.1 subunit constructs. Cylinders: Kir2.1 transmembrane domains; blue: mutation location; green: GFP; Red: HA-tag. Bottom, HA-tag was immunostained (red), expressed GFP was detected (green) and the nucleus was stained with DAPI (blue). The three optical channels are superimposed (upper panel) and the red channel is also shown separately (lower panel). Arrows point to the cell surface signal. **(B)** Biotinylation of HEK cells transfected with Kir2.1-GFP monomers and Kir2.1 dimers (WT and mutant) as illustrated above and detected with the HA-tag antibody. Left, representative blots from one experiment. Right, normalized signals. *a*. Total Kir2.1 protein level. Total expression was normalized to WT in the same experiment. Low film exposure was used to quantify the difference in Kir2.1 monomers' level within a dynamic range (upper panel, N = 4). Statistical analysis: one-way ANOVA. The differences between Kir2.1 monomers and dimers were shown in high film exposure of the blot, where Kir2.1 monomer signal was saturated (lower panel, N = 3). Statistical analysis: one-way ANOVA (Dunnett's test, comparison to WT Group). *b*. biotin-labeled Kir2.1 level. As a control for non-specific signals, Kir2.1-GFP WT and WT dimer expressing groups were not incubated with biotin. The amount of protein on the plasma membrane relative to total was quantified by a division of the biotinylated with input level in high exposure (N = 3). Statistical analysis: one-way ANOVA.

To investigate whether protein synthesis and trafficking in these loss-of-function Kir2.1 variants were impaired, two methods were employed: imaging of immunofluorescent Kir2.1 and biochemical detection of cell-surface Kir2.1 by biotinylation (**Figure 3**).

Cultured HL-1 atrial cells (Claycomb et al., 1998) were transfected with the WT and mutated Kir2.1-GFP that included an extracellular HA-tag. We used Kir2.1-GFP WT construct that did not include the extracellular HA-tag, as control. HL-1 cells were gently fixed and immunostained with HA-tag antibody. Green fluorescence following the expression of the Kir2.1-GFP was observed, mainly as aggregates in cytoplasmic organelles (probably the endoplasmic reticulum and Golgi apparatus), but also at the cell periphery. Following immunostaining, red fluorescence was detected at the plasma membrane of cells expressing Kir2.1-GFP WT, V77E, and M307V, but not when the HA-tag was not expressed. When the red and green signals were superimposed, a yellow signal was detected on the cell border, demonstrating the expression of Kir2.1-GFP WT, V77E, and M307V at the cell surface (**Figure 3A**).

Next, HEK cells were transfected with Kir2.1-GFP and incubated with biotin. Biotin-labeled cell-membrane proteins and total protein fractions were analyzed using Western blot. Kir2.1-GFP WT, V77E, and M307V were detected at the cell surface with no significant difference between groups, indicating that V77E and M307V did not affect Kir2.1 cellular expression, or cell surface expression that possibly reflects trafficking [**Figures 3Ba** (upper panel), B*b*].

In order to investigate the functional and biochemical properties of each of the two variants, V77E and M307V, expressed in a heterozygotic context, we used a subunit concatenation strategy where two Kir2.1 subunits were fused as dimers. In the Kir2.1 dimers, the first Kir2.1 subunit was WT and the second subunit was either a WT subunit ("WT dimer") or a mutated subunit ("mutant dimers"). Kir2.1 subunits were connected with a flexible 10 a.a. linker that included eight glycines. When the same amount of DNA was used for the transfection of Kir2.1-GFP monomers and Kir2.1 dimers, total expression levels of Kir2.1 dimers were 20%–30% of the monomers, with no significant difference between the WT and mutant dimers (**Figure 3Ba**, lower panel, **Supplemental image 1**). The expressed Kir2.1 dimers were exported to the cell surface so that the biotinylated fractions of WT and mutant dimers were not significantly different from each other (**Figure 3Bb**, **Supplemental image 2**). These experiments show that the expression of Kir2.1 dimer on the plasma membrane is reduced compared to Kir2.1-GFP monomers, but the mutations do not affect the surface expression of either Kir2.1 monomers or dimers.

A reduction in WT dimer function correlated with the reduction in its expression level: normalized current density at −120 mV of the WT dimer was 28% ± 5% of the Kir2.1-GFP WT monomer (**Figure 4A**). The normalized current waveform elicited by voltage ramp from −120 to 0 mV showed only a small change in current rectification and selectivity properties of the WT dimer compared to the Kir2.1-GFP WT monomer (**Figure 4B**). These results demonstrate that Kir2.1 subunit concatenation partially affected protein expression, but the cell-surface expressed Kir2.1 composed of the WT dimers had functional properties similar to the Kir2.1-GFP WT monomers.

Both V77E and M307V Induce a Dominant-Negative Effect on Current Amplitude but Do Not Change the Selectivity and Rectification Properties

The construction of Kir2.1 dimers enabled functional investigation of loss-of-function mutant with a fixed stoichiometry of WT:mutant subunits within a Kir2.1 tetramer. Kir2.1 is expected to be an assembly of 2 dimers, therefore the expression of mutant dimers is expected to form Kir2.1 tetramer composed of two WT and two mutated subunits. As a control, we used the loss-of-function Kir2.1-R67W variant, previously reported as a dominant-negative mutant (Andelfinger et al., 2002) with no effect on cell surface expression (Kalscheur et al., 2014). When each of the mutant dimers were expressed (WT-V77E, WT-M307V, and WT-R67W), typical rectifying Kir2.1 currents were recorded in HEK cells (**Figure 4C**, left). However, when equal amounts of DNA were used for transfection of WT and mutant dimers, the normalized current densities of mutant dimers were 22% ± 3%, 19% ± 2%, and 30% ± 5%, for WT-V77E, WT-M307V, and WT-R67W, respectively, compared to WT dimer (**Figure 4C**, right). The prominent reduction in current indicates that V77E and M307V mutated subunits possibly exert a dominant-negative effect on the functional WT subunits since the reduction in current was beyond their expected relative expression (of 50%) in a Kir2.1 tetramer.

In order to confirm the dominant-negative effect of the mutants, RNA's of Kir2.1 dimers were injected in *Xenopus* oocytes, and currents were measured. RNA injection in *Xenopus* oocytes enabled to control protein expression and to limit variability between cells, compared to DNA transfection in HEK cells. Similar to HEK cells, oocytes' current amplitudes in mutants dimers were reduced to 18% ± 1%, 17% ± 1%, and 28% ± 3% of WT dimer, for WT-V77E, WT-M307V, and WT-R67W, respectively (**Figure 4Da**). These results in *Xenopus* oocytes corroborate the putative dominant-negative effect of the loss-of-function Kir2.1 variants M307V and V77E, as shown in HEK cells.

Although a dominant-negative effect is highly plausible, the subunits within the dimer may have additional features not seen in the native channel. Nonetheless, the previously reported dominant-negative variant R67W (Andelfinger et al., 2002) showed a similar reduction in amplitude within the dimer as the two novel mutations V77E and M307V.

Channel selectivity and rectification properties of the mutant dimers were analyzed in *Xenopus* oocytes. The calculation of these parameters in oocytes was reliable due to the large current amplitude compared to HEK cells. Oocytes were perfused with 24 mM K^+ solution (the cytosolic K^+ concentration in *Xenopus* oocytes is estimated ~100 mM (Dascal, 1987) and the calculated Nernst

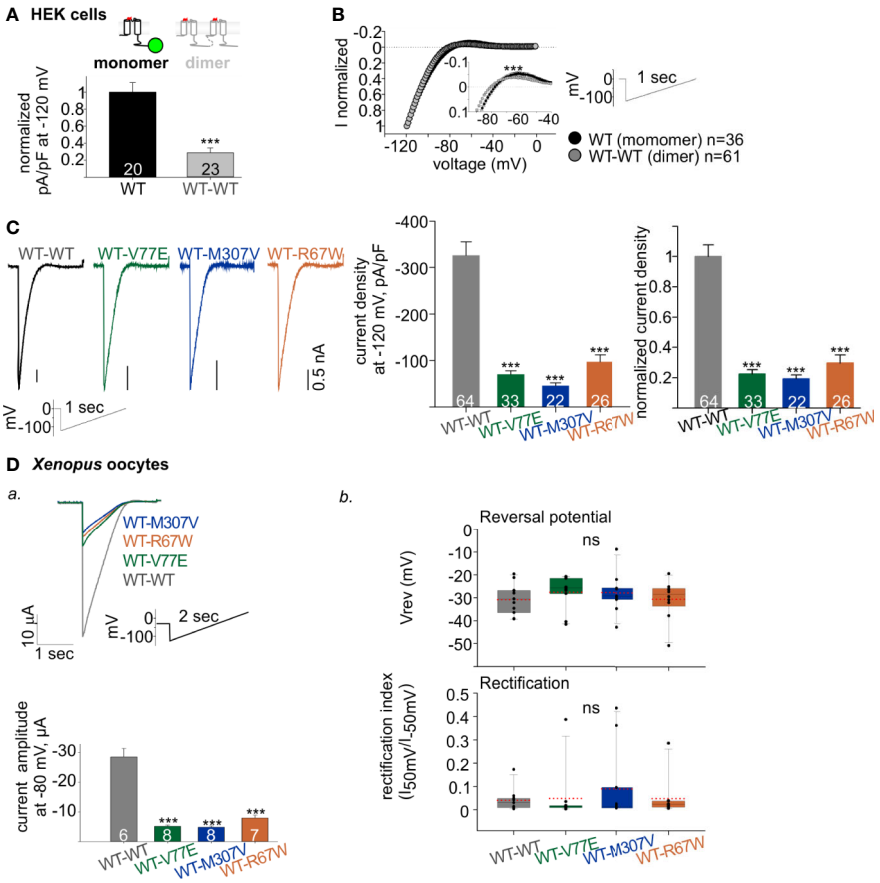

FIGURE 4 | Functional properties of Kir2.1 dimers. **(A)** Normalized current densities of Kir2.1-GFP WT monomer and WT dimers, recorded in HEK cells transfected with equal amounts of DNA. Normalization was performed to the mean current density of Kir2.1-GFP from the same experiment (N = 3). Statistical analysis: t-test. **(B)** Normalized currents (left) elicited by a ramp protocol (right). Every 10^{th} recorded point is presented. This is a summary of all cells from different experiments (N = 7 experiments for Kir2.1-GFP WT monomer and N = 12 for WT dimer). Inset, zoom on the reversal potential and the outward currents. Statistical analysis: two-way ANOVA with repeated measures, $p < 0.001$. **(C)** Left, representative currents elicited by ramp protocol of HEK cells expressing Kir2.1 dimers. Middle, current densities at −120 mV. Right, current density at −120 mV normalized to mean current density from cells expressing Kir2.1 WT dimers from the same experiment (WT-WT was compared to WT-V77E in N = 7, to WT-M307V in N = 4 and to WT-R67W in N = 6 experiments). Statistical analysis: one-way ANOVA (Dunn's test, comparison to WT Group). **(D)** Kir2.1 dimers RNA (1 ng/oocyte) was injected in *Xenopus* oocytes and recorded in 24 mM K^+ bath solution. *a.* Top, representative evoked currents by a voltage ramp protocol. Bottom, average current amplitudes at −80 mV. Statistical analysis: t-test compared to the WT-WT group. N = 1 experiment. *b*. Reversal potentials (Vrev) and rectification index calculated from the current elicited by voltage ramps, n = 10–11, N = 2 experiments. Statistical analysis: one-way ANOVA.

potential is ~−36 mV). The reversal potential and rectification index did not show a significant change when mutant dimers were compared to the WT dimer (**Figure 4Db**). Thus, although the dominant-negative mutants strongly reduced the whole-cell conductance in cells expressing Kir2.1 composed of the mutant dimers (WT-V77E, WT-M307V, and WT-R67W), the selectivity and rectification properties of the residual Kir2.1 currents were not affected, compared to Kir2.1 composed of the WT dimers.

Kir2.1 Mutations V77E, M307V, and R67W Increase Current Sensitivity to PIP_2 Depletion

We next characterized the functional sensitivity of Kir2.1 to PIP_2. We depleted PIP_2 membrane levels by voltage activation of VSP phosphatase that dephosphorylates plasma membrane phosphoinositide at 5′ position upon depolarization (Murata et al., 2005). PIP_2 depletion *via* VSPs results in a decay of Kir2.1 current (Murata and Okamura, 2007; Sakata and Okamura, 2014; Rjasanow et al., 2015).

We aimed to design a calibrated VSP activation protocol in order to quantify the VSP effect on Kir2.1 currents within a dynamic range. We coexpressed Kir2.1 and VSP in HEK cells and recorded the changes in Kir2.1 current amplitudes following a gradual increase in VSP activation time (**Figures 5A, B**) or voltage (**Figure 5C**). We employed a double-pulse voltage ramp protocol and measured the current amplitudes at −120 mV before VSP activation (I1) and after VSP activation (I2). We then calculated the I2/I1 ratio (left Y-

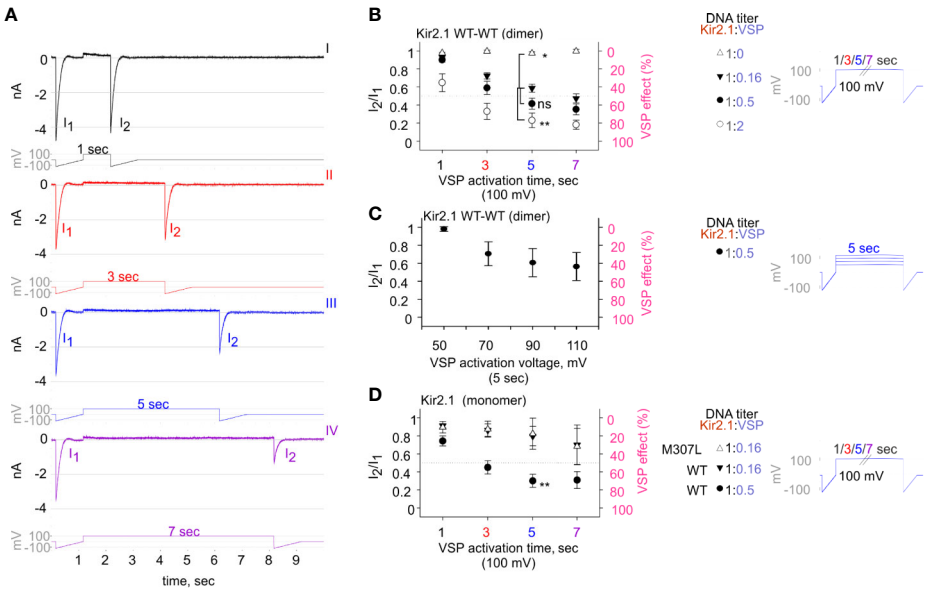

FIGURE 5 | The calibrated VSP activation protocol testing Kir2.1 sensitivity to PIP_2 depletion by VSP in HEK cells. **(A)** A representative four sweeps (I–IV)-protocol used to quantify Kir2.1 current amplitude reduction following VSP activation by depolarization. Each sweep started with a voltage ramp, followed by a 100-mV voltage step (for 1, 3, 5, or 7 s) and ended with a second voltage ramp. An example of currents elicited in a HEK cell transfected with Kir2.1 WT dimer and VSP in 1:0.16 DNA ratio. **(B–D)** Summary of the maximal amplitude ratio in each sweep after/before VSP activation (left Y-axis), also displayed as % VSP effect (right Y-axis, in pink). Voltage-protocol on the right. **(B)** At DNA ratio Kir2.1:VSP 1:0 (△), n = 10, 6, 4, 3; 1:0.16 (▼), n = 63, 63, 52, 44; 1:0.5 (•), n = 26, 22, 19, 18; 1:2 (○), n = 13, 10, 9, 8 for VSP activation at 100 mV for 1, 3, 5, and 7 s, respectively. Statistical analysis: one-way ANOVA at 5-s VSP activation [comparison to 1:0.16 (▼) group]. **(C)** VSP activation by steps to increasing voltages in each sweep (right). Currents amplitude ratio and the corresponding VSP effect from HEK cells transfected with WT dimer and VSP in 1:0.5 DNA ratio (left). n = 8, 8, 7, 6 for 5-s VSP activation at 50, 70, 90, and 110 mV, respectively. **(D)** Currents amplitude ratio and the corresponding VSP effect in Kir2.1-GFP monomers. At DNA ratio 1:0.16 of Kir2.1-GFP M307L:VSP (△), n = 5, 5, 4, 3; Kir2.1-GFP WT : VSP 1:0.16 (▼), n = 8, 9, 4, 4; Kir2.1-GFP WT : VSP 1:0.5 (•), n = 22, 19, 14, 9 for 1, 3, 5, and 7 s, respectively. Statistical analysis: t-test at 5-s VSP activation of the WT expressing groups, p = 0.004.

axis, **Figures 5B–D**) and the corresponding % VSP effect (right Y-axis, **Figures 5B–D**). VSP activation by 5-s depolarization to 100 mV was chosen as the standard duration for the following analysis.

VSP activation protocol was additionally calibrated using variable Kir2.1:VSP DNA ratios for transfection. In the group that did not express VSP (Kir2.1:VSP DNA ratio 1:0), the depolarizing pulses did not change the amplitude ratio of I2/I1 and the VSP effect was nearly 0 (**Figure 5B**, empty triangle). Raising the DNA proportion of VSP-to-WT dimers exacerbated the reduction in current amplitudes following VSP activation. After 5 s of depolarization to 100 mV, the second ramp evoked a slight reduction of 2.6% ± 1.7% in the current, in the absence of expressed VSP. When VSP was expressed, current reductions of 41% ± 4.5%, 58% ± 6%, and 77% ± 8% were evoked when the WT dimer:VSP DNA ratios were 1:0.16, 1:0.5, and 1:2, respectively (**Figure 5B**). Augmenting the depolarizing voltage of the 5-s step gradually increased the VSP effect on WT dimer current. VSP effect increased from 2% ± 2.6% to 29.5% ± 13.3%, 39.3% ± 15.6%, and 43.64% ± 15.6% for 50, 70, 90, and 110 mV, respectively (**Figure 5C**).

Current reduction following the VSP activation protocol was also observed in Kir2.1-GFP composed of monomers. The VSP effect was dependent on the transfected DNA proportion Kir2.1:VSP. After 5 s at 100 mV, the VSP effect increased from 20% ± 10% to 70% ± 7% when Kir2.1-GFP WT : VSP DNA ratios were 1:0.16 and 1:0.5, respectively (**Figure 5D**). VSP effect on the functional variant Kir2.1-GFP M307L was similar to that of Kir2.1-GFP WT. After 5 s of VSP activation at 100 mV, the VSP effect on Kir2.1-GFP M307L monomer was 17% ± 17% (Kir2.1:VSP DNA ratio 1:0.16, **Figure 5D**).

We then employed the calibrated VSP activation protocol on Kir2.1 mutant dimers, with the parameters that allowed quantification of Kir2.1 current response within a dynamic range. We transfected HEK cells with Kir2.1 WT and mutant dimers, at a Kir2.1:VSP DNA ratio of 1:0.16, and measured the VSP effect on Kir2.1 currents. Using the calibrated VSP activation protocol, with the 5-s step to 100 mV, the VSP effect increased from 41% ± 4.5% in Kir2.1 WT dimers, to 82% ± 3.7%, 81% ± 4.5%, and 74% ± 5.8% in mutant dimers (**Figures 6A, B**), representing a 197% ± 9%, 192% ± 11%, and 179% ± 14% increase in the normalized VSP effect of WT-V77E, WT-M307V, and WT-R67W currents, respectively (**Figure 6C**).

The current amplitude of the Kir2.1 mutant dimers WT-V77E and WT-M307V was 19%–22% of the WT-WT dimer (**Figure 4C**). This reduced current is expected to be the result of a reduced conductance and not due to low protein expression

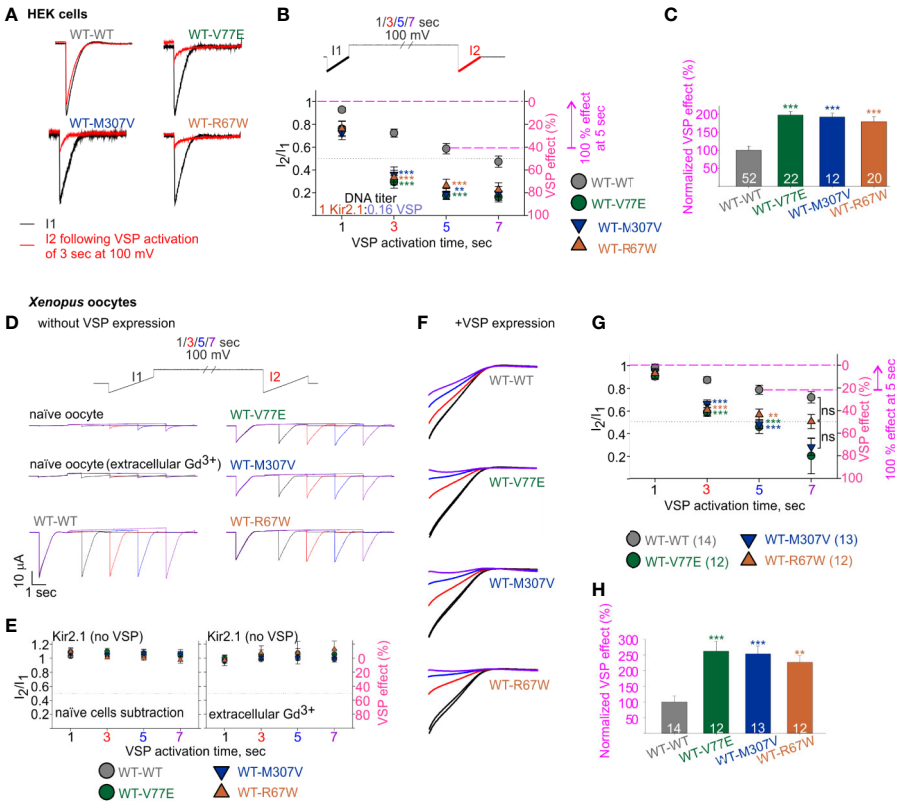

FIGURE 6 | Increased sensitivity of mutant dimers to PIP_2 depletion using the calibrated VSP activation protocol. **(A–C)** Currents in HEK cells expressing Kir2.1 dimers and VSP. **(A)** Representative ramp currents before (black) and after (red) VSP activation by a 3-s step to 100 mV. Traces of the WT dimer are the same as sweep II in **Figure 5A**. **(B)** Currents amplitude ratio and the corresponding VSP effect recorded from cells transfected with Kir2.1 dimer:VSP DNA ratio of 1:0.16. WT-WT is as summarized in **Figure 5B** (n = 63, 63, 52, 44). WT-V77E, n = 20, 20, 22, 17; WT-M307V, n = 16, 15, 12, 7; WT-R67W, n = 26, 24, 20, 15 for VSP activation by 100 mV step for 1, 3, 5, and 7 s, respectively. Statistical analysis: one-way ANOVA (Dunn's test, comparison to WT-WT group). At 5-s VSP activation: WT-V77E and WT-R67W, $p < 0.001$; WT-M307V, $p = 0.003$. The dashed magenta lines in panel B illustrate the normalizing value for the VSP effect on panel C. **(C)** Normalized VSP effect at a 5-s VSP activation compared to WT dimer. Statistical analysis: one-way ANOVA (Dunn's test, comparison to WT-WT Group). **(D–H)** Currents in *Xenopus* oocytes expressing Kir2.1 dimers without **(D, E)** and with VSP **(F–H)**. Representative currents in naïve and Kir2.1 dimers expressing oocytes **(D)**, and the average current amplitude ratio and the corresponding VSP effect (left, n = 7–8; right, n = 3–4) **(E)**. **(F)** Representative currents elicited in oocytes using the VSP activation protocol, and following subtraction of the averaged current from naïve cells. I1 and I2 of sweep I are in black, I2 of the sweeps II in red, III in blue, and IV in purple. Current amplitude ratio and the corresponding VSP effect **(G)** and the normalized VSP effect per experiment, at 5-s VSP activation **(H)**. N = 2 experiments. Statistical analysis at 3- and 5-s VSP activation was one-way ANOVA (Dunnett's test, comparison to WT-WT group). In panel G, at 5-s VSP activation, WT-R67W, $p = 0.005$. At 7-s VSP activation: statistical analysis was using Kruskal–Wallis one-way ANOVA. In panel H, statistical analysis was using Kruskal–Wallis one-way ANOVA. WT-R67W, $p = 0.003$. The dashed magenta lines in panel G illustrate the normalizing value for the VSP effect in panel **(H)**.

(**Figure 3B**). Thus, the Kir2.1:VSP expression ratio is expected to be similar in mutant compared to WT dimers, suggesting that the strong VSP effect reflects an increased sensitivity to PIP_2 depletion in Kir2.1 mutant dimers.

We sought to test the calibrated VSP activation protocol in *Xenopus* oocytes (**Figures 6D–H**). We started by applying the VSP activation protocol in naïve *Xenopus* oocytes. We detected time- and voltage-dependent endogenous inward currents. The current amplitude evoked by the voltage ramp increased following depolarization steps, and at −120 mV it often reached a few µA following a 7-s depolarization to 100 mV (**Figure 6D**, a representative naïve oocyte out of six, and one oocyte out of nine in the presence of Gd^{3+}). Thus, when we wanted to test VSP effect on Kir2.1 expressing oocytes, we either subtracted the mean current of naïve cells obtained by the VSP activation protocol or applied 50 µM Gd^{3+} in the external solution. Gd^{3+} partially inhibited the increase in the endogenous currents following the depolarization (**Figure 6D**), while Kir2.1 current amplitude and the VSP effect did not change (not shown). When VSP was not expressed in oocytes, the depolarizing pulses did not reduce the currents of WT and mutant dimers, when either method to avoid artifacts by endogenous currents was applied (**Figure 6E**).

We wanted to test whether the reduction in basal current amplitude itself in the mutant dimers' current (**Figure 4Da**) underlies the difference in VSP effect. Thus, we adjusted RNA amounts of WT and mutant dimes by injecting 10- to 20-fold less RNA of the WT dimer than of mutant dimers, to attain similar amplitudes. When Kir2.1:VSP RNA ratio was 0.1:10 or 0.05:10 in WT dimer and 1:10 in mutant dimers, the average

current amplitudes at −80 mV of WT dimer were −10 ± 1.1 μA for 0.1 ng RNA (n = 8) and −1.8 ± 0.11 μA for 0.05 ng RNA (n = 6), while the amplitudes of the mutant dimers were −3 ± 0.3 μA (n = 12), −2.3 ± 0.27 μA (n = 13), and −5 ± 1 μA (n = 12) for WT-V77E, WT-M307V, and WT-R67W, respectively.

Oocytes expressing both VSP and Kir2.1 dimers showed current amplitude decays during the VSP activation protocol (**Figure 6F**). The VSP effect was stronger in all mutant dimers compared to WT dimer, despite the lower Kir2.1:VSP RNA ratio used for WT dimer. The VSP effect, following a 5-s depolarization step to 100 mV, was 21% ± 4% in WT dimer and 54% ± 6%, 52% ± 64%, and 43% ± 65% in mutant dimers (**Figure 6G**), corresponding a normalized VSP effect of 262% ± 631%, 254% ± 625%, and 226% ± 621% in WT-V77E, WT-M307V, and WT-R67W, respectively (**Figure 6H**). These results demonstrate that the mutant dimers WT-V77E, WT-M307V, and WT-R67W have an increased sensitivity to PIP_2 depletion (and to a similar extent), compared to WT dimers of Kir2.1.

BGP-15 Decreases Kir2.1 Sensitivity to VSP-Induced PIP_2 Depletion

We studied the effect of BGP-15 on Kir2.1 current. BGP-15 has been previously shown to have cardio-protective properties and to reduce cardiac arrhythmias, possibly *via* lipid regulation (Gombos et al., 2011; Zhang et al., 2011; Gungor et al., 2014; Sapra et al., 2014). We hypothesized that BGP-15 affects lipid-regulated ion channels' function, consequently leading to an improvement in cardiac muscle function and reducing cardiac arrhythmia. HEK cells expressing Kir2.1 dimers and VSP were incubated overnight with BGP-15 (50 μM) and currents were recorded on the following day. Kir2.1 current density was not affected by BGP-15 incubation (**Figure 7A**, left). Selectivity and rectification of Kir2.1 current were barely affected by BGP-15 incubation, as shown by the normalized current waveform elicited by a voltage-ramp (**Figure 7A**, right).

We then examined the effect of BGP-15 incubation on the PIP_2 sensitivity of Kir2.1 WT dimers, using the VSP activation protocol (**Figure 7B**). Within the dynamic range of VSP action, BGP-15 incubation reduced the VSP effect. After 5 s of depolarization to 100 mV, VSP effect in BGP-15 treated cells decreased from 42% ± 7% to 12% ± 3% at 1:0.16 DNA ratio (**Figure 7C**, top) and from 59% ± 8% to 27% ± 7% at 1:0.5 DNA ratio (**Figure 7C**, middle). Basically, when normalized to the VSP effect without BGP-15 from the same experiment, VSP effect in BGP-15 treated cells was reduced to 30% ± 9% and 45% ± 12%, in cells transfected with Kir2.1:VSP DNA ratios of 1:0.16 and 1:0.5, respectively (**Figure 7E**). However, when the VSP proportion was raised to a DNA ratio of 1:2 Kir2.1:VSP, BGP-15 incubation did not reduce the VSP effect. After 5-s depolarization to 100 mV, VSP effect was 77% ± 8% in untreated cells, and 74% ± 7% in BGP-15 treated cells (**Figure 7C**, bottom), and the normalized VSP effect following BGP-15 incubation was 95% ± 6% (**Figure 7E**). To summarize, within a dynamic response range, BGP-15 incubation reduced the VSP effect and stabilized Kir2.1 amplitudes in the calibrated VSP activation protocol.

The VSP activation protocol was then used to test the effect of BGP-15 incubation on the PIP_2-sensitivity of Kir2.1 mutant dimers. Within the dynamic Kir2.1:VSP DNA ratio of 1:0.16 determined for WT dimers (**Figure 7C**), BGP-15 treatment reduced the VSP effect and increased its variability in the three mutant dimers, compared to the non-treated cells (**Figure 7D**). After 5-s depolarization to 100 mV, the normalized VSP effect following BGP-15 incubation was 74% ± 9%, 49% ± 14%, and 58% ± 9% of the corresponding non treated groups, for the mutant dimers WT-V77E, WT-M307V, and WT-R67W, respectively (**Figure 7E**).

In all, in this set of experiments BGP-15 incubation reduced Kir2.1 current susceptibility to PIP_2 depletion and stabilized Kir2.1 amplitudes in the calibrated VSP activation protocol, of both Kir2.1 WT and the ATS-associated mutant dimers.

DISCUSSION

In this study, we report on ATS associated with two mutations in *KCNJ2*, both induce a loss-of-function and exert a dominant-negative effect on the Kir2.1 tetramer. The major outcomes and findings include 1) development of a calibrated functional assay to assess PIP_2 sensitivity of Kir2.1 current that was tested by VSP activation, and 2) Kir2.1 mutants V77E, M307V, and R67W showed high sensitivity to PIP_2 depletion, which we interpret as lability in the PIP_2-Kir2.1 interaction, 3) BGP-15 incubation decreased the sensitivity to PIP_2 depletion, of both WT and mutant Kir2.1, possibly stabilizing the Kir2.1 open state.

Phenotypic Variability in ATS

ATS is a rare genetic disease, with a prevalence of 0.08–0.1:100,000 (Horga et al., 2013; Stunnenberg et al., 2018). Cardiac ventricular arrhythmias may include prolonged QT interval, prominent U-wave or ventricular ectopy. Bidirectional VTs were also reported with ATS, although clinical distinction from CPVT is challenging in the absence of other characteristics (Kimura et al., 2012; Chakraborty et al., 2015; Nguyen and Ferns, 2018).

Mutations in Ca^{2+}-handling proteins contribute to the etiology of CPVT, while impaired activity of inward-rectifier K^+-channels is the main cause of ATS (Napolitano et al., 2004; Veerapandiyan et al., 2004). In our report, identification of loss-of-function *KCNJ2* variants established an ATS-1 diagnosis. Although ATS-1 is considered a relatively benign channelopathy, some affected members had malignant ventricular arrhythmias that necessitated an ICD implantation.

The mode of inheritance of the familial M307V mutation was autosomal dominant. Expression was variable and gender-dependent: from six affected family members, three females reported palpitations and presented with incessant bidirectional VT. Two of them had symptomatic arrhythmia events and were implanted with an ICD. In contrast, the three males presented with PVCs, all with normal QT interval, and

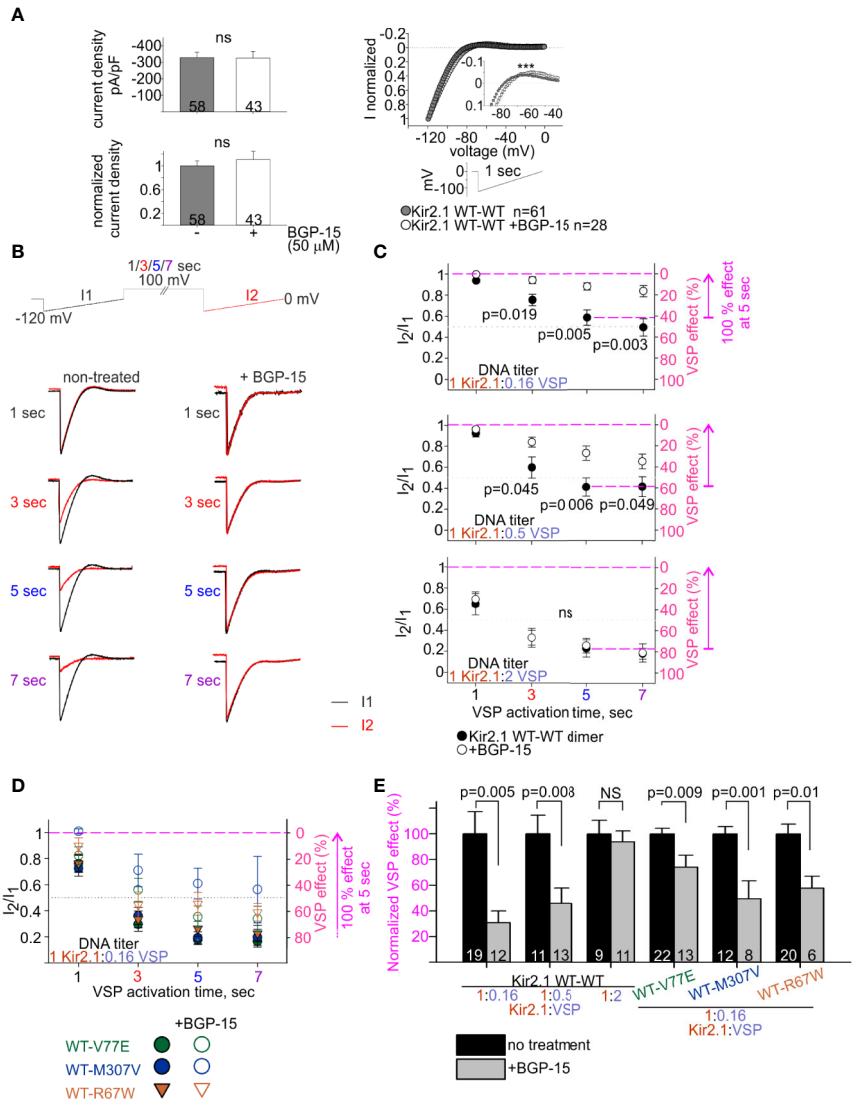

FIGURE 7 | BGP-15 reduces the sensitivity of mutant dimers to PIP_2 depletion using the calibrated VSP activation protocol. **(A)** Left, averaged current densities at −120 mV from HEK cells expressing Kir2.1 WT dimers with and without BGP-15 treatment. Top, current densities, bottom, current densities in cells that were incubated with BGP-15 and normalized to the mean current density in non-treated cells from the same experiment. Statistical analysis: Mann–Whitney rank-sum test. Right, ramp current waveform normalized to the current at −120 mV, from non-treated cells (same as WT dimer in **Figure 4B**), and BGP-15 treated cells. Statistical analysis: two-way ANOVA with repeated measures, $p < 0.001$. **(B)** Representative currents elicited in non-treated and 50 μM BGP-15 incubated HEK cells. Example in cells transfected with Kir2.1 WT dimer and VSP in 1:0.5 DNA ratio. **(C)** Average current amplitude ratio and the corresponding VSP effect of WT dimer and VSP expressing cells, following BGP-15 treatment. Top, n = 13, 12, 12, 11 for BGP-15-treated and n = 25, 21, 19, 15 for non-treated cells. N = 3 experiments. Middle, n = 16, 13, 13, 13 for BGP-15-treated and n = 17, 14, 11, 10 for non-treated cells. N = 2 experiments. Bottom, n = 12, 11, 11, 5 for BGP-15-treated and n = 13, 10, 9, 7 for non-treated cells. N = 2 experiments. Statistical analysis: t-test comparing treated with non-treated groups in the same protocol. **(D)** Average current amplitude ratio and the corresponding VSP effect of mutant dimer and VSP expressing cells with and without BGP-15 treatment. Kir2.1:VSP DNA ratio was 1:0.16. VSP effect from non-treated mutant dimers is the same as in **Figure 6B**. For BGP-15 treated groups, WT-V77E n = 18,16,13,7 from N = 3 experiments, WT-M307V n = 5,7,8,3 from N = 1 experiment, WT-R67W n = 7, 8, 6, 6 from N = 2 experiments. **(E)** Normalized VSP effect on Kir2.1 currents following a 5-s depolarization step to 100 mV. The mean VSP effect in non-treated cells (represented by dashed magenta lines in **(C, D)**, of each experiment, is the normalizing value for the VSP effect in panel **(E)**. Statistical analysis: t-test.

remained asymptomatic (Nof et al., 2004). The variant M307V was previously reported a *de novo KCNJ2* mutation in a 15-year-old male with ATS manifestations including muscular weakness and dysmorphic features, although his ECG findings were within a normal range (Liu et al., 2015). The V77E mutation occurred *de-novo*, as reported in 30-50% of *KCNJ2* mutations (Tristani-Firouzi et al., 2002; Hasegawa et al., 2015).

TABLE 1 | Missense variants in Kir2.1 slide helix.

Kir2.1 variant	Diagnosed disease	Reference
R67Q, R67W	ATS, long QT, periodic paralysis	(Eckhardt et al., 2007; Haruna et al., 2007; Andelfinger et al., 2002; Luo et al., 2019)
Y68D	ATS	(Davies et al., 2005)
A70S, A70T	Uncertain significance	ExAc, gnomAD
D71N, D71V, D71Y, D71H, D71E	ATS, long QT, periodic paralysis	(Plaster et al., 2001; Donaldson et al., 2003; Marrus et al., 2011; Luo et al., 2019), LOVD, ClinVar
I72M	Uncertain significance	ExAc, gnomAD
T74A	ATS	(Zhang et al., 2005)
T75M, T75A, T75R	ATS	(Donaldson et al., 2003; Fodstad et al., 2004; Davies et al., 2005)
C76G	Conflicting interpretations of pathogenicity	ClinVar
D78H, D78G, D78Y	ATS, long QT	ClinVar (Davies et al., 2005; Yoon et al., 2006)

ClinVar database obtained the data here from the genetic testing companies Blueprint Genetics, Invitae. and GeneDx.
LOVD, Leiden Open Variation Database, https://www.lovd.nl/; ExAc, The Exome Aggregation Consortium, http://exac.broadinstitute.org/; gnomAD, The Genome Aggregation Database, https://gnomad.broadinstitute.org; ATS, Andersen–Tawil syndrome.

Structural Analysis of the Mutated Kir2.1

The mutation V77E, located in the amphipathic slide helix of Kir2.1 N-terminus, is a substitution of a non-polar, hydrophobic, residue with a negatively charged residue. Most disease-associated variants in Kir2.1 slide helix were detected in polar residues facing the CTD (**Table 1**, **Figure 8A**). Inter and intra-subunit interactions in the interface of CTD and polar residues in the slide helix were suggested to transduce Kir2.1 opening (Decher et al., 2007; Bavro et al., 2012). The position of V77 side chain, in vicinity to the PIP_2 docking site and particularly the switch to a charged residue, may be implicated in the formation of a new molecular interaction that may have altered the channel interaction network and affected the activation dynamics or Kir2.1-PIP_2 docking, directly or indirectly. Positively charged residues K182, K185 and K187 on Kir2.1 inner TMD and the tether helix structure (equivalent to K183, R186, and K188 in Kir2.2), are candidates for such interaction. These residues directly interact with 5′ phosphate in the inositol ring of PIP_2 in a Kir2.2-PIP_2 structural model (Hansen et al., 2011; Lu et al., 2016).

We performed a limited structural analysis of Kir2.1 valine 77 substitution to glutamic acid, based on Kir2.2-PIP_2 crystal structure (PDB ID: 3SPI) where the corresponding residue is valine 75. The mutated residue E75 formed a putative polar contact with the residue R186 in Kir2.2, which is homologous to K185 in Kir2.1, a residue between the inner TMD and the tether helix (**Figure 8A**, right). Following the energy minimization simulation, we have seen that the R186 side chain is expected to rotate and face the E75 side chain, with a minimal distance of 1.9 Å between the charged residues. This interaction may reduce the flexibility of the tether helix or destabilize the interaction with the agonist PIP_2, consequently leading to the observed loss-of-function in Kir2.1-V77E.

Methionine 307 is located at the G-loop, a cytoplasmic gating structure in the apex of the CTD (Pegan et al., 2005) (**Figure 1C**). The functional role of the G-loop, its conformation in different gating states and its reciprocated modulation by Kir ligands remain incompletely understood (Pegan et al., 2006; Nishida

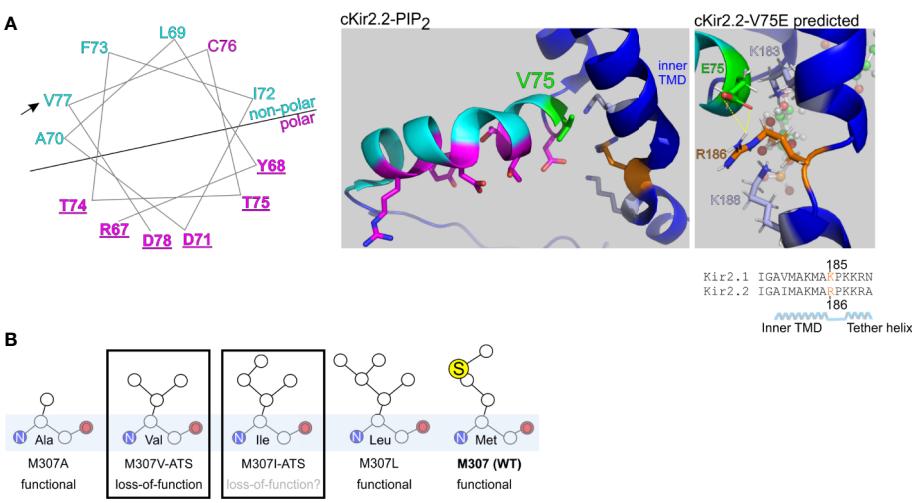

FIGURE 8 | Structural predictions of ATS-associated Kir2.1 variants. **(A)** Left, wheel plot illustration of the residues in Kir2.1 N-terminal slide helix. Polar residues in magenta, non-polar residues in cyan. Mutations in the underlined residues are disease-associated (**Table 1**). Arrow points on the ATS-associated residue in this report. Middle, polar (magenta) and non-polar (cyan) residues in chicken Kir2.2 + PIP_2 structure (PDB ID:3SPI). V75 in Kir2.2 (green) is the homolog of V77 in Kir2.1. Side chains of K183, K188 (light blue) and R186 (orange) are illustrated. Right, V75E mutation was introduced in Kir2.2 + PIP_2 structure and underwent a structural refinement. Putative interaction with R186 is shown in yellow. **(B)** Functional properties of Kir2.1 variants in position 307.

et al., 2007; Whorton and Mackinnon, 2011; Whorton and Mackinnon, 2013). However, alterations in the pore diameter, shape and biochemical properties conveyed by the G-loop residues' side chains are expected to lead to functional impairment (Ma et al., 2007). Our functional results show that unlike in the loss-of-function variant Kir2.1-M307V, currents measured in Kir2.1-M307L were indistinguishable from Kir2.1-WT (**Figure 2**), like in the previously reported Kir2.1 variant M307A (Pegan et al., 2005). However, the mutation M307I was found in ATS patients, presumably inducing Kir2.1 loss-of-function (Choi et al., 2007). Remarkably, the size of the hydrophobic side chain did not reflect a structural/functional tolerance (**Figure 8B**), and the potential of methionine to form disulfide bonds seems redundant. Further investigation is needed to shed light on the role of M307 residue, and G-loop in general, in the transition to the open state of Kir2.1.

Applying the Calibrated VSP Activation Protocol to Study PIP_2 Regulation of Kir2.1

PIP_2 is Kir2 primary agonist (Rohacs et al., 2003) and VSP activation reduces Kir2.1 current amplitude by depleting available PIP_2 molecules at the plasma membrane. We designed a protocol that correlated the changes in Kir2.1 amplitude ratios induced by a calibrated VSP activation, in two heterologous expression systems. We propose that the rate of Kir2.1 current reduction following VSP-induced PIP_2 depletion reflects Kir2.1 sensitivity to PIP_2 interaction so that an accelerated response rate is the consequence of a lower gating efficiency due to low PIP_2 affinity to Kir2.1.

In the calibrated VSP activation protocol we compared functional properties of dimer-composed Kir2.1 channels: the homomeric WT channel and the three heteromeric Kir2.1 mutants. We assumed that two dimers assembled into a tetrameric protein, but in a less-likely scenario four WT subunits originated from four mutated dimers might have assembled into one functional homomeric WT channel. This scenario cannot explain the increase in the VSP effect that occurred in mutant dimers but not in WT dimers (**Figure 6**).

The three Kir2.1 mutants putatively represent three mechanisms of Kir2.1 loss-of-function: V77E that destabilizes the tether helix, M307V that affects G-loop structure and R67W that is involved in inter-subunit interaction with the tether helix and the CTD. Yet, the three Kir2.1 mutant dimers showed a similar reduction in the amplitude compared to the WT dimer (**Figure 4**), and the calibrated VSP activation protocol did not reveal a difference in the VSP effect of the three mutant dimers (**Figure 6**), in two expression systems. We propose that the mechanisms of the pathogenic variants V77E, M307V, and R67W converge onto a similar impairment in the gating mechanism. One potential mechanism is a reduced affinity to the agonist PIP_2 in mutated Kir2.1 subunits and a total reduction in PIP_2 interaction in the heteromeric channel that destabilizes an open state. Based on available crystal structures, we propose a direct impairment of PIP_2 interaction in the V77E variant (**Figure 8**) and an allosteric effect in R67W and M307V variants that may impair an open state conformational transduction.

Finally, we tested the effect of BGP-15 on Kir2.1 currents and its therapeutic potential in ATS-associated Kir2.1 mutants. In a previous report, the oral administration of BGP-15 reduced AF episodes in genetically-engineered mice (Sapra et al., 2014). The AF was induced by age-dependent electrical remodeling that accompanied atrial enlargement in two transgenic mouse models with a dilated and failing heart. The AF mouse model had reduced ion channel expression, including *KCNJ3* (Kir3.1) and *KCNA5* (Kv1.5) genes (Sapra et al., 2014). Normalization of the fibrillation episodes by BGP-15 may have been related to the stabilization of the resting potential by an increased activity of potassium channels. In this study, following BGP-15 incubation, Kir2.1 currents were more resistant to PIP_2 depletion by VSP activation. We propose that BGP-15 is associated with the regulation of PIP_2 level, availability or localization, resulting in stabilization of Kir2.1 open-state. An indirect effect on other lipid regulators of Kir2.1 is plausible, e.g. *via* molulation of the interaction with Kir2.1 suppresor cholesterol, as BGP-15 was shown to remodel cholesterol-enriched lipid platforms (Romanenko et al., 2004; Gombos et al., 2011).

To note, Kir2.1 is predominantly expressed in the cardiac ventricles and ATS is an electrophysiologic disorder of the ventricle (Melnyk et al., 2002). However, other PIP_2-dependent inward rectifier potassium channels are expressed in the atria, mainly Kir2.2, Kir2.3, and acetylcholine-activated Kir3.1 and Kir3.4, in addition to other potassium channels such as Kv11.1 (hERG), Kv7.1 (KCNQ1), and Kir6.2 (Schram et al., 2002). Further investigation will shed light on whether the BGP-15 effect is shared by other PIP_2-dependent ion channels or is unique to Kir2.1.

CONCLUSION

In this study, two cases of ATS with cardiac arrhythmias were described, highlighting ATS phenotypic variability and resemblance with CPVT. The ATS-associated mutations, V77E and M307V, expand the spectrum of known *KCNJ2* mutations. Mutations were functionally and biochemically studied and showed loss-of-function with a dominant-negative effect. A calibrated protocol quantitated Kir2.1 current amplitude sensitivity to PIP_2 depletion and was tested on ATS-associated variants. The Kir2.1 variants showed increased PIP_2 sensitivity, which was partially restored by BGP-15.

DATA AVAILABILITY STATEMENT

The datasets generated for this study can be found in the LOVD [https://databases.lovd.nl/shared/variants/0000630833].

AUTHOR CONTRIBUTIONS

RH-J performed TEVC experiments. EM designed the study and prepared DNA constructs. DY performed simulations. LV performed biochemical studies. RB, MG, and EN evaluated the patients. ND, MG, JM, and SO acquired financial support for the

project. ND, JM, and SO conceived and planned the experiments. SO designed the study, performed patch-clamp experiments, and wrote the manuscript with input from all authors.

FUNDING

This work was supported by Dizengoff Trading Company (1952) Ltd. (MG), Israel Science Foundation (1282/18; ND), and Melbourne Biomedical Precinct Grant, Victorian Government's Trade and Investment Office for Israel Funding Program (JM and SO).

ACKNOWLEDGMENTS

We thank the patients and their families. We also thank Dr. Ronit S. Cherki for preliminary data and Prof. Yasushi Okamura (Osaka University, Japan) for dr-VSP construct.

SUPPLEMENTARY MATERIAL

The Supplementary Material for this article can be found online at: https://www.frontiersin.org/articles/10.3389/fphar.2020.00672/full#supplementary-material

REFERENCES

Andelfinger, G., Tapper, A. R., Welch, R. C., Vanoye, C. G., George, A. L. Jr., and Benson, D. W. (2002). KCNJ2 mutation results in Andersen syndrome with sex-specific cardiac and skeletal muscle phenotypes. *Am. J. Hum. Genet.* 71, 663–668. doi: 10.1086/342360

Balogi, Z., Multhoff, G., Jensen, T. K., Lloyd-Evans, E., Yamashima, T., Jaattela, M., et al. (2019). Hsp70 interactions with membrane lipids regulate cellular functions in health and disease. *Prog. Lipid Res.* 74, 18–30. doi: 10.1016/j.plipres.2019.01.004

Barajas-Martinez, H., Hu, D., Ontiveros, G., Caceres, G., Desai, M., Burashnikov, E., et al. (2011). Biophysical and molecular characterization of a novel de novo KCNJ2 mutation associated with Andersen-Tawil syndrome and catecholaminergic polymorphic ventricular tachycardia mimicry. *Circ. Cardiovasc. Genet.* 4, 51–57. doi: 10.1161/CIRCGENETICS.110.957696

Baud, C., Kado, R. T., and Marcher, K. (1982). Sodium channels induced by depolarization of the Xenopus laevis oocyte. *Proc. Natl. Acad. Sci. U. S. A.* 79, 3188–3192. doi: 10.1073/pnas.79.10.3188

Bavro, V. N., De Zorzi, R., Schmidt, M. R., Muniz, J. R., Zubcevic, L., Sansom, M. S., et al. (2012). Structure of a KirBac potassium channel with an open bundle crossing indicates a mechanism of channel gating. *Nat. Struct. Mol. Biol.* 19, 158–163. doi: 10.1038/nsmb.2208

Chakraborty, P., Kaul, B., Mandal, K., Isser, H. S., Bansal, S., and Subramanian, A. (2015). Bidirectional ventricular tachycardia of unusual etiology. *Indian Pacing Electrophysiol. J.* 15, 296–299. doi: 10.1016/j.ipej.2016.02.007

Choi, B. O., Kim, J., Suh, B. C., Yu, J. S., Sunwoo, I. N., Kim, S. J., et al. (2007). Mutations of KCNJ2 gene associated with Andersen-Tawil syndrome in Korean families. *J. Hum. Genet.* 52, 280–283. doi: 10.1007/s10038-006-0100-7

Claycomb, W. C., Lanson, N. A.Jr., Stallworth, B. S., Egeland, D. B., Delcarpio, J. B., Bahinski, A., et al. (1998). HL-1 cells: a cardiac muscle cell line that contracts and retains phenotypic characteristics of the adult cardiomyocyte. *Proc. Natl. Acad. Sci. U. S. A* 95, 2979–2984. doi: 10.1073/pnas.95.6.2979

Crul, T., Toth, N., Piotto, S., Literati-Nagy, P., Tory, K., Haldimann, P., et al. (2013). Hydroximic acid derivatives: pleiotropic HSP co-inducers restoring homeostasis and robustness. *Curr. Pharm. Des.* 19, 309–346. doi: 10.2174/138161213804143716

Dascal, N., and Lotan, I. (1992). "Expression of exogenous ion channels and neurotransmitter receptors in RNA-injected *Xenopus* oocytes," in *Protocols in Molecular Neurobiology*. Eds. A. Longstaff and P. Revest (Totowa, NJ: Humana Press), 205–225.

Dascal, N. (1987). The use of Xenopus oocytes for the study of ion channels. *CRC Crit. Rev. Biochem.* 22, 317–387. doi: 10.3109/10409238709086960

Davies, N. P., Imbrici, P., Fialho, D., Herd, C., Bilsland, L. G., Weber, A., et al. (2005). Andersen-Tawil syndrome: new potassium channel mutations and possible phenotypic variation. *Neurology* 65, 1083–1089. doi: 10.1212/01.wnl.0000178888.03767.74

Decher, N., Renigunta, V., Zuzarte, M., Soom, M., Heinemann, S. H., Timothy, K. W., et al. (2007). Impaired interaction between the slide helix and the C-terminus of Kir2.1: a novel mechanism of Andersen syndrome. *Cardiovasc. Res.* 75, 748–757. doi: 10.1016/j.cardiores.2007.05.010

Donaldson, M. R., Jensen, J. L., Tristani-Firouzi, M., Tawil, R., Bendahhou, S., Suarez, W. A., et al. (2003). PIP2 binding residues of Kir2.1 are common targets of mutations causing Andersen syndrome. *Neurology* 60, 1811–1816. doi: 10.1212/01.WNL.0000072261.14060.47

Eckhardt, L. L., Farley, A. L., Rodriguez, E., Ruwaldt, K., Hammill, D., Tester, D. J., et al. (2007). KCNJ2 mutations in arrhythmia patients referred for LQT testing: a mutation T305A with novel effect on rectification properties. *Heart Rhythm.* 4, 323–329. doi: 10.1016/j.hrthm.2006.10.025

Fodstad, H., Swan, H., Auberson, M., Gautschi, I., Loffing, J., Schild, L., et al. (2004). Loss-of-function mutations of the K(+) channel gene KCNJ2 constitute a rare cause of long QT syndrome. *J. Mol. Cell Cardiol.* 37, 593–602. doi: 10.1016/j.yjmcc.2004.05.011

Gehrig, S. M., Van Der Poel, C., Sayer, T. A., Schertzer, J. D., Henstridge, D. C., Church, J. E., et al. (2012). Hsp72 preserves muscle function and slows progression of severe muscular dystrophy. *Nature* 484, 394–398. doi: 10.1038/nature10980

Gombos, I., Crul, T., Piotto, S., Gungor, B., Torok, Z., Balogh, G., et al. (2011). Membrane-lipid therapy in operation: the HSP co-inducer BGP-15 activates stress signal transduction pathways by remodeling plasma membrane rafts. *PloS One* 6, e28818. doi: 10.1371/journal.pone.0028818

Gungor, B., Gombos, I., Crul, T., Ayaydin, F., Szabo, L., Torok, Z., et al. (2014). Rac1 participates in thermally induced alterations of the cytoskeleton, cell morphology and lipid rafts, and regulates the expression of heat shock proteins in B16F10 melanoma cells. *PloS One* 9, e89136. doi: 10.1371/journal.pone.0089136

Hansen, S. B., Tao, X., and Mackinnon, R. (2011). Structural basis of PIP2 activation of the classical inward rectifier K+ channel Kir2.2. *Nature* 477, 495–498. doi: 10.1038/nature10370

Haruna, Y., Kobori, A., Makiyama, T., Yoshida, H., Akao, M., Doi, T., et al. (2007). Genotype-phenotype correlations of KCNJ2 mutations in Japanese patients with Andersen-Tawil syndrome. *Hum. Mutat.* 28, 208. doi: 10.1002/humu.9483

Hasegawa, K., Ohno, S., Kimura, H., Itoh, H., Makiyama, T., Yoshida, Y., et al. (2015). Mosaic KCNJ2 mutation in Andersen-Tawil syndrome: targeted deep sequencing is useful for the detection of mosaicism. *Clin. Genet.* 87, 279–283. doi: 10.1111/cge.12357

Horga, A., Raja Rayan, D. L., Matthews, E., Sud, R., Fialho, D., Durran, S. C., et al. (2013). Prevalence study of genetically defined skeletal muscle channelopathies in England. *Neurology* 80, 1472–1475. doi: 10.1212/WNL.0b013e31828cf8d0

Hosaka, Y., Hanawa, H., Washizuka, T., Chinushi, M., Yamashita, F., Yoshida, T., et al. (2003). Function, subcellular localization and assembly of a novel mutation of KCNJ2 in Andersen's syndrome. *J. Mol. Cell Cardiol.* 35, 409–415. doi: 10.1016/S0022-2828(03)00046-4

Hossain, M. I., Iwasaki, H., Okochi, Y., Chahine, M., Higashijima, S., Nagayama, K., et al. (2008). Enzyme domain affects the movement of the voltage sensor in ascidian and zebrafish voltage-sensing phosphatases. *J. Biol. Chem.* 283, 18248–18259. doi: 10.1074/jbc.M706184200

Huang, C. L., Feng, S., and Hilgemann, D. W. (1998). Direct activation of inward rectifier potassium channels by PIP2 and its stabilization by Gbetagamma. *Nature* 391, 803–806. doi: 10.1038/35882

Kalscheur, M. M., Vaidyanathan, R., Orland, K. M., Abozeid, S., Fabry, N., Maginot, K. R., et al. (2014). KCNJ2 mutation causes an adrenergic-dependent rectification abnormality with calcium sensitivity and ventricular arrhythmia. *Heart Rhythm.* 11, 885–894. doi: 10.1016/j.hrthm.2014.02.015

Kimura, H., Zhou, J., Kawamura, M., Itoh, H., Mizusawa, Y., Ding, W. G., et al. (2012). Phenotype variability in patients carrying KCNJ2 mutations. *Circ. Cardiovasc. Genet.* 5, 344–353. doi: 10.1161/CIRCGENETICS.111.962316

Kokunai, Y., Nakata, T., Furuta, M., Sakata, S., Kimura, H., Aiba, T., et al. (2014). A Kir3.4 mutation causes Andersen-Tawil syndrome by an inhibitory effect on Kir2.1. *Neurology* 82, 1058–1064. doi: 10.1212/WNL.0000000000000239

Krieger, E., Joo, K., Lee, J., Lee, J., Raman, S., Thompson, J., et al. (2009). Improving physical realism, stereochemistry, and side-chain accuracy in homology modeling: Four approaches that performed well in CASP8. *Proteins* 77 (Suppl 9), 114–122. doi: 10.1002/prot.22570

Lacin, E., Aryal, P., Glaaser, I. W., Bodhinathan, K., Tsai, E., Marsh, N., et al. (2017). Dynamic role of the tether helix in PIP2-dependent gating of a G protein-gated potassium channel. *J. Gen. Physiol.* 149 (8), 799–811. doi: 10.1085/jgp.201711801

Literati-Nagy, B., Tory, K., Peitl, B., Bajza, A., Koranyi, L., Literati-Nagy, Z., et al. (2014). Improvement of insulin sensitivity by a novel drug candidate, BGP-15, in different animal studies. *Metab. Syndr. Relat. Disord.* 12, 125–131. doi: 10.1089/met.2013.0098

Liu, X. L., Huang, X. J., Luan, X. H., Zhou, H. Y., Wang, T., Wang, J. Y., et al. (2015). Case report: A Chinese child with Andersen-Tawil syndrome due to a de novo KCNJ2 mutation. *J. Neurol. Sci.* 352, 105–106. doi: 10.1016/j.jns.2015.02.027

Lopes, C. M., Zhang, H., Rohacs, T., Jin, T., Yang, J., and Logothetis, D. E. (2002). Alterations in conserved Kir channel-PIP2 interactions underlie channelopathies. *Neuron* 34, 933–944. doi: 10.1016/S0896-6273(02)00725-0

Lu, S., An, H., Zhang, H., and Long, M. (2016). Structural Basis for Differences in Dynamics Induced by Leu Versus Ile Residues in the CD Loop of Kir Channels. *Mol. Neurobiol.* 53, 5948–5961. doi: 10.1007/s12035-015-9466-x

Luo, S., Xu, M., Sun, J., Qiao, K., Song, J., Cai, S., et al. (2019). Identification of gene mutations in patients with primary periodic paralysis using targeted next-generation sequencing. *BMC Neurol.* 19, 92. doi: 10.1186/s12883-019-1322-6

Ma, D., Tang, X. D., Rogers, T. B., and Welling, P. A. (2007). An andersen-Tawil syndrome mutation in Kir2.1 (V302M) alters the G-loop cytoplasmic K+ conduction pathway. *J. Biol. Chem.* 282, 5781–5789. doi: 10.1074/jbc.M608776200

Ma, D., Taneja, T. K., Hagen, B. M., Kim, B. Y., Ortega, B., Lederer, W. J., et al. (2011). Golgi export of the Kir2.1 channel is driven by a trafficking signal located within its tertiary structure. *Cell* 145, 1102–1115. doi: 10.1016/j.cell.2011.06.007

Marrus, S. B., Cuculich, P. S., Wang, W., and Nerbonne, J. M. (2011). Characterization of a novel, dominant negative KCNJ2 mutation associated with Andersen-Tawil syndrome. *Channels (Austin)* 5, 500–509. doi: 10.4161/chan.5.6.18524

Melnyk, P., Zhang, L., Shrier, A., and Nattel, S. (2002). Differential distribution of Kir2.1 and Kir2.3 subunits in canine atrium and ventricle. *Am. J. Physiol. Heart Circ. Physiol.* 283, H1123–H1133. doi: 10.1152/ajpheart.00934.2001

Murata, Y., and Okamura, Y. (2007). Depolarization activates the phosphoinositide phosphatase Ci-VSP, as detected in Xenopus oocytes coexpressing sensors of PIP2. *J. Physiol.* 583, 875–889. doi: 10.1113/jphysiol.2007.134775

Murata, Y., Iwasaki, H., Sasaki, M., Inaba, K., and Okamura, Y. (2005). Phosphoinositide phosphatase activity coupled to an intrinsic voltage sensor. *Nature* 435, 1239–1243. doi: 10.1038/nature03650

Napolitano, C., Priori, S. G., and Bloise, R. (2004). *Catecholaminergic Polymorphic Ventricular Tachycardia*. (University of Washington, Seattle, USA: GeneReviews) Bookshelf ID: NBK1289.

Nascimento, T. L., Silva, M. T., and Miyabara, E. H. (2018). BGP-15 improves contractile function of regenerating soleus muscle. *J. Muscle Res. Cell Motil.* 39, 25–34. doi: 10.1007/s10974-018-9495-y

Nguyen, D., and Ferns, S. J. (2018). Asymptomatic ventricular tachycardia: diagnostic pitfalls of Andersen-Tawil syndrome-a case report. *Eur. Heart J. Case Rep.* 2, yty083. doi: 10.1093/ehjcr/yty083

Nishida, M., Cadene, M., Chait, B. T., and Mackinnon, R. (2007). Crystal structure of a Kir3.1-prokaryotic Kir channel chimera. *EMBO J.* 26, 4005–4015. doi: 10.1038/sj.emboj.7601828

Nof, E., Lahat, H., Constantini, N., Luria, D., Rosenfeld, G., Eldar, M., et al. (2004). A novel form of familial bidirectional ventricular tachycardia. *Am. J. Cardiol.* 93, 231–234. doi: 10.1016/j.amjcard.2003.09.049

Nof, E., Vysochek, L., Meisel, E., Burashnikov, E., Antzelevitch, C., Clatot, J., et al. (2019). Mutations in NaV1.5 Reveal Calcium-Calmodulin Regulation of Sodium Channel. *Front. Physiol.* 10, 700. doi: 10.3389/fphys.2019.00700

Oz, S., Pankonien, I., Belkacemi, A., Flockerzi, V., Klussmann, E., Haase, H., et al. (2017). Protein kinase A regulates C-terminally truncated CaV 1.2 in Xenopus oocytes: roles of N- and C-termini of the alpha1C subunit. *J. Physiol.* 595, 3181–3202. doi: 10.1113/JP274015

Pegan, S., Arrabit, C., Zhou, W., Kwiatkowski, W., Collins, A., Slesinger, P. A., et al. (2005). Cytoplasmic domain structures of Kir2.1 and Kir3.1 show sites for modulating gating and rectification. *Nat. Neurosci.* 8, 279–287. doi: 10.1038/nn1411

Pegan, S., Arrabit, C., Slesinger, P. A., and Choe, S. (2006). Andersen's syndrome mutation effects on the structure and assembly of the cytoplasmic domains of Kir2.1. *Biochemistry* 45, 8599–8606. doi: 10.1021/bi060653d

Plaster, N. M., Tawil, R., Tristani-Firouzi, M., Canun, S., Bendahhou, S., Tsunoda, A., et al. (2001). Mutations in Kir2.1 cause the developmental and episodic electrical phenotypes of Andersen's syndrome. *Cell* 105, 511–519. doi: 10.1016/S0092-8674(01)00342-7

Racz, I., Tory, K., Gallyas, F.Jr., Berente, Z., Osz, E., Jaszlits, L., et al. (2002). BGP-15 - a novel poly(ADP-ribose) polymerase inhibitor - protects against nephrotoxicity of cisplatin without compromising its antitumor activity. *Biochem. Pharmacol.* 63, 1099–1111. doi: 10.1016/S0006-2952(01)00935-2

Rjasanow, A., Leitner, M. G., Thallmair, V., Halaszovich, C. R., and Oliver, D. (2015). Ion channel regulation by phosphoinositides analyzed with VSPs-PI(4,5)P2 affinity, phosphoinositide selectivity, and PI(4,5)P2 pool accessibility. *Front. Pharmacol.* 6, 127. doi: 10.3389/fphar.2015.00127

Rohacs, T., Lopes, C. M., Jin, T., Ramdya, P. P., Molnar, Z., and Logothetis, D. E. (2003). Specificity of activation by phosphoinositides determines lipid regulation of Kir channels. *Proc. Natl. Acad. Sci. U. S. A* 100, 745–750. doi: 10.1073/pnas.0236364100

Romanenko, V. G., Fang, Y., Byfield, F., Travis, A. J., Vandenberg, C. A., Rothblat, G. H., et al. (2004). Cholesterol sensitivity and lipid raft targeting of Kir2.1 channels. *Biophys. J.* 87, 3850–3861. doi: 10.1529/biophysj.104.043273

Sakata, S., and Okamura, Y. (2014). Phosphatase activity of the voltage-sensing phosphatase, VSP, shows graded dependence on the extent of activation of the voltage sensor. *J. Physiol.* 592, 899–914. doi: 10.1113/jphysiol.2013.263640

Sapra, G., Tham, Y. K., Cemerlang, N., Matsumoto, A., Kiriazis, H., Bernardo, B. C., et al. (2014). The small-molecule BGP-15 protects against heart failure and atrial fibrillation in mice. *Nat. Commun.* 5, 5705. doi: 10.1038/ncomms6705

Schram, G., Pourrier, M., Melnyk, P., and Nattel, S. (2002). Differential distribution of cardiac ion channel expression as a basis for regional specialization in electrical function. *Circ. Res.* 90, 939–950. doi: 10.1161/01.RES.0000018627.89528.6F

Shistik, E., Ivanina, T., Blumenstein, Y., and Dascal, N. (1998). Crucial role of N terminus in function of cardiac L-type Ca2+ channel and its modulation by protein kinase C. *J. Biol. Chem.* 273, 17901–17909. doi: 10.1074/jbc.273.28.17901

Stunnenberg, B. C., Raaphorst, J., Deenen, J. C. W., Links, T. P., Wilde, A. A., Verbove, D. J., et al. (2018). Prevalence and mutation spectrum of skeletal muscle channelopathies in the Netherlands. *Neuromuscul. Disord.* 28, 402–407. doi: 10.1016/j.nmd.2018.03.006

Tawil, R., Ptacek, L. J., Pavlakis, S. G., Devivo, D. C., Penn, A. S., Ozdemir, C., et al. (1994). Andersen's syndrome: potassium-sensitive periodic paralysis, ventricular ectopy, and dysmorphic features. *Ann. Neurol.* 35, 326–330. doi: 10.1002/ana.410350313

Tristani-Firouzi, M., Jensen, J. L., Donaldson, M. R., Sansone, V., Meola, G., Hahn, A., et al. (2002). Functional and clinical characterization of KCNJ2 mutations associated with LQT7 (Andersen syndrome). *J. Clin. Invest.* 110, 381–388. doi: 10.1172/JCI15183

Veerapandiyan, A., Statland, J. M., and Tawil, R. (2004). *Andersen-Tawil Syndrome*. (University of Washington, Seattle, USA: GeneReviews) Bookshelf ID: NBK1264.

Whorton, M. R., and Mackinnon, R. (2011). Crystal structure of the mammalian GIRK2 K+ channel and gating regulation by G proteins, PIP2, and sodium. *Cell* 147, 199–208. doi: 10.1016/j.cell.2011.07.046

Whorton, M. R., and Mackinnon, R. (2013). X-ray structure of the mammalian GIRK2-betagamma G-protein complex. *Nature* 498, 190–197. doi: 10.1038/nature12241

Yang, X. C., and Sachs, F. (1989). Block of stretch-activated ion channels in Xenopus oocytes by gadolinium and calcium ions. *Science* 243, 1068–1071. doi: 10.1126/science.2466333

Yoon, G., Oberoi, S., Tristani-Firouzi, M., Etheridge, S. P., Quitania, L., Kramer, J. H., et al. (2006). Andersen-Tawil syndrome: prospective cohort analysis and expansion of the phenotype. *Am. J. Med. Genet. A* 140, 312–321. doi: 10.1002/ajmg.a.31092

Zhang, L., Benson, D. W., Tristani-Firouzi, M., Ptacek, L. J., Tawil, R., Schwartz, P. J., et al. (2005). Electrocardiographic features in Andersen-Tawil syndrome patients with KCNJ2 mutations: characteristic T-U-wave patterns predict the KCNJ2 genotype. *Circulation* 111, 2720–2726. doi: 10.1161/CIRCULATIONAHA.104.472498

Zhang, D., Ke, L., Mackovicova, K., Van Der Want, J. J., Sibon, O. C., Tanguay, R. M., et al. (2011). Effects of different small HSPB members on contractile dysfunction and structural changes in a Drosophila melanogaster model for Atrial Fibrillation. *J. Mol. Cell Cardiol.* 51, 381–389. doi: 10.1016/j.yjmcc.2011.06.008

Conflict of Interest: The authors declare that the research was conducted in the absence of any commercial or financial relationships that could be construed as a potential conflict of interest.

The authors declare that this study received funding from Dizengoff Trading Company (1952) Ltd. The funder was not involved in the study design, collection, analysis, interpretation of data, the writing of this article, or the decision to submit it for publication.

frontiers in Pharmacology

ORIGINAL RESEARCH
published: 20 May 2020
doi: 10.3389/fphar.2020.00704

Monoterpenes Differently Regulate Acid-Sensitive and Mechano-Gated K_{2P} Channels

Eden Arazi[1], *Galit Blecher*[1] *and Noam Zilberberg*[1,2]*

[1] Department of Life Sciences Ben-Gurion University of the Negev, Beer-Sheva, Israel, [2] The Zlotowski Center for Neuroscience, Ben-Gurion University of the Negev, Beer-Sheva, Israel

Potassium K_{2P} ("leak") channels conduct current across the entire physiological voltage range and carry leak or "background" currents that are, in part, time- and voltage-independent. The activity of K_{2P} channels affects numerous physiological processes, such as cardiac function, pain perception, depression, neuroprotection, and cancer development. We have recently established that, when expressed in *Xenopus laevis* oocytes, K_{2P}2.1 (TREK-1) channels are activated by several monoterpenes (MTs). Here, we show that, within a few minutes of exposure, other mechano-gated K_{2P} channels, K_{2P}4.1 (TRAAK) and K_{2P}10.1 (TREK-2), are opened by monoterpenes as well (up to an eightfold increase in current). Furthermor\e, carvacrol and cinnamaldehyde robustly enhance currents of the alkaline-sensitive K_{2P}5.1 (up to a 17-fold increase in current). Other members of the K_{2P} potassium channels, K_{2P}17.1, K_{2P}18.1, but not K_{2P}16.1, were also activated by various MTs. Conversely, the activity of members of the acid-sensitive (TASK) K_{2P} channels (K_{2P}3.1 and K_{2P}9.1) was rapidly decreased by monoterpenes. We found that MT selectively decreased the voltage-dependent portion of the current and that current inhibition was reduced with the elevation of external K^+ concentration. These findings suggest that penetration of MTs into the outer leaflet of the membrane results in immediate changes at the selectivity filter of members of the TASK channel family. Thus, we suggest MTs as promising new tools for the study of K_{2P} channels' activity *in vitro* as well as *in vivo*.

Keywords: K_{2P} channel, TREK-1, TRAAK, TASK-1, TALK, monoterpenes, leak channels, voltage-dependent current

OPEN ACCESS

Edited by:
Moran Rubinstein, Tel Aviv University, Israel

Reviewed by:
Sharon Weiss, Tel Aviv University, Israel
Yael Stern-Bach, Hebrew University of Jerusalem, Israel

***Correspondence:**
Noam Zilberberg
noamz@bgu.ac.il

Specialty section:
This article was submitted to Pharmacology of Ion Channels and Channelopathies, a section of the journal Frontiers in Pharmacology

Received: *17 September 2019*
Accepted: *29 April 2020*
Published: *20 May 2020*

Citation:
Arazi E, Blecher G and Zilberberg N (2020) Monoterpenes Differently Regulate Acid-Sensitive and Mechano-Gated K_{2P} Channels. Front. Pharmacol. 11:704. doi: 10.3389/fphar.2020.00704

INTRODUCTION

Potassium channels selectively and rapidly enable the movement of K^+ ions across biological membranes down the electrochemical K^+ gradient at a rate close to that of diffusion (Mackinnon, 2003). Members of the potassium leak channel family are structurally unique among potassium channels since each subunit possesses four transmembrane segments and two pore-forming domains (2P/4TM architecture). As such, these channels are often referred to as two pore-domain K^+ or K_{2P} channels (Goldstein et al., 2001; Choe, 2002). These channels conduct current

Abbreviations: MTs, monoterpenes; K_{2P}, two pore-domain potassium channels.

across the entire physiological voltage range and are essential for neurophysiological function, while their activity modulates excitability. It was shown that K_{2P} channels could also increase excitability by supporting high-frequency firing once an action potential threshold is reached (Brickley et al., 2007). It was recently reported that the majority of K_{2P} channels are gated by membrane potential in spite of their lack of a voltage sensor, as the outward current of K^+ ions through the selectivity filter was found to open this gate (Schewe et al., 2016). Members of this family may react to membrane stretch, as well as to intracellular and extracellular pH changes, phosphorylation, the activity of various G-protein coupled receptors, and more (Goldstein et al., 2001; Brickley et al., 2007; Demeure et al., 2011; Feliciangeli et al., 2015). K_{2P} channels activity was shown to modulate various important physiological processes such as pain perception (Alloui et al., 2006) and cardiac activity (Ellinghaus et al., 2005; Decher et al., 2017; Schmidt et al., 2017). Human K_{2P}3.1 channels (TASK-1) are expressed mainly in the atria and possess a promising target for atrial fibrillation treatment (Schmidt et al., 2014; Schmidt et al., 2018). A mutation in K_{2P}9.1 (TASK-3) is connected to the Birk–Barel syndrome, mental retardation, and unique dysmorphism syndrome (Barel et al., 2008). Also, the effect of several volatile analgesics is mediated, in part, through their action on K_{2P}2.1 and K_{2P}4.1 (TRAAK) (Franks and Honore, 2004).

Terpenes are a large group of structurally diverse organic chemicals that are mostly produced in plants. Monoterpenes (MTs) are terpenes that are composed of two five-carbon isoprene units. For centuries, MTs have been known for their beneficial effects as antifungal agents (Marei et al., 2012), antibacterial (Garcia et al., 2008), and analgesic (Khalilzadeh et al., 2016) agents. Terpenes have been proposed as remedies for the treatment of pain (Quintans-Junior et al., 2013; Quintans Jde et al., 2013; Guimaraes et al., 2014) and cardiovascular diseases (Magyar et al., 2004; Aydin et al., 2007; Menezes et al., 2010; Peixoto-Neves et al., 2010; Santos et al., 2011), and were shown to possess antitumor, local anesthetic, and anti-ischemic abilities (Koziol et al., 2014).

Several MTs were found to affect ion channels, both in excitable cells (Oz et al., 2015) and in other tissues (Muruganathan et al., 2017). To name a few, carvacrol and thymol were found to activate and sensitize the murine and human transient receptor potential (TRP) channel TRPV3, and acyclic MTs like citronellol, nerol, and their derivatives were found to modulate the activity of TRPA1 (Ortar et al., 2014). MTs were found to act upon other TRP channels (Xu et al., 2006; Parnas et al., 2009), as well as on voltage-gated ion channels and GABA receptors (Czyzewska and Mozrzymas, 2013; Kawasaki et al., 2013). However, their activity on members of the K_{2P} potassium channels had not yet been studied.

Recently (Arazi et al., 2020), we reported the activation of K_{2P}2.1 by various MTs. Here, we report that MTs activate the other two mechano-gated K_{2P} channels (*i.e.*, K_{2P}4.1 and K_{2P}10.1), in addition to members of other groups of K_{2P} channel families (*e.g.*, TALK, TRESK). Moreover, we found that MTs display remarkable selectivity towards the different K_{2P} channels, and we report that they selectively inhibited the voltage-dependent current of TASK family members.

METHODS

Animals

All experiments using animals were performed following the guidelines of the Institutional Animal Care and Use Committee. The project approval number is IL-61-09-2015.

Cloning

Channels were cloned into plasmid pRAT that included a T7 RNA polymerase promoter to enable cRNA synthesis, as well as the 3′-UTR and 5′-UTR sequences of the *Xenopus laevis* β-actin gene to ensure efficient expression in *Xenopus* oocytes. Competent *Escherichia coli* DH5α cells were transformed by heat shock. Plasmid DNA was purified with a Wizard Plus SV Miniprep kit (Promega). Restriction enzyme digestions were performed according to the manufacturer's instructions (Fermentas or NEB). Point mutations were generated according to the Quickchange site-directed mutagenesis technique (Stratagene) and confirmed by sequencing. cRNA was transcribed *in vitro* by T7 polymerase using an AmpliCap High Yield Message Maker (Epicentre) kit.

Electrophysiology

Xenopus laevis oocytes were isolated and injected with 20–40 nl of solutions containing 0.3–40 ng cRNA using a 3.5″ Drammond#3-000-203-G/X glass capillary, pulled in a Sutter P97 capillary puller and a Drummond manual oocyte microinjection pipette (3-000-510-X). Whole-cell currents were measured 1–3 days after injection by the two-electrode voltage-clamp technique (GeneClamp 500B, Axon Instruments). Data were filtered at 2 kHz and sampled at 5 kHz with Clampex 9.0 software (Axon Instruments). For two-electrode voltage-clamp experiments, the pipette contained 3M KCl and the bath solution contained (in mM) unless otherwise noted: 4 KCl, 96 NaCl, 1 $MgCl_2$, 0.3 $CaCl_2$, 5 HEPES, pH 7.4 with NaOH (standard solution). All measurements of K_{2P}5.1 and K_{2P}17.1 channels were performed at pH = 9.0. When needed, bath solution sodium ions were isotonically replaced by potassium ions and *vice versa*. When testing MT activity, the standard bath solution was supplemented with the same concentration of the solvent (ethanol) as of the tested chemical.

Injection of cRNA into oocytes was done in OR-2 solution (in mM: 5 HEPES, 1 $MgCl_2$, 2.5 KCl, 82.5 NaCl, pH = 7.4). Post-injection oocytes were maintained in ND-91 solution (in mM: 5 HEPES, 1 $MgCl_2$, 1.8 $CaCl_2$, 2 KCl, 91 NaCl, pH = 7.4). Specific recording protocols are mentioned in the relevant figure legends. To determine the voltage-dependent fraction of the current, the initial, voltage-independent (instantaneous) current was estimated by fitting the current to an exponential decay slope as the initial currents are masked by the capacitive transient current, as was previously described (Arazi et al., 2020).

Chemicals

Carvacrol (cat#282197), thymol (cat#T0501), p-cymene (cat#C121452), 4-isopropylphenol (cat# 175404), eugenol (cat#E51791, cinnamaldehyde (cat#W228613), menthol (cat#M2772), beta-citronelol (cat# C83201), geraniol (cat#16333, 4-methylcatechole (cat# M34200), and arachidonic acid (cat#A3611) were all purchased from Sigma-Aldrich.

Preparation of Compounds

Compounds delivered as powders were dissolved into stock solutions (4–6 M) in 100% ethanol. Compounds delivered as liquid oils (6.5–7.5 M) were diluted 1:1 with ethanol to form stock solutions and were kept at −20°C for up to two weeks. Just before testing, stock solutions were diluted in the bath solution to the desired concentration, and diluted compounds were vigorously vortexed until completely dissolved. All solutions were supplemented with ethanol to a final concentration of 0.1% (v/v) (confirmed not to harm the oocytes). The pH was corrected to 7.4 ± 0.05 using NaOH or HCl.

Statistical Analysis

Data were expressed as the mean ± standard error of the mean (SEM) and analyzed and presented using Microsoft Excel 2016. Groups of two paired data sets were analyzed using a Wilcoxon Signed Ranks test and groups of two unpaired data sets were analyzed using Mann–Whitney U test with IBM SPSS Statistics ver. 20 software. Values were considered to be significantly different when the z-value was ≤0.05 (*), ≤0.01 (**), or ≤0.001 (***). All experiments were repeated with at least five oocytes.

RESULTS

Activation of Mechano-Gated Channels by Monoterpenes

As we have recently reported (Arazi et al., 2020), the activity of K_{2P}2.1 is modulated by various MTs. K_{2P}2.1 is a member of the mechano-gated K_{2P} channel clade that includes K_{2P}4.1 (TRAAK) and K_{2P}10.1 (TREK-2). We, therefore, investigated whether MTs modulate all mechano-gated K_{2P} channels. An external application of MTs resulted in the increase in currents of K_{2P}10.1 channels by seven compounds and in the increase in currents of K_{2P}4.1 channels by eight of the tested compounds, although to lower levels (**Figure 1A**). As was found for K_{2P}2.1 (Arazi et al., 2020), the phenol-containing compounds (carvacrol and thymol) were more potent in opening both channels, while linear compounds and compounds containing no hydroxyl group were less effective (**Figure 1A**). Under standard testing conditions, currents of most K_{2P} channels are composed of two components: an instantaneous "leak" current (voltage-independent, VI) and a voltage-dependent (VD) current (Schewe et al., 2016), as demonstrated in **Figure 1B**. We, thus, looked at whether MTs affect the voltage sensitivity of the channels by looking at the change in the proportion of the two current components. For K_{2P}4.1 and K_{2P}10.1 channels, no change in voltage dependency was detected (**Figure 1C**). However, for K_{2P}2.1 channels, voltage dependency was reduced during carvacrol application, as was previously reported (Arazi et al., 2020). As expected (Schewe et al., 2016), arachidonic acid had a similar effect to carvacrol (**Figure 1C**).

Activation of TALK and TRESK Channels

The activity of members of the TALK clade of potassium channels (K_{2P}5.1, K_{2P}16.1, and K_{2P}17.1; TASK-2, TALK-1, and TALK-2, respectively) is sensitive to external pH, as these channels are activated at an alkaline pH (Decher et al., 2001; Girard et al., 2001). K_{2P}5.1 (TASK-2) is expressed mostly at the tubular epithelial and is involved in pathological conditions such as Balkan endemic nephropathy (BEN) (Toncheva et al., 2014; Reed et al., 2016). While most tested compounds had almost no effect on this channel, carvacrol and cinnamaldehyde (**Figure 2**) activated it by up to 17-fold (15.7 ± 3.0, n = 7 and 4.7 ± 0.5, n = 5, respectively, 0.3 mM for both compounds), although at different rates (**Figure 2B**). While activation by carvacrol was reversible, activation by cinnamaldehyde was not, even after a 5-min wash. It should be noted that irreversible activation of TRPA1 channels by cinnamaldehyde was previously reported (Macpherson et al., 2007). The minimal concentration that showed substantial activation of the channel was 12 μM for carvacrol (albeit not statistically significant) (1.9 ± 0.1-fold, n = 5, **Figure 2C**) and 30 μM for cinnamaldehyde (2.8 ± 0.3-fold, n = 5; statistically significant).

K_{2P}16.1 and K_{2P}17.1 are expressed predominantly in the pancreas and may be involved in the exocrine secretion of bicarbonate. A gain of function mutation in K_{2P}17.1 was associated with progressive cardiac conduction disorder (Friedrich et al., 2014). While K_{2P}16.1 was not affected by any of the tested MTs (not shown), K_{2P}17.1 was moderately activated by menthol, thymol, β-citronellol, 4MC, and carvacrol (**Figure 3A**). K_{2P}18.1 (TRESK, KCNK18) is unique among other K_{2P} channels by having an extra-long cytoplasmatic domain that is located between the two pore-forming domains (Sano et al., 2003). This channel is expressed in the dorsal root ganglion, trigeminal ganglion neurons, and spinal cord (Sano et al., 2003; Kang and Kim, 2006; Dobler et al., 2007). Mutation in this channel was linked to familial migraine with aurora (Lafreniere et al., 2010). K_{2P}18.1 was opened rapidly and robustly by carvacrol and to a lesser degree by thymol and 4-isopropylphenol (4IPP) (**Figure 3B**). Other compounds displayed mild to no effect on this channel. Since with mechano-gated K_{2P} channels, we observed a reduction in the proportion of the voltage-dependent current as a result of activation by carvacrol (**Figure 1C**), we tested this feature in these channels as well. In K_{2P}5.1 channels, the share of the voltage-dependent current indeed decreased (**Figure 3C**). In contrast, for K_{2P}17.1 channels, the share of the voltage-dependent current did not change. In K_{2P}18.1 channels, where the basal share of the voltage-dependent current was low, currents displayed more sensitivity to voltage after incubation with carvacrol (**Figure 3C**).

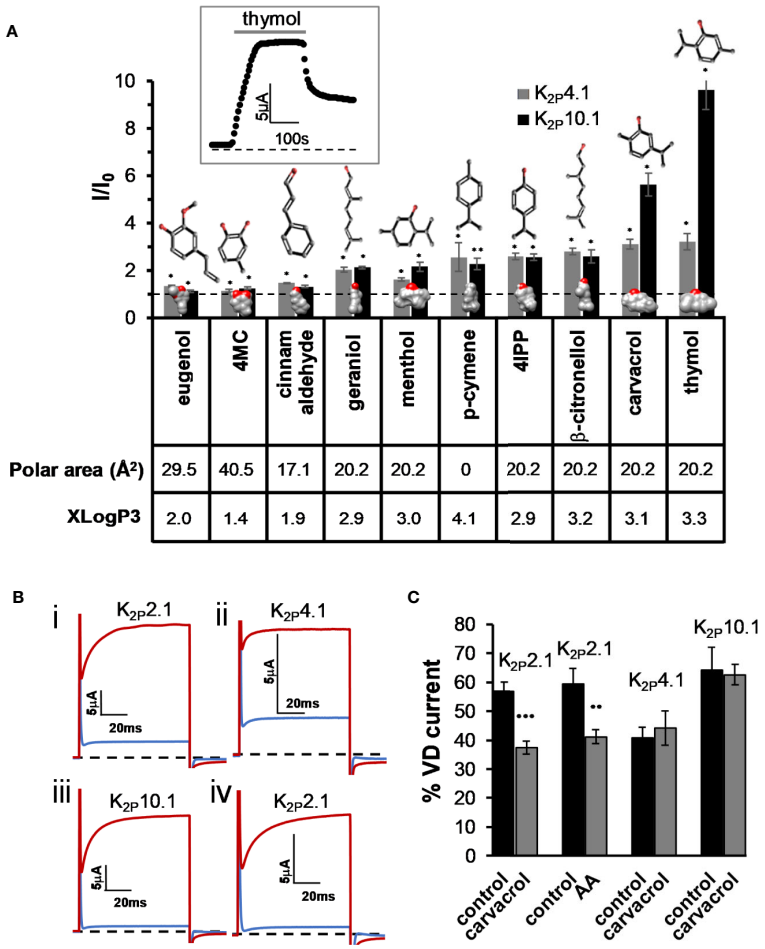

FIGURE 1 | Activation of K_{2P}4.1 and K_{2P}10.1 by monoterpenes. **(A)** Activation of K_{2P}4.1 and K_{2P}10.1. Oocyte membrane potential was held at −80 mV and pulsed to +25 mV for 75 ms with 5 s interpulse intervals. All MTs were applied at the same concentration (0.3 mM), and currents were measured after 4 min (mean ± S.E., n = 5–10). Polar area (Å^2) and octanol–water partition coefficient (logP) prediction (XLogP3) were obtained from PubChem (Kim et al., 2016). 2D structures and the coordinates for the 3D structures of the terpenes were obtained from ChemSpider. 3D models were performed with the UCSF Chimera package (Pettersen et al., 2004). Oxygen molecules are colored red. The dashed line represents no change from the initial current. Inset- currents of a representative oocyte expressing K_{2P}10.1 before, during and after thymol application. **(B)** Currents at 60 mV before (in red) and during (in blue) application of carvacrol (i–iii) or arachidonic acid (AA) (iv), on K_{2P}2,1 (i, iv), K_{2P}4.1 (ii), and K_{2P}10.1 (iii) **(C)**. Fraction of voltage-dependent current (in %) before (black) and after (gray) application of 0.3 mM carvacrol or arachidonic acid (AA, 100 μM). A fit of the current (at 60 mV) to an exponential decay slope was used to identify the initial current (mean ± S.E., n = 6–9).

Acid-Sensitive K_{2P}3.1 and K_{2P}9.1 (TASK) Channels Are Inhibited by Monoterpenes

K_{2P}3.1 and K_{2P}9.1 (TASK-1 and TASK-3, respectively) channels are expressed in the pancreas and placenta and to a lesser degree in the brain, heart, and kidneys (Duprat et al., 1997; Kim et al., 2000). Unlike all other tested K_{2P} channels, current levels of K_{2P}3.1 and K_{2P}9.1 decreased by all tested MTs (**Figure 4A**). In contrast to mechano-gated channels, which were affected mostly by cyclic phenolic compounds like thymol and carvacrol, TASK channels were affected mostly by linear MTs such as *β*-citronellol and geraniol (**Figure 4A**). Inhibition was rapid (*e.g.* τ = 3.8 ± 0.2, 6.2 ± 1.2, and 5.6 ± 1.5 s for thymol, *β*-citronellol, and carvacrol, respectively, n = 7–11) and within the solution change rate in our system (τ = 7.7 ± 1.0 s, n = 5). When using thymol, a monoterpene that affects both channel types, it was obvious that the inhibition rate was remarkably faster than that observed for activation of mechano-gated K_{2P} channels (**Figure 4B**). To make sure that the differences in rates were not merely a result of a difference in affinities ($K_{inhibition}$ of K_{2P}3.1 by thymol is 20 ± 5 μM and $K_{activation}$ of K_{2P}2.1 by thymol is 290 ± 50 μM, not shown), we measured the current change rates at three different concentrations for each channel (**Figure 4C**). As expected, no measurable change in the rate of K_{2P}3.1 channels inhibition was observed, while the activation rate for K_{2P}2.1 channels was much slower at all concentrations.

To further examine the unique activity of MTs on TASK channels, we tested the activity of carvone on K_{2P}3.1 channels as a model, as this monoterpene had no activity on K_{2P}2.1 channels (**Figure 5A**), while readily and rapidly (**Figure 5B**) decreasing

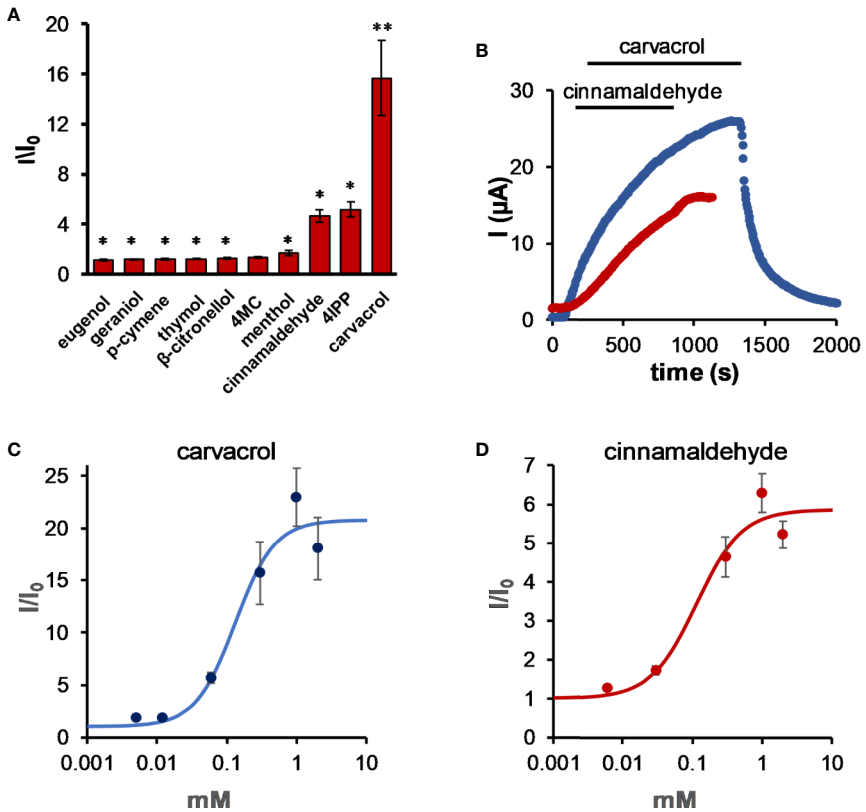

FIGURE 2 | Carvacrol and cinnamaldehyde robustly activate K_{2P}5.1. **(A)** Activation of K_{2P}5.1 by monoterpenes. Oocyte membrane potential was held at −80mV and pulsed to +25 mV for 75 ms with 5 s interpulse intervals. All MTs were applied at the same concentration (0.3 mM), and currents were measured after 5 min of incubation (mean ± S.E., n = 6–10). **(B)** Time course for activation by 0.3 mM carvacrol and 0.3 mM cinnamaldehyde for representative oocytes expressing K_{2P}5.1 channels. Currents were measured as in **(A)**. **(C)** Carvacrol dose-response for K_{2P}5.1 channels (mean ± S.E., n = 5–8) (EC_{50} = 0.13 ± 0.05 mM). **(D)** Cinnamaldehyde dose–response for K_{2P}5.1 channels (mean ± S.E., n = 5–8) (EC_{50} = 0.11 ± 0.07 mM). Currents were measured at 25 mV, as in **(A)**, after incubation for 5 min. $^{*}p \leq 0.05$, $^{**}p \leq 0.01$.

K_{2P}3.1 channel currents with a $K_{inhibition}$ of 0.90 ± 0.16 mM (**Figure 5C**). As in most K_{2P} channels, when held at −80 mV, K_{2P}3.1 currents are comprised of two components: an instantaneous, voltage-independent (VI), and a time- and voltage-dependent component (VD) (**Figure 5D**, control). As was observed with other MTs, the VD component of the current was dramatically reduced due to application of carvone (**Figures 5D, E**). The inhibition of the VD currents resulted, as anticipated, in the disappearance of K_{2P}3.1 channels tail currents (**Figure 5F**).

External K^+ concentration is known to affect the open probability of the selectivity filter gate of potassium channels (Hille, 2001) and, in particular, that of K_{2P} channels (Zilberberg et al., 2001). We, thus, tested the effect of external K^+ on carvone-induced current inhibition. The concentration of external K^+ had a profound effect on K_{2P}3.1 currents. A significant current decrease was observed under low (0 and 4 mM) external K^+ concentration (**Figure 6A**). At all external potassium concentrations, carvone reduced K_{2P}3.1 currents (**Figures 6B, C**). Currents at 0 mM (no added potassium) external K^+ were too low to allow further accurate analysis. When we analyzed the effect of carvone on each current component (VD or VI) at three external K^+ concentrations, we found that the VD current was almost completely eliminated at all concentrations, while the VI current was only mildly affected (**Figures 6C–G**). At 60 mV, inhibition was reduced by high external K^+ (**Figure 6C**).

DISCUSSION

In this study, we used an exogenous expression system to measure the impact of MTs on the activity of various human K_{2P} channels. MTs were found to affect various types of ion channels at high micromolar to millimolar concentrations (Lauritzen et al., 2005; Joca et al., 2012; Johnson et al., 2012; Brohawn et al., 2014; Pham et al., 2015; Bavi et al., 2016; Cabanos et al., 2017; Li Fraine et al., 2017), comparable to the concentrations that were found here to affect K_{2P} channels. Mechano-gated K_{2P}4.1 and K_{2P}10.1 were activated mainly by the cyclic aromatic phenolic MTs, carvacrol, and thymol, with the latter being the most effective. This is in accordance with our finding that the same MTs are the best activators of the other mechano-gated K_{2P} channel, K_{2P}2.1 (Arazi et al., 2020). Unlike in K_{2P}2.1 channels, the voltage dependency of

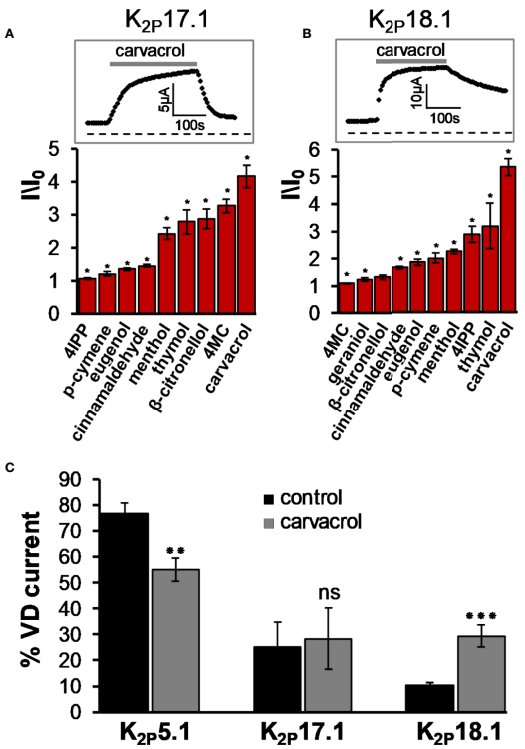

FIGURE 3 | K_{2P}17.1 and K_{2P}18.1 are activated by monoterpenes. **(A)**, **(B)** Activation of K_{2P}17.1 **(A)** and K_{2P}18.1 **(B)** by monoterpenes. Oocyte membrane potential was held at –80 mV and pulsed to +25 mV for 75 ms with 5 s interpulse intervals. All MTs were applied at the concentration of 0.3 mM, and currents were measured 4 min after application of the indicated monoterpene (mean ± S.E., n = 5–10). Insets: currents of representative oocytes expressing K_{2P}17.1 **(A)** and K_{2P}18.1 **(B)** during application of 0.3 mM carvacrol. **(C)** Fraction of voltage-dependent (VD) current (in %) under control conditions and after application of 0.3 mM carvacrol for three channel types, as indicated. Oocytes were held at –80mV, and currents were measured at 30 mV. A fit of the results to an exponential decay slope was used to identify the initial current (mean ± S.E., n = 6–9). $^{*}p \leq 0.05$, $^{**}p \leq 0.01$, $^{***}p \leq 0.001$, ns, not significant.

the current did not change as a result of MT activation. Our findings suggest that for best activation of mechano-gated K_{2P} channels, terpenes should be moderately hydrophobic (XLogP3 ~ 3, as is the case for carvacrol and thymol) and to be able to penetrate, yet not become embedded in, the bilayer due to the presence of a small polar area. Also, a phenol moiety was necessary to obtain high channel-stimulating activity. We believe that such molecules are embedded into the outer leaflet of the bilayer and perturbed its structure and/or curvature. Less hydrophobic and more polar molecules (a polar area larger than 20 $Å^2$ and XLogP value lower than 3) will stay in the polar area of the outer leaflet, while more hydrophobic molecules will sink deeper into the bilayer. We showed that for K_{2P}2.1, the cytoplasmic carboxyl-terminal of the channel is needed for the activity of MTs (Arazi et al., 2020). It is yet to be determined whether this is the mechanism by which the other two mechano-gated K_{2P} channels are activated by MTs.

The alkaline-sensitive K_{2P}5.1 and K_{2P}17, but not K_{2P}16.1, were also found to be activated by MTs. While K_{2P}17.1 was only mildly activated (up to a fourfold increase in current, **Figure 3A**), K_{2P}5.1 currents increased by up to 17-fold (0.3 mM, **Figure 2A**). Even at 60 μM carvacrol, K_{2P}5.1 currents increased by 5.5-fold (**Figure 2C**). The selectivity of the MTs towards these channels was not the same as for mechano-gated channels. While carvacrol activated, to a degree, all channels, K_{2P}5.1 was uniquely activated by cinnamaldehyde, but not by thymol, and K_{2P}17.1 was uniquely activated by β-citronellol and 4MC (**Figure 3A**). K_{2P}18.1 channels were activated by the same MTs, up to 5.3-fold (**Figure 3B**). Our findings indicate a certain degree of selectivity in the sensitivity of different K_{2P} channels to MTS, as some channels are activated by MTs that are inactive against other channels. The origin for this apparent selectivity is unclear since whether membrane-adhered hydrophobic molecules directly bind to channels or if they change membrane properties, causing each channel to react differently to those changes is an ongoing debate (Cristani et al., 2007; Ogawa et al., 2009; Lee, 2011; Nury et al., 2011; Epand et al., 2015; Sacchi et al., 2015). This dilemma applies not only to monoterpenes but also to other lipophilic molecules such as general anesthetics and alcohols (Howard et al., 2014), as well as for endocannabinoids (Oz, 2006) and steroids (Hill et al., 2015), all are allosteric modulators of several structurally different ion channels (Sanchez-Borzone et al., 2014; Oz et al., 2015; Ton et al., 2015). By changing the physicochemical properties of the surrounding membrane environment (Sanchez et al., 2004; Turina et al., 2006; Zunino et al., 2011; Reiner et al., 2013), and energetic requirements for gating-related conformational changes monoterpenes could affect ligand-gated ion channels (LGICs) (Fantini and Barrantes, 2009; Barrantes et al., 2010), and voltage-gated ion channel (VGICs) as reviewed by Oz at al. 2015 (Oz et al., 2015). On the other hand, evidence for direct binding of lipophilic monoterpenes, such as carvacrol and thymol, to specific amino acid residues in the transmembrane domain of Human 5-Hydroxytryptamine Type 3 (5-HT3Rs) were found (Lansdell et al., 2015). Similarly, the different potency of menthol stereoisomers (Walstab et al., 2014) on 5-HT3Rs or GABA(A) receptor (Corvalan et al., 2009) suggest also a degree of selectivity in monoterpenes action on ion channels.

For K_{2P}2.1, it was shown that channel opening would result in a reduction in its voltage dependency (Bockenhauer et al., 2001; Lopes et al., 2005; Cohen et al., 2008). Schewe et al. displayed that, for all mechano-gated K_{2P} channels, activation causes a gating mode shift within the selectivity filter and that these channels can be converted into a "classical" leak mode when stimulated by arachidonic acid or PIP_2 (Schewe et al., 2016). This phenomenon was observed in our experiments with K_{2P}2.1, but not with K_{2P}4.1 or K_{2P}10.1 channels. Reduction in the percent of voltage-dependent current was observed with K_{2P}5.1, but not with K_{2P}17.1, while with K_{2P}18.1, an increase in the voltage-dependent current was recorded (**Figure 3C**). The voltage-dependency of the K_{2P} channels' current is directly related to their open probability. Since in our experiments, only a relative estimation of the open probability of the channel is measured, we believe that it is plausible that "leak-like" behavior of the channel is achieved only at high open probabilities and that under our experimental conditions, this was not always achieved.

The acid-sensitive TASK channels, K_{2P}3.1 and K_{2P}9.1, were affected differently by MTs: a. most tested MTs caused a decrease

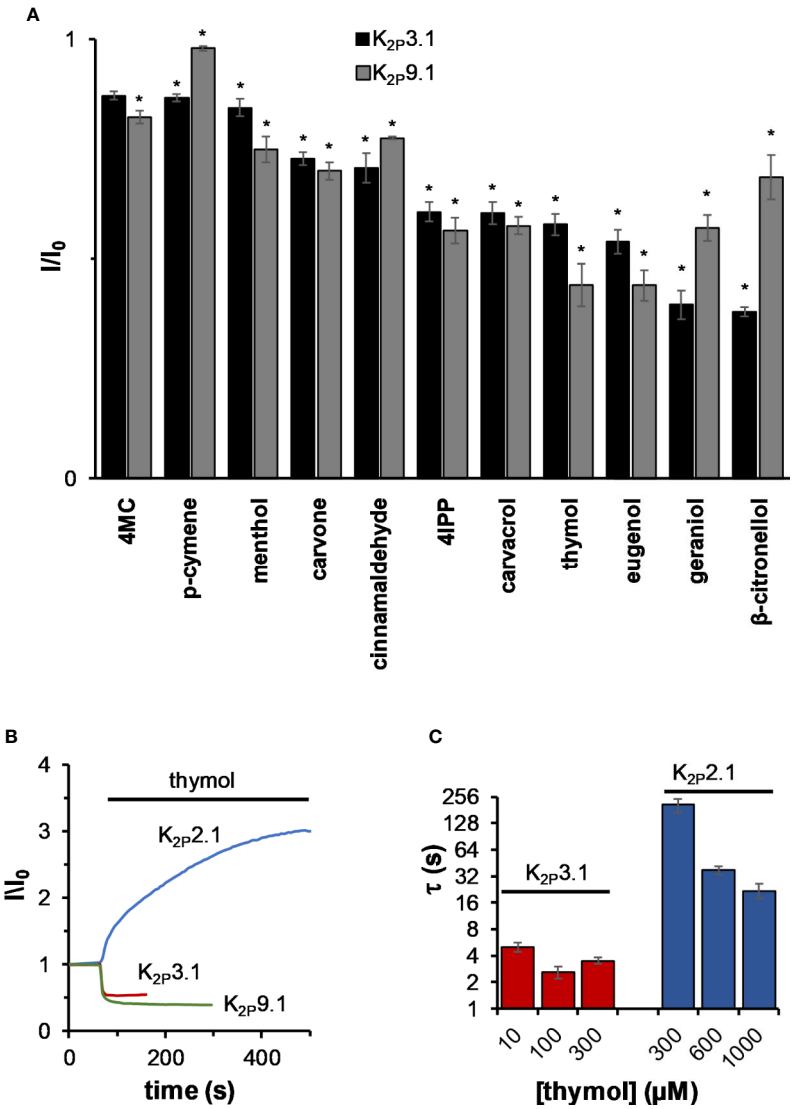

FIGURE 4 | The effect of monoterpenes on acid-sensitive K_{2P} channels. **(A)** Inhibition of K_{2P}3,1 and K_{2P}9.1 currents. Currents were measured before and after 2 in incubation with the indicated MT (mean ± S.E., n = 5–10). All MTs were applied at a concentration of 0.3 mM. **(B)** Normalized currents during 0.3 mM thymol application for representative oocytes expressing either K_{2P}2.1, K_{2P}3.1, and K_{2P}9.1. **(C)** The time constant (τ) of current changes during the application of thymol at different concentrations for K_{2P}2.1 or K_{2P}3.1 (mean ± S.E., n = 6–10). *$p \leq 0.05$.

in TASK channel currents (**Figure 4A**); b. the current decrease rate was high (a few seconds), while the activation rate of other channels was at least an order of magnitude slower (**Figures 4B, C** and not shown); and c. unlike other tested K_{2P} channels, TASK channels were affected mostly by linear MTs (*β*-citronellol and geraniol, **Figure 4A**). These three observations suggest that TASK channels are affected by MTs by a different mechanism than the other tested channels. Thus, we further studied the characteristics of the current inhibition of TASK channels by MTs using K_{2P}3.1 and carvone as a model.

It was clearly evident that carvone almost completely eliminated the voltage-gated portion of K_{2P}3.1 currents (**Figures 5D–F**). Since voltage-dependent gating was shown to originate from the movement of three to four potassium ions into the high electric field of an inactive selectivity filter (Schewe et al., 2016) and since the stability of the selectivity filter was shown to be affected by the concentration of external potassium ions in potassium channels in general (Hille, 2001) and in K_{2P} channels in particular (Zilberberg et al., 2001), we looked at the influence of external potassium concentrations on K_{2P}3.1 activity and sensitivity to carvone. External potassium ion levels had a clear effect on channel gating, as currents decreased dramatically at low external levels (**Figure 6A**). At all potassium levels, carvone reduced K_{2P}3.1 current, while specifically targeting the voltage-dependent portion (**Figures 6C–G**). While the voltage-independent portion of the current behaved, as expected, like a potassium GHK-leak, the voltage-dependent portion displayed

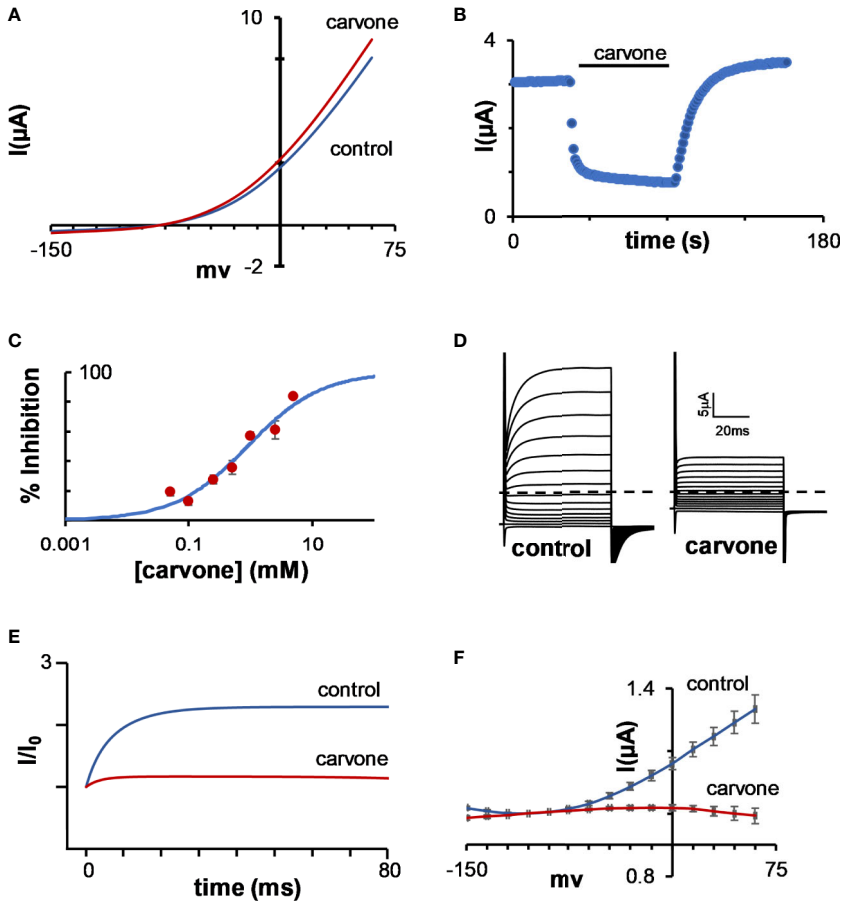

FIGURE 5 | Inhibition of $K_{2P}3.1$ by carvone. **(A)** Current–voltage relationship of a representative oocyte expressing $K_{2P}2.1$, before and after application of 1mM carvone. **(B)** The current of a representative oocyte expressing $K_{2P}3.1$ during incubation with 1 mM carvone. Oocyte membrane potential was held at –80 mV and pulsed to +25 mV for 75 ms with 1 s interpulse intervals. **(C)** Carvone dose–response for $K_{2P}3.1$ channels (mean ± S.E., n = 6–10) ($K_{inhibition}$ = 0.90 ± 0.16 mM). **(D)** Currents of a representative oocyte expressing $K_{2P}3.1$ channels before and during incubation with 1 mM carvone at 20 mM potassium at the bath. The oocyte was held at –80 mV, then at –135 mV for 30 ms, and then pulsed from –150 mV to 60 mV in 15 mV intervals. The dashed line represents zero current. **(E)** Currents at 60 mV of a representative oocyte before and during incubation with 1 mM carvone. Currents were normalized to the initial current. A fit of the results to an exponential decay slope was used to identify the initial current. **(F)** Tail analysis of currents before and during incubation with 1 mM carvone at external potassium concentration of 100 mM (mean ± S.E., n = 6). For each oocyte, currents were normalized to the current at –105 mV.

an outward rectification behavior that was partly dependent on potassium concentration (**Figure 6F**). We suggest that as external potassium ions stabilize the selectivity filter at its conductive state, they minimize the destabilizing structural changes caused by carvone. For this reason, we suggest that MTs might serve as a useful tool in studying the voltage-dependency of TASK channels as they specifically target the voltage-dependent portion of the current. Recently, it was reported that bupivacaine blocks TASK channels in a voltage-dependent manner by disrupting the K^+-flux gating mechanism (Rinne et al., 2019), and that it is located laterally in the side fenestrations of $K_{2P}3.1$ channels and interacts with residues of the pore helix, and the M2, M3, and M4 segments. It is conceivable that both bupivacaine and MTs bind to a similar binding site within the membrane and, thus, affect channels through a similar mechanism.

K_{2P} channels play a role in various physiological processes such as pain signaling (Li and Toyoda, 2015) heart function (Hancox et al., 2016), and more (Lesage and Barhanin, 2011; Bandulik et al., 2015; Renigunta et al., 2015; Riegelhaupt et al., 2018). For example, activation of mechano-gated K_{2P}, as well as $K_{2P}18.1$ channels, is expected to result in reduced pain sensation and neuroprotection. Terpenes have been proposed as analgesic agents (Khalilzadeh et al., 2016), as remedies for the treatment of pain and cardiovascular diseases (Magyar et al., 2004; Aydin et al., 2007; Menezes et al., 2010; Peixoto-Neves et al., 2010; Santos et al., 2011; Quintans-Junior et al., 2013; Quintans Jde et al., 2013; Guimaraes et al., 2014) and were shown to possess antitumor, local anesthetic, and anti-ischemic abilities (Koziol et al., 2014). Any of these activities of terpenes that stem from their activity on K_{2P} channels remains to be determined. Even though MTs are regularly consumed by people as food additives,

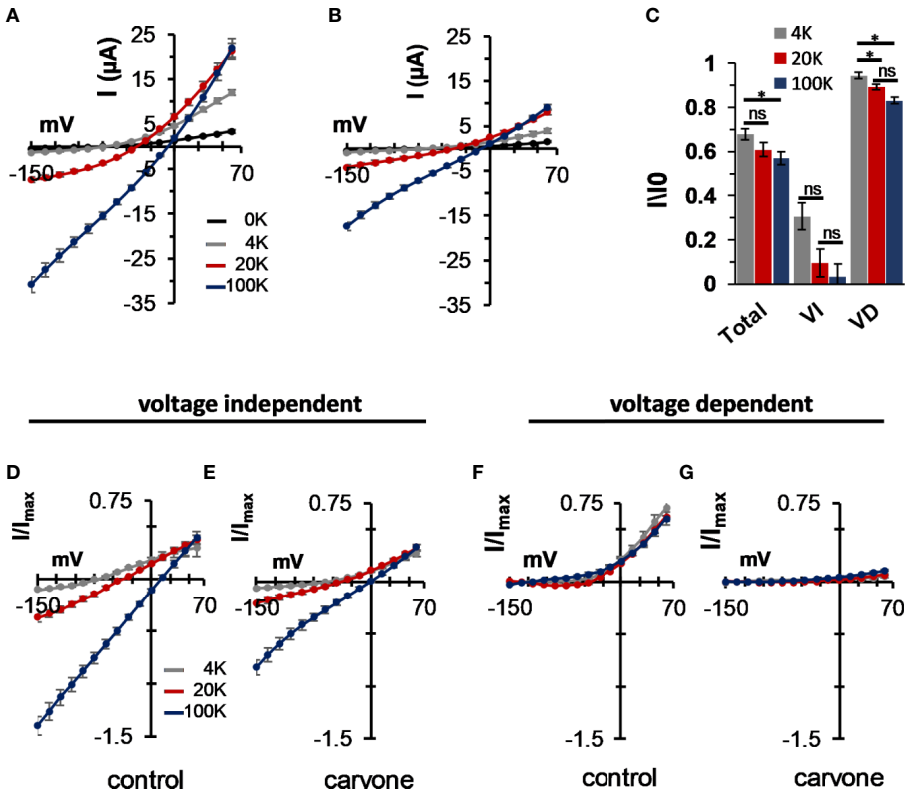

FIGURE 6 | The effect of external K^+ on the inhibition of the voltage-dependent current in $K_{2P}3.1$. **(A, B)** Steady-state current–voltage relationships for oocytes expressing $K_{2P}3.1$ at four external potassium concentrations (0, 4, 20, and 100 mM) under control conditions **(A)** or after incubation with 1 mM carvone **(B)**. Oocytes were held at −80 mV, pulsed to −135 mV for 30 ms, and then pulsed from −150 mV to 60 mV in 15 mV voltage intervals (mean ± S.E., n = 6–9). **(C)** The fraction of inhibited current due to carvone application of the total current (Total) and its components: the voltage-independent (VI) and the voltage-dependent (VD) currents. Currents at 60 mV were tested at three external potassium concentrations (4, 20, and 100 mM) (mean ± S.E., n = 6–9). **(D–G)** Current–voltage relationships for oocytes expressing $K_{2P}3.1$ channels at three different external potassium concentrations, as indicated (mean ± S.E., n = 6–9). Currents were measured as in **(A)**. The voltage-independent **(D, E)** and the voltage-dependent **(F, G)** fractions of the current were calculated as in **Figure 1C** and are presented individually. Measurements were performed before **(D, F)** and after **(E, G)** application of 1 mM carvone. *$p \leq 0.05$, ns, not significant.

due to their low concentration in food, they are unlikely to have any pharmacological effect. However, the extensive use of MTs in traditional medicine might raise the possibility of their beneficial pharmacological use when given in high concentrations.

DATA AVAILABILITY STATEMENT

All datasets generated for this study are included in the article/supplementary material.

ETHICS STATEMENT

The animal study was reviewed and approved by Institutional Animal Care and Use Committee, Ben Gurion University. The project approval number is IL-61-09-2015.

AUTHOR CONTRIBUTIONS

Conception and design of the study: EA and NZ. Acquisition of data: EA and GB. Analysis and interpretation of data: EA. Writing the manuscript: EA and NZ.

FUNDING

This work was supported by a grant from the Israel Science Foundation (1877/15) to NZ.

ACKNOWLEDGMENTS

The authors thank Prof. Dierk Thomas for his generous gift of the $K_{2P}4.1$, $K_{2P}10.1$, $K_{2P}16.1$, and $K_{2P}17.1$ clones.

REFERENCES

Alloui, A., Zimmermann, K., Mamet, J., Duprat, F., Noel, J., Chemin, J., et al. (2006). TREK-1, a K^+ channel involved in polymodal pain perception. *EMBO EMBO J.* 25, 2368–2376. doi: 10.1038/sj.emboj.7601116

Arazi, E., Blecher, G., and Zilberberg, N. (2020). A regulatory domain in the K2P2.1 (TREK-1) carboxyl-terminal allows for channel activation by monoterpenes. *Mol. Cell. Neurosci*. In press. doi: 10.1016/j.mcn.2020.103496.

Aydin, Y., Kutlay, O., Ari, S., Duman, S., Uzuner, K., and Aydin, S. (2007). Hypotensive effects of carvacrol on the blood pressure of normotensive rats. *Planta Med.* 73, 1365–1371. doi: 10.1055/s-2007-990236

Bandulik, S., Tauber, P., Lalli, E., Barhanin, J., and Warth, R. (2015). Two-pore domain potassium channels in the adrenal cortex. *Pflugers Arch.* 467, 1027–1042. doi: 10.1007/s00424-014-1628-6

Barel, O., Shalev, S. A., Ofir, R., Cohen, A., Zlotogora, J., Shorer, Z., et al. (2008). Maternally inherited Birk Barel mental retardation dysmorphism syndrome caused by a mutation in the genomically imprinted potassium channel KCNK9. *Am. J. Hum. Genet.* 83, 193–199. doi: 10.1016/j.ajhg.2008.07.010

Barrantes, F. J., Bermudez, V., Borroni, M. V., Antollini, S. S., Pediconi, M. F., Baier, J. C., et al. (2010). Boundary lipids in the nicotinic acetylcholine receptor microenvironment. *J. Mol. Neurosci.* 40, 87–90. doi: 10.1007/s12031-009-9262-z

Bavi, O., Cox, C. D., Vossoughi, M., Naghdabadi, R., Jamali, Y., and Martinac, B. (2016). Influence of global and local membrane curvature on mechanosensitive ion channels: A finite element approach. *Membranes* 6, 14. doi: 10.3390/membranes6010014

Bockenhauer, D., Zilberberg, N., and Goldstein, S. A. (2001). KCNK2: reversible conversion of a hippocampal potassium leak into a voltage-dependent channel. *Nat. Neurosci.* 4, 486–491. doi: 10.1038/87434

Brickley, S. G., Aller, M. I., Sandu, C., Veale, E. L., Alder, F. G., Sambi, H., et al. (2007). TASK-3 two-pore domain potassium channels enable sustained high-frequency firing in cerebellar granule neurons. *J. Neurosci.* 27, 9329–9340. doi: 10.1523/JNEUROSCI.1427-07.2007

Brohawn, S. G., Su, Z., and Mackinnon, R. (2014). Mechanosensitivity is mediated directly by the lipid membrane in TRAAK and TREK1 K^+ channels. *Proc. Natl. Acad. Sci. U. S. A* 111, 3614–3619. doi: 10.1073/pnas.1320768111

Cabanos, C., Wang, M., Han, X., and Hansen, S. B. (2017). A Soluble Fluorescent Binding Assay Reveals PIP_2 Antagonism of TREK-1 Channels. *Cell Rep.* 20, 1287–1294. doi: 10.1016/j.celrep.2017.07.034

Choe, S. (2002). Potassium channel structures. *Nat. Rev. Neurosci.* 3, 115–121. doi: 10.1038/nrn727

Cohen, A., Ben-Abu, Y., Hen, S., and Zilberberg, N. (2008). A novel mechanism for human K_{2P}2.1 channel gating. Facilitation of C-type gating by protonation of extracellular histidine residues. *J. Biol. Chem.* 283, 19448–19455. doi: 10.1074/jbc.M801273200

Corvalan, N. A., Zygadlo, J. A., and Garcia, D. A. (2009). Stereo-selective activity of menthol on GABA(A) receptor. *Chirality* 21, 525–530. doi: 10.1002/chir.20631

Cristani, M., D'arrigo, M., Mandalari, G., Castelli, F., Sarpietro, M. G., Micieli, D., et al. (2007). Interaction of four monoterpenes contained in essential oils with model membranes: implications for their antibacterial activity. *J. Agric. Food Chem.* 55, 6300–6308. doi: 10.1021/jf070094x

Czyzewska, M. M., and Mozrzymas, J. W. (2013). Monoterpene alpha-thujone exerts a differential inhibitory action on GABA(A) receptors implicated in phasic and tonic GABAergic inhibition. *Eur. J. Pharmacol.* 702, 38–43. doi: 10.1016/j.ejphar.2013.01.032

Decher, N., Maier, M., Dittrich, W., Gassenhuber, J., Bruggemann, A., Busch, A. E., et al. (2001). Characterization of TASK-4, a novel member of the pH-sensitive, two-pore domain potassium channel family. *FEBS Lett.* 492, 84–89. doi: 10.1016/s0014-5793(01)02222-0

Decher, N., Ortiz-Bonnin, B., Friedrich, C., Schewe, M., Kiper, A. K., Rinne, S., et al. (2017). Sodium permeable and "hypersensitive" TREK-1 channels cause ventricular tachycardia. *EMBO Mol. Med.* 9, 403–414. doi: 10.15252/emmm.201606690

Demeure, O., Lecerf, F., Duby, C., Desert, C., Ducheix, S., Guillou, H., et al. (2011). Regulation of LPCAT3 by LXR. *Gene* 470, 7–11. doi: 10.1016/j.gene.2010.09.002

Dobler, T., Springauf, A., Tovornik, S., Weber, M., Schmitt, A., Sedlmeier, R., et al. (2007). TRESK two-pore-domain K^+ channels constitute a significant component of background potassium currents in murine dorsal root ganglion neurones. *J. Physiol.* 585, 867–879. doi: 10.1113/jphysiol.2007.145649

Duprat, F., Lesage, F., Fink, M., Reyes, R., Heurteaux, C., and Lazdunski, M. (1997). TASK, a human background K^+ channel to sense external pH variations near physiological pH. *EMBO J.* 16, 5464–5471. doi: 10.1093/emboj/16.17.5464

Ellinghaus, P., Scheubel, R. J., Dobrev, D., Ravens, U., Holtz, J., Huetter, J., et al. (2005). Comparing the global mRNA expression profile of human atrial and ventricular myocardium with high-density oligonucleotide arrays. *J. Thorac. Cardiovasc. Surg.* 129, 1383–1390. doi: 10.1016/j.jtcvs.2004.08.031

Epand, R. M., D'souza, K., Berno, B., and Schlame, M. (2015). Membrane curvature modulation of protein activity determined by NMR. *Biochim. Biophys. Acta* 1848, 220–228. doi: 10.1016/j.bbamem.2014.05.004

Fantini, J., and Barrantes, F. J. (2009). Sphingolipid/cholesterol regulation of neurotransmitter receptor conformation and function. *Biochim. Biophys. Acta* 1788, 2345–2361. doi: 10.1016/j.bbamem.2009.08.016

Feliciangeli, S., Chatelain, F. C., Bichet, D., and Lesage, F. (2015). The family of K2P channels: salient structural and functional properties. *J. Physiol.* 593, 2587–2603. doi: 10.1113/jphysiol.2014.287268

Franks, N. P., and Honore, E. (2004). The TREK K_{2P} channels and their role in general anaesthesia and neuroprotection. *Trends Pharmacol. Sci.* 25, 601–608. doi: 10.1016/j.tips.2004.09.003

Friedrich, C., Rinne, S., Zumhagen, S., Kiper, A. K., Silbernagel, N., Netter, M. F., et al. (2014). Gain-of-function mutation in TASK-4 channels and severe cardiac conduction disorder. *EMBO Mol. Med.* 6, 937–951. doi: 10.15252/emmm.201303783

Garcia, R., Alves, E. S., Santos, M. P., Aquije, G. M., Fernandes, A. A., Dos Santos, R. B., et al. (2008). Antimicrobial activity and potential use of monoterpenes as tropical fruits preservatives. *Braz. J. Microbiol.* 39, 163–168. doi: 10.1590/S1517-838220080001000032

Girard, C., Duprat, F., Terrenoire, C., Tinel, N., Fosset, M., Romey, G., et al. (2001). Genomic and functional characteristics of novel human pancreatic 2P domain K^+ channels. *Biochem. Biophys. Res. Commun.* 282, 249–256. doi: 10.1006/bbrc.2001.4562

Goldstein, S. A., Bockenhauer, D., O'kelly, I., and Zilberberg, N. (2001). Potassium leak channels and the KCNK family of two-P-domain subunits. *Nat. Rev. Neurosci.* 2, 175–184. doi: 10.1038/35058574

Guimaraes, A. G., Serafini, M. R., and Quintans-Junior, L. J. (2014). Terpenes and derivatives as a new perspective for pain treatment: a patent review. *Expert Opin. Ther. Pat.* 24, 243–265. doi: 10.1517/13543776.2014.870154

Hancox, J. C., James, A. F., Marrion, N. V., Zhang, H., and Thomas, D. (2016). Novel ion channel targets in atrial fibrillation. *Expert Opin. Ther. Targets* 20, 947–958. doi: 10.1517/14728222.2016.1159300

Hill, M., Duskova, M., and Starka, L. (2015). Dehydroepiandrosterone, its metabolites and ion channels. *J. Steroid Biochem. Mol. Biol.* 145, 293–314. doi: 10.1016/j.jsbmb.2014.05.006

Hille, B. (2001). *Ion channels of excitable membranes* (Sunderland, Mass: Sinauer). doi:.

Howard, R. J., Trudell, J. R., and Harris, R. A. (2014). Seeking structural specificity: direct modulation of pentameric ligand-gated ion channels by alcohols and general anesthetics. *Pharmacol. Rev.* 66, 396–412. doi: 10.1124/pr.113.007468

Joca, H. C., Cruz-Mendes, Y., Oliveira-Abreu, K., Maia-Joca, R. P., Barbosa, R., Lemos, T. L., et al. (2012). Carvacrol decreases neuronal excitability by inhibition of voltage-gated sodium channels. *J. Nat. Prod.* 75, 1511–1517. doi: 10.1021/np300050g

Johnson, J. L., Erickson, J. W., and Cerione, R. A. (2012). C-terminal di-arginine motif of Cdc42 protein is essential for binding to phosphatidylinositol 4,5-bisphosphate-containing membranes and inducing cellular transformation. *J. Biol. Chem.* 287, 5764–5774. doi: 10.1074/jbc.M111.336487

Kang, D., and Kim, D. (2006). TREK-2 (K2P10.1) and TRESK (K2P18.1) are major background K^+ channels in dorsal root ganglion neurons. *Am. J. Physiol. Cell Physiol.* 291, C138–C146. doi: 10.1152/ajpcell.00629.2005

Kawasaki, H., Mizuta, K., Fujita, T., and Kumamoto, E. (2013). Inhibition by menthol and its related chemicals of compound action potentials in frog sciatic nerves. *Life Sci.* 92, 359–367. doi: 10.1016/j.lfs.2013.01.012

Khalilzadeh, E., Hazrati, R., and Saiah, G. V. (2016). Effects of topical and systemic administration of Eugenia caryophyllata buds essential oil on corneal anesthesia and analgesia. *Res. Pharmaceut. Sci.* 11, 293. doi: 10.4103/1735-5362.189297

Kim, Y., Bang, H., and Kim, D. (2000). TASK-3, a new member of the tandem pore K^+ channel family. *J. Biol. Chem.* 275, 9340–9347. doi: 10.1074/jbc.275.13.9340

Kim, S., Thiessen, P. A., Bolton, E. E., Chen, J., Fu, G., Gindulyte, A., et al. (2016). PubChem Substance and Compound databases. *Nucleic Acids Res.* 44, D1202–D1213. doi: 10.1093/nar/gkv951

Koziol, A., Stryjewska, A., Librowski, T., Salat, K., Gawel, M., Moniczewski, A., et al. (2014). An overview of the pharmacological properties and potential applications of natural monoterpenes. *Mini Rev. Med. Chem.* 14, 1156–1168. doi: 10.2174/1389557514666141127145820

Lafreniere, R. G., Cader, M. Z., Poulin, J. F., Andres-Enguix, I., Simoneau, M., Gupta, N., et al. (2010). A dominant-negative mutation in the TRESK potassium channel is linked to familial migraine with aura. *Nat. Med.* 16, 1157–1160. doi: 10.1038/nm.2216

Lansdell, S. J., Sathyaprakash, C., Doward, A., and Millar, N. S. (2015). Activation of human 5-hydroxytryptamine type 3 receptors via an allosteric transmembrane site. *Mol. Pharmacol.* 87, 87–95. doi: 10.1124/mol.114.094540

Lauritzen, I., Chemin, J., Honore, E., Jodar, M., Guy, N., Lazdunski, M., et al. (2005). Cross-talk between the mechano-gated K_{2P} channel TREK-1 and the actin cytoskeleton. *EMBO Rep.* 6, 642–648. doi: 10.1038/sj.embor.7400449

Lee, A. G. (2011). Biological membranes: the importance of molecular detail. *Trends Biochem. Sci.* 36, 493–500. doi: 10.1016/j.tibs.2011.06.007

Lesage, F., and Barhanin, J. (2011). Molecular physiology of pH-sensitive background K(2P) channels. *Physiol. (Bethesda)* 26, 424–437. doi: 10.1152/physiol.00029.2011

Li, X. Y., and Toyoda, H. (2015). Role of leak potassium channels in pain signaling. *Brain Res. Bull.* 119, 73–79. doi: 10.1016/j.brainresbull.2015.08.007

Li Fraine, S., Patel, A., Duprat, F., and Sharif-Naeini, R. (2017). Dynamic regulation of TREK1 gating by Polycystin 2 via a Filamin A-mediated cytoskeletal Mechanism. *Sci. Rep.* 7, 17403. doi: 10.1038/s41598-017-16540-w

Lopes, C. M. B., Rohács, T., Czirják, G., Balla, T., Enyedi, P., and Logothetis, D. E. (2005). PIP2 hydrolysis underlies agonist-induced inhibition and regulates voltage gating of two-pore domain K+ channels. *J. Physiol.* 564, 117–129. doi: 10.1113/jphysiol.2004.081935

Mackinnon, R. (2003). Potassium channels. *FEBS Lett.* 555, 62–65. doi: 10.1016/S0014-5793(03)01104-9

Macpherson, L. J., Dubin, A. E., Evans, M. J., Marr, F., Schultz, P. G., Cravatt, B. F., et al. (2007). Noxious compounds activate TRPA1 ion channels through covalent modification of cysteines. *Nature* 445, 541–545. doi: 10.1038/nature05544

Magyar, J., Szentandrassy, N., Banyasz, T., Fulop, L., Varro, A., and Nanasi, P. P. (2004). Effects of terpenoid phenol derivatives on calcium current in canine and human ventricular cardiomyocytes. *Eur. J. Pharmacol.* 487, 29–36. doi: 10.1016/j.ejphar.2004.01.011

Marei, G. I. K., Abdel Rasoul, M. A., and Abdelgaleil, S. (2012). Comparative antifungal activities and biochemical effects of monoterpenes on plant pathogenic fungi. *Pesticide Biochem. Physiol.* 103 (2012), 56–61. doi: 10.1016/j.pestbp.2012.03.004

Menezes, I. A., Barreto, C. M., Antoniolli, A. R., Santos, M. R., and De Sousa, D. P. (2010). Hypotensive activity of terpenes found in essential oils. *Z. Naturforsch. C.* 65, 562–566. doi: 10.1515/znc-2010-9-1005

Muruganathan, U., Srinivasan, S., and Vinothkumar, V. (2017). Antidiabetogenic efficiency of menthol, improves glucose homeostasis and attenuates pancreatic beta-cell apoptosis in streptozotocin-nicotinamide induced experimental rats through ameliorating glucose metabolic enzymes. *BioMed. Pharmacother.* 92, 229–239. doi: 10.1016/j.biopha.2017.05.068

Nury, H., Van Renterghem, C., Weng, Y., Tran, A., Baaden, M., Dufresne, V., et al. (2011). X-ray structures of general anaesthetics bound to a pentameric ligand-gated ion channel. *Nature* 469, 428–431. doi: 10.1038/nature09647

Ogawa, H., Shinoda, T., Cornelius, F., and Toyoshima, C. (2009). Crystal structure of the sodium-potassium pump (Na^+,K^+-ATPase) with bound potassium and ouabain. *Proc. Natl. Acad. Sci. U. S. A* 106, 13742–13747. doi: 10.1073/pnas.0907054106

Ortar, G., Schiano Moriello, A., Morera, E., Nalli, M., Di Marzo, V., and De Petrocellis, L. (2014). Effect of acyclic monoterpene alcohols and their derivatives on TRP channels. *Bioorg. Med. Chem. Lett.* 24, 5507–5511. doi: 10.1016/j.bmcl.2014.10.012

Oz, M., Lozon, Y., Sultan, A., Yang, K. H., and Galadari, S. (2015). Effects of monoterpenes on ion channels of excitable cells. *Pharmacol. Ther.* 152, 83–97. doi: 10.1016/j.pharmthera.2015.05.006

Oz, M. (2006). Receptor-independent effects of endocannabinoids on ion channels. *Curr. Pharm. Des.* 12, 227–239. doi: 10.2174/138161206775193073

Parnas, M., Peters, M., Dadon, D., Lev, S., Vertkin, I., Slutsky, I., et al. (2009). Carvacrol is a novel inhibitor of Drosophila TRPL and mammalian TRPM7 channels. *Cell Calcium* 45, 300–309. doi: 10.1016/j.ceca.2008.11.009

Peixoto-Neves, D., Silva-Alves, K. S., Gomes, M. D., Lima, F. C., Lahlou, S., Magalhaes, P. J., et al. (2010). Vasorelaxant effects of the monoterpenic phenol isomers, carvacrol and thymol, on rat isolated aorta. *Fundam Clin. Pharmacol.* 24, 341–350. doi: 10.1111/j.1472-8206.2009.00768.x

Pettersen, E. F., Goddard, T. D., Huang, C. C., Couch, G. S., Greenblatt, D. M., Meng, E. C., et al. (2004). UCSF Chimera–a visualization system for exploratory research and analysis. *J. Comput. Chem.* 25, 1605–1612. doi: 10.1002/jcc.20084

Pham, Q. D., Topgaard, D., and Sparr, E. (2015). Cyclic and Linear Monoterpenes in Phospholipid Membranes: Phase Behavior, Bilayer Structure, and Molecular Dynamics. *Langmuir* 31, 11067–11077. doi: 10.1021/acs.langmuir.5b00856

Quintans Jde, S., Menezes, P. P., Santos, M. R., Bonjardim, L. R., Almeida, J. R., Gelain, D. P., et al. (2013). Improvement of p-cymene antinociceptive and anti-inflammatory effects by inclusion in beta-cyclodextrin. *Phytomedicine* 20, 436–440. doi: 10.1016/j.phymed.2012.12.009

Quintans-Junior, L. J., Barreto, R. S., Menezes, P. P., Almeida, J. R., Viana, A. F., Oliveira, R. C., et al. (2013). beta-Cyclodextrin-complexed (-)-linalool produces antinociceptive effect superior to that of (-)-linalool in experimental pain protocols. *Basic Clin. Pharmacol. Toxicol.* 113, 167–172. doi: 10.1111/bcpt.12087

Reed, A. P., Bucci, G., Abd-Wahab, F., and Tucker, S. J. (2016). Dominant-Negative Effect of a Missense Variant in the TASK-2 (KCNK5) K^+ Channel Associated with Balkan Endemic Nephropathy. *PloS One* 11, e0156456. doi: 10.1371/journal.pone.0156456

Reiner, G. N., Delgado-Marín, L., Olguín, N., Sánchez-Redondo, S., Sánchez-Borzone, M., Rodríguez-Farré, E., et al. (2013). Gabaergic Pharmacological Activity of Propofol Related Compounds as Possible Enhancers of General Anesthetics and Interaction with Membranes. *Cell Biochem. Biophysics* 67, 515–525. doi: 10.1007/s12013-013-9537-4

Renigunta, V., Schlichthörl, G., and Daut, J. (2015). Much more than a leak: structure and function of K2P-channels. *Pflügers Archiv. Eur. J. Physiol.* 467, 867–894. doi: 10.1007/s00424-015-1703-7

Riegelhaupt, P. M., Tibbs, G. R., and Goldstein, P. A. (2018). HCN and K2P Channels in Anesthetic Mechanisms Research. *Methods Enzymol.* 602, 391–416. doi: 10.1016/bs.mie.2018.01.015

Rinne, S., Kiper, A. K., Vowinkel, K. S., Ramirez, D., Schewe, M., Bedoya, M., et al. (2019). The molecular basis for an allosteric inhibition of K^+-flux gating in K2P channels. *eLife* 8, e39476. doi: 10.7554/eLife.39476

Sacchi, M., Balleza, D., Vena, G., Puia, G., Facci, P., and Alessandrini, A. (2015). Effect of neurosteroids on a model lipid bilayer including cholesterol: An Atomic Force Microscopy study. *Biochim. Biophys. Acta* 1848, 1258–1267. doi: 10.1016/j.bbamem.2015.01.002

Sanchez, M. E., Turina, A. V., Garcia, D. A., Nolan, M. V., and Perillo, M. A. (2004). Surface activity of thymol: implications for an eventual pharmacological activity. *Colloids Surf. B. Biointerf.* 34, 77–86. doi: 10.1016/j.colsurfb.2003.11.007

Sanchez-Borzone, M., Delgado-Marin, L., and Garcia, D. A. (2014). Inhibitory effects of carvone isomers on the GABAA receptor in primary cultures of rat cortical neurons. *Chirality* 26, 368–372. doi: 10.1002/chir.22328

Sano, Y., Inamura, K., Miyake, A., Mochizuki, S., Kitada, C., Yokoi, H., et al. (2003). A novel two-pore domain K^+ channel, TRESK, is localized in the spinal cord. *J. Biol. Chem.* 278, 27406–27412. doi: 10.1074/jbc.M206810200

Santos, M. R. R. V., Moreira, F. V. V., Fraga, B. P., Souza, D. O. P. D., Bonjardim, L. R., and Quintans-Junior, L. J. (2011). Cardiovascular effects of monoterpenes: a review. *Rev. Bras. Farmacogn.* 21, 764–771 doi: 10.1590/S0102-695X2011005000119

Schewe, M., Nematian-Ardestani, E., Sun, H., Musinszki, M., Cordeiro, S., Bucci, G., et al. (2016). A Non-canonical Voltage-Sensing Mechanism Controls Gating in K_{2P} K^+ Channels. *Cell* 164, 937–949. doi: 10.1016/j.cell.2016.02.002

Schmidt, C., Wiedmann, F., Schweizer, P. A., Katus, H. A., and Thomas, D. (2014). Inhibition of cardiac two-pore-domain K+ (K2P) channels–an emerging antiarrhythmic concept. *Eur. J. Pharmacol.* 738, 250–255. doi: 10.1016/j.ejphar.2014.05.056

Schmidt, C., Wiedmann, F., Zhou, X. B., Heijman, J., Voigt, N., Ratte, A., et al. (2017). Inverse remodelling of K2P3.1 K^+ channel expression and action potential duration in left ventricular dysfunction and atrial fibrillation: implications for patient-specific antiarrhythmic drug therapy. *Eur. Heart J.* 38, 1764–1774. doi: 10.1093/eurheartj/ehw559

Schmidt, C., Wiedmann, F., Gaubatz, A. R., Ratte, A., Katus, H. A., and Thomas, D. (2018). New Targets for Old Drugs: Cardiac Glycosides Inhibit Atrial-Specific K2P3.1 (TASK-1) Channels. *J. Pharmacol. Exp. Ther.* 365, 614–623. doi: 10.1124/jpet.118.247692

Ton, H. T., Smart, A. E., Aguilar, B. L., Olson, T. T., Kellar, K. J., and Ahern, G. P. (2015). Menthol Enhances the Desensitization of Human alpha3beta4 Nicotinic Acetylcholine Receptors. *Mol. Pharmacol.* 88, 256–264. doi: 10.1124/mol.115.098285

Toncheva, D., Mihailova-Hristova, M., Vazharova, R., Staneva, R., Karachanak, S., Dimitrov, P., et al. (2014). NGS nominated CELA1, HSPG2, and KCNK5 as candidate genes for predisposition to Balkan endemic nephropathy. *BioMed. Res. Int.* 2014, 920723. doi: 10.1155/2014/920723

Turina, A. V., Nolan, M. V., Zygadlo, J. A., and Perillo, M. A. (2006). Natural terpenes: self-assembly and membrane partitioning. *Biophys. Chem.* 122, 101–113. doi: 10.1016/j.bpc.2006.02.007

Walstab, J., Wohlfarth, C., Hovius, R., Schmitteckert, S., Roth, R., Lasitschka, F., et al. (2014). Natural compounds boldine and menthol are antagonists of human 5-HT3 receptors: implications for treating gastrointestinal disorders. *Neurogastroenterol. Motil.* 26, 810–820. doi: 10.1111/nmo.12334

Xu, H., Delling, M., Jun, J. C., and Clapham, D. E. (2006). Oregano, thyme and clove-derived flavors and skin sensitizers activate specific TRP channels. *Nat. Neurosci.* 9, 628–635. doi: 10.1038/nn1692

Zilberberg, N., Ilan, N., and Goldstein, S. A. (2001). KCNKO: opening and closing the 2-P-domain potassium leak channel entails "C-type" gating of the outer pore. *Neuron* 32, 635–648. doi: 10.1016/S0896-6273(01)00503-7

Zunino, M. P., Turina, A. V., Zygadlo, J. A., and Perillo, M. A. (2011). Stereoselective effects of monoterpenes on the microviscosity and curvature of model membranes assessed by DPH steady-state fluorescence anisotropy and light scattering analysis. *Chirality* 23, 867–877. doi: 10.1002/chir.20998

Conflict of Interest: The authors declare that the research was conducted in the absence of any commercial or financial relationships that could be construed as a potential conflict of interest.

frontiers in Pharmacology

BRIEF RESEARCH REPORT
published: 12 June 2020
doi: 10.3389/fphar.2020.00903

Endogenous and Exogenous Vanilloids Evoke Disparate TRPV1 Activation to Produce Distinct Neuronal Responses

Rakesh Kumar[†‡], *Matan Geron*[‡], *Adina Hazan and Avi Priel*[*]

Institute for Drug Research (IDR), School of Pharmacy, The Faculty of Medicine, The Hebrew University of Jerusalem, Jerusalem, Israel

OPEN ACCESS

Edited by:
Antonio Ferrer-Montiel, Universidad Miguel Hernández de Elche, Spain

Reviewed by:
Felix Viana, Institute of Neurosciences of Alicante (IN), Spain
Karel Talavera, KU Leuven, Belgium

***Correspondence:**
Avi Priel
avip@ekmd.huji.ac.il

[†]**Present address:**
Rakesh Kumar, Zoology Department, Ravenshaw University, Cuttack, India

[‡]*These authors have contributed equally to this work*

Specialty section:
This article was submitted to Pharmacology of Ion Channels and Channelopathies, a section of the journal Frontiers in Pharmacology

Received: *13 February 2020*
Accepted: *02 June 2020*
Published: *12 June 2020*

Citation:
Kumar R, Geron M, Hazan A and Priel A (2020) Endogenous and Exogenous Vanilloids Evoke Disparate TRPV1 Activation to Produce Distinct Neuronal Responses. Front. Pharmacol. 11:903. doi: 10.3389/fphar.2020.00903

Neuronal signals are processed along the nociceptive pathway to convey discriminative information, which would manifest in the produced pain sensation. The transient receptor potential vanilloid 1 (TRPV1), an important signaling complex in nociceptors termini, is activated by different noxious stimuli that underlie distinct pain sensations. For example, while endovanilloids are associated with inflammatory pain and hypersensitivity through TRPV1 activation, the exovanilloid toxin, capsaicin, evokes an acute pain by activating this channel. Differences in the TRPV1 activation profile evoked by exogenous and endogenous vanilloids were suggested to underlie this disparity in pain sensations. However, the cellular processes that lead to these differences in pain sensation mediated by the same channel are not fully understood. Here, we sought to describe the neuronal response of TRPV1-expressing nociceptors to exo-and endovanilloids. To this end, we performed current-clamp recordings in rat trigeminal neurons exposed to either capsaicin or intracellular endovanilloids produced downstream of the bradykinin receptor BK2. Our results show that lipoxygenase metabolites generate persistent TRPV1-dependent action potential firing while capsaicin evokes robust depolarization and high-frequency firing that is quickly terminated by depolarization block. Additionally, we found that a weak TRPV1 activation prolongs action potential firing. Overall, our results indicate different firing patterns evoked by inflammatory mediators and capsaicin *via* TRPV1 that correlate with the respective subsequent pain sensation. These findings also suggest that differences in neuronal activation stem from the variable degree of TRPV1 activation they produce.

Keywords: TRPV1, endovanilloids, exovanilloids, capsaicin, bradykinin, Gq- GPCR, nociceptors, inflammatory pain

INTRODUCTION

TRPV1 has been identified as an essential component of the nociceptive mechanisms underlying different pain conditions and pain sensations (Davis et al., 2000; Patapoutian et al., 2009; Mishra et al., 2011; Fattori et al., 2016). This non-selective cation channel, which is mainly found in nociceptors is a polymodal receptor that detects a wide array of noxious stimuli such as heat (>42°C), protons (low

pH), plant, and animal toxins, as well as bioactive lipids (Julius, 2013). TRPV1 activators engage diverse binding domains producing a modulatory effect on this multi-steric channel (Winter et al., 2013). One main binding domain is the intracellular vanilloid binding site (VBS), located between S3 and S4, with which both plant toxins and bioactive lipids interact (Jordt and Julius, 2002). Vanilloid plant toxins, such as the prototypical capsaicin (found in chili peppers), activating TRPV1, and produce acute pain (Yang et al., 2015). In contrast, TRPV1 bioactive lipids are endogenous vanilloids mainly produced during inflammation (Levine and Alessandri-Haber, 2007; Julius, 2013). This TRPV1 activation following injury was shown to be essential for heat hyperalgesia and pain hypersensitivity (Caterina et al., 2000; Shin et al., 2002). Thus, TRPV1 mediates both the acute burning pain following the ingestion of hot peppers and the dull and prolonged pain as well as hypersensitivity that often accompany inflammation.

The endovanilloid lipids, such as 12-Hydroeicosatetraenoic acid (12-HETE), are products of arachidonic acid (AA) metabolism by lipoxygenases (LOX), downstream of the Gq/GPCR pathway (Hwang et al., 2000; Starowicz et al., 2007; Veldhuis et al., 2015; Kumar et al., 2017). Thus, different components of the inflammatory soup such as bradykinin and histamine indirectly activate TRPV1 by inducing the Gq signaling cascade through their respective receptors co-expressed with TRPV1 in nociceptors (Shin et al., 2002; Shim et al., 2007). PKC is also activated in this signaling pathway and is essential for endovanilloid activity as it phosphorylates and sensitizes TRPV1 (Premkumar and Ahern, 2000; Kumar et al., 2017). Also, LOX metabolites are highly labile as they are quickly reduced to products with reduced potency (Hwang et al., 2000; Starowicz et al., 2007). Thus, endovanilloids are components of a highly regulated machinery essential for the initial recognition and subsequent healing of tissue injury, in contrast to exovanilloid toxins that provide the evolutionary advantage of evoking a deterring intense pain.

We previously showed that endovanilloids produced through Gq signaling evoke reduced open probability in TRPV1 and thus a weak channel activation in comparison to capsaicin (Kumar et al., 2017). The different properties of TRPV1 activation by exogenous and endogenous vanilloids were suggested to underlie the distinct pain sensations experienced during acute and inflammatory settings (Kumar et al., 2017). Indeed, it was suggested that while endovanilloids evoke prolonged action potential firing in nociceptors, exovanilloids produce a short burst of action potentials followed by a depolarization block, a cessation of firing despite suprathreshold membrane potential due to the inactivation of voltage-gated sodium (Na_V) channels (Liu et al., 2001; Shin et al., 2002; Blair and Bean, 2003). However, these observations were obtained using different experimental settings for endo- and exovanilloids. Moreover, in both cases, recordings were performed in ruptured cells where intracellular signaling (i.e., Gq signaling) is disrupted. Thus, exactly how these two types of vanilloids exert a different effect in neurons remains to be elucidated.

Here, we sought to further describe the neuronal response of TRPV1 expressing nociceptors to exo- and endovanilloids. To this end, we performed electrophysiological recordings in perforated trigeminal neurons in which the intracellular signaling apparatus is preserved. We show that endovanilloids produced downstream to bradykinin receptor activation evoke prolonged action potentials firing, which is TRPV1 dependent, while capsaicin-evoked firing is short-lived. Firing evoked by bradykinin requires the generation of endovanilloids catalyzed by PLC and LOX in the Gq signaling pathway. Also, we found that the lower depolarization induced by endovanilliods could underlie the prolonged firing as lower capsaicin concentrations partially emulate this firing pattern. Overall, our results indicate that the highly regulated, reduced activation of TRPV1 by endovanilloids produced by LOX enables prolonged firing in nociceptors in contrast to the robust firing quickly followed by depolarization block obtained following the application of the highly efficacious capsaicin. Thus, these findings demonstrate that different neuronal activation patterns could be evoked through the same binding site in TRPV1, potentially encoding different pain sensations.

MATERIALS AND METHODS

Neuronal Cell Culture and Viral Infection

The Institutional Animal Care Committee of The Hebrew University approved all procedures that involved the use of animals. Acute culture of rat TG neurons (n = 42) was performed as previously described (Bohlen et al., 2010). In brief, dissected ganglia from two to four rat pups (P0–3) were collected in ice-cold DPBS (with Ca^{2+} and Mg^{2+}) (Sigma-Aldrich, St. Louis, MO, USA), followed by digestion with 0.025% collagenase type IV (Worthington Biochemical Corp., Lakewood, NJ, USA) and then 0.25% Trypsin (Sigma-Aldrich, St. Louis, MO, USA). After enzymatic digestion, ganglia were triturated with fire-polished Pasteur glass pipettes of decreasing tip diameter. Cells were re-suspended in Dulbecco's modified Eagle's medium (DMEM, Gibco, Waltham, MA, USA) supplemented with 10% fetal bovine serum (FBS, Gibco), 1% penicillin-streptomycin (Gibco), and 25 mM 4-(2-hydroxyethyl)-1-piperazineethanesulfonic acid (HEPES; pH 7.3; Gibco, Waltham, MA, USA) (hereafter: complete DMEM) and plated on Poly-D-Lysine (PDL; Sigma, St. Louis, MO, USA) coated glass coverslips. Cells were allowed to recover for 3 h at 37°C in a 5% CO_2 atmosphere before patch-clamp experiments. Dissociated rat TG neurons (n = 4) were infected with 0.5 ng/ml adeno-associated virus vector, serotype 2 (rAAV2) containing hSyn-HA-hM3D(Gq)-IRES-mCitrine or hSyn-EGFP (University of North Carolina Vector Core, Chapel Hill, NC, USA), in a complete media supplemented with 50 ng/ml nerve growth factor (NGF) (Alomone Labs, Jerusalem, Israel) and 1 ng/ml glial cell-derived neurotrophic factor (GDNF) (Alomone Labs, Jerusalem, Israel) for one week before electrophysiological analysis. Infected neurons were selected based on their fluorophore expression.

Electrophysiology

Current-Clamp Recordings

Membrane voltages were recorded under the current-clamp mode (I = 0) using an Axopatch 200B patch-clamp amplifier (Molecular Devices, Sunnyvale, CA, USA). Membrane voltages were digitized using a Digidata 1440A interface board and pCLAMP 10.6 software (Molecular Devices, Sunnyvale, CA, USA) at room temperature. Sampling frequency was set to 20 kHz and low-pass filtered at 5 kHz. Patch electrodes were fabricated from borosilicate glass using the P1000 Micropipette Puller (Sutter Instrument) and fire-polished using the Microforge MF-900 (Narishige, East Meadow, NY, USA) to a resistance of 2 to 4 MΩ for whole-cell and perforated patch recordings. Perforated patch or standard whole-cell configurations of the patch-clamp technique were obtained in voltage-clamp mode before proceeding to current-clamp recording mode. The perforated patch configuration was carried out as previously described (Priel and Silberberg, 2004). Briefly, the pipette solution constituted (mM): 75 K_2SO_4, 55 KCl, 5 $MgSO_4$, 10 HEPES, adjusted to pH 7.2 with KOH. Nystatin (Sigma, St. Louis, MO, USA) was used for patch perforation at a working concentration of 180 μM. To this end, it was dissolved in Dimethyl Sulfoxide (DMSO; Sigma, St. Louis, MO, USA) to obtain a 55 mM stock solution, which following 1 min ultra-sonication was diluted in pipette solution to obtain a working solution of 180 μM. Nystatin solutions were freshly prepared in the dark every 2 h. Only cells with a series resistance of ≤15 MΩ were used for analysis. The extracellular solution contained (mM): 140 NaCl, 2.8 KCl, 2 $MgSO_4$, 1.8 $CaCl_2$, 10 HEPES, 10 D-glucose, adjusted to pH 7.4 with NaOH (Ringer solution). Once the perforated-patch or the standard whole-cell configuration was established, cells were continuously superfused with extracellular solutions *via* the ValveBank perfusion system (AutoMate Scientific, Berkeley, CA, USA). Cells were incubated with U73122 for 5 minutes before recording, whereas other drugs and chemicals were applied as indicated in the figures. For the standard whole-cell configuration pipette solution contained (mM): 130 potassium-gluconate ($KC_6H_{11}O_7$), 2 $MgSO_4$, 6 KCl, 10 NaCl, 10 HEPES, 5 MgATP, 0.5 Li_2GTP, adjusted to pH 7.4 with KOH. Small TG neurons, (~25 μm), shown to be nociceptors based on their capsaicin-sensitivity (Cardenas et al., 1995; Le Pichon and Chesler, 2014) were selected for recording. Small TG neurons with stable (<10% variation) resting membrane potentials (≤−50 mV), action potentials with overshoots >40 mV, and amplitudes >85 mV were analyzed (Blair and Bean, 2003; Cummins et al., 2009; Gudes et al., 2015). Only neurons with a threshold of −35 ± 3 mV, determined according to the first action potential elicited under the fast current-clamp mode of a single ramp of depolarizing current injection (500 ms; 0–150 pA) (Gudes et al., 2015), were selected for analysis. In perforated current-clamp recordings, junction potential was calculated to be 9.3 mV (using Clampfit 10.6). The membrane potential was corrected accordingly. The phase plots of dV/dt vs. membrane voltage were formed by plotting the rate of change of membrane potential to time (dV/dt), following the application of bradykinin or capsaicin, as a function of membrane potential. The first two evoked APs in each cell were analyzed. Maximum upstroke velocity was obtained from (dV/dt) Max.

Voltage-Clamp Recordings

Recordings from TG neurons were performed as previously described (Kumar et al., 2016). Briefly, membrane currents were recorded under the voltage-clamp using an Axopatch 200B patch-clamp amplifier (Molecular Devices, Sunnyvale, CA, USA). Membrane currents were digitized using a Digidata 1440A interface board and pCLAMP 10.6 software (Molecular Devices, Sunnyvale, CA, USA) with sampling frequency set to 10 kHz and were low-pass filtered at 5 kHz. The holding voltage was −60 mV. All experiments were carried out at room temperature.

Data Analysis

The electrophysiological analysis was performed using pCLAMP 10.6 software (Molecular Devices, Sunnyvale, CA, USA). All statistical data were calculated using SigmaPlot 11 (Systat Software, San Jose, CA, USA) and Prism 7 (Graphpad Software, La Jolla, CA, USA) software. Student's *t*-test and ANOVA were used to determine statistical significance.

Drugs and Chemicals

All salts and buffers were purchased from Sigma-Aldrich (St. Louis, MO, USA). Capsaicin (Cap), Capsazepine (CPZ), U73122, and Bisindolylmaleimide I (BIM I; GF 109203X) were purchased from Tocris Bioscience (Bristol, UK). Bradykinin (Bk), Histamine dihydrochloride (His), Nordihydroguaiaretic acid (NDGA), Bupivacaine hydrochloride (bupivacaine), and Clozapine N-oxide (CNO) were purchased from Sigma-Aldrich (St. Louis, MO, USA). All drugs were dissolved according to manufacturer protocol.

RESULTS

Inflammatory Mediators and Exovanilloids Evoke Distinct Firing Patterns

Endo- and exovanilloids produce different activation profiles of TRPV1 expressed in a heterologous expression system (Kumar et al., 2017). To characterize the neuronal response to endogenous and exogenous vanilloids (i.e., capsaicin), we performed recordings in acutely dissociated trigeminal neurons from neonatal rats. In contrast to exovanilloids, endovanilloids are highly lipophilic, and thus their ability to cross the plasma membrane and reach the intracellular VBS in the TRPV1 channel when applied extracellularly is reduced as they can be trapped in the lipid bilayer (Hwang et al., 2000; Starowicz et al., 2007; Ursu et al., 2010). Under physiological conditions, endovanilloids were suggested to be LOX metabolites, produced downstream of Gq/GPCR (Hwang et al., 2000; Veldhuis et al., 2015). This pathway can be activated through receptors such as the bradykinin receptor BK2 and the histamine receptor H1 that were shown to co-express with TRPV1 (Carr et al., 2002; Shin et al., 2002; Pethő and Reeh, 2012). Thus, throughout this study, we sought to induce cell-autonomous

endovanilloid production by activating the Gq/GPCR pathway using the inflammatory mediators bradykinin and histamine. Accordingly, we employed the perforated whole-cell configuration of the patch-clamp technique, which in contrast to the standard whole-cell configuration, preserves the cellular milieu and allows signaling events downstream of GPCR activation (Knauer and Yoshida, 2019). Indeed, in perforated patch recordings, 18 out of 27 TRPV1-expressing nociceptors responded to bradykinin, whereas only 1 out of 6 were bradykinin- sensitive in whole-cell configuration recordings (**Figure 1A**). Of note, six out of the 33 small diameter neurons recorded under the perforated configuration were sensitive to bradykinin but not to capsaicin. Also, just four of 36 capsaicin-responsive nociceptors responded to histamine in the perforated configuration. This low rate of co-expression is expected as H1R expression in $TRPV1^+$ neurons is scarce, whereas TRPV1 is expressed in most $H1R^+$ neurons (Roberson et al., 2013). As shown in **Figures 1B, C**, while exposure to bradykinin or histamine evoked a long train of action potentials, exposure to capsaicin (0.2 μM) resulted in a robust depolarization with few action potentials that were followed by an immediate depolarization block. While the persistent neuronal activation by bradykinin allowed a higher number of action potentials firing, capsaicin evoked a higher firing frequency (**Figures 1D, E**). Therefore, our analysis indicates that inflammatory mediators and capsaicin (0.2 μM) produce distinctive neuronal firing patterns as both bradykinin and histamine evoke a more prolonged neuronal activation, albeit with reduced firing rate in TRPV1-positive nociceptors as compared to capsaicin. In order to further analyze the TRPV1-induced firing patterns, we compared the rate of change of membrane voltage as a function of membrane voltage, dV/dt vs. V, between the first and second APs. As shown in **Figure 2**, we found that sequential capsaicin-evoked APs present a significant decrease in maximal upstroke velocity [(dV/dt)max]. As (dV/dt) max is determined by the number of available Na_V channels (i.e., non-inactivated), this indicates that the fast and robust depolarization evoked by capsaicin causes the gradual inactivation of these channels until depolarization block is reached (Gudes et al., 2015). In contrast, bradykinin-evoked APs are mostly unchanged, suggesting the full recovery of Na_V channels between APs.

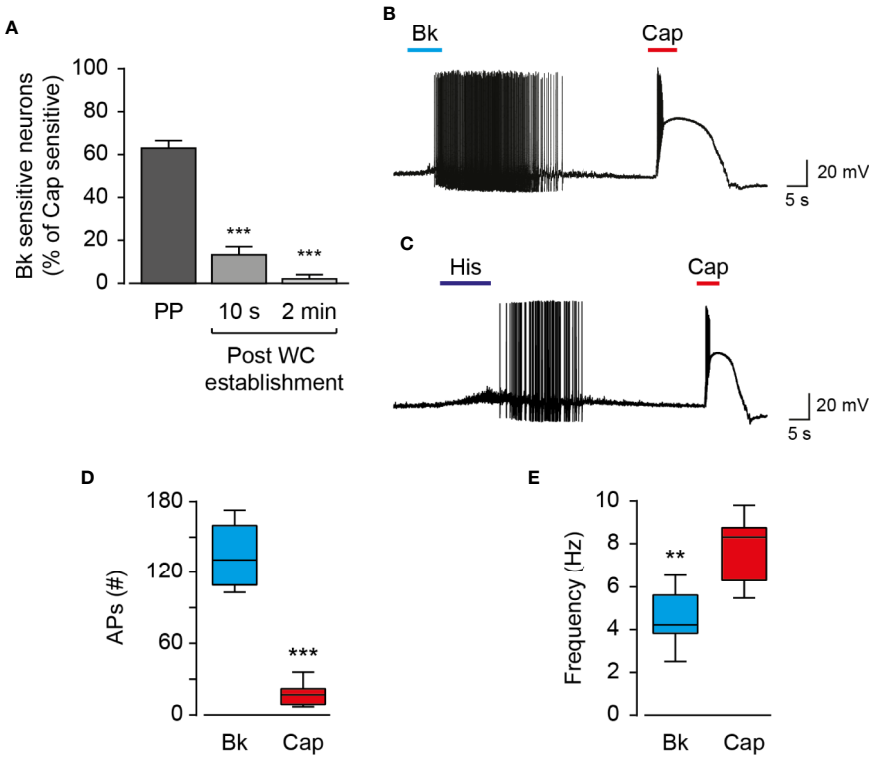

FIGURE 1 | Endo- and exovanilloids evoke distinct patterns of neuronal activation. **(A)** Bar diagram showing the average (± SEM) percentage of bradykinin ("Bk"; 0.5 μM) sensitive nociceptors (n = 6–27) at different configurations of the patch-clamp technique, normalized to the percentage of capsaicin ("Cap"; 0.2 μM) -sensitive cells. Sensitive cells were defined by the detection of agonist-evoked action potentials. Statistical significance between perforated whole-cell ("Perforated"; n = 27) and the whole-cell ("WC"; n = 6) configurations were determined using ANOVA with multiple comparisons, where *** represents $p \leq 0.001$. **(B)** Representative current-clamp recording (I = 0) from rat TG neurons using the perforated whole-cell configuration in response to capsaicin ("Cap"; red bar) and bradykinin ("Bk"; cyan bar) (n = 12). Bradykinin (0.5 μM) was applied for 15 s followed by capsaicin (0.2 μM) application for 5 s. **(C)** Representative current-clamp recording (I = 0) from rat TG neurons using the perforated whole-cell configuration in response to capsaicin ("Cap"; red bar) and histamine ("His"; dark blue bar) (n = 4). Histamine (20 μM) was applied for 15 s followed by capsaicin (0.2 μM) application for 5 s. **(D)** Box and whiskers plot shows the number of evoked action potentials (APs (#)) in response to bradykinin (0.5 μM) or capsaicin (0.2 μM) (n = 12). ***$p \leq 0.001$, paired Student *t*-test. **(E)** Box and whiskers plot shows the firing rate (Frequency) in response to bradykinin (0.5 μM) or capsaicin (0.2 μM) (n = 12). **$p \leq 0.01$ paired Student's *t*-test.

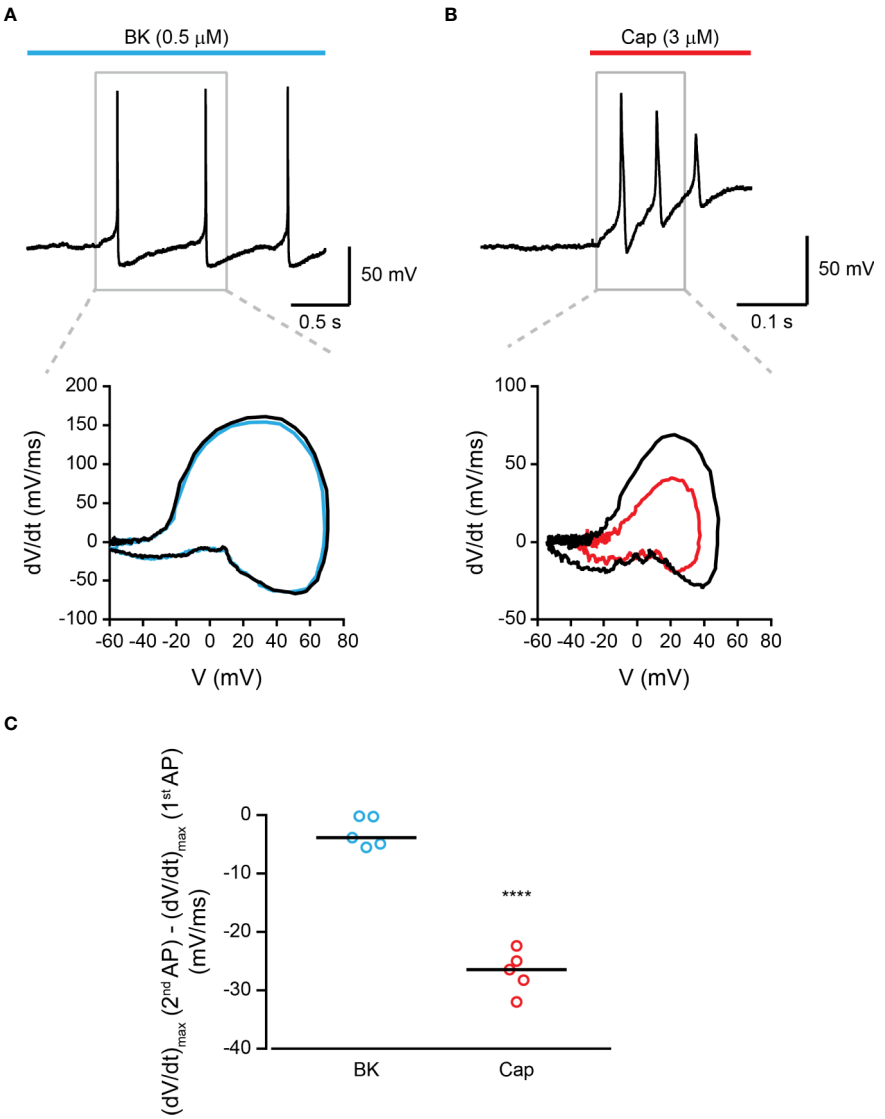

FIGURE 2 | Bradykinin-evoked activation of TRPV1 produces repetitive AP firing. **(A)** *Top:* Current-clamp recording (I = 0) from small-diameter dissociated rat trigeminal ganglion (TG) TRPV1+ neurons (P0) using the perforated whole-cell configuration of the patch-clamp technique. Representative trace of the first three APs following the application of bradykinin ("Bk"; cyan bar; 0.5 μM) is shown. *Bottom:* Phase plots of the rate of change of the membrane potential (dV/dt) during the first (black trace) and second (cyan trace) APs vs. membrane potential (V). **(B)** *Top:* Current-clamp recording (I = 0) from small-diameter dissociated rat trigeminal ganglion (TG) TRPV1+ neurons (P0) using the perforated whole-cell configuration of the patch-clamp technique. Representative trace of the first three APs following the application of capsaicin ("Cap"; red bar; 3 μM) is shown. *Bottom:* Phase plots of the rate of change of the membrane potential (dV/dt) during the first (black trace) and second (red trace) APs vs. membrane potential (V). **(C)** Mean/scatter-dot plot representing the difference in the maximal velocity (dV/dt) of the upstroke of the AP between the second and first APs evoked by either bradykinin ("Bk"; 0.5 μM; cyan circles) or capsaicin ("Cap"; red circles; 3 μM) (n = 5). ****p ≤ 0.0001, unpaired Student's *t*-test.

Bradykinin-Evoked Firing Is Mediated by TRPV1 and Requires LOX Metabolites

The bradykinin receptor, BK2, was previously shown to cause membrane depolarization by activating ion channels other than TRPV1 (Katanosaka et al., 2008). This includes the activation of ANO1, sensitization of TRPA1, and inhibition of Kv7 channels (Liu et al., 2010). However, as was previously shown by others (Shin et al., 2002), the application of the competitive TRPV1 antagonist, capsazepine, completely abolished action potential firing evoked by bradykinin as well as capsaicin (**Figure 3A**). Like other GPCRs, BK2 can activate various G protein signaling pathways (i.e., Gi, and Gq) (Miyamoto et al., 1997; Sandhu et al., 2019). In contrast, the engineered Gq-DREADD (hM3D (Gq)) receptor exclusively interacts with Gq proteins when it is bound to its selective activator, clozapine-N-oxide (CNO) (Roth, 2016). Nonetheless, in dissociated TRPV1-positive TG neurons infected with adeno-associated virus-carrying Gq-DREADD (hM3D(Gq)), CNO evoked a comparable response

to that evoked by bradykinin in EGFP-infected neurons (**Figure S1**). Thus, activation of the promiscuous BK2 mimics that of the Gq-DREADD that specifically induces Gq signaling, suggesting that other pathways have a minor effect on BK-evoked nociceptive firing. Inhibiting PLC, which initiates the signaling cascade downstream Gq, by incubating neurons with U73122, produced an attenuated response to bradykinin while the capsaicin response remained intact (**Figure 3B**). This further demonstrates that the neuronal response to bradykinin is Gq-dependent. To confirm the role of endovanilloids, produced by LOX in the neuronal response to bradykinin, neurons were incubated with the broad LOX inhibitor, nordihydroguaiaretic acid (NDGA). Similarly to PLC inhibition, neurons in which LOX was inhibited presented a diminished response to bradykinin, whereas the response to capsaicin was unaffected (**Figure 3C**). Thus, neuronal activation by bradykinin is mediated by endovanilloids, which are LOX metabolites. Sensitization of TRPV1 by PKC phosphorylation was shown to be essential to the activation of the channel by endovanilloids (Bhave et al., 2003; Kumar et al., 2017). Indeed, as shown in **Figure 3D**, inhibition of PKC by bisindoylmaleimide I (BIM) resulted in a reduced action potential firing evoked by bradykinin, thus demonstrating that PKC-mediated sensitization potentiates the neuronal response to endovanilloids. Together, these results confirm that the bradykinin-evoked prolonged firing in these neurons occurs through the activation of TRPV1 by endovanilloids produced downstream of the Gq signaling pathway (**Figure 3E**).

Reduced TRPV1 Current and Membrane Depolarization Result in Prolonged AP Firing

The properties of membrane depolarization affect the activity of ion channels that participate in the generation of action potentials (Bean, 2007). To examine the possibility that the different patterns of vanilloids-mediated neuronal activation result from differences in membrane depolarization, we measured voltage changes in TG neurons exposed to bradykinin or capsaicin (**Figure 4A**). To prevent the generation of action potentials and depolarization evoked by voltage-gated sodium channels, nociceptors were treated with bupivacaine throughout the analysis (Scholz et al., 1998). As summarized in **Figure 4B**, while capsaicin evoked a robust membrane depolarization ($\Delta V_{capsaicin}$ = 52 ± 7 mV), similarly to previous reports (Liu et al., 2001; Blair and Bean, 2003), exposure to bradykinin resulted in a moderate response ($\Delta V_{bradykinin}$ = 17 ± 5 mV). Therefore, our analysis indicates that endovanilloids evoke close-to-threshold neuronal depolarization, which is in contrast to the robust neuronal depolarization evoked by capsaicin. Thus, our findings indicate that endo- and exovanilloids induce different levels of neuronal membrane depolarization. The observed membrane depolarizations suggest the induction of different current

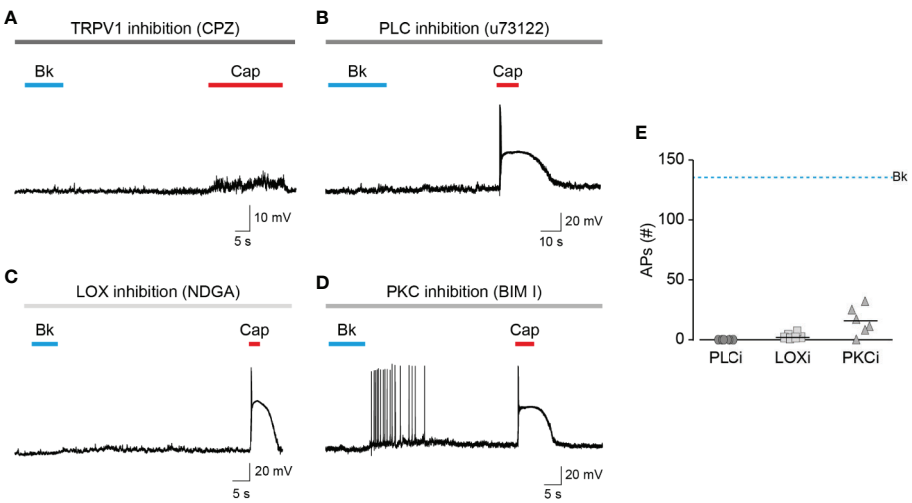

FIGURE 3 | Endovanilloids produced by LOX evoke TRPV1-dependent nociceptor firing. Current-clamp recordings (I = 0) from small-diameter dissociated rat trigeminal ganglion (TG) neurons (P0) using the perforated whole-cell configuration of the patch-clamp technique. **(A)** Representative recording in which bradykinin (0.5 μM) was applied for 15 s followed by capsaicin (1 μM) application for 20 s, in the continuous presence of capsazepine ("CPZ"; 40 μM; grey bar) (n = 6). **(B)** Representative recording in which bradykinin (0.5 μM) was applied for 15 s followed by capsaicin (0.2 μM) application for 5 s, in the continuous presence of U73122 (3 μM; bar) (n = 6). **(C)** Representative recording in which bradykinin (0.5 μM) was applied for 10 s followed by capsaicin (0.2 μM) application for 5 s, in the continuous presence of nordihydroguaiaretic acid ("NDGA"; 10 μM; bar) (n = 7). **(D)** Representative recording in which bradykinin (0.5 μM) was applied for 10 s followed by capsaicin (0.2 μM) application for 5 s, in the continuous presence of bisindolylmaleimide I ("BIM I"; 10 μM; grey bar) (n = 6). **(E)** Mean/scatter-dot plot representing the number of action potentials (APs) evoked by bradykinin while PLC ("PLCi"; dark grey circles), LOX ("LOXi"; light grey squares) or PKC ("PKCi"; grey triangles) are inhibited (n = 6–7). The dashed line indicates the average number of action potentials evoked by bradykinin in the absence of inhibitors.

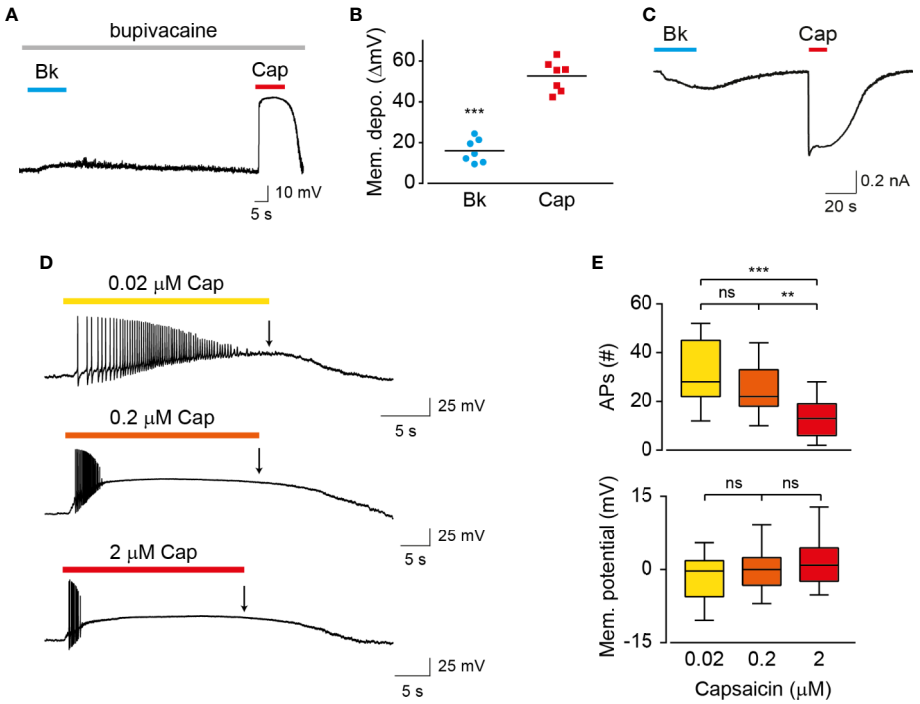

FIGURE 4 | Endo- and exovanilloids evoke distinct neuronal membrane depolarization. **(A)** Representative current-clamp recording (I = 0) from rat TG neurons using the perforated whole-cell configuration in response to bradykinin ("Bk"; 1 μM; cyan bar and circles) that was applied for 15 s followed by capsaicin ("Cap"; 3 μM; red bar and squares) application for 15 s in the continuous presence of bupivacaine (300 μM; light grey bar) (n = 7). **(B)** Mean/scatter-dot plot representing the evoked membrane depolarization ("Mem. depo."; ΔmV) in the presence of bupivacaine, as shown in A (n = 7). ***p ≤ 0.001, paired Student's *t*-test. **(C)** Representative perforated whole-cell recordings from a TG neuron at a holding potential of –60 mV. Cells were exposed to bradykinin ("Bk"; 0.5 μM; cyan bar) followed by applications of capsaicin ("Cap"; 1 μM; red bar) (n = 5). **(D)** Representative traces (n = 11–18) in which capsaicin ("Cap") was applied for 20 s in sub-EC_{50} (0.02 μM; yellow; top trace), EC_{50} (0.2 μM; orange; middle trace) and saturating (2 μM; red; bottom trace) concentrations. **(E)** Box and whiskers plots are showing the mean number of evoked action potentials ("APs (#)"; upper) and membrane potential at the end of agonist application (as indicated by an arrow in **D**; bottom) in response to the different capsaicin concentrations (n = 11–18). **p ≤ 0.01 and ***p ≤ 0.001 and ns- no statistical significance, ANOVA with multiple comparisons.

amplitudes by endo- and exovanilloids. To test this possibility, we measured currents in TG neurons under voltage clamp and found that while capsaicin evoked a typical robust current, endovanilloids downstream of bradykinin evoke lower current amplitude (**Figure 4C**). To test whether lowering capsaicin concentration could mimic the endovanilloids -evoked response, we measured neuronal firing in response to saturating (2 μM), EC_{50} (0.2 μM), and sub-EC_{50} (0.02 μM) capsaicin concentrations (Hazan et al., 2015; Kumar et al., 2016). Of note, we previously showed that 0.02 μM is at the lower limit of capsaicin that evokes TRPV1 activation in rat TRPV1 (rTRPV1) (**Figure S2**) (Hazan et al., 2015). As shown in **Figures 4D, E**, lowering capsaicin concentration allowed the development of more action potentials. However, bradykinin application evoked ~3-fold more action potentials as compared to capsaicin, even when the latter was applied at a sub-EC_{50} concentration (compare **Figure 1B** to **4D** and **1D** to **4E**). Importantly, for all analyzed capsaicin concentrations, depolarization block was reached. Therefore, our findings indicate that the different properties of endo- and exovanilloids, as well as their concentration, dictate the different neuronal response. Nonetheless, most exovanilloids produce depolarization block in neurons, while endovanilloids do not.

DISCUSSION

Endo- and exovanilloids are associated with distinct pain sensations. Here, we show that these vanilloids promote different neuronal responses. Our findings indicate that while exovanilloids produce robust but acute neuronal firing, endovanilloids–evoked TRPV1 activation supports a prolonged neuronal response (**Figure 1B**). In this work, we applied the inflammatory mediator, bradykinin, to rat TG neurons in order to induce the biosynthesis of endovanilloids intracellularly. Also, electrophysiological recordings were performed in perforated neurons in which the intracellular environment required for the production of these TRPV1 activators is intact. This experimental design better simulates the physiological conditions in which endovanilloids activate TRPV1 in comparison to either the direct application of these bioactive lipids or recordings using configurations that cause the dilution of the intracellular milieu. In our experimental settings, endovanilloids evoke lower neuronal membrane depolarization, which is sufficient to evoke firing yet does not develop into the depolarization block associated with the potent exovanilloids (**Figures 1B**, **2**, and **4A**). The weaker depolarization evoked by

endovanilloids reflects their reduced activation of TRPV1 in comparison to capsaicin (**Figure 4C**) (Kumar et al., 2017). Also, we found that the reduced TRPV1 activation evoked by low capsaicin concentrations produces longer firing reminiscent of the effect of endovanilloids. However, even in sub-EC_{50} capsaicin concentrations, the neuronal firing is eventually terminated by a depolarization block, suggesting that additional molecular mechanisms may underlie TRPV1-induced neuronal firing (**Figure 4C**). Thus, we propose that the different profiles of TRPV1 activation by endo- and exovanilloids and subsequent membrane depolarization may determine the duration, and potentially the intensity, of the evoked pain response.

Our results demonstrate that individual TG neurons can produce diverse firing patterns in response to different stimuli. Indeed, the different patterns of pain sensation evoked by endo- and exo-vanilloids may reflect their contradictory functions. The prototypical, exovanilloids, capsaicin, and resiniferatoxin (RTX), are phytotoxins believed to have evolved as plants' defense mechanism as they induce a robust response by harnessing central functional protein sites (such as the TRPV1 VBS) (Cromer and McIntyre, 2008; Bohlen et al., 2010; Cao et al., 2013). As such, exposure to these toxins produces acute and intense pain. In contrast, endovanilloids are essential components in the process through which tissue injury and inflammation are detected and resolved, which requires tight regulation of their concentration and activity (Hwang et al., 2000; Hylands-White et al., 2017; Kumar et al., 2017). Thus, we propose that while exo- and endovanilloids act through the same binding site in TRPV1, they produce distinct neuronal activations that underlie their different painful effects.

It is noteworthy that not all exovanilloids produce robust TRPV1 activation and pungency. Namely, capsaicin analogs were found to cause desensitization of sensory neurons without evoking a pungent sensation (Jancsó-Gábor et al., 1970). In addition, the synthetic exovanilloids, olvanil, arvanil, and SDZ249-665, were shown to evoke little or no pungency when applied to the eye in guinea pigs (Ursu et al., 2010). While the exact mechanism of this lack of pungency remains unclear, it was shown that non-pungent exovanilloids evoke slower kinetics of TRPV1 activation and depolarization, resulting in lower probability for AP generation (Ursu et al., 2010; Viana, 2011). The reduced rate of TRPV1 activation was suggested to stem from slow penetration through the membrane, further supporting our experimental design of inducing endovanilloid synthesis intracellularly (Ursu et al., 2010). Nonetheless, we show here that slowly developing depolarization induced by TRPV1 activation allows for the recovery of Na_V channels, resulting in prolonged AP firing (**Figures 2** and **4**). Regardless, these findings demonstrate that the kinetics of the activation profile of TRPV1 is a significant factor affecting neuronal firing and consequent response.

We have previously shown that the submaximal activation of TRPV1 by endovanilloids stems from a low open probability of the channel compared to capsaicin–evoked activation (Kumar et al., 2017). Another TRPV1 activator which elicits reduced TRPV1 activation is the peptide spider toxin, double-knot toxin (DkTx), as it locks the channel in a sub-conducting state (Geron et al., 2018). The injection of DkTx-containing venom following this spider's bite produces prolonged pain that was attributed to the persistent activation of TRPV1 by this toxin (Liang, 2004; Bohlen et al., 2010). It is also possible that the lower TRPV1 activation by this toxin evokes weaker depolarization and avoidance of depolarization block that facilitates a continuous pain sensation. However, this spider's venom was also reported to produce an immediate intense pain similarly to capsaicin (Liang, 2004). While effects of the isolated DkTx on the neuronal and behavioral levels were not yet thoroughly tested, this toxin further demonstrates the ability of different TRPV1 activators to produce various activation profiles which may underlie distinct pain sensations.

Bradykinin affects ion channels other than TRPV1, such as ANO1 and Kv7 channels, to produce excitation in nociceptors (Liu et al., 2010). Nonetheless, as demonstrated in **Figure 3A**, the TRPV1 inhibitor, capsazepine, completely inhibits AP firing. Thus, at least in $TRPV1^+$ neurons, TRPV1 activation by endovanilloids is necessary for the generation of AP firing. This does not preclude other effects induced by BK2 that may cause other changes in the firing properties of these neurons (Choi and Hwang, 2018). These effects produced by the bradykinin receptor are mainly Gq dependent, a signaling pathway that is also activated by other inflammatory mediators and is required for the endovanilloid activation of TRPV1 (Choi and Hwang, 2018). Thus, the effects of bradykinin on other ion channels are physiologically relevant and are part of TRPV1 activation by endovanilloids during inflammation.

Overall, our results suggest that the regulated activity of TRPV1 by endovanilloids allows a prolonged, low-frequency neuronal response. When toxins (such as capsaicin) bypass this regulation, neuronal membrane depolarization block is achieved, and the response is rapidly terminated. Thus, although capsaicin is a powerful tool to study this pivotal pain receptor, its activity may not reproduce the endogenous receptor response. The hydrophobicity of endovanilloids and the transient nature of their synthesis make them challenging to investigate (Starowicz et al., 2007). Nevertheless, a full understanding of TRPV1's physiological role necessitates studying its response to multiple endogenous stimuli. Elucidating the mechanisms through which inflammatory pain is generated may facilitate the identification of new targets as well as the development of new tools for pain management.

DATA AVAILABILITY STATEMENT

The datasets generated for this study are available on request to the corresponding author.

ETHICS STATEMENT

The animal study was reviewed and approved by Ethics Committee of the Hebrew University.

AUTHOR CONTRIBUTIONS

AP designed research. RK, MG, and AH performed research. RK, MG, AH, and AP analyzed data. MG and AP wrote the paper.

FUNDING

This work was supported by the Israel Science Foundation (Grant 1444/16 to AP), the Brettler Center and David R. Bloom Center, School of Pharmacy (The Hebrew University of Jerusalem; to AP), a Jerusalem Brain Committee Postdoctoral Fellowship (to RK) and the Paula Goldberg fellowship (to MG).

ACKNOWLEDGMENTS

We thank the AP laboratory members for the insightful comments on the manuscript.

SUPPLEMENTARY MATERIAL

The Supplementary Material for this article can be found online at: https://www.frontiersin.org/articles/10.3389/fphar.2020.00903/full#supplementary-material

REFERENCES

Bean, B. P. (2007). The action potential in mammalian central neurons. *Nat. Rev. Neurosci.* 8, 451–465. doi: 10.1038/nrn2148

Bhave, G., Hu, H.-J., Glauner, K. S., Zhu, W., Wang, H., Brasier, D. J., et al. (2003). Protein kinase C phosphorylation sensitizes but does not activate the capsaicin receptor transient receptor potential vanilloid 1 (TRPV1). *Proc. Natl. Acad. Sci. U. S. A.* 100, 12480–12485. doi: 10.1073/pnas.2032100100

Blair, N. T., and Bean, B. P. (2003). Role of tetrodotoxin-resistant Na+ current slow inactivation in adaptation of action potential firing in small-diameter dorsal root ganglion neurons. *J. Neurosci.* 23, 10338–10350. doi: 10.1523/JNEUROSCI.23-32-10338.2003

Bohlen, C. J., Priel, A., Zhou, S., King, D., Siemens, J., and Julius, D. (2010). A bivalent tarantula toxin activates the capsaicin receptor, TRPV1, by targeting the outer pore domain. *Cell* 141, 834–845. doi: 10.1016/j.cell.2010.03.052

Cao, E., Liao, M., Cheng, Y., and Julius, D. (2013). TRPV1 structures in distinct conformations reveal activation mechanisms. *Nature* 504, 113–118. doi: 10.1038/nature12823

Cardenas, C. G., Mar, L. P. D. E. L., Scroggs, R. S., and Del Mar, L. P. (1995). Variation in serotonergic inhibition of calcium channel currents in four types of rat sensory neurons differentiated by membrane properties. *J. Neurophysiol.* 74, 1870–1879. doi: 10.1152/jn.1995.74.5.1870

Carr, M. J., Kollarik, M., Meeker, S. N., and Undem, B. J. (2002). A Role for TRPV1 in Bradykinin-Induced Excitation of Vagal Airway Afferent Nerve Terminals. *J. Pharmacol. Exp. Ther.* 304, 1275–1279. doi: 10.1124/jpet.102.043422

Caterina, M. J., Leffler, A., Malmberg, A. B., Martin, W. J., Trafton, J., Petersen-Zeitz, K. R., et al. (2000). Impaired nociception and pain sensation in mice lacking the capsaicin receptor. *Science* 288, 306–313. doi: 10.1126/SCIENCE.288.5464.306

Choi, S.-I., and Hwang, S. W. (2018). Depolarizing Effectors of Bradykinin Signaling in Nociceptor Excitation in Pain Perception. *Biomol. Ther. (Seoul)* 26, 255–267. doi: 10.4062/biomolther.2017.127

Cromer, B., and McIntyre, P. (2008). Painful toxins acting at TRPV1. *Toxicon* 51, 163–173. doi: 10.1016/j.toxicon.2007.10.012

Cummins, T. R., Rush, A. M., Estacion, M., Dib-Hajj, S. D., and Waxman, S. G. (2009). Voltage-clamp and current-clamp recordings from mammalian DRG neurons. *Nat. Protoc.* 4, 1103–1112. doi: 10.1038/nprot.2009.91

Davis, J. B., Gray, J., Gunthorpe, M. J., Hatcher, J. P., Davey, P. T., Overend, P., et al. (2000). Vanilloid receptor-1 is essential for inflammatory thermal hyperalgesia. *Nature* 405, 183–187. doi: 10.1038/35012076

Fattori, V., Hohmann, M., Rossaneis, A., Pinho-Ribeiro, F., and Verri, W. (2016). Capsaicin: Current Understanding of Its Mechanisms and Therapy of Pain and Other Pre-Clinical and Clinical Uses. *Molecules* 21, 844. doi: 10.3390/molecules21070844

Geron, M., Kumar, R., Zhou, W., Faraldo-Gómez, J. D., Vásquez, V., and Priel, A. (2018). TRPV1 pore turret dictates distinct DkTx and capsaicin gating. *Proc. Natl. Acad. Sci.* 115, 201809662. doi: 10.1073/PNAS.1809662115

Gudes, S., Barkai, O., Caspi, Y., Katz, B., Lev, S., and Binshtok, A. M. (2015). The role of slow and persistent TTX-resistant sodium currents in acute tumor necrosis factor-α-mediated increase in nociceptors excitability. *J. Neurophysiol.* 113, 601–619. doi: 10.1152/jn.00652.2014

Hazan, A., Kumar, R., Matzner, H., and Priel, A. (2015). The pain receptor TRPV1 displays agonist-dependent activation stoichiometry. *Sci. Rep.* 5, 12278. doi: 10.1038/srep12278

Hwang, S. W., Cho, H., Kwak, J., Lee, S. Y., Kang, C. J., Jung, J., et al. (2000). Direct activation of capsaicin receptors by products of lipoxygenases: endogenous capsaicin-like substances. *Proc. Natl. Acad. Sci. U. S. A.* 97, 6155–6160. doi: 10.1073/pnas.97.11.6155

Hylands-White, N., Duarte, R. V., and Raphael, J. H. (2017). An overview of treatment approaches for chronic pain management. *Rheumatol. Int.* 37, 29–42. doi: 10.1007/s00296-016-3481-8

Jancsó-Gábor, A., Szolcsányi, J., and Jancsó, N. (1970). Irreversible impairment of thermoregulation induced by capsaicin and similar pungent substances in rats and guinea-pigs. *J. Physiol.* 206, 495–507. doi: 10.1113/jphysiol.1970.sp009027

Jordt, S.-E., and Julius, D. (2002). Molecular Basis for Species-Specific Sensitivity to "Hot" Chili Peppers. *Cell* 108, 421–430. doi: 10.1016/S0092-8674(02)00637-2

Julius, D. (2013). TRP channels and pain. *Annu. Rev. Cell Dev. Biol.* doi: 10.1146/annurev-cellbio-101011-155833

Katanosaka, K., Banik, R. K., Giron, R., Higashi, T., Tominaga, M., and Mizumura, K. (2008). Contribution of TRPV1 to the bradykinin-evoked nociceptive behavior and excitation of cutaneous sensory neurons. *Neurosci. Res.* 62, 168–175. doi: 10.1016/J.NEURES.2008.08.004

Knauer, B., and Yoshida, M. (2019). Switching between persistent firing and depolarization block in individual rat CA1 pyramidal neurons. *Hippocampus* 29, 817–835. doi: 10.1002/hipo.23078

Kumar, R., Hazan, A., Basu, A., Zalcman, N., Matzner, H., and Priel, A. (2016). Tyrosine Residue in TRPV1 Vanilloid Binding Pocket Regulates Deactivation Kinetics. *J. Biol. Chem.* 1997, 13855–13863. doi: 10.1074/jbc.M116.726372

Kumar, R., Hazan, A., Geron, M., Steinberg, R., Livni, L., Matzner, H., et al. (2017). Activation of transient receptor potential vanilloid 1 by lipoxygenase metabolites depends on PKC phosphorylation. *FASEB J.* 31, 1238–1247. doi: 10.1096/fj.201601132R

Le Pichon, C. E., and Chesler, A. T. (2014). The functional and anatomical dissection of somatosensory subpopulations using mouse genetics. *Front. Neuroanat.* 8, 21. doi: 10.3389/fnana.2014.00021

Levine, J. D., and Alessandri-Haber, N. (2007). TRP channels: Targets for the relief of pain. *Biochim. Biophys. Acta - Mol. Basis Dis.* 1772, 989–1003. doi: 10.1016/j.bbadis.2007.01.008

Liang, S. (2004). An overview of peptide toxins from the venom of the Chinese bird spider Selenocosmia huwena Wang [=Ornithoctonus huwena (Wang)]. *Toxicon* 43, 575–585. doi: 10.1016/j.toxicon.2004.02.005

Liu, L., Oortgiesen, M., Li, L., and Simon, S. A. (2001). Capsaicin inhibits activation of voltage-gated sodium currents in capsaicin-sensitive trigeminal ganglion neurons. *J. Neurophysiol.* 85, 745–758. doi: 10.1152/jn.2001.85.2.745

Liu, B., Linley, J. E., Du, X., Zhang, X., Ooi, L., Zhang, H., et al. (2010). The acute nociceptive signals induced by bradykinin in rat sensory neurons are mediated by inhibition of M-type K+ channels and activation of Ca2+-activated Cl– channels. *J. Clin. Invest.* 120, 1240–1252. doi: 10.1172/JCI41084

Mishra, S. K., Tisel, S. M., Orestes, P., Bhangoo, S. K., and Hoon, M. A. (2011). TRPV1-lineage neurons are required for thermal sensation. *EMBO J.* 30, 582–593. doi: 10.1038/emboj.2010.325

Miyamoto, A., Laufs, U., Pardo, C., and Liao, J. K. (1997). Modulation of bradykinin receptor ligand binding affinity and its coupled G-proteins by nitric oxide. *J. Biol. Chem.* 272, 19601–19608. doi: 10.1074/jbc.272.31.19601

Patapoutian, A., Tate, S., and Woolf, C. J. (2009). Transient receptor potential channels: targeting pain at the source. *Nat. Rev. Drug Discovery* 8, 55–68. doi: 10.1038/nrd2757

Pethő, G., and Reeh, P. W. (2012). Sensory and Signaling Mechanisms of Bradykinin, Eicosanoids, Platelet-Activating Factor, and Nitric Oxide in Peripheral Nociceptors. *Physiol. Rev.* 92, 1699–1775. doi: 10.1152/physrev.00048.2010

Premkumar, L. S., and Ahern, G. P. (2000). Induction of vanilloid receptor channel activity by protein kinase C. *Nature* 408, 985–990. doi: 10.1038/35050121

Priel, A., and Silberberg, S. D. (2004). Mechanism of ivermectin facilitation of human P2X4 receptor channels. *J. Gen. Physiol.* 123, 281–293. doi: 10.1085/jgp.200308986

Roberson, D. P., Gudes, S., Sprague, J. M., Patoski, H. A. W., Robson, V. K., Blasl, F., et al. (2013). Activity-dependent silencing reveals functionally distinct itch-generating sensory neurons. *Nat. Neurosci.* 16, 910–918. doi: 10.1038/nn.3404

Roth, B. L. (2016). DREADDs for Neuroscientists. *Neuron*. 89 (4), 683–694. doi: 10.1016/j.neuron.2016.01.040

Sandhu, M., Touma, A. M., Dysthe, M., Sadler, F., Sivaramakrishnan, S., and Vaidehi, N. (2019). Conformational plasticity of the intracellular cavity of GPCR-G-protein complexes leads to G-protein promiscuity and selectivity. *Proc. Natl. Acad. Sci. U. S. A.* 116, 11956–11965. doi: 10.1073/pnas.1820944116

Scholz, A., Kuboyama, N., Hempelmann, G., and Vogel, W. (1998). Complex Blockade of TTX-Resistant Na $^{+}$ Currents by Lidocaine and Bupivacaine Reduce Firing Frequency in DRG Neurons. *J. Neurophysiol.* 79, 1746–1754. doi: 10.1152/jn.1998.79.4.1746

Shim, W.-S., Tak, M.-H., Lee, M.-H., Kim, M., Kim, M., Koo, J.-Y., et al. (2007). TRPV1 mediates histamine-induced itching via the activation of phospholipase A2 and 12-lipoxygenase. *J. Neurosci.* 27, 2331–2337. doi: 10.1523/JNEUROSCI.4643-06.2007

Shin, J., Cho, H., Hwang, S. W., Jung, J., Shin, C. Y., Lee, S.-Y., et al. (2002). Bradykinin-12-lipoxygenase-VR1 signaling pathway for inflammatory hyperalgesia. *Proc. Natl. Acad. Sci. U. S. A.* 99, 10150–10155. doi: 10.1073/pnas.152002699

Starowicz, K., Nigam, S., and Di Marzo, V. (2007). Biochemistry and pharmacology of endovanilloids. *Pharmacol. Ther.* 114, 13–33. doi: 10.1016/j.pharmthera.2007.01.005

Ursu, D., Knopp, K., Beattie, R. E., Liu, B., and Sher, E. (2010). Pungency of TRPV1 agonists is directly correlated with kinetics of receptor activation and lipophilicity. *Eur. J. Pharmacol.* 641, 114–122. doi: 10.1016/J.EJPHAR.2010.05.029

Veldhuis, N. A., Poole, D. P., Grace, M., McIntyre, P., and Bunnett, N. W. (2015). The G protein-coupled receptor-transient receptor potential channel axis: molecular insights for targeting disorders of sensation and inflammation. *Pharmacol. Rev.* 67, 36–73. doi: 10.1124/pr.114.009555

Viana, F. (2011). Chemosensory properties of the trigeminal system. *ACS Chem. Neurosci.* 2, 38–50. doi: 10.1021/cn100102c

Winter, Z., Buhala, A., Otvös, F., Jósvay, K., Vizler, C., Dombi, G., et al. (2013). Functionally important amino acid residues in the transient receptor potential vanilloid 1 (TRPV1) ion channel – an overview of the current mutational data. *Mol. Pain* 9, 30. doi: 10.1186/1744-8069-9-30

Yang, F., Xiao, X., Cheng, W., Yang, W., Yu, P., Song, Z., et al. (2015). Structural mechanism underlying capsaicin binding and activation of the TRPV1 ion channel. *Nat. Chem. Biol.* 11 (7), 518–524. doi: 10.1038/nchembio.1835. advance on.

Conflict of Interest: The authors declare that the research was conducted in the absence of any commercial or financial relationships that could be construed as a potential conflict of interest.

frontiers in Pharmacology

ORIGINAL RESEARCH
published: 12 August 2020
doi: 10.3389/fphar.2020.01216

A Collision Coupling Model Governs the Activation of Neuronal GIRK1/2 Channels by Muscarinic-2 Receptors

Shai Berlin[1‡], Etay Artzy[2†], Reem Handklo-Jamal[2‡], Uri Kahanovitch[2†], Hanna Parnas[3], Nathan Dascal[2‡] and Daniel Yakubovich[2,4*‡]*

[1] Department of Neuroscience, Rappaport Faculty of Medicine, Technion, Haifa, Israel, [2] Department of Physiology and Pharmacology, Sackler Faculty of Medicine, Tel-Aviv University, Tel Aviv-Yafo, Israel, [3] Silberman Institute of Life Sciences, Hebrew University, Jerusalem, Israel, [4] Department of Neonatology, Schneider Children's Hospital, Petah Tikva, Israel

The G protein-activated Inwardly Rectifying K^+-channel (GIRK) modulates heart rate and neuronal excitability. Following G-Protein Coupled Receptor (GPCR)-mediated activation of heterotrimeric G proteins ($G\alpha\beta\gamma$), opening of the channel is obtained by direct binding of $G\beta\gamma$ subunits. Interestingly, GIRKs are solely activated by $G\beta\gamma$ subunits released from $G\alpha_{i/o}$-coupled GPCRs, despite the fact that all receptor types, for instance $G\alpha_q$-coupled, are also able to provide $G\beta\gamma$ subunits. It is proposed that this specificity and fast kinetics of activation stem from pre-coupling (or pre-assembly) of proteins within this signaling cascade. However, many studies, including our own, point towards a diffusion-limited mechanism, namely collision coupling. Here, we set out to address this long-standing question by combining electrophysiology, imaging, and mathematical modeling. Muscarinic-2 receptors (M2R) and neuronal GIRK1/2 channels were coexpressed in *Xenopus laevis* oocytes, where we monitored protein surface expression, current amplitude, and activation kinetics. Densities of expressed M2R were assessed using a fluorescently labeled GIRK channel as a molecular ruler. We then incorporated our results, along with available kinetic data reported for the G-protein cycle and for GIRK1/2 activation, to generate a comprehensive mathematical model for the M2R-G-protein-GIRK1/2 signaling cascade. We find that, without assuming any irreversible interactions, our collision coupling kinetic model faithfully reproduces the rate of channel activation, the changes in agonist-evoked currents and the acceleration of channel activation by increased receptor densities.

Keywords: collision-coupling, G-protein cycle, kinetic model, GIRK channel, G-Protein Coupled Receptor

OPEN ACCESS

Edited by:
Rami Yaka,
Hebrew University of Jerusalem, Israel

Reviewed by:
Michel Vivaudou,
UMR5075 Institut de Biologie Structurale (IBS), France
David J. Adams,
University of Wollongong, Australia

****Correspondence:***
Nathan Dascal
dascaln@tauex.tau.ac.il
Daniel Yakubovich
danial@tauex.tau.ac.il

†Present addresses:
Etay Artzy,
Paragon Ltd., Even Yehuda, Israel
Uri Kahanovitch,
Virginia Tech School of Neuroscience, Blacksburg, VA, United States

‡ORCID:
Shai Berlin
orcid.org/0000-0002-5153-4876
Reem Handklo-Jamal
orcid.org/0000-0001-6237-5412
Nathan Dascal
orcid.org/0000-0002-5397-4146
Daniel Yakubovich
orcid.org/0000-0003-2871-1026

Specialty section:
This article was submitted to Pharmacology of Ion Channels and Channelopathies, a section of the journal Frontiers in Pharmacology

Received: *07 April 2020*
Accepted: *24 July 2020*
Published: *12 August 2020*

Citation:
Berlin S, Artzy E, Handklo-Jamal R, Kahanovitch U, Parnas H, Dascal N and Yakubovich D (2020) A Collision Coupling Model Governs the Activation of Neuronal GIRK1/2 Channels by Muscarinic-2 Receptors. Front. Pharmacol. 11:1216. doi: 10.3389/fphar.2020.01216

INTRODUCTION

GIRK (G protein-activated Inwardly Rectifying K^+-channel) channels play fundamental physiological roles, such as control of heart rate and neuronal excitability, and are also highly implicated in disease such as addiction, depression, bipolar disorder, and cardiac arrhythmias (Dascal, 1997; Hibino et al., 2010; Luscher and Slesinger, 2010; Voigt et al., 2014; Mayfield et al., 2015; Rifkin et al., 2017). Opening of the channel is achieved by a highly recognized signaling cascade involving agonist binding to a G-protein Coupled Receptor (GPCR), which in turn activates

heterotrimeric G-proteins (of the $G\alpha_{i/o}$-type), to promote 'release' of $G\beta\gamma$ subunits. Then, direct interaction of $G\beta\gamma$ subunits with GIRK leads to channel opening and the appearance of the agonist-evoked current, I_{evoked} [(Logothetis et al., 1987; Reuveny et al., 1994; Lim et al., 1995; Slesinger et al., 1995); reviewed in (Clapham and Neer, 1997; Dascal and Kahanovitch, 2015)].

Despite more than four decades of studies, the details behind this prototypical activation scheme remain highly debated. For instance, it remains unclear how the different signaling proteins are arranged at the membrane to bring about robust and efficient channel opening, fast activation kinetics and, importantly, signaling specificity (the strong preference for GIRK activation by $G\beta\gamma$ derived from $G_{i/o}$ rather than G_s or G_q). Two contrasting mechanisms have been proposed [reviewed in (Hein and Bunemann, 2009)]. The first, denoted collision coupling (Tolkovsky and Levitzki, 1981; Tolkovsky et al., 1982; Shea and Linderman, 1997; Shea et al., 1997; Shea et al., 2000), assumes unrestricted diffusion of GPCRs, G-proteins, and effectors in the plasma membrane. After GPCR activation, GIRK activation occurs through random collisions with proteins of this cascade (Vorobiov et al., 2000; Hein et al., 2005; Touhara and MacKinnon, 2018). According to this model, a single receptor may activate several G-proteins (as in visual system; (Arshavsky et al., 2002)) and, therefore, an increase in the number of receptors is expected to accelerate activation kinetics of I_{evoked}. Indeed, this was observed for several GPCR-GIRK cascades (Vorobiov et al., 2000; Wellner-Kienitz et al., 2000; Hein et al., 2005; Kahanovitch et al., 2017). The second mechanism posits long-lived "preformed" complexes of GPCRs, G-proteins, regulatory proteins (e.g., Regulators of G Protein Signaling; RGS) and GIRKs in various combinations (Huang et al., 1995; Lavine et al., 2002; Fowler et al., 2006; Jaen and Doupnik, 2006; Dupre et al., 2007; Rusinova et al., 2007; Dupre et al., 2009; Nagi and Pineyro, 2014; Tateyama and Kubo, 2018). In support, several lines of evidence indicate that $G\beta\gamma$ and $G\alpha_{i/o}$ can associate with GIRKs, as early as in the endoplasmic reticulum ((Rebois et al., 2006; Robitaille et al., 2009); reviewed in (Zylbergold et al., 2010)), recruit G-proteins to the plasma membrane (Rishal et al., 2005; Kahanovitch et al., 2014), and possibly remain associated at the plasma membrane (Fowler et al., 2006; Rebois et al., 2006; Riven et al., 2006; Berlin et al., 2011; Kano et al., 2019). Further, in neurons, cardiomyocytes and heterologous expression models, some GIRKs exhibit an agonist-independent (basal) current (I_{basal}) that is $G\beta\gamma$-dependent, suggesting some kind of pre-coupling of GIRK with the G protein before the receptor has been engaged (reviewed in (Dascal and Kahanovitch, 2015)). We have also shown that GIRK1/2, but not the GIRK2 homotetramers, recruit G-proteins to the plasma membrane, favoring $G\beta\gamma$ over $G\alpha$ (Rishal et al., 2005; Kahanovitch et al., 2014). The preferential association with $G\beta\gamma$ explains the high, $G\beta\gamma$-dependent I_{basal} of GIRK1/2, contrasting the small and $G\beta\gamma$-independent I_{basal} of GIRK2 homotetramers (Rubinstein et al., 2009; Yakubovich et al., 2015). Together, these findings support the existence of dynamic G protein-GIRK complexes; however, whether they require permanent association is debated (Yakubovich et al., 2015). It is conceivable that different signaling cascades may proceed at different modes, namely collision or preformed modes, or a mixture of the two (e.g., only G protein and effector are pre-coupled).

The preformed complex model can seamlessly account for specificity (i.e., preferential activation of the channel by $G\beta\gamma$ released from a particular type of $G\alpha$-subunit) as well as for the high speed of GPCR-induced activation of GIRKs (Hille, 1992; Huang et al., 1995), limited mainly by the kinetics of G protein cycle (Vorobiov et al., 2000; Lohse et al., 2008; Hein and Bunemann, 2009). However, specificity can also be quantitatively described in purely kinetic terms, i.e. collision coupling (Touhara and MacKinnon, 2018). For instance, if a particular $G\alpha$-type, namely $G\alpha_{i/o}$, is quicker to provide $G\beta\gamma$ to the channel than other $G\alpha$'s, it would appear as though the channel solely responds to $G\beta\gamma$ derived from that specific $G\alpha$ (Touhara and MacKinnon, 2018). Indeed, heterologous overexpression of proteins of the β-adrenergic-$G\alpha_s$ cascade can lead to activation of GIRK *via* $G\alpha_s$-derived $G\beta\gamma$ (Lim et al., 1995; Bender et al., 1998; Touhara and MacKinnon, 2018). These results show that the system can indeed proceed, at least in some instances, *via* a collision coupling mechanism. Lastly, at high levels of expression of the reactants (proteins participating in the cascade), especially the GPCR, the kinetics and magnitude of effector activation *via* a collision coupling cascade would be indistinguishable from those attained by a preformed complex (Lauffenburger and Linderman, 1996). Therefore, the nature and concentrations of the reactants strongly affect the speed and specificity of the responses, thereby making it hard to distinguish between different modes of activation. It is therefore critical to study these mechanisms by systematic "titration" of the interactors.

In the current work, we set out to understand the mode of coupling in the classical M2R-$G\alpha_{i/o}$-GIRK cascade, by combining electrophysiological, fluorescence, and biochemical measurements in *Xenopus* oocytes with kinetic modeling. Specifically, we studied this cascade by systematically varying and quantifying surface densities of proteins involved in it, and monitored outcomes on GIRK activation. Next, we combine a Thomsen-Neubig-like mathematical model of GPCR activation (Thomsen and Neubig, 1989; Zhong et al., 2003) with extant models of GIRK activation by $G\beta\gamma$ to quantitatively describe GIRK activation in detail. We find that a collision coupling model faithfully reproduces both the fast activation kinetics of agonist-induced GIRK responses, and their dependence on GPCR surface density.

METHODS

Ethical Approval and Animals

Experiments were approved by Tel Aviv University Institutional Animal Care and Use Committee (permits M-08-081 and M-13-002). All experiments were performed in accordance with relevant guidelines and regulations. *Xenopus laevis* female frogs were maintained and operated as described (Dascal and Lotan, 1992). Briefly, frogs were kept in dechlorinated water tanks at

20 ± 2°C on 10 h light/14 h dark cycle, anesthetized in a 0.17% solution of procaine methanesulphonate (MS222), and portions of ovary were removed through a small incision in the abdomen. The incision was sutured, and the animal was held in a separate tank until it had fully recovered from the anesthesia and then returned to post-operational animals' tank. The animals did not show any signs of post-operational distress and were allowed to recover for at least 3 months until the next surgery. Following the final collection of oocytes, after 4 surgeries at most, anesthetized frogs were killed by decapitation and double pithing.

DNA Constructs and mRNA Injection

cDNA constructs of GIRK subunits, $G\beta_1$, $G\gamma_2$, M2R, YFP-GIRK1 were described in detail in previous publications (see (Tabak et al., 2019) for a detailed list). Fluorescent proteins (CFP and YFP) contained the A207K mutation to prevent dimerization (Zacharias et al., 2002). DNAs of M2R-CFP and M2R-YFP were produced by inserting the PCR product of the human M2R (Lechleiter et al., 1990), flanked by EcoRI on both sides, in pGEM-HJ vector containing CFP (cerulean) or YFP flanked by EcoRI and HindIII, yielding M2R-C/YFP_{CT}. The M2R-$G\alpha_{i3\text{-}C351G}$ tandem cDNA was created by ligating the M2R cDNA sequence in frame with the $G\alpha_{i3\text{-}C351G}$ cDNA, connected *via* a 6 nucleotide sequence GAATTC (EcoRI restriction site). Thus, the full primary sequences of M2R and $G\alpha_{i3\text{-}C351G}$ are connected by a 2-amino acid linker, Glu-Phe. The DNA of $GluR1_{L507Y}$ (Stern-Bach et al., 1998) was generously provided by Y. Stern-Bach (Hebrew University). All DNAs were cloned into pGEM-HE, pGEM-HJ or pBS-MXT vectors, which are high expression oocyte vectors containing 5' and 3' untranslated sequences of *Xenopus* β-globin (Liman et al., 1992), as previously described (Rishal et al., 2005; Berlin et al., 2011). mRNA was transcribed *in vitro* as described in (Dascal and Lotan, 1992) and precipitated overnight at -20°C with 4 M LiCl. mRNAs were divided into 1 to 2 µl aliquots and stored at -80°C. 50 nl of mRNA were injected into the equatorial part of oocytes, two to three days before the experiments.

Electrophysiology

Whole-cell GIRK currents were measured using two-electrode voltage clamp (TEVC) with Geneclamp 500 (Molecular Devices, Sunnyvale, CA, USA), sampled at 1 kHz and filtered at 200 Hz, at room temperature (21-23°C), as previously described (Rubinstein et al., 2009), using agarose cushion electrodes (Schreibmayer et al., 1994) filled with 3M KCl, with resistances of 0.1–0.6 MΩ. Data acquisition and analysis were done using pCLAMP software (Molecular Devices). For recording, oocytes were placed in a fast-perfusion chamber (see **Figure S1A** and below). Holding potential was set to -80 mV. Basal GIRK currents (I_{basal}) were measured by switching from physiological solution (low K^+, ND96: 96 mM NaCl, 2 mM KCl, 1 mM $CaCl_2$, 1 mM $MgCl_2$, 5 mM Hepes, pH 7.5) to a high K^+ solution (high K^+, in mM: 24 KCl, 2 NaCl, 1 $CaCl_2$, 1 $MgCl_2$, HEPES, pH 7.5). For recording evoked currents (I_{evoked}), solution was then switched to high K^+ solution containing 10 µM acetylcholine (ACh). Addition of 5 mM Ba^{2+} (blocker of GIRK) was typically applied at the end of each recording to isolate non-GIRK currents and to calculate net GIRK currents. Total current (I_{total}) was assessed by summing basal and evoked currents (I_{total}= I_{basal}+ I_{evoked}).

In the perfusion system employed in these experiments, each perfusion tube (inlet) is directly incorporated into the bath chamber (shaped like a thin elongated bar), rather than *via* a manifold, ending ~3 mm from the oocyte in large diameter openings (see **Figure S1A**). The suction has also been incorporated directly into the bath, 1 mm above the level of the oocyte, to reduce the bath solution volume and to allow fast exchange of the solution. In order to access the solution exchange time, we employed an AMPA receptor (AMPAR) mutant; $GluR1_{L507Y}$, which lacks fast desensitization (Stern-Bach et al., 1998). The activation time constant (τ_{act}) of AMPAR activation is below 1 ms (Grosskreutz et al., 2003) and can therefore be considered essentially instantaneous compared to the slower kinetics of GIRK activation. 1 ng RNA of $GluR1_{L507Y}$ was injected into *Xenopus* oocytes. 50 nl of 20 mM solution of EGTA was injected 2 hours before experiment, to prevent the appearance of Ca^{2+}-dependent Cl^- currents (Dascal, 1987). AMPAR was activated by applying saturating glutamate concentration (1 mM) to the bathing solution. A representative recording of AMPAR current is shown in **Figure S1B**. The rising phase of the response to glutamate, fitted to a single exponential function, was 88.6 ± 14.5 ms (n=9), indicating that the average solution exchange rate time constant of our perfusion system was about 90 ms.

Whole Oocyte Radioactive Quinuclidinyl Benzilate (QNB*) Labeling

Whole oocyte binding experiments were performed as described in (Ben-Chaim et al., 2003). Briefly, three days following mRNAs injection, oocytes were dropped into 200 µl of 0.67 nM QNB* (Halvorsen and Nathanson, 1981). After 1 min of incubation, the oocyte was taken to a washing chamber that contained 4000 µl of ligand-free solution (washing stage) and rapidly (after 1–2 s) removed to the scintillation liquid by use of a custom device. The device is composed of plastic holder that enables insertion of a pipetor with a standard pipette tip (volumes up to 200 µl) trimmed 4 mm from the edge. This ensures extraction of the oocyte with minimal amount of liquid. Then, individual oocytes were placed in vials to which 4 ml of scintillation fluid was added and counted with Packard 2100TR TriCarb Liquid Scintillation Analyzer. Specific binding was determined by subtracting the binding from native, uninjected oocytes.

Fluorescence Imaging

Imaging of fluorescence in the plasma membrane (PM) of whole oocytes was performed as previously described (Berlin et al., 2010; Berlin et al., 2011). Briefly, whole oocytes were placed in a glass-bottom dish, and all images were obtained from the animal hemisphere close to oocyte's equator (see Berlin et al, 2010; **Figure 2**-micrographs showing homogenous fluorescence in the animal pole). Imaging experiments were performed on a confocal laser scanning microscope (LSM 510 Meta, Zeiss, Germany) with 20x or 5x objective lenses, digital zoom = 2, pinhole 3 Airy units, equipped with a HFT 405/514/633 beam splitter. CFP was excited by 405 nm and emission was collected

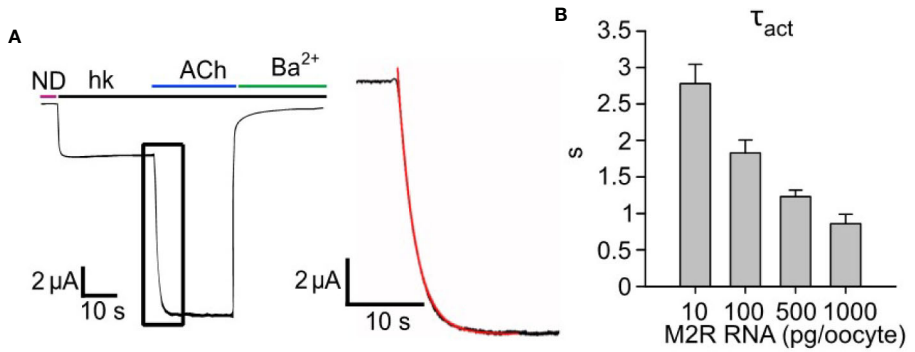

FIGURE 1 | Increasing expression levels of M2R accelerates the activation of GIRK1/2. **(A)** – a representative GIRK1/2 activation experiment. Oocytes were injected with the following RNAs: GIRK1 and GIRK2 (2 ng/oocyte each) and 500 pg/oocyte M2R. I_{evoked} was elicited by 10 μM ACh. Inset- zoom-in on the activation phase of I_{evoked} (black plot) and a mono-exponential fit (red). **(B)** – kinetics of GIRK1/2 activation. Oocytes expressed a constant amount of GIRK1/2 (2 ng RNA/oocyte), with increasing levels of M2R, in the range 10-1000 pg/oocyte, and τ_{act} was determined by monoexponential fitting as shown in A (N=2-7 experiments, n= 13-25 cells).

in the wavelength interval of 449-500 nm, peak emission 481 nm; YFP was excited by 514 nm and emission collected in the interval of 524-609 nm, peak emission: 534 nm. Analysis was done using Zeiss LSM software. The net intensity of fluorescence in the PM was measured by averaging the signal obtained from three standard regions of interest along the membrane with background subtraction (Berlin et al., 2010). In each experiment, uninjected oocytes were tested for intrinsic fluorescence with the use of either lasers: 405 and 514 nm excitation. In all confocal imaging procedures, care was taken to completely avoid saturation of the signal. In each experiment, all oocytes from the different groups were studied using constant LSM settings.

Statistical Analysis

Statistical analysis was performed using SigmaPlot software (Systat Software, San Jose, California, USA). Data are presented as mean ± S.E.M. Two group comparisons were done using two-tailed student's t-test. Multiple group comparison was done using one-way analysis of variance (ANOVA), with *post hoc* Tukey tests. Activation kinetics (τ_{act}) were obtained by fitting evoked currents by a mono-exponential fit.

Modeling and Simulation

Steady state calculations for estimation of initial conditions were done with Matlab for Windows (Mathworks Inc., Natick, Massachusetts). System of algebraic equations is shown in **Supplemental Material 2** and was solved numerically. Time-course simulation was done utilizing Berkeley Madonna 8.3.23.0 (R. Macey and G. Oster, University of California, Berkeley) for Windows. System of ordinary differential equations was generated based on schemes shown in **Figures 4A, B** and **Figure 5B**, and solved numerically by the 4th order Runge-Kutta method.

Estimation of GIRK-Gβγ Interaction Parameters

Reported GIRK-Gβγ affinity values span several orders of magnitude depending on estimation method (nM – mM range, (Dascal, 1997)). Considering this we utilized available crystal structure of GIRK2-Gβγ (Protein Data Bank number 4KFM, (Whorton and MacKinnon, 2013)) and two structures of GIRK1-Gβγ complex generated by homology modeling and protein-protein docking procedure (Mahajan et al., 2013) for structure-based prediction of protein-protein interaction free energy and affinity. In particular, the above mentioned structures were submitted to PRODIGY server (Xue et al., 2016) that calculated both free energy of interaction and K_D values utilizing algorithm which is based on correlation between number of interfacial contacts at the interface of a protein–protein complex and its experimental binding affinity together with properties of the non-interacting surface as described by Kastritis et al. (2011). The k_{on} (association rate constant values) were predicted utilizing Transcomp software (Qin et al., 2011). This software utilizes transient-complex theory developed by Alsallaq and Zhou (2008) for predicting protein-protein association rate constants. Coordinates supplied by structural data supplied in PDB format are used to generate the transient complex and rate constant is calculated based on the electrostatic interaction energy in the transient complex.

RESULTS

Collision Coupling Between M2R and $G_{i/o}$ in GIRK Cascade in *Xenopus* Oocytes

In previous publications, we presented evidence for catalytic collision coupling between M2R and $G\alpha_z$ (Vorobiov et al., 2000) and $GABA_B$ receptors with endogenous or coexpressed $G\alpha_{i/o}$ (Kahanovitch et al., 2017) in the GPCR-G protein-GIRK cascade reconstituted in *Xenopus* oocytes. To examine whether this is also the case for the M2R-$G_{i/o}$-GIRK cascade, and for the following quantitative description and kinetic modeling of the cascade, we first characterized the mode of M2R-$G_{i/o}$ coupling using our previously developed strategy (Vorobiov et al., 2000). Specifically, we initially assessed how changes in GPCR (M2R)

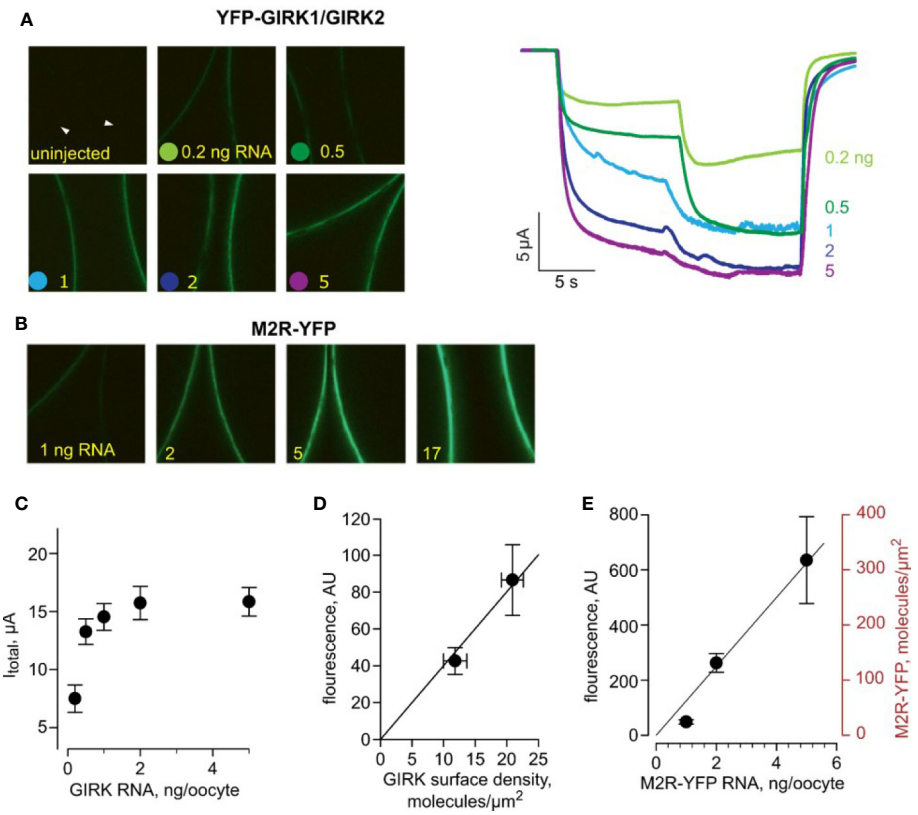

FIGURE 2 | Estimating the surface density of M2R-YFP. All data are from one experiment. **(A)** - (left) Representative micrographs of oocytes (membrane at equator) expressing equal amounts of RNAs of YFP-GIRK1 and GIRK2, and 1 ng M2R (wt). Injected YFP-GIRK1 mRNA amounts are indicated. (right) Representative currents from oocytes from the same experiment (from the same groups as in left panels). Note the gradual increase in I_{basal} and I_{total}, reaching a plateau at 2 ng/oocyte of channel's RNA. The current measurements in this experiment were done with a slower perfusion rate and were not included in the kinetic analysis. **(B)** – Representative micrographs of oocytes, injected with the indicated amounts of M2R-YFP, imaged at the same day and under identical settings as those in A. **(C)** – I_{total} of YFP-GIRK1/GIRK2 channels as a function of channel's RNA dose. **(D)** – calibration of the surface density of YFP. YFP-GIRK1 fluorescence (in arbitrary units, AU) is plotted versus channel density induced by the two lowest doses of GIRK RNA (<1 ng/oocyte), within the linear range of fluorescence-current relationship. Channel density was calculated from I_{total} as explained in the text. The correlation between fluorescence and number of YFP-GIRK1 molecules is shown with superimposed linear regression line, extended to origin of coordinates. The regression equation was y=4x, i.e. one channel/µm^2 corresponds to fluorescence intensity of 4 AU. Note that, since each channel has two YFP molecules, the calibration factor in this experiment is: 1 YFP molecule/µm^2 = 2 AU. **(E)** –estimating the surface density of M2R-YFP, for RNA concentrations of 1, 2 and 5 ng/oocyte. YFP fluorescence, in AU, is shown on the left Y-axis. M2R-YFP surface density (right axis) was calculated using the calibration factor derived from YFP-GIRK1/GIRK2 measurements. The relationship between M2R-YFP RNA dose and M2R-YFP surface density was fitted with linear regression, extended to the origin of coordinates, in the form y=62.5x.

concentration impacts the kinetics of activation (τ_{act}) of I_{evoked} of heterotetrameric GIRK1/2 channels. Here, we used a saturating concentration of acetylcholine (ACh; 10 µM) to activate different densities of ectopic M2R, whereas the signal transduction from GPCR to the channel relied on endogenous $G_{i/o}$ proteins. We employed a fast perfusion system with a time constant of solution exchange below 100 ms (see *Methods* and **Figure S1**). Importantly, in neurons and cardiomyocytes the τ_{act} of I_{evoked} is in the range 200-700 ms (Pott, 1979; Sodickson and Bean, 1996). Thus, our measurements of τ_{act} in the oocyte introduces an overestimation of GIRK1/2 activation kinetics. However, this overestimation is relatively minor, especially at low densities of M2R (see below). Our results show that the increase in the amount of mRNA of M2R per oocyte (i.e., increase in surface density) speeds up the activation of GIRK1/2 (**Figure 1A**, red plot- mono-exponential fit from which we extract τ_{act}), with a corresponding decrease in the time constant of activation (**Figure 1B**). These results are consistent with those obtained for M2R-G_z-GIRK and $GABA_BR$-$G_{i/o}$-GIRK cascades in this heterologous model (Vorobiov et al., 2000; Kahanovitch et al., 2017).

Estimation of Membrane Protein Density

For detailed kinetic analysis of GIRK1/2 activation, we sought to estimate the densities of proteins involved in our system, explicitly GIRK1/2, M2R and G-protein subunits- Gα and Gβγ, by a quantitative approach previously developed in our lab (Yakubovich et al., 2015). Briefly, channel density is typically calculated based on the maximal GIRK1/2 current (i.e., $I_{\beta\gamma}$) measured in oocytes that coexpress Gβγ at saturating concentration

(usually 5 ng/oocyte of Gβ RNA and 1-2 ng Gγ RNA). Under these conditions, the channel's open probability (P_o) is ~ 0.105. Channel density in M2R-expressing oocytes can also be calculated from the total current obtained upon activation with saturating 10 μM dose of ACh (I_{total}). I_{total} is the sum of agonist-independent GIRK1/2 current, I_{basal}, and the ACh-elicited I_{evoked}. We found that, for GIRK1/2, there is a stable relationship between I_{total} and $I_{\beta\gamma}$ over a wide range of channel densities such that, on average, $I_{\beta\gamma} = 2I_{total}$ (Yakubovich et al., 2015). If $I_{\beta\gamma}$ or I_{total} are known, GIRK1/2 density could be estimated using a modification of the classical equation (Hille, 2002):

$$\text{Eq.1 } I_{\beta\gamma} = 2 \cdot I_{total} = i_{single} \cdot P_o \cdot N$$

where i_{single} is the single channel current and N is the number of functional channels in the PM. The channel's surface density is defined as N/S, where S is the surface area of the cell (210^7 μm^2, deduced from oocyte's capacitance of ~200 nF (Dascal, 1987)). Based on data and calculations from (Yakubovich et al., 2015), under the conditions used here (24 mM K^+ external solution), the surface density for GIRK1/2 or YFP-GIRK1/GIRK2 can be estimated using a simple translation factor:

$$\text{Eq.2 density}(\text{channels}/\mu m^2) = 0.79\, I_{\beta\gamma} \quad (\mu A)$$

$$= 1.58\, I_{total}(\mu A)$$

In most experiments reported here, oocytes were injected with 1-2 ng or GIRK1 and GIRK2 m-RNA each. This generally elicited strong channel activity that corresponds to a "high density" group with an average surface density of ~21 GIRK1/2 channels/μm^2 (Yakubovich et al., 2015). There is a possibility of formation of functional GIRK2 homotetramers under these experimental conditions. However, the basal current we measured ranged between 3 to 5 μA (see **Figure 2A**). In oocytes, injection of 1 ng mRNA of GIRK2 gives rise to basal currents of 0.05 - 0.2 μA (Rubinstein et al., 2009). Therefore, under our experimental conditions, it is most likely that the predominant channels recorded are indeed GIRK1/2 heterotetramers. Moreover, the preferred stoichiometry of the homologous GIRK1/4 channel is two subunits of GIRK1 and two subunits of GIRK4, rather than GIRK4 homotetramers (Silverman et al., 1996).

Next, we employed YFP-GIRK1/GIRK2 as a "molecular ruler" to translate surface densities of the channel, obtained from current, to fluorescence measurements. Here, YFP density was assumed to be twice that of the channel, since each GIRK1/2 heterotetramer is believed to contain two GIRK1 subunits, by analogy with GIRK1/4 (Silverman et al., 1996; Corey et al., 1998). First, we determined the conditions for optimal channel expression for the calibration procedure. We injected increasing amounts of YFP-GIRK1, GIRK2 and Gβγ RNAs and observed a linear relationship between $I_{\beta\gamma}$ and YFP-GIRK1 fluorescence over the range of channel RNA doses of 0.2-1 ng/oocyte, in line with the assumption that fluorescence corresponds to functional channels (**Figure S2**). Linearity was lost at high RNA doses, suggesting that at high expression levels, some channels are non-functional (possibly not at membrane).

In the experiment shown in **Figure 2**, we expressed a range of doses of YFP-GIRK1/2 with 1 ng M2R RNA and measured surface levels of channel fluorescence and total GIRK currents in response to ACh (**Figures 2A, C, D**). We also expressed a range of doses of M2R-YFP and monitored YFP surface levels (**Figures 2B, E**). A linear relationship between YFP-GIRK surface density and I_{total} of YFP-GIRK1/GIRK was observed at low doses of RNA (below 1 ng) and this range was used for the estimation of YFP-GIRK1 density for calibration purposes (**Figure 2D**). In the same experiment and with identical imaging settings, we measured the PM expression of M2R-YFP at different RNA doses and, using the calibration factor from **Figure 2D**, calculated the PM density of M2R-YFP. **Figure 2E** shows that the relationship between the RNA dose and M2R-YFP density was linear in the range 1 – 5 ng RNA, yielding receptor densities of ~20 to ~300 M2R molecules/μm^2.

There are reports showing that the density of ion channels can be higher at the animal hemisphere or enriched around the injection site, which may effectively increase the density of PM proteins (M2R) in these areas (Robinson, 1979; Lopatin et al., 1998; Machaca and Hartzell, 1998). The assumption of homogeneity of M2R and GIRK distribution is therefore an approximation, which gives very good agreement with experiment. Note that, even if all the receptors and channels are located exclusively in the animal hemisphere, the surface density will only be changed two-fold.

Quantifying the Relationship Between M2R-YFP Surface Density and GIRK1/2 Activation Parameters

To compare the PM expression of different M2R constructs used in this study, we injected a range of RNA doses of wild-type (*wt*) M2R, M2R-YFP and M2R-CFP and measured the number of QNB binding sites in the PM of intact oocytes utilizing the methodology developed by Ben-Chaim et al. (Ben-Chaim et al., 2003). All three M2R constructs rendered similar number of QNB binding sites (**Figure 3A**), showing that they express at similar levels. We could therefore extend the M2R-YFP RNA – density relationship shown in **Figure 2E** towards M2R*wt* and M2R-CFP.

We next studied the impact of M2R-CFP surface density on activation parameters of YFP-GIRK1/GIRK2. We expressed a range of M2R-CFP receptor densities (with a constant amount of channel's RNA), by injecting 1-15 ng RNA/oocyte, and monitored the PM level of M2R-CFP (**Figure 3B**) and YFP-GIRK1 (**Figure 3C**) along with currents amplitude and τ_{act} of I_{evoked} (**Figures 3D–F**). The level of YFP-GIRK1/GIRK2 remained unchanged at all doses of M2R RNA except when the receptor was injected at excessively high doses, 25 ng. This yielded a decrease in the PM level of the channel (**Figure 3C**), likely due to non-specific competition of RNAs for the same pool of ribosomes (Richter and Smith, 1981) or a trafficking interference. We have, therefore, adjusted the amplitude of I_{evoked} for the change (even if slight) in channel's PM level (**Figure 3F**). Together, we find that increase in M2R density (validated by fluorescence) is associated with a sharp rise in both

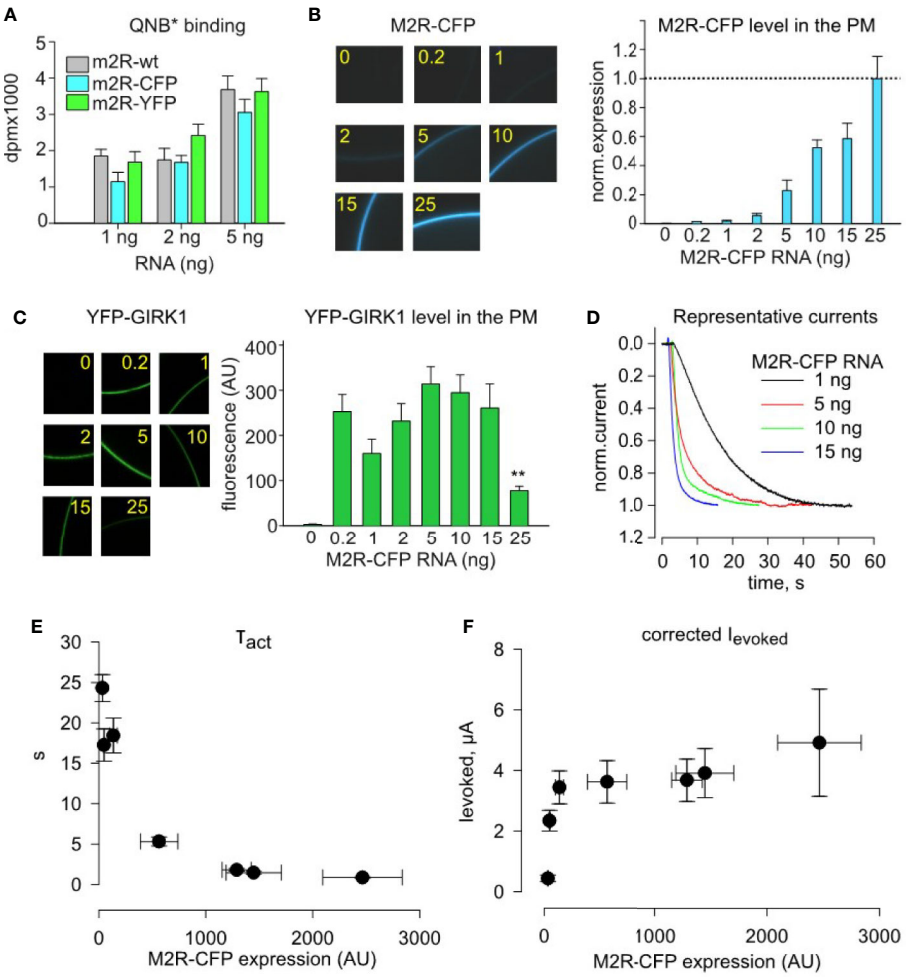

FIGURE 3 | Quantitative analysis of dose-dependency of τ_{act} and amplitude of I_{evoked} on plasma membrane density of M2R-CFP. **(A)**-Whole cell radioligand-labeling by quinuclidinyl benzilate (QNB*) shows that identical doses of injected RNA produce similar surface expression of M2R, M2R-CFP and M2R-YFP, for three different amounts of receptor RNAs. B-F, quantitative analysis of incremental expression of M2R-CFP reveals collision-coupling activation of YFP-GIRK1/GIRK2 channels. Oocytes were injected with constant mRNA amounts of YFP-GIRK1 and GIRK2 (1 ng each) but with increasing doses of M2R-CFP RNA. **(B)** – RNA dose-dependent increase in the surface levels of M2R-CFP. Representative micrographs of oocytes (left) expressing m2R-CFP and summary of expression (right). RNA amounts of M2R-CFP RNA, in ng/oocyte, are indicated in yellow. n=7-12 oocytes in each group. **(C)** – expression of M2R-CFP does not affect the surface level of YFP-GIRK1/GIRK2 except for the decrease at the highest dose of M2R-CFP, 25 ng/oocyte (**, p<0.01). Left panel shows representative micrographs of YFP-GIRK1/GIRK2 – expressing oocytes. Numbers within the images indicate the amounts of M2R-CFP RNA, in ng/oocyte. Right panel shows summary of expression data (n=7-12 oocytes in each group). **(D)** – representative normalized I_{evoked}, elicited by 10 μM ACh in oocytes injected with the indicated amounts of M2R-CFP RNA. For simplicity, only the initial (activation) phase of I_{evoked} is shown. **(E, F)** – τ_{act} is reduced **(E)** and I_{evoked} amplitude **(F)** is increased with increased surface density of M2R-CFP. AU, arbitrary units. τ_{act} and I_{evoked} data are from cells exemplified in B – D; n=5-12 in each group.

the speed and amplitude of channel activation (**Figures 3D–F**). Notably, maximal amplitude of I_{evoked} is obtained at lower PM densities of the receptor than those required to obtain the fastest activation (lowest τ_{act}; compare **Figures 3E**, **F**). These observations are in-line with the predictions of the catalytic collision coupling model. Unexpectedly, we note that, though M2R-CFP expresses at equivalent levels as M2R*wt* (**Figure 3A**), it exhibits slower kinetics at all RNA doses (compare **Figures 1D**, **3D–F**). Therefore, M2R-CFP was solely used to assess surface density of the receptor, but not for quantitative description of the native cascade, where we use M2R*wt*.

Modeling: G Protein Cycle Model

For quantifying the M2R-$G_{i/o}$-GIRK1/2 cascade, we elaborated the Thomsen et al. (1989) model of G-protein cycle by combining it with the ternary complex model developed by De Lean et al. (1980). Of note, a similar approach was used by Falkenburger et al. for the description of another muscarinic receptor and cascade, namely the M1R-G_q-phosphoinositide signaling mechanism and regulation of the KCNQ channels (Falkenburger et al., 2010; Hille et al., 2014). A schematic representation of the G-protein cycle model is shown in **Figure 4A**. List of reactions with corresponding rate constants

is shown in **Table 1**. To maintain microscopic reversibility, we incorporated into the G-protein cycle model a G-protein dissociation step (i.e. $RG\alpha_{GTP}G\beta\gamma$ dissociation, reaction 7) and also a GPCR-independent dissociation step (reaction 10) (Sarvazyan et al., 1998; Yakubovich et al., 2005). It must be emphasized that the rate constants for the latter reaction have been incorporated in the model of Touhara and MacKinnon (2018). $G\alpha_{GTP}G\beta\gamma$ dissociation rate has been reported by Hollins et al. (2009) and association rate could be estimated based on the microscopic reversibility assumption (**Table 1**, reaction 7). Furthermore, GDP/GTP exchange is split into two reversible reactions. Rate constants of GDP and GTP binding have been determined experimentally (Higashijima et al., 1987; Zhong et al., 2003). We also incorporated $G\alpha G\beta\gamma$ nucleotide free state in the process which leads from $G\alpha_{GDP}$ bound state to GTP bound state as proposed by Ross (Ross, 2008).

In order to estimate kinetic parameters of reactions of the model that have not been determined experimentally, we used the open-source software tools PRODIGY for the estimation of K_D values (Xue et al., 2016) and TRANSCOMP for estimating association rate constants (Qin et al., 2011). Lastly, we scrutinized the crystal structure of M2R with heterotrimeric G-protein (PDB: 6OIK) (Maeda et al., 2019) for deriving the kinetic parameters related to M2R-G protein coupling (**Table 1**).

Modeling: Channel Activation Model

We made use of our previously described GIRK1/2 gating model (Yakubovich et al., 2015), denoted "graded contribution model" (**Figure 4B**). This model is based on the assumption that a channel that is occupied by 1 to 4 Gβγ molecules can reach the open conformation, but the contribution of each Gβγ-occupied state is different; the higher Gβγ occupancy, the higher the contribution to open probability. This model is based on studies of Sadja et al. and Ivanova-Nikolova et al. (Ivanova-Nikolova et al., 1998; Sadja et al., 2002) on a highly homologous channel; GIRK1/4. To estimate the parameters of interaction between GIRK1/2 and Gβγ for the graded contribution model, we proceeded in a similar approach as done for the unknown parameters of M2R-G-protein interaction, namely we analyzed two structural models of GIRK-Gβγ complex. The first is the crystal structure of GIRK2 in complex with Gβγ (Whorton and MacKinnon, 2013) (PDB: 4KFM) and the second is a docking model for the GIRK1-Gβγ complex (Mahajan et al., 2013) (termed "best scoring model", or BS). Both models were

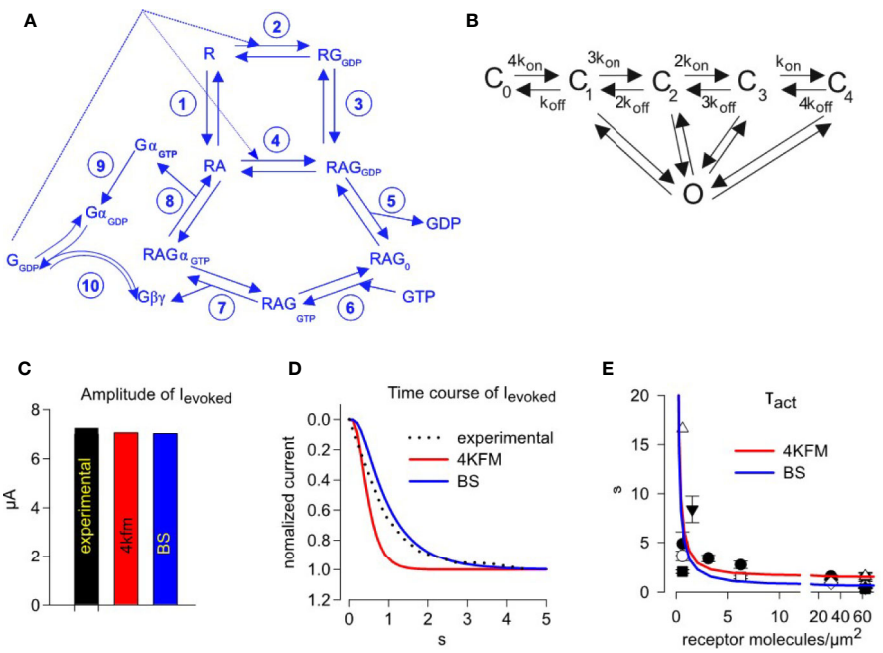

FIGURE 4 | Simulating activation kinetics and its dependence on M2R surface density. **(A)** – scheme of the G-protein cycle. **(B)** – graded contribution model of GIRK1/2 activation. Rate constants of reactions shown in A and B are summarized in **Table 1**. **(C)** –comparison of the experimentally observed and predicted ACh-evoked currents, with GIRK-Gβγ interaction parameters from two structural models, 4KFM and BS. **(D)** - representative analysis of the time course of GIRK1/2 activation. The experimental result (dotted black line) is from an oocyte injected with 0.5 ng M2R RNA. Superimposed are simulated currents according to graded contribution model of GIRK1/2 activation. The experimental parameters in this cell were: I_{basal} = 15.5 μA, I_{total}= 22.8 μA. Estimated channel density was 36 channels/μm^2. Initial concentrations of Gα and Gβγ available to the channel are: for the case of 4KFM model 3.23 molecules $G\alpha_i$/channel and 0.45 molecules Gβγ/channel; for the case of BS model, 3.24 molecules $G\alpha_i$/channel and 0.46 molecules Gβγ/channel. Each plot represents the recorded or simulated current normalized to its maximum. **(E)** – mean τ_{act} values from all experiments with wild-type M2R, superimposed on data obtained from fitting of simulated time-courses according to different models. Each experimental point shows mean value of τ_{act} ± SEM from one experiment (n=3-7 oocytes). Simulated time courses were generated for the case described by Yakubovich et al. as "high density group", i.e. I_{basal} =13.36 μA, I_{total} =17.2 μA, n=21 channels/μm^2. Amounts of available Gα and Gβγ molecules per one channel, that are required to obtain the observed I_{evoked}, were calculated using the graded contribution model: with the BS structure-based parameters, 3.65 Gβγ and 0.39 Gα molecules/channel; with the for 4kfm structure-based parameters, 3.62 Gβγ and 0.38 Gα molecules/channel.

TABLE 1 | Rate constants of GPCR mediated GIRK activation.

Reaction	k_{on} $M^{-1}s^{-1}$	k_{off} s^{-1}	Reference	Calculation
1. R + A ⟺ RA	$3.33 \cdot 10^2$ (k_{1f})	$7 \cdot 10^{-3}$ (k_{1b})	(Schreiber et al., 1985)	
2. R+G_{GDP}⟺RG_{GDP}	$5.51 \cdot 10^6$ (k_{2f})	$1.6 \cdot 10^{-1}$ (k_{2b})		(*)
3. RG_{GDP} + A ⟺ RAG_{GDP}	$4.5 \cdot 10^6$ (k_{3f})	$4.87 \cdot 10^{-1}$ (k_{3b})	(Schreiber et al., 1985)	
4. RA+G_{GDP}⟺ RAG_{GDP}	$3.68 \cdot 10^8$ (k_{4f})	$5. = 5 \cdot 10^{-2}$ (k_{4b})	(Ilyaskina et al., 2018)	(**)
5. RAG_0+GDP⟺ RAG_{GDP}	10^6 (k_{5b})	5 (k_{5f})	(Zhong et al., 2003)	
6. RAG_0+GTP⟺ RAG_{GTP}	10^6 (k_{6f})	.1 (k_{6b})	(Zhong et al., 2003)	
7. $RAG\alpha_{GTP}$ +Gβγ⟺ RAG_{GTP}	10^6 (k_{7b})	15 (k_{7f})	(Hollins et al., 2009)	(**)
8. RA+$G\alpha_{GTP}$⟺ $RAG\alpha_{GTP}$	10^7 (k_{8b})	2 (k_{8f})	(Zhong et al., 2003)	
9. $G\alpha_{GTP}$→ $G\alpha_{GDP}$		.02 (k_{9f})	(Zhong et al., 2003)	
10. $G\alpha_{GDP}$ + Gβγ ⟺ G_{GDP}	$0.7 \cdot 10^6$ (k_{10f})	0.0013 (k_{10b})	(Sarvazyan et al., 1998)	
C_n+ Gβγ⟺$CG\beta\gamma_{n+1}$	$(4\text{-}n) \cdot 0.23 \cdot 10^6$ $(4\text{-}n) \cdot 1.01 \cdot 10^6$	$(n+1) \cdot 0.037$ $(n+1) \cdot 0.14$	Best scoring model, (Mahajan et al., 2013) 4KFM, (Whorton and MacKinnon, 2013)	(*)

Notations in brackets are used in ordinary differential equations shown in ***Supplemental Material 2****.*
(*) k_{on} and k_{off} estimated by PRODIGY and TRANSCOMP.
(**) k_{on} adjusted, see text.

subjected to analysis by PRODIGY and TRANSCOMP software from which we obtained K_D and k_{on} values of GIRK-Gβγ interaction. For calculating initial values for all channel and G-proteins states (i.e. before agonist application), a system of algebraic equations was numerically solved assuming that the reaction between GIRK-G protein is in steady-state (**Supplemental Material 1**). Time-course of activation of GIRK1/2 was simulated as a solution of system of ordinary differential equations (**Supplemental Material**, **Eq. 19–34**).

Simulation of GIRK1/2 Activation Time-Course and Amplitude

In order to validate our model, we simulated the experimentally observed GIRK1/2 activation by a step application of 10 μM ACh. We chose a representative recording in which 0.5 ng/oocyte M2R mRNA was injected. This corresponds to a PM expression of about 31 receptors/μm^2, according to our calibrations (see **Figure 2E**). We used available values of Gα and Gβγ for the activation of GIRK from its I_{basal} and I_{total} as previously described (Yakubovich et al., 2015) (see **Supplemental Material 1**). We then simulated the evoked current of GIRK1/2 and compared with experimental values (**Figures 4C, D**). We find that our developed model satisfactorily reproduces the fast kinetics and the amplitude of I_{evoked}, with kinetic parameters of GIRK-Gβγ interaction obtained from both structural models tested (4KFM and BS).

Subsequently, we ran time-course simulations over a wide range of M2R receptor densities, 0.1 – 100 receptors/μm^2. The initial parameters of I_{basal} and I_{total} for these simulations were adopted from the "high density group" of GIRK1/2 channel expression obtained by injection of 1-2 ng (21.7 channels/μm^2, I_{basal} = 13.36 μA and I_{total} = 17.2 μA; (Yakubovich et al., 2015)). In each simulation, τ_{act} was extracted from mono-exponential fit of the activation phase of I_{evoked}, and the calculated values of τ_{act} versus receptor density were superimposed on the experimentally measured τ_{act} obtained from a large number of experiments with M2R*wt* (**Figure 4E**). We find that that our model satisfactorily predicts the acceleration of activation rate with the increase in GPCR density. It also faithfully reproduces the real kinetics of the receptor, namely it reproduces the fastest kinetics of activation obtained when using high receptor densities.

Modeling Kinetics of M2R-$G\alpha_{i3}$ Fusion Protein

We were curious as to how would our model behave, and how would the simulated results look, should we be able to force some players to be in complex with each other. We have previously achieved forcing the precoupling of GPCR to Gα by fusing M2R to $G\alpha_z$ (tandem) (Vorobiov et al., 2000). Notably, we found that the kinetics of GIRK activation were independent of the concentration of the tandem protein (see *Introduction*). Here, we similarly made a tandem protein consisting of M2R and $G\alpha_{i3}$. Our initial tests showed that this tandem was functional and, furthermore, engendered faster activation than that obtained by the M2R-$G\alpha_z$ tandem (**Figure 5A**). This was expected because of the much slower G protein cycle kinetics of $G\alpha_z$ (Vorobiov et al., 2000). We also introduced the C351G mutation into $G\alpha_{i3}$ to impart pertussis toxin resistance (West et al., 1985). This allowed us to silence endogenous $G\alpha_{i/o}$ by expressing the A protomer of pertussis toxin, to avoid incidental collision coupling of the tethered M2R to non-tethered endogenous $G\alpha_{i/o}\beta\gamma$ and the ensuing Gβγ activation of GIRK (Vorobiov et al., 2000). We find that the activation kinetics of I_{evoked} were remarkably stable and independent on the doses of M2R-$G\alpha_{i3\text{-}G351G}$ (**Figure 5A**,

red plot), whereas the amplitude of I_{evoked} persistently increased with higher RNA dose of M2R-G$\alpha_{i3\text{-}G351G}$ (**Figure 5A**, black plot). These results confirm that increase in RNA dose of the tandem is accompanied by an increase in its surface density and, more importantly, indicate that low doses of the tethered receptor-Gα pair cannot provide enough Gβγ to activate the large number of channels. We then proceeded to develop a scheme of GPCR-Gα_{i3} tandem-mediated activation of GIRK1/2 (**Figure 5B**) and subsequently simulated time-course of GIRK1/2 activation by a range of GPCR-Ga_{i3} tandem densities. Three possible scenarios were simulated: 1) M2R-Gα concatemer was assumed to have the same affinity to Gβγ as Gα, and no change in Gβγ concentration was assumed with concatemer expression; 2) M2R-Gα concatemer was assumed to have same affinity to Gβγ as Gα, and 1:1 increase in Gβγ concentration was assumed with concatemer expression; 3) M2R-Gα concatemer was assumed to have 10 fold lower affinity to Gβγ than Gα and no change in Gβγ concentration was assumed with concatemer expression. Simulated evoked currents and τ_{act} values show that, whereas I_{evoked} values increase with the increase in GPCR-Gα_{i3} density, τ_{act} values remain constant (**Figures 5C, D**). These simulations thereby fully recapitulate the outcomes on channel activation *via* a preformed complex between the GPCR and the G protein and provide a unique and contrasting picture than what we obtain when all components are free (i.e., non-fused). Thus, these observations further support the collision-coupling nature of M2R to G protein signaling in the M2R-GIRK cascade reconstituted in *Xenopus* oocytes.

Comparison to Cooperative Gating Model

We next tested another detailed model of the GPCR-GIRK cascade based on collision-coupling published by Touhara and MacKinnon (2018), termed here cooperative gating model. This model incorporates the Thomsen et al. model of the G-protein cycle (Thomsen et al., 1988; Thomsen and Neubig, 1989), and the receptor independent G-protein heterotrimer dissociation (Sarvazyan et al., 1998; Sarvazyan et al., 2002). This model assumes that channel activation is cooperative, i.e., each Gβγ binds to the channel with stronger affinity than the previous one. It also assumes that GIRK can open only when all four Gβγ-binding sites have been occupied. In the model, we applied affinities and rate constants from (Touhara and MacKinnon, 2018),

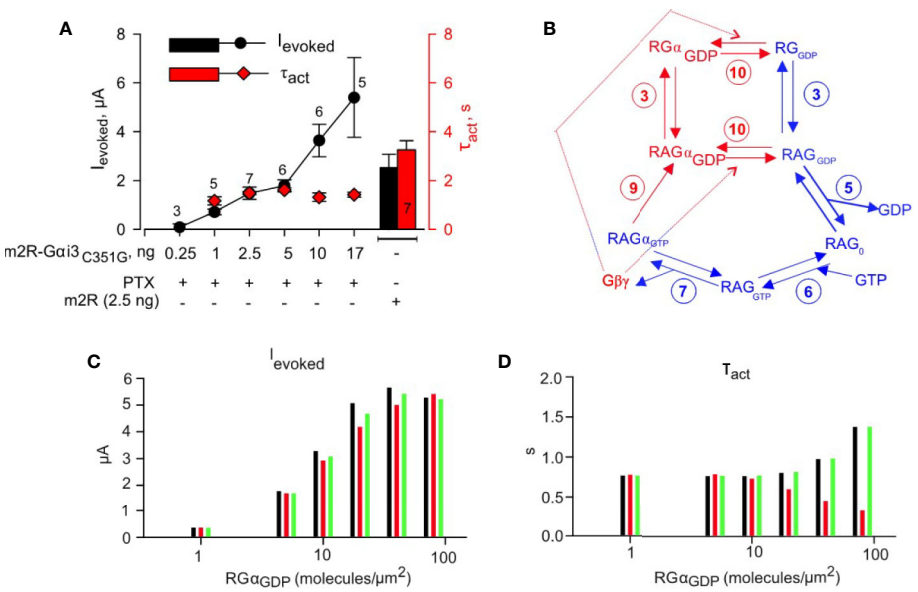

FIGURE 5 | Physical tethering of M2R and Gαi3 converts a collision coupling mechanism to a preformed-complex: experiment and simulation. **(A)** – Incremental expression of fused M2R-Gα_{i3}C351G (PTX-insensitive) in the presence of coexpressed A-protomer of pertussis toxin (PTX; 0.2 ng RNA/oocyte) shows increase in I_{evoked} with growing amounts of injected RNA (black plot), but kinetics of activation remain unchanged (red plot). Right- Histogram of evoked currents (black) and τ_{act} (red) of GIRK1/2 coexpressed with M2R-*wt*. Result shown are from one experiment; number of cells (n) tested in each group are shown above experimental points or in the bar. No significant change in τ_{act} was found (one way ANOVA, P = 0.154). Spearman correlation coefficient calculated for analysis of evoked currents ~ 1, P = 0.0167. **(B)** – scheme of G-protein utilized to simulate GIRK1/2 activation by M2R-Gα_{i3}C351G. Blue arrows and numbering denote reactions that are shared with M2R wt activation pathway, as described in **Figure 4**. Red arrows denote reactions present only in the current scheme. The numbering of reactions and the rate constants are the same as in **Table 1**. **(C)** – simulated I_{eoked} values obtained assuming a range of expression level of fused M2R-Gα_{i3}C351G. **(D)** – summary of τ_{act} obtained from fitting time-course of activation of GIRK1/2 by range of M2R-Gα_{i3}C351G densities with mono-exponential function. Three possible scenarios were simulated for analysis of M2R-G$\alpha_{i3C351G}$ experiments. Black bars; M2R-Gα concatemer is assumed to have same affinity to Gβγ as Gα, and no change in Gβγ concentration is assumed with concatemer expression. Red bars; M2R-Gα concatemer is assumed to have same affinity to Gβγ as Gα, and 1:1 increase in Gβγ concentration is assumed with concatemer expression. Green bars; M2R-Gα concatemer is assumed to have 10-fold lower affinity to Gβγ than Gα and no change in Gβγ concentration is assumed with concatemer expression. For simulation it was assumed that GIRK1/2 is expressed at levels similar to "intermediate density group" described in Yakubovich et al. (2015) i.e. under pre-expression conditions there are ~ 9.7 channels/μm^2 and 3.5 Gβγ molecules/channel. It is also assumed that under PTX expression conditions most endogenous Gα_{i3} is ADP-ribosylated and subsequently degraded.

including K_D of binding of the first Gβγ to GIRK of 60 μM, with a cooperativity factor μ=0.3 for the binding of each next Gβγ, to generate a system of differential equations analogous to Eq. 19-34 for the simulation of GIRK1/2 activation. The densities of Gβγ and Gα were as for standard conditions, specifically ~21 channels/μm^2 and 31 M2R receptors/μm^2 (as for simulation of "high density group" (Yakubovich et al., 2015); 0.5 ng/oocyte RNA of M2R corresponds to ~ 31 receptors/μm^2; see **Figure 2**).

Since GIRK1/2 has a substantial GPCR-independent but Gβγ-dependent I_{basal} [see (Rubinstein et al., 2009) for details], a certain excess of free Gβγ over Gα in the vicinity of the channel must be assumed (Yakubovich et al., 2015), whatever the mathematical approach used to describe channel's behavior. Using the cooperative gating model equations (Eq.14-18) and parameters of GIRK-Gβγ interaction, as described by (Touhara and MacKinnon, 2018), we calculate that ~7 free Gβγ molecules are needed to account for the I_{basal} measured at "high density". We next tested various pairs of Gβγ and Gα densities and selected those which most closely recapitulated experimental measures for I_{basal} and I_{total} (**Figure S3**). Furthermore, for analysis, we selected the minimal number of Gβγ (out of tested pairs), with the corresponding amount of Gα molecules per channel that best reproduced the experimental data (**Figure S3**, **see legend**).

Using the abovementioned initial conditions, we simulated the time-course of GIRK1/2 activation for a range of M2R densities similar to as shown in **Figure 4E**. Similar to data shown in **Figure 3** (for M2R-CFP), **Figures 1B** and **4E**, the amplitude of the simulated I_{evoked} increased with receptor density,whereas τ_{act} showed persistent decrease with the growing densities. However, the τ_{act} obtained was much faster than that observed in our experiments or predicted by our model, and varied less (i.e., of narrow range; **Figure 6B**). In order to determine the nature of this discrepancy, we compared similar kinetic steps between our model and that of cooperative gating model. We noticed that the GTP hydrolysis rate used by Touhara et al. is 100 times faster that used in other reports (Zhong et al., 2003). We also note that this fast rate of GTP hydrolysis is characteristic for conditions in which RGS is present, such as observed in cardiac myocytes (Doupnik, 2015). In our case, *Xenopus* oocytes lack RGS and thus slower GTP hydrolysis rates are expected (Keren-Raifman et al., 2001). Indeed, substituting slower hydrolysis rate constant into cooperative gating model restored channel activation kinetics to as obtained in our experiments (**Figures 6C, D**).

DISCUSSION

Summary of Findings

The main goal of this work was to develop a detailed kinetic model for the GPCR-G-protein-effector cascade based on experimental data obtained in a prototypical expression system, the *Xenopus* oocyte. As many key features for this cascade are still missing, we deemed it quintessential to measure reactant densities in the plasma membrane along a detailed description of current features (amplitudes and kinetics). We used fluorescently labeled GIRK1/2 as a 'molecular ruler" (Yakubovich et al., 2015) and conducted a controlled and quantitatively monitored expression of the component proteins of the signaling cascade, the GPCR (M2R)

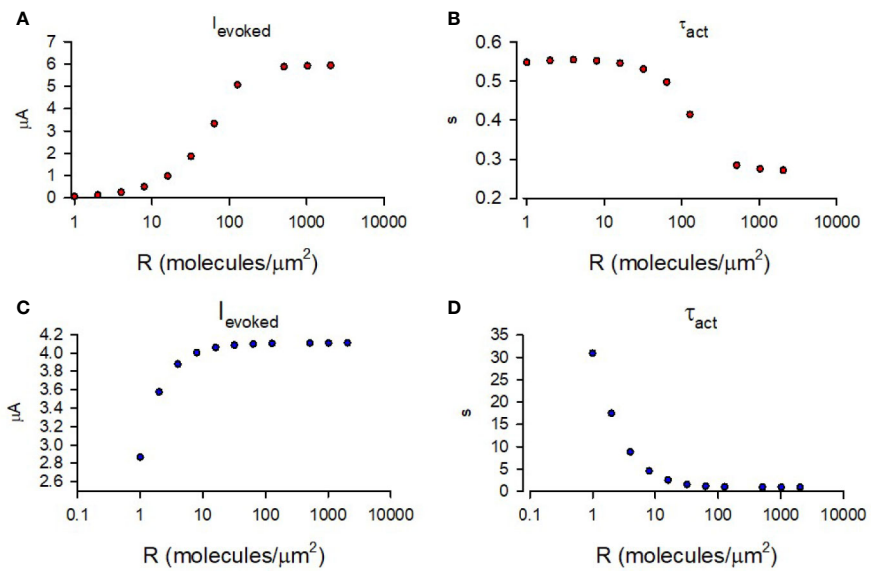

FIGURE 6 | Simulation of GIRK1/2 activation according to cooperative gating model. **(A)** – Simulated values of I_{evoked} obtained for a range of M2R densities. **(B)** – τ_{act} of mono-exponential fit of simulated I_{evoked} obtained for a range of M2R densities. For A and B, the rate constants were taken from Touhara et al. (1) and it was assumed that Gβγ =16 molecules/channel and Gα = 9 molecules/channel (red circles). **(C)** – Simulated I_{evoked} obtained from simulation with $k_{hydrolysis}$ = 0.02 s^{-1} and a range of M2R densities. **(D)** - τ_{act} of mono-exponential fit of time-course from simulation of I_{evoked} with $k_{hydrolysis}$ = 0.02 s^{-1} and a range of M2R densities. For calculations done in **(C, D)**, $k_{hydrolysis}$ was assumed to be 0.02 s^{-1} and Gβγ = 9 molecules/channel and Gα = 2 molecules/channel (blue circles).

and the effector (GIRK1/2). G-protein concentrations were measured in a previous work using two independent methods, the fluorescence measurements with YFP-GIRK1/2 as caliper, and by quantitative Western blots (Yakubovich et al., 2015). Using a titrated expression approach (as previously developed by us; (Vorobiov et al., 2000)), we demonstrate that incremental expression of both wild-type and CFP-tagged M2R, M2R-CFP, is accompanied by acceleration (decrease in τ_{act}) of channel activation, i.e., I_{evoked}. In contrast, activation kinetics of GIRK responses elicited by an M2R-Gα_{i3} tandem, which necessarily mimics the case of a "preformed GPCR-G protein complex", were fast and invariable over a wide range of expression levels of the fusion protein. We combined these observations and data to develop a comprehensive mathematical model for the M2R-G-protein-GIRK1/2 signaling cascade with free M2R based on free diffusion of all components, and a modification of this model for the case of M2R-Gα_i "preformed complex". Our model faithfully recapitulates and predicts all the quantitative aspects of GIRK1/2 activation explored here: the acceleration of activation with increasing densities of M2R, the τ_{act} and the amplitude of I_{evoked}, and the dependence of the amplitude, but not the kinetics, of GIRK currents elicited *via* the activation of the M2R-Gα_{i3} fusion protein. Our results strongly support the collision coupling mode of signaling between M2R and the $G_{i/o}$ protein in the GPCR-G protein-GIRK cascade reconstituted in *Xenopus* oocytes. More broadly, our model, and a similar collision coupling type of model of Touhara et al. demonstrate that a purely diffusion-limited coupling mechanism can fully account for the fast kinetics of GIRK responses in excitable cells, without the need to assume a preformed complex. Importantly, our results emphasize the utility of our approach of controlled incremental GPCR expression to distinguish between different coupling modes in G protein-mediated signaling cascades.

Model of G Protein Cycle

The mathematical approach used to describe the GPCR-G-protein-effector cascade is well elaborated (Lamb and Pugh, 1992; Turcotte et al., 2008; Falkenburger et al., 2010). Several models have been developed specifically for the analysis of GIRK activation. The first model of GIRK activation that also incorporated a G protein cycle of GIRK activation was published in 1988 (Breitwieser and Szabo, 1988). Subsequently, updated models have been developed by groups of Kurachi and Mackinnon (Murakami et al., 2010; Murakami et al., 2013; Touhara and MacKinnon, 2018). Though all these models implement Thomsen-Neubig style G-protein activation model (Thomsen and Neubig, 1989; Zhong et al., 2003), they differ in certain key details. In particular, the model proposed by Murakami et al. (2013) assumes two affinity states of GIRK to Gβγ and two affinity states of GPCR to agonist; however, the GPCR-agonist affinity states are not kinetically interconnected and unrelated to coupling to G-protein. These are incompatible with the well-established dependency of agonist affinity upon the G protein-GPCR association (Maguire et al., 1976; De Lean et al., 1980; Haga et al., 1986; Weis and Kobilka, 2018). The model proposed by Touhara and MacKinnon (2018) does not include an explicit bimolecular reaction of agonist binding to GPCR. Both models describe $G\alpha_{GTP}G\beta\gamma$ heterotrimeric complex dissociation as an irreversible reaction, which precludes the implementation of the microscopic reversibility principle (Colquhoun et al., 2004).

The G-protein cycle model presented here (**Figure 4A**) is a logical development and, in a way, a synthesis of previously proposed models with certain improvements. In particular, receptor-agonist-G-protein interaction is formulated as a complete ternary complex model (De Lean et al., 1980). Both $G\alpha_{GTP}$-Gβγ and $G\alpha_{GDP}$-Gβγ interactions are described as reversible reactions. To enable the implementation of microscopic reversibility in the cycle, we have excluded the obligatorily irreversible GTP hydrolysis (**Figure 4A**, reaction 9) from the main cycle. Including only reversible reactions in the circular parts of G-protein activation model makes the model more thermodynamically plausible. Moreover, we do not assume that the proteins in the cascade are in unlimited supply, and the equations of the model completely take into account "depletion" of proteins by excess of their binding counterparts. The only exception is GTP and GDP that are assumed to be in unlimited supply ("free ligand approximation", e.g. as is done for agonist in standard descriptions of agonist-receptor interactions).

Combining G-protein cycle model with GIRK1/2 gating model successfully reproduced the experimental observations. In particular, simulation of M2R*wt* expression experiment demonstrated similar decremental τ_{act} dependence on receptor density (**Figure 4**), a feature that was subsequently nearly abolished when modeling the M2R-Gα tandem activation process (**Figure 5**). These findings strengthen the notion that, in *Xenopus leaves* oocytes, M2R and G-proteins are not in "preformed complex", rather interact reversibly.

Channel Activation Models

The process that leads to GIRK opening following the binding of Gβγ is still unclear (Glaaser and Slesinger, 2017). Currently there are three detailed GIRK gating models developed chronologically by Kurachi group (Hosoya et al., 1996; Murakami et al., 2010; Murakami et al., 2013), our group (Yakubovich et al., 2005; Yakubovich et al., 2015) and MacKinnon's group (Touhara et al., 2016; Wang et al., 2016; Touhara and MacKinnon, 2018). The model proposed by Kurachi's group is based on Monod-Wyman-Changeux allosteric model of GIRK activation and formulates two binding states of Gβγ for each channel subunit. To complete the model, the authors used sub-nanomolar affinity for the GIRK-Gβγ interaction. The model developed by MacKinnon's group includes a detailed binding reaction of Gβγ to GIRK2 and GIRK1/4 and is based on elegant experiments with purified GIRK2 and Gβγ incorporated into bilayer membranes. In their work, they suggest that Gβγ binding is cooperative and that only channels occupied by four Gβγ undergo the closed-open transition (Wang et al., 2016). The model presented in the current work is based on sequential binding of Gβγ molecules to GIRK1/2 with graded contribution of each Gβγ-occupied state to open probability. Notably, this is based on ample experiments using the homologous heterotetrameric GIRK1/4 (Ivanova-Nikolova and Breitwieser, 1997; Ivanova-Nikolova et al., 1998; Sadja et al., 2002). Considering the different affinity values, reported in the literature, for GIRK-Gβγ interaction (see below), we derived the K_D values of this interaction from

analyzing the available crystal structure of GIRK2-Gβγ (Whorton and MacKinnon, 2013) and the docking model of GIRK1-Gβγ (Mahajan et al., 2013). Notably, both estimates rendered K_D values (100-200 nM) on par with those measured in biochemical experiments, 100-800 nM (Krapivinsky et al., 1995; Doupnik et al., 1996). Furthermore, our model of channel activation, combined with the G protein cycle model, reliably reproduced the amplitudes of GIRK1/2 activations when we used the surface densities of the channel, GPCR and G-protein directly measured under physiological conditions. We note that, with an appropriate adjustment for the oocyte expression system, the cooperative gating model of Touhara and MacKinnon (2018) also reproduced the experimental data reported here, in terms of GIRK1/2 currents, τ_{act} and the dependence of τ_{act} on M2R density (**Figure 6**). Interestingly, simulations done with the original parameters of the G-protein cycle model of Touhara et al. initially yielded a relatively shallow dependence of τ_{act} on M2R density, despite the fact that it is a collision coupling-type model. Analysis of this discrepancy lead us to the finding that τ_{act} dependence on receptor density even in "collision-coupling model" can be masked by a rapid rate of GTP hydrolysis, as can be obtained when RGS proteins are present (**Figure 6**).

A more consistent discrepancy of this model's estimate with our estimates is related to estimations of the number of Gβγ and Gα molecules required for channel activation. The endogenous levels of Gβγ in oocyte's plasma membrane is in the range of 20-40 molecules/μm^2, and is further increased to ~80 molecules/μm^2 (Yakubovich et al., 2015) upon overexpression of GIRK1/2 that recruits additional Gβγ to the plasma membrane (Rishal et al., 2005; Kahanovitch et al., 2014). Calculations with the Touhara et al. model showed that a minimum of 7 free Gβγ molecules need to be available at any time to account for the basal, GPCR-independent GIRK1/2 activity; at least 9 Gβγ and 2 Gα are needed to account for the observed I_{total} (I_{basal}+I_{evoked}) (**Figure S3**). For 21 GIRK1/2 channel/μm^2 (as observed after injection of 1 ng RNA of each subunit; (Yakubovich et al., 2015)), ~75 Gβγ molecules per m^2 are required to attain the total GIRK1/2 current according to our model, but ~180 Gβγ molecules per m^2 are needed with the cooperative gating model. The differences in Gβγ estimates stem mainly from the distinct GIRK-Gβγ affinity estimates used: 60 μM for the first Gβγ bound, with progressively improved affinity for each following Gβγ in Touhara and MacKinnon (2018), vs. ~0.15 μM in our model (**Table 1**). An even greater discrepancy may be expected if one uses the K_D of ~300 μM for GIRK2-first Gβγ interaction, as estimated experimentally in lipid bilayer in the presence of Na^+ (the natural condition in a living cell's cytosol) (Wang et al., 2016). Touhara and MacKinnon (2018) also note that, with such low affinity of interaction between GIRK and Gβγ, Gβγ surface densities needed for GIRK activation should be much higher than the physiological range. This leads them to propose that the GPCRs, G-proteins and GIRK channels interact in hot spots (Sungkaworn et al., 2017), where all components of the cascade are highly concentrated. Another possible explanation is that the actual affinity of GIRK-Gβγ interaction is higher than 200-300 μM K_D despite the measurements in lipid bilayer experiments (Wang et al., 2016) or in solution by nuclear magnetic resonance (Yokogawa et al., 2011). Notably, these studies employed a mutant Gγ lacking lipid modification (geranylgeranylation, in the case of $G\gamma_2$) and it is established that lipid modification of Gγ is an important determinant of high-affinity interaction between Gβγ and its binding partners such as Gα and phosducin (Myung et al., 1999; Lukov et al., 2004). Further study is needed to better determine the affinity of GIRK-Gβγ interactions in living cells.

Collision-Coupling Versus Preformed Complex

There is a longstanding debate regarding the existence, or lack, of diffusion-dependent steps in the GPCR-G-protein cycle. A large body of data suggests pre-formed (or dynamic) complexes between these proteins. For instance, measurement of diffusion coefficients of GPCRs demonstrate non-homogeneity, pointing to partial restriction of diffusion and possible organization of GPCRs in "islands" (Daumas et al., 2003; Suzuki et al., 2005; Baker et al., 2007). Similar restriction in lateral mobility is noted for G protein (Kwon et al., 1994). These observations are supported by studies showing that immobilized GPCRs can activate G-protein molecules with the same rate as mobile GPCRs (Lober et al., 2006). Going downstream in the cascade, the dissociation of Gα from Gβγ during the activation process also remains questioned. Whereas the dogma states full dissociation and diffusion of the latter, it has been shown that some Gα and Gβγ may not undergo dissociation, rather undergo spatial rearrangement after activation (Bunemann et al., 2003; Lambert, 2008). Onwards, complexes between G-protein and effectors, such as GIRK, have been noted (Robitaille et al., 2009; Zylbergold et al., 2010) as well as even larger supramolecular complexes consisting of GPCRs, G-proteins and modulating molecules, such as RGS, have been demonstrated (Lavine et al., 2002; Doupnik, 2008).Despite this body of work, pure collision coupling has also been demonstrated in many other cases (see introduction). Notably, the distinction between the two different modes is not trivial. In the current study, we elaborate our protocol using "titration" of proteins densities at the membrane, specifically those of the GPCR (Vorobiov et al., 2000) and show that it allows to quantitatively distinguish between the modes of GPCR-G protein coupling.

We compared the kinetic properties of two different settings of M2R-G-protein interaction. The first consists of M2R-Gα fusion protein; a one-to-one relationship between the GPCR and Gα is enforced, giving rise to a *bona fide* "preformed complex". Notably, in the scenario, we also assume that the complex necessarily includes $G\alpha_{GDP}$-Gβγ (in view of their very high nanomolar affinity), resulting in a full GPCR-G protein "preformed" complex. The second setting involves independent, untethered proteins. These two scenarios reveal that, whereas the kinetics of activation of GIRK by M2R*wt* are highly dependent on the receptor density, those of M2R-Gα fusion are not. This clear distinction strengthens the idea that, at least in *Xenopus* oocytes, M2R*wt* can indeed diffuse in the plasma membrane to activate several G-protein molecules (and GIRK subsequently). This conclusion is supported by studies, specifically conducted in *Xenopus* oocytes, demonstrating that, M2Rs and G-proteins are

not permanently co-localized and diffuse unrestrictedly in the plasma membrane (Hein and Bunemann, 2009).

In summary, the current concept of GPCR-G-protein effector signaling may be schematically presented as three possible, and not mutually exclusive, paradigms. The first, the preformed complex model, is expected to follow first order kinetics, in which the rate of activation is concentration-independent. In the second, the catalytic collision coupling model, the rate of activation is anticipated to be highly concentration-dependent, at least for diffusion-limited cases. Of note, the dependence of activation kinetics on receptor density might also be influenced by G-protein inactivation rate. Indeed, we demonstrate this by employing the simulation of Touhara et al. with the slower GDP hydrolysis rate (**Figure 6**). The third, is a mixture of the two. Importantly, the relationship of activation rate and concentration of the reactants is not trivial and is formulated, in most cases, as differential rate laws rather than as integrated rate law utilized for first order kinetic processes (useful for preformed complexes). It was previously shown that coupling reaction rate constant under diffusion limited conditions is equal to diffusion transport constant (Lauffenburger and Linderman, 1996) and is therefore expected to be dependent on receptor density (Mahama and Linderman, 1994; Shea et al., 1997). Together, the dependence of GIRK's activation rate on the density of M2R most likely originates from this phenomenon as a result of collision coupling of GPCR and G-protein. The recently proposed "hot spot" interaction model of GPCR-G-protein activation (Suzuki et al., 2005; Sungkaworn et al., 2017) represents a particular case of collision coupling model (but not preformed complexes) and elegantly describes cases in which there is relatively low affinity between the reactants, because restrictions of molecules within a tight hot spot is expected to robustly increase their effective concentration. Further studies based on stochastic analysis of GPCR-G-protein-GIRK system and measurement of GIRK-Gβγ affinity will deepen our understanding of the above described phenomena.

DATA AVAILABILITY STATEMENT

The raw data supporting the conclusions of this article will be made available by the authors, without undue reservation.

ETHICS STATEMENT

The animal study was reviewed and approved by Tel Aviv University Institutional Animal Care and Use Committee (permits M-08-081 and M-13-002).

AUTHOR CONTRIBUTIONS

SB, EA, RH-J, UK—electrophysiological and imaging experiments. DY, HP—generation of the model. ND, SB, DY—planning of the study. DY, ND, SB—writing the first draft of the manuscript. All authors contributed to the article and approved the submitted version.

FUNDING

This work was supported by the Israel Science Foundation (N.D.- grant #1282/18, and S.B.- grant #1096/17) and the Mauerberg Cathedra for Neuropharmacology (N.D.).

SUPPLEMENTARY MATERIAL

The Supplementary Material for this article can be found online at: https://www.frontiersin.org/articles/10.3389/fphar.2020.01216/full#supplementary-material

SUPPLEMENTAL FIGURE S1 | Kinetic measurements of time course of AMPA-R activation. **(A)** –configuration of the experimental chamber used for fast perfusion experiments. **(B)**– a representative record (black dots) of current evoked by 1 mM glutamate. The red dots represent mono-exponential fit of the activation time course of the current (τ_{act}=49.5 s).

SUPPLEMENTAL FIGURE S2 | Linear relationship between Gβγ-activated YFP-GIRK1/GIRK2 current and total surface density is observed in the range 0-1 ng of YFP-GIRK1 RNA. **(A)** – representative confocal images of oocytes expressing YFP-GIRK1/GIRK2. Channels were expressed by injecting the indicated doses of RNA of YFP-GIRK1 and GIRK2 (1:1) and activated by coexpression of 5 ng Gβ and 1 ng Gγ RNA. **(B)** – correlation between total GIRK surface density and the Gβγ-dependent GIRK current, $I_{\beta\gamma}$. $I_{\beta\gamma}$ is the total agonist-independent current in Gβγ-expressing oocytes. It was measured in 24 mM K^+ solution by subtracting the non-GIRK currents remaining after inhibition of >95% GIRK activity by 5 mM Ba^{2+} (Rubinstein et al., 2007). Total surface density is reflected in YFP fluorescence levels, functional channel density is proportional to $I_{\beta\gamma}$. Correlation between $I_{\beta\gamma}$ and fluorescence is linear for RNA doses of YFP-GIRK1/GIRK2 up to 1 ng/oocyte of each subunit. n = 6-12 for each point.

SUPPLEMENTAL FIGURE S3 | Estimation of Gβγ and Gα densities for simulation with cooperative gating model. **(A)** – I_{basal} currents rendered by different pairs of Gβγ and Gα densities selected for simulation. **(B)** – I_{total} currents rendered by different pairs of Gβγ and Gα densities selected for simulation.Red bars indicate Gβγ and Gα densities used for calculations in **Figures 6A, B**. Blue bars indicate Gβγ and Gα densities used for calculations in **Figures 6C, D**. All calculations except the 9:2 Gβγ/Gα pair (blue bar) have been made for the condition of fast hydrolysis of GTP, $k_{hydrolysis}$=2 s^{-1}. The 16:9 Gβγ/Gα pair was the lowest dose of G protein subunits per channel that reproduced I_{total} under this condition. Lower doses of Gβγ/Gα produced lower I_{total}. The 9:2 Gβγ/Gα pair was the lowest G protein subunits combination that reproduced I_{total} under the condition of low GTP hydrolysis rate ($k_{hydrolysis}$=0.02 s^{-1}).

REFERENCES

Alsallaq, R., and Zhou, H. X. (2008). Electrostatic rate enhancement and transient complex of protein-protein association. *Proteins* 71, 320–335. doi: 10.1002/prot.21679

Arshavsky, V. Y., Lamb, T. D., and Pugh, E. N. Jr. (2002). G proteins and phototransduction. *Annu. Rev. Physiol.* 64, 153–187. doi: 10.1146/annurev.physiol.64.082701.102229

Baker, A., Sauliere, A., Dumas, F., Millot, C., Mazeres, S., Lopez, A., et al. (2007). Functional membrane diffusion of G-protein coupled receptors. *Eur. Biophys. J.* 36, 849–860. doi: 10.1007/s00249-007-0214-7

Ben-Chaim, Y., Tour, O., Dascal, N., Parnas, I., and Parnas, H. (2003). The M2 muscarinic G-protein-coupled receptor is voltage sensitive. *J. Biol. Chem.* 278, 22482–22491. doi: 10.1074/jbc.M301146200

Bender, K., Wellner-Kienitz, M. C., Meyer, T., and Pott, L. (1998). Activation of muscarinic K^+ current by b-adrenergic receptors in cultured atrial myocytes

transfected with b1 subunit of heterotrimeric G proteins. *FEBS Lett.* 439, 115–120. doi: 10.1016/S0014-5793(98)01350-7

Berlin, S., Keren-Raifman, T., Castel, R., Rubinstein, M., Dessauer, C. W., Ivanina, T., et al. (2010). $G\alpha_i$ and $G\beta\gamma$ jointly regulate the conformations of a $G\beta\gamma$ effector, the neuronal G protein-activated K^+ channel (GIRK). *J. Biol. Chem.* 285, 6179–6185. doi: 10.1074/jbc.M109.085944

Berlin, S., Tsemakhovich, V. A., Castel, R., Ivanina, T., Dessauer, C. W., Keren-Raifman, T., et al. (2011). Two distinct aspects of coupling between Gαi protein and G protein-activated K^+ channel (GIRK) revealed by fluorescently labeled $G\alpha_{i3}$ protein subunits. *J. Biol. Chem.* 286, 33223–33235. doi: 10.1074/jbc.M111.271056

Breitwieser, G. E., and Szabo, G. (1988). Mechanism of Muscarinic Receptor Induced K+ Channel Activation as Revealed by Hydrolysis-Resistant Gtp Analogs. *J. Gen. Physiol.* 91, 469–493. doi: 10.1085/jgp.91.4.469

Bunemann, M., Frank, M., and Lohse, M. J. (2003). Gi protein activation in intact cells involves subunit rearrangement rather than dissociation. *Proc. Natl. Acad. Sci. U. S. A.* 100, 16077–16082. doi: 10.1073/pnas.2536719100

Clapham, D. E., and Neer, E. J. (1997). G protein βγ subunits. *Annu. Rev. Pharmacol. Toxicol.* 37, 167–203. doi: 10.1146/annurev.pharmtox.37.1.167

Colquhoun, D., Dowsland, K. A., Beato, M., and Plested, A. J. (2004). How to impose microscopic reversibility in complex reaction mechanisms. *Biophys. J.* 86, 3510–3518. doi: 10.1529/biophysj.103.038679

Corey, S., Krapivinsky, G., Krapivinsky, L., and Clapham, D. E. (1998). Number and stoichiometry of subunits in the native atrial G-protein-gated K+ channel, IKACh. *J. Biol. Chem.* 273, 5271–5278. doi: 10.1074/jbc.273.9.5271

Dascal, N., and Kahanovitch, U. (2015). The roles of Gβγ and Gα in gating and regulation of GIRK channels. *Int. Rev. Neurobiol.* 123, 27–85. doi: 10.1016/bs.irn.2015.06.001

Dascal, N., and Lotan, I. (1992). "Expression of exogenous ion channels and neurotransmitter receptors in RNA-injected Xenopus oocytes," in *Protocols in Molecular Neurobiology*. Eds. A. Longstaff and P. Revest (Totowa, NJ: Humana Press), 205–225.

Dascal, N. (1987). The use of Xenopus oocytes for the study of ion channels. *CRC Crit. Rev. Biochem.* 22, 317–387. doi: 10.3109/10409238709086960

Dascal, N. (1997). Signalling *via the* G protein-activated K^+ channels. *Cell Signal* 9, 551–573. doi: 10.1016/S0898-6568(97)00095-8

Daumas, F., Destainville, N., Millot, C., Lopez, A., Dean, D., and Salome, L. (2003). Confined diffusion without fences of a g-protein-coupled receptor as revealed by single particle tracking. *Biophys. J.* 84, 356–366. doi: 10.1016/S0006-3495(03)74856-5

De Lean, A., Stadel, J. M., and Lefkowitz, R. J. (1980). A ternary complex model explains the agonist-specific binding properties of the adenylate cyclase-coupled β-adrenergic receptor. *J. Biol. Chem.* 255, 7108–7117.

Doupnik, C. A., Dessauer, C. W., Slepak, V. Z., Gilman, A. G., Davidson, N., and Lester, H. A. (1996). Time resolved kinetics of direct Gb_1g_2 interactions with the carboxyl terminus of Kir3.4 inward rectifier K^+ channel subunits. *Neuropharmacology* 35, 923–931. doi: 10.1016/0028-3908(96)00125-6

Doupnik, C. A. (2008). GPCR-Kir channel signaling complexes: defining rules of engagement. *J. Recept Signal Transduct. Res.* 28, 83–91. doi: 10.1080/10799890801941970

Doupnik, C. A. (2015). RGS redundancy and implications in GPCR-GIRK signaling. *Int. Rev. Neurobiol.* 123, 87–116. doi: 10.1016/bs.irn.2015.05.010

Dupre, D. J., Baragli, A., Rebois, R. V., Ethier, N., and Hebert, T. E. (2007). Signalling complexes associated with adenylyl cyclase II are assembled during their biosynthesis. *Cell Signal* 19, 481–489. doi: 10.1016/j.cellsig.2006.07.021

Dupre, D. J., Robitaille, M., Rebois, R. V., and Hebert, T. E. (2009). The role of Gβγ subunits in the organization, assembly, and function of GPCR signaling complexes. *Annu. Rev. Pharmacol. Toxicol.* 49, 31–56. doi: 10.1146/annurev-pharmtox-061008-103038

Falkenburger, B. H., Jensen, J. B., and Hille, B. (2010). Kinetics of M1 muscarinic receptor and G protein signaling to phospholipase C in living cells. *J. Gen. Physiol.* 135, 81–97. doi: 10.1085/jgp.200910344

Fowler, C. E., Aryal, P., Suen, K. F., and Slesinger, P. A. (2006). Evidence for association of $GABA_B$ receptors with Kir3 channels and RGS4 proteins. *J. Physiol. (Lond)* 580, 51–65. doi: 10.1113/jphysiol.2006.123216

Glaaser, I. W., and Slesinger, P. A. (2017). Dual activation of neuronal G protein-gated inwardly rectifying potassium (GIRK) channels by cholesterol and alcohol. *Sci. Rep.* 7, 4592. doi: 10.1038/s41598-017-04681-x

Grosskreutz, J., Zoerner, A., Schlesinger, F., Krampfl, K., Dengler, R., and Bufler, J. (2003). Kinetic properties of human AMPA-type glutamate receptors expressed in HEK293 cells. *Eur. J. Neurosci.* 17, 1173–1178. doi: 10.1046/j.1460-9568.2003.02531.x

Haga, K., Haga, T., and Ichiyama, A. (1986). Reconstitution of the muscarinic acetylcholine receptor. Guanine nucleotide-sensitive high affinity binding of agonists to purified muscarinic receptors reconstituted with GTP-binding proteins (Gi and Go). *J. Biol. Chem.* 261, 10133–10140.

Halvorsen, S. W., and Nathanson, N. M. (1981). In vivo regulation of muscarinic acetylcholine receptor number and function in embryonic chick heart. *J. Biol. Chem.* 256, 7941–7948.

Hein, P., and Bunemann, M. (2009). Coupling mode of receptors and G proteins. *Naunyn Schmiedebergs Arch. Pharmacol.* 379, 435–443. doi: 10.1007/s00210-008-0383-7

Hein, P., Frank, M., Hoffmann, C., Lohse, M. J., and Bunemann, M. (2005). Dynamics of receptor/G protein coupling in living cells. *EMBO J.* 24, 4106–4114. doi: 10.1038/sj.emboj.7600870

Hibino, H., Inanobe, A., Furutani, K., Murakami, S., Findlay, I., and Kurachi, Y. (2010). Inwardly rectifying potassium channels: their structure, function, and physiological roles. *Physiol. Rev.* 90, 291–366. doi: 10.1152/physrev.00021.2009

Higashijima, T., Ferguson, K. M., Sternweis, P. C., Smigel, M. D., and Gilman, A. G. (1987). Effects of Mg2+ and the beta gamma-subunit complex on the interactions of guanine nucleotides with G proteins. *J. Biol. Chem.* 262, 762–766.

Hille, B., Dickson, E., Kruse, M., and Falkenburger, B. (2014). Dynamic metabolic control of an ion channel. *Prog. Mol. Biol. Transl. Sci.* 123, 219–247. doi: 10.1016/B978-0-12-397897-4.00008-5

Hille, B. (1992). G protein-coupled mechanisms and nervous signaling. *Neuron* 9, 187–195. doi: 10.1016/0896-6273(92)90158-A

Hille, B. (2002). *Ion Channels of Excitable Membranes* (Sunderland: Sinauer).

Hollins, B., Kuravi, S., Digby, G. J., and Lambert, N. A. (2009). The c-terminus of GRK3 indicates rapid dissociation of G protein heterotrimers. *Cell Signal* 21, 1015–1021. doi: 10.1016/j.cellsig.2009.02.017

Hosoya, Y., Yamada, M., Ito, H., and Kurachi, Y. (1996). A functional model for G protein activation of the muscarinic K^+ channel in guinea pig atrial myocytes. Spectral analysis of the effect of GTP on single-channel kinetics. *J. Gen. Physiol.* 108, 485–495. doi: 10.1085/jgp.108.6.485

Huang, C. L., Slesinger, P. A., Casey, P. J., Jan, Y. N., and Jan, L. Y. (1995). Evidence that direct binding of Gbg to the GIRK1 G protein- gated inwardly rectifying K^+ channel is important for channel activation. *Neuron* 15, 1133–1143. doi: 10.1016/0896-6273(95)90101-9

Ilyaskina, O. S., Lemoine, H., and Bunemann, M. (2018). Lifetime of muscarinic receptor-G-protein complexes determines coupling efficiency and G-protein subtype selectivity. *Proc. Natl. Acad. Sci. U. S. A.* 115, 5016–5021. doi: 10.1073/pnas.1715751115

Ivanova-Nikolova, T. T., and Breitwieser, G. E. (1997). Effector contributions to Gbg-mediated signaling as revealed by muscarinic potassium channel gating. *J. Gen. Physiol.* 109, 245–253. doi: 10.1085/jgp.109.2.245

Ivanova-Nikolova, T. T., Nikolov, E. N., Hansen, C., and Robishaw, J. D. (1998). Muscarinic K^+ channel in the heart. Modal regulation by G protein bg subunits. *J. Gen. Physiol.* 112, 199–210. doi: 10.1085/jgp.112.2.199

Jaen, C., and Doupnik, C. A. (2006). RGS3s and RGS4 differentially associate with GPCR-Kir3 channel signaling complexes revealing 2 modes of RGS modulation: precoupling and collision-coupling. *J. Biol. Chem.* 281, 34549–34560. doi: 10.1074/jbc.M603177200

Kahanovitch, U., Tsemakhovich, V., Berlin, S., Rubinstein, M., Styr, B., Castel, R., et al. (2014). Recruitment of Gβγ controls the basal activity of G-protein coupled inwardly rectifying potassium (GIRK) channels: crucial role of distal C terminus of GIRK1. *J. Physiol.* 592, 5373–5390. doi: 10.1113/jphysiol.2014.283218

Kahanovitch, U., Berlin, S., and Dascal, N. (2017). Collision coupling in the $GABA_B$ receptor - G protein - GIRK signaling cascade. *FEBS Lett.* 591, 2816–2825. doi: 10.1002/1873-3468.12756

Kano, H., Toyama, Y., Imai, S., Iwahashi, Y., Mase, Y., Yokogawa, M., et al. (2019). Structural mechanism underlying G protein family-specific regulation of G protein-gated inwardly rectifying potassium channel. *Nat. Commun.* 10, 2008. doi: 10.1038/s41467-019-10038-x

Kastritis, P. L., Moal, I. H., Hwang, H., Weng, Z., Bates, P. A., Bonvin, A. M., et al. (2011). A structure-based benchmark for protein-protein binding affinity. *Protein Sci.* 20, 482–491. doi: 10.1002/pro.580

Keren-Raifman, T., Bera, A. K., Zveig, D., Peleg, S., Witherow, D. S., Slepak, V. Z., et al. (2001). Expression levels of RGS7 and RGS4 proteins determine the mode of regulation of the G protein-activated K^+ channel and control regulation of RGS7 by Gb5. *FEBS Lett.* 492, 20–28. doi: 10.1016/S0014-5793(01)02220-7

Krapivinsky, G., Krapivinsky, L., Wickman, K., and Clapham, D. E. (1995). Gbg binds directly to the G protein-gated K^+ channel, I_{KACh}. *J. Biol. Chem.* 270, 29059–29062. doi: 10.1074/jbc.270.49.29059

Kwon, G., Axelrod, D., and Neubig, R. R. (1994). Lateral mobility of tetramethylrhodamine (TMR) labelled G protein α and β γ subunits in NG 108-15 cells. *Cell Signal* 6, 663–679. doi: 10.1016/0898-6568(94)90049-3

Lamb, T. D., and Pugh, E. N.Jr. (1992). G-protein cascades: gain and kinetics. *Trends Neurosci.* 15, 291–298. doi: 10.1016/0166-2236(92)90079-N

Lambert, N. A. (2008). Dissociation of heterotrimeric g proteins in cells. *Sci. Signal* 1, re5. doi: 10.1126/scisignal.125re5

Lauffenburger, D., and Linderman, J. J. (1996). *Receptors: Models for Binding, Trafficking, and Signaling* (New York: Oxford University Press).

Lavine, N., Ethier, N., Oak, J. N., Pei, L., Liu, F., Trieu, P., et al. (2002). G protein-coupled receptors form stable complexes with inwardly rectifying potassium channels and adenylyl cyclase. *J. Biol. Chem.* 277, 46010–46019. doi: 10.1074/jbc.M205035200

Lechleiter, J., Hellmiss, R., Duerson, K., Ennulat, D., David, N., Clapham, D., et al. (1990). Distinct sequence elements control the specificity of G protein activation by muscarinic acetylcholine receptor subtypes. *EMBO J.* 9, 4381–4390. doi: 10.1002/j.1460-2075.1990.tb07888.x

Lim, N. F., Dascal, N., Labarca, C., Davidson, N., and Lester, H. A. (1995). A G protein-gated K channel is activated *via* b2-adrenergic receptors and Gbg subunits in *Xenopus* oocytes. *J. Gen. Physiol.* 105, 421–439. doi: 10.1085/jgp.105.3.421

Liman, E. R., Tytgat, J., and Hess, P. (1992). Subunit stoichiometry of a mammalian K^+ channel determined by construction of multimeric cDNAs. *Neuron* 9, 861–871. doi: 10.1016/0896-6273(92)90239-A

Lober, R. M., Pereira, M. A., and Lambert, N. A. (2006). Rapid activation of inwardly rectifying potassium channels by immobile G-protein-coupled receptors. *J. Neurosci.* 26, 12602–12608. doi: 10.1523/JNEUROSCI.4020-06.2006

Logothetis, D. E., Kurachi, Y., Galper, J., Neer, E. J., and Clapham, D. E. (1987). The βγ subunits of GTP-binding proteins activate the muscarinic K+ channel in heart. *Nature* 325, 321–326. doi: 10.1038/325321a0

Lohse, M. J., Hein, P., Hoffmann, C., Nikolaev, V. O., Vilardaga, J. P., and Bunemann, M. (2008). Kinetics of G-protein-coupled receptor signals in intact cells. *Br. J. Pharmacol.* 153 Suppl 1, S125–S132. doi: 10.1038/sj.bjp.0707656

Lopatin, A. N., Makhina, E. N., and Nichols, C. G. (1998). A novel crystallization method for visualizing the membrane localization of potassium channels. *Biophys. J.* 74, 2159–2170. doi: 10.1016/S0006-3495(98)77925-1

Lukov, G. L., Myung, C. S., Mcintire, W. E., Shao, J., Zimmerman, S. S., Garrison, J. C., et al. (2004). Role of the isoprenyl pocket of the G protein β γ subunit complex in the binding of phosducin and phosducin-like protein. *Biochemistry* 43, 5651–5660. doi: 10.1021/bi035903u

Luscher, C., and Slesinger, P. A. (2010). Emerging roles for G protein-gated inwardly rectifying potassium (GIRK) channels in health and disease. *Nat. Rev. Neurosci.* 11, 301–315. doi: 10.1038/nrn2834

Machaca, K., and Hartzell, H. C. (1998). Asymmetrical distribution of Ca-activated Cl channels in Xenopus oocytes. *Biophys. J.* 74, 1286–1295. doi: 10.1016/S0006-3495(98)77842-7

Maeda, S., Qu, Q., Robertson, M. J., Skiniotis, G., and Kobilka, B. K. (2019). Structures of the M1 and M2 muscarinic acetylcholine receptor/G-protein complexes. *Science* 364, 552–557. doi: 10.1126/science.aaw5188

Maguire, M. E., Van Arsdale, P. M., and Gilman, A. G. (1976). An agonist-specific effect of guanine nucleotides on binding to the β-adrenergic receptor. *Mol. Pharmacol.* 12, 335–339.

Mahajan, R., Ha, J., Zhang, M., Kawano, T., Kozasa, T., and Logothetis, D. E. (2013). A computational model predicts that Gβγ acts at a cleft between channel subunits to activate GIRK1 channels. *Sci. Signal* 6, ra69. doi: 10.1126/scisignal.2004075

Mahama, P. A., and Linderman, J. J. (1994). A Monte Carlo study of the dynamics of G-protein activation. *Biophys. J.* 67, 1345–1357. doi: 10.1016/S0006-3495(94)80606-X

Mayfield, J., Blednov, Y. A., and Harris, R. A. (2015). Behavioral and genetic evidence for GIRK channels in the CNS: role in physiology, pathophysiology, and drug addiction. *Int. Rev. Neurobiol.* 123, 279–313. doi: 10.1016/bs.irn.2015.05.016

Murakami, S., Suzuki, S., Ishii, M., Inanobe, A., and Kurachi, Y. (2010). Cellular modelling: experiments and simulation to develop a physiological model of G-protein control of muscarinic K^+ channels in mammalian atrial cells. *Philos. Trans. A Math Phys. Eng. Sci.* 368, 2983–3000. doi: 10.1098/rsta.2010.0093

Murakami, S., Inanobe, A., and Kurachi, Y. (2013). Short-term desensitization of muscarinic K^+ current in the heart. *Biophys. J.* 105, 1515–1525. doi: 10.1016/j.bpj.2013.08.009

Myung, C. S., Yasuda, H., Liu, W. W., Harden, T. K., and Garrison, J. C. (1999). Role of isoprenoid lipids on the heterotrimeric G protein γ subunit in determining effector activation. *J. Biol. Chem.* 274, 16595–16603. doi: 10.1074/jbc.274.23.16595

Nagi, K., and Pineyro, G. (2014). Kir3 channel signaling complexes: focus on opioid receptor signaling. *Front. Cell Neurosci.* 8, 186. doi: 10.3389/fncel.2014.00186

Pott, L. (1979). On the time course of the acetylcholine-induced hyperpolarization in quiescent guinea-pig atria. *Pflugers Arch.* 380, 71–77. doi: 10.1007/BF00582615

Qin, S., Pang, X., and Zhou, H. X. (2011). Automated prediction of protein association rate constants. *Structure* 19, 1744–1751. doi: 10.1016/j.str.2011.10.015

Rebois, R. V., Robitaille, M., Gales, C., Dupre, D. J., Baragli, A., Trieu, P., et al. (2006). Heterotrimeric G proteins form stable complexes with adenylyl cyclase and Kir3.1 channels in living cells. *J. Cell Sci.* 119, 2807–2818. doi: 10.1242/jcs.03021

Reuveny, E., Slesinger, P. A., Inglese, J., Morales, J. M., Iniguez-Lluhi, J. A., Lefkowitz, R. J., et al. (1994). Activation of the cloned muscarinic potassium channel by G protein bg subunits. *Nature* 370, 143–146. doi: 10.1038/370143a0

Richter, J. D., and Smith, L. D. (1981). Differential capacity for translation and lack of competition between mRNAs that segregate to free and membrane-bound polysomes. *Cell* 27, 183–191. doi: 10.1016/0092-8674(81)90372-X

Rifkin, R. A., Moss, S. J., and Slesinger, P. A. (2017). G protein-gated potassium channels: A link to drug addiction. *Trends Pharmacol. Sci.* 38, 378–392. doi: 10.1016/j.tips.2017.01.007

Rishal, I., Porozov, Y., Yakubovich, D., Varon, D., and Dascal, N. (2005). Gβγ-dependent and Gβγ-independent basal activity of G protein-activated K^+ channels. *J. Biol. Chem.* 280, 16685–16694. doi: 10.1074/jbc.M412196200

Riven, I., Iwanir, S., and Reuveny, E. (2006). GIRK channel activation involves a local rearrangement of a preformed G protein channel complex. *Neuron* 51, 561–573. doi: 10.1016/j.neuron.2006.08.017

Robinson, K. R. (1979). Electrical currents through full-grown and maturing Xenopus oocytes. *Proc. Natl. Acad. Sci. U. S. A.* 76, 837–841. doi: 10.1073/pnas.76.2.837

Robitaille, M., Ramakrishnan, N., Baragli, A., and Hebert, T. E. (2009). Intracellular trafficking and assembly of specific Kir3 channel/G protein complexes. *Cell Signal* 21, 488–501. doi: 10.1016/j.cellsig.2008.11.011

Ross, E. M. (2008). Coordinating speed and amplitude in G-protein signaling. *Curr. Biol.* 18, R777–R783. doi: 10.1016/j.cub.2008.11.032

Rubinstein, M., Peleg, S., Berlin, S., Brass, D., and Dascal, N. (2007). Ga_{i3} primes the G protein-activated K^+ channels for activation by coexpressed Gbg in intact *Xenopus* oocytes. *J. Physiol.* 581, 17–32. doi: 10.1113/jphysiol.2006.125864

Rubinstein, M., Peleg, S., Berlin, S., Brass, D., Keren-Raifman, T., Dessauer, C. W., et al. (2009). Divergent regulation of GIRK1 and GIRK2 subunits of the neuronal G protein gated K^+ channel by Ga_iGDP and Gbg. *J. Physiol.* 587, 3473–3491. doi: 10.1113/jphysiol.2009.173229

Rusinova, R., Mirshahi, T., and Logothetis, D. E. (2007). Specificity of Gβγ signaling to Kir3 channels depends on the helical domain of pertussis toxin-sensitive Galpha subunits. *J. Biol. Chem.* 282, 34019–34030. doi: 10.1074/jbc.M704928200

Sadja, R., Alagem, N., and Reuveny, E. (2002). Graded contribution of the Gbg binding domains to GIRK channel activation. *Proc. Natl. Acad. Sci. U. S. A.* 99, 10783–10788. doi: 10.1073/pnas.162346199

Sarvazyan, N. A., Remmers, A. E., and Neubig, R. R. (1998). Determinants of $G_{i1}a$ and bg binding. Measuring high affinity interactions in a lipid environment using flow cytometry. *J. Biol. Chem.* 273, 7934–7940. doi: 10.1074/jbc.273.14.7934

Sarvazyan, N. A., Lim, W. K., and Neubig, R. R. (2002). Fluorescence analysis of receptor-G protein interactions in cell membranes. *Biochemistry* 41, 12858–12867. doi: 10.1021/bi026212l

Schreiber, G., Henis, Y. I., and Sokolovsky, M. (1985). Rate constants of agonist binding to muscarinic receptors in rat brain medulla. Evaluation by competition kinetics. *J. Biol. Chem.* 260, 8795–8802.

Schreibmayer, W., Lester, H. A., and Dascal, N. (1994). Voltage clamping of *Xenopus laevis* oocytes utilizing agarose-cushion electrodes. *Pflugers Arch. Eur. J. Physiol.* 426, 453–458. doi: 10.1007/BF00388310

Shea, L., and Linderman, J. J. (1997). Mechanistic model of G-protein signal transduction. Determinants of efficacy and effect of precoupled receptors. *Biochem. Pharmacol.* 53, 519–530. doi: 10.1016/S0006-2952(96)00768-X

Shea, L. D., Omann, G. M., and Linderman, J. J. (1997). Calculation of diffusion-limited kinetics for the reactions in collision coupling and receptor cross-linking. *Biophys. J.* 73, 2949–2959. doi: 10.1016/S0006-3495(97)78323-1

Shea, L. D., Neubig, R. R., and Linderman, J. J. (2000). Timing is everything - The role of kinetics in G protein activation. *Life Sci.* 68, 647–658. doi: 10.1016/S0024-3205(00)00977-2

Silverman, S. K., Lester, H. A., and Dougherty, D. A. (1996). Subunit stoichiometry of a heteromultimeric G protein-coupled inward-rectifier K+ channel. *J. Biol. Chem.* 271, 30524–30528. doi: 10.1074/jbc.271.48.30524

Slesinger, P. A., Reuveny, E., Jan, Y. N., and Jan, L. Y. (1995). Identification of structural elements involved in G protein gating of the GIRK1 potassium channel. *Neuron* 15, 1145–1156. doi: 10.1016/0896-6273(95)90102-7

Sodickson, D. L., and Bean, B. P. (1996). $GABA_B$ receptor-activated inwardly rectifying potassium current in dissociated hippocampal CA3 neurons. *J. Neurosci.* 16, 6374–6385. doi: 10.1523/JNEUROSCI.16-20-06374.1996

Stern-Bach, Y., Russo, S., Neuman, M., and Rosenmund, C. (1998). A point mutation in the glutamate binding site blocks desensitization of AMPA receptors. *Neuron* 21, 907–918. doi: 10.1016/S0896-6273(00)80605-4

Sungkaworn, T., Jobin, M.-L., Burnecki, K., Weron, A., Lohse, M. J., and Calebiro, D. (2017). Single-molecule imaging reveals receptor–G protein interactions at cell surface hot spots. *Nature* 550, 543–547. doi: 10.1038/nature24264

Suzuki, K., Ritchie, K., Kajikawa, E., Fujiwara, T., and Kusumi, A. (2005). Rapid hop diffusion of a G-protein-coupled receptor in the plasma membrane as revealed by single-molecule techniques. *Biophys. J.* 88, 3659–3680. doi: 10.1529/biophysj.104.048538

Tabak, G., Keren-Raifman, T., Kahanovitch, U., and Dascal, N. (2019). Mutual action by Gγ and Gβ for optimal activation of GIRK channels in a channel subunit-specific manner. *Sci. Rep.* 9, 508. doi: 10.1038/s41598-018-36833-y

Tateyama, M., and Kubo, Y. (2018). Gi/o-coupled muscarinic receptors co-localize with GIRK channel for efficient channel activation. *PLoS One* 13, e0204447. doi: 10.1371/journal.pone.0204447

Thomsen, W. J., and Neubig, R. R. (1989). Rapid kinetics of α 2-adrenergic inhibition of adenylate cyclase. Evidence for a distal rate-limiting step. *Biochemistry* 28, 8778–8786. doi: 10.1021/bi00448a015

Thomsen, W. J., Jacquez, J. A., and Neubig, R. R. (1988). Inhibition of adenylate cyclase is mediated by the high affinity conformation of the α 2-adrenergic receptor. *Mol. Pharmacol.* 34, 814–822.

Tolkovsky, A. M., and Levitzki, A. (1981). Theories and predictions of models describing sequential interactions between the receptor, the GTP regulatory unit, and the catalytic unit of hormone dependent adenylate cyclases. *J. Cyclic Res.* 7, 139–150.

Tolkovsky, A. M., Braun, S., and Levitzki, A. (1982). Kinetics of Interaction between β-Receptors, Gtp Protein, and the Catalytic Unit of Turkey Erythrocyte Adenylate-Cyclase. *Proc. Natl. Acad. Sci. U. States America* 79, 213–217. doi: 10.1073/pnas.79.2.213

Touhara, K. K., and MacKinnon, R. (2018). Molecular basis of signaling specificity between GIRK channels and GPCRs. *eLife* 7, e42908. doi: 10.7554/eLife.42908

Touhara, K. K., Wang, W., and Mackinnon, R. (2016). The GIRK1 subunit potentiates G protein activation of cardiac GIRK1/4 hetero-tetramers. *Elife* 5, e15750. doi: 10.7554/eLife.15750

Traut, T. W. (1994). Physiological concentrations of purines and pyrimidines. *Mol. Cell Biochem.* 140, 1–22. doi: 10.1007/BF00928361

Turcotte, M., Tang, W., and Ross, E. M. (2008). Coordinate regulation of G protein signaling *via* dynamic interactions of receptor and GAP. *PLoS Comput. Biol.* 4, e1000148. doi: 10.1371/journal.pcbi.1000148

Voigt, N., Abu-Taha, I., Heijman, J., and Dobrev, D. (2014). Constitutive activity of the acetylcholine-activated potassium current $I_{K,ACh}$ in cardiomyocytes. *Adv. Pharmacol.* 70, 393–409. doi: 10.1016/B978-0-12-417197-8.00013-4

Vorobiov, D., Bera, A. K., Keren-Raifman, T., Barzilai, R., and Dascal, N. (2000). Coupling of the muscarinic m2 receptor to G protein-activated K^+ channels *via* Ga_z and a receptor-Ga_z fusion protein. Fusion between the receptor and Ga_z eliminates catalytic (collision) coupling. *J. Biol. Chem.* 275, 4166–4170. doi: 10.1074/jbc.275.6.4166

Wang, W., Touhara, K. K., Weir, K., Bean, B. P., and Mackinnon, R. (2016). Cooperative regulation by G proteins and Na^+ of neuronal GIRK2 K^+ channels. *Elife* 5, e15751. doi: 10.7554/eLife.15751

Weis, W. I., and Kobilka, B. K. (2018). The Molecular Basis of G Protein-Coupled Receptor Activation. *Annu. Rev. Biochem.* 87, 897–919. doi: 10.1146/annurev-biochem-060614-033910

Wellner-Kienitz, M. C., Bender, K., Meyer, T., Bunemann, M., and Pott, L. (2000). Overexpressed A1 adenosine receptors reduce activation of acetylcholine-sensitive K^+ current by native muscarinic M2 receptors in rat atrial myocytes. *Circ. Res.* 86, 643–648. doi: 10.1161/01.RES.86.6.643

West, R. E.Jr., Moss, J., Vaughan, M., Liu, T., and Liu, T. Y. (1985). Pertussis toxin-catalyzed ADP-ribosylation of transducin. Cysteine 347 is the ADP-ribose acceptor site. *J. Biol. Chem.* 260, 14428–14430.

Whorton, M. R., and MacKinnon, R. (2013). X-ray structure of the mammalian GIRK2-βγ G-protein complex. *Nature* 498, 190–197. doi: 10.1038/nature12241

Xue, L. C., Rodrigues, J. P., Kastritis, P. L., Bonvin, A. M., and Vangone, A. (2016). PRODIGY: a web server for predicting the binding affinity of protein-protein complexes. *Bioinformatics* 32, 3676–3678. doi: 10.1093/bioinformatics/btw514

Yakubovich, D., Rishal, I., and Dascal, N. (2005). Kinetic modeling of Na^+-induced, Gbg -dependent activation of G-protein-gated K^+ channels. *J. Mol. Neurosci.* 25, 7–20. doi: 10.1385/JMN:25:1:007

Yakubovich, D., Berlin, S., Kahanovitch, U., Rubinstein, M., Farhy-Tselnicker, I., Styr, B., et al. (2015). A quantitative model of the GIRK1/2 channel reveals that its basal and evoked activities are controlled by unequal stoichiometry of Gα and Gβγ. *PLoS Comput. Biol.* 11, e1004598. doi: 10.1371/journal.pcbi.1004598

Yokogawa, M., Osawa, M., Takeuchi, K., Mase, Y., and Shimada, I. (2011). NMR analyses of the Gβγ binding and conformational rearrangements of the cytoplasmic pore of G protein-activated inwardly rectifying potassium channel 1 (GIRK1). *J. Biol. Chem.* 286, 2215–2223. doi: 10.1074/jbc.M110.160754

Zacharias, D. A., Violin, J. D., Newton, A. C., and Tsien, R. Y. (2002). Partitioning of lipid-modified monomeric GFPs into membrane microdomains of live cells. *Science* 296, 913–916. doi: 10.1126/science.1068539

Zhong, H., Wade, S. M., Woolf, P. J., Linderman, J. J., Traynor, J. R., and Neubig, R. R. (2003). A spatial focusing model for G protein signals. Regulator of G protein signaling (RGS) protien-mediated kinetic scaffolding. *J. Biol. Chem.* 278, 7278–7284. doi: 10.1074/jbc.M208819200

Zylbergold, P., Ramakrishnan, N., and Hebert, T. (2010). The role of G proteins in assembly and function of Kir3 inwardly rectifying potassium channels. *Channels (Austin)* 4, 411–421. doi: 10.4161/chan.4.5.13327

Conflict of Interest: The authors declare that the research was conducted in the absence of any commercial or financial relationships that could be construed as a potential conflict of interest.

The handling editor declared a shared affiliation, though no other collaboration, with one of the authors HP.

Advantages of publishing in Frontiers

OPEN ACCESS
Articles are free to read for greatest visibility and readership

FAST PUBLICATION
Around 90 days from submission to decision

HIGH QUALITY PEER-REVIEW
Rigorous, collaborative, and constructive peer-review

TRANSPARENT PEER-REVIEW
Editors and reviewers acknowledged by name on published articles

Frontiers
Avenue du Tribunal-Fédéral 34
1005 Lausanne | Switzerland

Visit us: www.frontiersin.org
Contact us: frontiersin.org/about/contact

REPRODUCIBILITY OF RESEARCH
Support open data and methods to enhance research reproducibility

DIGITAL PUBLISHING
Articles designed for optimal readership across devices

FOLLOW US
@frontiersin

IMPACT METRICS
Advanced article metrics track visibility across digital media

EXTENSIVE PROMOTION
Marketing and promotion of impactful research

LOOP RESEARCH NETWORK
Our network increases your article's readership